OAK RIDGE NATIONAL LABORATORY LIBRARY
3 4456 0021546 1

CENTRAL RESEARCH LIBRARY
DOCUMENT COLLECTION

3

ORNL-4007
UC-41 – Health and Safety

HEALTH PHYSICS DIVISION
ANNUAL PROGRESS REPORT
FOR PERIOD ENDING JULY 31, 1966

CENTRAL RESEARCH LIBRARY
DOCUMENT COLLECTION
LIBRARY LOAN COPY
DO NOT TRANSFER TO ANOTHER PERSON
If you wish someone else to see this document, send in name with document and the library will arrange a loan.

OAK RIDGE NATIONAL LABORATORY
operated by
UNION CARBIDE CORPORATION
for the
U.S. ATOMIC ENERGY COMMISSION

Printed in USA. Price $7.00 . Available from the Clearinghouse for Federal Scientific and Technical Information, National Bureau of Standards, U.S. Department of Commerce, Springfield, Virginia 22151

LEGAL NOTICE

This report was prepared as an account of Government sponsored work. Neither the United States, nor the Commission, nor any person acting on behalf of the Commission:

A. Makes any warranty or representation, expressed or implied, with respect to the accuracy, completeness, or usefulness of the information contained in this report, or that the use of any information, apparatus, method, or process disclosed in this report may not infringe privately owned rights; or

B. Assumes any liabilities with respect to the use of, or for damages resulting from the use of any information, apparatus, method, or process disclosed in this report.

As used in the above, "person acting on behalf of the Commission" includes any employee or contractor of the Commission, or employee of such contractor, to the extent that such employee or contractor of the Commission, or employee of such contractor prepares, disseminates, or provides access to, any information pursuant to his employment or contract with the Commission, or his employment with such contractor.

ORNL-4007
UC-41 – Health and Safety

Contract No. W-7405-eng-26

HEALTH PHYSICS DIVISION ANNUAL PROGRESS REPORT

For Period Ending July 31, 1966

K. Z. Morgan, Director
W. S. Snyder, Assistant Director
E. G. Struxness, Assistant Director

OCTOBER 1966

OAK RIDGE NATIONAL LABORATORY
Oak Ridge, Tennessee
operated by
UNION CARBIDE CORPORATION
for the
U. S. ATOMIC ENERGY COMMISSION

OAK RIDGE NATIONAL LABORATORY LIBRARY
3 4456 0021546 1

Contents

SUMMARY ix

PART I. RADIOACTIVE WASTE DISPOSAL

1. FATE OF NUCLIDES IN TERRESTRIAL ENVIRONMENT 3
   - Field Plot Studies 3
   - Cobalt Sorption by Pulverized Minerals and Clays 7
2. DISPOSAL BY HYDRAULIC FRACTURING 10
   - Rock Mechanics 10
   - Mix Development 12
3. DISPOSAL IN NATURAL SALT FORMATIONS 15
   - Preparation for Project Salt Vault 15
   - Startup of Project Salt Vault 17
   - Preliminary Results in Project Salt Vault 18
   - First Fuel Assembly Changeout 23
   - Pillar Model Studies 23
   - Disposal of High-Level Waste in Selected Rock Formations 26
4. APPLICATION OF MINERAL EXCHANGE TO REACTOR TECHNOLOGY 27
   - Disposal of Gases into Permeable Formations 27
   - Nonequilibrium Ion Exchange 30
   - Hydroxide Consumption by Conasauga Shale 31
   - Behavior of Curium in Mineral Exchange Systems 31
   - Interpretation of Cation Exchange by Alumina 32
5. ENGINEERING, ECONOMIC, AND SAFETY EVALUATIONS 34
   - Clinch River Safety Analyses 34
   - ^{85}Kr and Tritium in an Expanding World Nuclear Power Industry 35
   - Long-Range Waste Management Study 37
6. RELATED COOPERATIVE PROJECTS 40
   - Cooperation of Other Agencies in ORNL Studies 40
   - Special Project 40
   - Visiting Investigators from Abroad 40
   - Visiting Investigator Abroad 40
   - Nuclear Safety Review 40
   - *Health Physics* Journal 40

Committee Work 40
Participation in Educational Programs 41
Nuclear Safety Information Center 41

PART II. RADIATION ECOLOGY

7. RESPONSES OF ANIMAL POPULATIONS TO IONIZING RADIATION 45
Radiation Sensitivity in Indigenous Small Mammals 45
Incorporation of a Thymidine Analog into Indigenous Rodents 47
Radiation Effects on Carp Reproduction 48
Population Genetics and Radiation Effects Studies 48

8. RESPONSES OF PLANTS TO IONIZING RADIATION 51
Growth and Mortality Responses of Conifers to Fast-Neutron Irradiation 51
Radiation Dose to Roots of Potted Plants from Reactor Fast Neutrons and Soil Activation Products 52
Mineral Uptake Mechanism Affected by Fast-Neutron Radiation 53
Effects of Fast-Neutron Radiation on Physiological Processes 53
Environmental and Genetic Modifications of Radiosensitivity 55
Structural Changes in Irradiated Plants 56

9. RADIONUCLIDE CYCLING IN TERRESTRIAL ECOSYSTEMS 58
Trends of ^{137}Cs in the *Liriodendron* Forest Vegetation 58
Foliage Biomass and Primary Productivity in the ^{137}Cs-Tagged *Liriodendron* Forest 58
^{137}Cs Distribution in Canopy Food Chains of the *Liriodendron* Forest 60
Equilibration of ^{137}Cs Body Burdens in Forest Myriapoda 63
^{134}Cs Turnover by Isopods Under Natural and Laboratory Conditions 65
Relationship Between Metabolism and ^{134}Cs Turnover by Forest Isopods 67
Isotopic Determination of Food Consumption and Utilization by Isopods 68
Trophic Efficiencies of Insect Herbivory Using ^{86}Rb and ^{32}P Tracers 70
Efficiency of Radioisotope Transfer in Predator-Prey Systems 71
^{106}Ru Elimination by Brown Crickets (*Acheta domesticus*) 72
Losses of ^{137}Cs and ^{60}Co from Leaf Litter 73
^{137}Cs Transfer in Terrestrial Microcosms 73
Accumulation and Production in a Pioneer Ecosystem of Kudzu Vine at Copperhill, Tennessee 73
Movement of ^{137}Cs in Pine Forest Floor Subsystems 74
Soil Studies in Herbaceous Ecosystems 74
Possible Mechanisms of Cobalt Sorption on Soil Clays 77
Precision and Accuracy of Basal Cover Estimates 78
Value of a Vacuum Clipper in Harvesting Herbage 81
Electronic Data Processing of Floristic Records 82
Forest Management 82

10. RADIONUCLIDE CYCLING IN AQUATIC ECOSYSTEMS 84
Cesium and Potassium in White Crappie and Other Clinch River Fish 84
Feeding Rate of Carp in White Oak Lake 87
Effect of Trophic Level on Radionuclide Accumulation by Fish 88
Radionuclides in Periphyton 88
Use of Artificial Substrata to Estimate the Productivity of Periphyton 90
Estimate of Periphyton Mass and Stream Bottom Area Using ^{32}P 90
Primary Productivity Measurement 92
Trace Elements in Plankton 93
Trace Elements in Seston 98
Transfer of ^{137}Cs, ^{106}Ru, and ^{60}Co Between Detritus and Benthic Macroinvertebrates in Microcosms 100
Accumulation of ^{32}P by Biota and Their Substrates in a Tagged Stream 101
11. THEORETICAL AND SYSTEMS ECOLOGY 102
A Systems Philosophy 102
Mathematical Modeling of Natural Populations 103
Ecosystem Maintenance and Transformation Models as Markov Processes with Absorbing Barriers 104
Model Simulation of Oak Ridge Vegetation Succession 106
Kinetics of ^{134}Cs in Terrestrial Microcosms 107
Nonlinear Programming in Ecology 109
Computer Programs for Ecological Problems 110
Productivity of a Planktonic Diatom Determined from Data on Mixed Species Populations 113
Growth Models for Plants 114
The Optimum Site Problem 117
Year-to-Year Prediction of ^{137}Cs Movement in the Tagged Forest 119

PART III. RADIATION PHYSICS

12. THEORETICAL RADIATION PHYSICS 123
High-Energy Dosimetry 123
General Concepts in Radiation Dosimetry 123
The Static Dielectric Constant of a Free-Electron Gas 124
The Screening Constant of an Electron Gas 125
Positron Annihilation in Metals 125
Positron Effective Mass in a Free-Electron Gas 126
Electron Mean Free Paths in a Free-Electron Gas 127
The Penetration of Low-Energy Electrons in Condensed Matter 127
Coupled Electron-Hole Cascade in a Free-Electron Gas 128
Photoelectric Emission from Thin Foils 128
The Excitation of Surface Plasmons by Photons 128
Double Plasmon Excitation by Charged Particles 129

13. ATOMIC AND MOLECULAR RADIATION PHYSICS 130
Alpha-Particle Ionization of Binary Gas Mixtures 130
Electron Impact Excitation of Atoms and Molecules Using a Low-Energy Electron Scavenger Technique 131
Finite-Medium Effects in Irradiated Gases 133
Time-of-Flight Determinations of Electron Diffusion Coefficients and Electron Drift Velocities in Ethylene, Water Vapor, and Hydrogen 133
Effects of Experimental Boundaries on the Measurement of Diffusion Coefficients and Drift Velocities in Swarm Methods 134
Electron Time-of-Flight Studies Using Electron Multiplier Techniques 134
Effect of Capture and Loss Processes on Time Distributions of Diffusing Electrons 135
Swarm Determination of the Cross Section for Momentum Transfer in Ethylene and in Ethylene Mixtures 136
Studies of Electronic Bound States in the Field of a Permanent Electric Dipole 137
Analysis of Electron Swarm Data to Obtain Transport Cross Sections 137
Swarm-Beam Studies of Polyatomic Molecules 138
Lifetimes of Temporary Negative Ions 140
Studies of Dissociative Electron Attachment in H_2O and D_2O 141
Interaction of Low-Energy Electrons with Atomic Oxygen 142
Potential Energy Curves for Diatomic Molecules 144
Molecular Orbitals of Magnesium Porphin 144
Approximate Representation of the Hartree-Fock Equations Through a Pseudopotential 144
14. INTERACTION OF RADIATION WITH LIQUIDS AND SOLIDS 147
Transition Radiation Due to Nonnormally Incident Electrons 147
Transition Radiation and Bremsstrahlung from Ag and Al Foils Bombarded by Nonnormal Incidence Electrons 148
Reflectance of Evaporated Aluminum Films in the Wavelength Region 800 to 2000 A 150
Optical and Photoelectric Properties of Evaporated Ag and Al Films 151
Optical and Electronic Properties of Tin 153
Optical and Electronic Properties of Sodium in the Wavelength Region 420 to 2000 A 155
Electron Slowing-Down Spectra in Aluminum 157
15. PROFESSIONAL HEALTH PHYSICS TRAINING 161
16. PHYSICS OF TISSUE DAMAGE 164
Excimer-Scintillator Investigations 164
Radiation Interactions with Liquids 166
Optical Properties of Polystyrene 167
Electronically Excited Amino Acids 168
Low-Energy Electron Transmission in Solids 168

PART IV. RADIATION DOSIMETRY

17. ICHIBAN STUDIES 173
Ichiban Liaison 173

18. SPECTROMETRY AND DOSIMETRY RESEARCH 175
An Absolute Neutron Dosimeter Based on a Generalized Concept for Radiation Dosimetry 175
Prediction of Biological Damage from Stopping-Power Theory 179
Transistorized Fast-Neutron Integrator – Radsan Mark II 182
Production of Gamma Rays by Neutrons in Air 183
Neutron Cross Sections for the Elements in Tissue 186
Ionization Recombination Studies 186

19. DOSIMETRY APPLICATIONS 189
Metaphosphate Glass Dosimetry 189
A Neutron-Energy Threshold Detector System Employing Solid-State Nuclear Track Detectors 190
Nuclear Accident Dosimeter Intercomparison Study 192
Depth-Dose Studies 195
Experimental Depth-Dose Studies in Water Phantoms 196
Sensitivity of Cellulose Acetate Butyrate for Alpha-Particle Track Registration 198
Irradiation of Plastics in DOSAR Low-Energy Accelerator 200
Radsan Correction-Factor Studies 203

20. SPECIAL PROJECTS AND HPRR OPERATIONS 205
Operation HENRE Accelerator 205
DOSAR Low-Energy Accelerator 207
Health Physics Research Reactor 209

PART V. INTERNAL DOSIMETRY

21. INTERNAL DOSE ESTIMATION 213
Revision of Standard Man 213
The Estimation of Exposure to an Aerosol Based on a Revised Standard Lung Model 216
Variation of Dose Delivered by ^{137}Cs as a Function of Body Size from Infancy to Adulthood 221
Iodine Retention 228
Computer Studies of Linear Combination of Exponentials Representing Power Functions 232

22. STABLE ELEMENT METABOLISM 237
Tissue Analysis Laboratory 237
Inorganic Composition of Ashed Biological Materials 237
Elemental Composition of Standard Man 240

PART VI. HEALTH PHYSICS TECHNOLOGY

23. AEROSOL PHYSICS 245
Adhesion of Solid Particles to Solid Surfaces 245
Survey of Adventitious Electrical Fields in the Working Environment 250
Studies of Surface Contamination 251
Environmental Studies 254
Empirical Dose Model for Reactor Debris Particles 256
Dosimetry of Small Particles 257

24. APPLIED INTERNAL DOSIMETRY 260
ORNL In Vivo Gamma-Ray Spectrometry Facility 260
In Vivo Detection and Measurement of ^{90}Sr-^{90}Y Internal Contamination 261
Computer Analysis of Whole-Body Count Data 261
Correction of ^{239}Pu-^{241}Am Wound Count for Attenuation in Tissue and for Different Ratios of ^{241}Am to ^{239}Pu 264
Absorption of ^{90}Sr from a Puncture Wound 266
Preventing Radiostrontium Loss in the Precipitation of Alkaline-Earth Phosphates from Urine with NH_4OH 267

THESES, PAPERS, PUBLICATIONS, AND LECTURES

THESES 271
PAPERS 271
PUBLICATIONS 277
LECTURES 287

Summary

PART I. RADIOACTIVE WASTE DISPOSAL

1. Fate of Nuclides in Terrestrial Environment

Continuing studies of the field plots show a reduced rate of loss of ^{137}Cs in the fall and winter months of the second year. There is a logarithmic relationship between ^{137}Cs loss and the soil loss. Mass balance analyses do not provide a satisfactory accounting of the total ^{137}Cs applied to the clipped meadow plot.

Studies of the selective adsorption of cobalt by layer lattice silicates show that adsorption is influenced by the method of sample preparation. With identical sample preparation techniques, trioctahedral lattices sorb more cobalt than comparable minerals with dioctahedral lattices.

2. Disposal by Hydraulic Fracturing

The most probable failure mechanisms limiting the ultimate capacity of the shale formation in the hydraulic-fracturing waste-disposal method appear to be related to the stresses induced in the rocks surrounding the injection by the injection itself. The problem of defining the number and size of injections required to produce a failure condition is under investigation using elastic analysis.

Examination of the nuclide retention properties of the set grouts, especially those containing low-cost fly ash, continued.

3. Disposal in Natural Salt Formations

Final preparations for Project Salt Vault were completed during the first half of fiscal year 1966. In addition to experimental equipment, a hoist and ventilation fan were installed at the waste shaft. Prior to startup of the experiment, a number of preoperational tests were conducted using both empty fuel assembly canisters and canisters loaded with 500 curies of ^{60}Co. A number of minor modifications to both the equipment and the handling procedures were made as a result of these tests.

On November 15, 1965, operation of Project Salt Vault was commenced. By November 19, seven canisters, containing 14 ETR fuel assemblies and a total of 1,000,000 curies, had been lowered into the mine and installed in hole liners in the floor of the newly mined areas. The demonstration is proceeding without difficulty. Preliminary results indicate that the rapidity of the transference of thermally induced stresses from the floor, through the supporting pillars, and into the roof is the only effect so far which was not anticipated.

On June 13–16, 1966, an additional set of fuel assemblies were placed in the mine. Roof bolts have been installed to strengthen the roof in the experimental area. Pillar model studies have shown that shale partings at the floor or roof allow an accelerated rate of deformation of the pillars.

4. Application of Mineral Exchange to Reactor Technology

In the event of a nuclear incident involving fuel element meltdown, ^{131}I appears to present the most serious short-term hazard. If the radioactive gases could be pumped underground, the delay time afforded by adsorption and by physical movement through the porous medium and dilution would cause a reduction in the relative hazard by a few orders of magnitude. Strontium-90 would present the most serious potential for contaminating groundwater near the site of discharge.

Laboratory studies conducted on the sorption of iodine by clays suggest that the iodine consists of condensed I_2 and chemisorbed I_2. Samples leached with water retain a finite quantity of I_2, also suggesting a fixed capacity for the chemisorption of iodine.

A computer program has been written to describe the transient behavior of radionuclides in the ground when the transporting solution is of a different concentration than the original groundwater. Experimental data, obtained on a Berea sandstone for different sets of conditions, confirm the suitability of Glueckauf's model for the passage of a wide band of solute through a chromatographic column, modified for changes in the adsorptive capacity due to changes in the total electrolyte concentration and for nonequilibrium sorption conditions.

Preliminary data on curium behavior suggest that mechanisms other than ion exchange may play dominant roles in its behavior in the ground.

5. Engineering, Economic, and Safety Evaluations

An age-dependent metabolic model was used to estimate dose equivalents received by the skeleton from ingestion of Clinch River water. For the age groups considered, this model gave an average dose 15% larger than the adjusted ICRP model. The dose rate associated with buildup of ^{85}Kr in the atmosphere and ^{3}H in the atmosphere and circulating water was estimated for an expanding free-world nuclear power economy. For complete releases to year 2000, the estimated whole-body dose rate from ^{85}Kr was 1.8 millirems/year in the first $\frac{1}{4}$ mile of the atmosphere and the body tissue dose rate from ^{3}H was 7.2×10^{-4} millirem/year by inhalation and 1.4×10^{-3} millirem/year by ingestion of water. A long-range waste management study was initiated.

6. Related Cooperative Projects

Other agencies continued to participate in our studies. Three alien guests were in residence during the year. One staff member was assigned to work in Belgium and France. Members of the section participated in Project Arkose of the Department of Defense, ASCE Committee on Sanitary Engineering Aspects of Nuclear Energy, and NAS-NRC Committee on Pollution.

One member has also served as assistant news editor for the United States for *Health Physics* and as an assistant editor of *Nuclear Safety*. Two members of the section taught a course at the University of Tennessee, and a series of lectures have been given to the U.S. Public Health Service.

PART II. RADIATION ECOLOGY

7. Responses of Animal Populations to Ionizing Radiation

Six species of rodents in the family Cricetidae, two species in the Muridae, and two species of shrews in the family Soricidae were irradiated at seven dose levels ranging from 500 to 2000 rads. Estimates of LD_{50-30} ranged from 535 to 1050 rads. The most radioresistant and most radiosensitive species were both in the Cricetidae.

The thymidine analog 5-^{131}iodo-2′-deoxyuridine can be used as an index of radiation damage, cell proliferation rates, and general metabolism in free-ranging native rodents. Acute radiation doses of 100, 500, and 1000 rads depressed whole-body incorporation of this antimetabolite in cotton rats to 76, 38, and 28%, respectively, of controls, and activity levels in the radiosensitive intestines were reduced to 47, 18, and 1.5% respectively. Rate of cell proliferation was related to the general metabolism of the three species tested.

Study of the natural population of *Chironomus tentans* in White Oak Lake and White Oak Creek has continued since the preliminary investigations in 1960. Two hundred larvae of another species of *Chironomus* belonging to the *plumosus* group were collected from White Oak Lake and analyzed for chromosomal aberrations. In contrast to *C. tentans*, which is chromosomal polymorphic, previous examinations of this species from nonirradiated populations revealed no endemic inversions; and the species is considered to be chromosomal monomorphic in this area. One aberration, a small inversion, was found in the larvae from the irradiated population. This finding agrees with previous conclusions based on our studies with *C. tentans*, that ionizing radiation from the contaminated environment increased the frequency of new chromosomal aberrations, but that these new aberrations were eliminated rapidly by natural selection.

8. Responses of Plants to Ionizing Radiation

Two species of pine, white pine (*Pinus strobus* L.) and shortleaf pine (*Pinus echinata* Mill.), were exposed to four levels of fast-neutron radiation (75, 100, 150, and 200 rads – tissue dose in air) at the DOSAR facility. Growth inhibitions occurred in all radiation treatment groups and reached maxima about two months following irradiation. Needle mortality of old leaves appeared in the 150- and 200-rad treatments within two to four weeks following irradiation. Over winter, plants in the 75- and 100-rad treatment groups exhibited 100% needle mortality. Under the greenhouse conditions in this study the minimum lethal dose (LD_{100}) was 75 rads for all plants.

A study was conducted to determine the neutron dose distribution and additional gamma and beta dose delivered to plant roots by activation products in the potting soil used for plant irradiation studies at the DOSAR facility. The experimental packages were exposed 1.0 m from the reactor core to 2056 rads (tissue dose in air) of fast neutrons delivered over a 10-min period. The major activation products were ^{56}Mn, ^{51}Cr, ^{86}Rb, ^{181}Hf, and ^{95}Zr-^{95}Nb in decreasing order of abundance. Manganese constituted 96% of the measured activity from activation products.

The effects of fast-neutron radiation on the growth and uptake of ^{65}Zn were studied in three-year-old red oak (*Quercus rubra* L.) seedlings. Potted seedlings received shoot irradiations of 505 and 1011 rads (tissue dose in air) delivered over a period of 8 min. Primary and secondary stem growth, root growth, and new leaf development were inhibited. An initial stimulation of ^{65}Zn uptake was observed following irradiation but disappeared by about 20 days. Retardation of uptake was found about ten weeks following exposure of seedlings to the higher dose.

In studies of the predictability of the interphase nuclear volume technique for radiation sensitivity it was found that plants growing under field conditions were found to suffer severe growth inhibitions at gamma radiation exposures two to three times less than those necessary to produce the same effect on plants in growth chambers with optimized environmental conditions. Experimental stress conditions, particularly moisture stress, given postirradiation lowered exposure requirements even more. Under growth chamber conditions, fast-neutron exposures were an order of magnitude less than the gamma exposures necessary to produce severe growth inhibition or death. Seasonal changes in nuclear volume of 14 plant species suggest that radiosensitivity would change by a factor of 1.5 to 3.0 during the year for dormant vs actively growing plants.

9. Radionuclide Cycling in Terrestrial Ecosystems

Year-to-year changes in distribution of ^{137}Cs in the tagged *Liriodendron* forest have been measured and accounted for in terms of major above- and below-ground transfers of ^{137}Cs. Concentrations in the forest canopy decreased each year since 1962. Annual transfers out of the canopy decreased accordingly from 1962 through 1965. Production and energy studies in the forest showed that annual production was 554 leaves/m^2. In caloric terms annual net foliage production by all tree species in the tagged forest was calculated to be 1.55×10^3 kcal/m^2.

Cesium-137 concentrations in the sessile canopy arthropods were greatest in leaf-eating herbivores and were least in sap-feeding herbivores. Food chain analyses showed a general decrease in ^{137}Cs concentrations during movement along food chains, with herbivorous insects (except for sap feeders) having the highest concentrations, omnivores intermediate concentrations, and predators the lowest concentrations per unit weight.

Radiotracer tags of ^{86}Rb and ^{32}P of plants growing in the field were used to measure food consumption and the efficiencies of trophic transfer for beetle populations under natural environmental conditions. Consumption of vegetation by beetles averaged 15.9 mg/day or (56.8 ± 1.40)% of their dry body weight. The respective turnover times for these food constituents were ^{86}Rb, 1.44 days; dry matter, 3.66 days; energy (calories), 4.42 days.

A comparison of ^{106}Ru and ^{137}Cs elimination by the brown cricket (*Acheta domesticus*) showed similar biological half-lives for the longer components of cesium and ruthenium elimination. Radiocesium was found in the muscle, fat body, and other soft tissues, whereas ^{106}Ru concentrated mainly in the intestinal walls and was not detected in the fat body. Neither radionuclide accumulated in the integument.

A mathematical interpolation scheme of contour mapping was used to develop maps of soil prop-

erties. To test the validity of a "limited field–computer mapping" approach, the study area was first surveyed by conventional techniques. Then elevations were taken on a 50 × 50 ft grid and used as inputs for a computer program which produced contour maps with a Calcomp plotter.

10. Radionuclide Cycling in Aquatic Ecosystems

Studies of cesium and potassium concentrations in the white crappie (*Pomoxis annularis*) showed that potassium concentrations in the flesh were relatively constant throughout the year, whereas stable cesium concentrations varied by a factor of 2. The period of low cesium concentration did not coincide completely with a reduced summer feeding activity by fish. In other Clinch River species potassium also was relatively constant, whereas cesium concentrations differed by a factor of 4. Bluegills and channel catfish had the lowest cesium concentrations, white bass and white crappie had the highest concentration, and freshwater drum had intermediate concentrations. There was no concise relationship between trophic position of the fish and their cesium content, although white bass and white crappie, the most piscivorous species, also had the highest cesium concentrations.

An investigation of fish in White Oak Lake to determine if the trophic position of the fish was correlated with its concentration of a radionuclide yielded negative results. Five species were analyzed for ^{137}Cs, ^{60}Co, and ^{90}Sr. The species, in order of increasing relative trophic position, were carp, gizzard shad, bullhead, bluegill, and largemouth bass.

A technique for using ^{32}P to indirectly measure periphyton mass and stream bottom area was developed and used successfully on a small stream. Three standard methods of measuring aquatic primary productivity, pH, ^{14}C, and O_2 evolution, were compared in seven 48-hr experiments performed in situ in Melton Hill Lake. The methods yielded different results. Based on similar results in other experiments with a variety of planktonic material, it was concluded that productivity values obtained by indirect procedures applied under field conditions are a function primarily of the measurement method. Differences between methods were both quantitative and qualitative.

11. Theoretical and Systems Ecology

A survey was made of literature from ecology, natural resource management, systems analysis, and operations research in order to better define the area of work called systems ecology. Ecological compartment models were treated as Markov processes with absorbing barriers to simulate succession of vegetation on the Oak Ridge Reservation. The study of radiocesium kinetics in microecosystems consisting of different combinations of tagged white oak leaf litter, soil microflora, millipedes, and aqueous leachate was completed. Turnover data indicate (1) that identical compartments turned over radiocesium at variable rates in the different microcosms and (2) that turnover rates of compartments increased with greater system complexity. The results showed that material transfers in connected systems are influenced by the organizational networks which define interactions between component parts. Consequently, network characteristics should be regarded as significant ecological variables in studies of energy and material movements, including transfers of radioactive substances.

Several growth models for plants were investigated for their predictive value. Equations were developed to show the residual influence of the nitrogen and phosphorus on height growth.

PART III. RADIATION PHYSICS

12. Theoretical Radiation Physics

Work in theoretical radiation dosimetry has included the calculation of dose due to protons and neutrons having energies up to 400 Mev for a cylindrical tissue phantom with elliptical cross section. This work is being extended to the Bev region using simplified models for the interaction processes. Further research into general concepts in radiation dosimetry has been carried out. Quantum mechanical collision theory has been applied in an attempt to elucidate those physical characteristics of radiation and its interaction with matter that are most relevant in producing biological responses.

Theoretical work in the area of solid-state plasma physics has involved a large number of related topics. Monte Carlo techniques have been ap-

plied to the determination of the static dielectric constant of the electron gas, which in turn has been employed in the calculation of the annihilation rates of thermalized positrons in electron gases of various densities. These rates are in good agreement with experimental data in free-electron-like metals. Using many-body perturbation theory, the contribution to the effective mass of a thermalized positron in a free-electron-like metal due to Coulomb interaction with conduction electrons has been evaluated. This contribution is found to amount to about 10% of the electron mass in an electron gas at a density corresponding to the conduction band in metallic Na.

The mean free path of hot electrons in a free-electron gas is of great interest in connection with recent experimental work done in this Division and elsewhere. Calculations of this quantity from a Bethe-Goldstone equation for the scattering of a hot electron from a particular electron in the Fermi gas are being carried out. This calculation accounts for both the operation of the exclusion principle in intermediate states and for dielectric screening by the electron gas. A Monte Carlo calculation of low-energy electron penetration in thin metal foils has been compared with experimental results of Nakai and Birkhoff, yielding fair agreement. An analytical approximation to the low-energy end of the electron-hole cascade spectrum in an electron gas has been found. This solution predicts an inverse fourth-power dependence of the flux of electrons or holes upon energy measured from the top of the conduction band.

A study of the theoretical photoelectron yield from thin metal foils by photons incident such that the electric vector has a nonzero component normal to the foil surface has shown that a peak should exist at the volume plasma frequency. In addition, it is found that the yield at this frequency should fluctuate as the foil thickness is varied. The probability of surface plasmon excitation by photons incident upon a thick metal foil has been found to increase linearly above the threshold energy. The phenomenon of two-plasmon excitation in characteristic energy loss experiments is being investigated theoretically. This process may be important at low electron energies, where the first Born approximation becomes suspect.

13. Atomic and Molecular Radiation Physics

Studies of the ionization produced by alpha particles in gas mixtures have been extended to cases involving at least one noble gas. The data yield empirical parameters which may be interpreted as describing the partitioning of dose between the components. Kinetic interpretation of the ensuing Hornbeck-Molnar processes may then be made. A novel technique has been developed for investigating inelastic scattering mechanisms of electrons. At the threshold for each new transition the scattered electron is left with approximately zero energy and may thus be scavenged and detected as SF_6^-. A computational investigation of the diffusion of ions to a boundary in irradiated gases has been completed and suggests that thermal convection currents are responsible for much of the wall neutralization inferred from chemical yields.

The time-of-flight technique for measuring the transport properties of electrons in gases has been given a more reliable foundation. Errors arising from experimental boundaries, counter dead time, and instrumental fluctuations are either negligible or may be removed at the data-treatment stage. Diffusion coefficients thus obtained in several gases and mixtures are often in marked disagreement with results from the Townsend-Huxley method; occasional deviations from the Nernst-Einstein relation have also been noted. An expression has been derived that shows the effect of temporary electron capture on diffusion coefficients. This mechanism may be partially responsible for the above discrepancies.

Electron drift velocity measurements continue to provide information on momentum transfer cross sections. Temperature effects in pure ethylene suggest, surprisingly, that it has a velocity-independent cross section. The cross sections previously found for polar molecules in an ethylene medium remain anomalously large. Temporary electron capture by an electric dipole is being investigated as a source of these anomalies. Finally, improved analytical techniques have been devised for extracting electron transport cross sections in the rare gases from the macroscopic transport properties.

Electron beam and swarm techniques have been successfully combined to yield the mechanism and energy-resolved cross sections for electron

attachment by large organic molecules. Dissociative capture occurs for all halogenated benzene compounds, although the nitro derivatives of benzene may also capture thermal electrons nondissociatively. The lifetimes of these long-lived parent molecule ions with respect to autoionization can be measured in the time-of-flight mass spectrometer. With the measured cross sections and lifetimes, one may calculate the density of negative ion states from detailed balance. Comparison with thermodynamic estimates of these level densities then yields lower limits to molecular electron affinities. The swarm-beam combination is being extended to study the dissociative attachment of simple molecules (e.g., H_2O and D_2O) to obtain information concerning the primary interactions responsible for electron capture. Hartree-Fock calculations have been completed on still another mechanism of electron capture – the radiative attachment to oxygen atoms.

Calculations of potential energy curves of diatomic molecules are being continued. The Rydberg-Klein method is used to analyze spectroscopic data. The molecular orbitals of magnesium porphin, a chlorophyll constituent, are being classified as a means of interpreting the electronic absorption spectrum of this molecule. A tractable formalism for coping with Hartree-Fock calculations is being developed and applied to systems of large atomic number.

14. Interaction of Radiation with Liquids and Solids

The vacuum ultraviolet spectra of light emitted by electron-beam-bombarded metal films gives much detailed information about the electronic transitions taking place. Recently a German laboratory has found that Ag targets bombarded with electrons not entering normal to the surface emit a monochromatic component at the surface plasmon wavelength, and they have attributed this to surface plasmon decay, although there were strong theoretical arguments that such decay should be radiationless. A theoretical and experimental program at ORNL has corroborated their experimental findings for Ag and found a similar peak in Al. Studies of polarization and of dependence on electron energy, film thickness, and electron incidence angle show, however, that the light is bremsstrahlung rather than surface plasmon radiation. Interesting optical interference effects are found in thin Al films both theoretically and in the laboratory.

Optical studies in the vacuum ultraviolet were carried out for Al, Ag, Sn, and Na. The Al data were taken under ultrahigh vacuum conditions ($\sim 10^{-8}$ torr) but still required correction for surface oxidation. Reflectances were free-electron-like down to 790 A and showed a small absorption at 1250 A attributed to surface plasmon excitation. Also, photoelectric studies showed a large decrease in yield of photoelectrons beyond the threshold photon energy for surface plasmon excitation. This absorption of photoelectrons is thought to be similar to the absorption phenomena noted in electron transmission experiments described in "Physics of Tissue Damage," Chap. 16, this report. Reflectivity studies on Ag and Sn helped separate free-electron and interband components in the dielectric constants. Interference studies in Na between 420 and 2000 A, the region of transparency, were successful in determining the index of refraction and setting an upper limit to the extinction coefficient. Here also interband contributions to the dielectric constant were measured.

Electron slowing-down spectra were obtained in Al, a more nearly tissue-equivalent medium than those studied heretofore. Alloys of radioactive Cu, Au, or Pd ($\sim$1% by weight) in Al yielded absolute spectra in reasonable agreement with the Spencer-Attix theory above 10 kev, but these spectra were more than an order of magnitude higher than theory at low energies. LET spectra derived from the data and theoretical stopping powers substantiate the assumption usually made in radiobiology that the electron spectrum in a beta-irradiated medium is mono-LET in character.

15. Professional Health Physics Training

The Health Physics Training Program included 16 fellowship students from Vanderbilt University and the University of Tennessee who reported to ORNL for summer on-the-job instruction in applied and research health physics. Division personnel visited 33 colleges and universities to give seminars on various research problems of current interest and also to recruit qualified students into the program. The Health Physics Di-

vision provided research facilities and advisors for 22 graduate students who were conducting thesis research. Teaching assistance was given to the University of Tennessee for its program in Radiation Physics and to Vanderbilt University for its course in Radiation Physics. Numerous short courses and lectures were presented for other groups and agencies.

16. Physics of Tissue Damage

Several liquid organic scintillators have been developed which utilize excimer formation to enhance the fluorescent efficiency. Although the primary purpose of the studies is to understand energy absorption and transfer in these liquids, the enhanced light emission, exceeding the best liquid scintillators by at least a factor of 3, promises to have important uses in many practical applications. Equipment to measure the optical constants of liquid water in the vacuum ultraviolet has been designed, constructed, and tested. Such optical data can be used to determine which electronic levels are excited in liquid water by ionizing radiation. Techniques developed may be applied to body fluids and to photochemical studies on liquids in the vacuum ultraviolet, where no work has previously been reported. Optical studies on solid polystyrene in the same spectral region have revealed resonance absorptions at 6.5 and 19.2 ev, which are attributed to π-electron excitation and a collective resonance involving all 40 noncore electrons respectively.

Preliminary studies on electron-bombarded aromatic amino acids show unusually large transmissions through layers 200 to 600 A thick. These observations are not understood at present but may make easier the ultimate purpose of the research, namely, the observation of fluorescence and phosphorescence of these films with the hope of obtaining information about initial excitation and subsequent events. Electron transmission of metallic films a few hundred angstroms in thickness was measured for Al, Mg, Tl, In, and Cu. Monoenergetic electrons between 3 ev and 3 kev were found to excite surface and volume plasmons and ionize inner electron shells with probabilities varying with electron energy. A Monte Carlo calculation for aluminum showed substantial agreement with transmission data for this metal. A sharp minimum in absorption was found for In and Mg just above the threshold for surface plasmon excitation.

PART IV. RADIATION DOSIMETRY

17. Ichiban Studies

The major efforts in the Ichiban studies were directed to liaison, depth-dose studies, and the shielding problems associated with heavily shielded survivors. During the visits to Japan detailed descriptions for computing final dose values, based on the new air-dose curves and shielding equations, were written and discussed with the shielding technicians.

18. Spectrometry and Dosimetry Research

Research in spectrometry and dosimetry was directed, in the main, to the spectrometry of indirectly ionizing radiations and to the calculation and measurement of energy loss functions for protons and heavy ions in tissue. Other studies included cross-section and reaction-product compilations for tissue, nuclear accident detector research, and advances in instrumentation.

19. Dosimetry Applications

There were several significant developments in dosimetry applications including: (1) improvements in the techniques of dosimetry with threshold detectors; (2) improvements in photoluminescent detectors; (3) development of methods and techniques for using insulating solids as track detectors for heavy ions; and (4) development of a convenient system for applying correction factors to pulse integrator responses.

20. Special Projects and HPRR Operations

The final testing of the HENRE accelerator was completed at ORNL, and the machine was shipped to Nevada and installed on the BREN tower. A low-energy accelerator was placed in service at the DOSAR facility and is being used extensively in the research program. The Health Physics Research Reactor has continued as a versatile irradiation facility for health physics and radiobiological research for ORNL and non-ORNL programs.

PART V. INTERNAL DOSIMETRY

21. Internal Dose Estimation

Revision of Standard Man

For approximately 17 years standard man has been a hypothetical adult man whose weight was 70 kg and who has been described by a limited amount of data. Due to the increased need for additional information, standard man is now being revised. This study represents the first attempt, as far as is determined by the authors, to define in detail a 70-kg man. A table of organ weights is included, and in some cases where the weights present a special problem, a short description also is included as to the basis for these weights.

The Estimation of Exposure to an Aerosol Based on a Revised Standard Lung Model

The Report of the ICRP Task Group on Lung Dynamics is the result of an intensive review of the literature on the subject. The lung model defined by this report is considerably more detailed than previous models and provides estimates of deposition and retention of an aerosol in each of three subregions of the lung. The report does not discuss the estimation of dose to these regions. In this study masses are assigned to the nasopharyngeal region (N-P), the tracheobronchial region (T-B), and the pulmonary region (P), which the report defines. Also, the question of the effective energy to be used for each of these regions is considered. Because of the unusual geometrical shapes of these regions, the estimates given here are not firm, and the difficulties are discussed.

Variation of Dose Delivered by ^{137}Cs as a Function of Body Size from Infancy to Adulthood

Six phantoms approximating the body size and shape of humans from birth to adulthood were mathematically constructed. A Monte-Carlo-type code was used to compute the gamma dose rate in about a hundred subregions of each phantom from a ^{137}Cs source uniformly distributed in a phantom. The distributions of gamma dose rate throughout the phantoms and the dose rate variation with phantom size or age were determined.

Iodine Retention

Using transfer coefficients for the normal individual, the differential equations for a three-compartmental model for iodine retention by the body are solved. The equilibrium iodine concentration in the body for a constant intake of iodine, as well as the total dose from a single intake of radioiodine, is expressed as a rational function of the transfer coefficients.

Computer Studies of Linear Combinations of Exponentials Representing Power Functions

It is found that the finite sum of N exponentials

$$\sum_{i=1}^{N} \alpha_i^{-n} e^{-\alpha_i t}$$

will generally approximate the power function

$$\frac{\Gamma(1-n)}{\Delta\alpha} t^{-(1-n)}$$

over a finite time period for cases in which $n \leqq 0.333$ and $\alpha_i = \alpha_1 + (i-1)\Delta\alpha$. Graphs showing the comparison between the exponential sum and the power function are presented.

22. Stable Element Metabolism

Tissue Analysis Laboratory

In the tissue analysis program, laboratory techniques have been extended to include methods for determining cesium and rubidium in teen-age diet samples.

Inorganic Composition of Ashed Biological Materials

In a separate study, laboratory methods have been developed for determining the anionic composition for diets and excreta from a balance study on two individuals.

Elemental Composition of Standard Man

Using the previous data obtained from this study and data from many different sources, the amounts of 38 elements in the total body of a 70-kg man have been calculated.

PART VI. HEALTH PHYSICS TECHNOLOGY

23. Aerosol Physics

Adhesion of solid particles to solid surfaces is being studied theoretically and experimentally. Since capillary and electrical forces predominate, emphasis is placed on these phenomena. A physical model is suggested to predict the magnitude of the capillary force between a glass particle and a glass surface. Experimental data confirm a predicted aging effect and the maximum expected force at 100% relative humidity; however, deviations from the simple model at lower relative humidity appear to be in contradiction with the Gibbs-Thomson relation concerning the vapor pressure over a curved surface. An empirical equation relating the electrical repulsion of a conductive spherical particle in contact with a charged conductive surface is derived from experimental data and is seen to agree approximately with theoretical calculations for a flat flake.

A survey of two local hot-cell facilities shows the existence of electrically charged surfaces which are of sufficient magnitude to enhance local deposition of airborne particles. All hot-cell and strip-chart recorder windows were charged, as were all floor tiles (vinyl asbestos) and sponge rubber floor mats; about half of the glass windows in partitions and doors were charged. The observed surface charges were all negative.

Studies of surface contamination measurement and resuspension potential have been continued using CuO dust in a room (8 × 12 × 8 ft) simulating a small laboratory of average cleanliness. This work has shown that the resuspension potential of a given contaminant can be assessed almost independently of surface composition – dry hard, dry dusty, dry porous, sticky, oily – on the basis of measurements made with a resuspension sampler (SMAIR) developed by this group. It is seen also that particles larger than about 2 μ in diameter are more readily resuspended than are smaller particles. The resuspension studies (bench-top scale) have been extended to liquid spills. A cupric nitrate deposit left on a stainless steel surface after drying of a liquid spill could not be resuspended by the action of air jets, although the smear test removed 80% of the deposited copper.

Deposition and retention of simulated radioactive particles on the skin is being studied using fluorescent wax spheres (50 μ to 1 mm diameter), and carbon-coated depleted uranium dicarbide spheres (230 μ diameter). Initial sticking amounted to about 55% for small wax spheres (104 to 125 μ diameter) and from 6 to 44% for larger wax spheres (297 to 500 μ diameter) on moderately dry skin but approached 100% on skin wet with perspiration. The relatively heavier UC_2 spheres were retained about the same length of time or somewhat longer than wax spheres of the same size. Decontamination tests using wax spheres (100 μ to 1 mm diameter) show that, except for very small particles (1 to 2 μ diameter), essentially complete decontamination is effected by simple actions such as brushing the arm, rinsing with water, or washing with soap and water.

Dosimetry of small radioactive particles in contact with the skin or the lining of the gastrointestinal tract is complicated by the fact that some of the particles may differ significantly from the composition of tissue. An empirical model is suggested whereby a library of beta-gamma energy spectra and the associated tissue depth dose data for certain specified geometries may be used to approximate the depth dose from an unknown source so long as the source spectrum is known. At present the library includes ^{45}Ca and ^{89}Sr in 1-cm-diam graphite spheres containing 17 wt % of uranium.

The principle of extrapolation dosimetry is being applied to determining the skin and gastrointestinal tract dose from small (~100-μ-diam) irradiated reactor fuel particles as a function of decay time. The anthracene extrapolation dosimeter, described in the annual report for last year, has been modified to include NE 102-A plastic scintillators in a variety of sizes from 11 mm diameter × 500 μ thick to 1 mm diameter × 5 μ thick. An example of dose measurement using an extrapolation ion chamber and the extrapolation scintillator is given for UC_2 fuel beads irradiated for 10 min and observed at decay times from 30 min to two days. The combination of the two extrapolation dosimeters provides a useful range extending over six orders of magnitude in dose rate.

24. Applied Internal Dosimetry

During the period July 1965 through May 1966 a total of 628 whole-body counts were made on 463 persons. Approximately 89% of the persons counted showed a normal human gamma-ray spectrum. Two employees, exposed to ^{90}Sr-^{90}Y ($SrTiO_3$) in January 1964, have been recounted at approximately one-month intervals for 849 days; the half-time for lung clearance appears to be in excess of 1000 days. Both routine and special whole-body gamma-ray spectra are now analyzed by a new computer program, ALPHA, which provides a wide selection of options including least-squares estimates of up to 20 radionuclides in each spectrum, automatic compensation for gain and threshold shifts, and an indication of "suspicious" channels where peaks may exist in the data but are not requested in the analysis.

Although most internal exposures examined by the Applied Internal Dosimetry group arise as a result of inhalation, the next most significant mode of intake results from wounds sustained on contaminated objects. An empirical approach is outlined for estimating the ratio of ^{241}Am to ^{239}Pu in an exposure mixture, and, using these data along with thin-crystal-probe absorption measurements on the wound, a method is given for estimating the quantities of ^{241}Am and of ^{239}Pu and the approximate depth of the deposit. An accidental exposure to ^{90}Sr-^{90}Y occurred when an employee received a puncture wound with a contaminated wire which penetrated four layers of gloves. The ^{90}Y content of the finger was determined by beta-absorption counting and has been followed for five months: absorption of ^{90}Sr into the bloodstream (~88% in <2 months) was estimated by urinalysis and analysis of blood samples; after the first two months the half-life for strontium elimination appears to be $\geqq 500$ days. An improved urinalysis procedure providing for efficient recovery of strontium and of various transuranic elements is shown to yield a constant recovery (95.0% ± 0.3) of strontium from urine samples ranging in volume from 500 to 1500 ml: essentially, this is a variation of the alkaline-earth phosphate precipitation, in which the key factors are the addition of excess calcium (60 mg per 500 ml of urine), excess H_3PO_4 (to give 0.1 *M*), excess NH_4OH (to give pH 9), and the exclusion of atmospheric CO_2 from the sample.

Part I. Radioactive Waste Disposal

F. L. Parker

1. Fate of Nuclides in Terrestrial Environment

Tsuneo Tamura A. S. Rogowski
E. R. Eastwood O. H. Myers
R. C. Reynolds[1]

The major long-term objectives of the soil studies continue to be in understanding the behavior of nuclides in soils and the synthesis of this information so that predictions can be made of the fate of nuclides released to the terrestrial environment. The study of the movement of radiocesium applied to field soil plots having different vegetative cover was continued, and laboratory studies of cobalt sorption were started.

FIELD PLOT STUDIES

A. S. Rogowski Tsuneo Tamura
E. R. Eastwood O. H. Myers

Comparison of First and Second Year Runoff from Field Plots

Investigations into the fate of ^{137}Cs, sprayed in the fall of 1964 on bare or fallow and vegetation-covered plots (8 × 8 ft), on an alluvial Captina silt loam soil were continued. Erosion losses for the first year of operation equivalent to 9.0, 0.92, and 0.32 tons/acre and ^{137}Cs losses of 31, 19, and 6.7% on fallow soil, clipped unfertilized meadow, and tall fertilized meadow, respectively, have been reported earlier. Initially, on the meadow plots all of the ^{137}Cs was on the vegetation, and, while more than $^{9}/_{10}$ of ^{137}Cs leached off the vegetation by rain was subsequently fixed on the soil, that part running off contributed more than half to the ^{137}Cs loss in runoff.

As shown in Table 1.1, the results for the five-month period (October to March) for the first and second years of operation are compared. Lower rainfall and lower EI (erosion index) values are reflected by lower soil losses, particularly on the bare soil plot. Although the soil loss for the equivalent EI value (loss values in brackets) on the bare plot stayed essentially the same, the reduction of soil loss on the meadow plots reflects the added protection afforded by good vegetative growth in the 1965 growing season. The erodibility factor[2] for Captina soil was found to be higher (0.45) than both the previously reported (0.40) and expected (0.42) values. The difference is due to seasonal variations and also to the formation of surface crust, which effectively reduced infiltration and increased runoff. On the other hand, increase in vegetation on plot 2 substantially decreased the runoff, while only a slight decrease of runoff was observed on plot 3, which had fair vegetation cover initially. The above data are further corroborated by the changes observed in the cover factor[3] values. The cover factor for plots 2 and 3 due to 1964 vegetation was 0.099 and 0.011, while the cover factor to the 1965 vegetation was 0.037 and 0.004 respectively. It is noteworthy that even in 1965 the cover factor was still four times larger on the unfertilized clipped meadow plot 2 than the expected value of 0.010 for poor meadow stands.

[1]Research Participant from Dartmouth College, Hanover, N.H.

[2]Erodibility factor, usually between 0.15 and 0.50, is the soil loss in tons per acre per unit EI (see footnote *b* of Table 1.1.) for a particular soil.

[3]Cover factor is the ratio of soil loss from vegetation covered plot/soil loss from identical bare soil plot; it ranges from 0.004 to 1.0.

Table 1.1. Comparison of the First and Second Year Runoff (October–March)[a]

Plot	Parameter	1st Year	2d Year
All	Total rain, in.	20.2	16.1
All	Total EI,[b] ergs cm^{-1} sec^{-1}	3421	2299
Plot 1[c]	Average runoff, %	37.7	49.1
Plot 2		44.4	20.1
Plot 3		13.3	10.8
Plot 1	Soil loss, g/m^2	408(313)[d]	307
Plot 2		97(71)	18
Plot 3		30(18)	5
Plot 1	^{137}Cs loss,[e] %	16.6(14.4)	2.0
Plot 2		13.4(11.2)	0.4
Plot 3		3.8(2.7)	0.1
Plot 1	Average specific ^{137}Cs loss, $\mu c/g$	0.50	0.08
Plot 2		1.43	0.18
Plot 3		0.70	0.07

[a]The five-month period for the first year extended from 10/20/64 to 3/12/65 and for the second year from 10/20/65 to 3/15/66.

[b]The erosion index EI is the product of rainfall energy and its maximum 30-min intensity, usually given in (foot-tons per acre) (inches/hours).

[c]Plots 1, 2, and 3 represent bare soil, clipped unfertilized meadow, and tall well-fertilized meadow respectively.

[d]Values in parentheses indicate soil and ^{137}Cs losses for the approximately equivalent EI value (2190 ergs cm^{-1} sec^{-1}) during the same period.

[e]The ^{137}Cs loss is given as percent of applied initial concentrations, which were 903, 937, and 925 $\mu c/m^2$ on plots 1, 2, and 3 respectively.

Concerning the total ^{137}Cs loss values and the specific activity of ^{137}Cs on eroded soils, it may be concluded that the primary cause of the decrease in ^{137}Cs loss, apart from the cover differences, might be the movement of it down the profile and dilution in the soil profile. Theoretical computations indicate that the peak ^{137}Cs concentration should be found at about 0.4 cm below the present ground surface. Since the total thickness of the eroded soil on the bare soil plot to date amounted to 0.2 cm on the average, it appears that under normal conditions of rainfall, ^{137}Cs movement into the soil is faster than the erosion process taking place at the surface. Depending on the energy and intensity of rain, as well as the infiltration capacity of a soil, initial losses of surface-deposited ^{137}Cs could be high, but losses should decrease as ^{137}Cs moves deeper into the profile.

^{137}Cs Loss as a Function of Soil Loss

In Fig. 1.1 the functional relationship between cumulative soil loss and cumulative ^{137}Cs loss is given. The data were fitted with the previously described equation $y = A(x/b)^m$ for values of soil loss $x \geqq 200$ g/m^2 (approximately 1 ton/acre), where y is the percent cumulative ^{137}Cs loss and the numerical values of A, b, and m are shown in the equation in Fig. 1.1. Maximum soil loss tolerance from agricultural fields in Tennessee is 5 tons/acre per year. These data indicate that under conditions similar to the fallow plot as much as one-fourth of the surface-deposited ^{137}Cs may move off the field by runoff and erosion under agriculturally acceptable standards. Other data (not shown here) indicate that six months after the application of the radionuclide on both the fallow and vegetation-covered plots the rate of

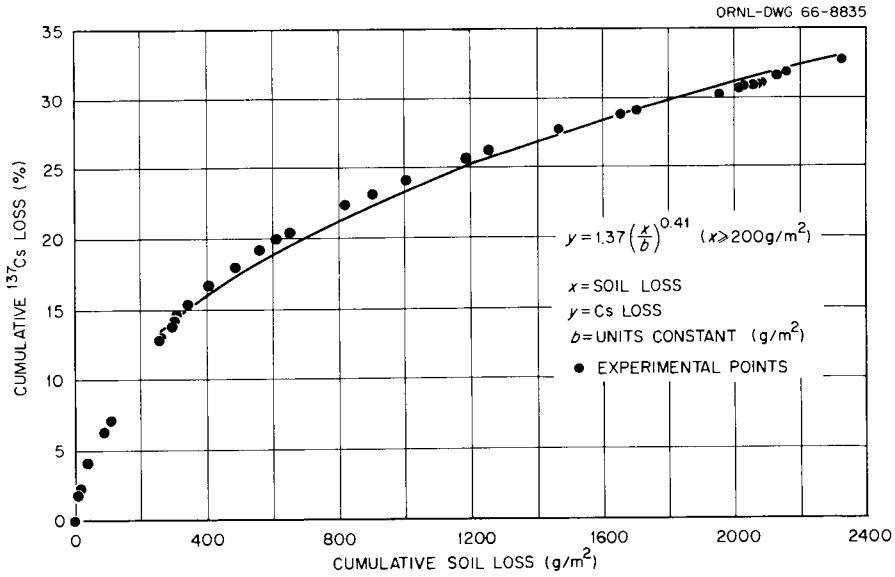

Fig. 1.1. ^{137}Cs Loss as a Function of Soil Loss on Plot 1, Bare Soil.

^{137}Cs loss decreased substantially and continued at this decreased rate through March 1966. This trend is particularly noticeable on the vegetation-covered plots, where the decreasing rate was further slowed by the appearance of new vegetation in 1965. The values in Fig. 1.1 of ^{137}Cs loss for $x > 800$ g/m^2 were obtained six months after the application of the radionuclide. Although the fit shown for $x \geqq 200$ g/m^2 is remarkably good (standard error, ± 0.1), it is felt that both in the case of the bare plot and particularly for the vegetation-covered plots the entire curve should best be approximated with two increments of the form

$$y = [A(x/b)^m]_{T_1} + [B(x/b)^n]_{T_2} ,$$

where T_1 and T_2 refer to the initial and final periods. A comprehensive model of radionuclide-soil loss relationship for other soils and other radionuclides is currently being developed based on the above equation. Since the model for determining the soil loss values (x) for different soils is already available, an attempt will be made to express the coefficients A, B and exponents m, n in terms of infiltration rate and field capacity, soil absorption coefficient (K_d), soil density, particle density, and porosity.

Distribution of ^{137}Cs in the Soil Profile

Detailed analyses of soil cores taken from each plot showed marked evidence of ^{137}Cs movement along the surface due to runoff and erosion and relatively little evidence of movement downward into the profile.

Three soil cores, 5 cm in diameter and 20 cm long, were taken from the upper, middle, and lower portion of each plot. (The lower portion of each plot adjoined the outlet drain.) The sampling was carried out one year after 5 mc of ^{137}Cs was applied to each plot. The original concentrations were 903, 937, and 925 μc/m^2 on plots 1, 2, and 3 respectively. The distribution with depth is shown in Table 1.2. The large standard errors listed reflect differences in concentration in the different portions of each plot. On the bare soil plot, the highest concentration of ^{137}Cs was found on a relatively flat area in the middle, and the lowest on a steeper portion close to the outlet. On the tall meadow plot, the highest concentration was found close to the outlet, where vegetation was dense, and lowest in the middle of the plot, which was more exposed, even though the slope near the outlet was six times as steep as the middle portion. On the clipped meadow plot, which had a gradual 4.6% slope, the concentration

Table 1.2. Average ^{137}Cs Distribution with Depth After One Year ($\mu c/m^2$)

Depth (cm)	Plot 1 (Bare Soil)	Plot 2 (Clipped Meadow)	Plot 3 (Tall Meadow)
Surface (0 to 2.5)	489 ± 184	349 ± 94	709 ± 260
2.5 to 10.0	89 ± 6	20 ± 9	55 ± 21
10.0 to 20.0	6 ± 4	1 ± 0.4	11 ± 10
Total (all depths)	586 ± 186	370 ± 101	776 ± 280
Initial application	903	937	925

was similar in the lower and middle portions of the plot and lowest in the upper portion. The results on the bare soil and tall meadow plot reflect differences in the mechanics of erosion and the effect of vegetative cover. Lowest loss of radionuclide from the bare soil plot would be expected from the area where the slope was minimum. The heavy meadow growth at the outlet of the tall meadow plot would tend to act as a filter of particulate soil material carrying adsorbed cesium and to increase localized deposition.

For the bare soil plot it was found that after one year of operation 83% of the ^{137}Cs present in the soil was concentrated in the upper 2.5 cm of the soil, 15% was in the 2.5-to-10-cm layer, and less than 1% was found in the 10-to-20-cm layer. On the vegetation-covered plots about 93% of cesium present in the soil was concentrated in the upper 2.5 cm of the profile, about 6% was in the 2.5-to-10-cm layer, and about 1% in the 10-to-20-cm layer. However, to explain the specific activity found in the eroded material from the plots (0.08 $\mu c/g$ on the average for four rains prior to sampling), the highest concentration of ^{137}Cs would have had to exist within the upper 1-cm zone of each plot, rather than the 2.5-cm zone analyzed.

Vegetation Uptake and Mass Balance

In Table 1.3 uptake by the vegetation in 1965 and in the spring of 1966 is given. It was previously reported that uptake by the vegetation in 1965 was negligible (1×10^{-10} $\mu c/g$). This value was found to be in error, and the recalculated data are presented here. In terms of total distribution and erosion losses the uptake by the vegetation is very small, amounting to about 0.1% of the total ^{137}Cs applied, as shown in the mass balance values in Table 1.4.

The mass balance values shown in Table 1.4 account satisfactorily for ^{137}Cs on the bare soil and tall meadow plot (plots 1 and 3). The cause of discrepancies observed on the clipped meadow plot is not fully understood. Low recovery of ^{137}Cs from the cores taken on the plot 2 (clipped meadow) suggested that more ^{137}Cs might be on the litter than the 6% reported earlier. Recent data, however, indicate that this is not the case. Two other possibilities exist. First, redistribution of radiocesium within the plot could create areas of both high and low concentration within the soil profile. To that end, additional small soil samples are being taken at random throughout the plot to check for the areas of high concentration. Second, since most of the initially applied ^{137}Cs was deposited on clipped litter material, the loss of loose litter through runoff could

Table 1.3. ^{137}Cs Concentration in the New Vegetation[a] of 1965 and 1966 Growing Seasons

Vegetation Sampled	Picocuries per Gram of Dry Plant Material[b]	
	Fall 1965	Spring 1966
Plot 2 (clipped meadow)	236 ± 59	341 ± 127
Plot 3 (tall meadow)	151 ± 41	70 ± 15

[a]Vegetation not contaminated by initial spray application of radiocesium.

[b]Values are for mixed grasses and weeds.

Table 1.4. Mass Balance of Radiocesium After One Year

Depth	Per Cent of Applied Radiocesium[a,b]		
	Plot 1 (Bare Soil)	Plot 2 (Clipped Meadow)	Plot 3 (Tall Meadow)
Vegetation		0.1	0.1
Litter		6.0	5.3
Eroded	30.7	18.9	6.7
0 to 2.5 cm (surface Ap)	54.1	37.2	76.6
2.5 to 10 cm (Ap)	9.8	2.1	5.9
10 to 20 cm (A_3)	0.7	0.1	1.2
Total	95.6	64.4	95.8

[a] ^{137}Cs was applied on Oct. 20, 1964.

[b] The rate of application was 903, 937, 925 $\mu c/m^2$ on plots 1, 2, and 3 respectively.

have contributed substantially to the radionuclide loss from clipped meadow plot, in contrast to the bare soil and tall meadow plots, where essentially no litter was present. Floating, relatively large litter material defies proportional sampling and would not have been adequately accounted for by the method used for determination of ^{137}Cs in the runoff. Hence, it is felt that unless additional soil samples disclose pockets of high activity in the soil profile, a very large loss of radionuclide associated with floating litter material in the runoff must be assumed.

It is concluded that all the cesium accounted for is associated with either the eroded and runoff material and litter, or the surface layer of soil. Concentration in the profile at this time appears to account for more cesium than uptake by the vegetation.

COBALT SORPTION BY PULVERIZED MINERALS AND CLAYS

R. C. Reynolds[1] Tsuneo Tamura
O. H. Myers

Cobalt sorption on various pulverized minerals and natural clays was measured; except as noted, all experiments were conducted in 5×10^{-2} *N* salt solutions to block nonspecific exchange reactions. One hundred milliliters of contacting solution, containing 2×10^{-6} *N* cobalt carrier spiked with ^{60}Co, was equilibrated for one week with 150 mg of mineral. The samples were continuously agitated, and pH adjustments were made periodically during the contact period.

Earlier work by Hodgson and co-workers has shown that specific sorption of cobalt is greatly enhanced by increasing pH, is better with minerals of trioctahedral lattices with the unexplained exception of dioctahedral muscovite, and is decreased when pulverized minerals are stored for several months.[4,5] This work has verified these observations and, in addition, has uncovered additional first-order factors that control specific sorption of cobalt.

Effect of Mineral Preparation and Treatment on Cobalt Sorption

As noted earlier, muscovite showed exceptionally high cobalt sorption for a dioctahedral mineral. Many soils are illitic, and illite is generally regarded as being similar chemically and structurally to muscovite. Yet Hodgson has shown that no soil shows specific cobalt sorption that approaches the values observed for muscovite.[6]

[4] K. G. Tiller and J. F. Hodgson, *Clays and Clay Minerals* **9**, 393–403 (1962).

[5] J. F. Hodgson, *Soil Sci. Soc. Am. Proc.* **24**, 165–68 (1960).

[6] K. G. Tiller, J. F. Hodgson, and M. Peech, *Soil Sci.* **95**, 392–99 (1963).

This anomaly has been studied by measuring cobalt sorption on muscovite samples which had been ground or filed to obtain the desired particle size and which had received prior treatment with acid or base. This was done not only to explain muscovite's behavior but to study the effect of sample preparation on the behavior of minerals in cobalt solutions. Table 1.5 lists the relevant data for several selected minerals.

Hodgson prepared his materials by dry-grinding the samples to obtain silt and clay-size particles. These results show that samples prepared in this manner sorb extremely high amounts of cobalt in 0.05 *N* $CaCl_2$ solutions. Wet-filing the material, which was intended to apply less shear to the mineral, did not cause decreased sorption consistently. To remove possible amorphous materials which were formed during the filing (and more likely during grinding) the samples were treated with acetic acid, sodium hydroxide, or both prior to testing. All treatments reduced cobalt sorption greatly. Considering the larger particle size of the muscovite, its sorption after the chemical treatments appears comparable to that of illite, which had not been subjected to any grinding, filing, or chemical treatment. These data make suspect the direct comparison of ground or filed mineral samples with naturally occurring clay-size particles.

Acid treatment was found to cause an increase in sorption of cobalt for biotite, which is the trioctahedral analog of muscovite. Visual examination of the centrifugate revealed that the mineral was attacked by the acid treatment. In contrast to biotite, trioctahedral talc was not attacked by the acid treatment and the sorption of cobalt remained relatively constant. The instability of biotite is generally ascribed to the presence of ferrous iron; talc, with its magnesium-bearing octahedral layer, is apparently more stable under

Table 1.5. Cobalt Sorption of Selected Minerals According to Sample Preparation and Chemical Treatment in 0.05 *N* $CaCl_2$

Material	Particle Size (μ)	Technique Used for Size Segregation	Chemical Treatment	Distribution Coefficient[a] (K_d) at pH = 7
Muscovite	20–2	Dry grinding	None	22,000
	20–2	Wet filing	None	1,450
	2–0.5	Dry grinding	None	30,000
	2–0.5	Wet filing	None	>100,000
	20–2	Wet filing	NaOH	<10
	20–2	Wet filing	Acetic acid (HAc)	<10
	20–2	Wet filing	NaOH + HAc	<10
Illite	2–0.5	Water soaked	None	43
	2–<0.5	Water soaked	None	63
Talc	20–2	Wet filing	None	690
	20–2	Wet filing	HAc	940
	20–2	Wet filing	NaOH + HAc	580
Biotite	20–2	Wet filing	None	870
	20–2	Wet filing	NaOH	520
	20–2	Wet filing	HAc	18,000
	20–2	Wet filing	NaOH + HAc	17,000

[a]Distribution coefficient is the ratio of cobalt sorbed per gram to that remaining per milliliter of solution.

conditions of lower pH. Further work is continuing with these minerals to establish the causes of the changes in sorption with the chemical treatment.

Sorptive Behavior of Di- and Trioctahedral Minerals

The data in Table 1.6 have been arranged to facilitate comparisons of related minerals. Despite the variable methods of sample preparation, the data show consistently higher cobalt sorption of trioctahedral as compared to dioctahedral materials. Note that talc shows high cobalt sorption in sodium and calcium systems. Both talc and pyrophyllite do not show measurable ion exchange capacities when determined by the conventional methods. Furthermore, the organic resin (IR-120), which has a very high exchange capacity, shows no measurable cobalt sorption in calcium system and minimal (K_d = 150) sorption in the sodium system. The high cobalt sorption exhibited by talc apparently involves mechanisms that are different from those of normal ion exchange reactions.

Magnesium ions exert a strong influence on cobalt sorption. Magnesium and cobalt have similar ionic radii (Co^{2+} = 0.72 A; Mg^{2+} = 0.65 A); therefore, it is possible that the blockage effects exhibited by magnesium arise from a direct competition between these two ions for similar sorption sites. Under these conditions, the behavior of the two ions should be treatable by simple mass action law considerations.

The influence of magnesium on cobalt sorption also is manifested by the greater affinity of the trioctahedral lattice (talc) for cobalt in distinction to dioctahedral materials (pyrophyllite). This difference may be simply a steric effect, which favors cobalt substitution at trioctahedral magnesium (or Fe^{2+}) sites, but diminishes cobalt substitution for the smaller aluminum ion (Al^{3+} = 0.50 A) in dioctahedral lattices.

The models proposed to explain cobalt sorption are tentative and incomplete. They are useful to an understanding of the sorption mechanisms and may help in predicting mineral responses. On the basis of these models, which emphasize the importance of trioctahedral lattices and their exposure at edges, it is not surprising that attapulgite has been found to be highly selective for cobalt.[7] This mineral not only is trioctahedral but it exposes many more magnesium octahedral sites along the pores of the structure. Sorption studies with attapulgite, other clay minerals, and the sesquioxides are continuing with cobalt as well as radiostrontium, since the selective sorption of both of these radionuclides appears to be controlled by edge effects in minerals.

[7] Y. A. Yousef and E. F. Gloyna, *The Transport of Co^{58} in an Aqueous Environment*, USAEC-EHE-12-6405, University of Texas, Austin (1964).

Table 1.6. Cobalt Sorption by Selected Minerals

Solution (concentration, 0.05 *N*)	Distribution Coefficient (K_d)[a]					
	Talc (Trioctahedral)	Pyrophyllite (Dioctahedral)	Vermiculite (Trioctahedral)	Montmorillonite (Dioctahedral)	Biotite (Trioctahedral)	Muscovite (Dioctahedral)
NaCl	770	13		1500	1900	
$CaCl_2$	690	10	11,500[b]	710	870	10
$MgCl_2$	53	10		56	270	10

[a]Distribution coefficient is defined as the ratio of the cobalt sorbed per gram of sorbent to that remaining per milliliter of solution.

[b]Results for the vermiculite sample were taken from ref. 4.

2. Disposal by Hydraulic Fracturing

W. C. McClain Tsuneo Tamura F. S. Brinkley

ROCK MECHANICS

W. C. McClain

The hydraulic shale fracturing technique has been shown to be a feasible, safe, and economical method for the disposal of low- and intermediate-level radioactive wastes.[1-3] Each injection of waste slurry pumped underground hardens in a horizontal grout sheet of finite thickness which disturbs the host formation and the overlying rock. This disturbance is typified by the surface uplifts occurring as a result of the injections. It is obvious that the rock material at a disposal site will not continue to accept further injections ad infinitum. Sooner or later the cumulative effects of previous injections will result in a failure of the system. The definition of the form of the failure and the determination of the failure criteria (i.e., when in the course of a series of injections the failure will occur) are the primary objectives of the rock mechanics investigation.

Possible Failure Mechanisms

It is possible to postulate a number of failure mechanisms of the hydraulic-fracturing technique simply from an understanding of the various parts of the system as installed at the Oak Ridge site:

1. Since the orientation of the fracture is controlled primarily by the direction of the least compressive stress[4] and since the effect of previous injections is such as to decrease the value of the existing horizontal compressive stress, failure may occur by the formation of a vertical fracture. This would constitute a failure of the system in that the waste-laden grout being injected would be released to the surface or into the ground water and a channel would be formed between the surface and the disposal level, allowing for vastly increased opportunities for leaching.

2. A sufficiently large number of nearly identically sized injections may be capable of inducing a shear stress in excess of the strength of the rocks so that a failure would occur in the form of "punching" an inverted cone-shaped mass up out of the ground. This would result in the same consequences as above.

3. There are many possibilities for failure of the system because of the numerous holes which have been drilled and cased through the disposal level. There are, in general, two types of failures associated with these drill holes: (1) a failure of the casing cement bond, which would be reparable; and (2) a failure of the rock due to the influence of the hole, which would not be reparable. This second condition would be visualized in the following manner:

The injections which intersect an existing cased hole will induce a compressive vertical stress in the strata in the vicinity of the hole, since the relatively rigid casing effectively "pins" together the rock above and below the injection level. When this induced stress has increased the total

[1] Wallace de Laguna, *Nucl. Struct. Eng. (Amsterdam)* 3(2), 338–52 (1956).

[2] Wallace de Laguna, *Nucl. Struct. Eng. (Amsterdam)* 3(3), 432–38 (1966).

[3] Herman Weeren, *Description of Shale Fracturing Pilot Plant and Analysis of Operating Hazards*, ORNL-TM-1003 (December 1964).

[4] M. K. Hubbert and D. G. Willis, *J. Petrol. Technol. Trans. AIME* **210**, 153–66 (June 1957).

vertical stress to the point where it exceeds the lesser of the two principal horizontal stresses, the next injection will approach the cased hole horizontally and then transform to a vertical fracture *in the rock.*

This list of possible failure mechanisms in the rock mass is by no means complete. Those listed, however, are the most probable.

Analytical Treatment

The first two failure mechanisms listed above are amenable to analysis by assuming that rocks behave elastically and, in the first case, isotropically. This assumption is open to the valid criticism that geologic materials do not usually exhibit elastic properties. However, it is felt, in view of the small strains induced and the greater probability of error in other assumptions, especially in the estimation of the original primitive, horizontal stresses, that the elastic solution will provide a more than acceptable first approximation.

Preliminary results of the analytical program indicate that failure by a vertical fracture at the injection well (item 1, above) is the most likely. Although a detailed discussion of the analytical method and procedure will not be presented at the present time, a number of interesting and relevant conclusions have already been drawn from the results of the program:

1. For injected grout sheets of specified size and shape (estimated for the actual case as being 1000 ft deep and circular), the surface uplift profile will take the shape of the normal distribution curve centered about the injection well and have a width several times the diameter of the grout sheet. A comparison of the actual measured uplifts due to injections 1 through 7 at the hydrofracture site[5] with the uplifts calculated from the theoretical analysis (normalized at the center point) is shown in Fig. 2.1. This figure shows a good correlation between the theoretical and measured results.

2. If assumptions are made of a constant slurry pumping rate and a proportional relationship between the radius of the grout sheet and its thickness, the theoretical analysis indicates that all points on the surface should be uplifted at a constant velocity. Measurement of surface tilts during grout injections made by the U.S. Geological Survey[6] (Fig. 2.2) confirm this conclusion, if due allowance is made for variations from a constant pumping rate.

3. Another important conclusion obtained from the theoretical analysis is that the surface uplift measurements cannot be used as an aid in determining the location and shape of the grout sheet. Figure 2.3 relates the eccentricity of an elliptical grout sheet to the eccentricity of the

[5]W. C. McClain, unpublished (1966).

[6]F. S. Riley, *Liquid-Level Tiltmeter Measures Uplift Produced by Hydraulic Fracturing,* USGS Professional Paper 424-B, pp. 317–19 (1961).

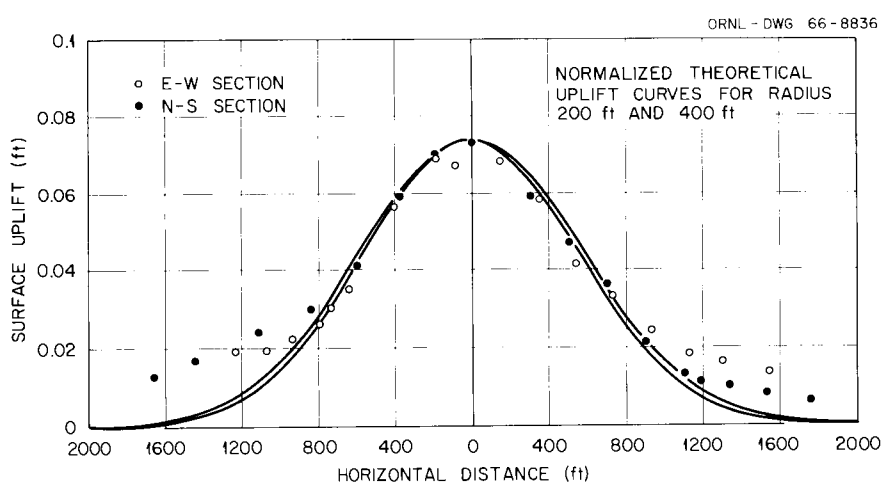

Fig. 2.1. Measured Uplifts, Injections 1 Through 7.

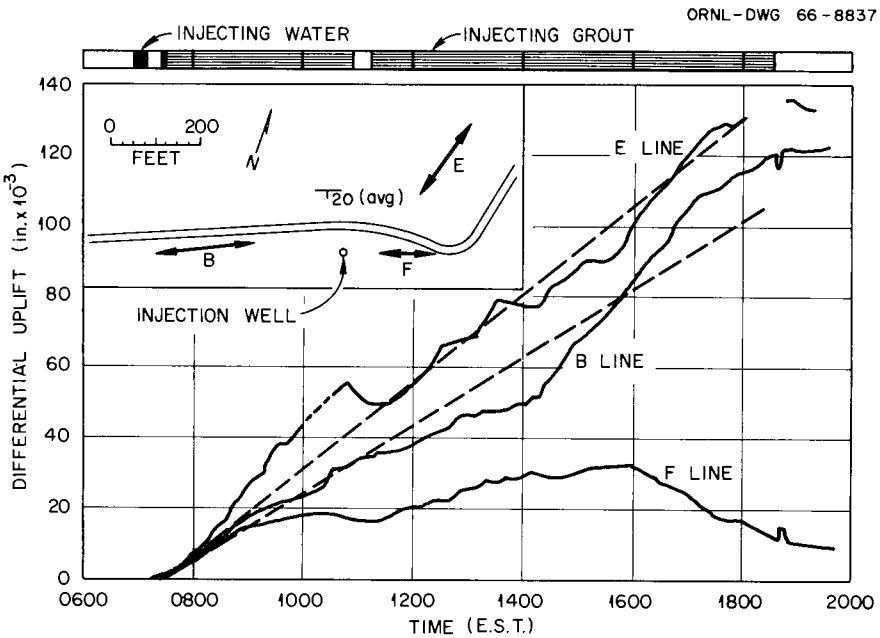

Fig. 2.2. Graph Showing Uplift of Closer Piers Relative to More Distant Piers, Sept. 10, 1960.

surface uplift contours. The relationship indicates that the surface uplift is very insensitive to changes in shape of the injection.

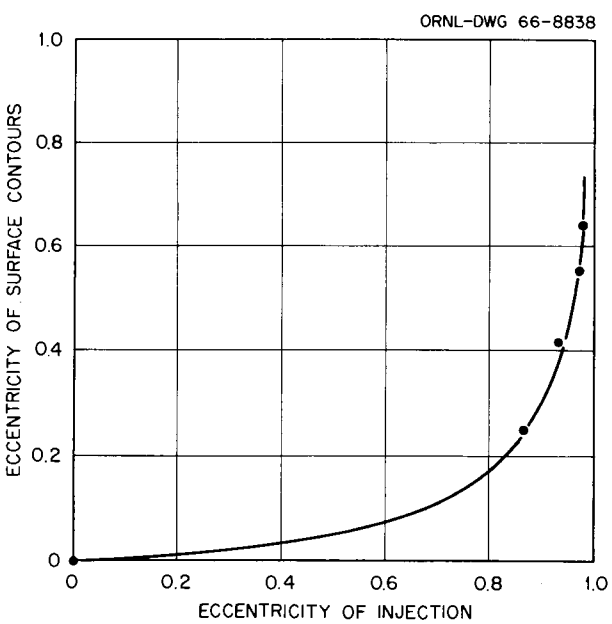

Fig. 2.3. Eccentricity of Injection.

Conclusions

The analytical technique is now being used to calculate the stresses induced in the rock around the injections. By making assumptions as to the original horizontal state of stress at the site, this information can be used to place a quantitative limit on the capacity of the host formation.

MIX DEVELOPMENT

Tsuneo Tamura F. S. Brinkley

In preparing mixes for possible routine use in the Oak Ridge plant, the cement content was reduced in the interest of economy. Since strontium retention was related to cement in the mix, it was desirable to investigate the retention of this nuclide in the grouts by leaching tests; these grouts had been prepared during the development of recipes for the different field injections. It was felt that the mix containing the highest cement

content would retain the most radiostrontium. Analysis of the data showed, in general, that higher cement content was favorable for strontium retention; however, this, in itself, was not a guarantee of highest retention. To get a better indication of the parameter which might be responsible for retaining radiostrontium, the solutions used to leach the grouts were analyzed for their chemical composition. Inspection of the data revealed that in addition to the chemicals originally present in the waste solution, the water contained a significant amount of calcium.

A plot of the calcium concentration and the radiostrontium concentration in the leach water showed a direct relationship, as seen in Fig. 2.4. The data show that the retention of radiostrontium depended on the retention of calcium in the grout. It was reasoned, therefore, that to reduce the leachable strontium from the grout, it would be necessary to reduce the leachable calcium. One way to do this would be to add pozzolanic material to the mix. With the addition of a pozzolanic material the calcium hydroxide, which is normally formed in the cement hydration reaction and which is readily subject to chemical attack, is removed and a cementitious lime-pozzolanic product is formed. A cheap local source of pozzolanic material is Kingston fly ash; addition of this material would not only reduce the cost of the mix but might improve the retention of radiostrontium. Laboratory tests showed that substituting a portion of the cement with Kingston fly ash reduced the "free lime" content of the grout, as well as the soluble calcium ion content, when the grout was leached with water. Figure 2.5 shows the reduction in "free lime" as a function of the amount of Kingston fly ash added. The reduction in "free lime" was also sensitive to the curing time; with increasing curing time the amount of "free lime" decreased. This behavior differs from normal cement mixes, which show an increase in "free lime" content with increasing curing time.

Bleedback from Injection 7

Following injection 7, the injection well was not plugged; after 14 days its valve was opened to measure the amount of bleedback. Although the mix had been designed originally to retain all the fluid, the proportioning device was not sufficiently precise, and the mix was approximately 15% low on solids. The lower solids content showed phase separation of approximately 15% in the laboratory; the bleedback data from the field showed at least 15% separation. The well had not stopped bleeding when the measurements were stopped; and at the last sampling date, which was approximately 70 days later, the flow rate was reduced to 35 gpd as compared to approximately 10,000 gpd on the first day. Extrapolation to no bleedback (45 days

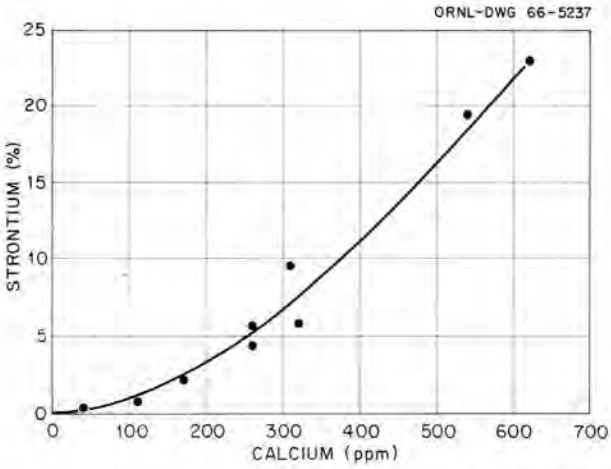

Fig. 2.4. Relationship of Strontium Leached and Amount of Calcium Dissolved from Cube Molds.

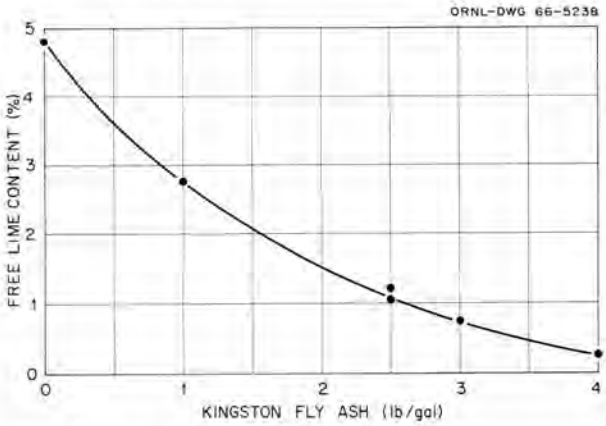

Fig. 2.5. Reduction in Free Lime as a Function of the Amount of Kingston Fly Ash Added.

later) gave an additional 800 gal. The total bleedback would have been approximately 19,000 gal of the 95,000 gal injected.

The principal activity in the bleedback solution was ^{137}Cs. On the basis of 19,000 gal, the total content of cesium in the liquid was about 1 curie, and 3200 curies had been injected. The ^{90}Sr in the liquid was approximately 0.3 curie; although difficult to calculate accurately, due to the strontium-bearing floccules in the waste, it was estimated that the total ^{90}Sr in the waste was approximately 400 curies. In addition to chemicals which had been in the waste solution, the bleedback solution contained about 0.7 *M* NaCl. This not only suggests the presence of halite in the shale but the high concentration indicates that the halite-shale interface may be the zone subjected to fracturing.

3. Disposal in Natural Salt Formations

PREPARATION FOR PROJECT SALT VAULT[1]

W. J. Boegly, Jr.
F. M. Empson
R. L. Bradshaw
W. C. McClain
F. L. Parker
W. F. Schaffer, Jr.[2]
R. C. Sexton[3]
B. L. Houser
T. W. Hodge, Jr.

Safety Analysis

A draft copy of the Safety Analysis for the operation of Project Salt Vault[4] was completed, and reviews were held with the ORNL Radiochemical Plants Committee[5] and the Kansas State Board of Health.

The maximum credible accident for Project Salt Vault is one in which the canister is dropped down the waste-charging shaft, resulting in the destruction of the canister and a failure of the cladding on some of the fuel assembly plates. Since fuel meltdown is not possible, it is assumed that 0.1% of the iodine and 100% of the rare gases contained in 19 fuel plates (each ETR assembly is composed of 19 plates) are released to the waste shaft. Because air flow is restricted in the waste shaft during transfers and the material released is not vented until the waste shaft fan is turned on, optimum meteorological conditions can be selected prior to release. Even if this were not the case, and the activity from the fuel assembly were released during atmospheric inversions, the following would occur: ^{131}I release would result in restrictions on milk production on land within a downwind distance of 1050 m, and at a distance of 100 m from the waste shaft an inhalation dose to the thyroid of 1.6 rems would be received; the ^{85}Kr and ^{131m}Xe released would result in submersion exposures to an individual standing 100 m from the source of 42 and 16 millirems respectively. Since milk production within 1050 m is negligible and it is possible to restrict personnel from an area 100 m from the waste shaft, the consequences of a maximum credible accident can be minimized.

Equipment Installation

Procurement and installation of the waste shaft fan were completed. The waste shaft fan will normally draw 5000 cfm of air up the waste shaft from the experimental area, but in an emergency the air flow can be reversed.

The hoist used to handle the canisters is equipped with three speeds: 100, 33, and 1.6 fpm. In normal operation the slow speeds are used when the canister is being raised into or lowered from the shipping carrier. The high speed is used for most of the canister travel in the shaft. The hoist is equipped with standard mine safety auxiliaries, such as independent dual brakes, slip clutch, and a depth indicator. The capacity of the hoist (2000 lb) is sufficient to handle 12-in. calciner pots and to remove personnel from the mine in the case of an emergency in the main hoisting shaft.

Figure 3.1 shows room 1 (main radioactive array) during the period when the experimental equipment was being installed. The tops of the hole liners may be seen in this figure, along with the trenches containing heater, thermocouple, and off-gas lines. The large white box on the wall contains the off-gas system flowmeters. In the upper right-hand corner of the picture may be seen the end of the main power control panel.

---

[1]Demonstration of high-level waste solids disposal.

[2]Chemical Technology Division.

[3]Plant and Equipment Division.

[4]W. J. Boegly, Jr., *Safety Analysis – Project Salt Vault*, ORNL report in preparation.

[5]Radiochemical Plants Committee, internal memorandum (1965).

Fig. 3.1. Room 1, Main Radioactivity Array.

Preoperational Tests

A number of handling operations were performed using empty fuel assembly canisters to check out the operating procedures. Minor changes in operating procedures were instituted after these tests.

Early in October, two canisters were loaded with 500 curies each of ^{60}Co and shipped to Lyons in the shipping carrier. A narrow fan-shaped beam was found to emanate from one section of the carrier (apparently due to a gap in the lead shielding), necessitating the addition of an auxiliary shielding ring. The canisters with ^{60}Co were lowered into the mine, placed in the array holes, and removed a number of times to obtain handling experience with radioactive canisters and to check the shielding calculations. It was also found that a "scatter" shield was needed inside the shot-retainer tubes in the hole liners in the floor.

All experimental equipment, such as the off-gas system and fission product leak detection system, was put through a shakedown test prior to startup. The chief difficulty encountered was failure of the Electrofilm heaters on the off-gas system tubes in the upper sections of the hole liners. During the shakedown tests, three of the seven heaters in the electrical array and two of the heaters in the radioactive array failed. There was no apparent reason for the failure, since the units were operating below their rated temperature. Three units were repaired and two were replaced. No additional trouble was encountered with the operation of the

electrical array off-gas heaters, but by the second week after startup, all seven (including the replacements) of the units in the radioactive array had failed. Since there has been no indication of a water problem in these arrays, there are no plans to make any further replacements. However, it was necessary to obtain more reliable units for installation of the array in the old mine floor, since water problems do exist there. Resistance-wire tape units were installed on the tubes in this array.

STARTUP OF PROJECT SALT VAULT

F. M. Empson
R. L. Bradshaw
W. J. Boegly, Jr.
W. F. Schaffer, Jr.
F. L. Parker
W. C. McClain
R. C. Sexton
B. L. Houser
T. W. Hodge, Jr.

ETR Fuel Assemblies

The 14 fuel assemblies from the Engineering Test Reactor cycle 73 were canned, the cans leak-tested, decontaminated, and loaded into the shipping carrier at the NRTS in Idaho without any major difficulties. Radiolysis of the ethylene glycol–water coolant was found to be a problem. This difficulty was circumvented by using plain water and installing a demineralizer in the cooling system.

The irradiation history of each of the fuel assemblies was taken into account in calculating the fission product decay heat, and the assemblies were paired so that the total heat content of each canister would be about the same. The calculated heat-generation rate as a function of time is shown in Fig. 3.2. Five of the canisters follow this curve almost exactly, while the other two deviate by less than 10% (lower). Note that on November 18, the heat generation per canister was about 520 w. On November 1 (the original target date) the heat-generation rate would have been about 630 w, as compared with the 750 w calculated under the assumptions of the original feasibility study. The total fission product activity in the seven canisters as of November 18 was calculated to have been about 1,000,000 curies.

Startup

In order that the peak salt temperature may be raised to the vicinity of 200°C within the duration of the test (two years) and with the limited number of heat sources, auxiliary heaters were attached to the hole liners. For the sake of simplicity in operation and in analysis of data, a fixed power input was chosen; all holes are to be operated with a power input of 1500 w.

On November 15 the electrical (control) array and the main radioactive array heaters were turned on at 1500 w each. The heaters were operated two days before the first canister was installed so that the relationships between the temperatures at the prime points of comparison in the arrays could be established. The prime comparison point is the one which is at the vertical center plane of the canisters but $1\frac{1}{2}$ ft from the central axis of the canister. Then, as each radioactive canister was placed, the electrical power was cut back so that the sum of the fission product power and electrical power was still 1500 w. Later, as the fission products decay, the electrical power will be boosted periodically in accordance with Fig. 3.2.

On November 17–19 all seven of the fuel assembly canisters were lowered into the mine and placed in

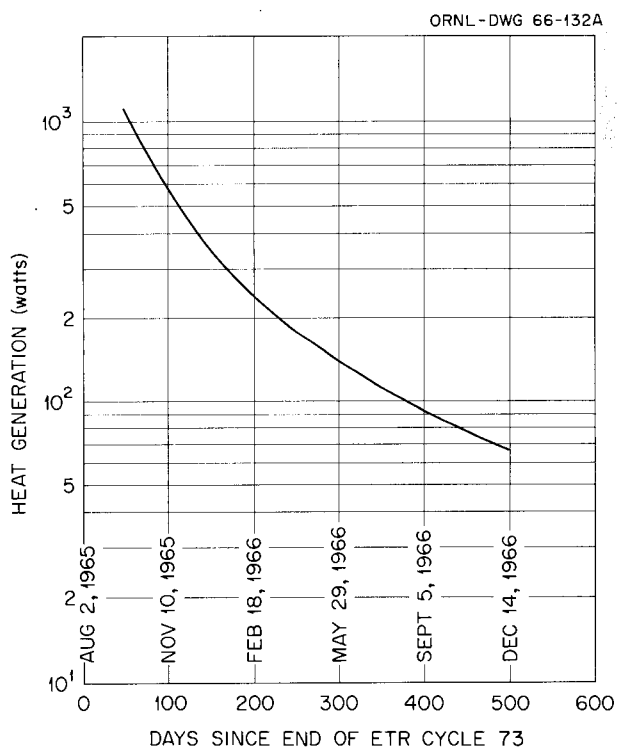

Fig. 3.2. Approximate Heat Generation Rate for All Canisters.

the floor. Only one of the seven caused any difficulty. This can could not be lowered out of the shipping carrier, and it finally had to be forced out by means of a steel rod inserted through the cable port. No trouble was encountered in placing the can in the hole liner. (Tolerances are greater than in the carrier.) A piece of tape was found inside that position in the carrier magazine. Thus it appears that the tape caused the trouble.

The maximum radiation dosage received by any of the personnel on the project during the entire loading period was 200 mr. Most of this was received in working with the stuck canister. Radiation levels immediately above the array holes (after installation of the scatter shields) are generally less than 10 mr/hr, and unlimited access is allowable everywhere except immediately over the holes.

PRELIMINARY RESULTS IN PROJECT SALT VAULT

R. L. Bradshaw W. C. McClain
F. M. Empson B. L. Houser
T. W. Hodge, Jr.

Salt Dose Measurements

During the first week of operation, the dose rates in the air annulus between the hole liner and the salt and at various depths into the salt were measured using the specially developed chemical and glass rod dosimeters. The results with the two types of dosimeter were in reasonable agreement with each other and with the theoretically calculated dose rates. The chief difference was that the peak dose rate appears to be at the surface of the salt, whereas the calculations showed the peak occurring at around 2 cm into the salt. The measured dose rate at the salt surface was about 5×10^4 rads/hr.

Additional dose rate measurements were taken during the first storage period. From these results it appears that the total dose delivered in seven months by the first set of fuel assemblies to the surface of the holes in the main radioactive array was about 1.2×10^8 rads.

Temperatures

Temperatures in both the electrical and radioactive arrays are satisfactorily close to each other and to the theoretical calculations. Most temperatures, including the fuel element temperatures, are running somewhat lower than calculated. This is in part due to the fact that heat losses were calculated as though the room were solid salt.

The peak fuel element temperatures ranged from about 225 to 265°C and were reached during the first day after placement of the canisters. As of the end of May the fuel element temperatures ranged from about 190 to 210°C. The highest salt temperature reached was at the wall of the central array hole and was about 145° in both the radioactive and electrical arrays. Peripheral hole temperatures were running about 120 to 130°C. Ten-degree temperature rises extended to about 15 ft from the array centers at the end of May.

Chlorine Measurements

Previous laboratory studies have indicated that radiation may produce small quantities of free chlorine within the salt structure; however, on the basis of the laboratory tests, it does not appear that this chlorine would be released at any significant rate. One of the objectives of Project Salt Vault is to investigate the possible release of chlorine under field conditions. Routine chlorine sampling is done on a periodic basis using indicator tubes with a sensitivity of about 0.1 ppm. To date there have been four occasions of short periods of time during which an indication has been obtained in the radioactive array (about 0.1 to 0.3 ppm). These occasions have coincided with the collection of a few milliliters of water in the off-gas system. Mass spectrometer analyses of grab samples taken during one of these periods failed to indicate the presence of chlorine. A cold trap collection is planned for the future.

Rheological Measurements

Thermal Stress Effects. – At the end of December 1965 (46 days after startup) the salt temperature at the wall of the peripheral holes of the main radioactive array was about 120°C, and at the wall of the center hole approximately 135°C. In the vertical center planes of the main radioactive and electrical arrays – about 9 ft below floor level – essentially the entire area within a circle formed by the peripheral holes (i.e., a horizontal circle of about a 10-ft diameter) was at or about 100°C.

Vertical thermal expansion of the floor in the center of the arrays had reached nearly an inch by the end of December. The floor uplift (measured in feet) as a function of time for each array at the center and 10 ft from the center is shown in Fig. 3.3*b*. It may be observed that the rate of rise in and near the array was slowing down. This is due to the fact that the rate of rise of the salt temperature was also slowing down. The total vertical expansion had reached about $1\frac{1}{4}$ in. in May.

In Fig. 3.3*a* are shown the uplift profiles for room 1 (radioactive array) along the north-south and east-west axes of the room. It is apparent that thermal expansion of the material in the floor extends to 40 or 50 ft from the center of the array. The north-south uplift profile shows the restraining effect produced by the presence of the adjacent pillars.

Figure 3.4*b* shows the transverse expansion (in inches) taking place in the pillar which borders the radioactive array room on the north side. The curve labeled 109-A-N-2 is a measure of the amount of horizontal expansion taking place between the surface of the pillar (about halfway up from the floor on the south face of the pillar) and a point about 10 ft in toward the center of the pillar. The curve labeled 118-A-S-1 is the corresponding measurement made from the north face of the pillar. (Locations of the gages are shown in Fig. 3.5.) The power was turned on in the array at 806 "standard days" (November 15, 1965), and almost immediately the expansion rate on the south side of the pillar increased from about 0.15 in./year to about 0.45 in./year, a threefold increase. This marked increase in expansion rate halfway up the pillar was due primarily to a transfer of thermal stress from the center of the floor, since the increased rate was detected before any appreciable temperature rise had taken place beneath the pillar. The fact that the expansion rate has not tended to decrease with time (as has the rate of floor uplift) is due to the fact that some temperature rise is now taking place beneath the pillar. It will be noticed that the north side of the pillar has also experienced a slight increase in strain rate (curve 118-A-S-1). A similar behavior has been observed in the wall on the south side of the room, and the behavior of the electrical array room is also essentially the same.

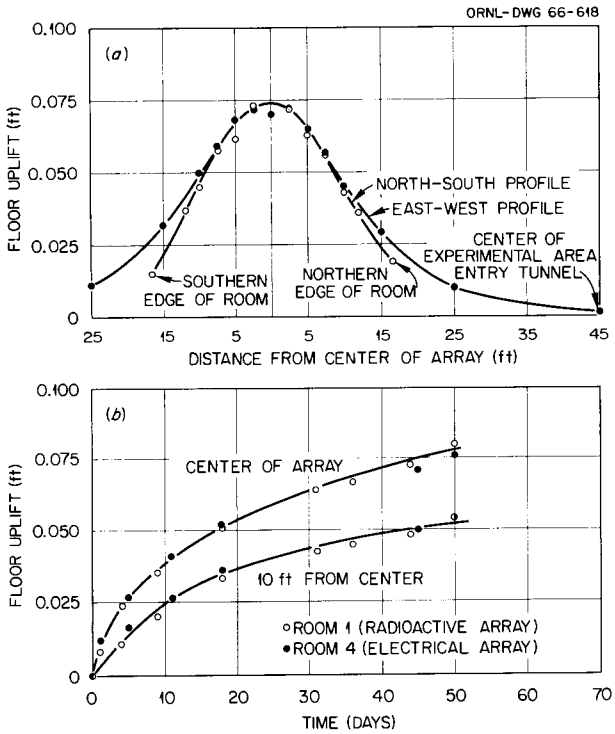

Fig. 3.3. Floor Uplift Due to Thermal Expansion. (*a*) Floor uplift profiles in room 1 as of December 30, 1965; (*b*) floor uplift in array rooms.

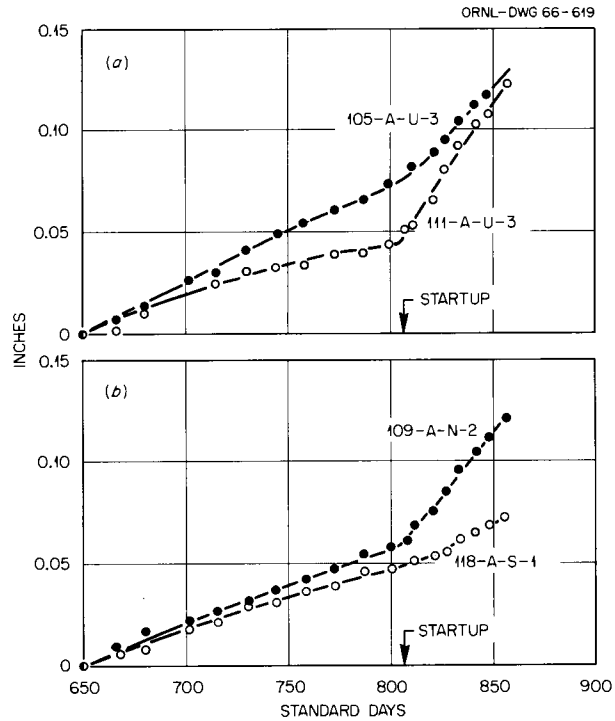

Fig. 3.4. Pillar and Roof Movement Due to Thermal Stresses. (*a*) Movement of ceiling relative to 6 ft up; (*b*) transverse expansion in pillar 1-2.

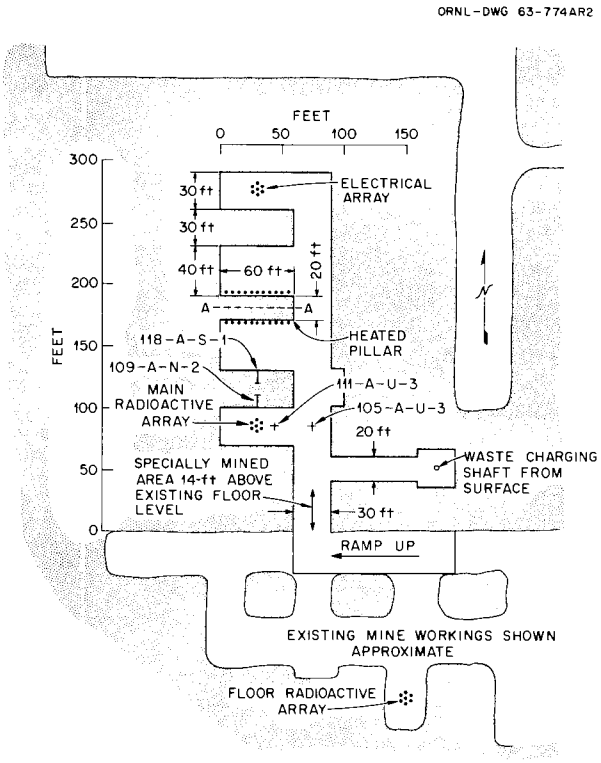

Fig. 3.5. Layout of Experimental Area, Showing Locations of Gages Referred to in Fig. 3.4.

The transfer of stress has not been limited to the adjacent pillars, but has extended to the ceiling as well. That this should be so is attested by the results of the pillar model tests, described separately. In the pillar model tests, an axially applied load resulted in movement of salt from above and below the pillar out into the roof and floor of the opening. Figure 3.4*a* shows the movement of the ceiling relative to a point 6 ft up into the roof. The curve labeled 111-A-U-3 is the roof-gage data for a point 10 ft from the center of the radioactive array (10 ft toward the mouth of the room, Fig. 3.5). The other curve (105-A-U-3) is for a point about 45 ft from the center of the array, out in the middle of the access corridor (Fig. 3.5). It will be noticed that almost immediately after startup (806 "standard days") there was about a fivefold increase in the rate of roof movement near the array (increase in rate of sag from about 0.12 to 0.55 in./year), and a substantial increase in the sag rate out in the entry corridor (from about 0.16 to 0.41 in./year). The data for the electrical array room show similar movements taking place. Most of this movement is separation of the 2-ft-thick salt layer in the roof from the thin shale layer immediately above it. Movement rates would be expected to be much lower if the salt layer were thick enough to resist buckling, as indicated by the results of the roof-bolt test described below.

Salt flow behavior in both the radioactive and electrical array rooms has been essentially the same. It is, therefore, concluded that thermal effects on salt flow are much more important than radiation effects.

Roof-Bolt Test. – In order to avoid possible problems associated with water in the interbedded shale in the floor of the Lyons mine, it was necessary to excavate the new experimental area in a stratum which had a shale parting about 2 ft up in the roof. Shale partings also existed at the original mine level, and this is a situation which will quite likely be encountered with a waste-disposal operation in any bedded salt deposit.

Based on mine observations and other considerations, it was felt that the 2-ft-thick roof slab would be safe under normal conditions. It was recognized, however, that the heated-pillar test might produce large salt movements in rooms 2 and 3 (Fig. 3.6), with consequent unknown effects on roof stability in these rooms. However, it was felt that there should be no roof trouble in rooms 1 and 4, since the pillars were larger and the rooms narrower. Thus it appeared that some form of protection from roof falls might be needed in rooms 2 and 3 and the experimental entry between the two rooms. Consequently, an investigation was begun to see if suitable protection could be provided in the event it became needed.

Roof bolts were considered first, but they appeared to be undesirable from a number of standpoints. Chief among these was the fact that there were no available data on installations of a similar nature in a salt mine. Secondly, assuming that they would work, it was felt that significant experimental data would be lost. One of the major aims of the heated-pillar test was to see what types of movement might take place as the salt beneath the pillar heated to temperatures which might be encountered in an actual waste-disposal operation. Would a 2-ft-thick salt layer in the roof prove hazardous in an actual operation? If the bolts were effective in sewing the 2- and 3-ft layers together, the answers would probably be lost. If the bolts didn't work, it might be neces-

sary to abandon at least the heated-pillar part of the demonstration prematurely.

The second method of protection which was given serious consideration was the "ceiling catcher." The object of this device was to provide a support which would prevent the roof slab from falling to the floor, while at the same time not preventing roof movement and ceiling sag from taking place. The third method studied was the "mobile umbrella." The concept here was essentially that of an armored vehicle. Neither of these alternatives appeared to be satisfactory.

During the study of the various methods of protection, the demonstration started. The arrays in rooms 1 and 4 were turned on with a power input of 10.5 kw per room. Considerable upward expansion of the floor and some change in pillar creep rates were expected from the thermal stresses

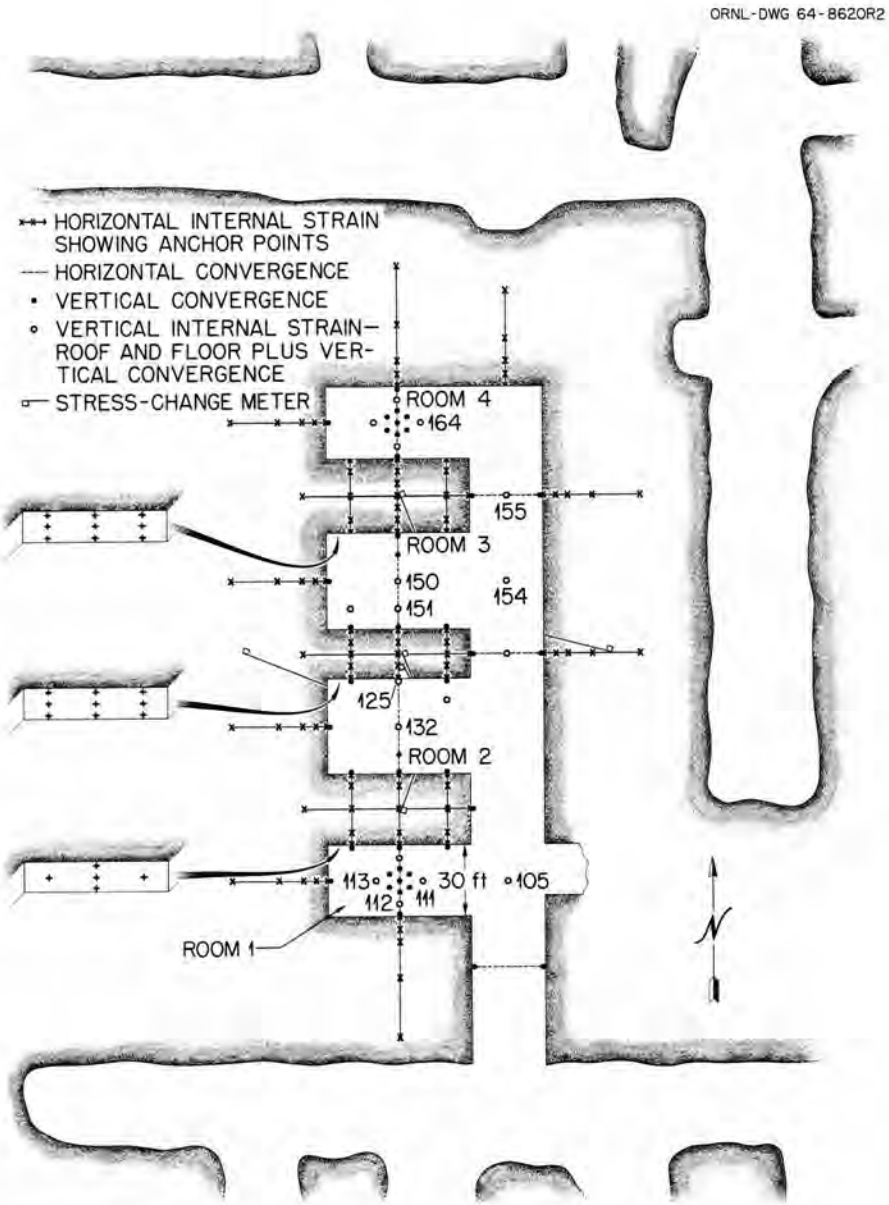

Fig. 3.6. Location of Stress and Strain Gages Inside Experimental Area.

produced in the centers of rooms 1 and 4. These results were found, but an additional unexpected result was a marked increase in the rate of sag of the 2-ft ceiling slab, discussed in the previous section (Fig. 3.4*a*). It is thus seen that the answer to the question posed previously (about the behavior of the 2-ft slab) has now been obtained. A 2-ft-thick roof slab could become a hazard in an actual disposal operation if the facility is not properly designed. Further, in the operation of the demonstration, rooms 1 and 4 could be jeopardized by startup of the pillar-heating test, since the increased sag rates have been found beyond the confines of the rooms containing the heat sources. (Since the separation rates are now decreasing with time, it is not felt that operation of the arrays alone will produce sufficient total separation to prove hazardous.) This being the case, it now seems desirable to provide some form of protection for the entire experimental area before starting the pillar-heating test. Since one of the two objections (loss of data) to roof bolts has been removed, roof bolts appeared to be the logical choice if they could be shown to be effective. In fact, roof bolts would now provide additional data which would be of considerable value; sewing the 2-ft slab to the 3-ft slab with roof bolts would allow us to determine the effectiveness of a 5-ft-thick roof system.

Consequently, a test installation, consisting of 37 bolts spaced 4 ft on centers, was made in the center of room 3. Figure 3.7 shows the effects of the roof bolts on the vertical closure and the roof movement in room 3. Note that strain gage 154, which is in front of room 3 (Fig. 3.6) in an area which is not bolted, shows no decrease in sag rate. Before the bolts were installed, the floor-to-ceiling convergence gage 150-E-V (in the center of room 3) had a rate (slope of the curve) of about 0.4 in./year. The movement of the ceiling, relative to a point 6 ft up into the roof in the center of room 3 (gage 150-A-U-3, Fig. 3.7) was about 0.2 in./year. The rate of movement in the roof at the center of the intersection of room 3 and the experimental entry was about the same as that at the side of room 3 (about 0.1 in./year, gages 154-A-U-3 and 151-A-U-3 respectively).

Gage 125-E-V (location shown in Fig. 3.6) in room 2 should indicate the floor-to-ceiling convergence which might be expected when no parting separation is taking place, since it is right next to the center pillar. The floor-to-ceiling convergence (gage 150-E-V) in the center of room 3 now (after bolting) has a rate (0.2 in./year) which is about equal to that next to the pillar in room 2 (125-E-V). The movement of the ceiling relative to points 6 ft up into the roof (150-A-U-3 and 151-A-U-3, Fig. 3.7) now appears (after bolting) to be about the same as that next to a pillar where no separation is taking place (about 0.03 in./year, 125-A-U-3).

As may be seen in Fig. 3.7, the gap at the parting (between the 2-ft layer and the 3-ft layer) in the center of room 3 was reduced by about 0.1 in. upon installation of the test bolts. In other words, the bolts have pulled up the 2-ft-thick slab. [If the 3-ft slab had been pulled down instead, the floor-to-ceiling convergence (gage 150-E-V) would not have decreased as it did in Fig. 3.7.] This result is to be expected, since the bolts are exerting a net upward force in the ceiling slab. Figure 3.8 shows the average roof bolt load as calculated from data obtained with the six load cells. Note that the force exerted by each bolt is around 10,000 lb. Each bolt is supporting an area of about 14 ft^2, and the deadweight load of a 2-ft-thick layer

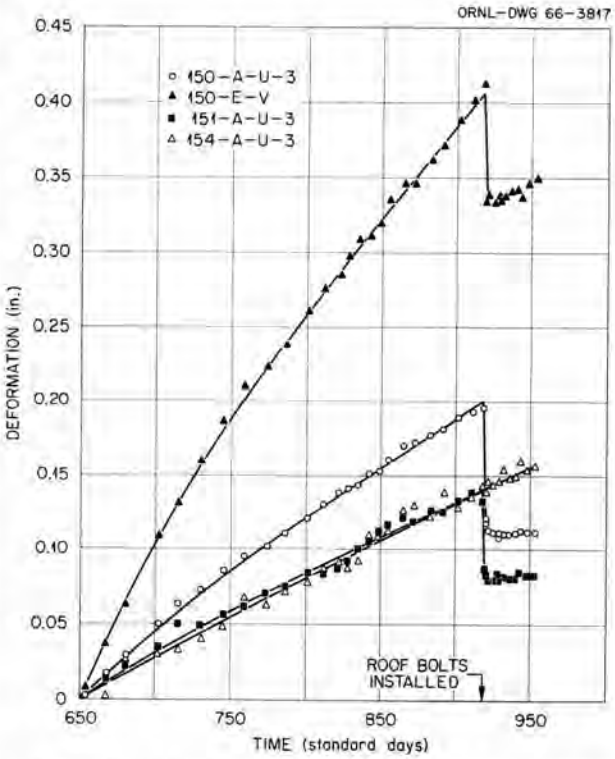

Fig. 3.7. Effects of Roof Bolts on Vertical Closure and Roof Movement in Room 3.

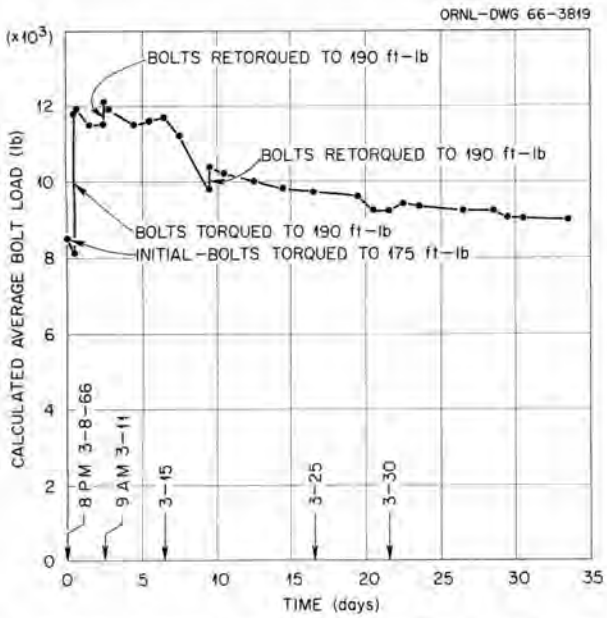

Fig. 3.8. Average Roof-Bolt Load in Test Installation.

would be about 3800 lb. Thus the net upward force is about 6000 lb per bolt or about 430 psf. The bolts have since been retorqued, and the load went back up above 10,000 lb.

The results have thus indicated that a patterned installation of bolts will effectively support the sagging 2-ft layer, and installation of about 1700 bolts in the entire experimental area is now under way. The system formed by bolting together the 2-ft and 3-ft layers, which has not yet shown any signs of separating from the material above it, should provide adequate support throughout the experimental area. Background data confirming this supposition will be obtained before starting the pillar-heating test.

FIRST FUEL ASSEMBLY CHANGEOUT

F. M. Empson — R. C. Sexton
R. L. Bradshaw — B. L. Houser
T. W. Hodge, Jr. — R. Rzekiecki[6]

The installation of the seven-hole array (radioactive array) in the floor of the existing mine was completed and all systems checked out. Transfer of the seven fuel assembly canisters from the main array to the floor array is scheduled to take place in June. One of the main array hole liners will be pulled for inspection. After that, seven new canisters will be loaded into the main array.

The seven new canisters will contain 14 assemblies from the ETR cycle 78. At the time of placement in the array, the fuel assemblies will be about 105 days out of the reactor, and each canister should have a heat generation rate of about 800 w. The decay curve is similar to that for the first set of fuel assemblies (Fig. 3.2).

PILLAR MODEL STUDIES

T. F. Lomenick — H. J. Wyrick

Effects of Shale Partings

Previous tests on scale-model specimens of rock salt mine pillars have shown the effects of temperature, compressive loads, and time on cavity closure.[7] Lithologic changes in the salt column can also markedly affect the deformation of mine pillars. Even though some salt deposits, such as salt domes, are essentially all salt, most bedded deposits contain lithologic discontinuities, or rock salt that is interbedded with layers of dolomite, shale, anhydrite, and other materials. For instance, the 300-ft-thick salt sequence at Lyons, Kansas, is only about 60% NaCl, with the other 40% being mostly shale and anhydrite.[8] In many cases these "other" materials may form a part of the roof, floor, or even the pillars in a mine and thus enter into the deformation of the openings. Shale layers (sometimes called "partings") are common in bedded salt deposits, and in many cases the salt is mined or falls to these layers since they form planes of weakness. The presence of these shale partings, even though they are quite thin, can have a significant effect on the rate of cavity deformation, depending on whether the shale is at the top and bottom of the pillar or in the center of it. This is shown in Fig. 3.9, where deformation curves are presented for model salt pillars that have been deformed without any simulated shale partings, with simulated shale partings at the top and bottom of a pillar, and with a simulated shale parting in the center of the pillar. Thin sheets of

[6]Visiting Scientist from French CEA.

[7]T. F. Lomenick and R. L. Bradshaw, *Nature* **207**(4993), 158–59 (1965).

[8]T. F. Lomenick, internal memorandum (1965).

Teflon lubricated with grease and graphite serve as friction reducers and thus simulate shale partings. (Analysis of data and observations from the Kansas mines indicates that the shale partings do have a lubricating effect, but it does not appear that they have so marked an effect as do the Teflon sheets. Therefore, the actual effects to be expected in a mine would lie somewhere between the two extremes shown in Fig. 3.9.) For the model having no simulated shale partings and for the model where the shale parting is in the center of the pillar, the deformational curves are almost identical, both showing about 0.03 in. or 3% deformation after 140 hr of testing. However, for the model with friction reducers at the top and bottom of the pillar, note that the deformation proceeds initially at a very fast rate before beginning to decrease with time. The model appears to then deform at a constant rate for a short period of time and then deforms at an increasing rate that results in sudden failure after less than 130 hr. It is also of interest that for models with no simulated shale partings, sudden or catastrophic pillar failure could not be induced even under stresses as high as 14,000 psi.

The accelerated rate of deformation of the models, when simulated shale partings occur at the top and bottom of the pillars, apparently results from the more or less independent deformation of the pillar from the roof and floor under these conditions. When there are no partings at the top and bottom of the pillar, or even if the parting is in the center of the pillar, there is an interlocking of salt crystals from the pillar with the roof and floor which serves to allow the pillar, roof, and floor to deform more or less as a single unit. However, when partings exist between the pillar and the roof and floor, they serve as effective friction reducers which consequently allow the pillar to deform more independently of the roof and floor, since horizontal confining pressures in the roof and floor are not transmitted into the pillar.

Deformational Behavior

Although the exact mechanisms of deformation within salt pillars are not fully understood at this time, some generalizations as to movement have been formulated through macroscopic observations of deformed specimens. Figure 3.10 shows cross-sectional views of two model pillars that have been cut vertically in half after deformation. Before deformation the pillars were 4 in. in diameter by 1 in. in height. In these specimens an attempt has been made to define the principal movement through observing the relation of the pillar and the material above and below it after deformation. The dark-colored, horizontal lines seen in the salt specimens are $\frac{1}{8}$-in.-diam holes that were bored horizontally through the top and bottom of the pillar and filled with colored salt before the specimens were deformed. In the model deformed at 22.5°C, it is seen that the pillar is only slightly more than 4 in. in diameter. However, a considerable amount of loose salt from the outermost portion of the pillar had accumulated in the surrounding cavity opening, but was subsequently removed. The cross-sectional view demonstrates that the pillar has not deformed independently of the roof and floor, but all three parts of the model have entered into the closure of the cavity. Note especially how the roof and floor have flowed into the cavity opening. The most resistance to deformation in the models is believed to be found in the center portion of the pillar (due to confining pressure) and immediately above and below the pillar in the roof and floor. Thus, movement here is at a minimum. This is shown in the photo by the greater distance between the lines in the center portion of the pillar than at the edge of the pillar. Toward the outside of the pillar, there is less resistance to deformation; thus, salt from the pil-

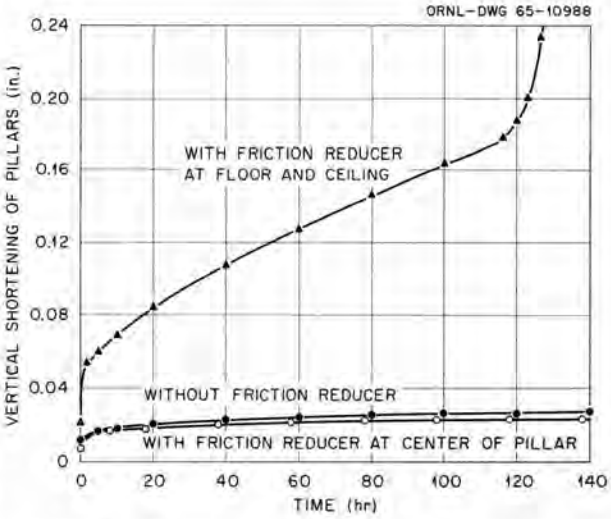

Fig. 3.9. Deformation of Model Rock Salt Pillars at 4000 psi.

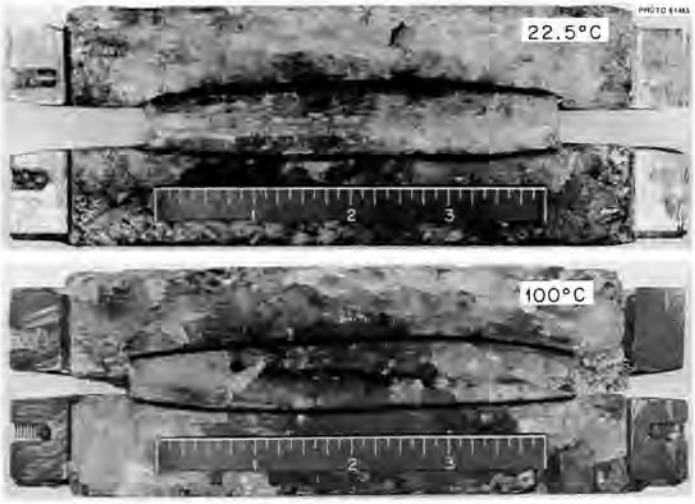

Fig. 3.10. Cross Sections of Model Pillars Deformed at 22.5 and 100°C.

lars tends to move horizontally into the opening while material from above and below also moves in to fill the cavity.

In the model pillar deformed at 100°C, the overall deformational pattern is similar to that for the sample tested at room temperature, but instead of the outermost portion of the pillar deforming through spalling, it has stayed intact and deformed more plastically. The pillar diameter in this case has increased from 4 in. to $4\frac{1}{2}$ in. as a result of the deformation.

In addition to Lyons, Kansas, salt, model pillar tests have been performed on salt from mines at Hutchinson, Kansas; Retsof, New York; Detroit, Michigan; and Grand Saline, Texas. The Kansas salt is from a bedded deposit of Permian age, while the New York and Michigan salts are bedded and of Silurian age. The Grand Saline salt is a dome deposit. In general, there appear to be only slight differences in the deformational behavior of the salt from the mines at Lyons, Hutchinson, Detroit, and Grand Saline. For the Retsof salt, there is initially a much greater rate of deformation upon application of load at room temperature than is the case with the salt from the other localities. However, after the initial deformation, the Retsof mine salt then deforms at a much slower rate. The reasons for these differences in behavior are not known at the present time.

Effects of Pillar Shapes

The width-to-height ratio of salt pillars is an important consideration in predicting mine closure. This is illustrated in Fig. 3.11, which shows pillar deformation with time for models having width (diameter) to height ratios of 2, 3, and 4. All pillars were originally 1 in. in height, while their widths were 2, 3, and 4 in. From the curves it is seen that pillar shortening proceeds at a faster rate with the smaller diameter-to-height models. Thus pillar strength increases with increasing width-to-height ratios. In addition to these tests, models having rectangular-shaped pillars were deformed. (All previously deformed model pillars were cylindrical in shape.) To date tests have been conducted only with the lengths of the pillars twice their widths, and under a pillar stress of

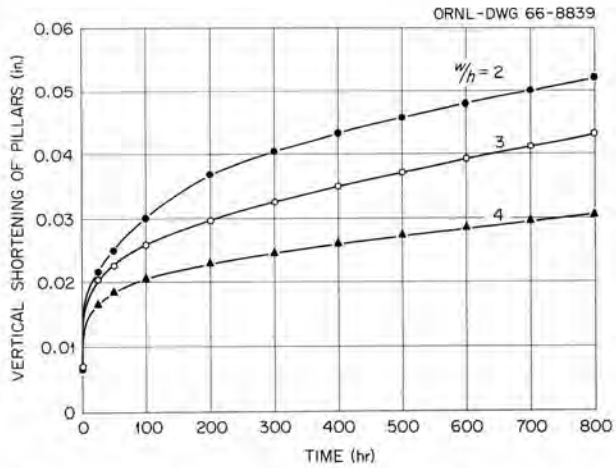

Fig. 3.11. Deformation of Model Salt Pillars at 4000 psi, 22.5°C, and Width-to-Height Ratios of 2, 3, and 4.

4000 psi at room temperature. Under these conditions, there do not appear to be any significant differences in pillar deformation as compared to the cylindrical-shaped specimens with the same horizontal cross-section area.

DISPOSAL OF HIGH-LEVEL WASTE IN SELECTED ROCK FORMATIONS

T. F. Lomenick

Even though salt is believed to be the most suitable environment for the ultimate disposal of high-level waste and its occurrences are rather widespread throughout the country, salt does not underlie any of the major AEC laboratories and plants that are currently engaged in fuel reprocessing or waste disposal. In addition, of the six geologic basins recently discussed by the AAPG for radioactive waste-disposal potential, only three contain salt deposits.[9] Thus, even though high-level waste could be shipped to areas where salt structures are available for ultimate disposal, it is likely that high-level wastes could be safely and economically disposed of in other rock types that may be available at any given site or possibly nearby.

Dry mine workings are probably not as commonplace as are wet mines in the United States. However, thick and relatively undisturbed beds of limestone and shale, and even granite and other crystalline rocks, exist that are essentially free of circulating water. For instance, in Barberton, Ohio, a dry 2000-ft-deep limestone mine is in operation.[10] Also, mined caverns in chalk near Demopolis, Alabama, have been found to be free of water.[11] Excavations in thick shale beds in Illinois have remained dry since they were opened.[12] In Ontario, Canada, it is reported that a mine in crystalline rocks has remained free of water even though the mine is directly beneath a large lake.[13] Loess deposits offer another possibility for the disposal of high-level waste in some areas above the water table.[14] Evaporite deposits other than rock salt, like potash, trona, anhydrite, gypsum, etc., may also be suitable.

For hard rock, such as limestone and granite, it is expected that mined cavities will remain stable under loads up to several thousand psi and temperatures up to a few hundred degrees centigrade. Recent model pillar tests on samples of dolomite from a local quarry show that there are negligible amounts of deformation in the rock up to loads of 10,000 psi and temperatures as high as 200°C. In comparison, it is of interest that under similar pillar model tests for rock salt at temperatures of 200°C and 6000 psi, the pillar deformation had exceeded 35% after only 1 hr.

---

[9] J. E. Galley (chairman), *Radioactive Waste Disposal Potential in Selected Geologic Basins*, SAN-413-2, AAPG (1964).

[10] Oliver Bowles, *Limestone and Dolomite*, U.S. Bur. Mines, Inform. Circ. 7738 (1956).

[11] W. G. Pierce and E. I. Rich, *Summary of Rock Salt Deposits in the United States as Possible Storage Sites for Radioactive Waste Materials*, Geological Survey Bulletin 1148, p. 78.

[12] H. H. Hess (chairman), *The Disposal of Radioactive Waste on Land*, Natl. Acad. Sci. – Natl. Res. Council, Report of Committee on Waste Disposal of the Division of Earth Sciences, Publ. 519, p. 100 (1957).

[13] *Ibid.*, p. 99.

[14] *Ibid.*, p. 98.

4. Application of Mineral Exchange to Reactor Technology

D. G. Jacobs Y. E. Kim[1]
O. M. Sealand

DISPOSAL OF GASES INTO PERMEABLE FORMATIONS

Estimation of the Behavior of Radionuclides Discharged to the Ground in a Gas

The fission product inventory was estimated for a reactor originally containing 5.82×10^{25} atoms of ^{235}U which had been operated for 1000 days at a flux of 1.5×10^{13} neutrons cm^{-2} sec^{-1}. It was assumed that in the case of an incident, the fission products would be released as gases into a containment shell with a volume of 2.5×10^6 ft^3 (7.1×10^4 m^3). In the unrealistic case of complete fission product release as radioactive gases, the critical nuclide would be ^{90}Sr and the critical organ would be bone. The initial concentration of radioactive contaminants in the containment shell would be about 2×10^{11} times the 40 hr/week occupational $(MPC)_a$. Reduction in the level of hazard would correspond to decay of the ^{90}Sr.

A more commonly accepted limit of release into the containment shell is 100% of the noble gases, 50% of the halogens, and 1% of the solids. In this case ^{131}I is the critical nuclide, and the thyroid is the critical organ for about the first month; thereafter, ^{90}Sr is again the critical nuclide. If the gases were pumped immediately from the containment shell into the ground, one would expect rather rapid condensation of the nuclides that are normally solid. Part of the iodine would probably be in the form of methyl iodide and noncondensable. If we assume that 100% of the noble gases and 10% of the halogens remain in a gaseous state, ^{131}I is the critical nuclide during the first four months. It decays, leaving ^{85}Kr the limiting mobile nuclide thereafter.

If a volume of groundwater equal to the volume of the containment shell moves into the discharge zone and dissolves the released radionuclides, the hazard is even further reduced. This is due to the fact that a smaller volume of liquid is ingested than air is inhaled during a given time interval and water is less mobile than air in a porous medium (by a factor of about 100). Most of the dissolved solid fission products could undergo ion exchange with the formation minerals and move at a much slower rate than the groundwater.

For the purposes of calculations, it was assumed that groundwater would flow at a rate of 1 ft/day and would be dispersed with a theoretical plate height of 50 ft. The delay factors due to ion exchange were assumed to be 100 for strontium and most other elements, 200 for rare earths, 10,000 for cesium, and 10 for ruthenium. Table 4.1 lists the nuclides that would present the most serious contamination problems. The times given are the times required before radioactive decay, plus dispersion and ion exchange, in the formation reduces the concentration levels to permissible limits. The distance of migration is the maximum extent of longitudinal movement of a front at the permissible concentration before decay occurs. If the flow occurred radially, or if there was appreciable lateral dispersion, the extent of movement could be considerably reduced.

[1]Alien guest from Korean AEC.

Table 4.1. Expected Extent of Movement of Fission Products in the Ground

Nuclide	Distance of Migration (ft)	Time Required for Decay and Dispersion (years)
^{90}Sr	1600	380
^{90}Y	400	220
^{106}Ru	400	11
^{131}I	300	0.4
^{132}I	200	0.4

From these exercises one can conclude that the relative hazard due to release of airborne activity from a reactor incident could be markedly reduced by pumping the gases into the ground. The delay time afforded, especially for condensable radionuclides, would greatly reduce the spread of contamination. Strontium would most likely present the most serious contamination of local groundwater, if it were released to the extent of 1%, but its extent of movement would be about 1600 ft in an area where the groundwater moves at a mean velocity of 1 ft/day. The vertical extent of movement would be expected to be at least an order of magnitude lower, so no contamination of a second aquifer should occur.

Adsorption of Iodine by Minerals

A numerical error was found in the previous calculations of the activation energy of desorption of iodine from Clinch River sediment. Subsequent calculations show that the corrected value for the activation energy for desorption ranges from 14.2 kcal/mole at a loading of 10^{-10} mole of I_2 per square centimeter to 54 kcal/mole at a loading of 10^{-11} mole of I_2 per square centimeter. These values for the activation energy of desorption are consistent for a system containing condensed I_2 (energy of sublimation = 14.66 kcal/mole) plus some chemisorbed iodine on the mineral surfaces. Previously, it has been necessary to postulate that some of the I_2 vapor had been converted to HI in order to account for the low values obtained for the activation energy.

It is difficult to compare the adsorption of iodine gas by different clays measured in individual nonflowing systems, because the equilibrium concentration of iodine in the gaseous phase is likely to be different. An ordinary flow system also presents difficulties. Iodine was so readily adsorbed that nothing could be detected at the effluent end of a 1½- by 12-in. core after several days of testing. Therefore, an arrangement was devised whereby several clays could be tested in a single flow system. A 1-in. double-thickness glass column was used as the main reaction vessel (Fig. 4.1). The clay samples consisted of ⅛-in.-diam glass rods, coated with a clay paste and then dried. Five samples could be placed on a rack that held the samples centered in the reaction vessel. At each end of the reaction vessel was placed a diffusion tube,[2] which consists of 1 ft of silver-plated copper tubing, 1 ft of rubber hose, and 1 ft of charcoal-coated copper tubing. The diffusion tubes give a relative measure of the concentration of iodine at the two ends of the reaction vessel. The influent end is attached to a U-tube, into which radioactive I_2 has been previously condensed. The effluent from the two diffusion tubes and from the reaction vessel can be regulated.

A run was made testing I_2 sorption by Wyoming bentonite, illite, kaolinite, vermiculite, and Clinch River floodplain sediment at room temperature. The total input was 1140 μc, and the recovery was 80% (Table 4.2). Based on the relative flow rates, one would have expected a total of 143 μc to have entered the first diffusion tube and 103 μc into the second. However, the concentration profile of iodine deposited in the diffusion tube indicated a loss of only about 2.5% of the amount entering each diffusion tube. A second run was made using a much lower amount of iodine tracer, and the losses from the diffusion tubes and the main reaction line were measured by collecting the effluent iodine in bubblers. The losses were quite low. In both runs the sorption of iodine by the clays was closely related to their surface area (Table 4.3). The amount sorbed by the Clinch River floodplain sediment was high in both runs; this may be due to the presence of organic material in this material.

[2]W. E. Browning, Jr., R. D. Ackley, and R. E. Adams, *Nuclear Safety Program Semiann. Progr. Rept. Dec. 31, 1963*, ORNL-3547, pp. 60–64 (1964).

ORNL-DWG 66-8840

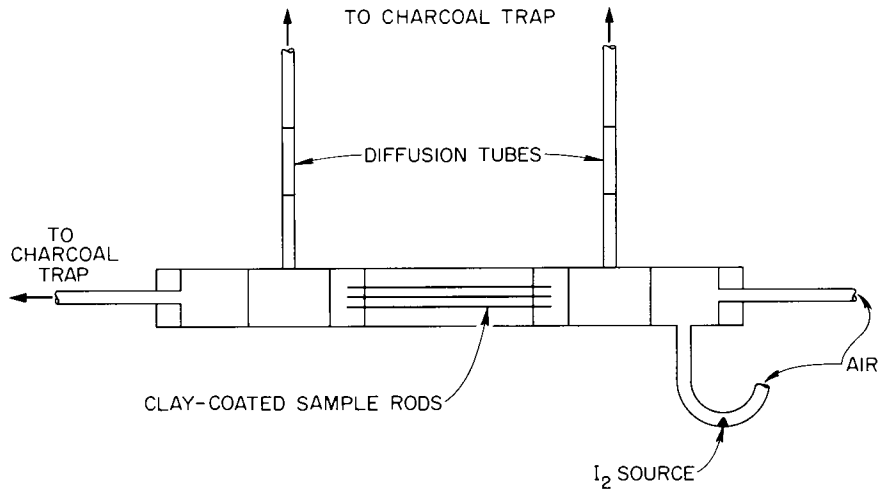

Fig. 4.1. Schematic of the System Used to Measure I_2 Sorption by Clays in a Flowing System.

Table 4.2. Mass Balance of Iodine in Flowing Sorption Experiments

	Run 1 (μc)	Run 2 (μc)
Total input	1140	5.105
Amount in U-tube after the experiment	554	4.191
Total adsorbed by clays	150	0.102
Amount recovered in first diffusion tube	39	0.097
Amount recovered in second diffusion tube	20	0.037
Total recovered	763	4.427
Estimated losses		
First diffusion tube	1	
Second diffusion tube	<1	
Reaction vessel	150	
Total accounted for	914	
Measured losses		
First diffusion tube		<0.001
Second diffusion tube		<0.001
Main reaction vessel		0.026
Total accounted for	914	4.453

Dissolution of Methyl Iodide by Water

Although methyl iodide (CH_3I) is not appreciably adsorbed onto mineral surfaces, it is soluble in water to the extent of 0.096 *M* at 22°C.[3] Methyl iodide was tagged with ^{131}I, and its vapor was bubbled through a container of distilled water and through a water-saturated Berea sandstone core. After the effluent showed no further increase in activity level, the water in the two systems was sampled and assayed for iodine. The concentration was found to correspond to 0.0061 ± 0.0003 *M* for the water in both systems. When the solution was allowed to stand over the weekend, the concentration dropped to 0.00014 *M* CH_3I.

These observations suggest that in moist formations the movement of part of the released CH_3I may be delayed by dissolution from the gas phase into the slower-moving phase.

Nuclear Safety Pilot Plant Runs

A sorption pack containing two 115-g samples of Berea sandstone followed by three 18-g sam-

[3]A. Seidell, *Solubilities of Organic Compounds*, p. 35, Van Nostrand, New York, 1941.

Table 4.3. Sorption of Iodine by Clays in a Flow System

Clay	Surface Area (m^2/g)	Run 1 Iodine Adsorbed ($\mu c/g$)	Run 1 Iodine Adsorbed ($\mu c/m^2$)	Run 2 Iodine Adsorbed ($\mu c/g$)	Run 2 Iodine Adsorbed ($\mu c/m^2$)
Wyoming bentonite	64	34	0.54	0.025	0.00039
Illite	58	32	0.55	0.019	0.00032
Vermiculite	3.6	5.7	1.58	0.0011	0.00031
Kaolin	14	4.2	0.31	0.011	0.00081
Clinch River floodplain sediment	4.3	3.5	0.81	0.012	0.00272

Table 4.4. Sorption of Iodine and Cesium by Clays in NSPP Run 11

	^{131}I (dis/min)	^{144}Ce (dis/min)
	$\times 10^3$	$\times 10^3$
Conasauga shale	540 ± 11	72 ± 9.8
BO-4 Zonolite	92 ± 2	12 ± 1.8
Exfoliated Zonolite	46 ± 1.1	4.1 ± 9.2
Berea sandstone	31 ± 0.7	4.4 ± 0.62
Charcoal	400 ± 5	34 ± 4.8
Charcoal	1.7 ± 0.15	0.32 ± 0.15

ples of charcoal was placed in the gaseous effluent line of the Nuclear Safety Pilot Plant for run 10. The activity levels of the released gas were too low to obtain satisfactory results, but the two samples of sandstone sorbed enough iodine to give 131 ± 31 and 88 ± 30 disintegrations of ^{131}I per minute, compared with 295 ± 44 for the first charcoal sample. No ^{85}Sr, ^{106}Ru, or ^{134}Cs was detected on any of the samples. On sandstone samples 1 and 2, 196 ± 90 and 102 ± 86 disintegrations of ^{134}Cs per minute were detected, but none was detected on the charcoal.

In run 11 the sorption pack contained, in order, Conasauga shale (62 g), BO-4 Zonolite (28 g), exfoliated Zonolite (16 g), Berea sandstone (84 g), and two 18-g samples of charcoal. No ^{85}Sr, ^{134}Cs, or ^{106}Ru was detected on any of the samples. Iodine-131 and cerium-144 were sorbed as shown in Table 4.4.

It has been suggested that the most important difference between runs 10 and 11 was a change in the furnace atmosphere from reducing conditions in run 10 to oxidizing conditions in run 11, causing HI release in run 10 and I_2 release in run 11.[4]

NONEQUILIBRIUM ION EXCHANGE

A computer program has been written to describe the transient behavior of radionuclides in the ground when the transporting solution is of a different concentration than the original groundwater. The program is based on Glueckauf's model for the passage of a wide band of solute through a chromatographic column, modified for changes in the adsorptive capacity due to changes in the total electrolyte concentration and for nonequilibrium sorption conditions.

Experimentally, a Berea sandstone core was presaturated with 0.001 *N* $CaCl_2$ to represent groundwater. Then radiostrontium was introduced in 0.05 *N* $CaCl_2$; volumes were injected corresponding to about 200%, 100%, etc., of the volume required to reach 50% breakthrough in a system containing only 0.05 *N* $CaCl_2$. Following the introduction of the tracer, leaching was accomplished using 0.001 *N* $CaCl_2$ to correspond to the return to the original conditions.

[4] *Oak Ridge National Laboratory Status and Progress Report, October 1965*, ORNL-3886, p. 18 (Nov. 4, 1965).

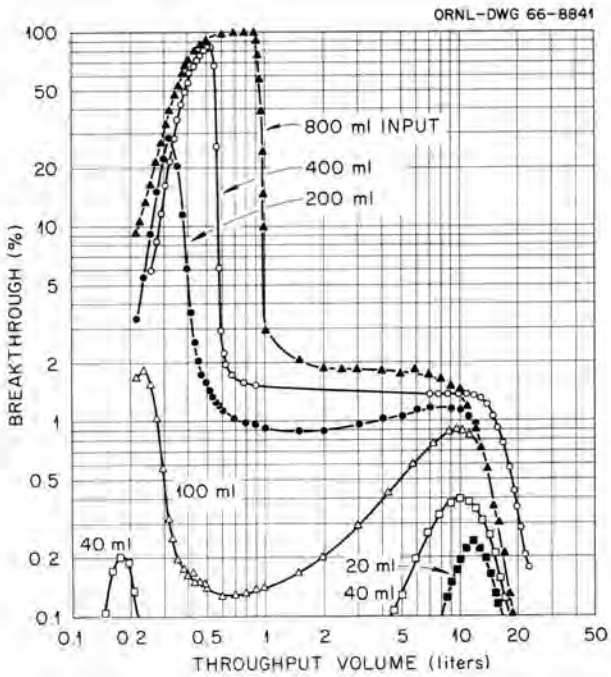

Fig. 4.2. Experimental Curves for the Breakthrough of ^{85}Sr from a Berea Sandstone Core when Injected in 0.05 *N* $CaCl_2$ and Leached with 0.001 *N* $CaCl_2$.

Experimental data show that the curves have the correct properties (Fig. 4.2). The computer program is being modified to process the data and, using K_d and the theoretical plate height as adjustable variables, to best fit the curves.

HYDROXIDE CONSUMPTION BY CONASAUGA SHALE

In the vicinity of the intermediate waste trenches small seeps have developed in which the pH of the seeping waters has been gradually increasing. It was felt that the increase in pH constituted a warning that only a small amount of the shale was being contacted by groundwater moving from the trench to this seep and that a breakthrough of ^{90}Sr might be expected.

Samples of Conasauga shale were placed in solutions of different pH and allowed to stand overnight. The equilibrium pH was measured, and the consumption of hydroxyl ions was calculated. The sorption of ^{85}Sr was also measured in each solution. At pH 12 in 0.1 *M* sodium the K_d for ^{85}Sr is 143 ml/g and the K_d for hydroxyl ion is about 10 ml/g. This indicates that the strontium front leaving the waste trench would require approximately 14 times as long to reach the seep as did the hydroxyl ion front. The severity of the problem will depend on the quantity of water carried through this seep.

BEHAVIOR OF CURIUM IN MINERAL EXCHANGE SYSTEMS

Preliminary experiments have begun on the behavior of curium in the ground. Because of the extreme hazard of the transuranic nuclides, the experiments must be confined in a glove box and the quantity of the nuclide used as a tracer must be kept to a minimum. As a result, data collection is slow.

Sorption of curium by several clays was measured in distilled water tagged with ^{242}Cm and adjusted to pH 7 by addition of NaOH or HNO_3 (Table 4.5). One gram of clay was used in 25 ml of solution. Sorption of the ^{242}Cm does not appear to be related to the exchange capacity. In fact, the increased sorption from 0.1 *M* NaCl suggests that ion exchange is probably not the major reaction. It is interesting to note that in the case of the distilled water systems the Wyoming bentonite would not centrifuge out; the higher salt concentration permits flocculation to occur. When the solutions were made basic (about pH 9), sorption was increased, whereas acidification to pH 2 to 3 reduced the sorption in all cases. This, again, suggests that precipitation reactions, rather than ion exchange, are the dominating removal mechanisms.

To check the effect of pH, 0.1 *M* NaCl solution, tagged with ^{242}Cm, was adjusted to various pH values ranging from 2 to 11 (Table 4.6). Three series were run with no clay added; in two other series illite and Conasauga shale were added after they had been equilibrated in untagged 0.1 *M* NaCl solution of the proper pH for several days. The results of these tests are shown in Table 4.6. Even without clay some of the ^{242}Cm is removed from solution at high pH. This can be due either to a precipitation reaction or to sorption on the glass centrifuge wall. The slight decline in removal above pH 8 suggests peptization of a radiocolloid, but the data are not sufficiently precise to warrant a positive statement. When clay is added, sorption is considerably increased,

Table 4.5. Sorption of Curium by Various Clays

1 g of clay per 25 ml solution

Clay	Exchange Capacity (meq/100 g)	Sorption (%)			
		Distilled Water		0.1 *M* NaCl	
		Neutral	Basic (pH ~9)	Neutral	Acid (pH 2–3)
Illite	15	99.6		99.98	79
Vermiculite	57	73		96.8	96
Kaolinite	7	68		99.96	91
Conasauga shale	12	89		99.6	92
Limestone	~1	99.8	99.8	99.96	88
Wyoming bentonite	71	6[a]	22[a]	99.94	98
Clinoptilolite	~150	99.8	99.9	99.9	76
Berea sandstone	7	77	98.8	99.1	81

[a]The Wyoming bentonite suspension would not centrifuge out after 20 min.

Table 4.6. Effect of pH on the Sorption of Curium from 0.1 *M* NaCl

pH	Curium Activity Removed from Solution (%)			
	No Clay[a]	Conasauga Shale[b]	Illite	Illite (Leach)
2	0	33	56	79
3	3	65	74	83
4	10	95	91	97.6
5	28	98	93	97.7
6	38	>99	>99	99.96
7	57	>99	>99	99.95
8	45	98	>99	99.95
9	47	99	>99	99.93
10	47	99	>99	99.98
11	42	86	>99	99.76

[a]The solution of pH 2 was used as the basis for comparison.

[b]One gram of clay per 25 ml of solution.

suggesting a need for a suitable surface for deposition of the precipitate formed or for exchange to occur.

When leaching of the contaminated illite was attempted under the same solution conditions as the sorption step, removal was less than expected (Table 4.6). This suggests that a portion of the original ^{242}Cm is not of the same form as that adsorbed and that in a continuous system there could well be a finite "leakage" even though the major portion of the curium was adsorbed. If this is the case, curium might be found to behave like ruthenium in the waste pits. This possibility will be checked in the next series of tests.

INTERPRETATION OF CATION EXCHANGE BY ALUMINA

Recent data on ion exchange by alumina published by Belot *et al.*[5] have been treated on the basis of weak acid exchange and Gouy-Chapman electric double-layer theory. The unextended electric double-layer theory provides a good framework for depicting the cation exchange behavior of alumina. However, attractive forces for alkaline-earth cations exceed those predicted by the Gouy-Chapman theory. The magnitude of the divalent cation attraction lies outside the range of deviation predicted by Bolt[6] on the basis of

[5]Y. Belot, C. Gailledreau, and R. Rzekiecki, "Retention du strontium-90, du calcium-45 et du baryum-140 par un oxyde d'aluminium de grande surface," *Health Phys.* (1966), in publication.

[6]G. H. Bolt, *J. Colloid Sci.* 10(2), 206 (1955).

extensions to the electric double-layer theory; this suggests specific attractive forces between divalent alkaline-earth cations and the alumina surface.

Alumina behaves like a weak acid exchanger with an effective acid dissociation constant of 2.0×10^{-10} having surface ionogenic groups to the extent of 4.5×10^{-7} meq/cm^2. When these parameters are used to calculate the effective exchange capacity of alumina in solutions used by Belot *et al.*,[5] the "equimolar" exchange exhibited by alumina can be readily explained (Table 4.7). This approach also predicts that the slope of a plot of log (Sr K_d) vs log sodium salt concentration should be about −0.7 in the range of concentrations employed by Belot *et al.*[5] and by Tamura[7] instead of a slope of −2 expected on the basis of strong acid ion exchange.[6] This predicted slope agrees quite well with the values of −0.69 reported by the workers.

Table 4.7. Comparison of Measured and Calculated Exchange Capacities of Alumina

pH	Concentration		Measured Exchange Capacity[a] (meq/g)	Calculated Exchange Capacity[b] (meq/g)
	Na^+ (*M*)	Ca^{2+} (*M*)		
10	0.1	0.0	0.12 ± 0.05	0.125
10	0.0	0.1	0.26 ± 0.02	0.225
12	0.1	0.0	0.43 ± 0.02	0.494
12	0.0	0.1	0.84 ± 0.04	0.810

[a]Data of Belot *et al.*[4]

[b]Calculated on the basis of a total concentration of ionogenic groups of 0.89 meq/g and an effective acid dissociation constant of 2.02×10^{-10}.

[7]T. Tamura, W. P. Bonner, and T. Murano, *Health Phys. Div. Ann. Progr. Rept. July 31, 1964*, ORNL-3697, pp. 49–52 (1964).

5. Engineering, Economic, and Safety Evaluations

K. E. Cowser W. J. Boegly, Jr. D. G. Jacobs

CLINCH RIVER SAFETY ANALYSES

Based on recent information, a preliminary assessment of the importance of metabolic processes of children and adults in estimating internal dose has been made. In particular, Kulp and Rivera have examined the effects of bone growth, rate of bone turnover, and the ratio of strontium to calcium in bone to that in diet on the retention of ^{90}Sr in the skeleton of man.[1,2] The difference equation for the age-dependent metabolic model developed by Kulp can be expressed as:

$$S_n = S_{n-1} - (f_n + \lambda)S_{n-1} + K_n \frac{I_n C_n}{G_n} [f_n \mathrm{Ca}_{n-1} + (\mathrm{Ca}_n - \mathrm{Ca}_{n-1})] ,$$

where

S_n = picocuries of ^{90}Sr skeleton burden at time n,

f_n = fractional bone turnover rate during the period from time $n - 1$ to time n,

λ = ^{90}Sr radiological decay constant per period,

K_n = $(\mathrm{Sr/Ca})_{\mathrm{bone}}/(\mathrm{Sr/Ca})_{\mathrm{diet}}$,

I_n = fluid intake (liters/day),

C_n = ^{90}Sr concentration in water (picocuries/liter),

G_n = calcium intake (g/day),

Ca_n = calcium content of skeleton (g).

The equation relates the loss and gain of ^{90}Sr during the period of interest and is based on calcium metabolism. Bone turnover is defined as the quantity of calcium that enters and is then excreted from the skeleton. The fractional bone turnover rate, f_n, is the bone turnover rate divided by the quantity of calcium contained in the skeleton. Strontium-90 in the skeleton is lost as a result of bone turnover and radiological decay and is gained by bone remodeling and bone growth.

With the age-dependent metabolic model, estimates were made of the dose received by the skeleton from ingestion of Clinch River water.[3] Values of calcium intake and calcium content of the body were taken from Albritton and Mitchell respectively;[4,5] values of bone turnover rate and the observed ratio were from Rivera. For the age groups considered, the metabolic model gave an average dose equivalent 15% larger than the adjusted ICRP model.[6] In all cases the cumulative dose was at least a factor of 10 less than permissible limits established by ICRP. Unquestionably, changes can be expected in values of metabolic factors as new information becomes available.

The operation of Melton Hill Dam at Clinch River mile (CRM) 23.1 has changed the hydraulic pattern of releases of radioactive waters from White Oak Creek (CRM 20.8) into the Clinch River. From field tests it was determined that the minimum

[1] J. L. Kulp, *Radioactive Fallout from Nuclear Weapons Tests, Proceedings of a Conference Held in Germantown, Maryland, November 15–17, 1961*, TID-7632, p. 457 (1962).

[2] J. Rivera and J. H. Harley, *The HASL Bone Program 1961–1964*, HASL-163, p. 7 (1965).

[3] Calculations were performed by H. J. Fisher, U.S. Public Health Service, while working with the Internal Dose Estimation Section, Health Physics Division.

[4] E. C. Albritton, *Standard Values in Nutrition and Metabolism*, W. B. Saunders Company, 1954.

[5] H. H. Mitchell *et al.*, *J. Biol. Chem.* **158**, 625 (1945).

[6] K. E. Cowser and W. S. Snyder, *Safety Analyses of Radionuclide Release to the Clinch River*, ORNL-3721, suppl. III (May 1966).

dilution at the peak concentrations at CRM 14.4 was 54 for summer conditions and 17 for winter conditions, compared with the previous medium daily dilution of 570.[7] These concentrations persist for only short periods of time. Since the concentrations can be averaged over a year for estimating dose equivalents and the total amounts of radionuclides released have decreased, it is felt that no additional hazard has been created by power releases at Melton Hill Dam. A proportional sampling station was completed at Melton Hill Dam, and another is under construction at Gallaher Bridge (CRM 14.5) to permit mass-balance analyses of data collected and to verify predictions of radionuclide concentration in the Clinch River.

^{85}Kr AND TRITIUM IN AN EXPANDING WORLD NUCLEAR POWER INDUSTRY

As the free world's nuclear power production increases, the buildup of ^{85}Kr and ^{3}H in the atmosphere may become important. Estimates of dose equivalents to the year 2000 from a uniform worldwide distribution of these radionuclides were made.

Estimates of the annual production rate of ^{85}Kr and ^{3}H were based on the AEC projected civilian nuclear power economy in the United States and the free world (Table 5.1).[8,9] The yield and physical half-life of ^{85}Kr were taken to be 3×10^{-3} atom/fission and 10.27 years respectively.[10] Tritium was considered to be produced at 10^{-4} atom/fission and to have a physical half-life of 12.36 years.[11,12] Additional assumptions included a load factor of 0.80 to year 1980 and 0.70 at year 2000, thermal efficiency of 0.31, irradiation level of 20,000 Mwd/metric ton, and specific power of 25 Mw/metric ton. Based on these assumptions, 3150 megacuries of ^{85}Kr and 96 megacuries of ^{3}H will be accumulated by the year 2000.

[7] F. L. Parker *et al.*, "Dilution, Dispersion, and Mass Transport of Radionuclides in the Clinch-Tennessee Rivers," presented at the *Symposium on the Disposal of Radioactive Wastes into Seas, Oceans, and Surface Waters, Vienna, Austria, May 16–20, 1966.*

[8] *Estimated Growth of Civilian Nuclear Power*, WASH-1055 (March 1965).

[9] *Civilian Nuclear Power, Appendices to a Report to the President*, USAEC, 1962.

[10] J. O. Blomeke and M. F. Todd, *Uranium-235 Fission-Product Production as a Function of Thermal Flux, Irradiation Time, and Decay Time. 1. Atomic Concentrations and Gross Totals*, ORNL-2127, Part 1, vol. 1 (August 1957).

[11] E. L. Albenesium and R. S. Ondrejcin, *Nucleonics* 18(9), 100 (1960).

[12] J. F. Eichelberger, G. R. Grove, and L. V. Jones, *Mound Laboratory Report for September 1963*, MLM-1176.

Table 5.1. ^{85}Kr and Tritium Production in the Free-World Nuclear Power Economy

Year	Mw (electrical)[a]	Mw (thermal)[b]	Process Load[c] (metric tons/day)	^{85}Kr Production Rate[d] (curies/year)	Accumulated ^{85}Kr (curies)	^{3}H Production Rate[d] (curies/year)	Accumulated ^{3}H (curies)
	$\times 10^3$	$\times 10^3$		$\times 10^6$	$\times 10^6$	$\times 10^6$	$\times 10^6$
1965	1.9	6.2	0.31	0.96	0.96	0.027	0.027
1970	9.6	31	1.55	4.8	13	0.14	0.32
1975	46	150	7.49	23	60	0.66	1.7
1980	120	390	19.7	62	210	1.7	6.3
1985	240[e]	780	39	120	540	3.4	16
1990	430[e]	1300	67	210	1100	5.9	32
1995	670[e]	2200	110	340	1900	9.5	58
2000	1030	3320	166	520	3150	14.6	96

[a] Assumed load factor of 0.80 to year 1980 and 0.70 at year 2000.

[b] Assumed thermal efficiency of 0.31.

[c] Assumed irradiation level of 20,000 Mwd/metric ton.

[d] Assumed specific power of 25 Mw/metric ton, average core lifetime of 800 days, 8600 curies of ^{85}Kr per metric ton and 240 curies of ^{3}H per metric ton.

[e] Interpolated values.

^{85}Kr Distribution and Dose Equivalent

The concentration of ^{85}Kr in the atmosphere was estimated by assuming complete mixing in the first 8 miles of the atmosphere. Within this zone, ^{85}Kr was distributed according to the mass of air. Above 8 miles the tropopause would inhibit rapid mixing into the stratosphere.[13] Rainout was considered negligible, since calculations indicated that the atmosphere contained more than 95% of the stable krypton when compared with the oceans.[14]

The estimated whole-body exposure from ^{85}Kr according to elevation is shown in Fig. 5.1. A maximum dose rate of 1.8 millirems/year in the first ¼ mile of the atmosphere can be compared to an average background radiation of 100 millirads/year (to gonads) near sea level and to permissible whole-body exposures of average population groups of 170 millirems/year as recommended by ICRP and FRC.[15,16]

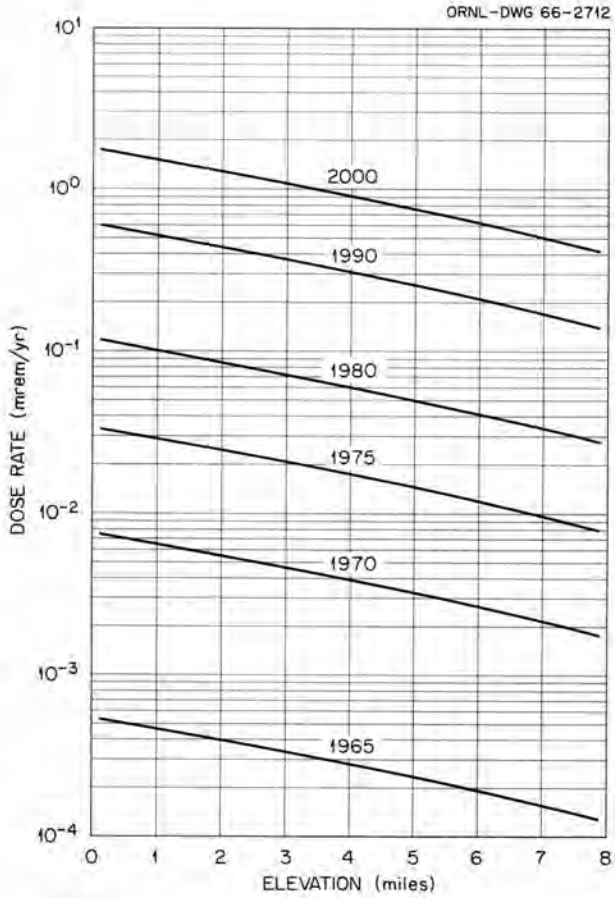

Fig. 5.1. Dose Rate from ^{85}Kr in the Atmosphere According to Elevation.

Tritium Distribution and Dose Equivalents

Practically all the tritium in irradiated fuel elements may be released to the environment during reprocessing.[17] This tritium will usually be converted to the oxide form quite rapidly and dispersed like ordinary water. The concentration of tritium in circulating waters of the world was estimated by assuming that tritium was mixed in oceans and seas to a depth of 40 m, that all the water in stream channels and in the atmosphere was circulating, that only that part of the groundwater in the root zone was available for mixing, and that complete isotopic dilution occurred with all circulating waters. The volumes of the various reservoirs of water are given in Table 5.2.

The estimated dose equivalents to body tissue due to inhalation of air and to ingestion of drinking water containing ^{3}H are shown in Fig. 5.2. At

Table 5.2. Volumes of Circulating Water in the World

	Volume of Water (m^3)	
	Total	30°–50° North Latitude
Oceans and seas (surface, 40 m)	1.44×10^{16}	1.43×10^{15}
Stream channels (average)	1.17×10^{13}	2.51×10^{12}
Atmospheric moisture (average)[a]	1.29×10^{14}	1.72×10^{13}
Subsurface water in the root zone	2.50×10^{14}	5.38×10^{13}
Total circulating	1.48×10^{16}	1.50×10^{15}

[a]Water vapor in the first 10 km of the earth's surface.

[13]L. Machta, "Status of Global Radioactive-Fallout Predictions," *Radioactive Fallout from Nuclear Weapons Tests, Proceedings of the Second Conference, Germantown, Maryland, November 3–6, 1964* (November 1965).

[14]H. Hintenberger *et al.*, *Z. Naturforsch.* **19a**, 1227–28 (1964).

[15]*Report of Committee II on Permissible Dose for Internal Radiation*, International Commission on Radiological Protection, Publication 2, Pergamon, London, 1959.

[16]*Background Material for the Development of Radiation Protection Standards*, Report No. 1, Staff Report of the Federal Radiation Council (May 18, 1960).

[17]J. O. Blomeke, internal memorandum, 1964.

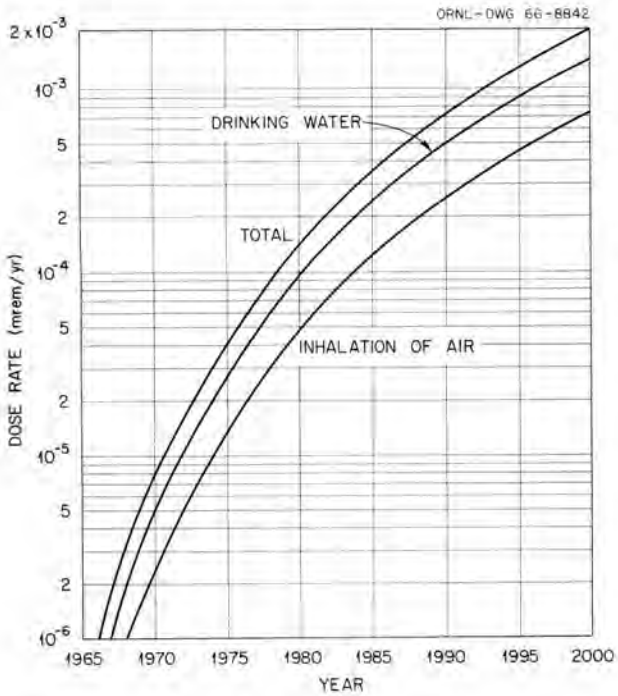

Fig. 5.2. Dose Rate to Body Tissue from ^3H by Inhalation and by Ingestion of Drinking Water.

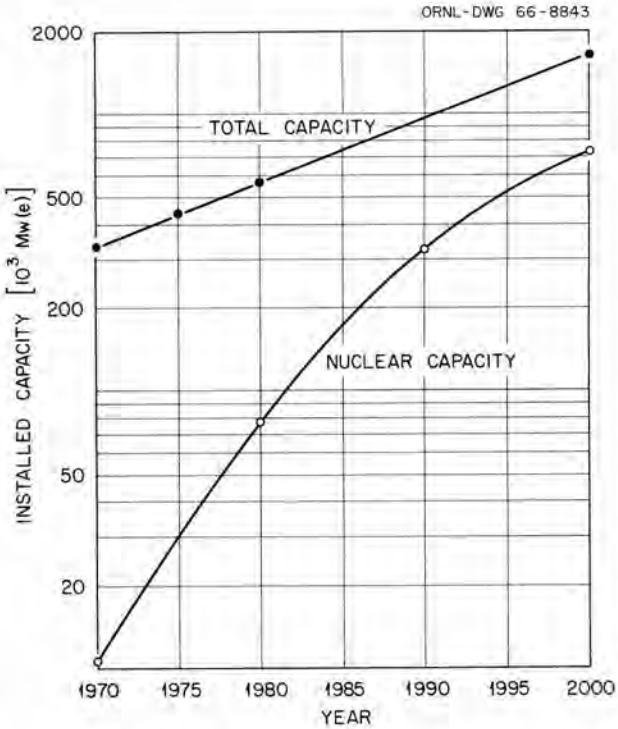

Fig. 5.3. Growth of Generating Capacity in the United States, 1970 to 2000.

year 2000 the average annual dose from inhalation is 7.2×10^{-4} millirem and from drinking water is 1.4×10^{-3} millirem. Nonuniform distribution of tritium has been indicated by Libby, such that half the tritium released from detonation of thermonuclear devices before the weapons test moratorium in 1958 had fallen between 30 and 50° north latitude.[18] If this remains true for releases of tritium from fuel-reprocessing plants, then approximately 10% of the earth's surface will receive half the total tritium. The average dose equivalents in this area may be five times the world average.

LONG-RANGE WASTE MANAGEMENT STUDY

The rapid growth of the nuclear power industry and the expanding use of radioisotopes by industry and government will influence the location, type, and magnitude of waste disposal. A long-range waste management plan is essential. Study has been initiated to estimate the regional productivity of radioactive wastes and their characteristics to the year 2000 and to provide guidelines for the management of these wastes. A committee composed of members of several ORNL divisions (Health Physics, Reactor, Chemical Technology, and Isotopes) has been organized to obtain input information for the waste management study.

A number of estimates have been made in the past five years of the growth of the electrical industry to the year 2000 and the portion of total electrical requirements that will be supplied by nuclear power plants. These include the estimates of the Atomic Energy Commission in 1962,[9] the estimates of Resources for the Future (RFF) in 1963,[19] and the Federal Power Commission (FPC) in its National Power Survey in 1963.[20] Since the estimates of the AEC and the FPC are in agreement, it has been decided to use the AEC estimates (the nuclear estimates for 1980 being further revised in 1965[8]) as the basis of the waste management study. Figure 5.3 shows the assumed growth in total and nuclear energy generation in the United States.

[18] W. F. Libby, *J. Geophys. Res.* **68**, 4485 (1963).

[19] H. Landsberg, L. Fischman, and J. Fisher, *Resources in America's Future*, published for Resources for the Future, Inc., by the Johns Hopkins Press, 1963.

[20] *National Power Survey*, vol. I and II, Federal Power Commission (October 1964).

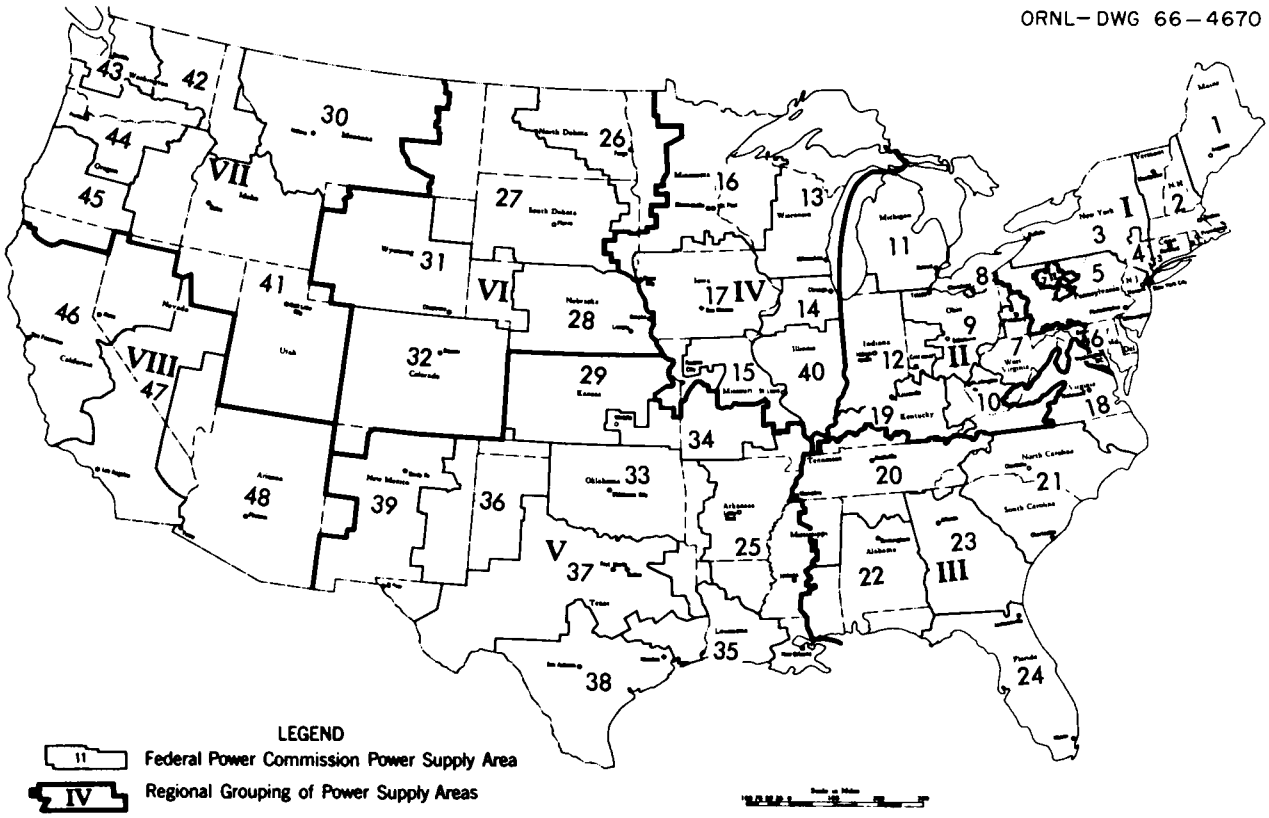

Fig. 5.4. Electric Power Supply Areas.

Using the information presented in Vol. II of the National Power Survey,[20] it is possible to forecast the growth in total electrical capacity required by various regional areas of the United States up to the year 2000. The regional areas selected for this study are the eight Regional Power Supply Areas defined by the Federal Power Commission and shown in Fig. 5.4.

Nuclear forecasts were developed using the total installed nuclear capacity estimated by the AEC,[9] the estimated regional installed capacity for 1980 from the National Power Survey,[20] and the estimating procedures used by the AEC in forecasting requirements from 1965 to 1980.[8] Table 5.3 shows the resulting estimates of nuclear capacities for the eight regions for the period 1970 to 2000.

Regional Waste Volumes

As a first approximation of the magnitude of the waste management problem from power reactors only, waste volumes were calculated for each region using the following assumptions:[21]

1. Reactor thermal efficiency increases linearly from 32% in 1970 to 44% in the year 2000.
2. The reactor capacity factor is 80% until 1980, after which it decreases linearly to 70% in 2000.
3. Fuel burnup is 20,000 Mwd/ton in 1970, 25,000 Mwd/ton in 1980, 40,000 Mwd/ton in 1990, and 60,000 Mwd/ton in 2000.
4. There is a three-year delay between power generation and fuel processing (waste production).
5. High-level waste volumes will be 100 gal of acid waste per 10,000 Mwd (thermal) of fuel burnup.

[21] J. O. Blomeke, Chemical Technology Division, ORNL, personal communication to W. J. Boegly, Jr., ORNL, May 1966.

6. Intermediate-level waste volumes will be 200 gal per ton of fuel processed.

The results of these calculations are shown in Table 5.4 for the period 1973 to 2000. Low-level waste volumes for each region have not been calculated, but they will approximate 10,000 gal per ton of fuel plus some volume from each processing plant generated from cell drainage, decontamination, laboratory drains, etc.

The volumes listed in Table 5.4 are estimates based on assumed thermal efficiencies and fuel burnups and are intended to serve only as interim values until more detailed estimates of reactor types predominating in the various time periods have been developed. Not shown in Table 5.4 are the volumes of liquid wastes generated from the production of isotopes and the reprocessing of reactor fuels used to supply heat for water desalination or advanced waste-treatment plants. However, based on current information, the volume of wastes from these sources will probably not significantly change the volumes shown in Table 5.4 prior to the year 2000.

Table 5.3. Installed Nuclear Electrical Capacity (Mw) by Region in the United States, 1970 to 2000

Region	1970[a]	1980	1990	2000
	$\times 10^3$	$\times 10^3$	$\times 10^3$	$\times 10^3$
I	4.2	21	78	171
II	1.0	8	38	88
III	1.4	14	70	170
IV	3.4	10	38	88
V	0	1	6	16
VI	0.1	1	5	11
VII	0	5	24	56
VIII	0.5	17	59	135
Total	10.6	77	318	735

[a]Based on operating plants, orders, and estimates of startup of new plants in 1970. The Hanford "N" reactor is not included.

Table 5.4. Volumes of High- and Intermediate-Level Wastes Generated in the United States by Region, 1973–2000 (gal/yr)

Region	1973[a]		1980		1990		2000	
	High Level	Intermediate Level	High Level	Intermediate Level	High Level	Intermediate Level	High Level	Intermediate Level
	$\times 10^3$	$\times 10^3$	$\times 10^3$	$\times 10^3$	$\times 10^3$	$\times 10^3$	$\times 10^3$	$\times 10^3$
I	38.3	38	120	100	390	230	880	320
II	9.1	10	41	40	180	110	450	170
III	12.8	12	65	60	330	200	870	310
IV	31.0	30	54	50	190	110	440	170
V	0	0	2	4	30	16	80	30
VI	1.0	1	5	6	20	14	60	20
VII	0	0	16	20	120	70	270	100
VIII	4.5	5	84	70	310	180	660	250
Total	96.7	96.0	387	350	1570	930	3710	1400

[a]Based on operating plants, utility orders, and estimates of startup of new plants in 1970. Hanford "N" reactor is not included.

6. Related Cooperative Projects

COOPERATION OF OTHER AGENCIES IN ORNL STUDIES

The research and development program of the Radioactive Waste Disposal Section of this Division is of special interest to various public and private agencies. Several study projects provide an opportunity for others to participate, both to supplement the Laboratory's research effort and to gain information and experience of value to the other agency. The ways in which another agency may cooperate include assignment of on-loan personnel as temporary additions to the ORNL staff, performance of specific work under cooperative agreements to augment ORNL programs, work authorized under ORNL subcontracts and performed by the contracting agency, or coordination of related work projects with ORNL projects for mutual benefit.

Disposal in Salt Formations

Agencies participating in this program during the past year have included the U.S. Bureau of Mines and the Carey Salt Company of Hutchinson, Kansas, an ORNL subcontractor. The results of this cooperative program are given in Chap. 3.

SPECIAL PROJECT

Project Arkose

Members of the Radioactive Waste Disposal Section participated in a field exercise for the Vela On-Site Inspection Program conducted in Utah September 13 to October 3, 1965, under the sponsorship of the Advanced Research Projects Agency of the Department of Defense. Presite reconnaissance and source design, fabrication, placement, testing, recovery, and analyses were included in this cooperative study.

VISITING INVESTIGATORS FROM ABROAD

During the year, three noncitizen guests participated as temporary members of the research staff of the Radioactive Waste Disposal Section.

VISITING INVESTIGATOR ABROAD

Wallace de Laguna, staff geologist, spent the year at Mol, Belgium, and Cadarache, France, working on geological problems involved in the disposal of radioactive wastes.

NUCLEAR SAFETY REVIEW

One member of the Section served on the staff of *Nuclear Safety* as assistant editor. During the year, several individuals in the Section contributed review articles which were published under the category "Consequences of Activity Release."

HEALTH PHYSICS JOURNAL

One member of the Section served as assistant news editor of *Health Physics* for the United States.

COMMITTEE WORK

American Standards Association

Several members of the staff of the Radioactive Waste Disposal Section have continued to serve on working groups of ASA Sectional Committee N5, Nuclear Fuel Cycle Engineering, its subcommittee

N5.2, Radioactive Waste Disposal, and working group N5.2.2, Site Selection Criteria.

ASCE – Committee on Sanitary Engineering Aspects of Nuclear Energy

The Section Leader served as a member of the Committee on Sanitary Engineering Aspects of Nuclear Energy of the American Society of Civil Engineers.

NAS-NRC – Committee on Pollution

The Section Leader served as a member of the study groups which helped prepare *Waste Management and Control,* NAS-NRC Publication 1400.

PARTICIPATION IN EDUCATIONAL PROGRAMS

Two members of the Section participated in the cooperative program with the University of Tennessee and taught a graduate course, Stream Sanitation, in the Civil Engineering Department.

During the ten weeks of field training of the AEC Fellowship course in applied radiation physics at ORNL, three students were assigned to work five weeks in the Radioactive Waste Disposal Section under the supervision of four staff members.

Four lectures and a field tour of the Laboratory's waste disposal facilities and ecological research activities were provided at ORNL by the staff of the Section as part of the course conducted by the U.S. Public Health Service on "Reactor Safety and Environmental Health Problems."

NUCLEAR SAFETY INFORMATION CENTER

Two members of the Section served as part-time staff members of the Nuclear Safety Information Center.

Part II. Radiation Ecology

S. I. Auerbach

7. Responses of Animal Populations to Ionizing Radiation

B. G. Blaylock[1]
P. B. Dunaway
N. A. Griffith[1]
N. R. Kevern[1]
Lovell L. Lewis
T. P. O'Farrell[2]
J. A. Payne
J. D. Story

RADIATION SENSITIVITY IN INDIGENOUS SMALL MAMMALS

P. B. Dunaway
Lovell L. Lewis
J. A. Payne
J. D. Story

Laboratory measurements of radiation sensitivity in native small mammals are necessary because (1) radiation effects in these species under controlled conditions must be known before interactions between radiation and other environmental variables can be evaluated in natural populations and (2) interspecies and interfamily comparisons of radiation effects may demonstrate to what extent radiation responses are related to taxonomic status of the mammals.

Six species of rodents in the family Cricetidae, two species in the Muridae, and two species of shrews in the family Soricidae were irradiated at seven dose levels ranging from 500 to 2000 rads. After preliminary analyses of LD_{50-30} for the species, additional doses were given above and below the estimated LD_{50} doses in order to refine the estimates. Final probit analyses were made by computer with the ORNL "PROBIT" program (Table 7.1).

Estimates of LD_{50-30} ranged from 535 to 1050 rads. The most radioresistant and most radiosensitive species were both in the Cricetidae. Interestingly, the most radioresistant species both belonged to the genus *Peromyscus*. Shrews are known to have very high metabolic rates,[3] but LD_{50} estimates for the two species of soricids are about the same as for the wild murids and higher than for the radiosensitive *Oryzomys palustris*. Most of the species died within relatively narrow dose ranges, but the confidence range of *Microtus pinetorum* was extremely wide. We suspect that caging conditions were not adequate for the pine mouse, and this species actually may be more radioresistant than indicated.

The LD_{50} estimate for the RF-strain mice caged singly is considerably higher than the estimate for the mice caged together and higher than the estimate for the wild house mice caged singly (Table 7.1). However, the estimate for the female wild house mouse caged together is not significantly lower than the estimate for males and females caged singly. No significant differences between sexes have been seen for radiation mortality under our experimental conditions, but final comments about differences in mortality between multiply caged wild and RF-strain *M. musculus* should be reserved until data are available for the wild males caged together.

Average survival times for the two species of soricids at the two highest dose levels (1625 and 2000 rads) were extremely short, 3.0 to 4.3 days. Survival times for the two wild murids at these highest doses also were relatively short, 4.4 to 5.1 days. The six species of cricetids lived longer than the soricids and murids at the highest doses; average survival times ranged from 5.5 to 8.1 days. Although the LD_{50} estimates for the two species of *Peromyscus* were the highest of all species tested, survival times for *P. leucopus*

[1]Dual capacity.

[2]AEC Postdoctoral Fellow.

[3]O. P. Pearson, *Ecology* **28**, 127–45 (1947).

Table 7.1. LD_{50-30} Estimates for Indigenous Rodents and Shrews and for RF-Strain *Mus musculus*

All animals were caged separately except in the experiment where five mice of the same sex were caged together

Family and Species	Number of Animals[a]	LD_{50-30} (rads)	95% Confidence Range (rads)	Total Range (rads)
Cricetidae				
Harvest mouse *Reithrodontomys humulis*	102	940	884–1008	124
White-footed mouse *Peromyscus leucopus*	126	1045	985–1110	125
Golden mouse *Peromyscus nuttalli*	101	1050	963–1136	173
Pine vole *Microtus pinetorum*	101	935	611–1331	720
Rice rat *Oryzomys palustris*	115	535	458–600	142
Cotton rat *Sigmodon hispidus*	123	960	916–1019	103
Muridae				
House mouse *Mus musculus*				
Wild				
One per cage	120	855	789–916	127
Five per cage[b]	50	800	659–928	269
RF Strain				
One per cage	136	1010	941–1093	152
Five per cage	124	795	698–883	185
Norway rat *Rattus norvegicus*	91	880	805–949	144
Soricidae				
Least shrew *Cryptotis parva*	35	855	711–1025	314
Short-tailed shrew *Blarina brevicauda*	28	770	663–893	230
Total	1252			

[a]Males and females combined.
[b]Females only.

were shorter and for *P. nuttalli* were longer than for all the other cricetids. A peculiar finding was that the multiply caged RF-strain mice died about one day earlier at the highest doses than the singly caged RF-strain mice, but the multiply caged wild mice lived about two days longer than the singly caged wild mice. Investigation of these differences will be initiated after completion of the present study of crowding stress.

So far, our studies suggest that (1) in terms of LD_{50-30}, radiosensitivity of different species within a family or higher classification may vary greatly; (2) mean survival times at higher doses are not obviously related to metabolism or size of species; (3) caging several individuals of the same sex together may cause alterations in mortality and survival times; (4) nutrition, parasitism, and disease can affect mortality and survival times in irradiated wild species; and (5) weight losses for all species were rapid at the highest doses, but at lower doses considerable variation was seen in onset and magnitude of weight loss among the various species.

INCORPORATION OF A THYMIDINE ANALOG INTO INDIGENOUS RODENTS

T. P. O'Farrell P. B. Dunaway

The thymidine analog 5-^{131}iodo-2′-deoxyuridine (^{131}IUDR) is incorporated into the DNA of proliferating cells. Radiation alters incorporation of this antimetabolite. The objective of this laboratory study was to test the usefulness of ^{131}IUDR as a physiological index of radiation effects in native rodents. This research has been completed, and a study is now under way to adapt this technique for use with free-ranging wild mammals.

Experiments were designed to characterize tissue distribution of activity in order to test the usefulness of whole-body retention curves, to measure incorporation of ^{131}IUDR by three species of rodents and relate the incorporation rates to general metabolic rates, and to ascertain the effects of acute gamma radiation on ^{131}IUDR uptake. Methods are reported in detail elsewhere.[4]

Over 95% of the 1 μc injected into *Sigmodon hispidus* as ^{131}IUDR was eliminated within 48 hr. The majority of the remaining activity was incorporated into the intestines and presumably was attached to the DNA. Since the whole-body retention curves largely reflected the activity in the intestinal cells, the whole-body curves apparently were a useful index to cell proliferation and DNA metabolism in this tissue. Lesser amounts of activity were found in bone marrow, muscle, stomach, kidneys, lungs, and spleen.

Acute ionizing radiation reduced incorporation of ^{131}IUDR, probably by damaging intestinal cells and altering the mitotic cycle. After absorbed doses of 100, 500, and 1000 rads, whole-body measurements of incorporation were depressed to 76, 38, and 28%, respectively, as compared with controls. Greatest reduction of total activity in tissues occurred in the intestines. Activity levels in this radiosensitive organ after 100, 500, and 1000 rads were reduced to 47, 18, and 1.5%, respectively, of control values.

A merging of whole-body retention curves for ^{131}IUDR and Na^{131}I with increased radiation was caused by coaction of reduced incorporation of ^{131}IUDR in proliferating tissues and changes in clearance time and elimination rate of iodine. After a dose of 1000 rads, the retention curves for

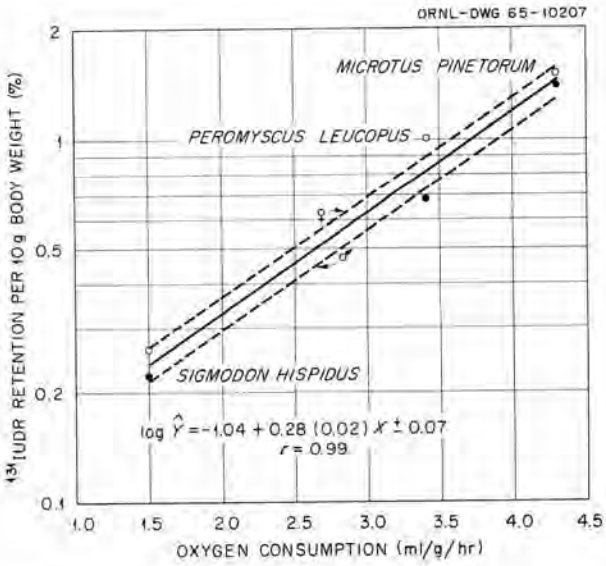

Fig. 7.1. Regression of ^{131}IUDR Incorporation at 48 hr Postinjection as a Function of Oxygen Consumption for Three Species of Rodents.

[4]T. P. O'Farrell, S. I. Auerbach, and P. B. Dunaway, *Incorporation of a Thymidine Analog by Indigenous Rodents* (thesis), ORNL-3907 (March 1966).

the two radioiodine-labeled chemicals could not be distinguished, indicating that free iodide rather than incorporated antimetabolite was being measured.

The rate of cell proliferation, indicated by the activity retained 48 hr postinjection of ^{131}IUDR, was related to the general metabolism of the species tested, as indicated by the amount of oxygen consumed per gram of body weight per hour (Fig. 7.1). Within the range measured, it appeared that for every 1-ml increase in oxygen consumption there was a corresponding doubling in cell proliferation.

Results of the study indicate that this thymidine analog can be used as an index to radiation damage, cell proliferation rates, and general metabolism in mammals living in natural environments. These measurements can be made without sacrificing individuals, which is of special advantage in studies of population dynamics.

RADIATION EFFECTS ON CARP REPRODUCTION

N. R. Kevern B. G. Blaylock
N. A. Griffith

The effect of chronic low-level irradiation on the reproductive capacity of carp in White Oak Lake was investigated further this year. Dominant lethal mutations can be caused by irradiation of germ cells and, if present, can lower the hatchability of fertilized fish eggs. Hatchability of fertilized eggs from White Oak Lake carp was compared with controls from Fort Loudon Reservoir. Studies in 1964 and 1965 provided background information on spawning time for carp in East Tennessee (late April), accumulated dose to gonads of five-year-old carp (about 800 rads), and laboratory techniques for collecting ova and sperm from ripe carp.[5] In 1966, carp spawned in late April and early May. Four pairs of spawning carp were taken from Fort Loudon Reservoir and two pairs from White Oak Lake. Eggs and sperm were stripped from the fish in the laboratory, and fertilized eggs were placed in glass trays in a water bath. A significant difference in hatchability existed between control and experimental fish (Table 7.2). The mean percent hatch for White Oak Lake carp was 78.3 compared to 95.7 for the control carp. Hatchability of eggs for a single pair of White Oak Lake carp in 1965 was 80.8%, similar to this year's White Oak Lake fish. The lower hatchability for White Oak Lake carp may be caused by chronic irradiation; however, other environmental factors also may be involved. Additional observations of the same type are needed. Also, crosses should be made between control and experimental fish to test for intermediate effects.

POPULATION GENETICS AND RADIATION EFFECTS STUDIES

B. G. Blaylock

Study of the natural population of *Chironomus tentans* in White Oak Lake and White Oak Creek

[5]S. I. Auerbach *et al.*, *Health Phys. Div. Ann. Progr. Rept. July 31, 1965*, ORNL-3849, p. 87.

Table 7.2. Hatchability of Carp Eggs from White Oak Lake and Fort Loudon Reservoir

Pair No.	Fort Loudon Reservoir		White Oak Lake	
	Number of Eggs	Percent Hatch	Number of Eggs	Percent Hatch
1	869	85.0	1187	77.7
2	1881	98.7	2147	78.9
3	1594	99.8		
4	704	99.4		
		95.7 ±3.3[a]		78.3 ±0.6[a]

[a] $\bar{x}$ ±1 SE.

has continued since the preliminary investigations in 1960. Annual samples have been taken from this population, which has been exposed to an estimated dose of 230 rads/year for over 120 generations. Salivary gland chromosomes of 755 larvae from the irradiated population and 714 from nonirradiated populations were scored for chromosomal aberrations. Twelve different aberrations were found in the irradiated population (at a very low frequency) that were not found in the nonirradiated populations. Three endemic inversions which occurred at relatively high frequencies (0.09 to 0.20) in both the irradiated and control populations were unaffected by the exposure to chronic irradiation from the radioactive bottom sediments.

Two hundred larvae of another species of *Chironomus* belonging to the Plumosus group were collected from White Oak Lake and analyzed for chromosomal aberrations. In contrast to *C. tentans*, which is chromosomally polymorphic, previous examinations of this species from nonirradiated populations revealed no endemic inversions; and the species is considered to be chromosomally monomorphic in this area. One aberration, a small inversion, was found in the larvae from the irradiated population. This finding agrees with previous conclusions based on our studies with *C. tentans*, that ionizing radiation from the contaminated environment increased the frequency of new chromosomal aberrations, but that these new aberrations were eliminated rapidly by natural selection.

Laboratory populations of *Drosophila melanogaster*, *D. tropicalis*, and *D. simulans* were used to study the effects of gamma radiation in interspecific competition. In laboratory populations started with equal numbers of *D. tropicalis* and *D. melanogaster*, the *D. tropicalis* were eliminated within two generations. When both species received an acute dose of 2000 rads, the *D. tropicalis* were not eliminated until the fourth generation; however, under chronic irradiation of 6 rads/hr the *D. tropicalis* were eliminated in one generation. Similar experiments were conducted with *D. simulans* and *D. melanogaster*. *Drosophila simulans* were not eliminated rapidly by *D. melanogaster*. In control populations the frequency of *D. melanogaster* after 21 days was slightly less than 50%, but increased thereafter. In populations where both species had received 2000 rads of gamma radiation, the frequency of *D. melanogaster* exceeded 70% after 21 days. At this time the irradiated populations were significantly smaller than the control populations. The decrease in population size was caused primarily by a decrease in the number of *D. simulans*. Although other similar experiments are being conducted, these data show that under these experimental conditions interspecific competition can be affected by ionizing radiation.

Laboratory populations of *D. melanogaster* established for chromosomal polymorphism studies were also used to study the viability – egg to adult emergence – of the population after exposure to acute and chronic gamma radiation. One of two populations of approximately 5000 flies that had been established for several generations was given an acute dose of 2000 rads of ^{60}Co gamma radiation; the other population received a chronic dose of 6 rads/hr of ^{60}Co gamma radiation. The egg to adult emergence in each population was tested prior to exposure and at intervals thereafter. The results are given in Table 7.3. The viability of the population exposed to the acute dose of radiation was reduced by 80%, but recovered rapidly. The rapid increase in viability indicated that factors other than genetic damage, such as damage to the egg cytoplasm, were responsible for the large decrease in viability. The genetic effects in the first generation were due primarily to dominant lethals and semilethals, which were eliminated and accounted for another large increase in viability in the second generation. The recovery thereafter was much slower. This was attributed to recessive lethals, which may be carried in the population for several generations before being eliminated. The viability of the population exposed to chronic radiation decreased slowly. This gradual decrease was expected, since lethal and deleterious genes were introduced gradually and were concurrently eliminated. The population was reaching an apparent equilibrium, at which the rate of induction of lethals and deleterious genes equals the rate of elimination of these mutations. Although the accumulated dose to the population from the exposure to chronic radiation exceeded the acute dose, the reduction in viability was never as great. This study differs from most studies of this type, since radiation exposure occurred during the entire life cycle, more closely resembling a nuclear warfare situation.

Table 7.3. Effects of Chronic and Acute Gamma Radiation on the Viability (Egg to Adult Emergence) in Laboratory Populations of *Drosophila melanogaster*

Acute Dose, 2000 rads				Chronic Dose, 6 rads/hr				
Days After Exposure	Number of Eggs	Number of Adults	Percent	Days After Start of Exposure	Accumulated Dose (rads)	Number of Eggs	Number of Adults	Percent
0	1022	933	91.3	0	0	1048	978	93.3
1	307	35	11.4	7	1008	170	125	73.5
9	308	117	38.0	13	1872	304	214	70.4
15	134	40	29.9	20	2880	100	59	59.0
22	152	60	39.5	27	3888	523	293	56.0
28	100	77	77.0					

8. Responses of Plants to Ionizing Radiation

G. N. Brown
J. W. Curlin[1]
F. G. Taylor, Jr.
J. P. Witherspoon

GROWTH AND MORTALITY RESPONSES OF CONIFERS TO FAST-NEUTRON IRRADIATION

J. P. Witherspoon F. G. Taylor, Jr.

Serious growth inhibition and mortality of conifers in forests surrounding the DOSAR facility have been reported.[2] This case of long-term, discontinuous exposure to fast-neutron radiation indicated the extreme radiosensitivity of conifers to this particular kind of radiation. A laboratory study was completed this year to ascertain conifer response to acute fast-neutron exposures. Results from this study help define parameters of radiosensitivity, and results may be compared with existing data on conifer response to acute gamma irradiation for RBE implications.

Two species of pine, white pine (*Pinus strobus* L.) and shortleaf pine (*P. echinata* Mill.), were exposed to four levels of fast-neutron radiation (75, 100, 150, and 200 rads – tissue dose in air) at the DOSAR facility. These total doses were delivered in a period of 8 min. The white pines were two-year-old seedlings, and two age groups (1 and 3 years) were represented in the shortleaf pines. Potted plants were irradiated in May 1965

[1]Dual capacity.

[2]J. P. Witherspoon, *Health Phys.* 11, 1637 (1965).

Table 8.1. Growth Response of Conifers to Acute Fast-Neutron Irrodiation at 65 Days Postirradiation

Fast-Neutron Dose (rads)	White Pine Two Years Old	Shortleaf Pine One Year Old	Shortleaf Pine Three Years Old
75	53.4 ± 5.7[a]	88.5 ± 12.5	83.7 ± 10.9
75	28.2 ± 6.4[b]	30.7 ± 7.3	39.0 ± 8.1
100	54.1 ± 8.0[a]	80.8 ± 10.3	90.0 ± 8.5
100	30.7 ± 5.6[b,c]	27.4 ± 4.9	31.3 ± 6.2
150	41.2 ± 7.5[a]	67.0 ± 9.3	59.0 ± 11.2
150	21.9 ± 6.1[b]	26.2 ± 6.4[c]	28.8 ± 7.9[c]
200	36.0 ± 4.4[a]	69.2 ± 10.1	55.1 ± 9.8
200	17.8 ± 4.0[b]	22.9 ± 5.1	19.4 ± 4.7

[a]Mean shoot height ± 1 SE as percent of controls.

[b]Mean apical needle length ± 1 SE as percent of controls.

[c]First appearance of mortality of new apical needles.

and maintained under greenhouse conditions for a period of one year. Terminal and lateral shoot growth and needle growth were measured weekly until needle and shoot mortality became evident.

Growth inhibitions occurred in all radiation treatment groups and reached maxima about two months following irradiation (Table 8.1). Needle mortality of old leaves appeared in the 150- and 200-rad treatments (all plants) within two to four weeks following irradiation. Mortality of old and new needles increased throughout the growing season, and at onset of dormancy all plants in the 150- and 200-rad treatments exhibited 100% needle mortality. Over winter, plants in the 75- and 100-rad treatment groups exhibited 100% needle mortality. Under the greenhouse conditions in this study the minimum lethal dose (LD_{100}) was 75 rads for all plants. Time required for 100% mortality varied in the 75-rad groups: white pine, 210 days; three-year-old shortleaf, 283 days; and one-year-old shortleaf, 311 days. Growth and mortality data indicate that the order of radiosensitivity is white pine > one-year shortleaf > three-year shortleaf. White pine is also more sensitive to gamma radiation than shortleaf pine. The greater sensitivity of the three-year-old shortleaf over the one-year-old shortleaf may be due to size differences (thickness of stem and apices) which allowed for more energy absorption by the larger plants.

RADIATION DOSE TO ROOTS OF POTTED PLANTS FROM REACTOR FAST NEUTRONS AND SOIL ACTIVATION PRODUCTS

J. W. Curlin J. P. Witherspoon

The fast-neutron dose delivered to shoots and foliage of potted plants can be estimated accurately for exposures made at the DOSAR facility, but the neutron dose distribution and additional gamma and beta dose delivered to plant roots by activation products in the potting soil are unknown. A study is being conducted to identify the nuclides responsible for secondary radiation, and to estimate total dose and dose distribution within the pot.

Emory silt loam, a soil commonly used for growing experimental plant material, was placed in polyethylene bags and molded into 11-cm-square plastic frames 3 cm thick to form a monolithic "soil sandwich." The reconstructed soil density averaged 1.57 g/cc, and moisture content was 32.4% of oven dry weight. Seven such units were arranged back to back to form a package 21 cm thick which simulated the tangential cross section of a planting pot. Gold and Cd + Au fission foils were inserted between each soil layer to measure thermalization of the fast neutrons as they passed through the soil mass. A second experimental package with ^{32}S threshold detectors measured the >2.5-Mev neutron dose distribution. Boron-shielded ^{239}Pu, ^{237}Np, and ^{238}U fission foils placed in front and behind the experimental package measured the entrance and exit fast-neutron fluence at three energy levels between 0.1 Mev and 2.5 Mev.

The experimental packages were exposed 1.0 m from the reactor core to 2056 rads (tissue dose in air) of fast neutrons delivered over a 10-min period. The major activation products identified by spectral analysis were: ^{56}Mn, ^{51}Cr, ^{86}Rb, ^{181}Hf, and ^{95}Zr-^{95}Nb in decreasing order of relative contribution to total gamma activity. Manganese-56 constituted 96% of the measured activity from activation products. The distribution of radionuclides within the experimental package followed the trend of the fast-neutron fluence, the highest activities being contained between 2.5 and 5.0 cm from the exposed face of the experimental package. Infinite mean dose estimates were calculated for gamma and beta radiation resulting from activation of soil minerals (Table 8.2). Estimated total dose to a well-ramified root system irradiated under these experimental conditions would have been:

Component	Dose (rads)
Activation products	
Beta	6.5
Gamma	5.8
Fission Gamma	140.0
Neutrons	
Thermal	0.2
Fast (>1 kev)	1061.0
Total	1213.5

Because of the short half-lives and small quantities ($\sim$0.2 μc/g) of nuclides present, the dose to plant roots from this secondary source contributes an extremely small proportion of the total dose.

Table 8.2. Dose Contributions from Soil Activation Products

Radionuclide	Percent of Total Activity	Percent of Total Mean Dose	
		$\overline{D}_{\beta\infty}$	$\overline{D}_{\gamma\infty}$
^{56}Mn	95.6	16.4	31.4
^{51}Cr	2.4		1.7
^{181}Hf	0.4	19.3	21.5
^{86}Rb	1.2	48.4	1.7
^{95}Zr	0.2	9.2	34.4
^{95}Nb	0.2	6.7	9.3

MINERAL UPTAKE MECHANISM AFFECTED BY FAST-NEUTRON RADIATION

G. N. Brown F. G. Taylor, Jr.

The effects of fast-neutron radiation on the growth and uptake of ^{65}Zn were studied in three-year-old red oak (*Quercus rubra* L.) seedlings. Potted seedlings received shoot irradiations of 505 and 1011 rads (tissue dose in air) delivered over a period of 8 min. Potted soil of irradiated plants and controls was inoculated with 50 μc of ^{65}Zn per pot. Leaf disks for radioanalysis and growth measurements were taken twice weekly throughout the growing season. Primary and secondary stem growth, root growth, and new leaf development were inhibited by radiation. Statistically significant differences appeared in shoot height of the high-dose group (1011 rads) after 25 days and in the lower-dose group (505 rads) after 50 days. By 90 days a 35% retardation in shoot height was present in the lower-dose group while retardation was 64% of controls in the high-dose group.

An initial stimulation of ^{65}Zn uptake was observed following irradiation but disappeared by about 20 days (Fig. 8.1). Retardation of uptake also was found about ten weeks following exposure of seedlings to the higher dose. At the end of the growing season distribution of ^{65}Zn in seedling components was ascertained. Highest concentrations were in secondary roots, followed by primary roots, stems, and leaves in decreasing order.

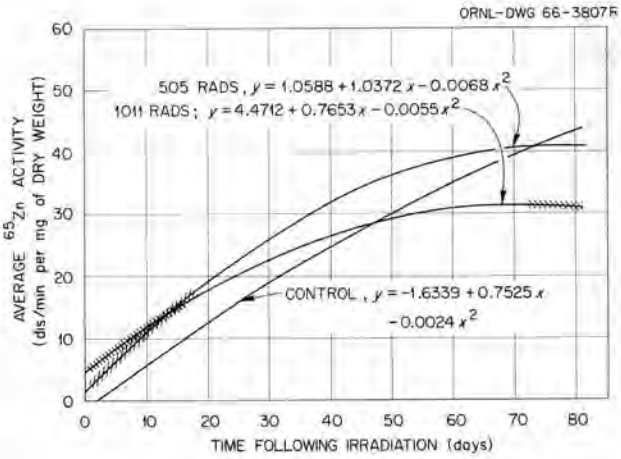

Fig. 8.1. Uptake of ^{65}Zn by Red Oak Seedlings Following Acute Fast-Neutron Irradiation. (Cross hatching indicates that treatment differs from control at the 5% level of significance.)

EFFECTS OF FAST-NEUTRON RADIATION ON PHYSIOLOGICAL PROCESSES

G. N. Brown F. G. Taylor, Jr.

Studies of the interactions of photoperiodic mechanisms and ionizing radiation in cocklebur have continued this year. Experiments were designed to ascertain the differences in radiosensitivity within photoinduction cycles.

Five-week-old *Xanthium pensylvanicum* plants received acute fast-neutron radiation simultaneous with photoinduction (12 hr of light per day). Groups of plants were irradiated (1570 rads, tissue dose in air) with respect to time in the photoinductive cycle: early day, early night, late day, and late night. A fifth group of nonirradiated, photoinduced plants served as controls.

Pre- and postirradiation and photoinduction growth was rigorously controlled in environment chambers on long day cycles of 17 hr of light per day. An inhibition to flowering was observed in all irradiated plants. By 48 days postirradiation staminate flowers of control photoinduced plants reached anthesis. Using this criterion to indicate maturation in flowering, all terminal apices in each group were collected, processed into permanent slides, and studied for effects on the development of the inflorescence and individual flowers.

In comparison to other groups, flowering appeared to be most sensitive in plants irradiated during the latter portion of the dark period. Plants irradiated during the beginning of the dark or light period, and during the latter portion of the light period did not differ between treatments, while all treatments varied from controls.

Two groups of *X. pensylvanicum* plants received a dose of 1927 rads of ^{60}Co gamma radiation during either the dark or light period of short-day photoinduction. Another group of control plants was photoinduced but not irradiated. Vegetative growth was initially stimulated in both groups of irradiated plants, but later suppression was not observed. Pistillate and staminate flowering were inhibited in both groups of irradiated plants, but pistillate flowering was inhibited to a greater extent. Both micro- and megasporogenesis were retarded in irradiated plants, with the greatest inhibition occurring in plants irradiated during the light period. Results are interpreted as responses to radiation-induced changes in nucleic acid and growth hormone metabolism.

Previous work[3] has suggested that RNA characteristics, particularly soluble RNA (sRNA) characteristics, vary with rates and stages of development in higher plants. A study was designed to determine quantities of total RNA, DNA, sRNA, and sRNA base compositions in control and irradiated mimosa (*Albizzia julibrissin* Durazzini) epicotyl tissue through a ten-day postirradiation period (fast neutrons, 1181 rads). Total RNA and DNA per unit dry weight decreased during this ten-day period in both control and irradiated epicotyls, with total RNA decreasing at a greater rate in both groups (Fig. 8.2). However, total RNA decreased more rapidly in irradiated epicotyls, while total DNA did not vary significantly between control and irradiated epicotyls. Soluble RNA (responsible for the transfer of amino acids to the ribosomal site of protein synthesis) did not vary between control and irradiated epicotyls during the ten-day period, even though a significant decline in sRNA was observed in both groups between six and ten days postirradiation (Fig. 8.3). The delayed decline in sRNA as compared to total RNA in both groups suggests a greater stability of sRNA than other fractions of total RNA (primarily ribosomal RNA) during epicotyl development, and that sRNA may be derived from ribosomal RNA. These two phenomena apparently were unaffected by the levels of fast-neutron radiation used in this study.

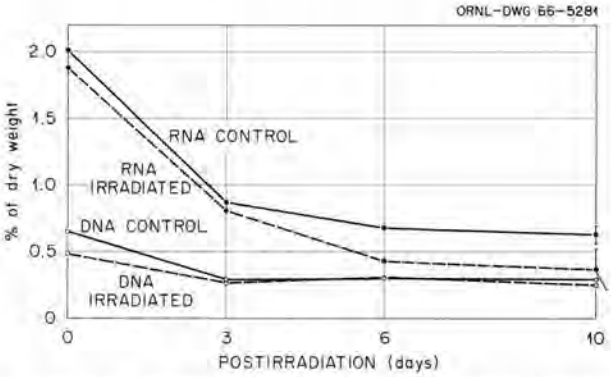

Fig. 8.2. Changes in Mimosa Epicotyl Total Nucleic Acid Following Fast-Neutron Irradiations.

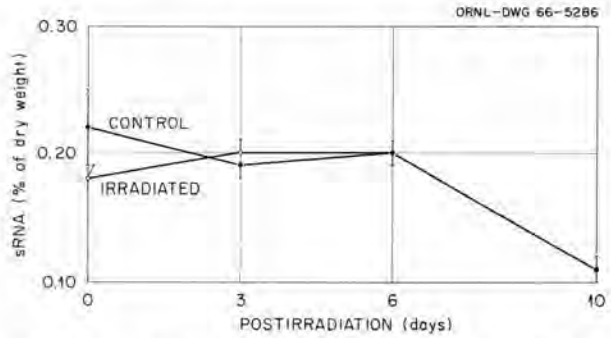

Fig. 8.3. Changes in Mimosa Epicotyl Soluble RNA Following Fast-Neutron Irradiation.

[3]G. N. Brown, *Plant Physiol.* 40, 557 (1965).

Early declines in quantities of total RNA, DNA, and sRNA in irradiated epicotyls within 4 hr following irradiation were observed. However, partial recovery of quantities of total RNA and complete recovery of quantities of DNA and sRNA were found at three days following irradiation (Fig. 8.2).

Slight changes were observed in sRNA base compositions in both control and irradiated epicotyls during the ten-day period, with adenylate, and possibly cytidylate, varying significantly more than guanylate and uridylate through time. An initial decrease in the relative concentration of sRNA guanylate and an increase in sRNA uridylate were observed in irradiated epicotyls up to six days following irradiation. Shifts in base compositions, either through time or as a result of irradiation, suggest changes in relative concentrations of the amino acid-specific sRNA's or changes in the stability of the CCA terminus of sRNA.

Significant decreases in both fresh weight and dry weight of irradiated epicotyls were found between three and ten days following irradiation, accompanied by a yellowing of irradiated epicotyls after five days, and drought stress in irradiated epicotyls after seven days. Other morphological aberrations were observed in microscopic sections of irradiated epicotyls. The slight declines in total RNA and insignificant changes in total DNA and sRNA between irradiated and control epicotyls would not appear to account for the relatively large inhibition of growth and morphological development. Such comparisons suggest that metabolic factors other than RNA and DNA metabolism and subsequent protein synthesis may play a major role in growth and developmental inhibition following irradiation. On the other hand, the slight declines in total RNA and sRNA base composition shifts observed in irradiated epicotyls may reflect sufficient molecular damage to result in rather large growth and developmental inhibition.

ENVIRONMENTAL AND GENETIC MODIFICATIONS OF RADIOSENSITIVITY

J. P. Witherspoon J. W. Curlin
F. G. Taylor, Jr.

In plants there is a high correlation between exposures of x or gamma rays required to produce certain biological effects and the average interphase chromosome volume of shoot apical meristem cells. When log chromosome volume is plotted against log exposure, a linear relationship shows that the larger the chromosome volume, the smaller the exposure required to produce severe growth inhibition or lethality. This relationship has great value in predicting biological effects for experimental design purposes or nuclear catastrophe assessment. Modifications, however, must be made for environmental factors and types of radiation. Plants growing under field conditions were found to suffer severe growth inhibitions (growth less than 50% of controls) at gamma radiation exposures two to three times less than those necessary to produce the same effect on plants in growth chambers with optimized environmental conditions (Fig. 8.4). Experimental stress conditions, particularly moisture stress, given postirradiation lowered exposure requirements even more. Exposure in all cases was correlated with chromosome volume, but the log-linear relationship changed as environmental factors became more optimal. Under growth chamber conditions, fast-neutron exposures were an order of magnitude less than the gamma exposures necessary to produce severe growth inhibition or death (Fig. 8.4). Seasonal changes in

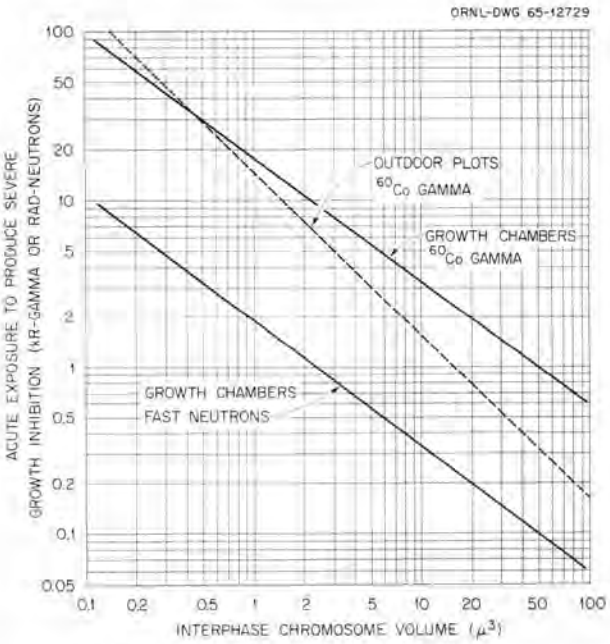

Fig. 8.4. Relation Between Interphase Chromosome Volume and Acute Exposure for Serious Growth Inhibition. Dotted line from BNL data [R. C. Sparrow and A. H. Sparrow, *Science* 147, 1449 (1965)]; solid lines are ORNL data.

nuclear volume of 14 plant species[4] suggest that radiosensitivity would change by a factor of 1.5 to 3.0 during the year for dormant vs actively growing plants. Information on environmental modifications of the chromosome volume method of predicting relative radiosensitivity in plants will increase the usefulness of this concept under field conditions and lead to more accurate interpolation of laboratory results.

Radiation studies have continued this year with clones of eastern cottonwood (*Populus deltoides* Marsh.) propagated asexually from cuttings. A genetic basis for radiosensitivity was found when results showed significant statistical differences in shoot height, growth rate, and biomass of irradiated clones grown under controlled environmental conditions.

Dormant cuttings of the same age and size were irradiated and grown with controls in aerated nutrient solutions in plant growth chambers. Figure 8.5 illustrates growth response after 21 days in ten clones exposed to ^{60}Co gamma radiation, total exposure 7600 r given at a rate of 11 r/sec. Significant growth differences were found between controls, with the best growth performers averaging 1.5 to 2.0 times more growth than other clones. Shoot height was inhibited 60 to 85% in irradiated clones, while other biological end points varied even more between clones.

This spring two clones (dormant cuttings) were irradiated with fast neutrons at the DOSAR facility (300 to 1200 rads, tissue dose in air) and with ^{137}Cs gamma radiation (300 to 12,000 rads). Both radiations were given at a rate of 600 rads/hr. These plants are now being maintained under constant environmental conditions, and growth measurements are being made to ascertain differences in clonal response to the two radiations and possible genetic bases for RBE differences. Mortality data indicate an RBE of 10 to 12 for fast neutrons, while end points of inhibition indicate RBE's in the range of 3 to 6.

To facilitate future work with these clones, a field nursery of 3000 cuttings representing 27 clones was planted. These clones represent stock from Alabama, Mississippi, Kentucky, Illinois, and Wisconsin.

[4]S. I. Auerbach *et al.*, *Health Phys. Div. Ann. Progr. Rept. July 31, 1965*, ORNL-3849, p. 49.

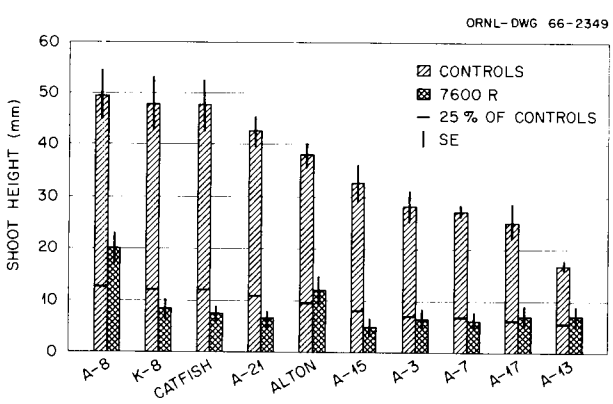

Fig. 8.5. Mean Shoot Height of Ten Gamma-Irradiated and Control Clones of Eastern Cottonwood Cuttings Grown Under Controlled Environmental Conditions.

STRUCTURAL CHANGES IN IRRADIATED PLANTS

J. P. Witherspoon F. G. Taylor, Jr.

The normal growth habit of higher plants is usually altered by exposure to ionizing radiation. Alterations of cellular or tissue structure often result in abnormal growth and development of roots, leaves, stems, or flowers. In past work many of these morphological effects of ionizing radiation have been defined in very general terms. Thickening, brittleness, color change, curling, fusing, and puckering are terms often used to describe anomalous leaf development. Terms describing effects in stems include growth stimulation (elongation), inhibition, and fasciation. Less is known concerning the histological detail of these general morphologic anomalies, and much less relative to possible consequences of these alterations to normal functions of plants and plant processes.

Last year a project was initiated wherein materials are collected routinely from control and irradiated plants. These materials are prepared for microscopic comparison and studied in an effort to catalog and reduce some of these general structural terms to histologic descriptions. Moreover, attempts are made to correlate some of these aberrations with changes in normal physiological processes. For example, Fig. 8.6 shows cross sections of leaf tissue from control (*a*) and irradiated (*b*, *c*, and *d*) yellow poplar leaves. These leaves developed from buds given an acute ^{60}Co gamma dose of 4500 rads. In *a* the normal condi-

tion is illustrated with well-formed epidermis, vascular bundle, mesophyll cells, and intercellular air spaces. In *b* note the irregular epidermal cells. Surface area is increased, with probable effects on moisture and light absorption phenomena. In *c* there is abnormal development of the vascular bundle, which could affect translocation, and compression of mesophyll cells, which might affect moisture and food storage capacity. Puckering of leaf surface (the general term) is shown (*d*) to be due to enlargement of cells in regions of the palisade parenchyma tissue.

Other histological series have been made of apical meristems and foliage of several forest tree species exposed to gamma and fast-neutron radiation and of floral development in cocklebur as part of the photoperiod study.

Studies on photosynthetic and mineral transport abilities of plants with such structural anomalies are being initiated this year. Results of these studies should enable us to interpret morphological changes due to radiation in terms of changes in plant function which alter survival or recovery patterns.

PHOTO-81379

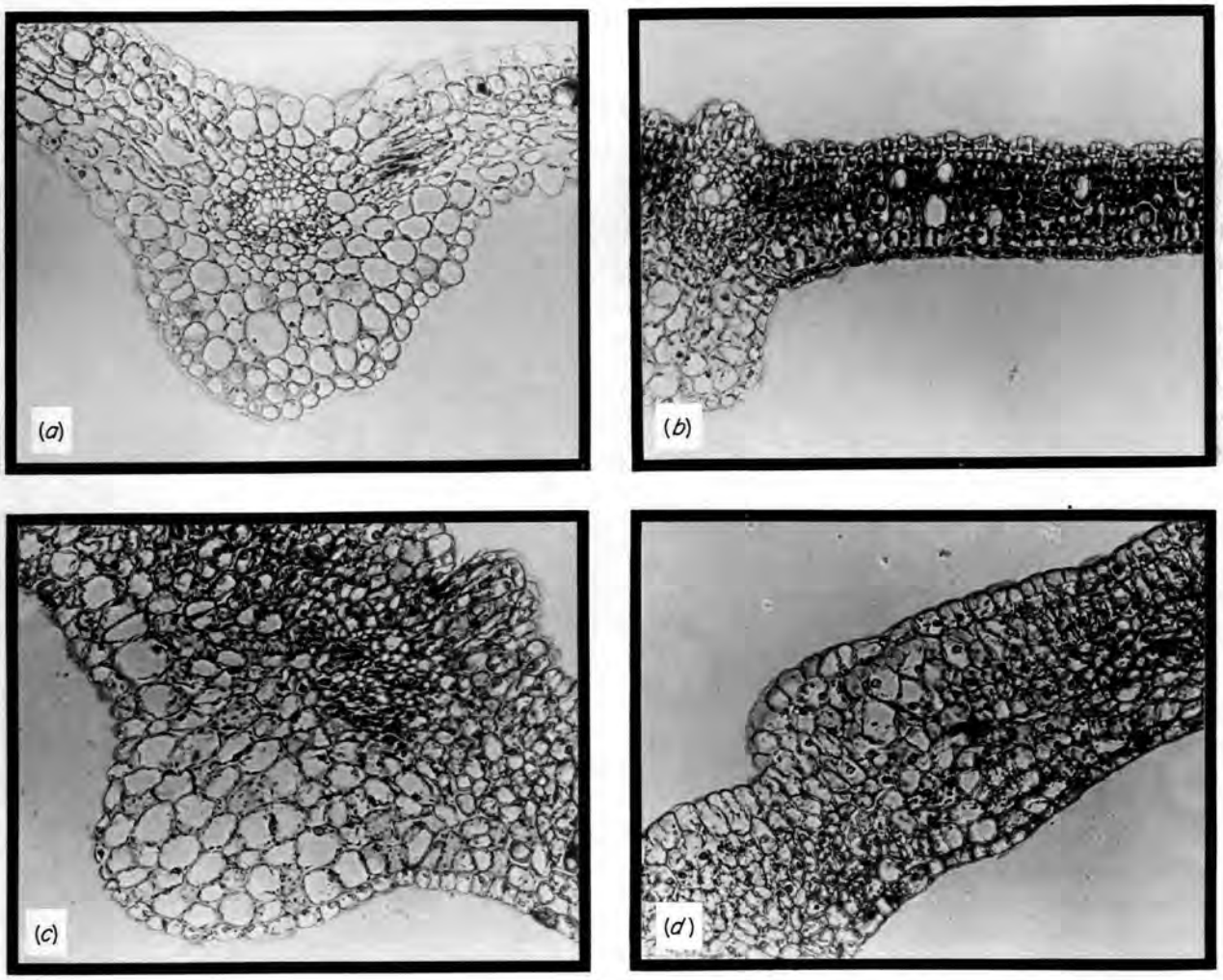

Fig. 8.6. Cross Sections of Control (*a*) and Gamma-Irradiated Leaves (*b*, *c*, and *d*) of Yellow Poplar.

9. Radionuclide Cycling in Terrestrial Ecosystems

D. A. Crossley, Jr.
J. W. Curlin[1]
J. S. Olson[1]
D. E. Reichle
G. M. Van Dyne[1]
Martin Witkamp[1]
T. Tamura[1]
G. Cristofolini[2]
S. Cristofolini[3]
R. C. Reynolds[3]
Regina M. Anderson
W. C. Cate
Gladys J. Dodson
Marilyn L. Frank
M. H. Shanks
R. L. Tabor
H. D. Waller
J. K. West

TRENDS OF ^{137}Cs IN THE *LIRIODENDRON* FOREST VEGETATION

J. S. Olson
R. L. Tabor
H. D. Waller
Regina M. Anderson

Year-to-year changes in the distribution of ^{137}Cs in a tagged *Liriodendron* forest have been measured and accounted for in terms of major above- and below-ground transfers of ^{137}Cs. Sampling of forest canopy showed that ^{137}Cs concentrations continued to decrease each year since 1962 (from $\frac{1}{3}$ to $\frac{1}{2}$ that of each preceding year). Annual transfers out of the canopy decreased accordingly from 1962 through 1965: rainout from the canopy was 12, 5.5, 3, and about 2 $\mu c\ m^{-2}\ year^{-1}$, and estimated litter fall inside the plot was 57, 26, 10, and 5 $\mu c\ m^{-2}\ year^{-1}$ respectively. About one-fifth of the litter fall moved into the fringe of untagged forest around the tagged plot each year. Preliminary estimates of these losses, plus more restricted export in roots, accounted for about 4% of the initial tag leaving the area. The second major soil-root sampling was completed and is proceeding through analysis and interpretation.

There has been a consistent tendency for a late spring maximum concentration of foliage activity, and also in total foliage content of ^{137}Cs, in spite of some further growth of new leaves after the main period of growth prior to early June. Detailed canopy level analysis for 1963 showed identical mean activity per leaf for all canopy levels. Slight differences in activity per gram were therefore due to the larger mean leaf size that is typical of the upper one-third of the canopy, as compared with the middle or lower one-third (Fig. 9.1). Increased ^{137}Cs in branches in late summer may reflect the translocation of radiocesium from leaves, on its way downward through the bole to the roots.

FOLIAGE BIOMASS AND PRIMARY PRODUCTIVITY IN THE ^{137}Cs-TAGGED *LIRIODENDRON* FOREST

J. S. Olson
D. E. Reichle
H. D. Waller
Gladys J. Dodson

During the 1963 growing season, litter fall consisted of 142 g/m^2 of tagged *Liriodendron tulipifera* leaves, 63 g/m^2 of nontagged *Liriodendron* leaves, 18 g/m^2 of *Liriodendron* flowering parts, 98 g/m^2 of leaves from other deciduous species (predominantly understory), and 18 g/m^2 of pine needles. If loss of tagged *Liriodendron* leaves from the

[1]Dual capacity.
[2]NATO Fellow.
[3]Consultant.

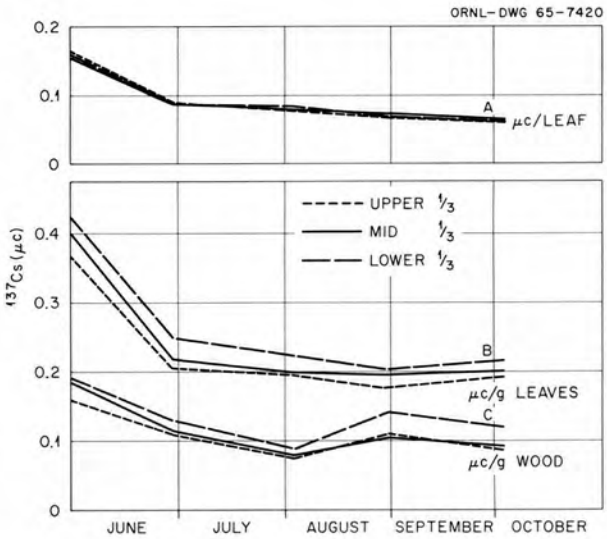

Fig. 9.1. Summer Decrease of ^{137}Cs in *Liriodendron* Leaves and Associated Branches. A, Uniform activity per leaf; B, differences in activity per gram due to canopy level differences in leaf size; C, corresponding activities in twigs.

PHOTO 83519A

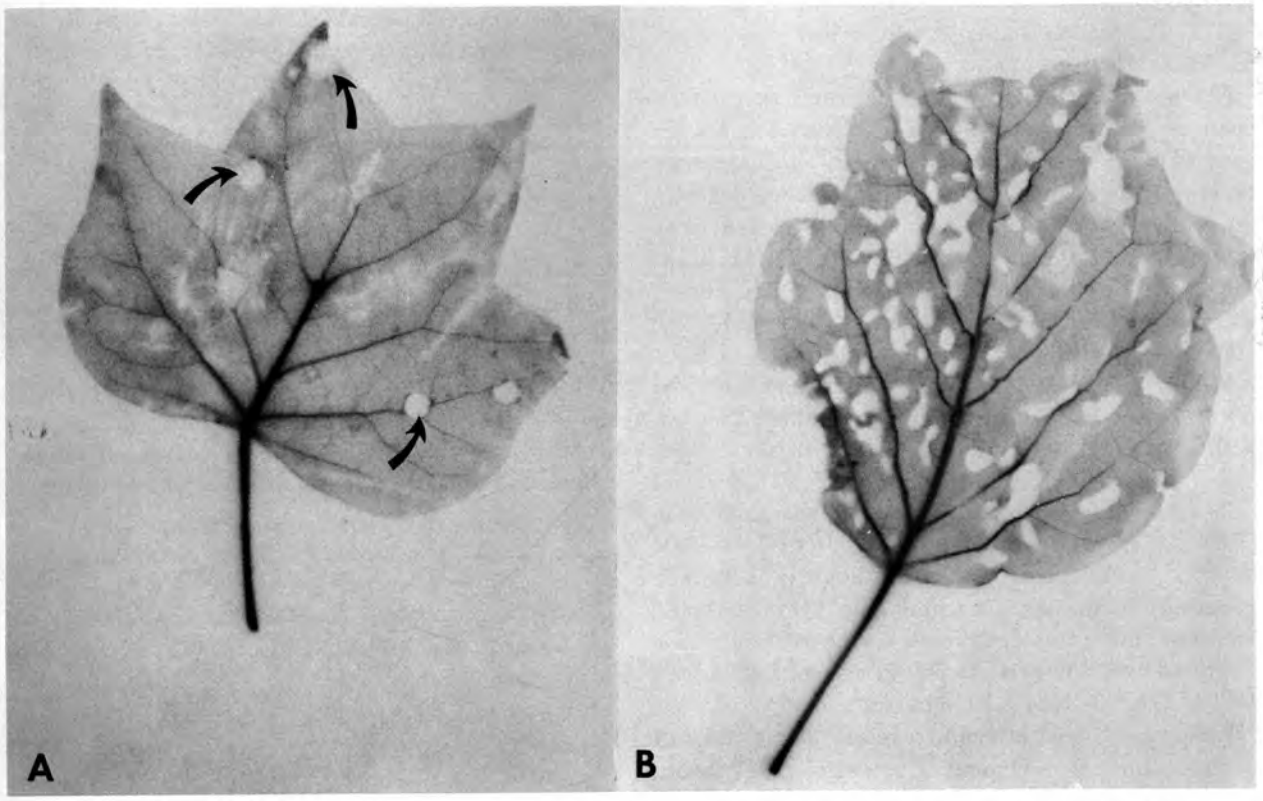

Fig. 9.2. Audioradiograms of *Liriodendron tulipifera* Leaves, Showing the Relative Distribution of ^{137}Cs. A, leaf with minor insect consumption and leaf punches (arrows) removed for radioanalysis; B, leaf exhibiting heavy insect consumption.

forest plot due to wind action is balanced by input of nontagged leaves from trees adjacent to the study plot, then total *Liriodendron* leaf biomass was 205 g/m^2 or approximately 60% of the total vegetative production (exclusive of woody material).[4] With a mean oven-dry weight (105°C for 24 hr) of 0.37 g/leaf, this is equivalent to the production of 554 leaves/m^2. The caloric content of *Liriodendron* leaves was 4.54 kcal per g of dry weight (4.95 kcal per g of ash-free dry weight). A general value for conifer leaves (*Juniperus virginiana*) was 5.04 kcal per g of dry weight. Using these values as approximations of the energy content of the various foliage constituents, annual net foliage production by all tree species was calculated[5] to be 1.55×10^3 kcal/m^2. This figure is based upon a net nonwoody production of 339 g/m^2 composed of 66% *Liriodendron* leaves and flowering parts, 29% foliage from other deciduous species, and 5% pine needles. Similar net annual foliage production of 1.57×10^3 kcal/m^2 has been reported[6] for a sugar maple (*Acer saccharum*) forest.

Estimation of foliage consumption was based upon a random sampling of *Liriodendron* leaves both between all of the major trees and within all levels of the canopy.[5] Leaf holes associated with insect herbivory averaged 5.6% of total leaf area (standard deviation of 8.8), with some leaves showing little effects and others considerable insect damage (Fig. 9.2). Bray[6] reported primary foliage consumption over a three-year period to average 6.6% for a mesic *Acer-Fagus* forest and 5.9% for a moist *Acer-Fagus* forest, both in southern Canada. With 205 g/m^2 of total tree foliage in the tagged forest represented by *Liriodendron*, 5.6% consumption by insects would raise the original production of foliage by this species to 217 g/m^2 or 0.99×10^3 kcal/m^2. Assuming the same degree of foliage consumption for the remaining tree species would increase the total (nonwoody) primary production estimate from 339 g/m^2 to 360 g/m^2 and from 1.55×10^3 kcal/m^2 to 1.64×10^3 kcal/m^2.

Future work will attempt to relate annual foliage consumption to seasonal fluctuations in insect biomass, as well as the depression in primary productivity due to the activity of sap-feeding insect species.

[4]S. I. Auerbach *et al.*, *Health Phys. Div. Ann. Progr. Rept. July 31, 1965*, ORNL-3849, pp. 65–66.

[5]D. E. Reichle and D. A. Crossley, Jr., "Investigations on Heterotrophic Productivity in Forest Insect Communities," Working Meeting on Principles and Methods of Secondary Productivity of Terrestrial Ecosystems, Warsaw, 1966 (in press).

[6]J. R. Bray, *Ecology* **45**, 165–67 (1964).

^{137}Cs DISTRIBUTION IN CANOPY FOOD CHAINS OF THE *LIRIODENDRON* FOREST

D. E. Reichle D. A. Crossley, Jr.
Gladys J. Dodson

To estimate ^{137}Cs content of canopy foliage with minimal damage, regression equations were developed to predict total leaf ^{137}Cs concentrations from analyses of subsamples using one, two, and three punches per leaf. Removal of leaf discs did not alter the distribution of ^{137}Cs in the remaining leaf area (Fig. 9.2*a*). The measurement of foliage concentrations of a given branch with 95% confidence limits within 10% of the mean required minimum sampling of 71 leaves with two discs removed from each. In Table 9.1 are listed the mean ^{137}Cs leaf concentrations (pc per mg of dry weight) for branches examined during 1965. The regression equation used in calculating leaf values was

$$\hat{Y} = 41.65 + 0.4284X ,$$

where $\hat{Y}$ is the whole leaf (petiole plus blade) concentration, and X is mean disc concentration.

Table 9.1. Weekly ^{137}Cs Concentrations in *Liriodendron* Leaves on Branches Sampled During the Study Period

Cesium values are pc per mg of dry weight

Date of Collection	No. of Leaves Examined	$\bar{x}$ Branch Concentration
June 18	83	42.3
June 23	88	43.3
June 29	73	49.5
July 6	96	43.7
July 14	81	50.6
July 28	70	32.9
August 3	95	56.4
August 13	83	46.0
August 16	86	58.4
Mean	84	47.0 ± 2.59

Table 9.2. ^{137}Cs Concentrations in Canopy Arthropods Expressed as a Percentage of Leaf Concentrations

Monthly values are means of three collections; $\bar{x}$ = mean, SD = one standard deviation; grand means are calculated from original weekly collections

Month and Trophic Position	Herbivore				Omnivore		Predator		
	Leaf Feeder		Sap Feeder						
	Geometridae	*Oecanthus*	*Macrosiphum*	Cicadellidae	Formicidae	Psocoptera	Araneida	*Chrysopa*	Coccinellidae
June									
$\bar{x}$	40.6	34.3	5.1		21.4	10.0	13.6		4.0
SD	22.9	4.3	1.6		1.5		9.9		0.9
July									
$\bar{x}$	58.1	48.5	5.3	5.1	20.1	12.6	10.7	6.2	7.4
SD		12.7	1.9	1.9	1.4	6.4	12.0	1.0	
August									
$\bar{x}$	49.7	12.1[a]	9.8	7.9	19.7		11.3		8.2
SD	4.6	6.2					9.2		
Grand									
$\bar{x}$	48.1	28.8	6.0	6.0	10.6	12.2	11.9	6.2	5.9
SD	12.5	17.9	2.4	2.1	1.3	6.0	9.1	1.0	2.3

[a]Immigration of untagged individuals.

Cesium-137 concentrations in foliage averaged 47.0 ± 2.59 pc per mg of dry weight. Due to individual branch differences, these data do not depict clearly the seasonal behavior of ^{137}Cs in the forest canopy. However, more extensive collections have demonstrated a consistent pattern of ^{137}Cs distribution in foliage during successive growing seasons.[4]

Cesium-137 concentrations in the sessile canopy arthropods were determined from hand collections of individuals on leaves (Table 9.2).[5] In the more mobile insect groups, for example, Diptera, flying Hymenopters, and Coleoptera, detectable levels of radiocesium were seldom found due to the mobility of these populations and the limited size (500 m^2) of the experimental area. Highest ^{137}Cs levels were found in the leaf-eating herbivores – the tree cricket *Oecanthus* sp. and larvae of geometrid moths. Sap-feeding herbivores such as aphids equilibrated at much lower levels than did leaf-feeding species. Radioactivity in aphids (*Macrosiphum liriodendroni*) averaged 6.0% of leaf values, which actually represented a factor of only 1.2% when compared with ^{137}Cs concentrations in sap. The Cicadellidae were another abundant group of sap feeders with radiocesium concentrations not significantly different from aphids. Aphidlions (*Chrysopa* sp.) exhibited ^{137}Cs concentrations (6.2%) similar to their aphid prey. Larval and adult coccinellid predators of aphids also had ^{137}Cs levels similar to their food base. Cesium-137 body burdens of predaceous spiders averaged about 12% of leaf concentrations. The large variances associated with spider concentrations in all months suggest a significant influx of uncontaminated individuals. Ballooning is a common means of dispersal for many canopy spiders, and this mechanism could account for a dilution of the tagged populations by spiders from adjacent untagged trees. Two species of ants in the canopy (*Camponotus nearcticus* and *Crematogaster lineolata:* Formicidae) showed constant radiocesium levels throughout the summer. The average ant/foliage ^{137}Cs concentration of 20.6% was intermediate between ^{137}Cs levels of predators and herbivores. Psocoptera concentrations were also intermediate. These data indicate a general decrease in ^{137}Cs concentrations during movement along food chains,

Table 9.3. Population Density and Biomass Estimates of the Dominant Canopy Arthropods on *Liriodendron tulipifera* June–August 1965

Data are based upon weekly samples of vegetation with arthropod densities per leaf converted to m^2 basis using 554 *Liriodendron* leaves/m^2

Trophic Position	Herbivore				Omnivore		Predator	Total
	Leaf Feeder		Sap Feeder					
Month	Geometridae	*Oecanthus*	*Macrosiphum*	Cicadellidae	Formicidae	Psocoptera	Araneida	mg/m^2
June								
$\bar{x}$ mg wt	3.77	2.89	0.058	2.26	0.65	0.25	2.94	
No./m^2	13.47	4.11	1248.42	6.08	2.51	7.01	6.71	
mg/m^2	50.82	11.87	72.78	13.75	1.64	1.79	19.73	172.38
July								
$\bar{x}$ mg wt	5.30	10.51	0.043	2.22	0.92	0.23	2.59	
No./m^2	8.16	3.59	221.92	15.12	1.19	20.18	38.07	
mg/m^2	43.24	37.69	9.48	33.52	1.09	4.68	98.07	228.40
August								
$\bar{x}$ mg wt	9.17	13.73	0.031	2.05	0.60	0.24	2.14	
No./m^2	6.86	1.20	209.05	26.98	0.75	71.35	30.36	
mg/m^2	62.94	16.48	6.48	55.31	0.45	16.90	65.02	223.58
$\bar{x}$ mg/m^2	52.33	22.01	29.58	34.19	1.06	7.79	61.15	208.11

with herbivorous insects (except for sap feeders) having the highest concentrations, omnivores intermediate concentrations, and predators the lowest concentrations per unit weight. Canopy collections during the first summer (1962) after tagging showed ^{137}Cs levels in herbivores to be 0.36 and predators 0.30 that of leaves. The efficiencies of radiocesium transfer were thus 36 and 83% for plant to herbivore and herbivore to predator respectively.

The observed biomass of omnivores was relatively low in comparison with that of herbivores and predators (Table 9.3). The biomass of ants was probably underestimated, since ants spent a major portion of their time on branches in movement between leaves. The biomass of Psocoptera averaged about 7.8 mg/m^2 for the summer, with populations increasing by an order of magnitude from June to August. Of the predators, spiders had unusually high mean biomass (61 mg/m^2). The densities of other predators, for example, Coccinellidae and Reduviidae, were low, and spiders are undoubtedly the most important predatory group in the canopy. The numbers of leaf-feeding herbivores (geometrid larvae and tree crickets *Oecanthus*) decreased progressively through the summer, but biomass increased due to the continued growth of individuals. The biomass represented by these two groups (74 mg/m^2) is only a partial estimate of the actual leaf-feeder biomass – early spring weevil damage has been difficult to assess. The sap feeders (Aphididae and Cicadellidae) constitute an equally important part of the total herbivore biomass. The biomass of aphids decreased abruptly from June to July, probably due to the effects of heavy predation. Reproduction continued as evidenced by the reduction in mean individual size. Leafhopper (Cicadellidae) biomass, however, progressively increased despite a slight reduction in individual size.

EQUILIBRATION OF ^{137}Cs BODY BURDENS IN FOREST MYRIAPODA

D. A. Crossley, Jr.

Arthropod research initiated with the tagging of a *Liriodendron* forest stand with ^{137}Cs involved measurement of steady-state radiocesium concentrations in animals feeding at various trophic levels.[7] The need for better information on radioisotope accumulation under steady-state and transient conditions was emphasized by Auerbach.[8] Following the tagging of trees (by trunk inoculation) in May 1962, ^{137}Cs was translocated into foliage and became available to arthropod food chains there. Leaching by rainout removed ^{137}Cs to the forest floor during the subsequent summer, and leaf drop in autumn added higher levels of radiocesium to the leaf litter and detritus of the forest floor.[9] Arthropods on the forest floor accumulated ^{137}Cs from the litter-detritus food base. Analyses completed to date have emphasized radiocesium accumulation by myriapod species (millipedes and centipedes) of the forest floor community.

Table 9.4 presents mean ^{137}Cs concentration (pc per mg of dry weight) in myriapod species for the collecting periods July 1962–July 1963 and September 1964–March 1965. Means show only slight decreases between the two collecting periods, indicating a relatively constant steady-state concentration of ^{137}Cs in these forest floor invertebrates. Previous experimentation in the field indicated that radiocesium is leached rapidly from leaf litter.[10] Laboratory experiments with millipedes (*Dixidesmus erasus*) demonstrated that these arthropods, feeding upon leaf litter tagged with ^{134}Cs, rapidly reached a maximum concentration which then declined in proportion to the loss of radiocesium from their food.[11] Results in Table 9.4 suggest that under field conditions the ^{137}Cs leached from new litter is held by the detritus of the forest floor and remains available to the detritus-feeding arthropods. Radiocesium concentrations in arthropods evidently do not decline at rates corresponding to loss from new litter.

Figure 9.3 illustrates accumulation of ^{137}Cs by two myriapod species during the first year following tagging of the trees. The large millipede

[7] S. I. Auerbach, J. S. Olson, and H. D. Waller, *Nature* 201 (4921), 761–64 (1964).

[8] S. I. Auerbach, *Health Phys.* 11, 1355–61 (1965).

[9] S. I. Auerbach *et al.*, *Health Phys. Div. Ann. Progr. Rept. July 31, 1963*, ORNL-3492, pp. 100–102.

[10] J. S. Olson and D. A. Crossley, Jr., "Tracer Studies in the Breakdown of Forest Litter," pp. 411–16 in *Radioecology*, ed. by V. Schultz and A. Klement, Jr. Reinhold, New York, 1963.

[11] S. I. Auerbach *et al.*, *Health Phys. Div. Ann. Progr. Rept. July 31, 1962*, ORNL-3347, pp. 61–62.

Table 9.4. ^{137}Cs Concentrations (pc per mg of dry weight) in Myriapoda from the Floor of the ^{137}Cs-Tagged *Liriodendron* Forest Stand

Species	Collecting Period	
	1962–1963	1964–1965[a]
Diplopoda		
Apheloria montana	4.30 (48)[b]	2.2 (5)
Cambala annulata	0.80 (5)	c
Dixidesmus erasus	12.35 (10)	11.0 (21)
Gyalostethus monticollis	1.01 (5)	
Ptyoiulus impressus	6.53 (63)	7.1 (47)
Scytonotus granulatus	5.36 (7)	5.5 (50)
Chilopoda		
Otocryptops nigridis	6.29 (2)	
Otocryptops sexspinosus	3.74 (198)	6.8 (33)
(Geophilidae sp.)	6.29 (2)	
(Lithobiidae sp.)	8.22 (4)	

[a]Data from D. E. Reichle and D. A. Crossley, Jr., *Health Phys.* 11, 1375–84, (1965).

[b]Number of observations in parentheses.

[c]No data.

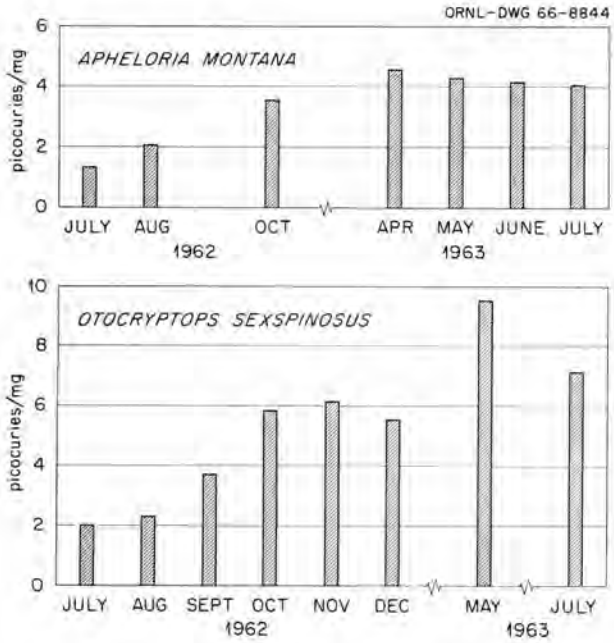

Fig. 9.3. Accumulation of ^{137}Cs by Two Myriapod Species Resident in Litter Layers in the ^{137}Cs-Tagged *Liriodendron* Forest Stand, Following Introduction of Tracer into Tree Trunks in May 1962.

Apheloria montana reached 2 pc/mg by August, when input into the forest floor still consisted largely of ^{137}Cs leached out by rain. Following leaf drop in autumn, concentrations reached 4.6 pc/mg, but then decreased slightly. The centipede *Otocryptops sexspinosus* is predaceous, yet it showed a pattern of ^{137}Cs accumulation similar to that of *Apheloria* (Fig. 9.3). Results for both species confirm the conclusion based on mean values, that under field conditions radiocesium lost from new litter remains available for accumulation by forest floor arthropods.

Local movements into and out of the tagged area proper may have resulted in some dilution of the ^{137}Cs body burdens for myriapods. Starting in the autumn of 1962, arthropods were collected outside the tagged stand in an attempt to evaluate the influence of these movements. Figure 9.4 presents ^{137}Cs concentrations in three of the species as a function of distance from the stand. Both millipede species (*Ptyoiulus* and *Apheloria*) had decreased concentrations at the periphery of the tagged area and at distances of 5, 10, or 15 m away. The centipede *Otocryptops*, however, showed no such trend for ^{137}Cs concentrations to decrease with distance from the tagged area. This finding suggests greater mobility for this predaceous species, and indicates that body burdens of ^{137}Cs in this species and possibly in

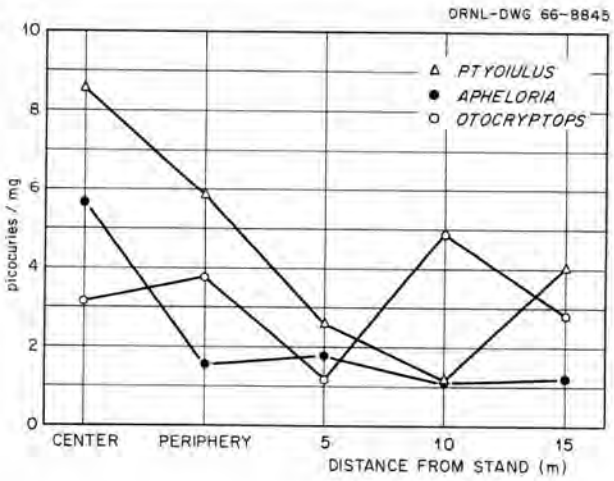

Fig. 9.4. Changes in ^{137}Cs Concentration in Myriapods Found at Distances from the Tagged *Liriodendron* Forest. Central and periphery traps were within the contaminated area; 5-, 10-, and 15-m distances measured from the boundary of the tagged area.

other predators may have been underestimated due to dilution of the population by immigrants from surrounding areas. Such a dilution should become less effective in subsequent years, as leaf litter in surrounding areas becomes increasingly contaminated by drifting leaves from the tagged stand.

^{134}Cs TURNOVER BY ISOPODS UNDER NATURAL AND LABORATORY CONDITIONS

D. E. Reichle Gladys J. Dodson

Ecological studies dealing with the turnover rates and behavior of radionuclides in natural environmental systems are often dependent upon laboratory determinations of biological half-lives for prediction of subsequent isotope movement in the field. Many environmental parameters interact to affect the biological retention of radiocesium in free-living species. Paramount among these factors is the influence of temperature. Recent studies[12] have demonstrated that ^{134}Cs retention in forest isopods is a function of environmental temperatures (Fig. 9.5), following a Q_{10} relationship of 2 ($P < 0.01$). Both components of the retention curves show a dependent relationship with

[12] D. E. Reichle, "Radioisotope Turnover and Energy Flow in Terrestrial Isopod Populations," submitted to *Ecology*.

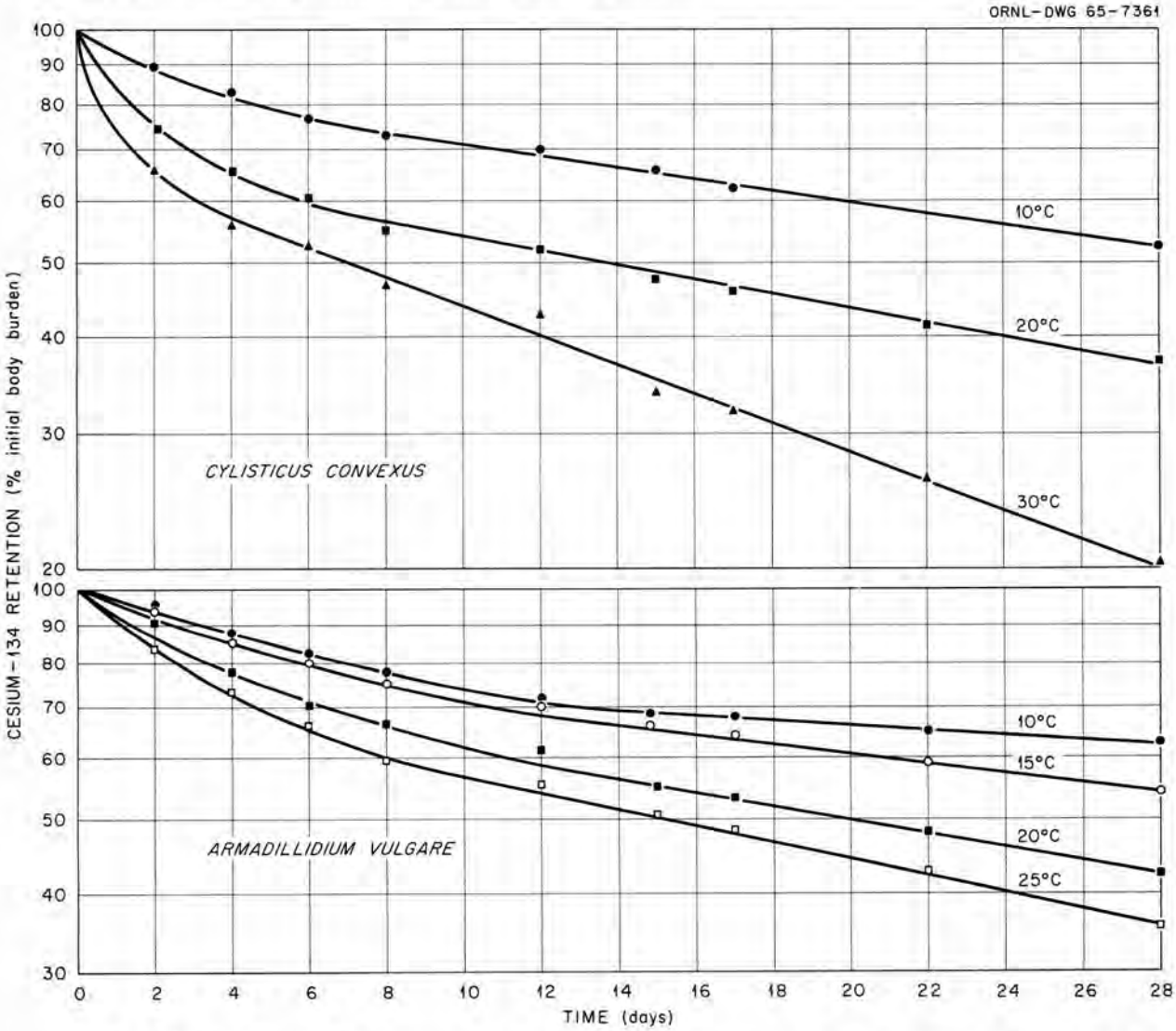

Fig. 9.5. ^{134}Cs Retention by *Armadillidium vulgare* and *Cylisticus convexus* Acclimated to Several Different Temperatures. Data points are means of ten individuals; curves are fitted by eye.

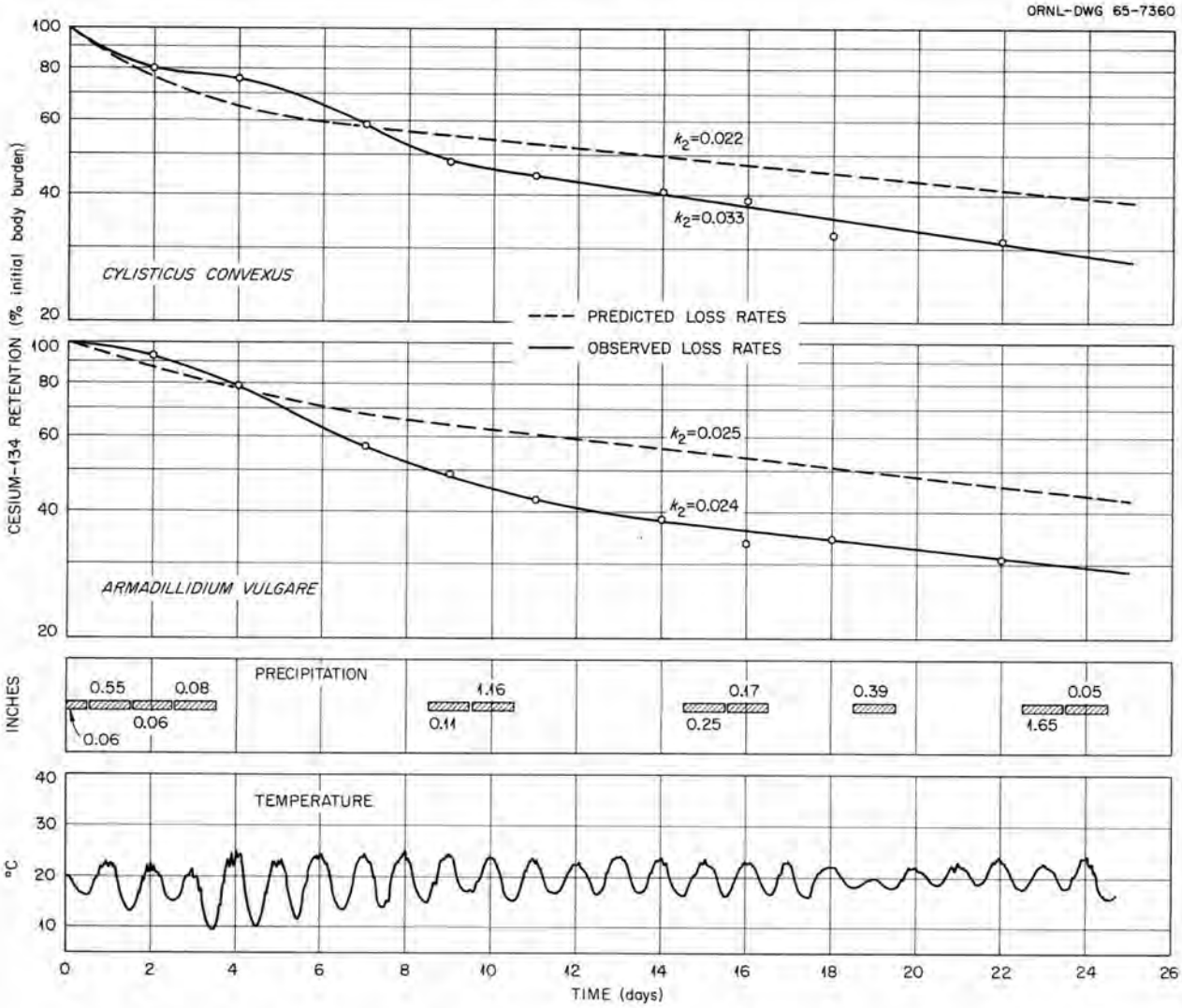

Fig. 9.6. Comparison of Radiocesium Turnover Under Laboratory and Field Conditions. Top, ^{134}Cs loss rates for *Armadillidium vulgare* and *Cylisticus convexus* (observed field rates based upon 50 individuals; predicted rates calculated from laboratory data). Center, precipitation records. Bottom, temperature regimes at soil-litter of field pens (mean 25-day temperature = 19.8°C).

temperature; that is, as temperature increases, the rate of radiocesium elimination is accelerated. The first component of the retention system represents the passage of the tagged food bolus through the intestinal tract; the second reflects excretion of metabolized wastes. Using the reciprocal of the rate constant of the first component, the turnover times of food for each species at respective increasing temperatures were calculated to be: *Armadillidium vulgare*, 3.2, 2.5, 1.9, and 1.4 days; *Cylisticus convexus*, 3.5, 1.6, and 1.3 days.

Predictions based upon these data for ^{134}Cs retention by field populations of isopods under known temperature regimes (mean $\simeq$ 20°C) closely approximated observed turnover rates (Fig. 9.6). *Armadillidium vulgare* exhibited a turnover rate of 2.4% per day and differed by a factor of only 0.1% per day from the expected rate. *Cylisticus convexus* had a turnover rate of 3.3% per day, which was 1.1% per day greater than that predicted. Increased activity of *C. convexus* in the field may have accelerated radiocesium turnover. These exponential

loss rates were derived from the second long-term retention component representing the egestion of metabolized wastes. Discrepancies in the first components (gut phase) arose, in part, from differential radiocesium assimilation from food. During early phases of the experiment, isopods retreated into refugia removed from the soil surface in response to rains and partial flooding of a previously saturated substratum. This behavior is a typical response of isopods to adverse moisture stresses in their microhabitats; drowning can be a significant mortality factor in natural populations.[13] Cessation of feeding while in refugia is expressed by a prolonged retention of the initial tagged food bolus in the gut. The significance of these data is the constancy of the second component loss rates under fluctuating temperature regimes and intermittent rains. The metabolism and turnover of radiocesium by isopods in laboratory cultures thus appear to be applied validly to field populations when corrected for temperature differences.

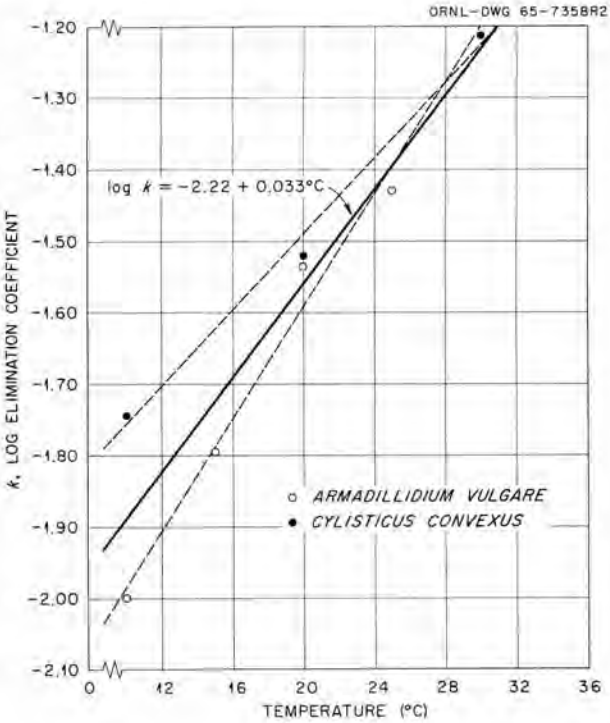

Fig. 9.7. Exponential Relationship Between Elimination Coefficients (k) and Temperature for *Armadillidium vulgare* and *Cylisticus convexus*. Solid line represents pooled regression of both species. Data points are means of ten individuals.

RELATIONSHIP BETWEEN METABOLISM AND ^{134}Cs TURNOVER BY FOREST ISOPODS

D. E. Reichle Gladys J. Dodson

A quantitative correlation between radiocesium retention and temperature for *Armadillidium vulgare* and *Cylisticus convexus* (Fig. 9.5) was made by comparing the elimination coefficients (k) with their respective temperatures (Fig. 9.7). A positive, linear relationship existed between the logarithm of k and increasing temperature. Neither of the individual species regressions (hatched lines) were significantly different ($P < 0.01$) from a Q_{10} of 2 (slope = 0.030) over the range of temperatures examined:

Armadillidium vulgare $\log k = -2.38 + 0.039°C$

Cylisticus convexus $\log k = -2.02 + 0.027°C$

Because temperature is known to limit the metabolic rate of poikilotherms, the data were also analyzed to ascertain whether there was any correlation between the metabolism of species and their retention of radiocesium. Although oxygen consumption was not measured simultaneously with bioelimination, the regressions of log microliters of oxygen consumed on temperature were also linear for this same temperature range (Fig. 9.8), with neither of the two species being significantly different ($P < 0.01$) from a Q_{10} of 2:

Armadillidium vulgare $\log \mu l = 1.56 + 0.030°C$

Cylisticus convexus $\log \mu l = 1.79 + 0.025°C$

By simultaneously solving for temperature the regression equations of log k on temperature and log μl of O_2 on temperature, expressions were derived describing the direct relationship between radiocesium turnover and oxygen consumption (Fig. 9.9). The resulting equations were as follows:

Armadillidium vulgare $\mu l = 2.46 \times 10^3 k^{0.77}$

Cylisticus convexus $\mu l = 4.68 \times 10^3 k^{0.93}$

Similar correlations between radionuclide turnover rates and temperature have been reported for other

[13] O. H. Paris, *Ecol. Monographs* **33**, 1–22 (1963).

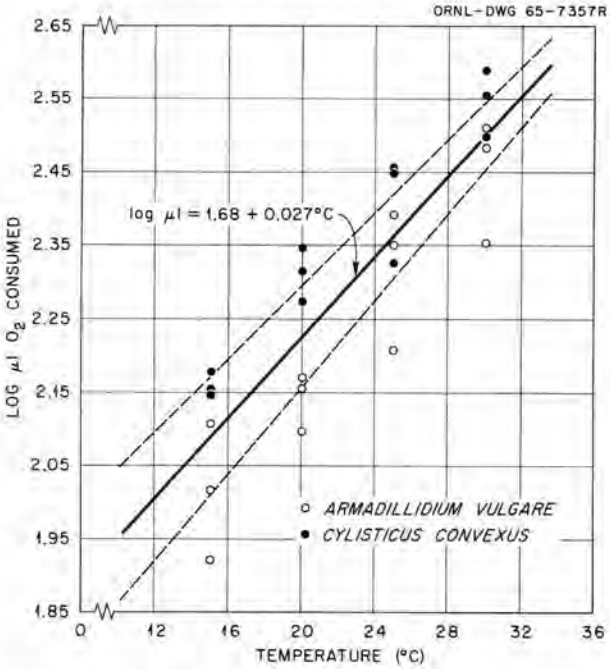

Fig. 9.8. Exponential Relationship Between Microliters Oxygen Consumption and Temperature for *Armadillidium vulgare* and *Cylisticus convexus*. Solid line represents pooled regression of both species. Data points are means of 15 individuals.

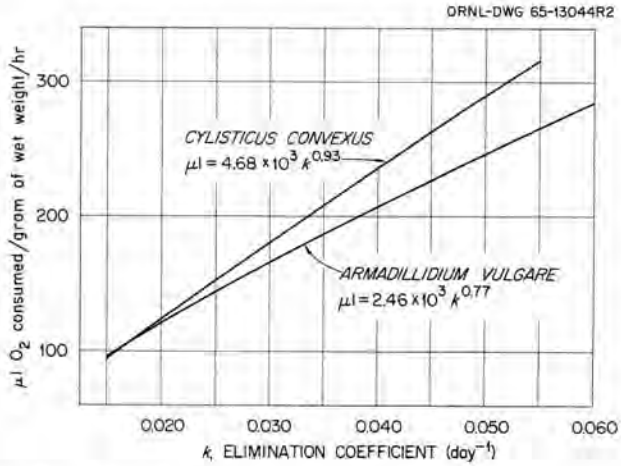

Fig. 9.9. Relationship Between Radiocesium Turnover and Metabolism for *Armadillidium vulgare* and *Cylisticus convexus*.

arthropods.[14,15] However, proceeding beyond this point and establishing a function relating radionuclide turnover and metabolic rate makes available a tool of considerable ecological value.[12] A model can now be developed which utilizes the turnover rates of an isotope as a means of measuring the metabolic activity of animal populations under natural environmental conditions.

ISOTOPIC DETERMINATION OF FOOD CONSUMPTION AND UTILIZATION BY ISOPODS

D. E. Reichle Gladys J. Dodson

Dry matter intakes for four isopod species from a lettuce food base, estimated by the isotope method, are presented in Table 9.5 as mean daily consumption. For closely related taxa, food consumption and energy requirements usually are considered to be a function of body size. To permit comparative analysis of dry matter utilization and energy flow between the several isopod species examined, the data were normalized by expressing all values relative to gram (dry weight) individuals. Energy inputs were computed from these values using a caloric equivalent of 3982 cal per g of dry weight of lettuce. Efficiencies of dry matter and caloric utilization by *Armadillidium vulgare* and *Cylisticus convexus* were determined from the relationship (daily food intake minus daily feces production/daily food intake) × 100. Since feces in arthropods are mixed with some metabolic wastes before elimination from the organism, it is not proper to consider these percentages as efficiencies of assimilation. They are, rather, the efficiencies for dry matter digestibility and metabolizable energy. The respective efficiencies (Table 9.6) were 64% digested and 73% metabolized for *A. vulgare* and 60% digested and 70% metabolized for *C. convexus*. Higher efficiencies for *A. vulgare* may be correlated with a longer time of food residence in the gut. The caloric values of metabolizable food were higher than the caloric value of the food ingested: 1.5 times higher for *A. vulgare* (4564 cal per g of dry weight) and 1.17 times higher for *C. convexus* (4665 cal per g of dry weight).

[14] D. E. Reichle and D. A. Crossley, Jr., *Health Phys.* 11, 1375–84 (1965).

[15] E. P. Odum and F. B. Golley, "Radioactive Tracers as an Aid to the Measurement of Energy Flow at the Population Level in Nature," pp. 403–10 in *Radioecology*, ed. by V. Schultz and A. W. Klement, Jr., Reinhold, New York, 1963.

Table 9.5. Estimation of Food Consumption by Isopods from Radiocesium Turnover Rates

k_2 is the second component loss rate coefficient, Q_e is the activity density, M is the mean species mass, a is the assimilation coefficient for radiocesium; intake (nc) = $k_2 Q_e M/a$; intake (mg) = nc/Q food; all food intake values are expressed as dry weights

Species	k_2 (day^{-1})	Q_e Isopod (nc/mg)	$M/\bar{x}$ mg Isopod	$k_2 Q_e M$	a	Intake (nc)	Q Food (nc/mg)	Intake (mg)	% Body wt per Day
Armadillidium vulgare	0.030	14.72	22.41	9.90	0.87	11.38	22.16	0.51	2.3 ± 0.42
Armadillidium nasatum	0.024	16.52	9.92	3.93	0.87	4.52	30.49	0.15	1.5 ± 0.30
Cylisticus convexus	0.037	17.71	11.59	7.59	0.87	8.72	23.03	0.38	3.3 ± 0.61
Metoponorthus pruinosus	0.050	19.46	5.21	5.07	0.87	5.83	31.74	0.18	3.5 ± 0.66

The food energy metabolized by an animal is subsequently utilized for the performance of several basic functions. As a result, the total energy budget may be partitioned between the requirements of basal metabolism, activity expenditures, and production. Presumably, a small fraction of this energy transfer may be lost due to the calorigenic effect. In partitioning the isopod energy budgets, two fundamental categories have been examined:[12] (1) maintenance metabolism, which included both the basal metabolic rate and a normal activity component, and (2) production, further subdivided into growth and production of young by females.

Estimates of the energy requirements for maintenance were based upon independent respirometry measurements of oxygen consumption which were converted to caloric equivalents using specific respiratory quotients. In *A. vulgare* 80% (52.5 cal per g of dry weight per day) of the metabolizable energy was utilized in maintenance. *Cylisticus convexus* had a slightly lower requirement of 79% (72.3 cal per g of dry weight per day) of the metabolizable energy used in maintenance. The gross maintenance efficiencies for these two species were 58 and 55% respectively. Since dry matter digestibility and metabolizable energy efficiencies were not obtained for *A. nasatum* and *Metoponorthus pruinosus*, it was not possible to consider their net efficiencies of utilization in maintenance. However, their respective gross efficiencies of 78 and 103% were considerably higher than those of the former two species. Errors incorporated into the measurements of maintenance metabolism for *M. pruinosus* may have resulted in an overestimate of this component, since individuals of this species exhibited above-normal activity in respirometers.

Growth rate calculations gave 20.4 cal per g of dry weight per day for *A. vulgare* and 15.4 cal per g of dry weight per day for *C. convexus*: 31 and 17% of the metabolizable energy respectively. Energy requirements of gravid females for reproduction were 7.6 cal per g of dry weight per day for *A. vulgare* and 16.4 cal per g of dry weight per day for *C. convexus* during their periods of gravidity. In experimental laboratory cultures, males and females were present in a 1:1 ratio. Therefore, on a population basis, the energy expenditure for reproduction in these cultures would be 50% of the above figures or 6 and 9%, respectively, of the metabolizable energy for *A. vulgare* and *C. convexus*. The total gross and net production efficiencies on an energy basis were: *A. vulgare*, 27 and 37%; *C. convexus*, 18 and 26%.

Table 9.6. Food Consumption and Energy Flow (per Gram Individual) at 20°C for Isopods on a Lettuce Food Base

Daily intake calculated by isotopic method; maintenance metabolism energy requirements calculated from respirometry determinations

Species	Daily Intake (Mean with 95% Confidence Limits)	Metabolizable (Digestible)	Maintenance Metabolism (Mean with 95% Confidence Limits)	Estimated Production[a]	
				Growth	Reproduction (♀)
Armadillidium vulgare					
Dry matter, mg	22.8 (13.8–31.7)	14.5			
Energy, cal	90.7 (54.9–126.2)	65.9	52.5 (47.5–57.5)	20.4	7.6
Armadillidium nasatum					
Dry matter, mg	15.1 (9.1–21.1)				
Energy, cal	60.1 (36.2–84.0)		46.7 (41.7–51.7)		
Cylisticus convexus					
Dry matter, mg	32.8 (20.4–45.2)	19.6			
Energy, cal	130.5 (81.2–179.9)	91.7	72.3 (65.3–79.3)	15.4	16.4
Metoponorthus pruinosus					
Dry matter, mg	34.5 (21.0–48.0)				
Energy, cal	137.3 (23.6–191.0)		141.2 (124.0–158.4)		

[a]S. P. Hatchett, *Ecol. Monographs* 17, 47–79 (1947).

TROPHIC EFFICIENCIES OF INSECT HERBIVORY USING ^{86}Rb AND ^{32}P TRACERS

D. E. Reichle

The predilection of certain herbivorous insects for specific plant hosts offers the opportunity for detailed trophic analyses of insect populations with delimitable food bases. An example of such a plant-insect relationship occurs with the chrysomelid beetle *Chrysochus auratus* (Fab.) and the Indian hemp plant *Apocynum canabinum* L. Radiotracer tags of ^{86}Rb and ^{32}P of plants growing in the field were used to measure food consumption and the efficiencies of trophic transfer for beetle populations under natural environmental conditions. Plant-to-insect concentration factors and the assimilation efficiencies from food are given in Table 9.7 for the various constituents of the foliage food base. Consumption of vegetation by beetles averages 15.9 mg per day or (56.8 ± 1.40)% of their dry body weight. The steady-state body levels (Q) of the various food constituents in beetles are

Table 9.7. Trophic Efficiencies for Herbivory by *Chrysochus auratus*

Factor	Plant	Insect	Concentration Ratio (Insect/Plant)	Efficiency of Assimilation from Food
^{86}Rb (pc per mg of dry weight) at steady state	1.58	1.09	0.69	0.87
^{32}P (cpm per mg of dry weight) at steady state	791	1149	1.45	0.74
Total ash content (% dry weight)	18	5.6	0.69	
Dry matter				0.48
Ash-free dry matter				0.46
Energy (cal per g of ash-free weight)	5640	5537	0.98	0.55
Water content (%)	48	60	1.25	

a function of the input rate (I), turnover rate (k), and assimilation efficiency (a), where

$$I = kQ/a .$$

The biological half-life (T_b) of ^{86}Rb in beetles was 1.0 day (k = 0.693 day^{-1}). A difference between sexes in ^{32}P turnover existed: T_b males, 7.5 days (k = 0.092 day^{-1}); T_b of ovipositing females, 5.3 days (k = 0.131 day^{-1}). The respective turnover times for these food constituents (calculated from body burden/daily input) were ^{86}Rb, 1.44 days; dry matter, 3.66 days; energy (calories), 4.42 days. Turnover times may be used to compare the metabolism of such constituents by the organism. Ranking of turnover times indicates that *Chrysochus* is most conservative in its utilization of energy, followed by dry matter and then rubidium. The turnover times of phosphorus in both sexes (7.63 to 10.87 days) were appreciably slower, due to the synthesis and incorporation of phosphorus in body tissues. The turnover time of energy can subsequently be used to estimate the metabolic rate of *Chrysochus* in the field. Assuming an RQ of 1, oxygen utilization would be 3950 μl per g of live weight per hr – comparable to the value (3400 μl per g of live weight per hr) found by Crossley[16] for mixed species populations of insects on White Oak Lake bed.

[16]D. A. Crossley, Jr., personal communication.

EFFICIENCY OF RADIOISOTOPE TRANSFER IN PREDATOR-PREY SYSTEMS

D. A. Crossley, Jr. M. H. Shanks

The translocation of radioactive substances along food chains in contaminated or tagged areas results in a standing distribution of radioactivity among soils, plants, herbivores, and predators. Data from such field studies are being used in evaluating food chain transfers of radioisotopes such as ^{137}Cs and ^{90}Sr. An additional important objective involves the use of radioisotopes as tools in the study of functional relationships in food chains. Radioisotopes of cesium have been employed to estimate rates of dry-matter movement and energy flow in plant-to-insect transfers. In order to extend the methods to include predators in food chains, additional laboratory experiments were initiated to analyze the efficiencies of radiocesium transfer in predator-prey trophic exchanges.

The brown cricket (*Acheta domesticus*) served as the prey species. A laboratory colony received ^{134}CsCl in drinking water (1.4 μc/ml); after one week, individuals were removed and offered to predators caged singly. After feeding, radiocesium accumulation in predators was evaluated by the relation

$$Cs_p = Cs_h - Cs_r - Cs_u ,$$

Table 9.8. Gross Predatory Efficiencies for Arthropod Species Preying on Crickets (*Acheta domesticus*)

	Transfer to Predator (%)		
	Tenodera	*Otocryptops*	Lycosidae
Weight	97.6 ± 1.02 (10)[a]	100 ± 0.00 (18)	93.3 ± 1.14 (8)
^{134}Cs	98.5 ± 0.60 (10)	100 ± 0.00 (18)	83.3 ± 4.16 (8)

[a]Mean ± standard error. Number of observations in parentheses.

where Cs_p is the radiocesium accumulated by the predator during a single feeding, Cs_h is the radiocesium in the prey at initiation of the feeding trial, Cs_r is the radiocesium in uneaten residues after feeding, and Cs_u is that unaccounted for (due to radioactivity in unrecoverable juices and loss through biological elimination). The quantity Cs_u was minimal when data were limited to those feeding events which occurred within a few hours after final counting of the prey. A mass balance obtained for the centipede *Otocryptops* indicated Cs_u to be less than 10%.

Gross predatory efficiency for transfer of ^{134}Cs from prey to predator was estimated from the ratio $(Cs_h - Cs_r)/Cs_h$. Similarly, transfer of dry matter was estimated from the ratio (wt prey – wt residue)/wt prey. Table 9.8 shows gross predatory efficiencies obtained for a preying mantis species (*Tenodera sinensis*), a centipede species (*Otocryptops sexspinosus*), and lycosid spiders. Gross predatory efficiencies were highest for *Otocryptops*, for which percentage transfer of both weight and ^{134}Cs was 100%. Mantids were nearly as efficient, accumulating about 98% of both weight and radiocesium. Residue uneaten by mantids consisted of cricket antennae and small appendages. Efficiencies were lowest for lycosid spiders, which accumulated weight more efficiently than ^{134}Cs. These spiders injected digestive fluids into their prey and are able to ingest only liquid matter. Evidently some radiocesium is lost during this feeding process.

These laboratory experiments demonstrate a highly efficient accumulation of radiocesium by predators during the feeding process. In analysis of field data it now appears feasible to use mean radionuclide concentration in herbivores as an estimate of concentration in the food intake of predators.

^{106}Ru ELIMINATION BY BROWN CRICKETS (*ACHETA DOMESTICUS*)

D. A. Crossley, Jr. M. H. Shanks

Ruthenium-106 is potentially hazardous in waste disposal areas because of its mobility when released into the environment, its relatively abundant fission yield, and its moderately long half-life.[17]

Some data on ^{106}Ru content of soils, plants, and animals in the upper White Oak Lake bed have been obtained previously.[18] To assist in interpretation of these field data, experiments were initiated on turnover rates for ^{106}Ru in a common insect species, the brown cricket, for comparison with radiocesium turnover rates.

Radionuclides ($^{106}RuCl$ or $^{134}CsCl$) were supplied to cricket colonies in drinking water for several days prior to measurement of biological half-lives. Following the accumulation phase, crickets were caged separately and counted several times daily at 3- to 6-hr intervals with an NaI well-type scintillation detector. Experimental animals were maintained at 85°F.

Results of the experiments suggested similar biological half-lives for longer components of cesium and ruthenium elimination (Fig. 9.10). Longer components of elimination appear to have half-times of approximately 40 hr for each nuclide, but absorption was different for these: About 60 to 70% of the radiocesium was eliminated at the longer rate, but only about 30% of the radioruthenium was attributable to the longer component.

[17]S. I. Auerbach and J. S. Olson, pp. 509–19 in *Radioecology*, ed. by V. Schultz and A. W. Klement, Jr., Reinhold, New York, 1963.

[18]S. I. Auerbach *et al.*, *Health Phys. Div. Ann. Progr. Rept. July 31, 1962*, ORNL-3492, pp. 81–84.

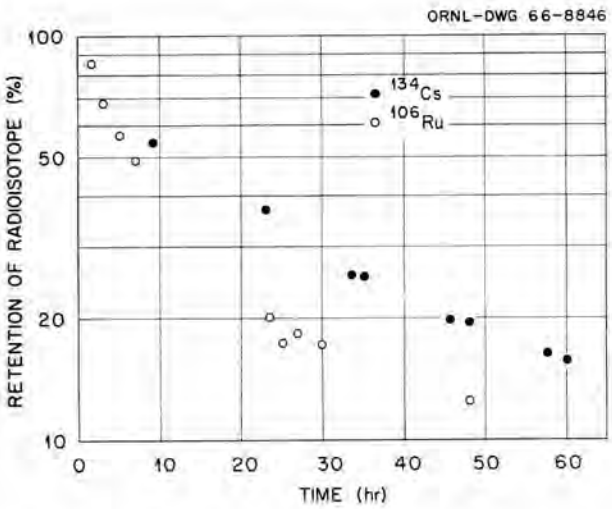

Fig. 9.10. Retention of ^{134}Cs and ^{106}Ru by Crickets (*Acheta domesticus*).

Dissections of crickets in additional experiments confirmed rapid clearance of ^{106}Ru from the crop and gizzard. Mid-gut and hind-gut concentrations decreased at rates similar to the whole-body longer components, probably as a result of elimination of absorbed material from the intestinal walls. Radiocesium also has been shown to concentrate in the intestinal walls of orthopterans.[19] However, radiocesium was also found distributed among muscle, fat body, and other soft tissues of insects, whereas ^{106}Ru concentrates mainly in the intestinal walls and was not detected in samples of fat body of *Acheta*. Neither radionuclide accumulated in the integument.

LOSSES OF ^{137}Cs AND ^{60}Co FROM LEAF LITTER

Martin Witkamp Marilyn L. Frank

Three types of leaf litter (alder, white oak, and sycamore) tagged with ^{137}Cs and ^{60}Co were exposed in natural environments with varied rates of leaching (forest floor, pond, stream) for showing contrasts in isotope solubility, in complexing with organic compounds, and in biological importance. The leaves were contained in nylon mesh bags. Loss rates of ^{137}Cs were from 2 to 12 times higher than for ^{60}Co. First year's loss of ^{137}Cs, ^{60}Co, and weight was greatest in a stream and least in a forest, whereas losses in a pond were intermediate. Microbial densities and activities on the leaves were not significantly correlated with these losses, indicating the dominant effect of leaching over microbial breakdown. Both losses and microbial activities and densities were greatest on sycamore leaves and least on alder leaves, with oak leaves in an intermediate position. Thus it appears that loss rates of nuclides in organic matter exposed to these contrasting environments are primarily determined by rates of leaching, whereas within any one of these environments, microbial breakdown regulates rate of release between leaf species.

[19] D. A. Crossley, Jr., and M. E. Pryor, *Health Phys.* 4, 16–20 (1960).

^{137}Cs TRANSFER IN TERRESTRIAL MICROCOSMS

Martin Witkamp Marilyn L. Frank

Terrestrial microcosms composed of differing numbers of compartments were leached by simulated rain to evaluate transfer of ^{137}Cs. After six months of leaching, the microflora of decomposing tulip poplar leaves retained more than one-third of the leachable ^{137}Cs. In the presence of millipedes, the microflora retained only 11% of the initial ^{137}Cs. The consumption of microflora by millipedes reduced total amounts that could be retained by microbes. Leaves lost half their weight and 73% of their ^{137}Cs. Most of the initial ^{137}Cs was held by the soil (51%), while 21% was in the organic fraction. Loss from the entire system amounted to only 8%. Results show that the microflora is the major biological ^{137}Cs accumulator, and that the soil after only six months retained more than half of the ^{137}Cs input.

ACCUMULATION AND PRODUCTION IN A PIONEER ECOSYSTEM OF KUDZU VINE AT COPPERHILL, TENNESSEE

Martin Witkamp Marilyn L. Frank

Development of biota and matter was measured during the fifth, seventh, and ninth years of succession of kudzu vine (*Pueraria lobata*) planted on cultivated and fertilized strips of a denuded

landscape at Copperhill, Tennessee. Masses of vegetation, litter, and humus and their contents of carbon and nitrogen; population densities of bacteria, fungi, and arthropods; and respiration rates, moisture content, and pH of litter and soil were measured at three stations in each of four stages of succession. After five years of growth (August 1960) the vine produced 550 g of dry matter per m^2 on the strip and had spread 30 m away from it. Subsequent measurements in August of 1962 and 1964 showed that further growth had been checked. This reduction of growth may be due to an immobilization of up to 80% of the cycling phosphorus and 50% of the nitrogen in litter and humus, which had been accumulating at the rate of 0.8 to 1.1 standing crops per year. Microbial densities and respiration increased at a faster rate than their litter and humus substrate. This result suggests (1) that the physical environment of the microflora improved and (2) that microbial immobilization of phosphorus and nitrogen was instrumental in the reduced expansion of kudzu.

Studies like these show the problems and possibilities of regeneration of denuded or degenerated landscapes which may result from strip mining, nuclear disaster, or general mismanagement.

MOVEMENT OF ^{137}Cs IN PINE FOREST FLOOR SUBSYSTEMS

Martin Witkamp Marilyn L. Frank

Retention of ^{137}Cs by moss, lichen, needle litter, and plant rosettes following three months of simulated rain was measured to evaluate their role in the cycle of ^{137}Cs in a local pine forest. Moss, lichen, litter, and rosettes retained 99, 92, 90, and 10% of the applied ^{137}Cs respectively. Dead mosses and lichens retained only about 3% less ^{137}Cs than living ones, indicating that retention was mainly nonbiological. The presence of 2.5 cm of subsoil under moss, lichen, and litter reduced their ^{137}Cs contents, but retention by these materials and subsoil combined was 98% or more. Moisture absorption of soil and the diffusion of the isotopes into the adsorptive soil sink appear to enhance downward movement of isotopes into the soil. The discretely bounded lichen and moss cushions naturally occurring in many pine forests evidently are capable of a similar high fallout retention, as has been found in the tundra and in tropical epiphyte food chains.

SOIL STUDIES IN HERBACEOUS ECOSYSTEMS

G. M. Van Dyne

In designing field facilities for a proposed study on mechanisms of secondary succession, it was necessary to characterize the edaphic and topographic characteristics of a field area for use in allocation of plots in future experiments. Since mapping or sampling the soil properties in detail would damage a considerable part of the study area, a hydraulically powered coring machine was used to obtain soil cores at selected points throughout the area.

A mathematical interpolation scheme of contour mapping was used to develop maps of soil properties. To test the validity of a "limited field–computer mapping" approach, the study area was first surveyed by conventional plane-table mapping techniques (Fig. 9.11). Then elevations were read with a transit, obtaining data points on a 50- by 50-ft grid. A mathematical interpolation scheme was used in a computer program to produce the contour maps in Fig. 9.12 with the Calcomp plotter. Excellent agreement of elevated contours is noted, even though the computer-based method required only a minimum of data points in the field.

This method was then applied for mapping soil properties. To gain familiarity with soil properties in the area, six pits were excavated to the water table, and a soils specialist was consulted in the examination and description of horizons and soil properties in the pits. Both black and white and color photographs were taken of these soil profiles to aid in recognition of horizons in core samples, which were obtained intact by using a hydraulically powered coring machine. Duplicate cores were taken on the 50- by 50-ft grid, horizon depths and depth to mottling were measured on the intact cores, and the horizons were separated for chemical and physical analyses. An example of the contour maps of a soil property is given in Fig. 9.12, where the depth of the *A* horizon is mapped. Comparison of the maps of elevation and *A* horizon depth shows that the latter was, in part, dependent on the former. This technique will be used in mapping other soil chemical and physical properties as a means of allocating comparable

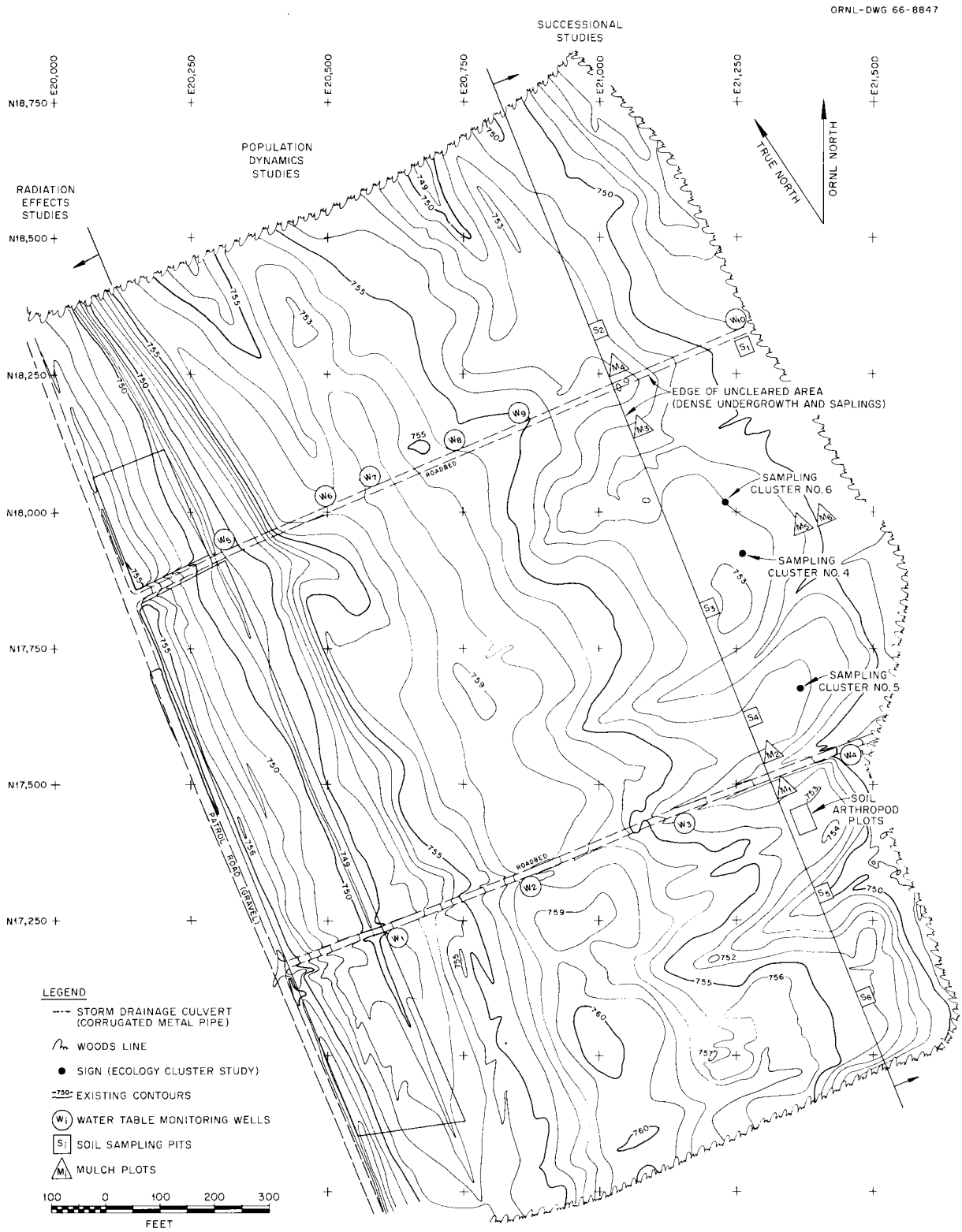

Fig. 9.11. Elevation Contour Map of the Old-Field (Ecology 0800) Area. The map was obtained by conventional plane-table surveying methods. The part of the area denoted by arrows is shown in Fig. 9.12 with computer-generated contour maps.

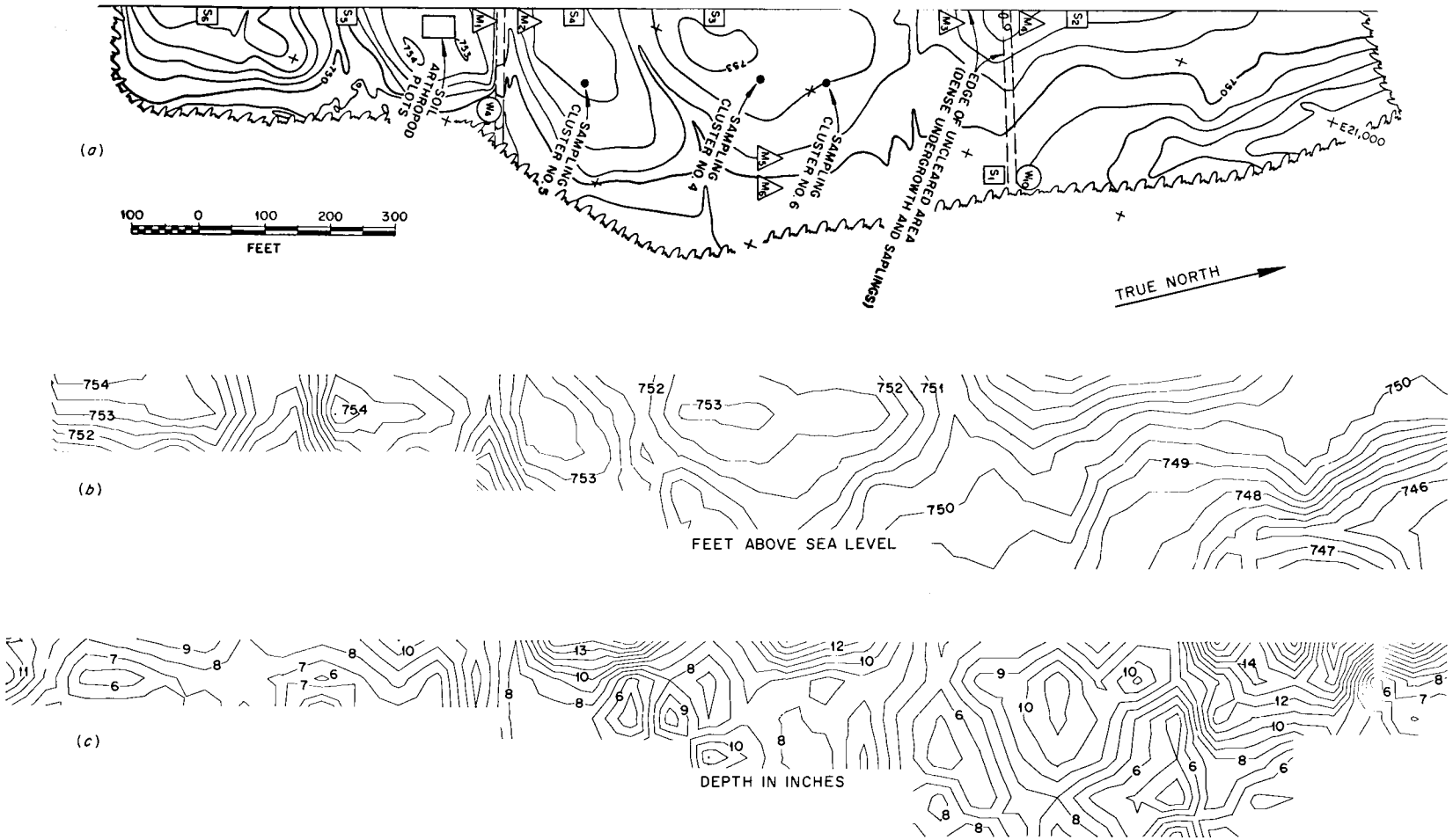

Fig. 9.12. Comparison of Elevational and Soil Features in Part of the Old-Field Area. Map *a* is a conventionally obtained elevation contour map; *b* is a computer-generated elevation contour map of the same area; c is a contour map of *a* horizon depth for the same area.

plot locations for factorial experiments for which it is necessary to minimize the random variance between plots.

POSSIBLE MECHANISMS OF COBALT SORPTION ON SOIL CLAYS

R. C. Reynolds Tsuneo Tamura

Studies have been made of cobalt sorption on clays and ground micas. A partial and tentative model of cobalt sorption on natural clays is presented here. Verification and completion of this model should allow predictions concerning soil-water interactions of cobalt in specific ecosystems, assuming that soil and fluid compositions are known.

All clay sorption experiments involved $\sim 10^{-6}$ *M* cobalt spiked with ^{60}Co; cobalt sorption was studied in the presence of high salt concentrations (0.05 to 0.1 *N*). The salt swamps normal non-specific exchange reactions; therefore data reported here apply to specific exchange reactions such as one might expect in situations where the ratio of indigenous cations to carrier-free radionuclide is large.

For the purposes of comparing sorption data, a sorption coefficient *S* is defined as $10 \times \log [1/(1 - Co_s)]$, where Co_s is the fraction of cobalt sorbed by the clay at equilibrium. The expression for *S* derives from a consideration of cobalt sorption as a first-order reaction

$$Co_e = Co_i e^{-S} ,$$

where Co_e is the fraction of cobalt in solution at equilibrium, and Co_i is the fraction of cobalt initially present. Inverting and taking the logarithm yields

$$S = 2.303 \log Co_i/Co_e ;$$

substituting $Co_i - Co_s$ for Co_e and assuming the value of unity for Co_i yields

$$S = \text{constant} \log [1/(1 - Co_s)] .$$

A direct comparison of sorption data requires that cobalt and clay concentrations be fixed.

All conclusions here are drawn from ratios of sorption coefficients, so that effects of aging, particle size, and reagent contamination are reduced. Interpretations of sorption data have led to a tentative model of cobalt sorption, which may be outlined as follows.

Depending upon the composition of the octahedral layer (magnesium or aluminum) and the surface charge density present on the mineral, cobalt sorption occurs at either or both of two exchange sites, namely, octahedral edges and 12-coordinated interlamellar or surface sites. Low-charged lattices, particularly those of trioctahedral composition, favor edge sorption, whereas high-charged lattices favor surface and/or interlamellar sorption. Because of the ionic similarity between cobalt and magnesium, the latter effectively blocks cobalt at all sites. Edge sorption is enhanced by high pH and is little affected by calcium ions. Conversely, surface of interlamellar sorption is little affected by pH and is significantly blocked by calcium.

Figure 9.13 shows the relative blocking efficiency, with respect to sodium, of calcium and magnesium on cobalt sorption. Experiments were carried out at pH 7, and all ionic concentrations are 0.05 *N*. The ordinate shows the sorption coefficient, normalized to S_{Na} (cobalt sorption from sodium solution) equal to 1. The abscissa shows the estimated net negative charge on the mica structural unit; this is a function of the charge density on the clay surface.

Figure 9.13 also shows that with increasing surface charge density, calcium assumes an increasingly significant role in blocking cobalt sorption. Magnesium appears to block cobalt sorption efficiently, regardless of surface charge. These relations have been interpreted as follows. Talc has little or no surface charge; therefore its rather significant cobalt sorption is explained largely by adsorption on the unsatisfied trioctahedral (magnesium) clay edge sites. Calcium is too large an ion to substitute for magnesium or cobalt at these sites. Therefore, calcium shows about the same blocking efficiency as sodium, namely, very little. At the other extreme, illite has a high surface charge and little affinity for cobalt on edge adsorption sites because of its aluminous dioctahedral layer. For illite, calcium blocks cobalt significantly better than does sodium, presumably because of calcium's divalent character. Magnesium blocks cobalt sorption effectively because of the similar ionic radii of these two elements. Montmorillonite is intermediate to illite and talc

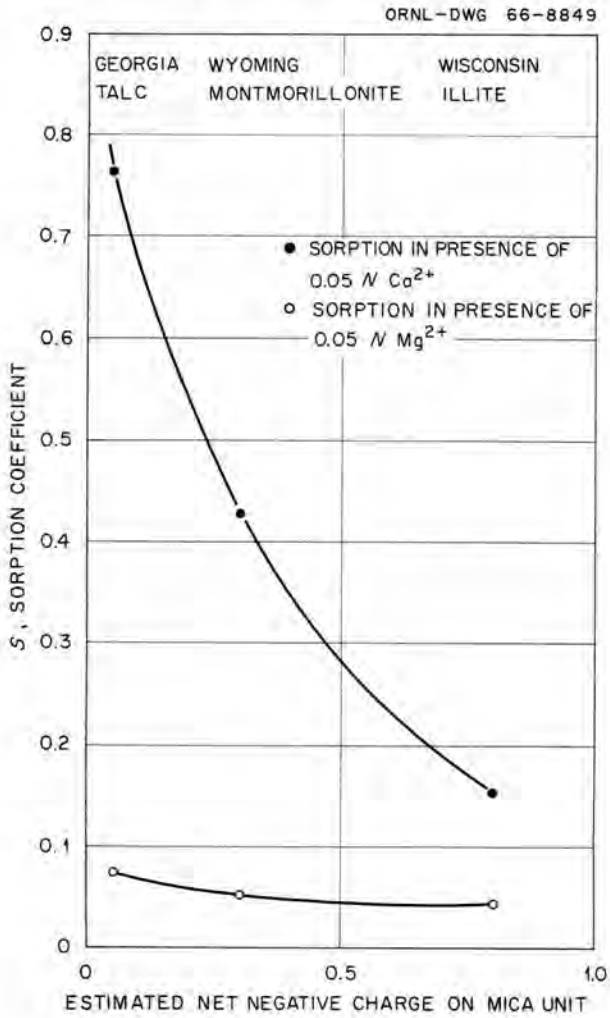

Fig. 9.13. Sorption as a Function of Lattice Charge. *S* values are normalized to $S_{Na} = 1$.

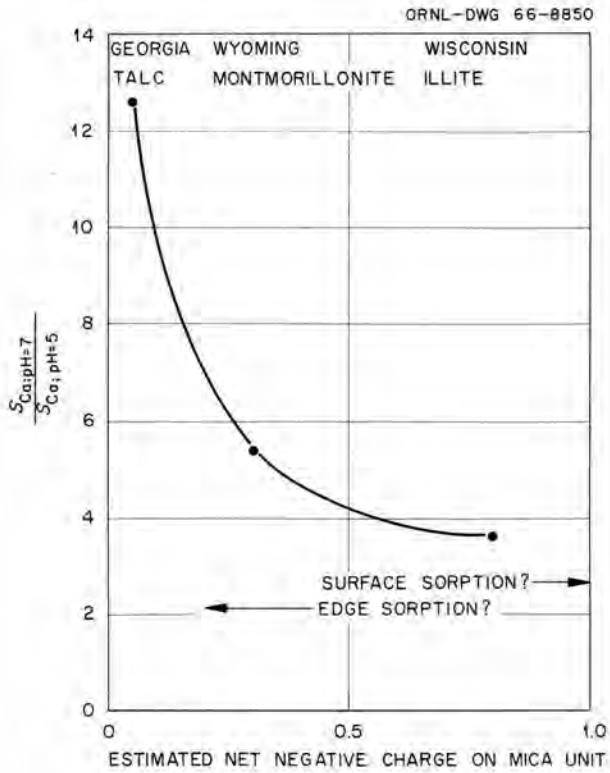

Fig. 9.14. Relation Between Lattice Charge and the pH Effect in Cobalt Sorption.

in surface charge and composition; its sorption characteristics also are intermediate. Presumably, the sorption on montmorillonite is partially at edges and partially on interlamellar surfaces.

Figure 9.14 tends to confirm the previous interpretations. Here the effect of pH on cobalt sorption is compared for these three minerals. The ordinate shows the sorption coefficient at pH 7 divided by the sorption coefficient at pH 5, both measured in calcium systems. A large value for the ratio indicates a large pH effect. Sorption at octahedral edge sites is thought to involve ionization of exposed OH groups with a concomitant increase in negative lattice charge. Because the magnitude of the charge is very pH sensitive, cobalt sorption by this mechanism should also show a large pH dependence. Note that for talc, with postulated edge adsorption, the pH effect is indeed large. Illite, on the other hand, shows a much reduced pH effect, probably because the sorption involves surface exchange sites which are activated by permanent lattice charge. Such sites should not be increased by higher pH values, and the data of Fig. 9.14 support this contention. As before, montmorillonite shows intermediate behavior.

PRECISION AND ACCURACY OF BASAL COVER ESTIMATES

G. M. Van Dyne

Two common methods of basal area or cover determination in ecological studies are the line intercept technique and the point analysis technique. The line intercept technique generally is considered to give accurate results and has been

Table 9.9. Population Characteristics for 12 Vegetation Groupings from 350 Transects

Plant Group	Frequency[a] (%)	Basal Cover[b] (%)	Cover Composition[c] (%)	Variance[d]
All live vegetation[e]	100	15.9	100	3977
All grasses	98	4.3	27	213
Bunchgrasses	79	2.3	14	151
Sod formers	73	2.0	12	164
Bluebunch wheatgrass	32	0.5	3	25
Needleandthread	38	0.4	3	18
Needleleaf sedge	32	0.1	1	3
All forbs	58	1.6	10	251
Upright forbs	33	0.4	3	27
Mat forbs	38	1.2	8	288
Small clubmoss	52	8.9	56	3514
Shrubs	17	0.3	2	44

[a]Based on presence or absence by transect.
[b]Based on total intercepts over all transects.
[c]Based on percent of total basal cover of all live vegetation.
[d]Based on number of 0.01-ft intercept units per 5-ft transect.
[e]Includes lichens and moss.

used as a standard for comparison in many methodological studies, but it is a time consuming procedure. Point analysis technique has frequently been used in vegetation analysis, but many factors including number, size, and spacing of points have influenced its success. The true values of the vegetation basal area or cover parameters seldom are known in field studies. Thus, the validity or accuracy of vegetation sampling techniques usually cannot be established. The precision or repeatability of different techniques is compared in field studies. Accuracy as well as precision of techniques may be compared when sampling artificial populations for which the values of the parameters are known.

A study[20] was made of a known but complex population constructed from census records of 350 line intercept transects from foothill grassland. This artificial population was sampled both systematically and randomly with 25, 50, and 100 points per line. Statistical analyses were made to compare point densities, point placements, and their interactions with each other and with 12 plant categories. Comparisons were also made of the various point-sample estimates to the population parameters.

Characteristics or parameters of the population of 350 transects are shown in Table 9.9. The degree to which statistics for point samples match these parameters is a measure of the accuracy of that technique. Frequency of occurrence of different vegetation categories as a function of number of points per line, and averaged for systematic and random placement, mean percent cover, and coefficients of variation in percent are given in Fig. 9.15. Some practical implications from these studies for sampling vegetation similar to that described herein are: (1) to sample sod-forming species; random placement of points would be better than systematic placement; (2) to sample the dominant bunch grasses; systematic placement would be better, especially if the distance between points is greater than the average basal diameter of the plants; (3) to sample plant categories with high basal cover; either point placement procedure would suffice; (4) generally, greater efficiency in sampling would occur within 25 than with more

[20]H. G. Fisser and G. M. Van Dyne, *J. Range Management* 19, 205–211 (1966).

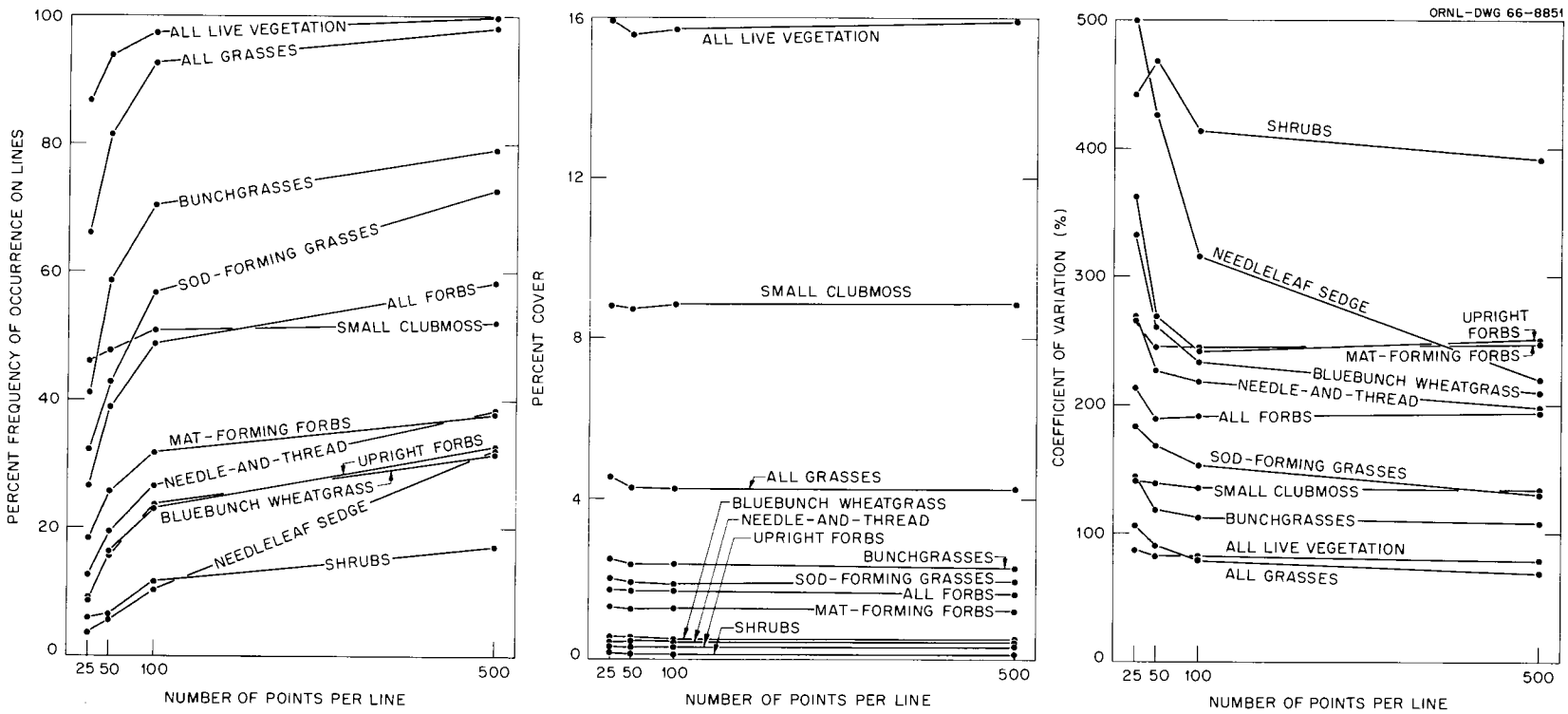

Fig. 9.15. Influence of Number of Points per Line in Artificial Populations on Percent Frequency of Occurrence on Lines, Percent Cover, and Coefficients of Variation of Individual Plants and Plant Groups.

points per line; and (5) basal cover of all species was estimated relatively accurately by point placements and all point densities.

Results of these studies will be used in devising sampling schemes for detecting cover changes due to irradiation and other treatments in old-field ecosystem successional studies.

VALUE OF A VACUUM CLIPPER IN HARVESTING HERBAGE

G. M. Van Dyne

Clipping herbage for yield determination or to obtain samples for chemical analyses is a costly part of many ecological experiments. This is especially true of harvesting low-growing vegetation, which requires considerable dexterity for accurate results, and for harvesting any type of vegetation during inclement weather. Numerous botanical analysis techniques based on estimating herbage yield have been developed, but they still require clipping plots for purposes of calibration, and estimation techniques do not provide herbage for chemical analyses. Statistical studies[21] were made of results obtained with a vacuum-clipper for harvesting low-growing herbage.

This clipper was constructed by modifying a portable vacuum cleaner and mounting it on an electrical clipper. Field data were collected in three studies on shortgrass rangeland, and time was reported for field effort and laboratory effort to separate litter and soil collected by the vacuum from the herbage. Regression equations were developed to predict herbage yield from total sample weight and from the weight or percentage weight of various contaminants. Equation (1),

$$R = \sqrt{\frac{C_s}{C_f + C_t} \cdot \frac{b^2 V_x}{V_{y \cdot x}}}, \qquad (1)$$

was used to predict the optimum ratio, R, of fast (vacuum clipping) to slow (laboratory sorting of clipped plots) measures. Here $V_{y \cdot x}$ is the variance of the estimates of the regression equation, b is the regression coefficient, V_x is the variance of the independent variable, C_s and C_f respectively are costs for obtaining measurements (slow and fast), and C_t is the combined travel time and setup time required per sample. In the computer study, to calculate the relative importance of field and fixed time, the time required to obtain one sample in the field was set at 1, the time required to separate samples was allowed to vary from 1 to 100, and the fixed time per sample was allowed to vary from 0.01 to 1.0. Results of these computer studies are presented as surfaces in Fig. 9.16 showing the optimum ratio of samples to be separated to the total number of samples to be clipped with the vacuum clipper.

These surfaces, of course, pertain only to a particular experiment but illustrate that use of such a double sampling technique can appreciably decrease the field time or, in all probability, result in more samples being taken in the same time period. This method can be used well by personnel with less training than that required by conventional harvesting procedures. In initial tests on shortgrass ranchland dominated by *Boutelova gracilis* and *Agropyron spicatum*, a two-man crew harvested five to ten times as many plots by this

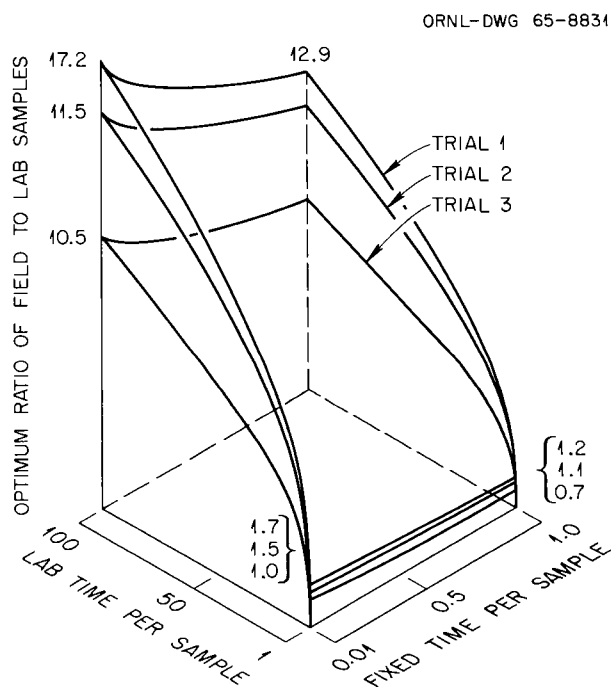

Fig. 9.16. Relative Effects of the Time Required to Separate Contaminants from Samples and of Fixed Time on the Optimum Ratio of Vacuum-Clipped Plots and Hand-Separated Plots.

[21] G. M. Van Dyne, "Use of a Vacuum-Clipper for Harvesting Herbage," *Ecology* 47 (in press).

method as by conventional hand-clipping procedures. However, on pasture and old-field vegetation in Oak Ridge, plants were so tall and heavy that the advantages of vacuum clipping were lost.

ELECTRONIC DATA PROCESSING OF FLORISTIC RECORDS

J. S. Olson Giovanni Cristofolini
Simonetta Cristofolini

A flora of Oak Ridge[22] was generated from a file of IBM cards, a 1401 computer, and a Friden Justowriter. Numerical coding of the International Plant Index[23] was used for sorting of data according to families and order or higher category. Alphabetical coding is based primarily on initial letters of the Latin names, with adjustments where necessary to avoid duplicate symbols.

Table 9.10 summarizes the results for five surrounding counties according to (1) representation within the ORNL Herbarium, (2) additional taxa in the University of Tennessee Herbarium in Knoxville, and (3) others represented by sight or other records. As of August 1965, nearly 1500 taxa (including varieties and forms) were included from the five-county area, but much smaller numbers have yet been recorded within any single county (Table 9.10). This suggests that field collections are far from complete and that more than 1500 taxa are represented near Oak Ridge.

This large number of taxa is significant for regional ecology, in providing contrasting genetic potentialities from which the actual vegetation dominants have been selected by environmental factors and by human disturbance. Furthermore, the diversity within many communities is enhanced by numerous minor species, which are available for prompt replacement of present dominants in the event of changing conditions of the landscape.

Three purposes of testing the electronic data processing methods were served well. One was to provide the flexibility needed for successive updating in the course of further botanical research in Oak Ridge and surrounding areas. A second was to make inaccessible information more widely available for educational and other public use. A third purpose was to demonstrate the workability of alphanumeric coding for more widespread use, for example, for International Biological Program records for the plant kingdom and perhaps for the animal kingdom and microbes, that is, a unified system of recording for all living components of the ecosystem.

A further test of all three objectives has been the use of slightly modified coding for horticultural records of more than 1300 woody-plant acquisitions from many parts of the world at the University of Tennessee Arboretum in Oak Ridge.[24] It is concluded that the International Plant Index numerical codes and procedures for coding families and higher categories has many merits, and that simple alphabetic coding can be adapted for genus-species-variety-form designations regardless of when strictly numerical coding is extended down to these taxonomic levels.

Table 9.10. Herbarium Inventory of Taxa[a] in Oak Ridge, Tennessee, Region[b]

County	ORNL Herbarium	Additional University of Tennessee	Other Record	Total
Morgan	3	218	138	359
Roane	342	330	237	909
Anderson	311	294	150	755
Knox	93	705	124	922
Loudon	58	112	98	268
Total	807	1659	747	3213

[a]Includes species, varieties, and forms.

[b]As of late 1965, records published in *Oak Ridge, Tennessee, Flora. I. Preliminary Alphabetic Inventory of Vascular Plants*, ORNL-TM-1232 (1966).

FOREST MANAGEMENT

J. W. Curlin W. C. Cate
J. K. West

Efforts have been continued to control an epidemic of the southern pine beetle (*Dendroctonus frontalis* Zimm.) which threatened several ecology

[22]J. S. Olson, G. Cristofolini, and S. Cristofolini, *Oak Ridge Flora. I. Preliminary Alphabetic Inventory of Vascular Plants*, ORNL-TM-1232 (1966).

[23]S. Gould, *Family Names of the Plant Kingdom*, International Plant Index, New Haven, Conn., 1966.

[24]R. D. MacDonald, *American Assoc. Bot. Gardens and Arboretums Quarterly Newsletter (66)*, pp. 13–15 (April 1966).

research study areas. Severe subzero weather late in January caused extensive mortality of the larvae brood. Control efforts during the past year included commercial salvage cutting, spraying with insecticide, and bulldozing and burning infested trees.

Indications are that the accelerated control program coupled with favorable weather will reduce the infestation to endemic levels by the end of the year.

An aerial photo technique for detection and appraisal of southern pine beetle damage was developed cooperatively with the U.S. Forest Service. Infrared color photographs (camouflage detection film) taken at a scale of 1:3960 proved efficient for identification of insect-infested trees and timber types. By flying a systematic pattern of flight lines $^3/_4$ mile apart and exposing stereo-triplicates at 1-mile intervals, a 7% coverage of the area was made. Interpretation of the photo plots provided information as to acreage infested, average number of trees per infested spot, and acreage of host type (southern pine). The conventional detection technique, aerial observer sketch-mapping from low-flying aircraft, involved an element of personal risk in addition to being imprecise. The new photo technique offers the advantage of statistical measures of accuracy, estimates of infested area, and an estimate of the host type, all of which are unattainable by conventional methods. The Forest Service has adopted this technique as a standard for insect surveys in the Appalachian Region.

The continuous forest inventory system of permanent plots described in the last annual report is presently being revised to provide additional information for use in the Forest Operations Simulator Program at the University of Georgia. This computer technique is a management tool designed to optimize yield on the basis of growth data, forest age, quality and type of structure, and silvicultural management decisions which are provided as input. Information from this program may be beneficial in developing other computer simulation routines for evaluating ecosystem responses to other disturbances such as fire or radiation damage. It might also provide valuable information for computer routines designed to maximize landscape productivity measured in units other than merely yield of commercial wood volume.

10. Radionuclide Cycling in Aquatic Ecosystems

D. A. Culver[1]
C. E. DePoe[2]
N. A. Griffith[3]
R. L. Iverson[1]
N. R. Kevern[3]
F. G. Lowman[4]
E. C. Neal
D. J. Nelson
B. C. Patten[3]
J. L. Wilhm[5]
G. M. Van Dyne[3]
Martin Witkamp[3]

CESIUM AND POTASSIUM IN WHITE CRAPPIE AND OTHER CLINCH RIVER FISH

D. J. Nelson N. A. Griffith

The series of white crappie (*Pomoxis annularis*) analyzed for strontium and calcium was also analyzed for stable cesium, potassium, and ^{137}Cs.[6] The objectives of these analyses were to determine (1) concentration factors for cesium and potassium in fish flesh, (2) whether there was a seasonality in the stable cesium and potassium concentrations in white crappies, and (3) to verify the use of the specific activity relationship for predicting ^{137}Cs activity in Clinch River fish.

White crappies were collected each month from the Clinch River at about Clinch River mile 10 (river miles are measured from the river mouth). An attempt was made to obtain ten specimens each month. The collected fish were frozen and later were dissected carefully to obtain flesh samples uncontaminated with extraneous tissues. Four additional species were sampled once to obtain comparative data on cesium and potassium concentrations. These species included drum, *Aplodinotus grunniens* Rafinesque; white bass, *Roccus chrysops* (Rafinesque); channel catfish, *Ictalurus punctatus* (Rafinesque); and bluegill, *Lepomis macrochirus* Rafinesque. With the bluegills ten composite samples were used for analyses since individual fish did not provide sufficient tissue for analytical determination of cesium. The minimum amount of sample required was about 50 g of fresh tissue, which would yield approximately 0.5 g of ash. Composite samples of selected internal organs were analyzed also. These analyses were limited because of the availability of tissue.

Potassium concentrations in white crappie flesh were relatively constant throughout the year (Table 10.1) in contrast to stable cesium concentrations, which varied by a factor of 2. Reasons for the lower cesium concentrations found from May through July are unknown. Generally, it is assumed that cesium uptake by fish is via the food chain. The period of low cesium concentrations does not coincide completely with reduced summer feeding activity by fish. An alternative suggestion is the mobilization of cesium in gonads prior to spawning. The white crappie gonads analyzed (Table 10.2) were from fish collected in the spring; these did not exhibit the unusually high cesium concentrations that would be indicated by the reduction in flesh concentrations.

The rapid changes in cesium concentrations during April–May and July–August imply a relatively short biological half-life for cesium. This may reflect a difference between laboratory-determined biological half-lives[7] of about 100 days at 20°C and those occurring in nature. The problem

[1]Temporary summer student.

[2]ORAU summer participant, 1965.

[3]Dual capacity.

[4]Puerto Rico Nuclear Center.

[5]ORAU Postdoctoral Fellow.

[6]S. I. Auerbach *et al.*, *Health Phys. Div. Ann. Progr. Rept. July 31, 1964*, ORNL-3697, p. 95.

[7]S. I. Auerbach *et al.*, *Health Phys. Div. Ann. Progr. Rept. July 31, 1964*, ORNL-3697, p. 101.

Table 10.1. Potassium, Cesium, and ^{137}Cs in Flesh of White Crappies Collected Monthly from the Clinch River[a]

All values are based on fresh weight of tissue

Collection Period	Number Analyzed	Potassium (mg/g)	Cesium ($\mu g/g$)	^{137}Cs (dis min^{-1} g^{-1})
			$\times 10^{-2}$	
1962				
May	6	3.31 ± 0.094	0.759 ± 0.058	1.409 ± 0.762
June	10	3.31 ± 0.067	0.847 ± 0.167	1.324 ± 0.348
July	7	3.49 ± 0.273	0.788 ± 0.091	0.612 ± 0.229
August	10	3.53 ± 0.125	1.69 ± 0.194	1.336 ± 0.181
September	9	3.06 ± 0.158	1.17 ± 0.216	1.216 ± 0.065
October	10	3.64 ± 0.067	1.28 ± 0.071	0.679 ± 0.293
November	10	3.65 ± 0.118	1.03 ± 0.074	1.163 ± 0.110
December	10	3.21 ± 0.051	1.35 ± 0.107	1.101 ± 0.141
1963				
January	10	3.48 ± 0.035	1.17 ± 0.084	0.605 ± 0.196
February	10	3.55 ± 0.056	1.66 ± 0.182	0.896 ± 0.141
March	10	3.69 ± 0.041	1.65 ± 0.157	1.038 ± 0.140
April	10	3.69 ± 0.030	1.65 ± 0.208	1.205 ± 0.390

[a] ±1 standard error.

is further complicated by the change in the size of the metabolic pool of cesium.

Comparative data on concentrations of potassium and cesium in flesh of five species of Clinch River fish, including white crappie, are shown in Table 10.3. Potassium is relatively constant among these species and is considered a conservative property. On the other hand, cesium concentrations differed by a factor of 4 among the species analyzed. It is unknown whether cesium concentrations in the four species other than white crappie varied seasonally. Bluegills and channel catfish had the lowest cesium concentrations, white bass and white crappies had the highest, and freshwater drum had intermediate concentrations. There was no concise relationship between trophic position of the fish and their cesium content, although white bass and white crappie, the most piscivorous species, also had the highest cesium concentrations.

Analyses of the internal organs showed some interesting differences in that bluegills, the species having the least cesium in flesh, generally had the highest potassium and cesium concentrations in internal organs. An exception occurred with cesium in the bluegill liver, which was about the same as in the other species. The concentrations of potassium and cesium in internal organs of all species did not constitute a significant reservoir of these elements. Since the major internal organs of white crappie did not contain high concentrations of cesium, it is unlikely that internal transfers of cesium can be postulated to account for the seasonal changes in flesh concentrations.

Potassium concentrations in organisms have been used with ^{137}Cs analyses to develop empirical relationships for prediction of the disposition of ^{137}Cs in the environment. Because cesium and potassium concentrations in flesh and internal organs varied, the ^{137}Cs to potassium ratio would be subject to a significant error among species and within the various tissues of a single species unless the stable cesium concentration was considered.

The specific activity concept was used successfully to predict ^{90}Sr concentrations in white

Table 10.2. Potassium and Cesium Concentrations in Selected Internal Organs of Five Species of Clinch River Fish

All values are based on fresh weight of tissue and are single analyses of organs composited from four or more fish

Organ and Species	Potassium (mg/g)	Cesium (μg/g)
		$\times 10^{-2}$
Liver		
White crappie	2.54	0.943
Drum	2.34	0.989
White bass	2.38	1.01
Channel catfish	2.56	0.258
Bluegill	3.31	0.841
Kidney		
White crappie	2.96	0.893
Drum	2.48	1.20
Channel catfish	2.56	0.294
Bluegill	8.85	14.88
Testes		
White crappie	3.05	1.02
Drum	2.51	2.45
White bass	2.71	6.85
Ovaries		
White crappie	2.98	1.06
Drum	1.83	0.665
Channel catfish	2.18	0.802
Bluegill	3.77	6.38
Spleen		
Channel catfish	2.97	1.54
Bluegill	4.35	9.78

crappie,[8] and the same technique may be used to predict ^{137}Cs concentrations. As a first approximation the average data on stable cesium and ^{137}Cs in river water and white crappie flesh (Table 10.4) were used to test the relationship between specific activities in water and fish tissue. The relationship and data give the following results:

$$\frac{^{137}\text{Cs}}{\text{Cs}}\,(\text{water}) = \frac{^{137}\text{Cs}}{\text{Cs}}\,(\text{fish})$$

$$\frac{1.767 \times 10^{-3}\ \text{dis min}^{-1}\ \text{ml}^{-1}}{2.5 \times 10^{-5}\ \mu\text{g/g}} \cong \frac{1.059\ \text{dis min}^{-1}\ \text{g}^{-1}}{1.289 \times 10^{-2}\ \mu\text{g/g}}$$

$$0.71 \times 10^{2}\ \text{dis min}^{-1}\ \mu\text{g}^{-1} \cong 0.82 \times 10^{2}\ \text{dis min}^{-1}\ \mu\text{g}^{-1}$$

The agreement was quite good and shows that one can predict average ^{137}Cs concentrations in fish tissue from average concentrations of ^{137}Cs in water. These results also suggest that ^{137}Cs released in waste water behaves chemically and biologically like stable cesium occurring in the environment. This is an important consideration in applying the specific activity concept.

These data will be analyzed further, taking into account the biological half-life of cesium in fish,

[8] S. I. Auerbach *et al.*, *Health Phys. Div. Ann. Progr. Rept. July 31, 1964*, ORNL-3697, p. 95.

Table 10.3. Mean Potassium and Cesium Concentrations in Flesh of White Crappie and Four Other Fish Species

All values are based on fresh weight

Species	Number Analyzed	Collection Date	Potassium (mg/g)	Cesium (μg/g)
				$\times 10^{-2}$
White crappie	112	*a*	3.48 ± 0.033	1.29 ± 0.054
Drum	10	July 1963	3.26 ± 0.123	0.873 ± 0.071
White bass	9	July 1963	3.52 ± 0.074	1.60 ± 0.306
Channel catfish	10	Oct. 1963	3.40 ± 0.070	0.408 ± 0.052
Bluegill	10	Oct. 1963	3.28 ± 0.048	0.344 ± 0.050

[a] Average of monthly samples May 1962 through April 1963.

Table 10.4. Mean Concentrations of Potassium, Cesium, and ^{137}Cs (± 1 standard error) in White Crappie Flesh and Clinch River Water

	Number of Samples	Potassium (mg/g)	Cesium ($\mu g/g$)	^{137}Cs (dis min^{-1} g^{-1})
			$\times 10^{-2}$	
Flesh	112	3.48 ± 0.033	1.29 ± 0.054	1.059 ± 0.845
River water (CRM 14.4)		1.3[a]	2.5×10^{-3}[b]	1.767×10^{-3}[c]

[a]R. J. Morton (ed.), *Status Report No. 5 on Clinch River Study*, ORNL-3721 (October 1965).

[b]Mean of three samples from CRM 21.6.

[c]Applied Health Physics Monitoring Data for Period May 1962 through April 1963.

in an effort to obtain the specific activity relationships between fish and their environment during transient conditions.

FEEDING RATE OF CARP IN WHITE OAK LAKE

N. R. Kevern

The daily food consumption for yearling carp in White Oak Lake was reported last year.[9] A radioisotopic method involving ^{137}Cs was used, and the total food consumption was calculated. Total consumption was subdivided graphically into the quantity of each diet item consumed for both maintenance metabolism and growth requirements. The equation developed since then for calculating daily food consumption for maintenance metabolism of an organism having several diet items is

$$r = \frac{Q_e k}{\sum_{i=1}^{n} a_i c_i f_i},$$

where

r = rate of feeding (g/day),

Q_e = equilibrium body burden of ^{137}Cs in the organism ($\mu\mu c$),

k = rate of elimination of ^{137}Cs by the organism (fraction/day),

a_i = assimilated fraction of radioisotope ingested with the ith diet item,

c_i = concentration of radioisotope in the ith diet item ($\mu\mu c/g$),

f_i = fraction of the diet made up by the ith item.

The quantity of the ith diet item ingested can be calculated by rf_i.

Another equation was developed for calculation of the food intake for growth requirements. An estimate of daily growth is necessary and is obtainable for fish by a standard age and growth study and length-weight relationship. New tissue is assumed to be in equilibrium with the rest of the organism and therefore has the same body-burden concentration. The radioisotope in the new tissue is also subject to turnover (elimination) at the same rate as that in other tissues. Daily food consumption for growth requirements is

$$r_g = \frac{\dot{Q} + (0.5)Q_g k}{\sum_{i=1}^{n} a_i c_i f_i},$$

where $\dot{Q}$ is the quantity of radioisotope ($\mu\mu c$/day) deposited with the new tissue and Q_g is equal to $\dot{Q}$ but is defined as the body burden of the new tissue ($\mu\mu c$) subject to turnover. New tissue is accumulated throughout the day, and the radioisotope being deposited increases from zero to Q_g; therefore, the average quantity subject to turnover is approximated by (0.5) Q_g. The daily quantity of the ith diet item consumed for growth can be calculated by $r_g f_i$.

[9]S. I. Auerbach *et al.*, *Health Phys. Div. Ann. Progr. Rept. July 31, 1965*, ORNL-3849, p. 86.

EFFECT OF TROPHIC LEVEL ON RADIONUCLIDE ACCUMULATION BY FISH

N. R. Kevern N. A. Griffith

To predict the fate of radionuclides in the environment, one must understand the ecological relationships involved in the accumulation of radionuclides by organisms. There is speculation in the literature that the concentrations of ^{137}Cs in organisms increase with each higher trophic position, that is, from herbivore to omnivore to carnivore. An investigation of fish in White Oak Lake was initiated to determine if the trophic position of the fish was correlated with its concentration of a radionuclide. Five species of fish were collected and analyzed for ^{137}Cs, ^{60}Co, and ^{90}Sr. The species, in order of increasing relative trophic position, were carp, gizzard shad, bullhead, bluegill, and largemouth bass. The results, in Table 10.5, revealed no correlation between the trophic level of the species and the concentration of any of the three radionuclides. Carp and bullhead had the lowest ^{137}Cs concentrations, shad intermediate, and bass and bluegill the highest; however, the differences were not significant between the two species with high concentrations and the two species with low concentrations. Relatively high concentrations of ^{60}Co and ^{90}Sr were present in bullhead, and a high concentration of ^{90}Sr was present in bluegill. Concentration factors and ratios of radionuclide concentration in the fish to that in the water were variable, especially for ^{90}Sr, and were low for ^{60}Co. Differences among species are not explainable at this time.

RADIONUCLIDES IN PERIPHYTON

B. C. Patten D. A. Culver
R. L. Iverson C. E. DePoe
E. C. Neal N. A. Griffith

Periphyton are the communities of aquatic organisms attached to aquatic plants and other submerged surfaces. Their growth is related to the dynamics of nutrients, and they develop readily on artificial substrates. During the summer of 1965 six continuous strips of polyethylene tape 5 ft long were suspended in the deepest part of White Oak Lake. The objective was to follow the development of periphyton at different levels of the water column and to observe the associated uptake of ^{137}Cs, ^{106}Ru, and ^{60}Co. One tape was removed 2, 3, 4, 5, 6, and 8 weeks after the start of the experiment to determine the vertical distribution of species, biomass, and radionuclides.

The succession of plant and animal species varied with depth, but in general was as follows. The principal forms were the blue-green algae *Microcystis* and *Oscillatoria*. *Microcystis* was most abundant at the 4-to-5-ft level, while *Oscillatoria* growth was more pronounced in the upper 4 ft. The diatom genera *Navicula, Cymbella,* and *Fragillaria* appeared on most tapes, but in lesser abundance than *Oscillatoria* and *Microcystis*. Succession was most noticeable as the green alga *Oedogonium* appeared the fifth week, followed by

Table 10.5. Concentration ($\bar{x} \pm 1$ standard error) and Concentration Factors of Three Radionuclides in Five Species of Fish from White Oak Lake

Species	Sample Size	^{90}Sr		^{137}Cs		^{60}Co	
		($\mu\mu c/g$)	C.F.	($\mu\mu c/g$)	C.F.	($\mu\mu c/g$)	C.F.
Carp	5	No data		20 ± 1.7	60	8.8 ± 1.6	6.4
Shad	5	18 ± 2.0	46	32 ± 1.9	140	15.0 ± 1.9	13.0
Bullhead	5	85 ± 8.5	220	23 ± 1.3	100	83.0 ± 15.0	70.0
Bluegill	5	93 ± 5.0	240	38 ± 8.5	170	6.0 ± 0.8	5.0
Bass	5	36 ± 7.6	93	35 ± 8.0	150	6.2 ± 0.6	5.5

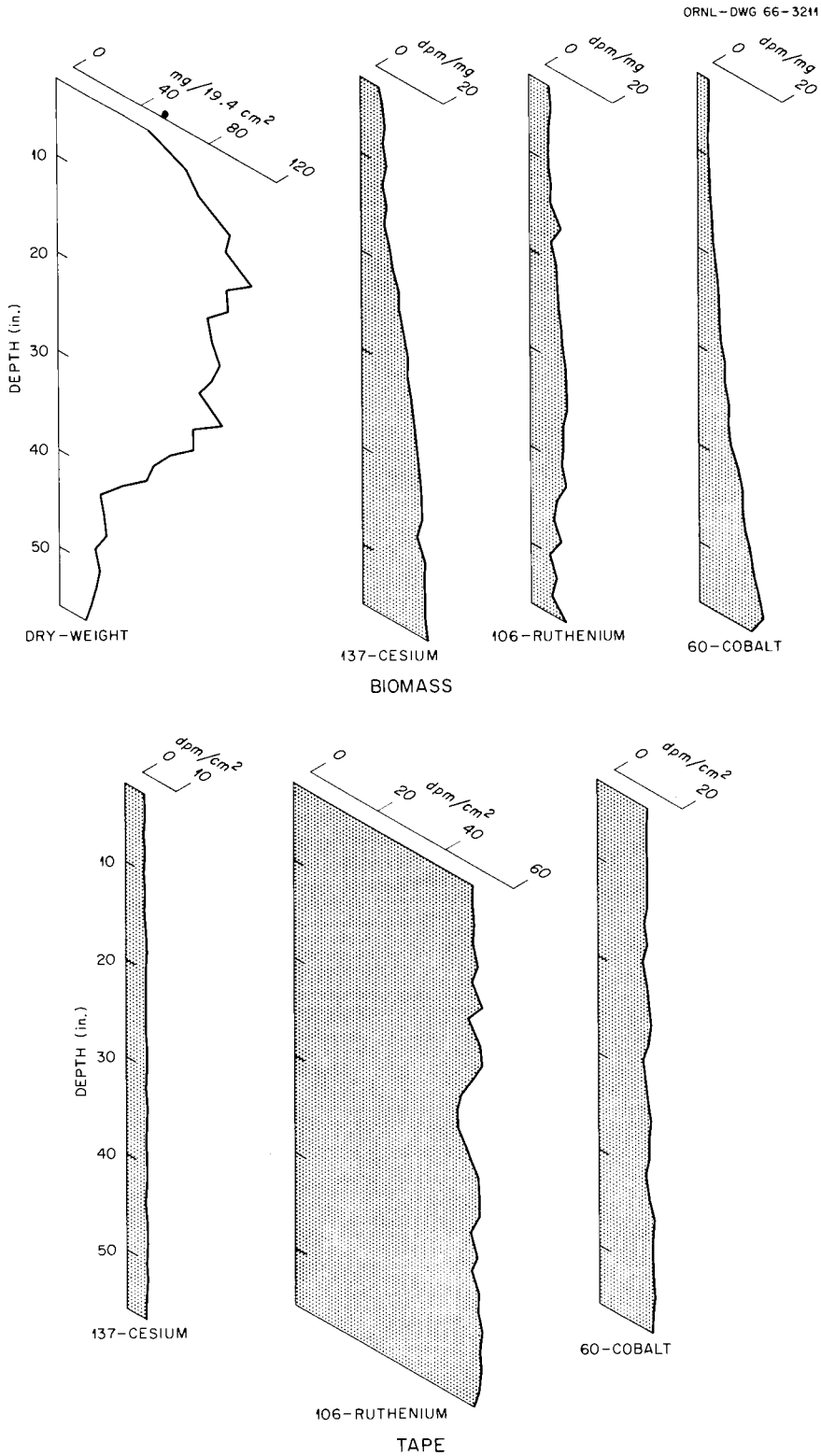

Fig. 10.1. Vertical Distribution of Periphyton Biomass and Assimilated Radioactivity and of Activity in the Artificial Substrates (Polyethylene Tape) Placed for Three Weeks in White Oak Lake.

other filamentous greens such as *Spirogyra, Chaetophora,* and *Stigeoclonium* developing successively through the eight-week period. Several genera of Protozoa appeared in the third week on the lower foot of the tape, and after four weeks were abundant at all depths. Nematodes were most prominent during the seventh week and were located on the lower 3 ft. Other algae genera observed during the eight-week period included *Ankistrodesmus, Aphanocapsa, Chlamydomonas, Chlorella, Chroococcus, Closterium, Cosmarium, Euglena, Gleocapsa, Lyngbya, Merismopedia, Nitzschia, Phormidium, Scenedesmus, Spirulina,* and *Ulothrix.*

Figure 10.1 shows biomass and radioisotope results three weeks after the tapes were placed in the lake. The vertical biomass (dry weight) distribution resembles a typical profile of photosynthesis in plankton communities, with greatest concentrations between 10 and 30 in. Distributions of ^{137}Cs, ^{106}Ru, and ^{60}Co in biomass appear in the upper part of the figure, and activities residual in the polyethylene tape after the periphyton was scraped off are illustrated in the lower part.

The uniform vertical distributions of tape radioactivity suggest homogeneous vertical distributions of the radionuclides in the water. The tape appears to concentrate ^{106}Ru to a considerable extent, but the possibility of error in this assay is currently being investigated. Tapes from other weeks did not concentrate this radioisotope to the extent shown in Fig. 10.1. In the periphyton biomass, concentrations of ^{137}Cs and ^{60}Co increased with depth. The uniform distribution of these isotopes on the tape tends to rule out greater concentrations in deeper water as the cause. The possibility of associating vertical trends in radionuclide concentration with particular populations of organisms remains to be looked into. Ruthenium-106 was uniformly distributed in biomass, unlike the other two elements. The basis of these differences as well as the influence of successional development should be clarified by analyses of the tapes from other weeks.

USE OF ARTIFICIAL SUBSTRATA TO ESTIMATE THE PRODUCTIVITY OF PERIPHYTON

N. R. Kevern J. L. Wilhm
G. M. Van Dyne

Artificial substrata placed in an aquatic habitat for a single extended time period provide a measurement of the average rate of biomass accumulation resulting from the process of colonization and ensuing growth of attached periphyton, but not a measurement of the rate of production of a well-established mat of periphyton. The colonization and growth phases can be recognized by measuring biomass accumulation on a series of substrate exposures of increasing duration. Plexiglas plates were placed in laboratory streams and in a spring and removed at two- to three-day intervals up to 35 days to determine the increase in standing crop of periphyton.

The data suggested two linear components and led to fitting a discontinuous, weighted linear regression model. The model used was

$$Y = c(bt) + d(a + b't) ,$$

where Y is the standing crop, t is time, and a, b, and b' are coefficients determined such that if $t < t_i$, $c = 1$, $d = 0$, and b = slope; if $t > t_i$, $c = 0$, $d = 1$, and b' = slope; and $t_i = a/(b - b')$.

The instantaneous growth rate, calculated from the exponential phase of the growth curve of periphyton in the stream, was 0.51 g m^{-2} day^{-1} as compared with an estimate of 0.60 g m^{-2} day^{-1} obtained by oxygen measurements for growth of periphyton on the stream bottom. The average growth rate of periphyton on plates in the streams over a single exposure period was 0.31 g m^{-2} day^{-1}. The instantaneous growth rate in the spring was 0.20 g m^{-2} day^{-1}. Under the conditions of the experiment, the instantaneous growth rate was a better estimate of productivity than was the average growth rate.

ESTIMATE OF PERIPHYTON MASS AND STREAM BOTTOM AREA USING ^{32}P

D. J. Nelson J. L. Wilhm
N. R. Kevern N. A. Griffith

When the behavior of a radionuclide in the environment is known, this knowledge can be used

to obtain ecological data that are difficult or impractical to obtain by conventional methods. As an example, quantitative data on the standing crop of periphyton and the actual bottom surface area of small rocky streams are limited because of the difficulty in making these measurements. The purpose of this study was to determine the standing crop of periphyton and the bottom surface area of a small, rocky stream by using ^{32}P.

Preliminary experiments and previously published[10] results on the behavior of introduced ^{32}P in streams have shown the following: (1) up to 95% of the introduced ^{32}P was retained within the study reach; (2) periphyton rapidly accumulated large quantities of ^{32}P; (3) small concentrations of ^{32}P occurred in inorganic sediments; (4) accumulation of ^{32}P by consumer organisms such as snails, odonates, hellgramites, crayfish, and salamanders was low initially and increased gradually for several days.

Because of this behavior, material balance techniques may be used to determine the amount of released ^{32}P that is retained in the reach of the stream being studied. By measuring ^{32}P concentrations per gram of periphyton, the standing crop in an entire stream section can be estimated, since most of the ^{32}P retained is associated with the periphyton. The actual surface area of the stream bottom can be estimated using the ^{32}P activity per unit area.

Phosphorus-32 was introduced by inverting a 4-liter polyethylene bottle over a funnel with a capillary tip. Empirical testing of the apparatus showed that a 30-min release would be obtained by diluting the ^{32}P solution to 3650 ml. Creek discharge was measured at a weir located about 30 m downstream from the study reach. Measured discharge at the time of the radionuclide release was 8.664×10^6 ml per 30 min. The maximum permissible concentration of ^{32}P in water for an occupational exposure (40-hr week) is 5×10^{-4} μc/ml. Accordingly, 4.332 mc of ^{32}P released during a 30-min period is permissible. The actual release was 4.325 mc (9.6×10^9 dis/min), giving a maximum ^{32}P concentration, assuming instantaneous dilution, of 11.07×10^2 dis/min per milliliter of creek water.

[10] R. C. Ball and F. F. Hooper, pp. 217–28 in *Radioecology*, ed. by V. Schultz and A. W. Klement, Jr., Reinhold, New York, 1963.

The quantity of ^{32}P retained in the stream section was determined by measuring the activity in the water at the end of the study reach and comparing this value with the activity introduced. Although the release lasted 30 min, downstream sampling continued for 100 min because of longitudinal dispersion. Total activity passing the downstream station was calculated by multiplying the mean activity by total discharge during the sampling period. In the initial hours after the ^{32}P release, most of the activity was incorporated in the periphyton. Then the following relationships existed:

$$P_s - P_d = P_r , \qquad (1)$$

where P_s is activity in spike or at an upstream station, P_d is activity at a point downstream, and P_r is activity retained in the section. All activities are expressed as disintegrations per minute. Further,

$$\frac{P_r \text{ (dis/min)}}{P_w \text{ (dis min}^{-1}\text{ mg}^{-1})} = \text{standing crop of periphyton in stream section (mg)}, \qquad (2)$$

where P_w is the activity per unit weight in periphyton as determined on natural or artificial substrata. Likewise,

$$\frac{P_r \text{ (dis/min)}}{P_a \text{ (dis min}^{-1}\text{ cm}^{-2})} = \text{total bottom area (cm}^2\text{)}, \qquad (3)$$

where P_a is activity per unit area of periphyton.

Activity of ^{32}P introduced at the upstream station was 9.602×10^9 dis/min, and activity leaving the study area, 100 m downstream, was 2.402×10^9 dis/min. By subtraction [Eq. (1)], 7.2×10^9 dis/min, or about 75% of the introduced ^{32}P, was retained within the study section.

Uptake of ^{32}P by periphyton was determined by collecting samples from both artificial glass slides and natural substrata 4 hr after introduction of ^{32}P. The mean and standard deviation of ash-free weight of periphyton on 50 slides was 0.304 ± 0.183 mg/cm^2. Periphyton on 20 rocks weighed 4.95 ± 3.04 mg/cm^2. A bias was introduced by selecting rocks with a heavy periphyton accumulation, and these data were not included in calculations of stream biomass.

The mean concentration and standard deviation of ^{32}P in periphyton on slides was 4890 ± 3155

dis min^{-1} mg^{-1}. Therefore, the total biomass of periphyton could be calculated by Eq. (2),

$$\frac{7.2 \times 10^9 \text{ dis/min}}{4.890 \times 10^3 \text{ dis min}^{-1} \text{ mg}^{-1}} = 1.47 \times 10^6 \text{ mg},$$

the biomass in the entire stream section.

Similarly, a mean concentration and standard deviation on the slides was 1264 ± 994 dis min^{-1} cm^{-2}. By Eq. (3) an estimate of bottom area is obtained,

$$\frac{7.2 \times 10^9}{1.264 \times 10^3} = 5.70 \times 10^6 \text{ cm}^2 .$$

The bottom area of the stream as calculated from surface measurements was 134 m^2, while total bottom area as estimated by ^{32}P uptake was 570 m^2. In view of the irregular topography of the stream bottom, the value obtained from uptake data is a better estimate of total bottom area than surface measurements of length and width.

The standing crop of periphyton expressed on a total area basis was 2.6 g/m^2 and on a surface area basis was 11.0 g/m^2. The first value is more realistic, since it is based on the area actually available for periphyton attachment.

This technique presents a new use for a radioactive isotope in ecological studies. The technique will be tested further, since it may be possible to detect differences between contrasting habitats within a stream.

PRIMARY PRODUCTIVITY MEASUREMENT

B. C. Patten R. L. Iverson
E. C. Neal D. A. Culver

Aquatic primary production can be estimated by enclosing water samples in dark and light bottles and measuring CO_2 uptake (pH and ^{14}C) or O_2 evolution[11–13] over a suitable interval of time. There is general feeling among investigators who use these methods that they do not assess production variables accurately, although their precision may be quite good. During the summer of 1965 the three methods were compared in seven 48-hr experiments performed in situ in Melton Hill Lake. Biological material included cultured algae and plankton populations produced by enriching samples of lake water with nutrients.

The experimental procedure was to fill approximately 100 dark and light bottles with an aliquot of sample material and then incubate them at a depth of 1.5 m in Melton Hill Lake. Replicate bottles were removed at dusk, dawn, and midday over a 48-hr period, and CO_2 assimilation and O_2 evolution were determined. Emphasis was placed upon obtaining maximum experimental precision under field conditions. Cell counts on the same samples were made with a Coulter counter, and biomass concentrations (organic + inorganic) were measured gravimetrically. Results of a typical experiment with the green alga *Spongiochloris excentrica* are shown in Fig. 10.2.

The cell count data indicate that the light bottle (LB) cultures became synchronous during the second night. Cell division in this period was much reduced in the dark bottles (DB). Biomass increased in both LB and DB during the first 18 hr, and growth in the first dark period was about 10 mg/liter. The lack of growth during the second night in both LB and DB suggests undesirable bottle effects, and this is further evidenced by decreases in biomass concentrations toward the end of the experiment. In view of the high and increasing cell counts during this period, the biomass losses must be in the form of excreted organic matter dissolved in the medium. Only particulate material was recorded as biomass.

The graph of results by the O_2 method shows net production (LB) and respiration (DB), not O_2 concentrations, in the light and dark bottles. For example, dark bottles lose O_2 to respiration, and it is the latter process and not DB O_2 concentration which is depicted in Fig. 10.2. The data indicate an O_2 increase of 35 mg/liter during the 48 hr. Figuring algal biomass at 40% O_2, a biomass increase of around 90 mg/liter would result. This is about double the levels indicated by direct measurement, as shown in Fig. 10.2. Qualitatively, the O_2 curves do not resemble those for biomass, and most particularly the biomass loss toward the end of the experiment is not reflected at all in the O_2 data.

[11] R. J. Beyers and H. T. Odum, *Limnol. Oceanog.* 4, 499–502 (1959); *Limnol. Oceanog.* 5, 228–30 (1960).

[12] E. Steemann Nielsen, *Nature* 167, 684 (1951); *J. conseil, Conseil Perm. Intern. Exploration Mer* 18, 117–40 (1952).

[13] T. Gaarder and H. H. Gran, *Rapp. Conseil Exploration Mer* 42, 1–48 (1927).

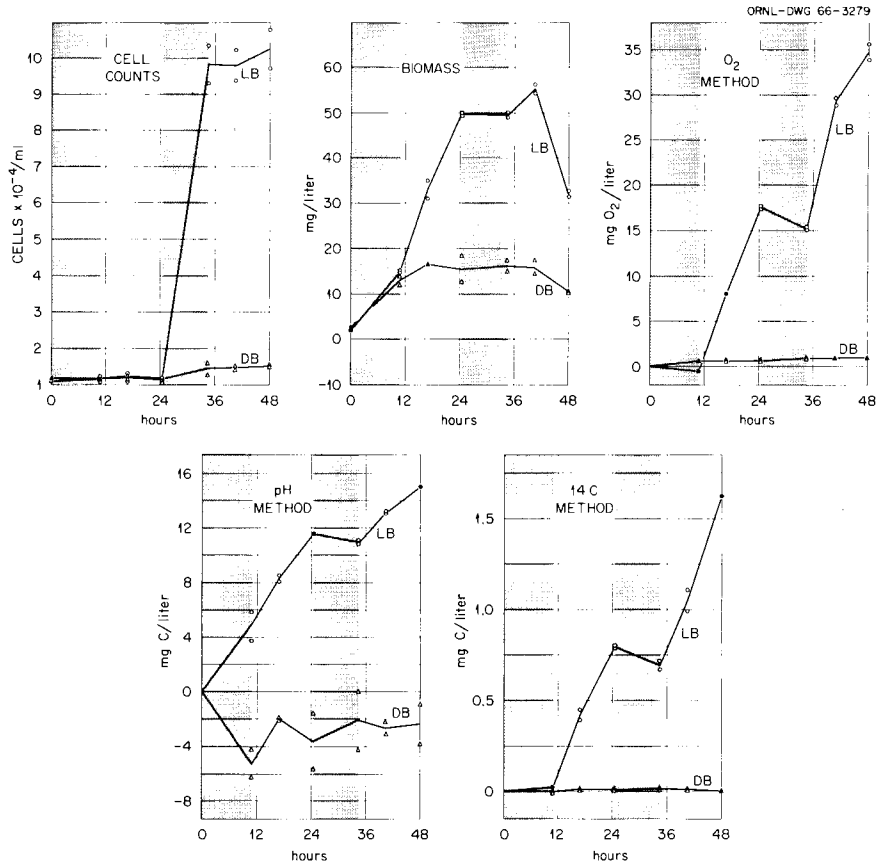

Fig. 10.2. Two-Day in situ Productivity Experiment with the Green Alga *Spongiochloris excentrica*. Day and night periods are indicated. Light bottle results are labeled LB and dark bottle results DB. Paired data points are shown, with identical values denoted by solid circles or triangles.

The pH and ^{14}C methods both measure carbon assimilation. If carbon is about 20% of biomass, then from the biomass data about 10 mg of carbon per liter should have been produced in the LB over the 48 hr. The pH method gave results in this range, but the ^{14}C method underestimated by nearly an order of magnitude. A principal criticism of the ^{14}C procedure for determining production is that much of the assimilated radioisotope may be excreted back into the medium as dissolved organic matter. In the present experiment the loss of biomass between 40 and 48 hr was not reflected by the ^{14}C results.

The O_2 and ^{14}C data are shown to be qualitatively similar. A persistent problem with the pH method is illustrated by the DB data. Variability between paired samples was high, and this did not appear to be a problem in the light bottles.

Based on similar results in other experiments with a variety of planktonic material, it is concluded that productivity values obtained by indirect procedures applied under field conditions are a function primarily of the measurement method. Differences between methods are both quantitative and qualitative.

TRACE ELEMENTS IN PLANKTON

B. C. Patten F. G. Lowman E. C. Neal

Investigations of trace element dynamics in plankton off the western coast of Puerto Rico have been initiated in cooperation with the Puerto Rico Nuclear Center (PRNC).

To date plankton samples have been obtained in October and December 1965 and March 1966.

Sampling is by 20-mesh net attached to a Clarke-Bumpus sampler. At seven stations (Fig. 10.3) material was collected from 5 m and at a deep level in or beneath the thermocline. Element concentrations determined were Mg, Ca, Mn, Cr, Fe, Co, Ni, Cu, Zn, Sr, Cd, and Pb. Manganese was assayed by nondestructive neutron activation; calcium, magnesium, and strontium by flame spectrophotometry; and all other elements by atomic absorption. Analyses were performed by the staff of PRNC. Plankton were enumerated from formalin-fixed aliquots returned to ORNL.

Table 10.6 shows the distribution by station of phytoplankton forms collected in the December samples. The principal genera, *Rhizosolenia* and *Chaetoceros*, remain to be speciated along with zooplankton, which dominated in terms of biomass. In these waters it takes an hour of towing to collect a few hundred milligrams dry weight of plankton material, in contrast to several minutes in most in-shore temperate waters. This is due to the low concentrations of both phyto- and zooplankton (Table 10.7). Much has been written about the relative infertility and lack of productivity of tropical waters, and results such as those presented in Table 10.7 lend further support. However, it seems unlikely in view of higher trophic level populations, such as fishes and birds, which are obviously maintained successfully in the region, that these waters are completely unproductive. The low organism counts occur even in enriched situations such as Mayaguez Harbor (station 1), suggesting that the food chain base may reside more with another group of plants than with net phytoplankton. Figure 10.4 is a photomicrograph of two species of algae common in phytoplankton along the east coast of the United States. The specimens shown are from Puerto Rico material. The photographs illustrate an abundance of microplankton scattered throughout the medium. These forms are too small to be concentrated by a 20-mesh net, and in fact the medium was diluted due to addition of formalin. General observations indicate the microplankton to be quite abundant in this region, and it is entirely possible that they are the principal forms supporting higher trophic levels. In addition, the dynamics of materials, such as trace elements and radionuclides, in plankton dominated by small organisms is probably quite different from that in communities in which net forms are important or predominant.

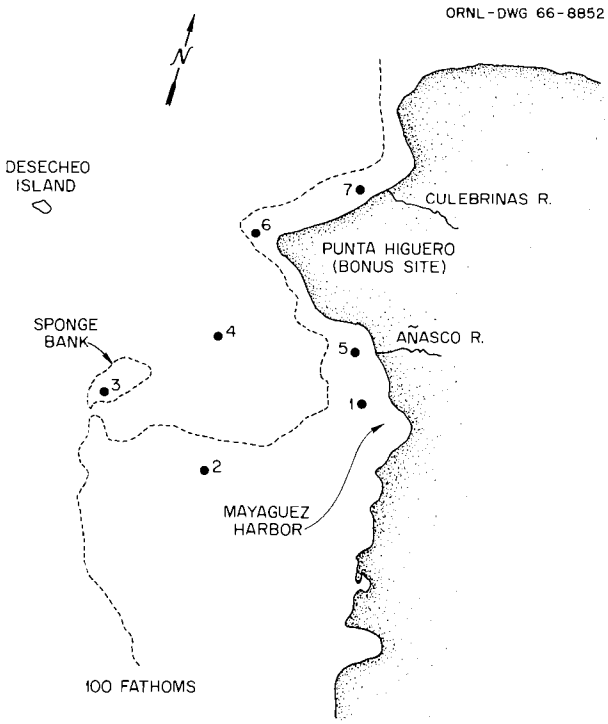

Fig. 10.3. Plankton Sampling Stations Off the Western Coast of Puerto Rico. The 100-fathom contour is shown.

Trace element results from the October 1965 collections indicate that none of the elements assayed were more concentrated in 5-m samples than in deep samples. Four elements – Ca, Fe, Mn, and Sr – tended to be more concentrated in deep than in shallow samples, and essentially no depth differences were observed for Mg, Cr, Co, Ni, Cu, Zn, Cd, or Pb. The preliminary general indication, then, is that different elements may be expected to have different patterns of vertical distribution in plankton.

Of particular interest in October were observations on strontium and calcium in the plankton. Strontium/calcium atom ratios in water, sediments, and organisms of both marine and freshwater environments generally run less than 10 atoms of strontium per 1000 atoms of calcium.[14] Exceptions have been noted, for example, in the marine Acantharia – protozoans which build their skeletons of celestite ($SrSO_4$). In these organisms strontium to calcium ratios approaching 3:1 in

[14] T. G. Thompson and T. J. Chow, *Deep-Sea Res., suppl.* 3, 20–39 (1955); H. T. Odum, *Inst. Marine Sci. (Texas)* 4, 39–113 (1957).

Table 10.6. List of Phytoplankton and Occurrence by Station in December 1965

The 5-m samples are denoted by S following station numbers and the deep samples by D

Phytoplankton	Station													
	1S	1D	2S	2D	3S	3D	4S	4D	5S	5D	6S	6D	7S	7D
Ceratium fusus	X	X	X	X	X		X		X	X	X	X	X	X
Ceratium macroceros	X	X	X	X	X	X	X	X	X	X	X	X	X	X
Ceratium bigelowii	X	X		X	X		X		X	X	X	X	X	
Ceratium furca			X	X					X	X	X	X		
Ceratium tripos	X	X	X	X	X		X	X	X	X	X	X	X	X
Ceratium candelabrum				X			X				X			
Rhizosolenia spp.	X[a]	X[a]	X[a]	X[a]	X[a]	X[a]	X[a]	X[a]	X[a]	X	X[a]	X[a]	X	X[a]
Chaetoceros spp.	X[a]	X[a]	X[a]	X[a]	X[a]	X[a]	X[a]	X[a]	X[a]	X	X[a]	X[a]	X	
Pleurosigma hippocampus			X		X				X	X				
Thalassiothrix sp.	X	X	X	X	X	X	X	X	X	X	X	X		
Asterionella japonica	X	X		X	X		X	X	X	X	X			
Pyxilla americana	X	X	X	X	X		X	X	X	X	X	X	X	
Rhizosolenia stolterfothii	X	X	X		X		X	X		X		X		
Bacteriastrum curvatum		X	X		X		X	X	X	X	X	X	X	
Rhizosolenia calyptra	X	X	X	X	X		X	X	X	X	X	X		
Bacillaria paradoxa	X							X	X	X				
Triceratium sp.									X	X				
Peridinium depressum	X	X		X			X		X		X	X	X	X
Pleurosigma elongatum									X					
Coscinodiscus grani	X			X			X		X			X	X	
Navicula sp.	X			X	X				X		X			
Coscinodiscus heteroporus				X										
Spirulina sp.		X		X	X		X						X	
Peridinium claudicans				X										
Biddulphia mobilensis				X	X				X					
Bacteriastrum varians	X		X	X	X		X				X			
Asteromphalus sp.							X				X		X	
Dictiocha fibula											X	X		
Bacteriastrum furcatum												X		
Licmophora sp.													X	
Campylodiscus sp.													X	
Silicoflagellates (zoo.)	X	X			X		X	X			X	X		
Various filament spp. (8–10)	X[a]	X[a]	X[a]	X[a]	X[a]	X[a]	X[a]	X[a]	X[a]	X	X[a]	X[a]	X[a]	X

[a]Predominant genera.

PHOTO 84605

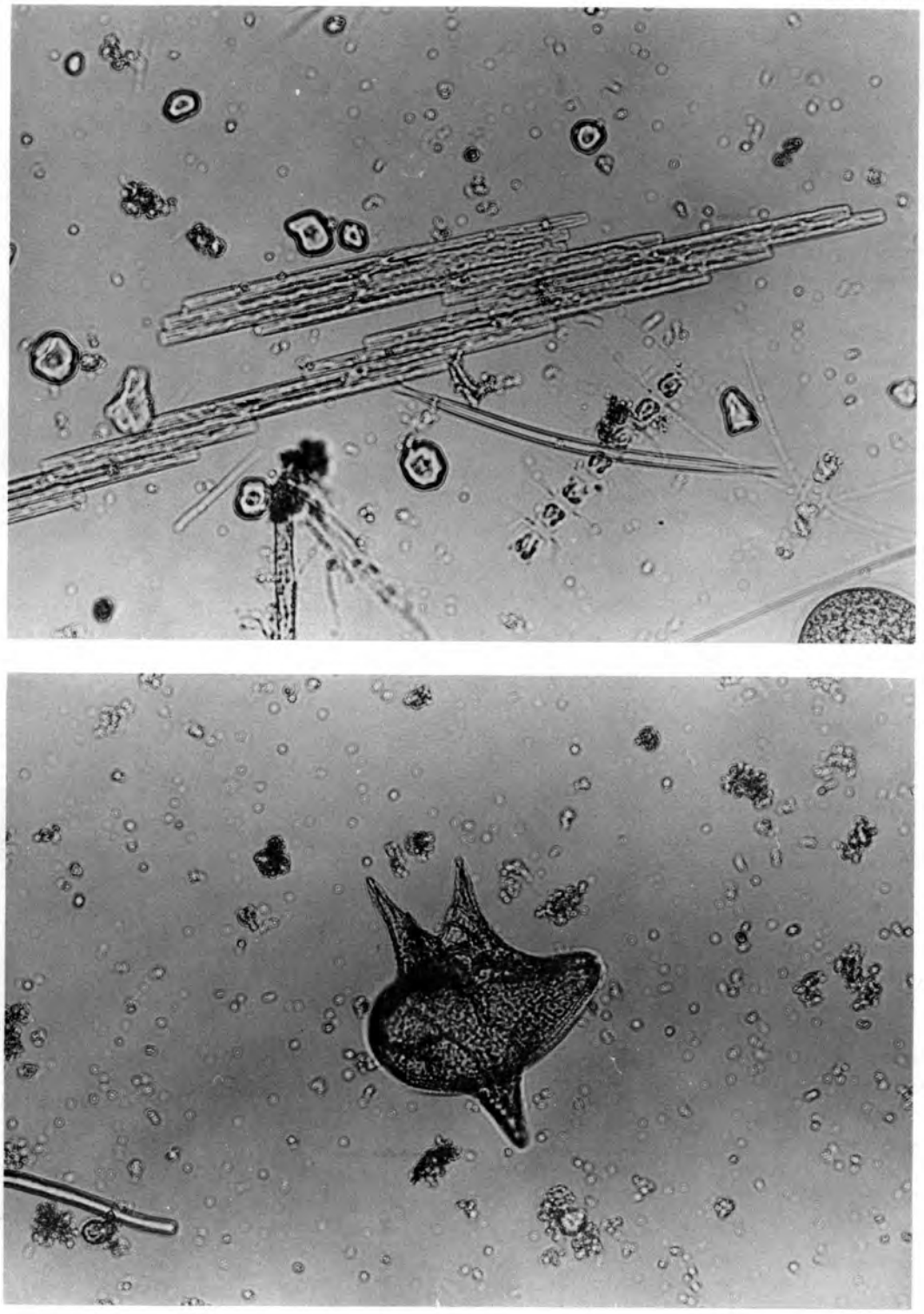

Fig. 10.4. Photomicrographs of *Bacillaria paradoxa* (Upper) and *Peridinium depressum* (Lower) from Puerto Rico, Showing Abundance of Microplankton (Somewhat Diluted by Formalin) in the Medium.

Table 10.7. Concentrations of Phyto- and Zooplankton by Station in December 1965

The 5-m samples are denoted by S following station numbers and the deep samples by D

Station	Date, 1965	Time (Atlantic Standard)	Depth (m)	Plankton Concentration	
				Phytoplankton (cells/m^3)	Zooplankton (individuals/m^3)
1S	12/15	1725–1825	5	132,768	51,907
1D	12/15	1832–1938	42	133,141	28,300
2S	12/15	1024–1130	5	113,645	15,084
2D	12/15	1133–1237	50	119,505	15,738
3S	12/13	1525–1630	5	463,731	59,309
3D	12/13	1635–1750	200	55,760[a]	630[a]
4S	12/13	1150–1255	5	98,841	6,865
4D	12/13	1307–1420	100	36,449	4,320
5S	12/14	1928–1020	5	293,253	50,716
5D	12/14	1055–1202	20	219,093	31,873
6S	12/14	1550–1655	5	80,417	8,406
6D	12/14	1656–1755	40	132,838	12,819
7S	12/10	1316–1425	5	29,094	26,666
7D	12/10	1535–1605	22	442,926[a]	221,475[a]

[a]Error in Clarke-Bumpus.

favor of strontium have been reported.[15] Previously reported data from the west coast of Puerto Rico indicated that water and sediments were in the normal range.[16]

The October 1965 results were as follows:

Station	Sr Atoms/Ca Atoms	Station	Sr Atoms/Ca Atoms
1S	0.052	4D	0.067
1D	0.048	5S	0.027
2S	0.025	5D	0.030
2D	0.034	6S	0.038
3S	0.073	6D	0.039
3D	0.042	7S	0.062
4S	0.062	7D	0.069

These values are consistently greater than normal. To determine how general this situation is, the PRNC staff undertook an intensive sampling (37 stations) of surface plankton in December 1965. The distribution of atom ratios revealed by this study is shown in Fig. 10.5. Ratios were in the normal range only inshore. Values tended to increase in an offshore direction to levels 10 to 100 times greater than those normally encountered. The distribution of calcium in plankton over the area was approximately constant, so that the offshore increase in strontium to calcium ratios was due to increased concentration of strontium (Fig. 10.6). Analysis of the species composition of samples obtained a week and a half earlier (December 10–13) at the regular stations, 1 to 7, indicated no Acantharia present nor other forms – either plant or animal – which would be expected to concentrate strontium to the levels indicated.

[15]B. Schreiber *et al.*, *Atti Accad. Naz. Lincei, Ser.* 8, **38**, 1–10 (1965).

[16]F. G. Lowman *et al.*, *Inter-Am. Symp. Peaceful Appl. Nucl. Energy, 5th, 1964*, pp. 241–49, Pan-American Union, Washington, D.C., 1965.

ORNL-DWG 66-3212

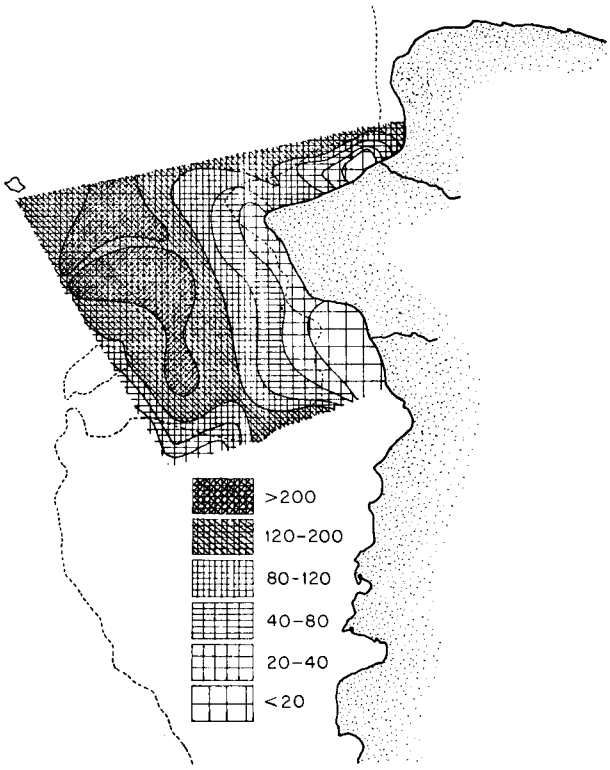

Sr/Ca atom ratio X 10^{-3}
DECEMBER 21, 1965

Fig. 10.5. Strontium-Calcium Atom Ratios in Surface Net Plankton Off the West Coast of Puerto Rico in December 1965.

ORNL-DWG 66-3213

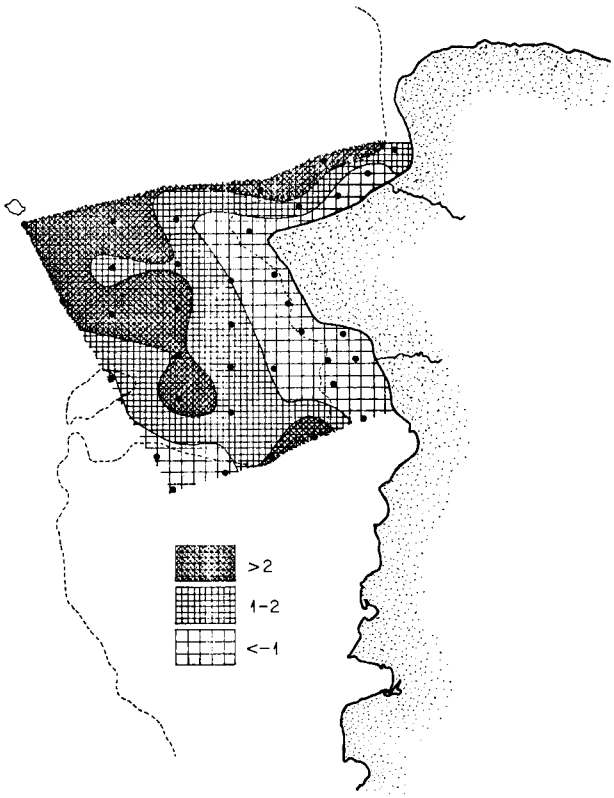

mg Sr/g ASH
DECEMBER 21, 1965

Fig. 10.6. Strontium Concentrations in Surface Net Plankton Off the West Coast of Puerto Rico in December 1965.

TRACE ELEMENTS IN SESTON

B. C. Patten F. G. Lowman E. C. Neal

The dynamics of materials, including radionuclides, in water masses is influenced by relationships between dissolved and particulate substances. To determine the role of particles in the sedimentation of matter out of water columns, an investigation of particulate trace element sinking characteristics is under way. Two stations have been established for study near the mouths of the Añasco and Culebrinas Rivers on the western coast of Puerto Rico. Sediment traps, unstoppered BOD bottles, are placed at various levels in these water columns to collect seston, which is then weighed and assayed for the trace elements Mg, Ca, Mn, Cr, Fe, Co, Ni, Cu, Zn, Cd, and Pb. This work is performed in cooperation with the Puerto Rico Nuclear Center. Manganese is assayed by nondestructive neutron activation, calcium and magnesium by flame spectrophotometry, and the remaining elements by atomic absorption. Results will be reported in greater detail in the annual report for fiscal year 1966 of the PRNC Marine Biology Program.

The downward flux $[ML^{-2}T^{-1}]$ of seston and its elemental components is represented by the material collected in the vertically oriented sediment traps. This flux can be related to the area of the collecting surface, which is the area of the collecting surface, which is the area of the orifice of the BOD bottles at the top of the neck. From flux data, sinking rates $[LT^{-1}]$ can be estimated

from initial seston concentrations $[ML^{-3}]$ by assuming that the latter are representative over the sampling period:

$$\text{sinking velocity } [LT^{-1}] = \frac{\text{flux } [ML^{-2}T^{-1}]}{\text{concentration } [ML^{-3}]}.$$

Flux and velocity values observed for total seston (dry weight) in October and December 1965 are shown in Table 10.8. The sinking velocity figures are comparable to others reported for the York River, a tributary of Chesapeake Bay, which were obtained by the same methods.[17] The fluxes are considerably lower, however, due to lower concentrations of suspended materials in these tropical waters. Typically in the York River, seston flux increased from surface to bottom and was quite high near the bottom due to sediment resuspension. This pattern was observed only in the Añasco in December (Table 10.8). The fact that large, dense particles, presumably resuspended, were involved is suggested by the sinking velocities, which were very high below 7 m.

Element fluxes in the October sampling are presented in Table 10.9. Sinking velocity data were not obtained for the individual elements. The data show variable flux rates for the different elements, although the flux of each element was generally similar at all depths. Station differences are also apparent, and these show to perhaps better advantage in Table 10.10. The Añasco River drains a region in which the parent materials are volcanic and igneous in origin, whereas the watershed of the Culebrinas is underlain by limestone. The sedimentation fluxes shown reflect the geology of the regions drained; for example, the flux of calcium is higher for the Culebrinas, whereas that of iron is higher for the Añasco.

Continuation of this work is expected to yield information which will be useful for making inferences about patterns and rates of radionuclide immobilization in aquatic systems.

[17] B. C. Patten, D. K. Young, and M. H. Roberts, Jr., *Chesapeake Sci.* **7**, 20–29 (1966).

Table 10.8. Sedimentation Flux and Velocity of Seston Dry Weights at Various Depths near the Mouths of the Añasco and Culebrinas Rivers, Puerto Rico

Depth (m)	Oct. 20–21, 1965		Dec. 10–13, 1965	
	Flux ($mg\ cm^{-2}\ day^{-1}$)	Sinking Velocity ($m\ day^{-1}$)	Flux ($mg\ cm^{-2}\ day^{-1}$)	Sinking Rate ($m\ day^{-1}$)
		Añasco		
1	7.23	4.83	2.01	1.00
4	4.58	3.97	1.05	0.89
7	3.79	3.12	7.47	7.33
10	3.69	3.38	8.77	7.67
13	3.41	3.11	9.84	8.99
16	4.05	3.62	11.16	11.76
$\bar{x}$	4.46	3.67	6.72	6.27
		Culebrinas		
1	3.61	1.52	1.02	0.91
4	3.09	2.97	0.81	0.73
7	2.69	3.02	0.81	0.74
10	2.75	2.67	0.80	0.73
13	2.71	2.55	0.83	0.76
16	3.07	3.17	0.94	0.88
$\bar{x}$	2.99	2.65	0.87	0.79

Table 10.9. Element Sedimentation Flux Rates near the Mouths of the Añasco and Culebrinas Rivers, October 20–21, 1965

Depth (m)	Element Flux ($\mu g\ cm^{-2}\ day^{-1}$)										
	Mg	Ca	Mn	Cr	Fe	Co	Ni	Cu	Zn	Cd	Pb
					Añasco						
1	16.67	4.62	0.28	0.77	193.54	0.34	0.64	0.52	2.04	0.97	2.31
4	13.53	1.29	0.09	0	125.37	0.08	0.33	0.04	0.96	0.04	0.53
7	22.59	5.38	0.07	0.35	96.80	0.16	0.32	0.25	0.86	0.05	0
10	15.12	2.58	0.08	0.17	91.26	0	0.82	0.24	0.85	0.04	0.85
13	25.39	6.92	0.07	0	80.78	0.25	0.25	0.26	1.02	0.04	0.44
16	29.16	7.89	0.11	0	106.35	0.27	0.34	0.38	0.96	0.03	0.28
$\bar{x}$	20.41	4.78	0.12	0.22	115.68	0.18	0.45	0.28	1.12	0.20	0.74
					Culebrinas						
1	22.07	15.86	0.05	0	71.26	0.19	2.09	0.17	1.13	Trace	0.25
4	22.30	13.18	0.03	0.18	56.77	0.08	0.69	0.23	0.73	Trace	0.28
7	19.61	10.30	0.02	0	44.13	0.26	2.29	0.11	0.85	0.04	0.28
10	21.36	8.69	0.02	0.16	42.72	0.19	0.30	0.14	0.83	Trace	0.17
13	22.22	8.73	0.02	0.32	46.04	0	0.24	0.16	6.19	0.02	0.79
16	23.65	9.83	0.02	0	50.95	0.20	0.33	0.12	1.00	Trace	0.44
$\bar{x}$	21.87	11.10	0.03	0.11	51.98	0.15	0.99	0.16	1.79	0.01	0.37

Table 10.10. Average Sedimentation Flux of Trace Elements in Water Columns off Mouths of Añasco and Culebrinas Rivers, October 20–21, 1965 ($\mu g\ cm^{-2}\ day^{-1}$)

	Añasco (Volcanic-Igneous)	Culebrinas (Limestone)
Total seston		
Flux, $\mu g\ cm^{-2}\ day^{-1}$	4460	2990
Sinking rate, m/day	367	265
Mg	20.41	21.87
Ca	4.78	11.10
Mn	0.12	0.03
Cr	0.22	0.11
Fe	115.68	51.98
Co	0.18	0.15
Ni	0.45	0.99
Cu	0.28	0.16
Zr	1.12	1.79
Cd	0.20	0.01
Pb	0.74	0.37

TRANSFER OF ^{137}Cs, ^{106}Ru, AND ^{60}Co BETWEEN DETRITUS AND BENTHIC MACROINVERTEBRATES IN MICROCOSMS

J. L. Wilhm

Experimental microcosms were used to study the transfer of radionuclides between detritus and benthic macroinvertebrates. Detritus containing ^{137}Cs, ^{106}Ru, and ^{60}Co was collected from White Oak Lake, and invertebrates were taken from a spring. Four species of detritus feeders, each with a different feeding mechanism, and one carnivorous species were studied. Microcosms were established in 2-liter Erlenmeyer flasks, and two microcosms each were sacrificed after 3, 7, 10, 14, 21, and 28 days.

Mean activity in picocuries per ash-free gram in detritus was 6630 for ^{137}Cs, 28,849 for ^{106}Ru, and 7509 for ^{60}Co. The detritus lost 48% of the ^{137}Cs, 21% of the ^{106}Ru, and 37% of the ^{60}Co to the water by day 3. *Limnodrilus* accumulated 1032 pc of ^{137}Cs per ash-free gram, twice the accumulation by *Stictochironomus*. Mean ^{106}Ru

concentration was 1128 pc per ash-free gram in *Stictochironomus*, and about twice this value was measured in the other detritus feeders. The mean ^{60}Co concentration was 1159 pc per ash-free gram in *Limnodrilus*, 444 in *Stictochironomus*, and 860 in *Physa*. Concentration factors (ratio of pc/ash-free g in organisms to pc/ash-free g in detritus) for ^{137}Cs was 0.13 in *Stictochironomus*, 0.16 in *Physa*, and 0.31 in *Limnodrilus*. Concentration factors for ^{60}Co approximated those for ^{137}Cs, while the factors for ^{106}Ru were less than half the ^{137}Cs values.

Broad trophic levels were distinguished by plotting concentrations in organisms as a function of time. Peak concentrations of the radioisotopes in the detritus feeders were reached by day 3, while the carnivore *Procladius* had a delayed uptake and increased in activity until day 14.

Concentration of ^{106}Ru in the different life stages of *Stictochironomus* was (pc/ash-free g) 947 in larvae, 1529 in pupae, 10,276 in exuviae, and 1068 in adults. The high concentration in exuviae is being investigated further.

The detritus feeders studied had different feeding mechanisms and used different size fractions of the detritus. The sizes ingested are being studied currently by separating the detritus into components and using the separated components as sources of nourishment in different microcosms. An analysis of the concentration curve should reveal the particular component of the detritus ingested by each species.

ACCUMULATION OF ^{32}P BY BIOTA AND THEIR SUBSTRATES IN A TAGGED STREAM

Martin Witkamp Marilyn L. Frank

Uptake of ^{32}P by biota, organic substrate, and inorganic substrate was measured in a stream to evaluate their roles in the phosphorus turnover in this environment. Organic substrate (alder leaves) in a tagged stream retained more ^{32}P than inorganic substrate (shale). In a near-stagnant pool the leaves retained 1.6 times and, in a nearby ripple, 2.9 times more ^{32}P than the shale. Three-week-old aufwuchs increased ^{32}P accumulation on leaves tenfold, and on shale 13 times in the pool. Biological accumulation of ^{32}P in the ripple was 30 times higher on leaves, and 24 times higher on shale than on these substrates without aufwuchs. Biological accumulation appears to be most stimulated on organic substrate with continuous mineral and oxygen supply by the stream. These results parallel the use of shaking cultures vs stationary cultures as a method to enhance mineral turnover rates by microbes.

11. Theoretical and Systems Ecology

J. S. Olson[1] Martin Witkamp[1]
B. C. Patten[1] Giovanni Cristofolini[2]
G. M. Van Dyne[1] V. R. R. Uppuluri[3]
P. J. Wangersky[4]

A SYSTEMS PHILOSOPHY

G. M. Van Dyne

A survey was made of literature from ecology, natural resource management, systems analysis, and operations research in order to better define the area of work called "systems ecology." A report[5] summarizing this survey discusses some of the properties of ecosystems and the ecosystem concept as a basis for defining this area of study. In this approach man is considered both a component and a manipulator of ecosystems (Fig. 11.1), those systems resulting from the integration of all

[1]Dual capacity.
[2]NATO Fellow.
[3]Mathematics Division, ORNL.
[4]Consultant.
[5]G. M. Van Dyne, *Ecosystems, Systems Ecology, and Systems Ecologists*, ORNL-3957 (1966).

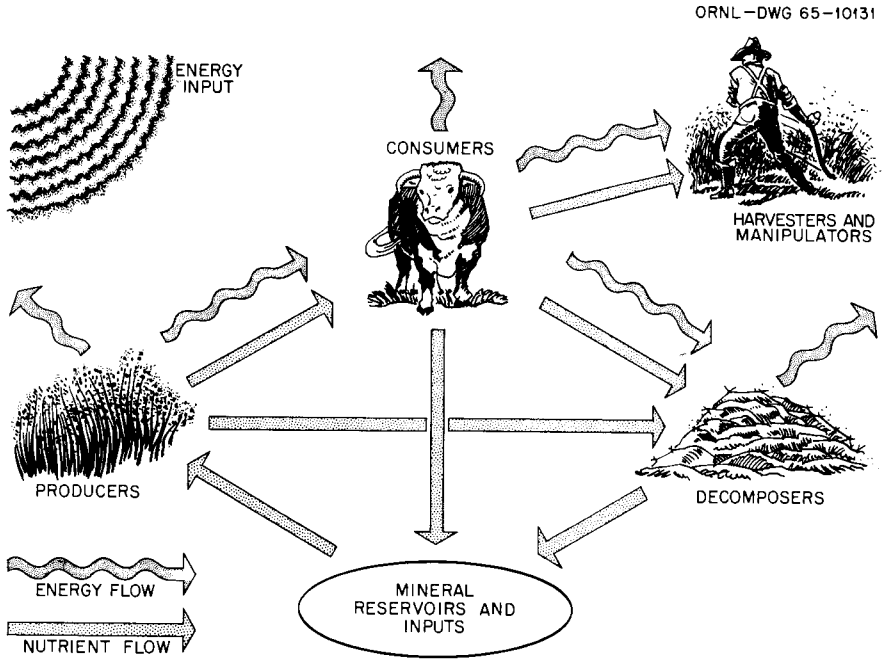

Fig. 11.1. Man is Both a Spectator and a Participant in the Functioning of Ecosystems. He has manipulated ecosystems to maximize the flow of nutrients and energy to him from the producers and primary consumers. He has attempted to minimize the respiratory losses of energy from producers, consumers, and decomposers.

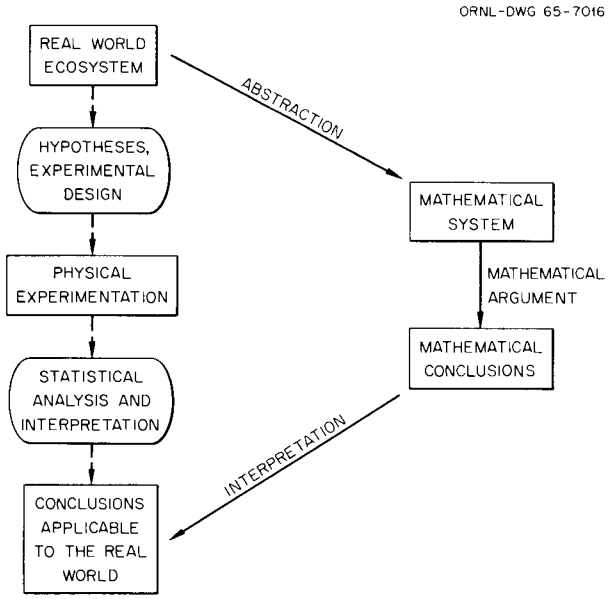

Fig. 11.2. Two Ways of Experimenting with Ecosystems. One involves the conventional process of formulating hypotheses, designing and conducting experiments, and analyzing and interpreting results. The second involves the abstraction of the system into a model, application of mathematical argument, and interpretation of mathematical conclusions.

of the living and nonliving factors of the environment. Problems, methods, tools, and approaches of systems ecology are considered in defining tasks, problems, and training of systems ecologists. Special consideration is given to the approach of modeling in ecological studies (Fig. 11.2) as a supplement to the conventional means of experimentation and analysis. The interdisciplinary nature of systems ecology research and the importance of computers, especially remote console systems, are considered in the report. Examples of ecological, natural resource management, and mathematical methods, concepts, and applications are drawn from a diverse body of literature, which further illustrate the interdisciplinary nature of systems ecology.

MATHEMATICAL MODELING OF NATURAL POPULATIONS

P. J. Wangersky

This project was originally concerned with the effects of the introduction of genetic variability into the Lotka-Volterra type of deterministic mathematical model of competition between two species. In the first years of the research, modified competition models were constructed, the modifications permitting calculation of the rates of population increase, r. The competition equations could thus be evaluated once the birth rate per animal, b, the concavity of the survivorship curve, p, and the time lags, $\tau_1 \equiv$ the gestation period, $\tau_2 \equiv$ the population reaction time, and $\tau_3 \equiv$ the maximum length of life, were known. These were the factors which were allowed to vary in the competing populations.

The mechanism of variation for each variable involved random selection from a given distribution, the interval between selections being an inverse function of population size. The genetic variability thus induced most closely resembled genetic drift. Some 530 competitions were run, with a variety of starting conditions and distribution of variables. In contests where the population growth curves were either logistic curves or damped oscillations, the outcome of competition was not influenced by the genetic variability, although the exact paths of the competing species could not be predicted. In those populations oscillating in a limit cycle, the numbers of each species present at the peak of one cycle were largely determined by the choice of variables at the lowest points in the cycle. It should thus be considered that genetic drift is important not only in small, isolated populations, but also in those populations undergoing large regular fluctuations in numbers.

This year the model was extended to include the effects of selection. Whenever a new choice of variables was made, the rate of population growth resulting from this choice was compared with that of the competing species. If the new rate of growth was greater than that of the competitor, the selection of variables was retained. If it were not as great, a new set of variables would be chosen. To date, 350 competitions have been run with this modification. Although the runs have not been completely analyzed, it is apparent that a much greater degree of variation in paths exists in these runs, along with some variability in the outcome of competition.

In the course of programming the competition equations it became apparent that the time lag equation for the growth of a population,

$$\frac{dN}{dt} = rN \frac{K - N}{K} (t - \tau_2) ,$$

was inadequate as a mathematical model of population growth, since it did not permit us to study the mechanisms of density-dependent population control. Therefore, a model was constructed in which the nonspecific damping term, $[(K - N)/K] \cdot (t - \tau_2)$, was replaced by descriptions of the ways in which the birth rate and survivorship curves were influenced by increased density. The new equation took the form

$$\frac{dN}{dt} = b_{(t-\tau_1)} N_{(t-\tau_1)} + \int_0^{\tau_3} S'_{z(t-\tau_1)} N_{(t-z-\tau_1)} dz ,$$

where $b = f'(N)$, $S'_z = f''(N)$, and $\tau_3 = f'''(N)$. Here $b \equiv$ birth rate per animal, $N \equiv$ number of animals, $\tau_1 \equiv$ gestation period, $\tau_3 \equiv$ maximum length of life, $S'_z \equiv$ derivative of the survivorship curve, and $z \equiv$ constant of integration. The most difficult part of this approach is the specification of functions for b, S'_z, and τ_3. These functions can be estimated from field data taken from a population during periods of high and low density.

This equation, describing density-dependent regulation of a population in the presence of an excess of food, has now been programmed. The functions for b, S'_z, and τ_3 have been estimated from field data on cotton rat populations collected at Oak Ridge. At the present time we are investigating the effects of different forms of these functions on the shape of the growth curves.

ECOSYSTEM MAINTENANCE AND TRANSFORMATION MODELS AS MARKOV PROCESSES WITH ABSORBING BARRIERS

J. S. Olson V. R. R. Uppuluri

Ecological compartment models discussed in previous reports[6,7] have been expressed in terms of a system of n differential equations for the continuous rates of change of the variables v_k ($k = 1, 2, \ldots, n$), that is, for the vector $\mathbf{v} = (v_k) = (v_1 v_2 \ldots v_n)$ describing the state of n compartments. In ecological applications one or more of the last compartments can be thought of as an absorbing compartment, in the sense that matter or energy arriving there has zero rate (or very low probability) of return to circulation within the remaining compartments, for example, $(v_1 v_2 \ldots v_{n-2})$.

For example, where the variable $\mathbf{v}$ is energy, v_n may be that energy which has been dissipated by respiratory processes (generating low-grade heat), and which cannot again furnish free energy for the operation of biological processes of the ecosystem according to the second law of thermodynamics; replenishment of biologically usable free energy requires photosynthetic input from solar radiation. Where $\mathbf{v}$ is carbon and the model is for the carbon cycle, v_n may be the C in CO_2 which has been respired and mixed with the air outside the local ecosystem; because of rapid turbulent mixing throughout the troposphere, the probability of reentry for any particular atom is exceedingly low, though not quite zero. Where $\mathbf{v}$ stands for a radionuclide, v_n can be defined as that which has finally undergone radioactive decay to another element, and which accordingly has entered a different chemical cycle and been permanently removed from the cycle of the original element in question.

Another class of absorbing barriers (here labeled as v_{n-1}) encompasses various exports from the local ecosystem to surrounding systems, possibly including harvest by man for food or raw materials in the energy or material technology of the human ecosystem. As before, return of units to the local system may be impossible in some cases, or may have sufficiently low probability that it is expressed as having probability 0 for purposes of modeling.

An extension of previous deterministic ecological compartment models in the context of Markov processes encompasses all possible transfers of a specified energy or mass unit by a matrix $\mathbf{P} = (p_{jk})$. Probabilities of transfer within the local ecosystem (i.e., excluding two absorbing compartments) are represented by the submatrix

$$\mathbf{Q} = \begin{bmatrix} p_{11} & \cdots & p_{1k} & \cdots & p_{1(n-2)} \\ \vdots & & \vdots & & \vdots \\ p_{j1} & \cdots & p_{jk} & \cdots & p_{j(n-2)} \\ \vdots & & \vdots & & \vdots \\ p_{(n-2)1} & \cdots & p_{(n-2)k} & \cdots & p_{(n-2)(n-2)} \end{bmatrix} . \quad (1)$$

[6] J. S. Olson, *Health Phys.* 11(12), 1385–92 (1965).

[7] S. I. Auerbach *et al.*, *Health Phys. Div. Ann. Progr. Rept. July 31, 1961*, ORNL-3189, pp. 124–31, and other references cited in these.

Probabilities of transfer to the absorbing states are given by another submatrix

$$\mathbf{R} = \begin{bmatrix} p_{1(n-1)} & p_{1n} \\ \vdots & \vdots \\ p_{j(n-1)} & p_{jn} \\ \vdots & \vdots \\ p_{(n-2)(n-1)} & p_{(n-2)n} \end{bmatrix} . \qquad (2)$$

By definition, the absorbing states have probability 1 for retention of units which have arrived there, as represented by the identity matrix (here 2×2):

$$\mathbf{I} = \begin{bmatrix} 1 & 0 \\ 0 & 1 \end{bmatrix} = \begin{bmatrix} p_{(n-1)(n-1)} & p_{(n-1)n} \\ p_{n(n-1)} & p_{nn} \end{bmatrix} . \qquad (3)$$

Another way of expressing this exclusion of a unit's return to the local ecosystem is the null matrix for the probabilities of contribution from variables v_{n-1} and v_n to the state vector of this system $(v_1 v_2 \ldots v_{n-2})$:

$$\mathbf{0} = \begin{bmatrix} 0 \ldots 0 \ldots 0 \\ 0 \ldots 0 \ldots 0 \end{bmatrix}$$

$$= \begin{bmatrix} p_{(n-1)1} & \cdots & p_{(n-1)k} & \cdots & p_{(n-1)(n-2)} \\ p_{n1} & \cdots & p_{nk} & \cdots & p_{n(n-2)} \end{bmatrix} . \qquad (4)$$

Matrices (1) to (4) are thus submatrices of the overall matrix

$$\mathbf{P} = (p_{jk}) = \begin{bmatrix} \mathbf{Q} & \mathbf{R} \\ \mathbf{0} & \mathbf{I} \end{bmatrix} , \qquad (5)$$

which expresses the transformations of matter or energy within and from any ecosystem.

The postulate that ecosystems are never isolated [$\mathbf{R} = (0)$ for energy] and with rare, artificial exceptions are not closed [$\mathbf{R} = (0)$ for materials] implies that an ecosystem would "run down" if its energy and nutrient losses were not replenished. In nature energy losses are counteracted by the input vector $\mathbf{w} = (w_1 \ldots w_k \ldots w_{n-1})$ including primary production by photosynthesis, and in some cases by immigration of plant propagules, or animals or other materials. Nutrient depletion (e.g., by erosion, leaching, harvesting) is counteracted by rainfall, dust, and, in agriculture, by fertilizer treatments. A quantitative theory of this deterioration, and of the means by which nature or man may counteract it, is being developed from the following implications of the preceding postulate and definitions.

If the initial state of the system is $\mathbf{v}^{(0)}$ at time 0, the expected values, $v^{(t)}$, for time $t = 1, 2, \ldots$ steps of operation of the system are given by the sequence:

$$\begin{aligned} \mathbf{v}^{(1)} &= \mathbf{v}^{(0)}\mathbf{Q}^{(0)} + \mathbf{w}^{(0)} , \\ \mathbf{v}^{(2)} &= \mathbf{v}^{(1)}\mathbf{Q}^{(1)} + \mathbf{w}^{(1)} = [\mathbf{v}^{(0)}\mathbf{Q}^{(0)} + \mathbf{w}^{(0)}]\mathbf{Q}^{(1)} \\ &\qquad + \mathbf{w}^{(1)} , \\ \mathbf{v}^{(3)} &= \mathbf{v}^{(2)}\mathbf{Q}^{(2)} + \mathbf{w}^{(2)} = [\mathbf{v}^{(1)}\mathbf{Q}^{(1)} + \mathbf{w}^{(1)}]\mathbf{Q}^{(2)} \\ &\quad + \mathbf{w}^{(2)} = \mathbf{v}^{(0)}\mathbf{Q}^{(0)}\mathbf{Q}^{(1)}\mathbf{Q}^{(2)} + \mathbf{w}^{(0)}\mathbf{Q}^{(1)}\mathbf{Q}^{(2)} \\ &\qquad + \mathbf{w}^{(1)}\mathbf{Q}^{(2)} + \mathbf{w}^{(2)} . \end{aligned} \qquad (6)$$

For the simple case of constant input (e.g., gross primary production) and constant transfer probability operator $\mathbf{Q}$, these equations simplify into a sum of two terms, one representing the product of the initial condition multiplied by a power of $\mathbf{Q}$, and the second representing the input vector multiplied by a sum of decreasing powers of $\mathbf{Q}$:

$$\mathbf{v}^{(t)} = \mathbf{v}^{(0)}\mathbf{Q}^{t} + \mathbf{w}(\mathbf{Q}^{t-1} + \mathbf{Q}^{t-2} + \ldots + 1) . \qquad (7)$$

If $\mathbf{R} \neq 0$, individual terms in $\mathbf{Q}$ contain terms which are progressively closer to zero ($\mathbf{Q}^n$ tends to a zero matrix).[8] It follows that the influence of the initial state $\mathbf{v}^{(0)}$ on the current state $\mathbf{v}^{(t)}$ diminishes with time, in a way that can be predicted from the tth power of the matrix $\mathbf{P}$ or $\mathbf{Q}$. The input vector influences the current state of the system in a way that can be predicted from the properties of the geometric series in the parentheses of Eq. (7). In the limit, the expected steady state for the local ecosystem can be shown to be

$$\mathbf{v}^{(\infty)} = \mathbf{w}[\mathbf{I} - \mathbf{Q}]^{-1} \qquad (8)$$

where $\mathbf{I}$ here is an $(n-2)(n-2)$ identity matrix. Digital and analog computer model simulations suggest that steady states predicted by this formula are commonly reached early enough to be of significance for interpreting the behavior of natural and managed ecosystems. Problems of fluctuation and stability in systems governed by random disturbances are under investigation.

[8] J. G. Kemeny and J. L. Snell, *Finite Markov Chains*, pp. 22–54, Van Nostrand, New York, 1960.

MODEL SIMULATION OF OAK RIDGE VEGETATION SUCCESSION

J. S. Olson Giovanni Cristofolini

The successional changes revealed by analysis of 1935 and 1959 air photos[9] were used as approximate estimates of the probability p_{jk} for a randomly chosen tract of the Oak Ridge Reservation to change from vegetation type j to type k, or to remain in the same vegetation "type" (i.e., where $j = k$) during the 24-year period. The matrix $P = (p_{jk})$ derived from Table 10.4 of the last report[9] was adjusted to express these probabilities of change in state on an annual basis. This matrix was then used as an operator for transforming the row vector $\mathbf{v} = (v_k)$ representing the distribution of proportions of area given by major types $k = 1, 2, \ldots, 8$ for times $t = 0, 1, 2, \ldots$:

$$\mathbf{v}^{(t)} = (v_k)^{(t)} = \mathbf{v}^{(t-1)}\mathbf{P} \tag{1}$$

$$= \mathbf{v}^{(0)}\mathbf{P}^t . \tag{2}$$

This example is thus a particularly simple, practical application involving the first term of Eq. (7) of the preceding article, where $\mathbf{v}$ is a vector of probabilities (or fractions of the total land, adding up to 1, but excluding those substantial areas of the Oak Ridge Reservation which have been transferred to the "absorbing barrier" represented by facilities, roads, and rights of way). With this exclusion, the matrix $\mathbf{P}$ here becomes identical with the submatrix $\mathbf{Q}$ in expression (1) of the preceding article. Equation (1) represents the calculations which were made through successive annual steps by adapting a previously discussed digital computer simulation program for calculating rates of change.[10] Computer-generated functions (Fig. 11.3) illustrate the rapid decrease in open

[9] S. I. Auerbach *et al.*, *Health Phys. Div. Ann. Progr. Rept. July 31, 1965*, ORNL-3849, pp. 76–77.

[10] S. I. Auerbach *et al.*, *Health Phys. Div. Ann. Progr. Rept. July 31, 1965*, ORNL-3849, p. 92.

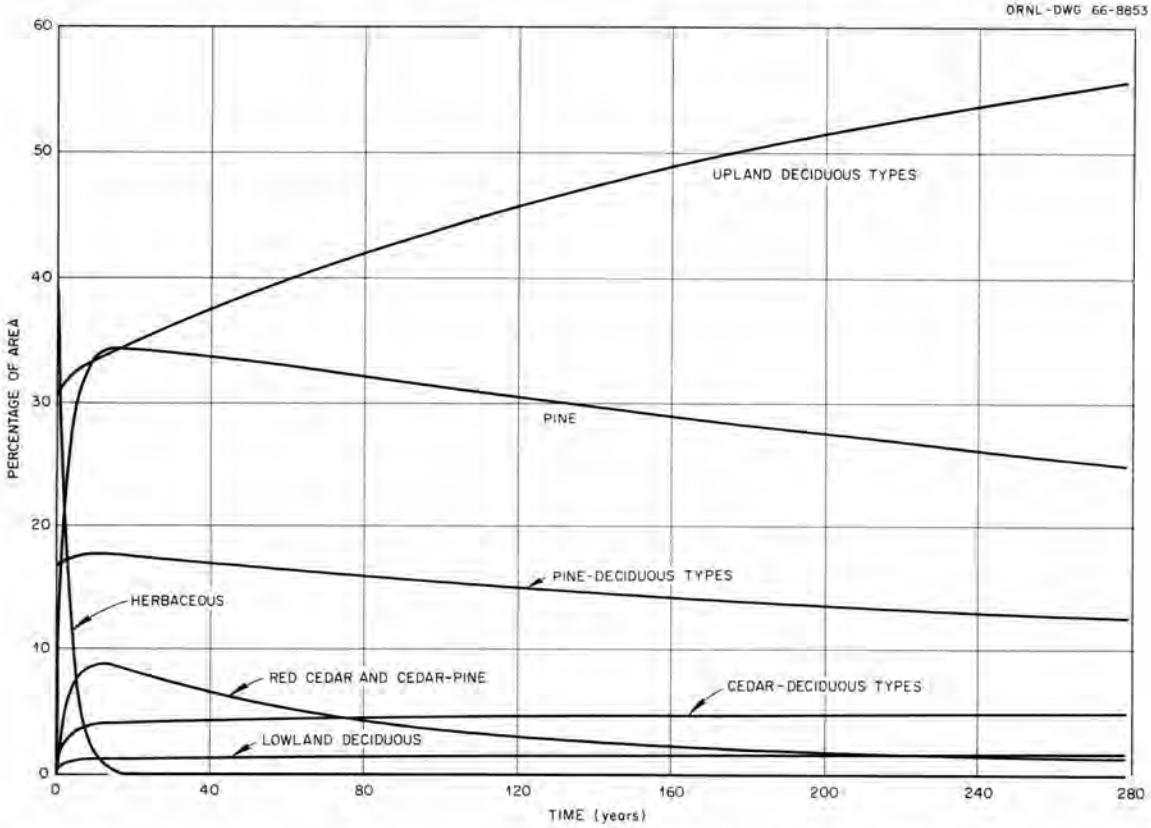

Fig. 11.3. Computer-Generated Curves Showing Predicted Areas of Major Oak Ridge Forest Types, Assuming a Constant Matrix of Transfers $\mathbf{P} = (p_{jk})$ of Area from Type j to Type k.

land which occurred during this interval due to abandonment of agricultural fields; natural reforestation would go essentially to completion in Tennessee's forest climate unless soil-ecosystem disruption were very drastic (as at Copperhill).[11] Red cedar forest type increased temporarily as a result of invading open land, but decreased soon afterward, primarily as a consequence of conversion to stands of pine (which soon overtop the cedar), pine-deciduous mixtures, or to red cedar–deciduous mixtures, which are surprisingly stable (at least on typical limestone outcrop belts).[9] The pine-deciduous mixtures increase temporarily, but are replaced in turn by the upland deciduous forest types, primarily oak-hickory. However, local data and simulations suggest how this classic successional sequence (cedar or pine to deciduous-pine to deciduous) is reversed locally, by disturbing processes like blowdown and fire; such disturbance presumably accounts for regeneration of pine-deciduous vegetation in much of the southeastern United States.

KINETICS OF ^{134}Cs IN TERRESTRIAL MICROCOSMS

B. C. Patten Martin Witkamp

The study of radiocesium kinetics in microecosystems consisting of different combinations of tagged white oak leaf litter, soil, microflora, millipedes, and aqueous leachate[12] has been completed. Results are shown in Fig. 11.4; these supersede the preliminary results reported last year. The principal result illustrated is that cesium kinetics varies with the system components. For example, litter loss rates, λ_{ij}, in the sequence of systems toward greater complexity (*a–f* in Fig. 11.4) were 0.037, 0.037, 0.036, 0.060, 0.110, and 0.199 day^{-1}. Millipede elimination rates increased from 0.525 day^{-1} in system *e* with soil absent to 0.660 in system *f* with soil present. Microflora transferred Cs to litter in system *f*, a pathway over which no transfers occurred in other systems which had microflora in them.

System characteristics which influence the concentration and turnover of radionuclides are important to identify in radioecology. Turnover data (Table 11.1) indicate (1) that identical compartments turned over radiocesium at variable rates in the different microcosms, and (2) that turnover rates of compartments increased with greater system complexity. Relative cesium-concentrating ability of the different systems was determined by performing computer simulations with the models. A typical simulation of 1200 days' duration is shown in Fig. 11.5 for system *e* of Fig. 11.4. Starting each compartment free of radioactivity, the system was driven by a constant 0.25 v/sec, representing an arbitrary input of radiocesium to litter. The equilibrium level in each compartment relative to this input was taken as a concentration factor. That cesium-concentrating ability of different compartments depends on the system kinetics, and hence on patterns of coupling, is illustrated in Table 11.1. For example, in system *e* microflora concentrated cesium 4.0 times while in system *f* it was concentrated only 1.9 times. Millipedes in system *e* had a concentration factor of 3.7, almost three times the value in system *f* (1.3).

Table 11.1. Turnover Rates and Hypothetical Concentration Factors of ^{134}Cs in the Experimental Microcosms

"∞" indicates compartments which did not equilibrate

Microcosm (Fig. 11.4)	Litter	Soil	Microflora	Millepedes	Leachate
Turnover, %/day					
a	3.7				0.0
b	3.7	0.0			0.0
c	3.6		0.0		0.0
d	6.0	0.0	0.0		0.0
e	11.0		37.5	52.5	0.0
f	19.9	0.0	75.0	66.0	0.0
Concentration factor					
a	14.2				∞
b	14.1	∞			∞
c	14.1		∞		∞
d	8.8	∞	∞		∞
e	20.4		4.0	3.7	∞
f	9.1	∞	1.9	1.3	∞

[11] See "Accumulation and Production in a Pioneer Ecosystem of Kudzu Vine at Copperhill, Tennessee," chap. 9, this report.

[12] S. I. Auerbach *et al.*, *Health Phys. Div. Ann. Progr. Rept. July 31, 1965*, ORNL-3849, pp. 94–95.

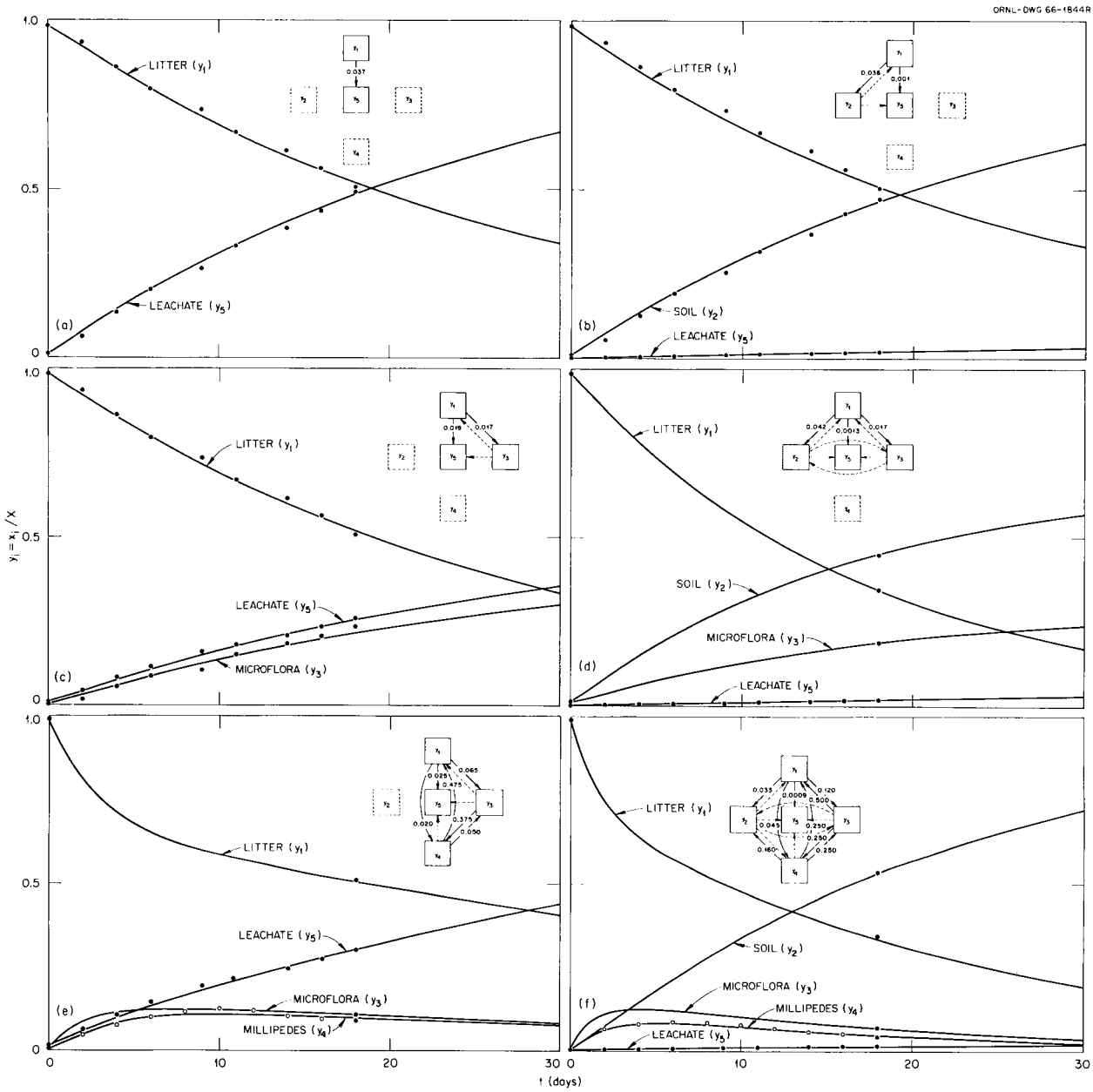

Fig. 11.4. Analog Computer Curves of Changes in Relative Distribution (y_j) of Radiocesium in the Experimental Microcosms. Means of two replicates are shown as solid circles. Open circles represent estimates of relative ^{134}Cs concentration in millipedes based on radioassays of animals which died. Insets show compartment combinations and rate constants (day^{-1}) over the indicated transfer routes. Pathways over which no cesium was transferred are illustrated by broken arrows.

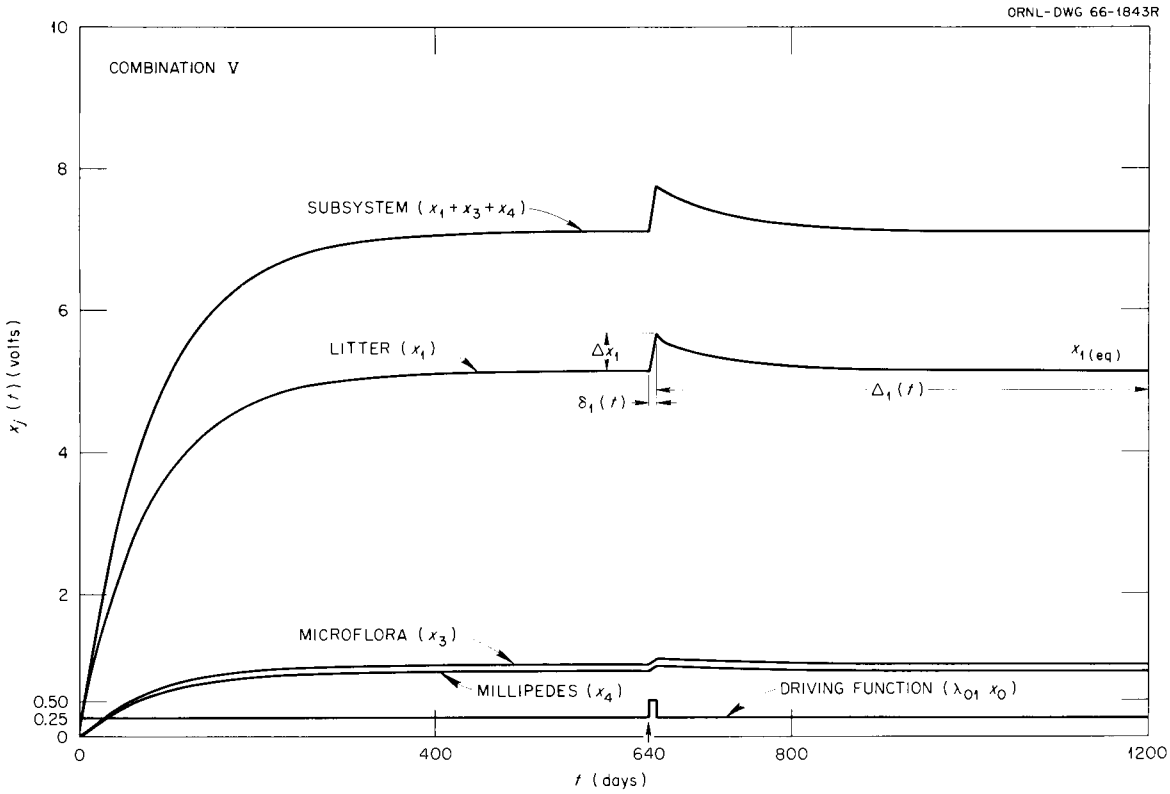

Fig. 11.5. Computer Simulation of Radiocesium Uptake in System (e) of Fig. 11.4 Under the Influence of a Constant Input, $\lambda_{01} = 0.0125\ \text{day}^{-1}$, to Litter. Soil and leachate did not equilibrate and are omitted. Perturbation of the system between 640 and 648 days by doubling of the input is illustrated.

Results like these show that material transfers in connected systems are influenced by the organizational networks which define interactions between component parts. Consequently, network characteristics should be regarded as significant ecological variables in studies of energy and material movements, including transfers of radioactive substances.

NONLINEAR PROGRAMMING IN ECOLOGY

G. M. Van Dyne

Nonlinear programming has been used in three dissimilar ecological analysis problems. In many ecological studies we obtain samples containing a mixture of species, and we measure some attributes of the sample and determine the percentage species composition in the samples. Often, however, because of practical or technical reasons, we are not able to measure the same attribute for each species in a sample. For example, dietary samples collected from esophageal fistulated animals may be analyzed for chemical composition by routine methods and may be analyzed for botanical composition by microscopic point analysis. However, we would like to know the content of a given chemical or radionuclide in each species in the sample. We could separate the sample into species, but we are prevented by practical considerations from separating samples and chemically analyzing each plant.

The method of applying nonlinear programming to this problem is as follows: Let C_i be the measured percent content (or say μc/g of a radionuclide) of a given chemical constituent by weight in the ith mixed sample; P_j is the predicted chemical content of the jth species, plant part, or plant group in the mixed sample, expressed as a percent; and W_{ij} is the measured proportional weight of the jth species, part, or group in the ith sample.

Best estimates of the vector P, in a least-squares sense, are obtained by minimizing the function Q as follows:

$$Q = \sum_i (C_i - \sum_j W_{ij}P_j)^2 ,$$

where $\sum_j W_{ij} = 1.0$ for all i, and $0 \leqq W_{ij} \leqq 1.0$ and $0 \leqq C_i \leqq 100$. Some 30 computer experiments were summarized in a paper considering this operations research technique and its application to ecological problems.[13]

An extension of this technique was made by considering simultaneously several chemical constituents in the mixed-species samples.[14] This is accomplished by defining C_{ik} to be the measured percent composition of the kth chemical in the ith mixed sample, W_{ij} remains the same as above, and P_{jk} is the predicted percent composition of the kth chemical in the jth plant. The new function, Q^*, to be minimized by nonlinear programming is:

$$Q^* = \sum_i \sum_k (C_{ik} - \sum_j W_{ij}P_{jk})^2$$

such that $P_{jk} \geqq 0$ for all j and k, and $\sum_k P_{jk} = 100$ for all j, as well as the constraints on W_{ij} given above.

Furthermore, if we let S_{ik} be defined as the percent digestibility of the kth chemical constituent in the ith mixed forage sample as determined by in vitro or in vivo techniques, we can predict the digestion coefficients, D_{jk}, for these samples by minimizing Q',

$$Q' = \sum_i \sum_k (S_{ik} - \sum_j W_{ij}P_{jk}D_{jk})^2 ,$$

subject to $0 \leqq D_{jk} \leqq 100$ for all j and k and where P_{jk} is given by the above method.

Another use of nonlinear programming has been in application of the dry-weight rank method of botanical composition analysis. In studies on White Oak Lake bed and in old-field areas (Ecology study area 0800) we have located quadrats randomly, recorded the species present in each, ranked each species according to its weight contribution, clipped the herbage and separated it in the laboratory, and obtained the following matrix and vector. Here X_{ij} is the proportion of the plots in which the ith species received the jth rank and W_i is the measured dry weight percentage contributed by the ith species. We estimate a vector of multipliers, K_j, to use to convert ranking data to percent weight composition by using nonlinear programming to minimize a function Q'' as follows:

$$Q'' = \sum_i (E_i - \sum_j K_jX_{ij})^2$$

subject to $\sum_j K_j = 100$. Statistical and field studies concerned with old-field vegetation at Oak Ridge are continuing to evaluate this method of nondestructively sampling botanical composition of herbaceous vegetation. This technique holds special promise for working in small areas where nondestructive sampling is especially important, or working in radioactively contaminated areas where field time must be kept to a minimum.

A third application of nonlinear programming to ecological problems is given by Patten and Van Dyne ("Productivity of a Planktonic Diatom Determined from Data on Mixed Species Populations," in Chap. 11, this report).

COMPUTER PROGRAMS FOR ECOLOGICAL PROBLEMS

G. M. Van Dyne

Major computer programs have been written for a variety of ecological problems, and a few are reported here. Also, several programs written elsewhere have been modified or extended for use in ecological analysis. Results of some of the latter programs are given in this report in the sections on "Nonlinear Programming in Ecology" (Chap. 11) and in "Soil Studies in Herbaceous Ecosystems" (Chap. 9).

REGRESS[15] is a general multiple regression and correlation program especially written to be simple yet flexible, and usable by those not intimately familiar with computer technology. This program

[13] G. M. Van Dyne, *Health Phys.* 11, 1511–19 (1965).

[14] G. M. Van Dyne, *Data on Chemical and Botanical Composition of Dietary Samples Grazed by Cattle and Sheep*, ORNL-TM-1376 (1965).

[15] G. M. Van Dyne, *REGRESS – a Multiple Regression and Correlation Program with Graphic Output for Model Evaluation*, ORNL-TM-1288 (1965).

is available as a main program or as a subroutine and will give summary statistics on the input variables (up to 60) as well as correlation and regression analyses. Deviations from the model are calculated and a variety of Calcomp plots are available. Options (Table 11.2) within the program allow reading data from cards or tape, variable format or standard format, names generated or names read in, weighted regression or non-weighted regression, a variety of transgenerations, and regression through the origin or not through the origin.

ENSLAVE is a program which calls a variety of subroutines to make a study of interspecies and intraspecies spacing or pattern relationships among plants. A variety of input data is accepted by variations in the reading subroutine. Data from line intercept records, line point records, or chart quadrat records can be accommodated by this program. Output from the program includes statistical and information-theoretic parameters concerning the observed and expected (for randomly distributed plants) spacing relationships among plants in field communities. An example of the graphic output from the program is given in Fig. 11.6, where the intraspecies spacing relations of two foothill range bunchgrasses and the interspecies relations between them are given. *Koeleria*

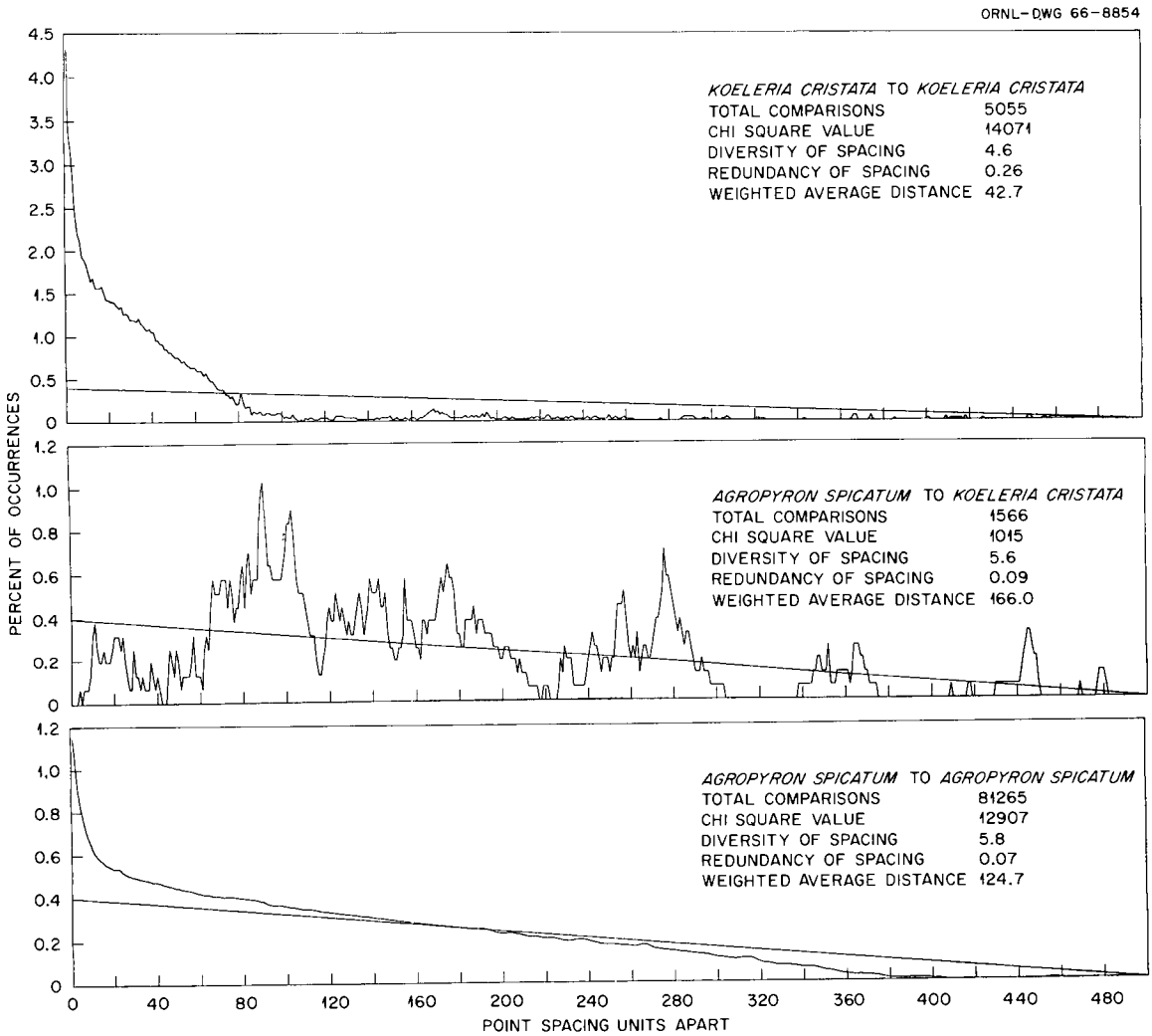

Fig. 11.6. Example Results from Program ENSLAVE for Pattern Analysis. These Calcomp-generated graphs show straight lines for expected random distributions and irregular lines for observed distributions of spacing relations of two grasses on 350 line intercept transects, each 5 ft long and measured in 0.01 ft.

Table 11.2. Description of the Control Card for REGRESS Showing Options Available in the Program

Card Column(s)	Designation on Output	Meaning and Coded Values
1–2	Printed statement	Controls use of input: < 0 read data from tape 0 read data from cards > 0 read from cards, write on tape
3–6	OBS	Number of data points or observations: $2 \leq \text{OBS} \leq 9999$
7–8	NBE	Number of variables before transgeneration: $2 \leq \text{NEB} \leq 61$
9–10	NAF	Number of variables after transgeneration: $2 \leq \text{NAF} \leq 60$
12	WGT	Control for weighted regression: < 1 do not weight, ≥ 1 weight data
14	PLT	Controls plots: no plots, variables against deviations, against each other, etc. (see ref. 15)
16	ORG	Controls forcing equation through the origin: ≤ 1 not through origin, ≥ 2 through origin
18	NAM	Controls labeling of variables: ≤ 1 generate numbers for names, ≥ 2 read names
20	FMT	Controls input format: 0 read standard, ≥ 1 read variable format
21–22	TRN	Controls transgenerations[a] 0 no transgenerations, ≥ 1 number to make
23–24	CON	Controls constant to be read in: 0 no constants, ≥ 1 number of constants
25–80	Printed	Alphanumeric identification

[a]Transgenerations: given as eight digits per transgeneration, NNIIJJKK, where NN is the code, II is index of variable (X) before transgeneration, JJ is the index after transgeneration, and KK is the index of a second variable or constant (C) used in the transgeneration.

Code	Meaning	Code	Meaning
1	$X_i = X_j$	10	$X_i = X_j \times C_k$
2	$= X_j \times X_k$	11	$= X_j^{C_k}$
3	$= X_j \div X_k$	12	$= \log_e X_j$
4	$= X_j + X_k$	13	$= \log_{10} X_j$
5	$= X_j - X_k$	14	$= e^{X_j}$
6	$= 1 \div X_j$	15	$= \sin X_j$
7	$= X_j + C_k$	16	$= \arctan X_j$
8	$= X_j \div C_k$	17	$= \sin (X_j - C_k) + 1$
9	$= C_k \div X_j$		

cristata shows a much greater degree of "bunchiness" than does *Agropyron spicatum*, as is reflected in the much greater percentage of the occurrences at close spacings. Chi-square tests substantiate that all three distributions are nonrandom. The weighted average distances apart for these plants were 0.42 ft for *Koeleria*, 1.25 ft for *Agropyron*, and 1.66 ft for the distance between them. Diversity of spacing relationships, in an information-theoretic sense, was 4.62 for *Koeleria*, 5.75 for *Agropyron*, and 5.65 for the interspecific relationship. This program is being used for continued studies on pattern relationships, using a variable distance between sampling units, that is, from 0.01 ft to greater distances, as a means of detecting the scale of pattern.

Other programs of special ecological interest include: RANK, a method of applying "tie-breaking" random decisions in ranking or estimating percent composition of plants in plots, and then organizing the data in suitable matrix formats for input into nonlinear programming analyses for the dry-weight rank method; ECOKINET, programs related to the compartmental analysis for the study of intraseasonal herbage dynamics, wherein field data are used to estimate transfer coefficients from compartment to compartment, and for which variance-covariance matrices are derived by combining iterative least-squares methods with those for solving sets of differential equations; BIAS, programs for studying the effect of human error in field studies estimating herbage yield in clipping studies involving circular plots of 0.5, 1.0, 1.5, and 2.0 m^2 in pasture or old-field areas (see clusters 4, 5, and 6 in Fig. 9.11); and SHRUBS, a program designed to evaluate the use of geometric properties such as volume, surface area, and projected area of shrubby plants for predicting yield, where linear measurements of the plants are used to classify the plant into one of six circular or elliptic solid geometric forms.

PRODUCTIVITY OF A PLANKTONIC DIATOM DETERMINED FROM DATA ON MIXED SPECIES POPULATIONS

B. C. Patten G. M. Van Dyne

In studies of plankton productivity, water samples containing a mixture of species are typically assayed for photosynthetic or respiratory activity by dark-and-light-bottle methods involving ^{14}C assimilation or oxygen evolution (see "Primary Productivity Measurement," Chap. 10). It is desirable to be able to estimate from such data the amount of production which is due to each species in the sample. This would permit following the energetics of each population, and a fuller understanding of community organization and succession would thereby be obtained. An approach to such an objective is possible through a combination of (1) factorial experiments in situ and (2) a mathematical programming procedure.[16] The latter has been applied previously to food chain analysis problems.[17]

In applying the procedure to productivity problems, it is necessary to design experiments meeting two criteria. First, the number of samples n must exceed the number of species m. Second, samples should be obtained such that a necessary assumption (that each individual of the same species in every sample have the same photosynthesis or respiration) can be applied and the method still yield meaningful information. These desiderata can be met through factorial experimental designs.

During the summer of 1963 eight factorial dark-and-light-bottle oxygen experiments[18] were performed in the York River, Virginia.[19] Water samples from seven depths were suspended throughout the water column (at all the sampling depths) for 24 hr; that is, samples from a given collection depth were suspended at all the other collection depths in a 7×7 factorial design. Thus, the number of samples was $n = 49$. Phytoplankton in each of the seven samples were identified and counted, giving seven species compositions for each experiment. The maximum number of taxa encountered in the samples of the eight experiments was $m = 18$. Thus, $n > m$ was always satisfied.

By sampling and resuspending in the manner described, the phytoplankton populations of the entire water column (surface to bottom) are rep-

[16] A. V. Fiacco and G. P. McCormick, *Management Sci.* 10, 601–17 (1964).

[17] G. M. Van Dyne, *Health Phys.* 11, 1511–19 (1965).

[18] T. Gaarder and H. H. Gran, *Rappt. Proces-Verbaux Reunions, Conseil Perm. Intern. Exploration Mer* 42, 1–48 (1927).

[19] B. C. Patten and B. F. Chabot, "Factorial Productivity Experiments in a Shallow Estuary," submitted to *Chesapeake Sci.*

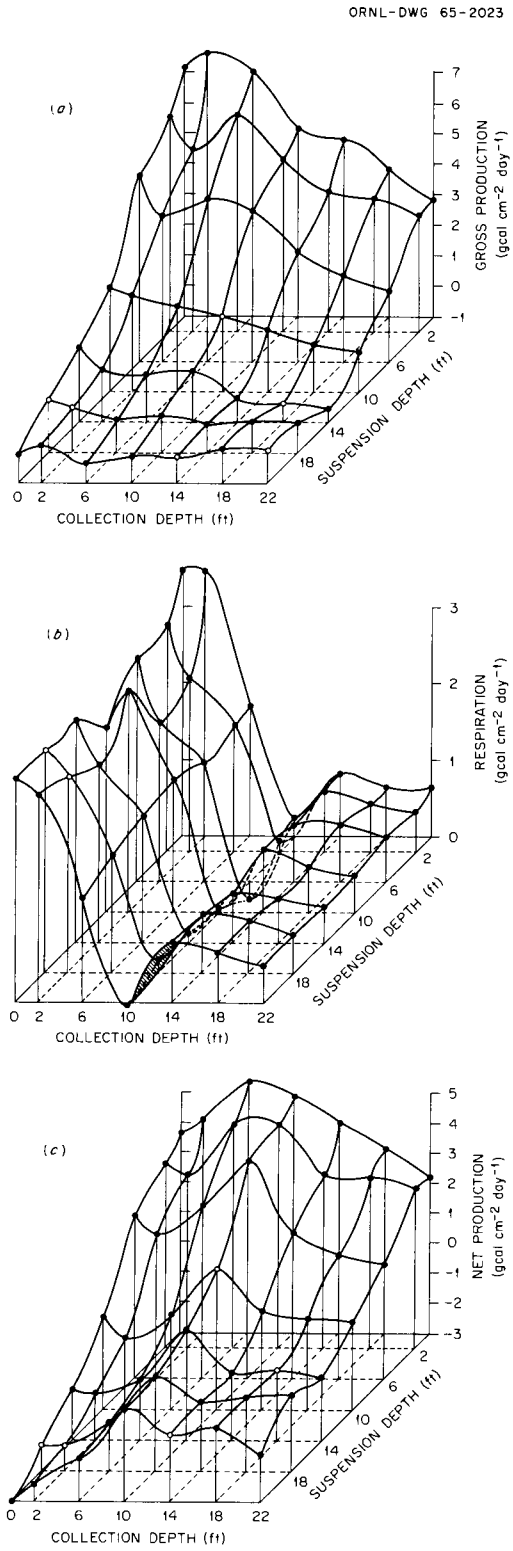

Fig. 11.7. Production and Respiration Response Surfaces Obtained for Phytoplankton Populations Sampled in the Fourth Experiment, July 15–16, 1963.

resented, and their average photosynthetic and respiratory responses under all conditions of light and temperature in the water column are assessed. Results of the fourth experiment are depicted in Fig. 11.7. Computation of the production or respiration per individual of each species *i* from such data gives meaningful information despite the assumption that each individual of the species in all the 49 samples had the same production or respiration per cell: the values represent an *average* response per cell of all populations of species *i* found in the water column at the time of sampling to all conditions in the water column over the incubation period. This information can be used to compare the states of component populations in a succession sequence.

To illustrate the application, average photosynthesis and respiration per cell of the diatom *Skeletonema costatum* and of all remaining species lumped together were computed for the eight experiments. Results are depected in Fig. 11.8.

The data show that average photosynthesis and respiration per individual of *S. costatum* varied over five decades during the course of the eight-week study. Photosynthesis and respiration, both of *Skeletonema* and the remaining species, appear strongly correlated. The succession of *Skeletonema* is indicated to have proceeded from populations with low average gross production and respiration per cell to populations with high values in mid-July (the fourth experiment, discussed above) to lowest levels in late July, followed again by high levels in August. Average net production per cell, the difference between gross production and respiration, was generally higher in the first half of the study. An inverse relationship between productivity and respiration per cell of *Skeletonema* and that of the remaining species is apparent during June and July.

GROWTH MODELS FOR PLANTS

G. M. Van Dyne

In many ecological studies it is desirable to represent height or weight growth of an individual or a population with a prediction function. Furthermore, when the equation and form of the model is obtained, properties of the equation may be used

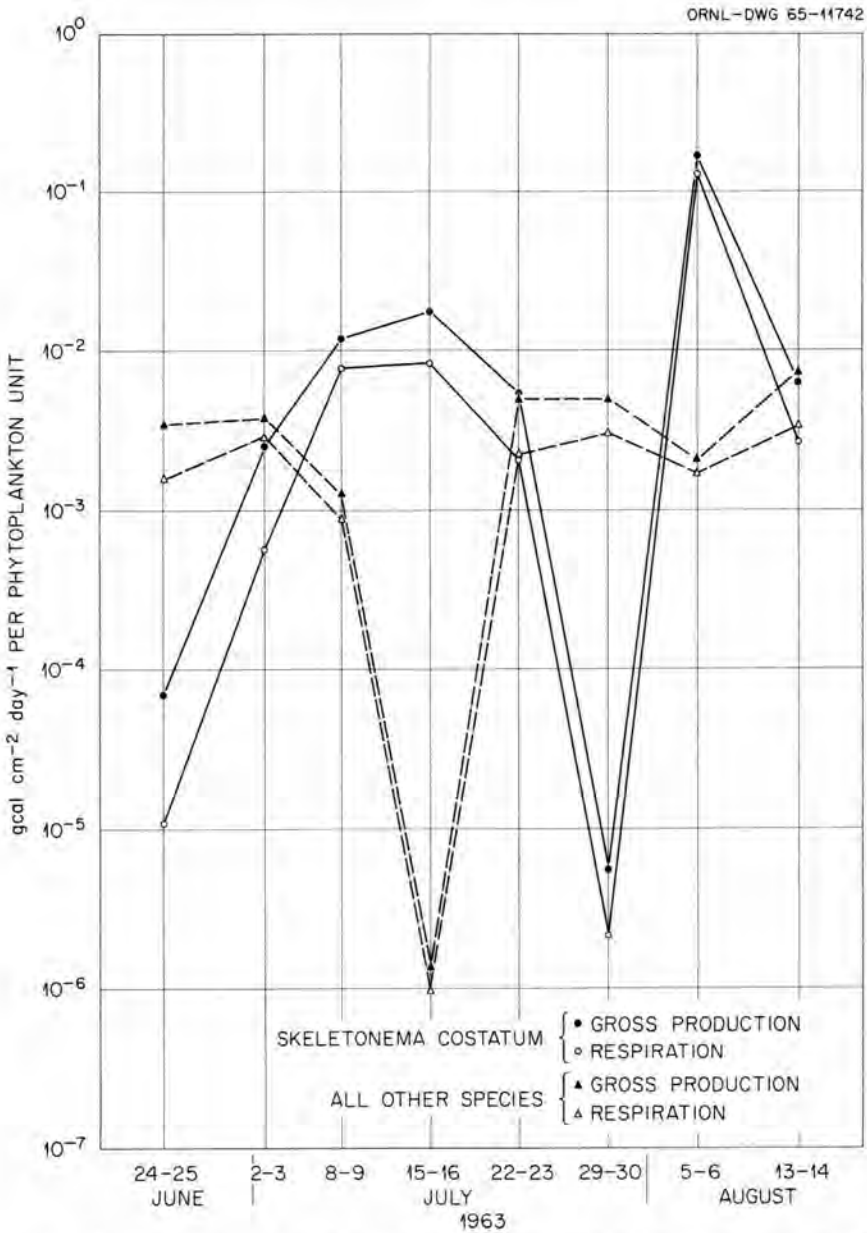

Fig. 11.8. Average Gross Production and Respiration per Cell of *Skeletonema costatum* Populations and per Cell of Remaining Species Lumped Together During Summer 1963.

to assess economic or ecological effects of treatments. Equations were developed[20] to show the residual influence of the nitrogen and phosphorus on height growth of the three cool-season plants. Growth properties examined included height of the plants in early spring at the time of flowering of a phenological index species, the maximum height-growth rates attained, the time and plant heights at which maximum growth rates were obtained, and the maximum heights attained during the season.

Using H to represent height in inches, and t to represent the day in the year, three nonlinear models were used to study height growth of *Oxytropis serecia*, *Stipa comata*, and *Agropyron*

[20] G. M. Van Dyne and I. Thorsteinsson, "Intra-seasonal Changes in Height Growth Rate of Range Plants in Response to Nitrogen and Phosphorus," *Proc. Xth International Grassland Congress* (in press).

spicatum in response to 0, 50, and 100 lb/acre of nitrogen and phosphorus applied in factorial combinations in two replicates in the preceding year:

$$H = \frac{1}{a + br^t}, \qquad (1)$$

$$H = \frac{a}{1 + be^{-ct}}, \qquad (2)$$

$$H = k_1 (ae^{bt}) + k_2 (c + dt), \qquad (3)$$

where

$$\text{for } t \leq t_c,\ k_1 = 1 \text{ and } k_2 = 0;$$
$$t > t_c,\ k_1 = 0 \text{ and } k_2 = 1;$$

and

t_c = date when decay of height began.

Equation (1) was inappropriate because of lower coefficients of determination than were obtained for (2) or (3). Equation (2), derived from the differential model $dH/dt = k_i H - k_2 H^2$, fitted the data comparatively well, but did not account for the very rapid increase in plant height growth early in the growing season. Plant height growth best fits Eq. (3) for many treatments because these cool-season plants made rapid growth early in the year and then, in general, heights of the grasses decreased in a linear manner or changed little during the remainder of the season. In Eqs. (2) and (3) coefficients of determination generally were above 90% for grasses, better predictive equations were found for no nitrogen as compared to either 50 or 100 lb/acre of nitrogen, but relatively little difference occurred among phosphorus treatments. For the legume, *Oxytropis serecia*, the predictive value varied widely, but better equations usually were found for 0 or 50 lb/acre of phosphorus than for 100 lb/acre and there was no consistent relation to nitrogen treatments.

The magnitudes of various parameters or properties of Eq. (2) derived for various phosphorus and nitrogen treatment combinations are shown in Table 11.3, and the curves are given in Fig. 11.9.

Table 11.3. Influence of Nitrogen and Phosphorus on Initiation of, Rate of, and Extent of Height Growth of Three Plants as Determined with a Kinetic Model, Eq. (2)

Nutrient Added (lb/acre)		Height at Time Zero,[a] $\frac{a}{1+b}$ (in.)	Maximum Growth Rate, $\dot{H}$ at t_m (in./day)	Time of Maximum Growth Rate, t_m (coded date)	Height at Maximum Growth Rate, H_m (in.)	Maximum Height, a (in.)
Nitrogen	Phosphorus					
			Agropyron spicatum			
0	0	0.43	0.16	46	4.7	9.5
0	100	0.75	0.12	49	4.7	9.4
100	0	0.37	0.16	40	4.2	8.3
100	100	0.54	0.16	37	4.2	8.5
			Stipa comata			
0	0	0.42	0.065	45	2.5	4.9
0	100	0.42	0.066	48	2.5	5.0
100	0	0.44	0.068	34	2.1	4.3
100	100	0.33	0.102	37	2.7	5.5
			Oxytropis serecia			
0	0	0.92	0.066	29	2.6	5.1
0	100	0.89	0.065	32	2.6	5.3
100	0	0.80	0.062	35	2.6	5.1
100	100	0.93	0.060	30	2.5	5.0

[a]Dates are referenced to the time when *Douglasia montana* was in full bloom, about April 1.

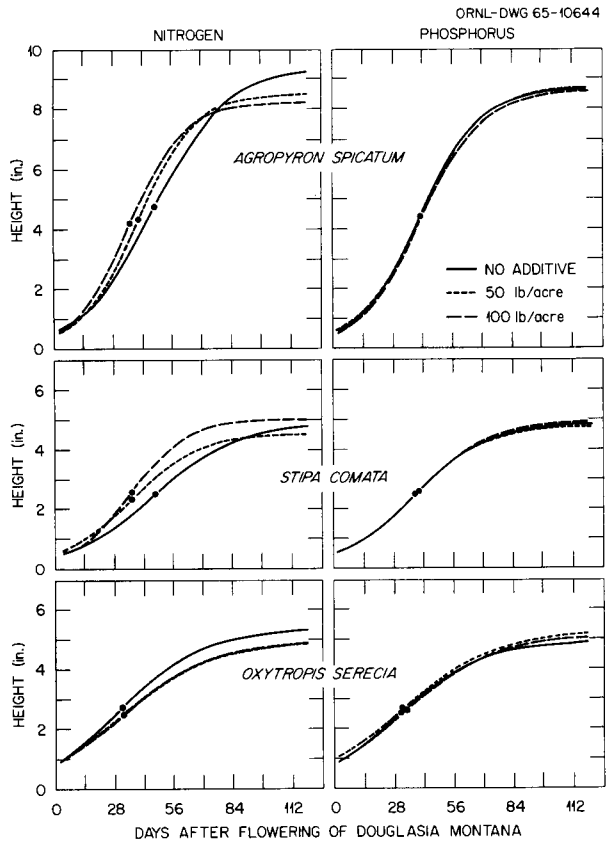

Fig. 11.9. Kinetic Model (Eq. 2) of Height Growth of Three Plants as Affected by Phosphorus and Nitrogen. The dots represent inflection points on the curves.

These models showed that nitrogen caused the grasses to grow rapidly during the period of greater soil moisture supply, and cessation of height growth corresponded to a rapid decrease in the percent moisture in the *A* horizon of the soil. Maximum height-growth rates usually were greater for the legumes in plots without nitrogen than for plots with high levels of nitrogen. Additional nutrients apparently influence the productivity of the legume by increasing competition from the grasses, which were benefited by either nitrogen alone or nitrogen and phosphorus in combinations. In many instances discontinuous models may provide more realistic results than such classical growth models as the logistic (1) or the kinetic model (2). The discontinuity in growth was, in this instance, related to changes in daylight-night ratios and to depletion of soil moisture supplies as well as to elevated temperatures in mid-summer. This is suggested in Fig. 11.10 for *Agropyron spicatum* receiving 100 lb/acre of nitrogen and 50 lb/acre of phosphorus. Kinetic models for productivity and nutrient cycles must ultimately take account of such seasonal influences.

THE OPTIMUM SITE PROBLEM

G. M. Van Dyne

Assessing the combined effects of site variables on measures of vegetation production has undergone long development, originating with qualitative site classifications and more recently turning to regression models for prediction purposes. In this study[21] multiple linear regression functions were used as objective functions in linear programming models, along with appropriate constraints to find optimum sites for nutrient production measures. Protein yield, grass and sedge composition, perennial grass yield, phosphorus yield, and lignin composition in the herbage (Y_i) from foothill grassland were expressed as linear functions of topographic factors of elevation, exposure, and slope, and soil factors of concentration or content of sand, rock, clay, phosphorus, organic matter, conductivity, and pH of the *A* horizon (X_i).

The regression equation (1),

$$\mathbf{Y}_{1x1} = \mathbf{X}_{1xm}\,\mathbf{B}_{mx1}\,, \tag{1}$$

became the objective function (2),

$$f_{max} = \mathbf{X}_{1xm}\,\mathbf{B}_{jx1}\,, \tag{2}$$

of a linear programming model which was to be maximized according to the constraints (3),

$$\mathbf{A}_{jxm}\,\mathbf{X}_{mx1} = \mathbf{C}_{jx1}\,, \tag{3}$$

where **A** and **C** respectively are a matrix and a column vector of constants.

The problem was to maximize protein production for use by cattle and sheep during the nonwinter period. Sites having higher-than-average grass

[21] G. M. Van Dyne, "The Optimum Site Problem — an Application and Integration of Multiple Linear Regression and Linear Programming Analyses," submitted to *J. Range Management*.

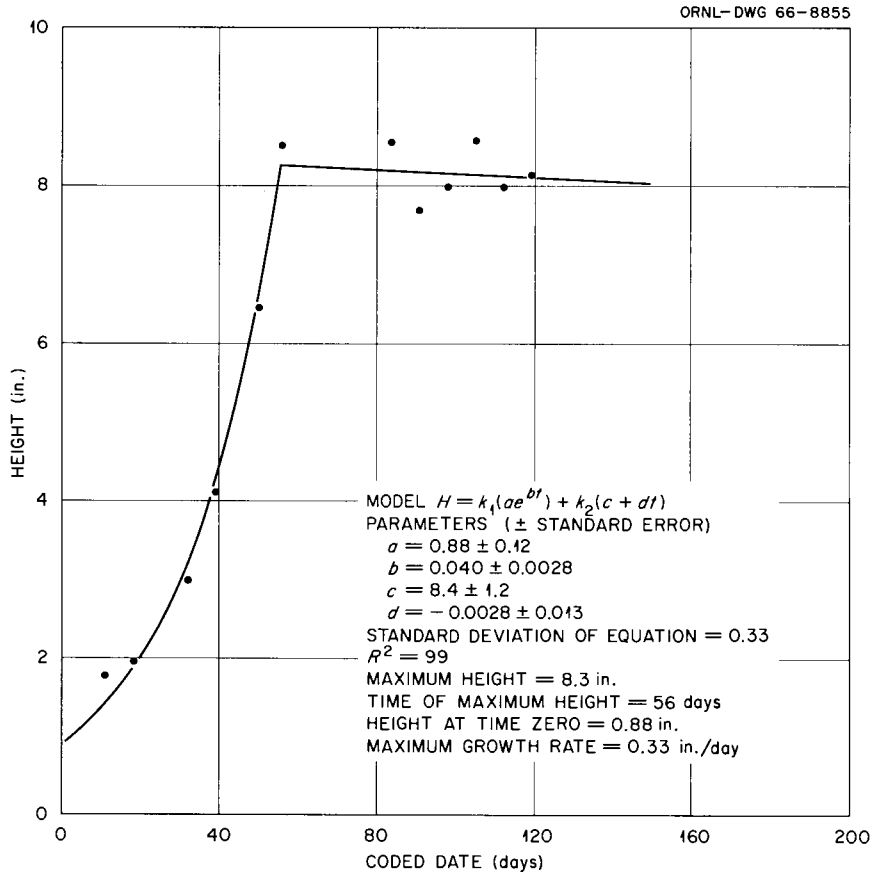

Fig. 11.10. Discontinuous Regression Model (Eq. 3) for Height Growth of *Agropyron spicatum* Which had Received 100 lb/acre of Nitrogen and 50 lb/acre of Phosphorus the Preceding Year.

and sedge composition in their herbage were being sought, in contrast to those having a large percentage of woody vegetation. The site must have better-than-average grass and sedge yield, better-than-average phosphorus yield, as well as having herbage with less-than-average lignin concentration. The four multiple linear regression equations relating site factors to grass and sedge composition and phosphorus yield, and lignin concentration were used to derive these inequality constraints (constraints 12 to 16 in Table 11.4).

The final model, with the objective function and constraints, is given in Table 11.4. The optimum site determined by linear programming analysis showed that the maximum protein yield, under these constraints, was about 139 lb/acre as compared to a measured range of protein yield of from 24 to 211 lb/acre with a mean of 77 lb/acre. To maximize protein yield under this particular set of constraints requires sites at relatively low elevation on north or east exposures. These sites need low sand and clay content, therefore implying a relatively high silt value. The soil would be relatively high in rock, phosphorus, and organic matter content, but relatively low in pH and conductivity. The optimum site needs nearly level topography and slightly deeper than average *A* horizons.

This example shows how combining linear programming and regression models provides a new means of evaluating macroenvironmental problems. This approach also can be used in forestry in determining site characteristics for simultaneous maximization of site index of several tree species. Another important use would be in renewable resource management in the situation where more

Table 11.4. The Objective Function and Constraints[a] of the Linear Programming Model for Determination of Site Characteristics (X_i) for Optimum Crude Protein Yield (Y)

Objective function:

$$Y = 14 + 0.02X_1 - 11X_2 - 0.78X_3 - 1.6X_4 + 0.47X_5 + 0.02X_6 + 3.4X_7 - 4.6X_8 - 22X_9 - 0.09X_{10} + 6.0X_{11}$$

Constraints:

(1) $4780 \leqq X_1 \leqq 5980$	(7) $0.3 \leqq X_7 \leqq 56$
(2) $0 \leqq X_2 \leqq 2.0$	(8) $5.8 \leqq X_8 \leqq 8.0$
(3) $46 \leqq X_3 \leqq 93$	(9) $0 \leqq X_9 \leqq 18$
(4) $2 \leqq X_4 \leqq 19$	(10) $1 \leqq X_{10} \leqq 55$
(5) $1.2 \leqq X_5 \leqq 62$	(11) $2 \leqq X_{11} \leqq 24$
(6) $33 \leqq X_6 \leqq 222$	

(12) $X_3 + X_4 \leqq 100$

(13) $0.01X_1 - 6.1X_2 - 1.7X_3 - 0.88X_4 - 0.36X_5 + 0.03X_6 - 3.4X_7 - 4.4X_8 + 3.2X_9 - 0.32X_{10} - 0.24X_{11} \leqq -150$

(14) $0.13X_1 - 79X_2 - 16X_3 - 12X_4 - 6.9X_5 + 0.26X_6 - 39X_7 + 140X_8 - 519X_9 - 4.3X_{10} + 24X_{11} \leqq 73$

(15) $0.01X_1 + 0.01X_2 - 0.02X_3 - 0.03X_4 + 0.01X_5 - 0.01X_6 - 0.07X_7 - 0.17X_8 + 4.7X_9 - 0.01X_{10} + 0.08X_{11} \leqq -2.1$

(16) $0.01X_1 - 1.0X_2 + 0.05X_3 - 0.03X_4 + 0.01X_5 + 0.01X_6 + 0.59X_7 - 0.28X_8 - 20X_9 + 0.04X_{10} + 0.12X_{11} \leqq 3.4$

[a]The first 11 constraints were imposed to keep the solution within the range of variables found in the field; the next constraint is due to definition of mechanical composition of the soil; the last four constraints are biological or economical considerations.

than one species of livestock and game animals utilize a given rangeland, and it is desired to select optimum combinations of grazing animals.

As we learn more about environmental complexes and the interrelationships of their components, we will be better able to express these factors mathematically and determine whether simplifying assumptions such as linearity of the model impose serious restrictions of such operations research methods in resource management.

YEAR-TO-YEAR PREDICTION OF ^{137}Cs MOVEMENT IN THE TAGGED FOREST

J. S. Olson

The compartment modeling approach which was used previously for simulating the very rapid redistribution of ^{137}Cs during the first growing season after the tagging of the *Liriodendron* forest in May 1962[22] has been extended for predicting nuclide movement through the landscape in future years. Growing season rates of transfer are higher than year-round average rates for a complete annual cycle, and imply even higher rates of depletion from the living organisms than have been observed in four years (see Chap. 9). A second approximation model treating year-to-year transfers as discrete steps (as in the Markov chain model described above), instead of as continuous flows, implies over 90% transfer into the soil compartment in slightly over four years; details of this model are still being tested, as a prelude to modeling the annual cycles of movement by linear differential equations with variable coefficients. In the context of the Markov chain models for environmental pollution in general, this case illustrates an important class of models in which soil is almost an absorbing barrier, but nevertheless provides a small percentage of its contaminant burden for recycling through the living part of the ecosystem.

[22]J. S. Olson, *Health Phys.* 11(12), 1385–92 (1965).

Part III. Radiation Physics

G. S. Hurst

12. Theoretical Radiation Physics

Jacob Neufeld
R. H. Ritchie

V. E. Anderson[1]
J. C. Ashley
E. E. Branstetter[2]
Julian Crowell[3]
Mary Feezell[1]
Kenneth Fox[4]
W. R. Garrett[5]
R. N. Hamm
H. C. Schweinler
W. S. Snyder
J. E. Turner
R. E. Wilems[6]
C. L. Wiginton[4]
H. A. Wright

HIGH-ENERGY DOSIMETRY

The calculations of dose due to protons and neutrons with energies up to 400 Mev are being refined using a modified tissue phantom having the shape of a cylinder with an elliptical cross section. Emphasis is being placed on the dose received at various locations within the cylinder representing the position of critical organs. A study of possible buildup in dose due to nucleons crossing an interface between soft tissue and bone is being completed.

Codes for the computation of dose due to protons and neutrons with energies into the Bev region are being developed. In contrast to the calculations up to 400 Mev, simplified models are being used in this work.

GENERAL CONCEPTS IN RADIATION DOSIMETRY

It has been shown that, within the framework of the first Born approximation in quantum mechanics, the number of primary quantum transitions per rad is a function of the velocity, but not charge, of an incident charged particle when most of its lost energy is absorbed locally.[7] It is known experimentally that the remaining dependence on velocity is slight. A primary quantum transition is defined as an excitation of a target atom or molecule resulting from inelastic scattering of the incident particle. If it is assumed that the same extent of biological damage is produced in two identical systems when the number of primary quantum transitions per unit volume is the same, then it follows that the relative biological effectiveness (RBE) is approximately independent of the charge and velocity of the incident radiation. Such a result is found experimentally for targets (e.g., viruses) that are small compared with the average distance between successive primary quantum transitions.

The work of ref. 7 has been applied to more general assumptions about the relation between a primary quantum transition and biological damage. If it is assumed that the same extent of damage results when r_0 or more primary quantum transitions occur in a critical track segment, then it can be shown that RBE depends on both charge and velocity.[8] The use of collision theory shows, however, that the resulting functional dependence is not

[1]On loan from Central Data Processing Facility (ORGDP).

[2]On loan from Mathematics Division (ORNL).

[3]Oak Ridge Graduate Fellow.

[4]Consultant.

[5]Temporary assignment.

[6]U.S. AEC Health Physics Fellow.

[7]J. E. Turner and H. Hollister, *Nature* **207**, 36 (1965).

[8]J. E. Turner and H. Hollister, submitted to *Nature*.

that of linear energy transfer (LET). An experimental test to measure the possible difference between a more general charge-velocity dependence of RBE than that of LET is proposed.[8]

THE STATIC DIELECTRIC CONSTANT OF A FREE-ELECTRON GAS

The response of an electron gas to an external, linear perturbation can be codified in the frequency- and wave-vector-dependent dielectric constant, $\epsilon(\mathbf{k}, \omega)$, of the electron gas.[9,10] The dielectric constant is obtainable from the irreducible part, $Q(\mathbf{k}, \omega)$, of the particle-hole pair propagator,[11,12] that is,

$$\epsilon(\mathbf{k}, \omega) = 1 - V(\mathbf{k})\, Q(\mathbf{k}, \omega) ,$$

where $V(\mathbf{k})$ is the Fourier transform of the Coulomb potential: $Q(\mathbf{k}, \omega)$ is calculated by summing the contributions from all the Feynman graphs in Fig. 12.1.

In the simplest approximation to $\epsilon(\mathbf{k}, \omega)$, that is, in the random phase approximation[9] (RPA), one ignores all graphs in Fig. 12.1 except the first one; it represents the excitation and subsequent de-excitation of a particle-hole pair. This approximation works very well at high electron densities, but at low electron densities it "underscreens," that is, it predicts too long a screening length. One can correct for this underscreening by replacing the first graph in Fig. 12.1 by the infinite series consisting of graphs 1, 2, 5, etc., that is, by taking account of repeated (ladder) scatterings between the hole-electron pair. In this approximation the static pair propagator $Q(\mathbf{k}) = Q(\mathbf{k}, 0)$ is given by

$$Q_{LAD}(\mathbf{k}) = \frac{-i\hbar}{\Omega} \sum_{\mathbf{p},\sigma} \int \frac{d\omega_1}{2\pi}\, G_0(\mathbf{p} - \mathbf{k}, \omega_1)\, G_0(\mathbf{p}, \omega_1)$$

$$\times \left[1 + \frac{i\hbar}{\Omega} \sum_{\mathbf{p}'} \mathcal{V}_{RPA}(|\mathbf{p}' - \mathbf{p}|) \right.$$

$$\left. \times \int \frac{d\omega_2}{2\pi}\, G_0(\mathbf{p}' - \mathbf{k}, \omega_2)\, G_0(\mathbf{p}', \omega_2) + \cdots \right] ,$$

where $\mathcal{V}_{RPA}(|\mathbf{p}' - \mathbf{p}|)$ is the static RPA potential and $G_0(\mathbf{p}' - \mathbf{k}, \omega_1)$ is a single-particle Green function.

A Monte Carlo procedure has been used to calculate $Q_{LAD}(\mathbf{k})$ and the effective potential

$$\mathcal{V}_{LAD}(zk_F) = \frac{4\pi e^2}{(zk_F)^2\, \epsilon_{LAD}(zk_F)} ,$$

where

$$z = k/k_f$$

$$\epsilon_{LAD}(zk_f) = 1 - V(zk_F)\, Q_{LAD}(zk_f).$$

The results of these calculations for $r_s = 3$ are shown in Fig. 12.2 (r_s is the interelectron spacing in units of the Bohr radius). For the sake of comparison, the RPA potential and an analytic approximation to $\mathcal{V}_{LAD}(zk_F)$ suggested by Hubbard[10] are also shown. The present work represents a

ORNL-DWG 65-13503R

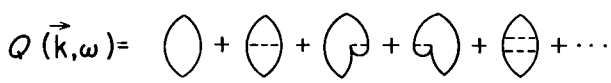

Fig. 12.1. Diagrammatic Representation of the Irreducible Polarization Propagator.

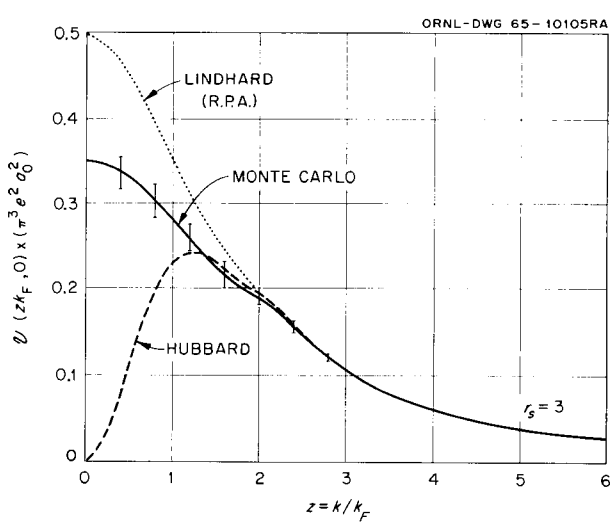

Fig. 12.2. Comparison of the Random Phase Approximation (Lindhard), Hubbard, and Improved Dielectric Constants for $r_s = 3$.

[9] J. Lindhard, *Kgl. Danske Videnskab. Selskab, Mat.-Fys. Medd.* **28**, 8 (1954).

[10] J. Hubbard, *Proc. Roy. Soc. (London)* **A243**, 336 (1958).

[11] D. F. DuBois, *Ann. Phys. (N.Y.)* **7**, 174 (1959).

[12] A. J. Glick, *Phys. Rev.* **129**, 1399 (1963).

substantial improvement in $\mathcal{V}(zk_F)$ in the region $k \lesssim 2k_F$.

To a good approximation, the results of the Monte Carlo calculations may be expressed by the following analytic approximation to the pair propagator:

$$Q_{LAD}(\mathbf{k}) = Q_{RPA}(\mathbf{k}) \Big/ \left[1 + \frac{2\pi e^2}{k^2 + \xi k_F^2} Q_{RPA}(\mathbf{k}) \right],$$

where $\xi = 1.5 + 0.6\, r_s$.

THE SCREENING CONSTANT OF AN ELECTRON GAS

The results from the preceding section ("The Static Dielectric Constant of a Free-Electron Gas") have been used to calculate the screening constant of an electron gas. The screening constant is given by

$$C = \lim_{z \to 0} z^2 \left[\epsilon_{LAD}(zk_F) - 1 \right],$$

where z is the wave number in units of the Fermi wave number.

In Fig. 12.3 the screening constant is plotted in units of the Fermi-Thomas screening constant.[13] For comparison a screening constant based on the work of DuBois[14] is also shown; it includes, to first order in r_s, the contributions from the first four diagrams in Fig. 12.1.

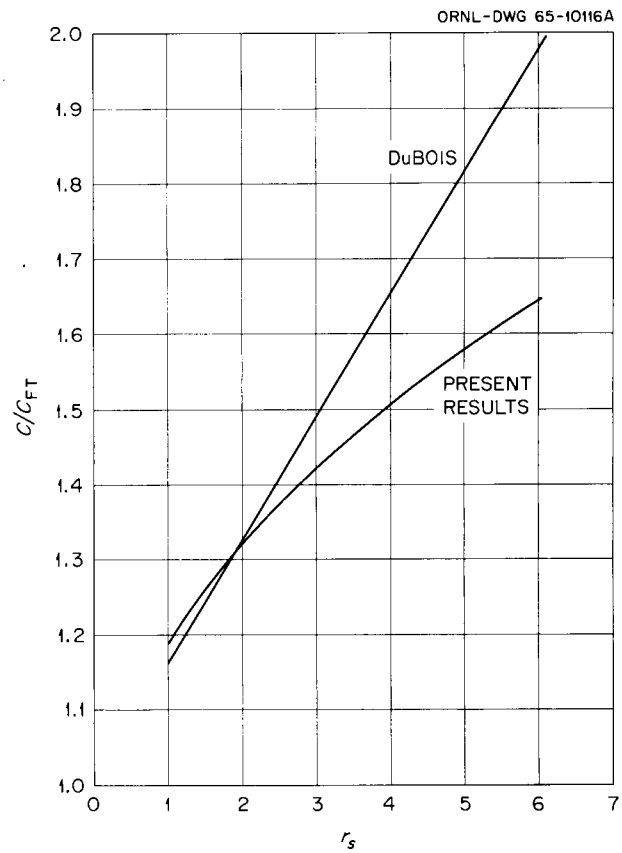

Fig. 12.3. The Screening Constant of an Electron Gas in Units of the Fermi-Thomas Screening Constant.

POSITRON ANNIHILATION IN METALS

First-order perturbation theory calculations[15] of the two-photon annihilation rate of positrons in an electron gas do not agree with experimental results[16] on annihilation in free-electron-like metals except in the case of aluminum. Kahana[17] has made use of the Bethe-Goldstone[18] equation for a positron-electron pair in an electron gas to obtain annihilation rates in the range $r_s \leqq 4$. In his work he used the static RPA dielectric constant to describe the response of the electron gas to the positron, and he approximated the effect of plasma oscillations on the annihilation rate.

In order to extend the annihilation rate calculations to lower densities (higher r_s), a high-order perturbation calculation has been made in which the improved, screened Coulomb potential described in "The Static Dielectric Constant of a Free-Electron Gas" has been used.

It has been assumed that the most important contributions to the annihilation amplitude come from those Feynman graphs in which the positron excites an electron out of the Fermi sea and interacts repeatedly with it outside of the sea before annihilating with it. Thus one ignores graphs, for example, in which the positron scatters with the

[13] D. Pines, *Elementary Excitations in Solids*, p. 97, W. A. Benjamin, Inc., New York, 1963.

[14] D. F. DuBois, *Ann. Phys. (N.Y.)* **8**, 24 (1959).

[15] R. A. Ferrell, *Rev. Mod. Phys.* **28**, 308 (1956).

[16] R. E. Bell and M. H. Jørgensen, *Can. J. Phys.* **38**, 652 (1960).

[17] S. Kahana, *Phys. Rev.* **129**, 1622 (1963).

[18] H. A. Bethe and J. Goldstone, *Proc. Roy. Soc. (London)* **A238**, 551 (1957).

hole vacated by the excited electron. This procedure has been justified for second-order exchange graphs; their contribution to the annihilation amplitude is negligible. To this approximation, the S-matrix element for the annihilation of a zero-momentum positron with an electron of wave vector $\mathbf{p}$ is given by

$$\left\langle f|S|i\right\rangle = \left\langle f|S^0|i\right\rangle \left[1 + \frac{1}{(2\pi)^3\hbar} \times \int_{k>K_F} \frac{d^3k\, \mathcal{V}(|\mathbf{k}-\mathbf{p}|\, H(\mathbf{k})}{\omega(\mathbf{k}) + \omega(\mathbf{k}-\mathbf{p}) - \omega(\mathbf{p})}\right],$$

where

$$H(\mathbf{k}) = 1 + \frac{1}{(2\pi)^3\hbar} \times \int_{k'>K_F} \frac{d^3k'\, \mathcal{V}(|\mathbf{k}'-\mathbf{k}|)\, H(\mathbf{k}')}{\omega(\mathbf{k}') + \omega(\mathbf{k}'-\mathbf{p}) - \omega(\mathbf{p})},$$

$\langle f|S^0|i\rangle$ is the annihilation amplitude for a noninteracting (Sommerfeld) free-electron gas, $\mathcal{V}(k)$ is the static, screened Coulomb potential, and $\omega(\mathbf{k}) = \hbar k^2/2m$.

The Neumann series solution of the above integral equation has been calculated by Monte Carlo methods, and the resulting annihilation rates are shown in Fig. 12.4. Three different effective potentials $\mathcal{V}(k)$ have been used: the improved potential discussed in the section on "The Static Dielectric Constant of a Free-Electron Gas," the RPA potential, and the Hubbard[10] potential. Also shown in Fig. 12.4 are the experimental results of Bell and Jørgensen[16] and the calculated results of Kahana.[17] It is seen that the Monte Carlo results are in fair agreement with Kahana's results for $r_s \leq 4$ and with experimental results for $r_s \lesssim 5$.

The upturn in the theoretical annihilation curves in the neighborhood of $r_s \approx 6$ may be real or may be due to statistical errors in the calculation. At low electron densities the probability of positronium formation increases, and more terms are required for convergence of the perturbation series. This in turn leads to a magnification of statistical fluctuations in the Monte Carlo process. Approximate calculations indicate that a bound state does exist for r_s just greater than 6 in the RPA and Hubbard electron gases. So it may well be that the upturn is evidence for an incipient bound state.

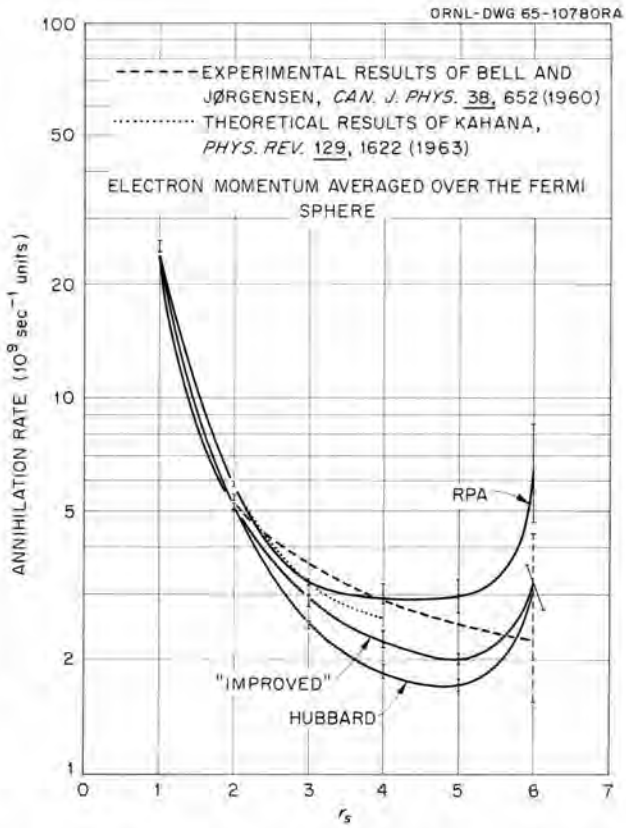

Fig. 12.4. High-Order Perturbation Calculations of the Annihilation Rate Using the RPA Interaction, the Hubbard Interaction, and an Improved "Ladder" Interaction.

POSITRON EFFECTIVE MASS IN A FREE-ELECTRON GAS

Experiments have indicated that the effective mass of a positron in sodium is about twice the electron mass.[19] The contribution to the positron effective mass due to the interaction of the positron with a free-electron gas (as formed approximately by the electrons in the conduction band of sodium) has been calculated using methods from many-body perturbation theory.

The calculation starts from the expression for the change in self-energy of the positron due to interaction with the medium:

$$\Delta E = \frac{4\pi i e^2}{(2\pi)^4} \int d\mathbf{k} \int d\omega \frac{1}{k^2} \left[\frac{1}{\epsilon(\mathbf{k},\omega)} - 1\right] \frac{1}{\omega - \omega_0 + i\delta},$$

[19] A. T. Stewart and J. B. Shand, *Bull. Am. Phys. Soc.* 10, 21 (1965); *Phys. Rev. Letters* 16, 261 (1966).

where $\epsilon(\mathbf{k},\omega)$ describes the properties of the free-electron gas,

$$\omega_0 \equiv \frac{\hbar}{m}\mathbf{k}_0 \cdot \mathbf{k} - \frac{\hbar^2 k^2}{2m},$$

with m and $\mathbf{k}_0$ the positron mass and wave vector, respectively, and $\delta \to +0$. The ω integration can readily be done if for the dielectric function $\epsilon(k, i\omega)$ we use the "quadratic approximation" discussed by Geldart *et al.*[20] If we consider thermalized positrons so that $\eta = v_0/v_F$, the ratio of the positron velocity to the Fermi velocity, is small compared to 1, we can expand ΔE in powers of η retaining only terms through η^2. Defining the fractional change of mass of the positron through

$$\Delta m/m_e = \frac{[\Delta E(\eta) - \Delta E(0)]}{m_e v_0^2/2},$$

m_e the electron mass, we find

$$\frac{\Delta m}{m_e} = -4X^4 \int_0^\infty dZ \frac{[Z R(Z)]^2}{[Z^2 + X^2 R(Z)]^{1/2}\{[Z^2 + X^2 R(Z)]^{1/2} + [3R(Z)]^{1/2} Z^2\}^3},$$

where $X^2 = e^2/\pi\hbar v_F$ and

$$R(Z) = \frac{1}{2}\left[1 + \frac{1 - Z^2}{2Z} \ln\left|\frac{1+Z}{1-Z}\right|\right].$$

Computer evaluation of this integral yields $\Delta m/m_e = -0.107$ or a positron effective mass $m = 0.893 m_e$, a value about 10% less than the electron mass for a free-electron gas corresponding to the sodium conduction band. These results indicate that the positron effective mass cannot be accounted for entirely by this many-body density polarization effect.

ELECTRON MEAN FREE PATHS IN A FREE-ELECTRON GAS

A theoretical expression giving the scattering of an excited electron in a free-electron gas has been derived. It is assumed that the electron has a sufficiently low energy so that only a static interaction between it and any electron in the Fermi sea need be considered. The interaction energy is given by summing terms corresponding to a series of ladder-type scatterings of the excited electron on electrons ejected from the Fermi sphere, taking the exclusion principle into account. The equation for the wave function of the pair of electrons, corresponding to scattering on a potential $v(r)$, is given by

$$\left\{-\frac{\hbar^2}{m}(\nabla^2 + k_0^2) + v(r)\right\} \Psi_{\mathbf{p},\mathbf{k}_0}(\mathbf{r}) = \int d\mathbf{r}'\, v(\mathbf{r}')\, \Psi_{\mathbf{p},\mathbf{k}_0}(\mathbf{r})\, g(\mathbf{r}, \mathbf{r}', \mathbf{p}),$$

where the integral term on the right corrects for the exclusion principle and where $\mathbf{k}_0$ is the relative momentum and $\mathbf{p}$ the center of mass momentum of the particles. In the special case $\mathbf{p} = 0$, g is a function only of the magnitude of $\mathbf{r} - \mathbf{r}'$ and the equation may be analyzed into partial waves. The equation for the s-wave state is

$$\left\{\frac{d^2}{ds^2} + K_0^2 - \omega(s)\right\} U(s) = -\frac{1}{\pi}\int_0^\infty ds'\, \omega(s')\, U(s') \left[\frac{\sin|s - s'|}{|s - s'|} - \frac{\sin(s + s')}{s + s'}\right]$$

in terms of the dimensionless variable $s = k_F r$, and where $\omega(s) = v(s)/2E_F$ and $K_0 = k_0/k_F$. The integral on the right again contains the exclusion principle correction. A numerical solution of this equation is being calculated using an iterative method. The scattering cross section σ is given, in terms of the phase shifts δ thus calculated, in the standard manner:

$$\sigma = \frac{4\pi}{K_0^2}\sin^2\delta.$$

THE PENETRATION OF LOW-ENERGY ELECTRONS IN CONDENSED MATTER

Our theoretical understanding of the various modes of energy loss by low-energy electrons (0 to

[20] D. J. W. Geldart, A. Houghton, and S. H. Vosko, *Can. J. Phys.* 42, 1938 (1964).

10 kev) in matter is only semiquantitative at present. However, recent advances in experimental technique have made it possible to measure with some precision the number of electrons penetrating to a given depth in a solid bombarded by a beam of monoenergetic low-energy electrons. It is of interest to carry out a parallel Monte Carlo analysis of the penetration process in order to assess the accuracy of existing theoretical cross sections. A code written along these lines is currently being tested and compared with the experiments of Nakai and Birkhoff. Cross sections for electrons interacting with electrons and ions in aluminum metal have been estimated using simple theoretical models for volume and surface plasmon excitation, single electron excitation, etc. These interactions may give rise to large numbers of secondary, tertiary, etc., electrons, each of which has similar possibilities for interaction in the foil. Preliminary results on the attenuation of 0- to 100-ev electrons in foils of a few hundred angstroms in thickness compare favorably with experimental results.

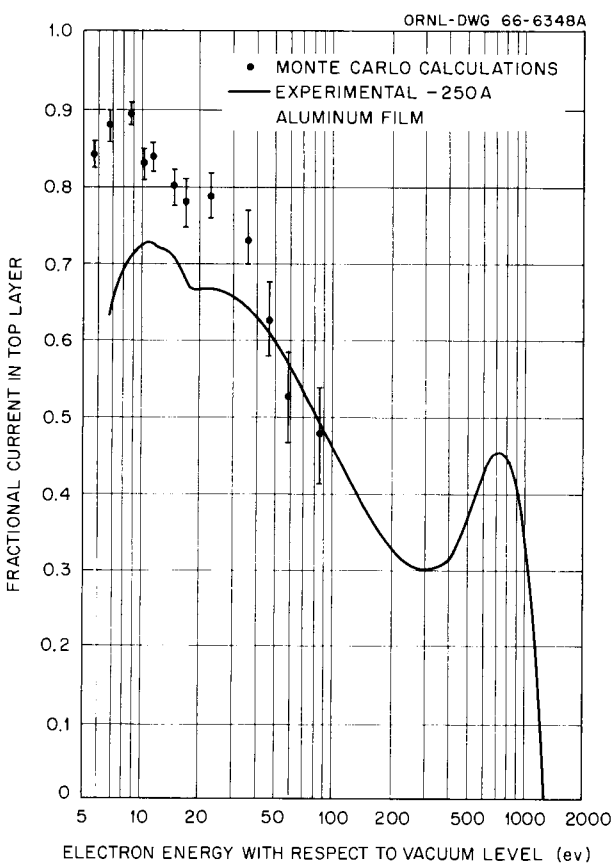

Fig. 12.5. Comparison of Experiment and Monte Carlo Calculations of Electron Penetration in a Thin Aluminum Foil.

Figure 12.5 compares experiment with the results of a calculation of the fractional number of electrons absorbed in an Al foil of 250 A thickness as a function of the energy of electrons incident normally upon the foil. A barrier potential of 2 ev at the exit side of the foil has been assumed. The Monte Carlo results are shown as points with associated probable error, while the experimental data are shown as a smooth curve. Calculations are being extended to higher energies.

COUPLED ELECTRON-HOLE CASCADE IN A FREE-ELECTRON GAS

The coupled electron-hole cascade in an electron gas may be described by a space- and angle-independent transport equation. Analytic cross sections employed for the various processes are appropriate to a high-density electron gas and for low to moderate excitation energies. An analytic solution of the integral transport equation has been found. It has been shown that the flux of both electrons and holes diverges as the inverse fourth power of the difference between the energy and the Fermi energy. An account of this work will be published elsewhere.

PHOTOELECTRIC EMISSION FROM THIN FOILS

A study of the surface photoelectron yield from an idealized thin metal foil has been made, using both classical and quantum mechanical analyses. It has been shown that the photo yield should exhibit a maximum at the volume plasma frequency if the incident light has a component of polarization normal to the foil surface. It is also predicted that the yield should be a periodic function of the foil thickness. The surface photoelectric yield effect is treated as the inverse of the transition radiation phenomenon. An account of this work will be submitted for publication soon.

THE EXCITATION OF SURFACE PLASMONS BY PHOTONS

The interaction of electromagnetic fields with collective electronic motion in metals has been studied experimentally using thin foils. A strong

coupling[21] occurs at the volume plasma frequency ω_p of the metal when photons are incident nonnormally on a foil thin compared with the photon. Absorption of photons due to such collective interactions at the surface has been measured experimentally.[22,23]

Absorption of photons due to electronic interactions involving the excitation of "one-surface" surface plasmons at the frequency $\omega_p/\sqrt{2}$ has been determined theoretically using second-order perturbation theory. Such absorption should occur for thick foils and for arbitrary angles of photon incidence. The absorption probability is predicted to rise linearly above the threshold frequency $\omega_p/\sqrt{2}$ and in the neighborhood of the threshold should be given approximately by

$$A_s = \frac{9\pi\sqrt{2}}{32}\frac{e^2}{\hbar c}\frac{\hbar(\omega - \omega_p/\sqrt{2})}{E_F},$$

where A_s is the probability of absorption per photon incident on the surface and E_F is the Fermi energy of the metal. Although this effect is small, it may be detectable in a very careful experimental investigation.

A brief account of this work has been published.[24]

DOUBLE PLASMON EXCITATION BY CHARGED PARTICLES

The second-order process in which an incident charged particle excites two plasmons in an electron plasma may be important in the interpretation of certain characteristic energy loss experiments. Employing the concept of the dielectric response function, second-order perturbation theory has been used to find the probability for the transition from an initial state containing a particle of momentum p_0 and no plasmons to a final state in which two plasmons and a particle of momentum p_f are present. This transition probability summed over the possible final states is used to calculate a mean free path for the double plasmon excitation process.

---

[21] R. A. Ferrell and E. A. Stern, *Am. J. Phys.* **30**, 810 (1962).

[22] A. H. McAlister and E. A. Stern, *Phys. Rev.* **132**, 1599 (1963).

[23] R. H. Huebner *et al.*, *J. Opt. Soc. Am.* **54**, 1434 (1964).

[24] R. H. Ritchie, *Surface Sci.* **3**, 497 (1965).

13. Atomic and Molecular Radiation Physics

G. S. Hurst

R. P. Blaunstein[1]
T. E. Bortner[2]
Ada E. Carter
L. G. Christophorou[2]
R. N. Compton
J. T. Cox
F. J. Davis
H. W. Dickson[3]
Kenneth Fox[2]
W. R. Garrett[4]
J. A. Harter
R. H. Huebner[1]
W. G. Hendrick[3]
A. G. Kenerly[5]
C. E. Klots
D. R. Nelson[6]
Devon Pittman
P. W. Reinhardt
R. H. Ritchie
H. C. Schweinler
J. E. Turner
E. B. Wagner
R. E. Wilems[7]

ALPHA-PARTICLE IONIZATION OF BINARY GAS MIXTURES

It has been recognized for some time that measurements of W (average energy per ion pair) in irradiated binary mixtures display a remarkable degree of empirical regularity. Thus, using the transformation $G_{\text{ions}} = 100/W$, ion yields from molecular gas mixtures can almost invariably be expressed in the form[8]

$$G_{ij} = G_i^0\left(\frac{P_i a}{P_i a + P_j}\right) + G_j^0\left(\frac{P_j}{P_i a + P_j}\right), \qquad (1)$$

where P_i and P_j are the partial pressures of the two components and a is an empirical parameter unique to each binary combination. An experimental survey of the a parameters in a large number of mixtures has supported the suggestion[9] that each such parameter is composed of two molecular coefficients in the sense

$$a = Z_i'/Z_j' . \qquad (2)$$

The several Z_i' may then be interpreted as weighting coefficients for each molecular species, dictating the partitioning of the radiation dose among the components of a given mixture. A scale of such coefficients for a number of molecular species has been established in this way.[10]

An extension of this work to mixtures containing at least one inert gas reveals that Eq. (1) is, with rare exceptions, inadequate to describe the observed ion yields. Figure 13.1 displays the measured ion yields from helium-methane mixtures; the observed behavior will clearly not yield to the simple one-parameter form of Eq. (1).

The mechanism which has been contrived to rationalize these results is based on the supposition that in pure helium, for example, part of the ion yield arises from the Hornbeck-Molnar process:

$$He^* + He \rightarrow He_2^+ + e . \qquad (3)$$

In the presence of a molecular additive this may be, in part, quenched:

$$He^* + CH_4 \rightarrow \text{neutral products} . \qquad (4)$$

A kinetic analysis of this scheme indicates that two additional parameters may then be necessary to describe the observed yields. A least-squares computer analysis has thus been used to extract,

[1]Radiological Health Physics Fellow.

[2]Consultant.

[3]U.S. AEC Health Physics Fellow.

[4]Temporary assignment.

[5]On loan from Instrumentation and Controls Division.

[6]U.S. AEC Advanced Health Physics Fellow.

[7]Oak Ridge Graduate Fellow.

[8]T. E. Bortner and G. S. Hurst, *Phys. Rev.* **93**, 1236 (1954).

[9]C. E. Klots, *J. Chem. Phys.* **39**, 1571 (1963).

[10]C. E. Klots, *J. Chem. Phys.* **44**, 2715 (1966).

for a number of rare-gas mixtures, the parameters relevant to the above quenching mechanism as well as the underlying Z_i' coefficients. These latter coefficients are of especial interest and are given in Table 13.1. They are normalized, as previously,[10] by arbitrarily assigning CH_4 the value 10.0. With these parameters it should now be possible to assess quantitatively the initial partitioning of energy in mixtures containing a rare gas and thus the extent of subsequent sensitization and energy transfer processes.

Table 13.1. Energy Partition Coefficients for the Inert Gases

Gas	Z_i'
(Methane	10.0)
Helium	2.25
Neon	4.6
Argon	6.5
Krypton	9.8
Xenon	14.9

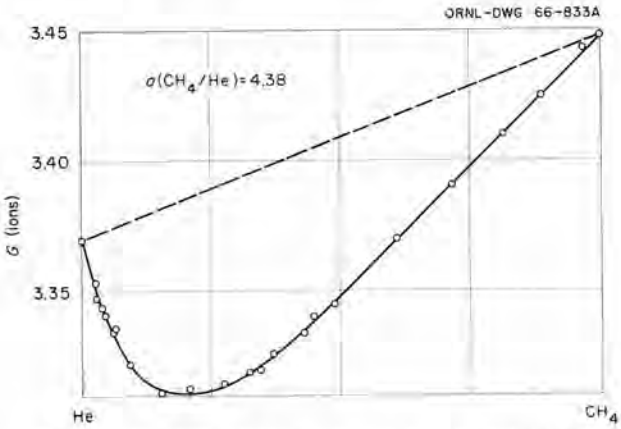

Fig. 13.1. Ion Yields from Alpha-Irradiated Helium-Methane Mixtures.

ELECTRON IMPACT EXCITATION OF ATOMS AND MOLECULES USING A LOW-ENERGY ELECTRON SCAVENGER TECHNIQUE

Electron impact excitation of atoms and molecules has been studied by many investigators and with almost as many different methods. A technique has been developed which is different from previous studies in that only electrons which have lost essentially all their energy upon collision are detected. The resulting energy loss spectrum might appropriately be called a "threshold" excitation spectrum. The technique utilizes a strong resonance capture process at approximately zero energy[11] to scavenge electrons which have suffered inelastic collisions with a sample gas present with the sulfur hexafluoride (SF_6) in a mass spectrometer.

The fact that SF_6^- ions can be formed by inelastically scattered electrons from atoms or molecules was demonstrated by Curran.[12] We have extended this idea to study excitation processes. The technique has been shown to be a valuable tool in studying the true shapes of electronic states, position of triplet states, and "threshold" excitation in general.

Figure 13.2 shows the "threshold" excitation spectrum of helium. The ratio of the 2^3S excitation probability to the 2^1S probability was found to be larger than that previously observed.[13] From the data in Fig. 13.2 it was concluded that the slope of the 2^3S excitation was approximately 1.5 times larger than the slope of the 2^1S excitation function over the energy range from 0 to ~0.03 ev.

The "threshold" excitation spectrum of N_2 is presented in Fig. 13.3. All the peaks were in good agreement with previously determined electronic states of the N_2 molecule with the exception of the peak between 13 and 14 ev. Excitation spectra of hydrogen and water vapor using the SF_6 scavenger technique were also in good agreement with previous investigations. In the case of water a broad, inelastic loss process extending from ~4 to ~6 ev was detected, in agreement with Schulz.[13] The process is believed to be the first triplet state of the water molecule.

The threshold excitation technique will be applied to the study of triplet states in organic molecules. As an example, the threshold excitation spectra of diacetyl [$(CH_3CO)_2$] and glyoxal [$(CHO)_2$] have been studied. Figure 13.4 shows the threshold excitation spectra in which diacetyl and glyoxal were used as "self-detectors" of low-energy electrons. (Diacetyl and glyoxal capture low-energy electrons in a manner similar to SF_6.) The SF_6^- ion current exhibited the same energy dependence. For diacetyl the first triplet state is clearly resolved, and a second triplet

[11] W. M. Hickam and R. E. Fox, *J. Chem. Phys.* 25, 642 (1956).

[12] R. K. Curran, *J. Chem. Phys.* 38, 780 (1963).

[13] G. J. Schulz, *Phys. Rev.* 112, 150 (1958).

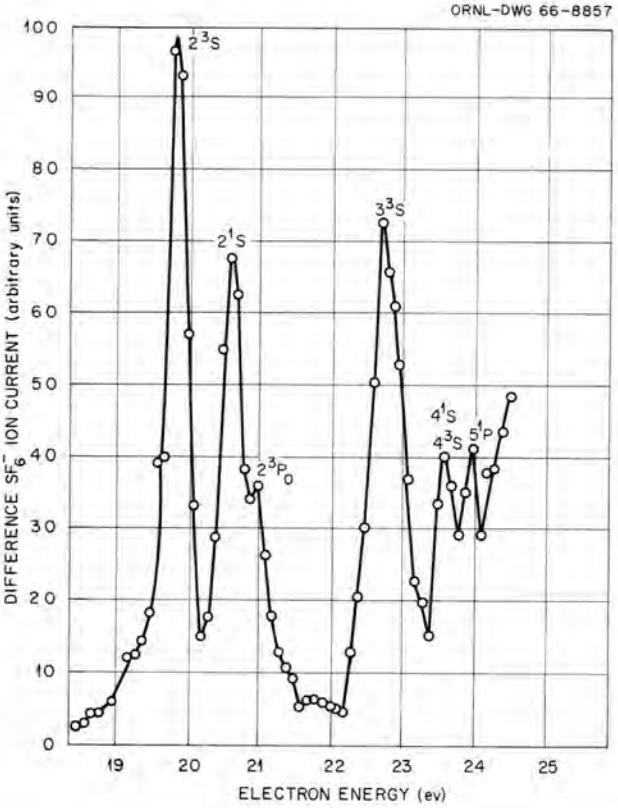

Fig. 13.2. Electron Energy Loss Spectrum of Helium Using SF_6 as a Zero Energy Electron Detector. Threshold excitation spectrum.

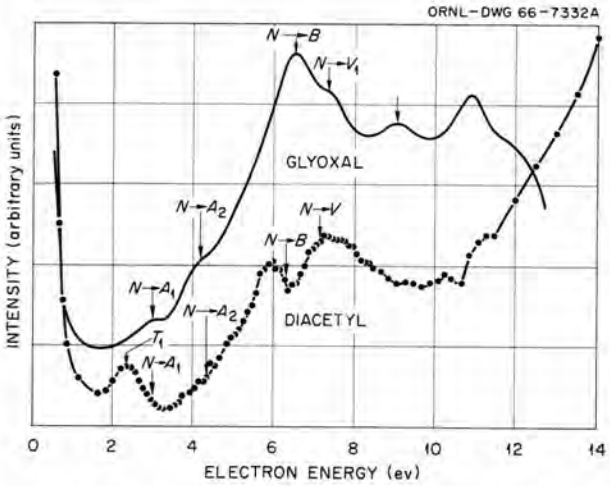

Fig. 13.4. Threshold Excitation Spectrum of Diacetyl and Glyoxal.

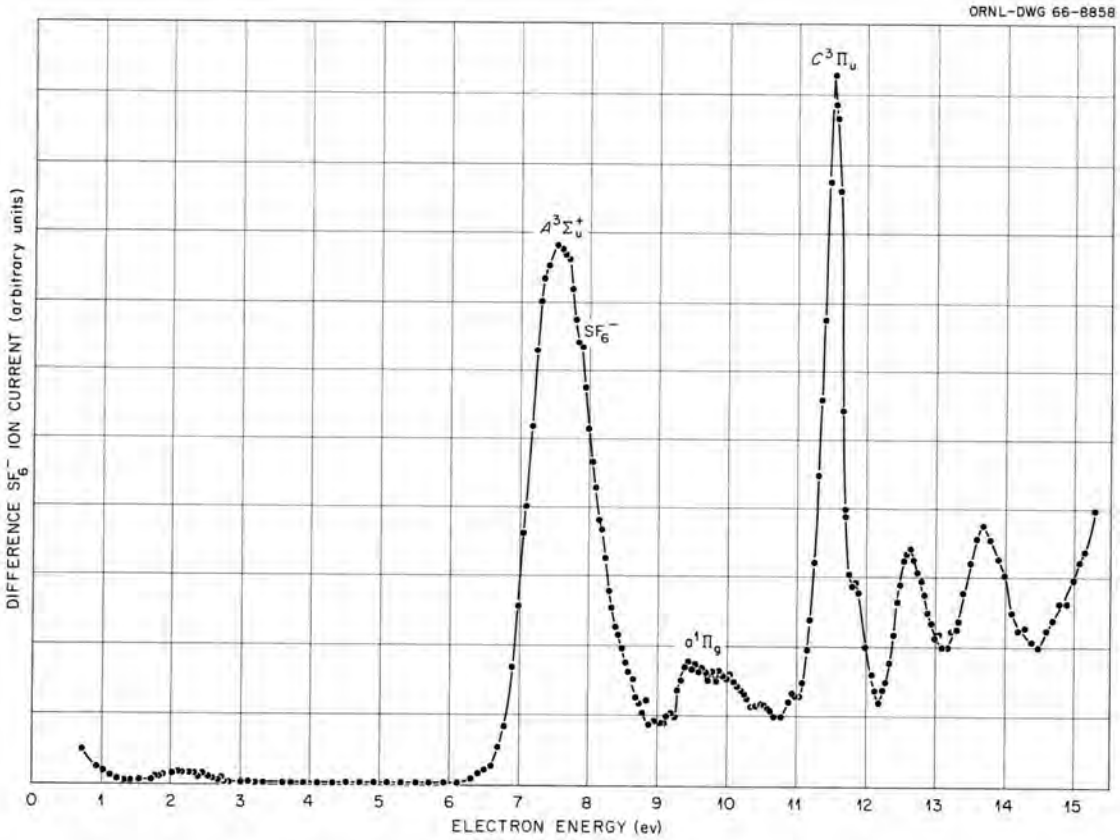

Fig. 13.3. Threshold Excitation Spectrum of Nitrogen.

state might explain the peak at ~6 ev. The vertical lines indicate the position of optical absorption bands which have been reported previously. The strong absorption at ~7 ev, responsible for the color of diacetyl, agrees well with the largest peak in the electron impact spectrum at ~7 ev.

The data presented in Fig. 13.2 to 13.4 were obtained from a tedious point-by-point plot employing the retarding potential difference technique for producing a monoenergetic electron beam. An apparatus is presently being developed which will automate the data-obtaining procedure as well as incorporate single-particle counting techniques to achieve greater sensitivity.

FINITE-MEDIUM EFFECTS IN IRRADIATED GASES

Radiation chemistry studies in gases are currently yielding a great deal of information concerning the nature and reactivity of the intermediates involved. Interesting variations in the observed chemical yields with changes in radiation parameters (e.g., the dose rate) have been plausibly attributed to a shift in the site of ion neutralization from the bulk volume to the wall (at, e.g., low dose rates).[14] Computer calculations have thus been undertaken to predict the extent of wall neutralization as a function of relevant parameters (dose rate, vessel size, diffusion coefficients, etc.). The results have been cast in terms of a single dimensionless parameter and include corrections for space-charge effects. The asymptotic behavior in the limit of negligible volume neutralization, as inferred from an analytic treatment appropriate to this limit, is reproduced by the calculations.

Comparison with experiment confirms qualitatively the earlier interpretations but suggests an uncontrolled role of thermal convection currents in much of the experimental work.

TIME-OF-FLIGHT DETERMINATIONS OF ELECTRON DIFFUSION COEFFICIENTS AND ELECTRON DRIFT VELOCITIES IN ETHYLENE, WATER VAPOR, AND HYDROGEN

The time-of-flight method for the determination of electron diffusion coefficients D and drift velocities w of electrons in gases has been improved in two essential ways. First, an accurate method has been developed for measuring all fluctuations in the time-of-flight distribution except those due to the diffusion process itself. Second, a data analysis procedure has been worked out in which the effects of instrumental fluctuations are removed and accurate values of the parameters D and w are found from a generalized least-squares procedure making use of a digital computer. Distortions in the electron time-of-flight distributions arising out of electron losses during detector dead times were calculated by assuming that single electron detection follows Poisson statistics. This assumption was examined experimentally and was not found to be in error. The improved method has been applied to ethylene, ethylene–water-vapor mixtures, and hydrogen over the range of E/P from 0.01 to 1.0 v cm^{-1} torr^{-1}. Independent measurements of the quantities D and w were made; the D/w ratios were compared with theory in the region of thermal electron energies. The ratio of the momentum transfer cross sections for H_2O compared with ethylene was essentially the same whether use was made of $D(E/P)$ or $w(E/P)$ data in the region of thermal energies. In the cases of ethylene and ethylene–water-vapor mixtures, it was found that the value of D/w for thermal electrons was 12% higher than the theoretical value.

The following numerical values were obtained:

The measured drift velocity in pure ethylene is essentially a linear function of E/P when $E/P \leqq 0.10$ v cm^{-1} torr^{-1} and has the value w_E (cm/sec) $= 9.50 \times 10^6\ E/P$.

For $E/P \leqq 0.10$ v cm^{-1} torr^{-1} and for $f_1P/(f_1P + f_2P) \leqq 0.04$, the measured drift velocity in ethylene–water-vapor mixtures is given by

$$w_m = w_E \left(1 + 133\ \frac{f_1P}{f_1P + f_2P}\right)^{-1},$$

where f_1P and f_2P are the partial pressures of water vapor and ethylene respectively.

The measured diffusion coefficient for thermal electrons in ethylene is 2.9×10^5 cm^2/sec when normalized at a pressure of 1 torr.

For $E/P \leqq 0.10$ v cm^{-1} torr^{-1} and for $f_1P/(f_1P + f_2P) \leqq 0.04$, the measured diffusion coefficient for a mixture of ethylene and water vapor is given by

$$D_m = 2.9 \times 10^5 \left(1 + 133\ \frac{f_1P}{f_1P + f_2P}\right)^{-1} \text{cm}^2/\text{sec},$$

[14] T. W. Woodward and R. A. Back, *Can. J. Chem.* 41, 1463 (1963).

where f_1P and f_2P are the partial pressures of water vapor and ethylene, respectively, when normalized to a total pressure of 1 torr.

The measured diffusion coefficient for thermal electrons in hydrogen is 1.1×10^5 cm^2/sec when normalized at a pressure of 1 torr.

EFFECTS OF EXPERIMENTAL BOUNDARIES ON THE MEASUREMENT OF DIFFUSION COEFFICIENTS AND DRIFT VELOCITIES IN SWARM METHODS

Further refinements for the measurement of diffusion coefficient D and drift velocity w from electron time-of-flight swarm experiments are being investigated. The effects of counting losses due to counter dead time and of fluctuation of photoelectron production on the measured D and w values have previously been discussed.[15]

Measurements of D and w are currently made by fitting the solution of the one-dimensional transport equation to the experimental data with the proper inclusion of the error function through an unfolding procedure. This solution is that obtained for an infinite space where boundaries are ignored. The solution is

$$n(xt) = \frac{N_0}{\sqrt{4\pi Dt}} e^{-(x - wt)^2/4Dt} .$$

We report here preliminary results where the two physical boundaries, photocathode and collecting anode, are considered. When only the photocathode boundary is considered for zero reflection ($\beta = 0$), back diffusion of photoelectrons to the photocathode results in only a small fraction escaping this process to permanently enter the drifting and diffusing electron swarm. Typical values of the fraction of electrons escaping back diffusion in ethylene range from 9.3 to 35.7% for E/P values from 0.02 to 0.1. It is found that the D and w values measured from the distribution of electrons escaping back diffusion are not significantly different from the infinite space, no boundary, solution.

When one similarly treats the transport problem with the collector anode boundary, larger errors in D and w are found than for the photocathode boundary, but these errors are still very small. The errors found when one assumes zero reflection at the anode boundary ($\beta = 0$) and the kinetic theory mean-free-path formula ($\bar{\ell} = 3D/\bar{v}$) are only 0.13% for D and 0.10% for w for the worst case of $E/P = 0.02$.

When one increases the initial mean-free-path distribution of photoelectrons and also allows for reflection of electrons at the boundary, then the electron distribution changes so as to further increase the errors in D and w measurements. For example, if the initial mean free path is increased by a factor of 5 [$\bar{\ell} = 5(3D/\bar{v})$] and the reflection coefficient (β) is set equal to 0.3, then one finds 0.24% error in D and 0.12% error in w for, once again, the worst case of $E/P = 0.02$. Therefore, we conclude from these preliminary considerations of physical boundary conditions that appreciable fractions of the photoelectrons are lost to the photocathode due to back diffusion, but the errors in the measured D and w values may be neglected for those experiments currently in progress.

ELECTRON TIME-OF-FLIGHT STUDIES USING ELECTRON MULTIPLIER TECHNIQUES

The measurements of electron diffusion in gases by the electron time-of-flight method[16] still show an unexplained discrepancy with measurements made by the Townsend-Huxley method. The values of the ratio of diffusion constant to mobility (D/μ) reported earlier[17] showed reasonable agreement with other experimenters for the polyatomic gases CO_2 and C_2H_4 but for N_2 and H_2 showed values which were lower by 40% than those obtained by the Townsend-Huxley method. The measurements for CH_4, helium, and argon are shown in Figs. 13.5 to 13.7. We show agreement with others for CH_4, but helium and especially argon are much lower. A few measurements made on neon showed D/μ values to be 60% lower than values obtained by the Townsend-Huxley method. The discrepancy seems to become more pronounced in accordance with the width of the electron time-of-flight distribution, which is associated with high agitation energy and low energy loss per collision. The values of D/μ for low E/P approach the value of 0.025 v required by the Einstein relation in all gases where data could be obtained.

[15] G. S. Hurst *et al.*, *Health Phys. Div. Ann. Progr. Rept. July 31, 1965*, ORNL-3849, p. 110.

[16] G. S. Hurst *et al.*, *J. Chem. Phys.* **39**, 1341 (1963).

[17] G. S. Hurst *et al.*, *Health Phys. Div. Ann. Progr. Rept. July 31, 1965*, ORNL-3849, p. 112.

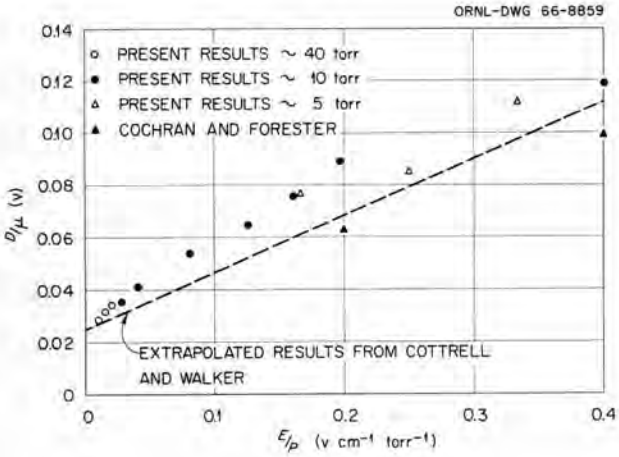

Fig. 13.5. Ratio D/μ as a Function of E/P in Methane. Data from L. W. Cochran and D. W. Forester, *Phys. Rev.* **126**, 1785 (1962), and T. L. Cottrell and I. C. Walker, *Trans. Faraday Soc.* **61**, 1591 (1965).

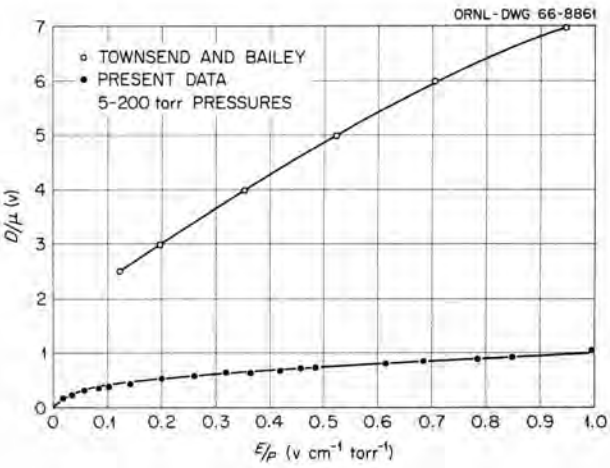

Fig. 13.7. Ratio D/μ as a Function of E/P in Argon. Data from J. S. Townsend and V. A. Bailey, *Phil. Mag.* **44**, 1033 (1922).

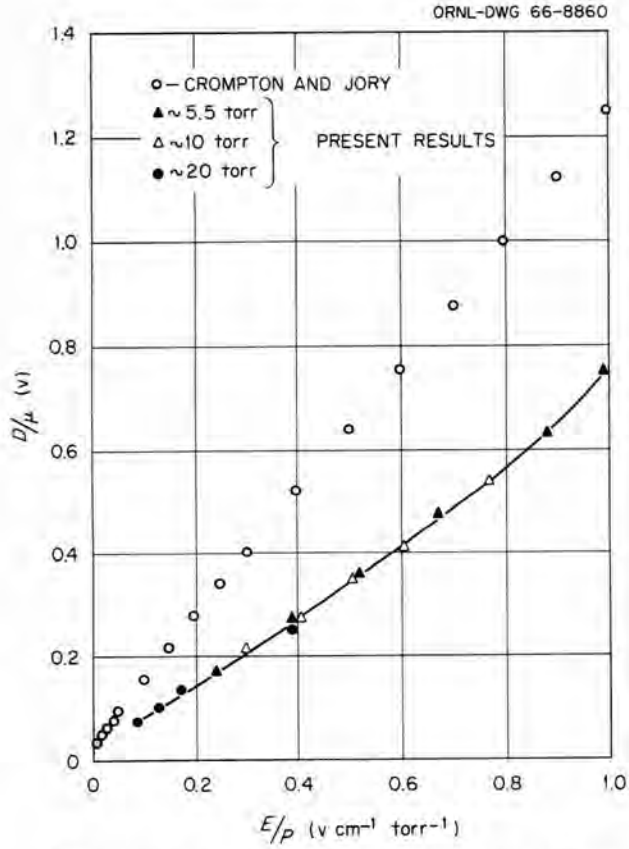

Fig. 13.6. Ratio D/μ as a Function of E/P in Helium. Data from R. W. Crompton and R. L. Jory, Fourth International Conf. Phys. Electronic and Atomic Collisions, Aug. 2–6, 1965, p. 118.

The values for drift velocity w agree very well with those of other experimenters; however, in wide electron time-of-flight distributions higher pressures were required to eliminate pressure dependence. In the case of argon, measurements were made at 200 torrs. One would not expect much variance in w among experimenters, since the most recent values have been determined by a time-of-flight method.

Effects of gas purity, stray magnetic fields, boundary effects, etc., do not seem to account for the disagreement in D/μ values. Most disturbing effects, such as variation in pressure, voltage, or temperature during a run, would widen the electron time-of-flight distributions, causing values of D/μ to be too high.

EFFECT OF CAPTURE AND LOSS PROCESSES ON TIME DISTRIBUTIONS OF DIFFUSING ELECTRONS

Further consideration has been given to the effect of temporary capture of electrons in time-of-flight swarm experiments.[18] It has been shown that when both t_c, the average time between captures in the gas, and t_r, the average lifetime of an electron in the captured state, are small compared with D/w^2, where D is the diffusion

[18] G. S. Hurst *et al.*, *Health Phys. Div. Ann. Progr. Rept. July 31, 1965*, ORNL-3849, p. 122.

coefficient and w the drift velocity of electrons in the gas, a simple expression may be obtained for D_a, the apparent diffusion coefficient of electrons in the gas. One finds that D_a is larger than D and is given approximately by

$$D_a \approx D + \frac{t_r^2 w^2}{2(t_c + t_r)} .$$

It has also been shown that in steady-state experiments of the Townsend type the effect of temporary attachment is nil; thus such experiments cannot be used to infer values of t_c and t_r for electrons undergoing capture on the gas atoms.

SWARM DETERMINATION OF THE CROSS SECTION FOR MOMENTUM TRANSFER IN ETHYLENE AND IN ETHYLENE MIXTURES

The apparatus for measurement of electron capture and electron drift velocities at high temperatures, which was described last year,[19] has been employed to study elastic electron scattering from ethylene and mixtures of ethylene with polar molecules.

Electron swarm drift velocities w in ethylene were measured for temperatures T ranging from 298 to 473°K. There is a substantial decrease in w with increasing T up to at least a pressure-reduced electric field E/P equal to 0.4 v cm^{-1} torr^{-1}. The observed dependence of w on temperature was used in an attempt to deduce both the velocity dependence and the magnitude of the cross section for electron momentum transfer in ethylene. In the region of low E/P ($\leqq 0.1$), where the applied field does not disturb appreciably the electron energy distribution, the electron energy distribution is assumed to be Maxwellian. Thus, we may write

$$w = -\frac{4\pi}{3}\frac{e}{mN}\frac{E}{P}\int_0^\infty \frac{v^2}{\sigma(v)}\frac{df_0}{dv}\,dv , \qquad (1)$$

where

$$f_0(v) = \left(\frac{m}{2\pi kT}\right)^{3/2} e^{-mv^2/2kT} . \qquad (2)$$

[19]G. S. Hurst *et al.*, *Health Phys. Div. Ann. Progr. Rept. July 31, 1965*, ORNL-3849, p. 114.

In these equations E/P is the pressure-reduced electric field; v, m, and e are the electron velocity, mass, and charge respectively; and N is the number of gas molecules per cm^3 when $P = 1$ torr and $T = 298$°K.

Assuming that the cross section for momentum transfer is expressed in powers of velocity, that is,

$$\sigma(v,\alpha) = \frac{A_\alpha}{v^\alpha} , \qquad (3)$$

where A_α is a constant depending only on α, we obtained

$$w = \frac{4}{3\sqrt{2\pi}}\frac{e}{mN}\frac{E}{P}\frac{2^{\alpha/2}}{A_\alpha}\Gamma\left(\frac{\alpha}{2}+2\right)\frac{m^{(1-\alpha)/2}}{kT} , \qquad (4)$$

where $\Gamma(x)$ is the gamma function of x, and α can be any quantity greater than -4. The temperature-dependent $w(T)$ follows immediately from Eq. (4).

Our results for the drift velocity in pure ethylene were compared with Eq. (4) for E/P from 0.01 to 0.10 v cm^{-1} torr^{-1} and for T from 298 to 473°K. It was found that when $\alpha = 0$, a good fit to Eq. (4) was obtained with the constant cross section $\sigma_E = A_0^E = (4.37 \pm 0.26) \times 10^{-16}$ cm^2, where the $\pm$ represents extreme variations in 54 data points.

Mixtures of Polar Molecules with Ethylene

In previous analyses[19–21] of the drift velocity of electrons in mixtures of ethylene with polar gases, it was assumed that the cross section for momentum transfer in the polar gas as well as in ethylene itself depended inversely on the square of the electron velocity. Because we now find that the cross section in ethylene is velocity independent, we have examined the consequences of combining a constant cross section for ethylene with a v^{-2}-dependent cross section for the polar gas. It was found that, while our previous comparisons[19–21] of theory and experiment are quantitatively changed, the substantial differences between theory[22,23] and experiment[19–21] remain almost unchanged.

[20]G. S. Hurst *et al.*, *J. Chem. Phys.* **38**, 2572 (1963).

[21]L. G. Christophorou *et al.*, *J. Chem. Phys.* **44**, 3506 (1966).

[22]S. Altshuler, *Phys. Rev.* **107**, 114 (1957).

[23]M. H. Mittleman and R. E. Von Holdt, *Phys. Rev.* **140**, A726 (1965).

STUDIES OF ELECTRONIC BOUND STATES IN THE FIELD OF A PERMANENT ELECTRIC DIPOLE

A summary of new results obtained for the motion of an electron in the field of a permanent electric dipole was prepared.[24] The solution in the Wentzel-Kramers-Brillouin (WKB) approximation gives the requirement that a minimum value of the dipole moment is necessary for binding an electron.[25] Although this result suggests that the existence of a minimum dipole moment is a result of the dipole potential rather than a feature of the WKB method, it does not establish this existence rigorously. A detailed variational calculation is now being carried out in an attempt to find the electronic ground-state binding energy as a function of dipole moment down to zero energy.

ANALYSIS OF ELECTRON SWARM DATA TO OBTAIN TRANSPORT CROSS SECTIONS

In the approximation that the thermal motion of atoms may be neglected, the drift velocity $w(\eta)$ of electrons diffusing through an assembly of elastically scattering gas atoms is given by

$$w(\eta) = -19.8\eta \frac{\displaystyle\int_0^\infty \frac{\epsilon}{\sigma(\epsilon)} \frac{d}{d\epsilon} f(\eta,\epsilon)\, d\epsilon}{\displaystyle\int_0^\infty \epsilon^{1/2} f(\eta,\epsilon)\, d\epsilon} \tag{1}$$

in the P_1 transport theory approximation. The equilibrium electron energy distribution

$$f(\eta,\epsilon) = \exp\left[-\frac{\gamma}{\eta}\int_0^\epsilon \epsilon'\,\sigma(\epsilon')\, d\epsilon'\right],$$

where $\eta = E/P$, the ratio of electric field intensity to gas pressure (v cm^{-1} torr^{-1}), $\sigma(\epsilon)$ (cm^{-1}) is the electron transport cross section of the gas at a pressure of 1 torr for electrons of energy ϵ (ev), $\gamma = 6/M$, where M is the mass of the gas atom in units of electron mass, and $w(\eta)$ is measured in cm/μsec. A similar expression may be written for the quantity PD (cm^2 torr μsec^{-1}), the product of the diffusion coefficient of electrons in the gas and the gas pressure,

$$PD(\eta) = 19.8 \frac{\displaystyle\int_0^\infty \frac{\epsilon}{\sigma(\epsilon)} f(\eta,\epsilon)\, d\epsilon}{\displaystyle\int_0^\infty \epsilon^{1/2} f(\eta,\epsilon)\, d\epsilon}. \tag{2}$$

The usual procedure used to infer the unknown cross section $\sigma(\epsilon)$ from measurements of $w(\eta)$ or $PD(\eta)$ using these integral equations is to assume some simple analytical expression for $\sigma_t(\epsilon)$, containing adjustable parameters, such that the integrations may be carried out analytically. The resulting expression for $w(\eta)$ or $D(\eta)$ is made to agree with experiment as well as possible by varying the adjustable parameters. This procedure is inefficient and unsystematic and probably is not useful in obtaining $\sigma_t(\epsilon)$ in any detail.

A different method of obtaining $\sigma_t(\epsilon)$ from $w(\eta)$ and $PD(\eta)$ data has been proposed and is in the process of being tested. This approach is based on the fact that $f(\eta,\epsilon)$ is a rather simple exponential function of $\sigma_t(\epsilon)$ so that one may use known theorems from Laplace transform theory to invert formally the integral equation (1) or (2).

One finds the following nonlinear "Volterra-type" integral equations for the unknown function $d\epsilon/dt$:

$$\frac{d\epsilon}{dt}(t) = \epsilon^{-3}(t)\left[\int_0^t w(t-\tau)\,\epsilon^{1/2}(\tau)\frac{d\epsilon}{dt}(\tau)\, d\tau\right]^2 \tag{3}$$

$$= \epsilon^{-1}(t)\left[\int_0^t \Delta(t-\tau)\,\epsilon^{1/2}(\tau)\frac{d\epsilon}{dt}(\tau)\, d\tau\right]^{2/3} \tag{4}$$

$$= \frac{\displaystyle\int_0^t \Delta(t-\tau)\,\epsilon^{1/2}(\tau)\frac{d\epsilon}{dt}(\tau)\, d\tau}{\displaystyle\int_0^t w(t-\tau)\,\epsilon^{1/2}(\tau)\frac{d\epsilon}{dt}(\tau)\, d\tau}, \tag{5}$$

where

$$\sigma_t(\epsilon) = \left[\gamma\epsilon(t)\frac{d\epsilon}{dt}\right]^{-1/2},$$

$$\epsilon(t) = \int_0^t \frac{d\epsilon}{dt}(t')\, dt'.$$

[24] J. E. Turner and Kenneth Fox, *On the Bound States of an Electron in the Field of a Permanent Electric Dipole*, ORNL-3895 (1965).

[25] Kenneth Fox and J. E. Turner, *Am. J. Phys.* (in press).

The quantities $w(t)$ and $\Delta(t)$ are inverse Laplace transforms of the quantities $w(s^{-1/2})/19.8[\gamma s]^{1/2}$ and $PD(s^{-1/2})/19.8\sqrt{\gamma}$, respectively, and may be obtained from analytical fits to the $w(\eta)$ and $PD(\eta)$ data. The quantity s is considered to be the Laplace transform parameter.

Numerical solution of the three different forms of the integral equation for $d\epsilon/dt$ has been carried out for a case in which the solution is known. The results are quite encouraging, and application of the method to the analysis of drift and diffusion coefficient data in the noble gases is under way.

SWARM-BEAM STUDIES OF POLYATOMIC MOLECULES

Electron swarm and electron beam techniques were combined as described earlier,[19,26] and absolute capture cross sections as a function of electron energy were obtained for a number of polyatomic molecules. The swarm-beam method not only provides absolute cross sections as a function of electron energy, but also establishes a new independent energy-scale calibration for as low as a few tenths of an electron volt.

Our investigation of the dissociative electron capture by halogenated benzene derivatives has been completed.[27] For this group of molecules, dissociative attachment leading to halogen negative ions peaks at ~0.8 ev and extends down to thermal electron energies. Our electron swarm-beam studies have been extended to $C_6H_5NO_2$, *o*- and *m*-$C_6H_4CH_3NO_2$, and SF_6. Figure 13.8 gives NO_2^- and *m*-$C_6H_4CH_3NO_2^-$ ion currents for *m*-$C_6H_4CH_3NO_2$. Similar data were obtained for $C_6H_5NO_2$ and *o*-$C_6H_4CH_3NO_2$. Table 13.2 summarizes our beam results for these three compounds. Beam data on SF_6 were reported earlier;[19,26,27] swarm data on SF_6 are now reported.

Due to the high sensitivity of the electron swarm method employed, the pressure of gases (such as SF_6) with large electron capture cross sections must be very low ($<1\ \mu$). Such pressures are very difficult to measure accurately. An expansion technique, however, was developed in which a few torrs of SF_6 was measured with a Wallace and Tiernan gage and was subsequently expanded into an expansion tank, where the SF_6 was premixed with the carrier gas (ethylene) at a pressure of ~100 torrs. Small quantities of this mixture were introduced into the attaching chamber through a solenoid valve. Therefore, the true pressure of SF_6 in the attachment experiment chamber was calculated from the predetermined expansion ratios and from the pressure of SF_6 before expansion (measured by the Wallace and Tiernan gage). During measurements at higher temperatures special attention was given to ensure that effects due to outgassing were not involved. The results were consistent and reproducible to within ±15%.

The absolute rates of electron attachment were determined in the carrier gas ethylene at low values of E/P (≤ 1 v cm^{-1} torr^{-1}), where the distribution of electron energies in the electron swarm is thermal.[27] For this E/P region (≤ 0.1) was measured a constant rate of attachment equal

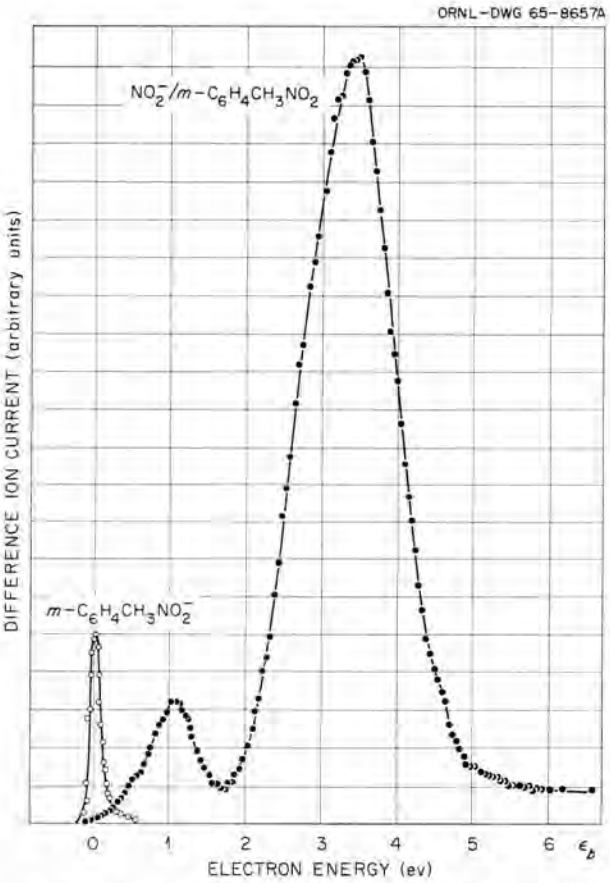

Fig. 13.8. Dissociative Electron Capture in *m*-Nitrotoluene.

[26] L. G. Christophorou *et al.*, *J. Chem. Phys.* 43, 4273 (1965).

[27] L. G. Christophorou *et al.*, *J. Chem. Phys.* (in press).

Table 13.2. Electron Beam Data for Nitrobenzene, o-Nitrotoluene, and m-Nitrotoluene

Compound	Formula	Ion	ϵ_{max} (ev)	Appearance Potential when SF_6^- Was Used for Energy Calibration (ev)
Nitrobenzene	$C_6H_5NO_2$	$C_6H_5NO_2^-$	0.03	0.0
		NO_2^-	1.06	0.42
		NO_2^-	3.53	1.9
o-Nitrotoluene	$o\text{-}C_6H_4CH_3NO_2$	$o\text{-}C_6H_4CH_3NO_2^-$	0.03	0.0
		NO_2^-	0.62	0.5
		NO_2^-	3.22	2.1
m-Nitrotoluene	$m\text{-}C_6H_4CH_3NO_2$	$m\text{-}C_6H_4CH_3NO_2^-$	0.03	0.0
		NO_2^-	1.06	
		NO_2^-	3.50	1.8

to 1.24×10^9 and 2.1×10^7 sec^{-1} $torr^{-1}$ for SF_6 and $C_6H_5NO_2$ respectively. The capture rates were independent of the total pressure ($250 \leqq P_{tot} \leqq 800$ torrs). For $E/P > 0.1$, the capture rates decreased slightly, indicating that at higher energies the capture process does not have the same velocity dependence as in the thermal energy region.

The temperature (T) dependence of the absolute rates of electron attachment in SF_6 was also investigated. For the high-temperature studies the pressures were normalized to $P(T = 300°K)$. Figure 13.9 shows that the capture rates, $\alpha \times w$, given by

$$\alpha \times w = N_0 \int_0^\infty v\, \sigma_c(v)\, f(v)\, dv\,, \qquad (1)$$

are independent of the temperature over the range 25 to 145°C. In Eq. (1), N_0 is the number of SF_6 molecules per torr at 300°K, $\sigma_c(v)$ is the capture cross section as a function of electron velocity, and

$$f(v)\, dv = (m/2\pi kT)^{3/2}\, e^{-(mv^2/2kT)} 4\pi v^2\, dv\,.$$

From Eq. (1) and the experimental results presented in Fig. 13.9, we conclude that $\sigma_c(v)$ depends inversely on the electron velocity v, that is,

$$\sigma_c(v) = \frac{A}{v}\,. \qquad (2)$$

For comparison with the experimental data we also plotted in Fig. 13.9 the temperature dependence of $\alpha \times w$ (broken line) which would be observed if $\sigma_c(v)$ were inversely proportional to the square of the electron velocity.

From Eqs. (1) and (2) the constant A for SF_6 is calculated to be 3.83×10^{-8} cm^3/sec. Using this value and the average velocity $\bar{v}$ of a thermal electron, we calculated an average capture cross section $\bar{\sigma}$ equal to 3.6×10^{-15} cm^2. This value is comparable with those of total ionization experiments but is in disagreement with values reported by the microwave technique.

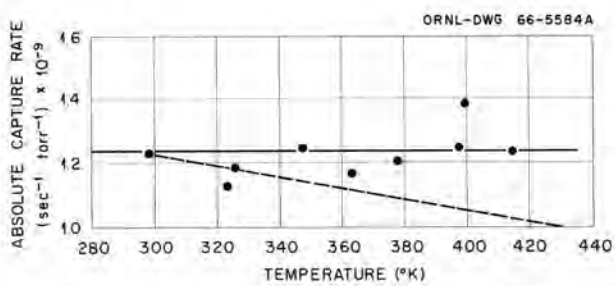

Fig. 13.9. Temperature Dependence of the Electron Capture Rates in SF_6.

The results on SF_6^- and $C_6H_5NO_2^-$ presented in this section are combined with data on the lifetimes of these temporary negative ions elsewhere in this report to derive information about the molecular structure.

LIFETIMES OF TEMPORARY NEGATIVE IONS

The existence of long-lived, temporary negative ions formed by unimolecular electron capture are of current interest.[28] Of particular physical and biological importance is the formation of long-lived organic negative ions. In this connection the problem of unimolecular electron capture by polyatomic molecules is under experimental and theoretical investigation.

A modification of a Bendix model 14-206 time-of-flight mass spectrometer was employed to determine the mean half-lives for autodetachment. The experimental details are given in ref. 28. The mean lifetimes for $C_6H_5NO_2^{-*}$, SF_6^{-*}, and $(CH_3CO)_2^{-*}$ were determined to be 40, 25, and 11.5 μsec respectively.

The fact that large molecules can possess large cross sections and long lifetimes for unimolecular electron attachment has suggested that the energy of the captured electron is shared with the many degrees of freedom of the molecule. We have adapted such a model, whereby the excess energy of negative ion formation is distributed among the various degrees of freedom of the molecule in connection with the principle of detailed balance in an attempt to interpret the experimental lifetime and cross-section measurements for SF_6, $C_6H_5NO_2$, and $(CH_3CO)_2$.

The lifetime τ of a negative ion possessing N vibrational degrees of freedom is related to the attachment cross section $\sigma(v)$ through the following:

$$\tau = \frac{2\pi^2\hbar^3}{W_M\, m^2 v} \frac{(\epsilon_e + \epsilon_A + a\epsilon_z)^{N-1}}{\Gamma(N)\prod_i^N h\nu_i} \frac{1}{v\,\sigma(v)}, \quad (1)$$

where ϵ_e and v are the energy and velocity of the incident electron, ϵ_z is the zero-point energy of the ion (i.e., one-half the sum of all the vibrational energies $h\nu_i$), ϵ_A is the electron affinity of the molecule, W_M is the number of states available to the molecule after electron ejection, $\Gamma(N)$ is the gamma function of N, and a is a parameter which is to be evaluated for each molecule and each value of $(\epsilon_e + \epsilon_A)/\epsilon_z$.[29] An analog of this equation, applicable when the ejected electron can take on a range of energies, is of the form

$$k_i = \int_0^{E-\epsilon_A} \frac{\sigma(\epsilon)}{\pi a_0^2} \frac{\epsilon}{R} \frac{\rho(E - \epsilon_A - \epsilon)}{\rho^-(E)} \frac{d\epsilon}{h},$$

where k_i is the rate of autoionization, a_0 is the Bohr radius, R is the Rydberg constant, and E is the internal energy of the ion.

The use of these equations is illustrated in Fig. 13.10, where the SF_6^- autoionization rate constant is given as a function of the internal energy; the rate constant k_d for a competing dissociation reaction is also given. At least qualitative agreement is obtained between the experimental and predicted lifetimes for SF_6.

[28] R. N. Compton *et al.*, *Electron Capture Cross Sections and Negative Ion Lifetimes*, ORNL-TM-1409 (March 1966).

[29] G. Z. Whitten and B. S. Rabinovitch, *J. Chem. Phys.* 38, 2466 (1963).

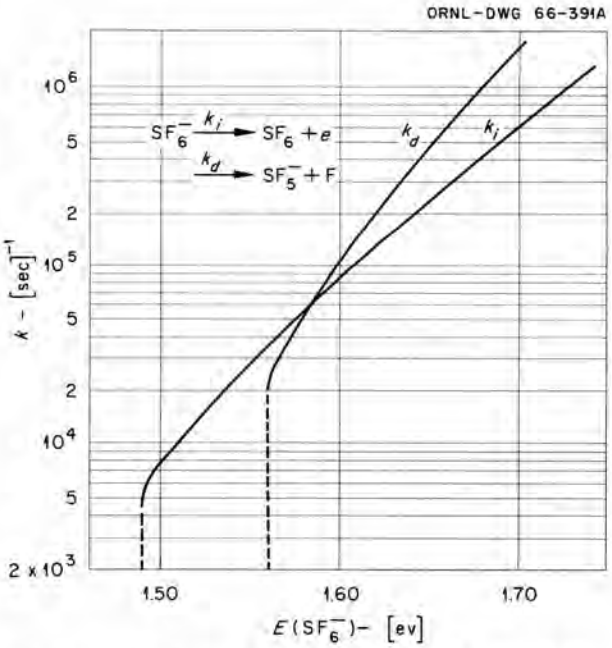

Fig. 13.10. Rate of Autoionization and Rate of Dissociation as a Function of Internal Energy for $(SF_6^-)^*$.

The extreme sensitivity of the product of τ and σ on ϵ_A strongly indicates the possibility of calculating electron affinities of molecules from a measurement of lifetimes and cross sections. Work is presently under way along this line.

A new apparatus designed to measure negative-ion lifetimes in the range 10^{-9} to 10^{-6} sec has been constructed, and the basic components have been tested and are functioning properly.

STUDIES OF DISSOCIATIVE ELECTRON ATTACHMENT IN H_2O AND D_2O

The electron swarm-beam method[26–28] has been applied to determine the cross section as a function of energy for the production of H^- from H_2O and D^- from D_2O. The swarm experimental rates and the rates calculated from the electron beam experiments (after optimum translation) are plotted in Fig. 13.11 as a function of E/P for H_2O and D_2O. A positive energy shift of 0.3 ev for the case of H_2O and 0.5 ev for D_2O was required to bring the experimental and calculated rates into agreement. The energy scale thus determined resulted in good agreement with previous experiments. The "swarm normalized beam cross sections" for H^- from H_2O and D^- from D_2O are presented in Figs. 13.12 and 13.13 respectively.

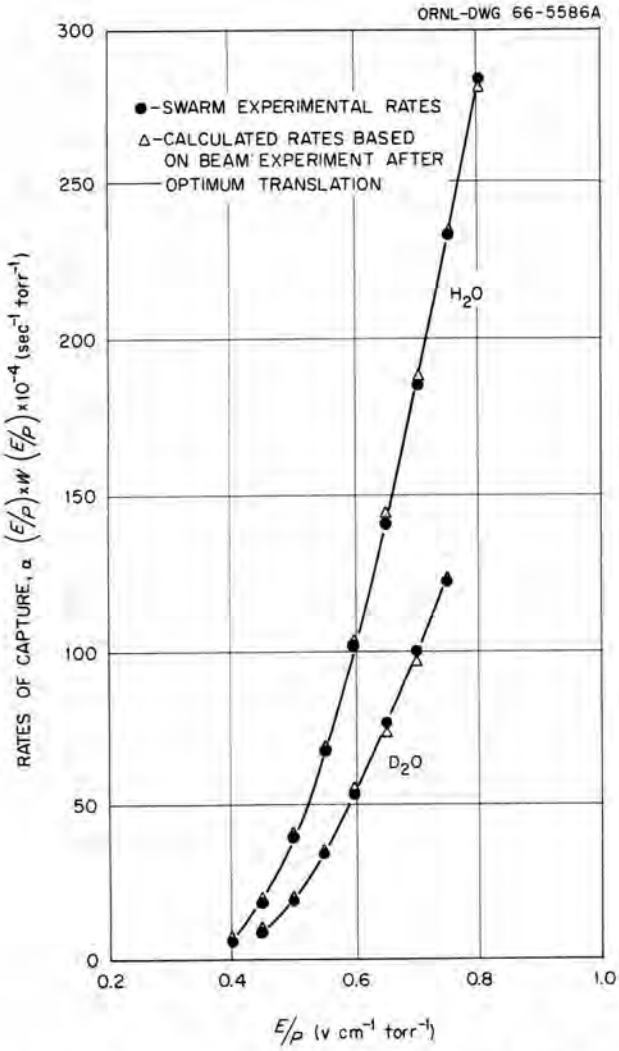

Fig. 13.11. Experimental and Calculated Rates of Capture vs E/P for Water and Heavy Water for Trial Functions Based on Beam Experiments.

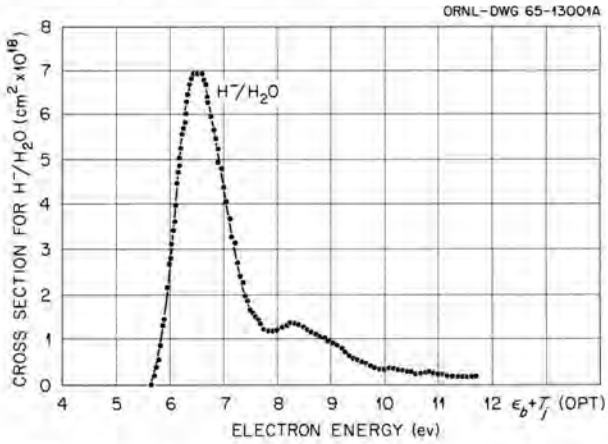

Fig. 13.12. Electron Capture Cross Section as a Function of Energy. Atomic hydrogen negative ions from water.

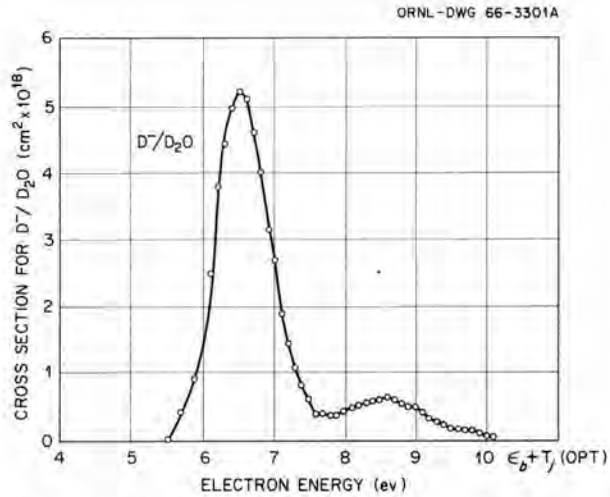

Fig. 13.13. Electron Capture Cross Section as a Function of Energy. Deuterium negative ions from heavy water.

The ratio of the cross section for H^-/H_2O to D^-/D_2O is found to be 1.33, consistent with the concept that electron emission is in competition with dissociative attachment. This result is being studied with respect to the existing theories of electron attachment.

Isotope effects were discovered in the production of O^- from H_2O and D_2O as well as in the magnitude of the cross section for formation of H^- from H_2O and D^- from D_2O. Figure 13.14 shows the relative ion current yields for O^- from H_2O and O^- from D_2O as a function of energy. The two curves have been normalized in magnitude at the second maximum. Calibration of the electron energy scale was obtained from the H^- and D^- peaks. The ratio of the ~11-ev peak to the ~9-ev peak for D_2O is seen to be much smaller than the corresponding ratio for the case of H_2O. Such isotopic effects have not been observed previously but are to be expected from theoretical considerations.

Experiments are also in progress to investigate isotope effects on dissociative electron capture in the simple diatomic molecules HCl, DCl, HBr, DBr, HI, and DI. The results will be employed to study the basic mechanisms involved in electron attachment.

Ion molecule reactions in water and water-oxygen mixtures were also studied. At high pressures ($\sim 10^{-4}$ torr), OH^- was produced by ion-molecule reactions involving H^- and O^- with water. Also, in water-oxygen mixtures charge exchange between H^- and O_2 producing O_2^- was observed. Figure 13.15 shows the OH^- and O_2^- ion currents as a function of electron energy. The H^- ion current is observed to follow the same energy dependence (see Fig. 13.12). Thus OH^- and O_2^- are produced via the reaction scheme

$$H^- + H_2O \rightarrow OH^- + OH ,$$

$$H^- + O_2 \rightarrow O_2^- + H .$$

Parent negative ions of water were not observed in H_2O or in the H_2O-O_2 mixtures.

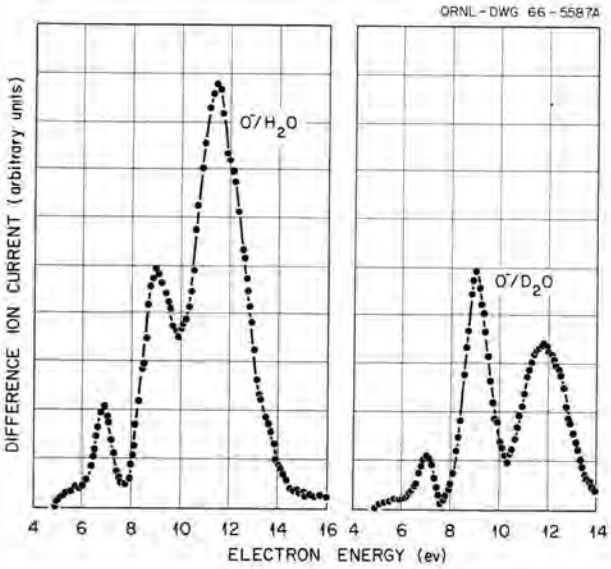

Fig. 13.14. Atomic Oxygen Negative Ions from Water and Heavy Water.

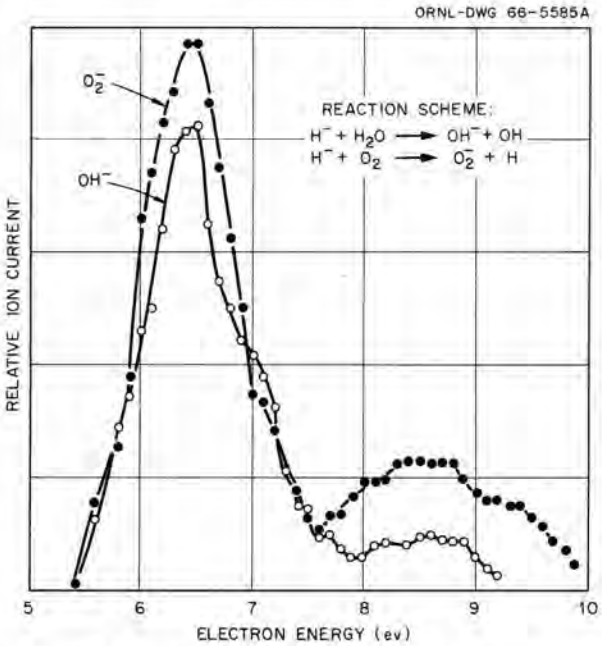

Fig. 13.15. Ion Molecule Reaction in Water-Oxygen Mixtures.

INTERACTION OF LOW-ENERGY ELECTRONS WITH ATOMIC OXYGEN[30]

A theoretical study of the interaction of low-energy electrons with atomic oxygen (0 to 25 ev) has been completed. The cross section for the elastic scattering of low-energy electrons by atomic

[30]Part of this work was done at the University of Alabama prior to the author's joining ORNL.

oxygen, the attachment cross section and attachment coefficient for electrons on neutral oxygen, and the photodetachment cross section for the negative atomic oxygen ions were determined.

In the present treatment[31] of these problems the bound-state functions of oxygen and of O^- were treated by a modified Hartree-Fock-Slater (H-F-S) technique, wherein the Slater exchange term in the Hartree-Fock (H-F) equations was varied over a range of values in order to obtain eigenvalues in agreement with experiment for O and O^-. The interaction potential between the neutral atom and the free electron in each of these problems was obtained from the modified H-F-S potential to which a polarization correction was added. The polarization potential was determined from a polarized orbital calculation on the neutral oxygen atom. This method has been used successfully in earlier calculations on alkali atoms,[32] where the polarization term in the total interaction potential is quite large.

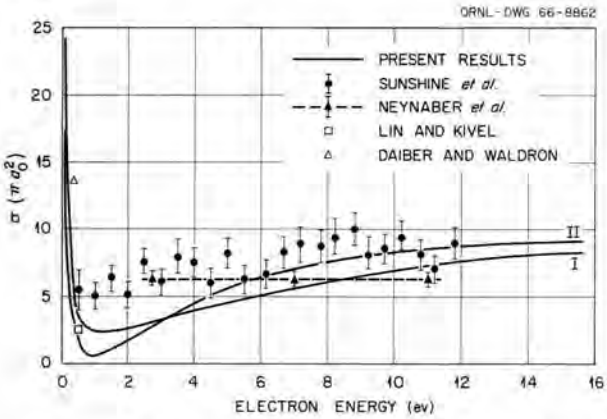

Fig. 13.16. Total Elastic Scattering Cross Section for Oxygen Compared with Available Experimental Data.

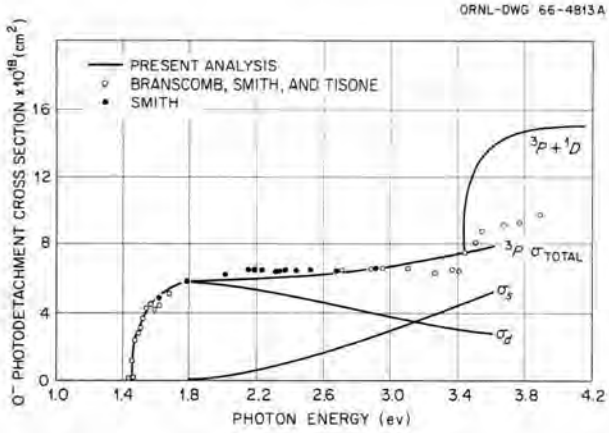

Fig. 13.17. Total Photodetachment Cross Section for O^-, Showing Contributions from the *s* and *d* Waves. Experimental values are those of Branscomb, Smith, and Tisone, and of Smith.

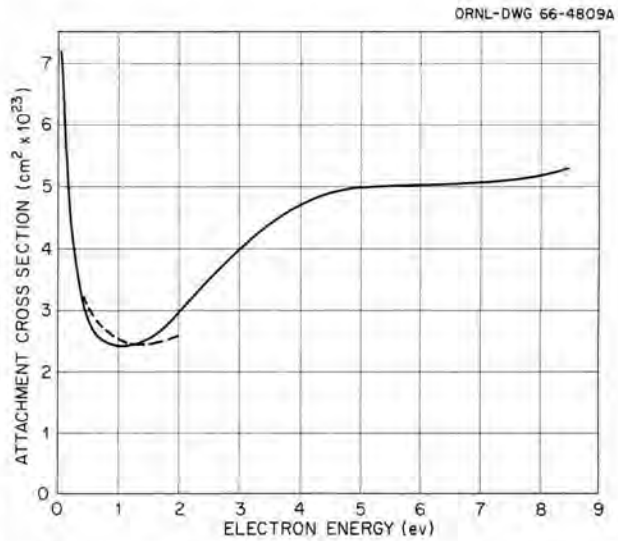

Fig. 13.18. Attachment Cross Section of Electrons to Atomic Oxygen Calculated by Detailed Balancing from the Photodetachment Cross Section.

The present theoretical results for elastic scattering on oxygen are compared with four experiments in Fig. 13.16.[33–36] Results for photodetachment cross sections are compared with experiment in Fig. 13.17,[37,38] and the attachment cross sections and attachment coefficients are compared with results obtained from experiment by Branscomb[39] in Figs. 13.18 and 13.19. In all cases the comparison of theoretical results with experiment is very good.

---

[31] H. T. Jackson, Jr., and W. R. Garrett, *Theoretical Photodetachment Cross Section for the Negative Atomic Oxygen Ion*, University of Alabama Research Institute Report No. 32 (December 1965).

[32] W. R. Garrett, *Phys. Rev.* **140**, A705 (1965).

[33] S. C. Lin and B. Kivel, *Phys. Rev.* **114**, 1026 (1959).

[34] R. H. Neynaber *et al.*, *Phys. Rev.* **123**, 148 (1961).

[35] G. Sunshine, B. B. Aubrey, and B. Bederson, *Proc. IVth International Conf. on Phys. of Electronic and Atomic Collisions, Quebec, 1965*, p. 130, Science Bookcrafters, Inc., New York, 1965.

[36] J. W. Daiber and H. F. Waldron, paper presented at the 18th Annual Gaseous Electronics Conference, Minneapolis, Minn., 1965.

[37] S. J. Smith, *Proc. Intern. Conf. Ionization Phenomena Gases, 4th, Uppsala, 1959*, paper IC219, North Holland, 1960.

[38] L. M. Branscomb, S. J. Smith, and G. Tisone, *J. Chem. Phys.* **43**, 2906 (1965).

[39] L. M. Branscomb, p. 100 in *Atomic and Molecular Processes* (ed. by D. R. Bates), Academic, New York, 1962.

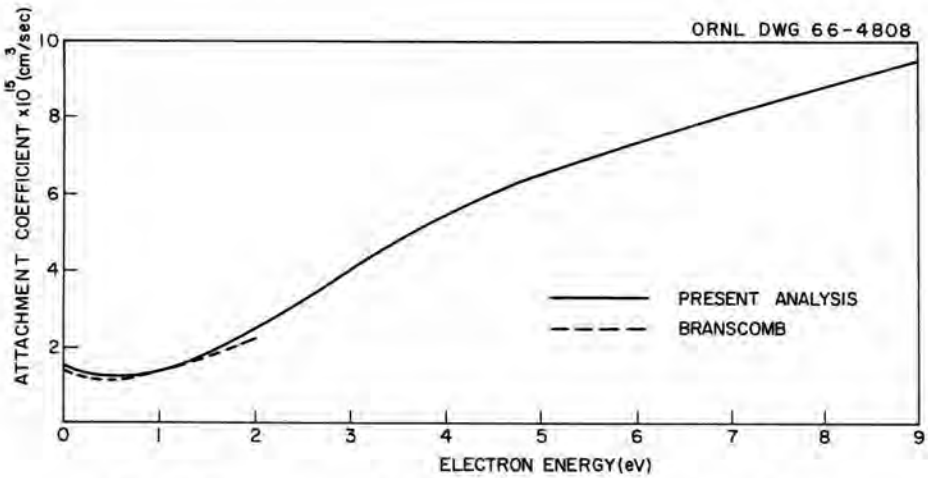

Fig. 13.19. Attachment Coefficient for Electrons on Atomic Oxygen.

POTENTIAL ENERGY CURVES FOR DIATOMIC MOLECULES

Rees's modification[40] of the semiclassical method of Rydberg and Klein for obtaining the potential energy U_e as a function of internuclear spacing R was programmed and run for the $^3\Pi_{0^+u}$ state of $^{79}Br^{81}Br$. The calculations agree with Rees's to vibrational quantum number $v' = 21$ and extend his results to $v' = 48$ (the latter being within one milli-electron volt of the dissociation limit).

MOLECULAR ORBITALS OF MAGNESIUM PORPHIN

Magnesium porphin, $MgN_4C_{20}H_{12}$, is essentially the kernel of the chlorophyll molecule. Molecular orbitals of D_{4h} spatial symmetry have been generated for the $2s$ and $2p$ orbitals of the nitrogen and of the carbon atoms, and for the $1s$ orbitals of the hydrogen atoms. Arguments based on the number of nodal surfaces of the molecular orbitals in excess of those of the constituent atomic orbitals lead to a unique specification of which orbitals are occupied, but the order of occupation is not yet definite. Further calculations are in process, with the aim of identifying the low-lying optical transitions of large oscillator strength.

[40] A. L. G. Rees, *Proc. Phys. Soc. (London)* 59, 998 (1947).

APPROXIMATE REPRESENTATION OF THE HARTREE-FOCK EQUATIONS THROUGH A PSEUDOPOTENTIAL[30]

In many important applications in atomic and molecular physics the representation of the appropriate system by the complete Hartree-Fock (H-F) formalism becomes excessively difficult. These occasions often arise in treating multielectron systems with a large number of electrons, or in cases where one or more electrons are in continuum states. Thus it is necessary in such problems to make approximations which reduce the equations to a more tractable form. A convenient method of approximating the H-F equations has been investigated, and preliminary results indicate that the method is quite accurate and becomes closer to the complete H-F treatment with increasing atomic number Z.

If one takes, as a representation of an n-electron atom, a single Slater determinant of one-electron orbitals,

$$\Phi = (N!)^{-1/2} \cdot \begin{vmatrix} \phi_1(1)\ \phi_1(2) \ldots \phi_1(n) \\ \phi_2(1)\ \phi_2(2) \ldots \phi_2(n) \\ \vdots \\ \phi_n(1)\ \phi_n(2) \ldots \phi_n(n) \end{vmatrix} \quad (1)$$

with

$$\langle \phi_i, \phi_j \rangle = \delta_{ij} , \quad (2)$$

then Fock's equations can be written as

$$-\nabla_1^2 \phi_i(1) + \left[-\frac{2Z}{r_1} + \sum_{j=1}^{n} \int \phi_j^*(2) \frac{2}{r_{12}} \phi_j(2)\, dv_2\right]$$

$$\times \phi_i(1) - \sum_j^n \delta(m_{s_i} m_{s_j}) \left[\int \phi_j^*(2) \frac{2}{r_{12}} \phi_i(2)\, dv_2\right]$$

$$\times \phi_j(1) = \epsilon_j \phi_i(1) . \quad (3)$$

The principal difficulty in solving these integro-differential equations lies in the second sum over the integrals on the left-hand side of Eq. (3), which is the familiar exchange term. The inhomogeneous equation (3) can be written in the form of a homogeneous equation by multiplying and dividing the exchange term by $\phi_i^*(1)\ \phi_i(1)$, in which case it takes the form:

$$[-\nabla_1^2 + V_c(1)]\ \phi_i(1)$$

$$-\left[\frac{\sum_j \delta(m_{s_i} m_{s_j}) \int \phi_i^*(1)\ \phi_j^*(2) \frac{2}{r_{12}} \phi_j(1)\ \phi_i(2)\, dv_2}{\phi_i^*(1)\ \phi_i(1)}\right]$$

$$\times \phi_i(1) = \epsilon_i \phi_i(1) , \quad (4)$$

where $V_c(1)$ has been written for the two Coulomb terms in Eq. (3). The equation is now homogeneous if one regards the term in brackets as a pseudopotential due to electron exchange, which is an additional attractive potential experienced by the ith electron. This term is, however, not well behaved in that it has singularities at the nodes of $\phi_i(1)$. In order to simplify the H-F equations, Slater has suggested two approximations to the above exchange term. In his first method Slater[41] defines an average exchange potential experienced by all electrons by multiplying the exchange term in brackets by the quantity

$$\frac{\phi_j^*(1)\ \phi_i(1)}{\sum_j \phi_j(1)\ \phi_j(1)} \quad (5)$$

and summing over i. Thus, in this approximation the exchange potential which any one electron experiences is the average of the exchange term for all electrons. In a second, more approximate treatment Slater[41] derives the exchange potential experienced in a free-electron gas and replaces the exchange term in Eq. (4) by an expression

$$V_{\text{exch}}(1) = -6\left[\frac{3}{8}\pi \sum_j \phi_j^*(1)\ \phi_j(1)\right]^{1/3} . \quad (6)$$

Though both of these techniques preserve much of the character of the H-F equations, they are rather inaccurate for many applications.

A method analogous to Slater's first technique is being investigated whereby a different average is taken in the exchange terms of Fock's equations. In the present method all electrons with common orbital angular momenta are treated through a common exchange potential similar to Slater's method. Here the exchange term of Eq. (4) is replaced, for a given angular momentum state, by the average of the terms for all orbitals of the given value of l (l = orbital angular momentum quantum number). Thus, we define

$$V^l_{\text{exch}}(1) = \frac{-\sum_k \sum_j \left[\delta(m_{s_k} m_{s_l}) \int \phi_k^{l*}(1)\ \phi_j^*(2) \frac{2}{r_{12}} \phi_j(1)\ \phi_k^l(2)\, dv_2\right]}{\sum_k \phi_k^{l*}(1)\ \phi^l(1)} , \quad (7)$$

where the notation $\phi_i^l(1)$ indicates orbital i having orbital angular momentum l. Thus, orbitals with common values of l share an equivalent exchange potential, but the exchange term is different for two orbitals having different orbital angular momenta. Calculations have been made for several atomic systems within this approximation, and results are quite close to those from the complete H-F treatment. Results for Ar and Cu^+ are shown in Table 13.3 and for Kr and Ag^+ in Table 13.4, where comparison is made with H-F results[42] and with the exchange approximation of Slater.[43] This

[41] J. C. Slater, *Quantum Theory of Atomic Structure*, vol. II, chap. 17, McGraw-Hill, New York, 1960.

[42] B. H. Worsley, *Proc. Roy. Soc. (London)* **A247**, 390 (1958).

[43] F. Hermann and S. Skillman, *Atomic Structure Calculations*, Prentice-Hall, Englewood Cliffs, N.J., 1960.

method promises to yield reliable wave functions for more complicated atomic systems and for important cases where continuum orbitals are included in the system.

Table 13.3. Comparison of Orbital Eigenvalues from Hartree-Fock, *l* Average H-F of Present Treatment, and Hartree-Fock-Slater Calculations

Energies in rydbergs

Orbital	ϵ		
	Hartree-Fock[a]	Present Results	Hartree-Fock-Slater[b]
	Argon ($Z = 18$)		
1*s*	−237.212	−236.026	−232.54
2*s*	−24.643	−24.425	−22.865
2*p*	−19.142	−18.525	−18.207
3*s*	−2.554	−2.648	−2.1068
3*p*	−1.182	−1.196	−1.065
	Cu^+ ($Z = 29$)		
1*s*	−658.4	−656.8	−650.4
2*s*	−82.30	−82.41	−78.87
2*p*	−71.83	−71.25	−69.74
3*s*	−10.651	−11.075	−9.355
3*p*	−7.279	−7.556	−6.429
3*d*	−1.613	−1.585	−1.459

[a]B. H. Worsley, *Proc. Roy. Soc. (London)* **A247**, 390 (1958).

[b]F. Hermann and S. Skillman, *Atomic Structure Calculations*, Prentice-Hall, Englewood Cliffs, N.J., 1960.

Table 13.4. Comparison of Eigenvalues for Ag^+ ($Z = 47$) and Kr ($Z = 36$) as in Table 13.3

Energies in rydbergs

Orbital	Hartree-Fock[a]	Present Results	Hartree-Fock-Slater[b]
	Ag^+ ($Z = 47$)		
1*s*	−1828.1	−1824.9	
2*s*	−270.1	−269.5	
2*p*	−250.8	−248.8	
3*s*	−52.22	−52.15	
3*p*	−44.30	−43.99	
3*d*	−29.85	−28.88	
4*s*	−8.458	−8.802	
4*p*	−5.823	−6.067	
4*d*	−1.69	−1.636	
	Kr ($Z = 36$)		
1*s*	−1040	−1037.9	−1030.6
2*s*	−139.8	−139.35	−135.53
2*p*	−126.2	−124.58	−123.25
3*s*	−21.7	−21.49	−19.728
3*p*	−16.67	−16.33	−15.249
3*d*	−7.60	−7.042	−7.0975
4*s*	−2.303	−2.411	−1.9456
4*p*	−1.06	−1.087	−0.9519

[a]B. H. Worsley, *Proc. Roy. Soc. (London)* **A247**, 390 (1958).

[b]F. Hermann and S. Skillman, *Atomic Structure Calculations*, Prentice-Hall, Englewood Cliffs, N.J., 1960.

14. Interaction of Radiation with Liquids and Solids

E. T. Arakawa
R. D. Birkhoff

A. E. Carter
J. G. Carter
L. S. Cram[1]
L. C. Emerson
J. A. Harter
A. G. Kenerly[2]
W. J. McConnell
M. Y. Nakai[3]
H. L. Pray[4]
L. L. Robinson[1]
J. C. Sutherland[5]
L. H. Toburen[5]
R. C. Vehse[1]
E. K. Yeargers[6]

TRANSITION RADIATION DUE TO NONNORMALLY INCIDENT ELECTRONS

Born-Approximation Method

The transition radiation from a thin film generated by electrons of nonnormal angle of incidence has been calculated using a simple approximation method. This Born-approximation treatment, valid when the electric susceptibility is small compared to unity, neglects the influence of the boundaries to a great extent (no reflection or refraction is included) but reproduces some general aspects of this problem, such as the dependence of the transition radiation on thickness, in simple and understandable fashion. For work on similar problems using this approximate method, see ref. 7. The calculation employs standard methods from electromagnetic theory to arrive at the photon number distributions, $d^2N/d\Omega d\omega$, the number of photons emitted into a solid angle $d\Omega$, and of frequency in the interval ω to $\omega + d\omega$, for both parallel and perpendicular polarizations of the photons. The geometry of this situation is depicted in Fig. 14.1, where ϕ is the azimuthal angle, measured from the x axis, of the point P. The photon distributions are given by

$$\frac{d^2N^{\parallel}}{d\Omega\, d\omega} = \frac{\alpha\beta^2}{\pi^2\omega}\cos^2\xi\left(\frac{\epsilon-1}{\epsilon}\right)^2 \times \left[\frac{\sin\theta\,(\rho-\beta^2\cos^2\xi) - \epsilon\beta\cos\theta\cos\xi\,(\sin\theta-\beta\sin\xi\cos\phi}{\rho^2-\beta^2\cos^2\theta\cos^2\xi}\right]^2 \cdot I$$

and

$$\frac{d^2N^{\perp}}{d\Omega\, d\omega} = \frac{\alpha\beta^2}{\pi^2\omega}(\epsilon-1)^2\left[\frac{\beta^2\sin\xi\sin\phi\cos^2\xi}{\rho^2-\beta^2\cos^2\theta\cos^2\xi}\right]^2 \cdot I\,,$$

where

$$I \equiv \frac{\sin^2\left[\dfrac{\omega d}{2v\cos\xi}(1-\beta\cos\theta')\right]}{(1-\beta\cos\theta')^2}$$

and $\beta \equiv v/c$, $\alpha \equiv e^2/\hbar c$, ϵ is the dielectric constant at frequency ω, $\rho = 1\text{-}\beta\sin\theta\cos\phi\sin\xi$, and $\cos\theta' = \cos\theta\cos\xi + \sin\theta\cos\phi\sin\xi$. The dependence of the distributions on d, the foil thickness, is given by I. The "sine-squared" term in I gives

[1]US AEC Health Physics Fellow.

[2]On loan from Instrumentation and Controls Division (ORNL).

[3]On loan from Thermonuclear Division (ORNL).

[4]Radiological Health Physics Fellow.

[5]Oak Ridge Graduate Fellow.

[6]AEC Postdoctoral Fellow.

[7]J. C. Ashley and R. H. Ritchie, *J. Appl. Phys.* 35, 2313 (1964).

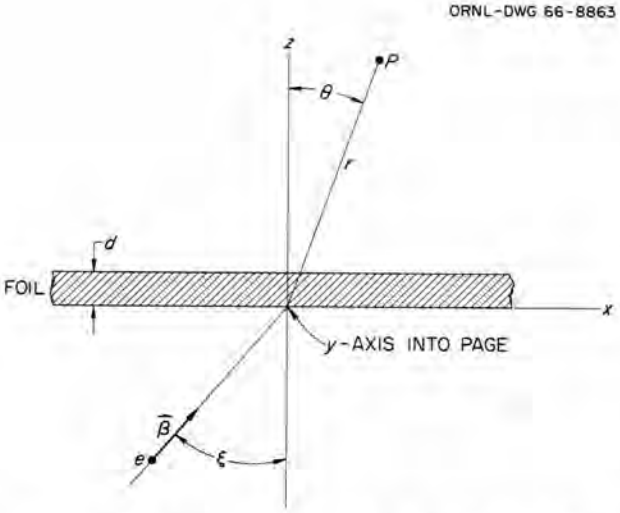

Fig. 14.1. Geometry for Transition Radiation Calculations.

rise to maxima and minima in the photon distributions when the parameters are varied, due to constructive and destructive interference of photons originating at different depths within the foil.

These equations have been used to compare with experimental work on aluminum. The experimental work and the comparison with theory are discussed in the next section.

Exact Method

An "exact" calculation of the transition radiation for the geometry of Fig. 14.1 has been carried out. This treatment is an improvement on the approximate procedure above in that the boundary conditions on the electromagnetic fields have been used in the analysis where they were only partially included in the Born-approximation method. A quite lengthy expression results, which has been programmed for computer evaluation. Some preliminary results are available and are encouraging, but further checks on the equations and program are being pursued.

TRANSITION RADIATION AND BREMSSTRAHLUNG FROM Ag AND Al FOILS BOMBARDED BY NONNORMAL INCIDENCE ELECTRONS

Recent investigation[8,9] of the optical emission spectrum from a thick Ag target bombarded by high-energy electrons at grazing incidence shows a peak at 3550 A. Boersch identified this peak as being due to the decay of surface plasmons. In an effort to verify this hypothesis, the radiation emitted by self-supporting Ag foils 700 to 1700 A in thickness and Al foils 300 A thick was investigated as a function of angle of electron incidence, foil thickness, and degree of polarization.

The spectra of light emitted by a self-supporting silver foil 700 A thick bombarded by electrons at various angles of incidence are shown in Fig. 14.2, along with the theoretical results of Howe and Ritchie[10] (henceforth abbreviated as HR). These spectra have been corrected for the spectrometer response and for the change in number of electrons per unit area for changing angles of electron incidence. The peak at 3300 A characteristic of transition radiation was found in the emission spectrum when the foil was bombarded by normally incident electrons ($\theta_i = 0°$). The wavelength at which the peak appeared increased monotonically until it

[8] H. Boersch *et al.*, *Z. Physik* 187, 97 (1965).

[9] G. E. Jones, L. S. Cram, and E. T. Arakawa, "Radiation from Thick Silver Foils Bombarded by Grazing-Incident Electrons" (to be published).

[10] H. J. Howe and R. H. Ritchie, *Transition Radiation and Low Energy Bremsstrahlung*, ORNL-TM-1105 (August 1965) (to be published).

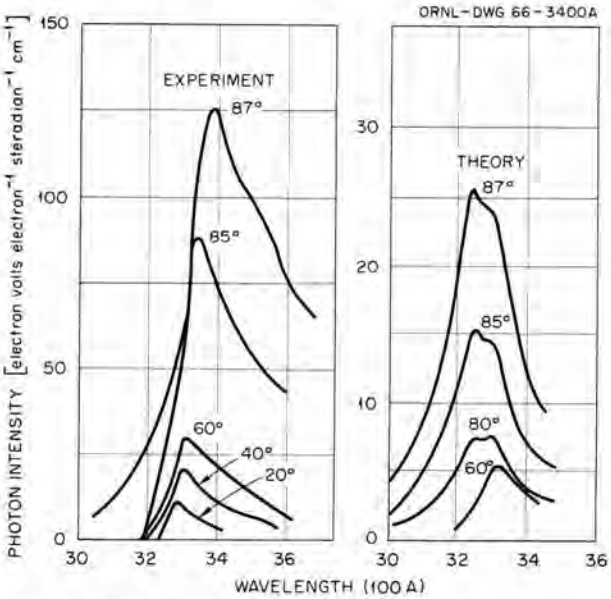

Fig. 14.2. Spectra of Light Emitted in the Parallel Plane of Polarization from Thin (t = 700 A) Self-Supporting Silver Foils Bombarded by 80-kev Electrons at Various Angles of Incidence.

appeared at $\lambda = 3400$ A for $\theta_i = 87°$. No peak was found at $\lambda = 3500$ A for this foil.

As electron incidence approaches grazing angles ($\theta_i > 80°$) there is a strong peaking of the photon intensity at approximately $\lambda = 3400$ A, which conforms to the $(\cos \theta_i)^{-1}$ dependence of bremsstrahlung calculated by HR for nonnormal electron incidence. This is because more scatters will occur close to the surface of the foils than in the case of normal incidence, resulting in a large number of photons escaping from the foil. Both the parallel and perpendicular components show the $(\cos \theta_i)^{-1}$ dependence.

An investigation of the energy dependence at $\theta_i = 80°$ (Fig. 14.3) for a 700-A silver foil exhibited a $1/E$ dependence for both the parallel and perpendicular components of the photon intensity. This $1/E$ dependence is typical of bremsstrahlung in this wavelength region and is predicted for grazing incidence electrons by the theory of HR.

The ratio of the parallel to the perpendicular polarization at the peak photon intensity in Fig. 14.3 is 4.5 at 80 kev, in excellent agreement with the ratio 4.6 calculated by HR.

The wavelength of maximum emission was observed to increase, up to 3600 A, as a function of foil thickness for grazing incidence electrons. This accounts for the wavelength of peak emission observed by Boersch ($\lambda = 3550$ A) for a thick silver film.

Aluminum foils 300 A thick were bombarded by 80-kev electrons at various angles of incidence to ascertain the presence of enhanced emission similar to that observed from silver foils. The maximum photon intensity for two experimental runs is plotted as a function of the angle of electron incidence in Fig. 14.4. In addition, the theoretical transition radiation, as calculated by Ashley[11] for a foil of finite thickness, is compared with the experimental results. Transition radiation intensity oscillates as a function of the angle of electron incidence due to the constructive and destructive interference of radiation originating at different depths in the foil. The oscillatory behavior of transition radiation in the experimental spectrum is not observable above $\theta_i = 75°$, due to the onset of a large bremsstrahlung component analogous to the bremsstrahlung peak seen in the silver optical emission spectrum for grazing incidence electrons.

The peak in the emission spectrum was seen to vary from 760 to 830 A as θ_i was increased from 20 to 89°. No peak was seen at 1200 A, the wavelength corresponding to the surface plasmon of aluminum.

We conclude from these results that the enhanced emission which arises when Ag and Al are bombarded by grazing incidence electrons is due to

[11] J. C. Ashley (to be published).

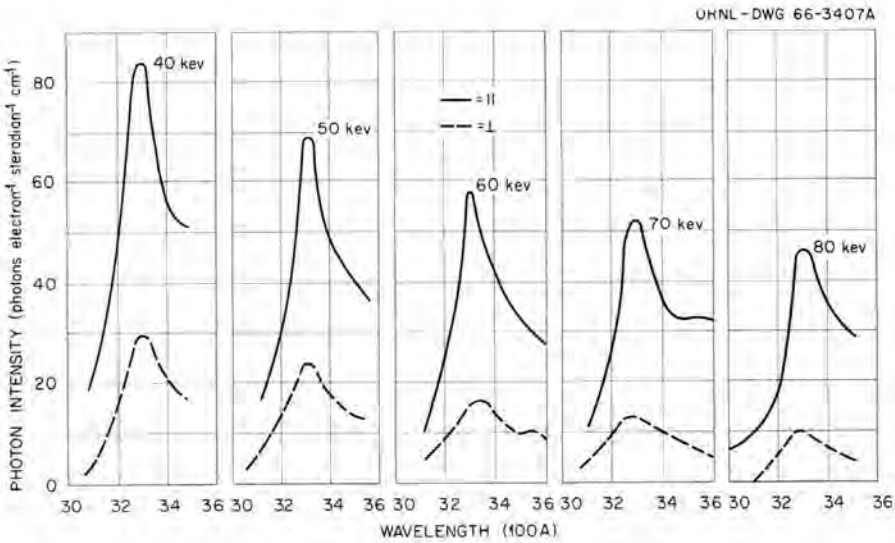

Fig. 14.3. Spectra of Light Emitted in the Parallel and Perpendicular Plane of Polarization from Thin (t = 700 A) Self-Supporting Silver Foils Bombarded by 40- to 80-kev Electrons at 80°.

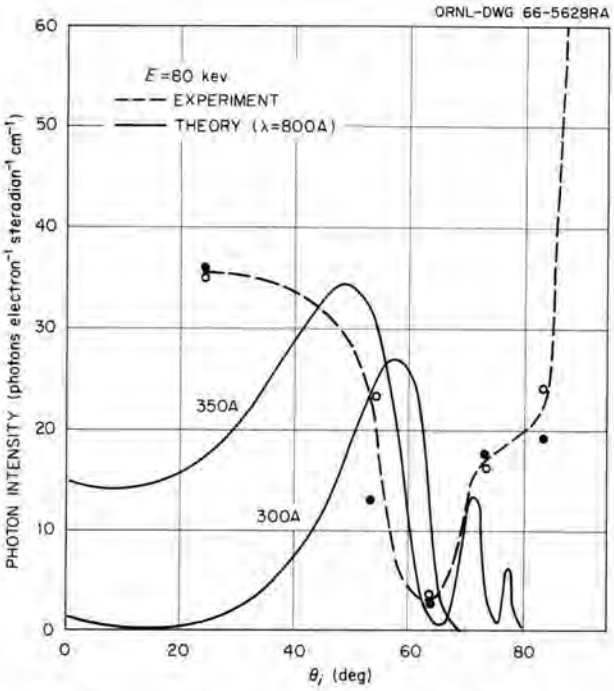

Fig. 14.4. Experimental and Theoretical Photon Intensities from Thin (t = 340 A) Self-Supporting Aluminum Foil as a Function of Angle of Electron Incidence. The experimental values have been multiplied by a factor of 10.

bremsstrahlung, and not from surface plasmons as suggested by Boersch *et al.*

REFLECTANCE OF EVAPORATED ALUMINUM FILMS IN THE WAVELENGTH REGION 800 TO 2000 A

Madden, Canfield, and Hass[12] have reported data on the normal incidence reflectance of aluminum films for wavelengths as low as 1025 A. We have extended these measurements through the critical region of rapidly changing reflectances to 790 A in vacua of about 3×10^{-8} torr. The composite results of our measurements and those of Madden *et al.* are presented in Fig. 14.5.

Due to the rapid oxidation of aluminum, even under ultrahigh vacuum conditions, it is necessary to plot reflectances as a function of time in order that extrapolations can be made to determine the "oxide-free" reflectances of the films. The arrows attached to the data points of Madden *et al.* represent the magnitude of the extrapolations relative to the first measured value. In our work, all extrapolations made amounted to an increase in reflectance of less than 1.5% for wavelengths lower than about 1000 A. For higher wavelengths no extrapolation was needed because the reflectances remained constant for as long as 6 min after the evaporation was completed. This behavior is attributed to the sharp onset of absorption by aluminum oxide for wavelengths below 1000 A. The essential difference between the two groups of experiments is in the pressure within the reflectance chamber. Our pressures were generally a factor of 10 below those of Madden *et al.*, so we considered the possibility of presenting the two sets of data on weighted time scales to compensate for this pressure difference. By reducing our times by a factor of 10, we find that the data match very well for long times after evaporation; however, there was disagreement between the values of the zero time reflectances which were chosen. It is not clear to us whether the reflectance for a particular wavelength of light should drop off as rapidly from zero time as described by Madden, or whether the reflectance

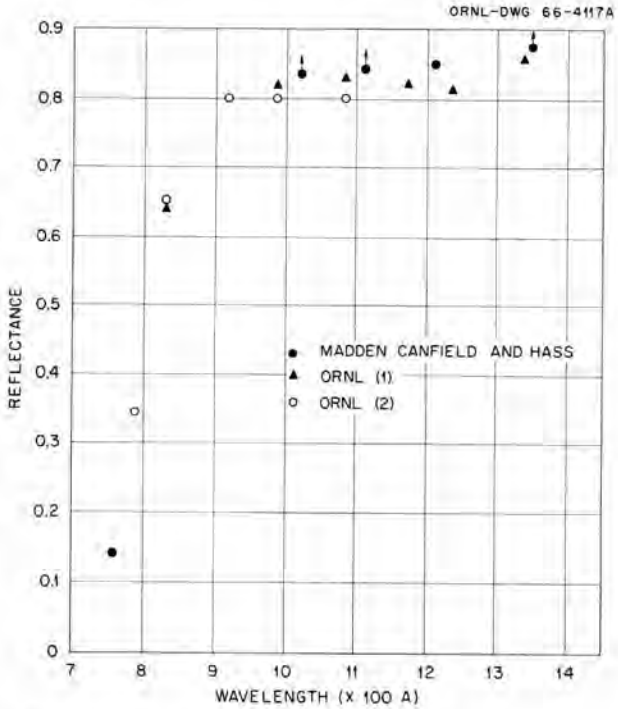

Fig. 14.5. Reflectance of Oxide-Free Aluminum Films Prepared by Vacuum Evaporation.

[12] R. P. Madden, L. R. Canfield, and G. Hass, *J. Opt. Soc. Am.* **53**, 620 (1963).

values might remain constant for a short time before falling off due to the oxidation of the sample as shown by our results. Finally, in agreement with the existing data, our results show evidence of a mode of absorption around 1250 A that can be attributed either to the excitation of surface plasmons in the metal or to the interband transitions x_1 to x_5' at 7.9 ev and x_4' to x_1 at 12.0 ev.

Using the free-electron model of metals it is possible to express the normal incidence reflectance of the metal in terms of two parameters, ω_p and τ, the plasma frequency and the relaxation time respectively. With $\omega_p = 835$ A the reflectance data for wavelengths in the near-ultraviolet and visible regions fit the model for which $\tau = 1.1 \times 10^{-15}$ sec. Our data show that in the region studied the value of τ for wavelengths below 1600 A drops to 0.7×10^{-15} sec at about 1350 A and remains essentially constant down to 800 A. Hunter[13] has reported that below 800 A the value of τ drops from 0.8×10^{-15} sec at 736 A to 0.6×10^{-15} sec at 584 A.

OPTICAL AND PHOTOELECTRIC PROPERTIES OF EVAPORATED Ag AND Al FILMS

The optical constants n and k have been obtained for an evaporated Ag film approximately 1000 A thick for photon energies between 4 and 25 ev. Peaks in the spectrum of the charged-particle-energy-loss function $-\mathrm{Im}\ (1/\epsilon)$ calculated from these values of n and k were found at 4.1, 7.3, and 17.2 ev and are in good agreement with similar data for bulk Ag[14] and the measured electron-energy-loss spectrum.[15]

The photoelectric yield curve for Ag shown in Fig. 14.6 exhibits a plateau between photon energies of 15 and 20 ev. This plateau is interpreted as being due to the onset of scattering of electrons corresponding to the broad loss near 18 ev observed in the spectrum of $-\mathrm{Im}\ (1/\epsilon)$ and the electron-energy-loss spectrum. The change in yield with time reflects the contamination of the surface due to slight oxidation or adsorption of diffusion pump oil at a pressure of 3×10^{-8} torr. Comparison of the ratio of the yields measured at an angle of incidence of 70° to the corresponding yields measured at 10° with the ratio of the secants of the corresponding angles of refraction indicates that the mean free path for electron-electron scattering in Ag is not extremely short compared with the photon attenuation length over most of the photon energy range studied. Analysis of the energy-distribution data, which yielded an estimate of the electron mean free path, verified the above result.

Photoelectron energy-distribution curves for photon energies of 14.9, 16.3, and 17.6 ev are shown in Fig. 14.7. The high-energy portion of the curves set off by the dashed lines is due to unscattered electrons excited from the d bands of Ag, where the density of electron states is high. The low-energy peaks in the curves for $h\nu = 14.9$ ev and $h\nu = 16.3$ ev are located about 4 ev below the high-energy peak; the low-energy peak in the curve for $h\nu = 17.6$ ev is located about 7 ev below the peak due to unscattered electrons.

These low-energy peaks have been attributed to losses of energy of about 4 and 7 ev, respectively, by electrons excited from the d bands of Ag. These losses agree with losses observed in both optical measurements and electron-energy-loss measurements using fast electrons. Fitting the energy-distribution curves calculated from the density of

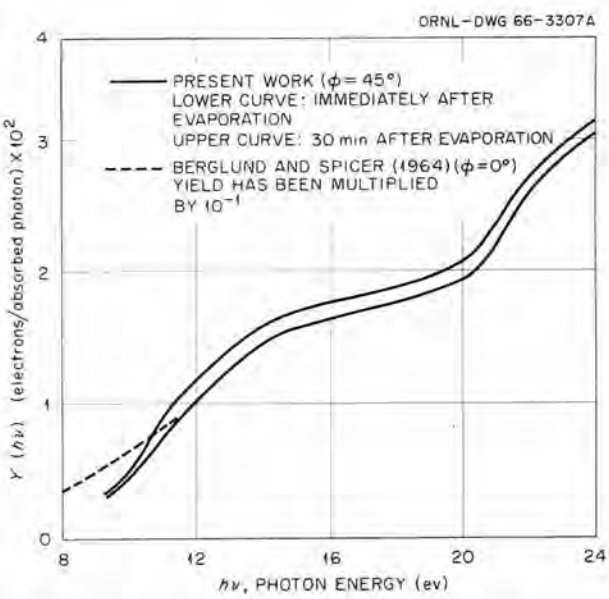

Fig. 14.6. Photoelectric Yield of Evaporated Silver for 45° Angle of Incidence, Showing Change in Yield with Time.

[13] W. R. Hunter, *J. Opt. Soc. Am.* **54**, 208 (1964).

[14] H. Ehrenreich and H. R. Philipp, *Phys. Rev.* **128**, 1622 (1962).

[15] J. L. Robins, *Proc. Phys. Soc. (London)* **78**, 1177 (1961).

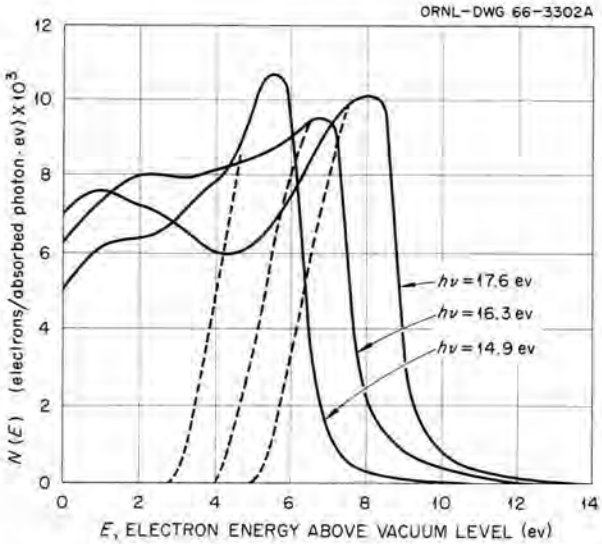

Fig. 14.7. Photoelectron Energy Distributions for Evaporated Silver for Photon Energies of 14.9, 16.3, and 17.6 ev with Estimate of the Portion of the Curve Due to Unscattered Electrons.

states according to the theory of Berglund and Spicer[16] to the measured curves resulted in the assumption of a more narrow peak in the *d*-band portion of the density-of-states curve than that indicated by Berglund and Spicer.

The photoelectric yields of oxide-free aluminum films were obtained for photon energies between 9 and 20 ev by extrapolating measurements of yield vs time to zero time. The yields were corrected for reflection using reflectance data for freshly evaporated films. Yield curves thus obtained are shown in Fig. 14.8, where it is seen that the yield decreases rapidly with photon energy beyond $h\nu$ = 10 ev, even though the photon absorption coefficient is practically constant out to 13 ev. This rapid decrease in yield is attributed to the loss of emitted electrons due to scattering by plasmon excitation at the surface of the film, in agreement with the results of Garber, Nakai, and Birkhoff.[17] An initial decrease of the yields with time for photon energies less than about 11.5 ev is interpreted as being due to the lowering of the surface-plasmon energy from 10.5 to about 7 ev by the presence of oxide on the surface; this results in a loss of electrons due to scattering at the lower photon energies.

The results of photoelectron-energy-distribution measurements on Al, obtained at a pressure of 3×10^{-8} torr for photon energies of 9.9, 12.4, 13.3, and 17.9 ev are shown in Fig. 14.9. The parabolic

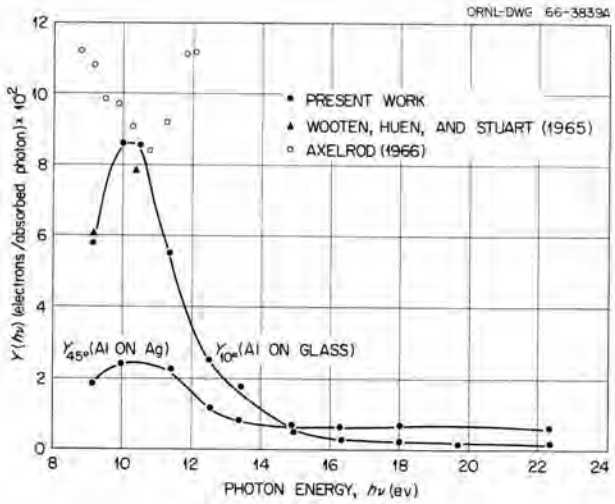

Fig. 14.8. Photoelectric Yields of Evaporated Aluminum Obtained by Extrapolation of Yield-vs-Time Data to Zero Time.

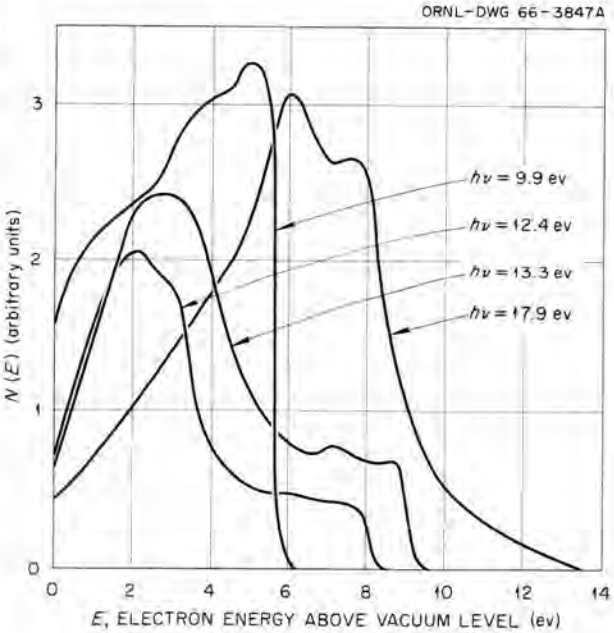

Fig. 14.9. Photoelectron Energy Distributions for Evaporated Aluminum for Photon Energies of 9.9, 12.4, 13.3, and 17.9 ev.

[16] C. N. Berglund and W. E. Spicer, *Phys. Rev.* **136**, A1044 (1964).

[17] F. W. Garber, Y. Nakai, and R. D. Birkhoff, *J. Phys. Chem. Solids* **26**, 1621 (1965).

shape of the energy-distribution curve for $h\nu = 9.9$ ev, characteristic of the free-electron nature of aluminum, is replaced at the higher photon energies by a shape resulting from the excitation of photoelectrons within the thin layer of oxide on the surface of the aluminum. If information about the electronic properties of aluminum for photon energies greater than about 10 ev is to be obtained for such measurements, the rate at which the measurements can be made must be increased or the measurements must be carried out under considerably better vacuum conditions than those obtained in the present study.

OPTICAL AND ELECTRONIC PROPERTIES OF TIN

The energy-dependent refractive index, $n(E)$, and the extinction coefficient, $k(E)$, have been determined in the energy region 5 to 14.5 ev from reflectance measurements made at 20 and 70° angles of photon incidence. In addition $n(E)$ has been determined in the energy region 14.5 to 27.5 ev by the critical angle method and combined with Hunter's[18] values of $k(E)$ obtained from transmission measurements in this energy region. These data and previously published data in the energy range 0.1 to 5 ev have been analyzed. Golovashkin and Motulevich's[19] values for n and k, determined from the change in polarization of radiation reflected from tin films, have been used in the energy range 0.1 to 1.33 ev. There are no recent determinations of the optical constants of tin in the energy range 1.3 to 5.0 ev, and a survey was made of the available data. We have used the values of k determined from transmission measurements by Smakula[20] and values of n determined from observations on the reflection of polarized light from molten tin by Erochin.[21] The real and imaginary parts of the energy-dependent dielectric constant $\epsilon(E) = \epsilon_1(E) + i\epsilon_2(E)$ were calculated from $\epsilon_1(E) = n^2 - k^2$ and $\epsilon_2(E) = 2nk$ and are plotted in Fig. 14.10 over the whole energy range 0.1 to 27.5 ev. In order to utilize logarithmic plots, the quantities $[1 - \epsilon_1(E)]$ and $[1 + \epsilon_2(E)]$ are shown as a function of energy.

It has been shown[22] that the complex dielectric constant of a metal can be written as

$$\epsilon(E) = \epsilon^{(f)}(E) + \delta\epsilon^{(b)}(E) , \qquad (1)$$

where $\epsilon^{(f)}(E)$ is the contribution due to free electrons and $\delta\epsilon^{(b)}(E)$ is that due to bound electrons.

From the free-electron theory we can express $\epsilon^{(f)}(E)$ in the following form:

$$\epsilon^{(f)}(E) = 1 - \frac{E_{pa}^{\ 2}}{E[E + (i\hbar/\tau)]} , \qquad (2)$$

where

$$E_{pa} = \hbar \left(\frac{4\pi N\, n_{\text{eff}} e^2}{m_{\text{eff}}} \right)^{1/2}$$

is the free-electron volume plasma energy, τ is the relaxation time, N is the atom density of the crystal, m_{eff} the effective mass of the electrons, and n_{eff} the effective number of electrons per atom contributing to the optical properties at energies below the threshold for transitions between electronic bands. X-ray absorption measurements show that tin has two $5p$ electrons in the valence band and two $5s$ electrons in a (overlapping) band at approximately 1.4 ev. The next lowest bands are $4d$ bands at 23.9 and 24.4 ev.[23] Thus, the free-electron formula for ϵ should be valid for energies below the threshold for transitions between bands, or below about 1.4 ev in tin.

We have assumed free-electron behavior at 0.1 ev. The following equations:

$$\epsilon_1(\text{exp}) = \epsilon_1^{(f)}(E) + \delta\epsilon_1^{(b)}(E)$$

$$= 1 - \frac{E_{pa}^{\ 2}}{E^2 + (\hbar/\tau)^2} + \delta\epsilon_1^{(b)}(E) \qquad (3)$$

$$\epsilon_2(\text{exp}) = \epsilon_2^{(f)}(E) + \delta\epsilon_2^{(b)}(E)$$

$$= \frac{\hbar}{\tau E}\left[\frac{E_{pa}^{\ 2}}{E^2 + (\hbar/\tau)^2}\right] + \delta\epsilon_2^{(b)}(E) \qquad (4)$$

[18] K. Codling *et al.*, *J. Opt. Soc. Am.* **56**, 189 (1966); W. R. Hunter, *Optical Properties and Electronic Structure of Metals and Alloys*, ed. by F. Abelès, p. 136, North Holland, Amsterdam, 1966.

[19] A. I. Golovashkin and G. P. Motulevich, *Soviet Phys. JETP* **20**, 44 (1965).

[20] A. Smakula, *Z. Physik* **88**, 114 (1934).

[21] P. Erochin, *Ann. Physik* **39**, 213 (1912).

[22] H. Ehrenreich and H. R. Philipp, *Phys. Rev.* **128**, 1622 (1962).

[23] A. E. Sandström, *Handbuch der Physik*, vol. 30, p. 226, 1957.

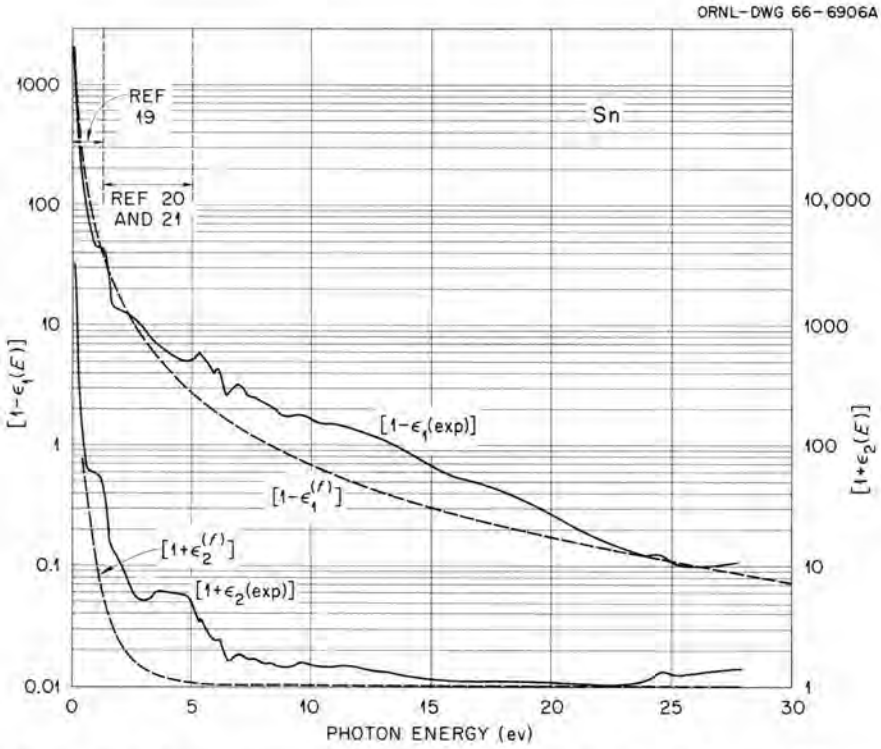

Fig. 14.10. Comparison of Experimental and Theoretical Values of ϵ_1 and ϵ_2 for Tin. In order to utilize a logarithmic scale, the quantities $[1 - \epsilon_1(E)]$ and $[1 + \epsilon_2(E)]$ are plotted.

for the experimental values of ϵ_1 and ϵ_2 then yield $E_{pa} = 8.3$ ev and $\tau = 4.1 \times 10^{-15}$ sec with $\delta\epsilon_1^{(b)}(E) = \delta\epsilon_2^{(b)}(E) = 0$ at 0.1 ev. With m_{eff} put equal to the free-electron mass, $n_{eff} = 1.36$. Electrical conductivity measurements also indicate that n_{eff} is much less than 4, the number of valence electrons usually assumed for tin. This indicates the existence of a zone which contains about four states per atom.[24]

In order to show the energies at which interband transitions occur, $\delta\epsilon_1^{(b)}(E)$ and $\delta\epsilon_2^{(b)}(E)$, calculated from Eqs. (3) and (4) with $E_{pa} = 8.3$ ev and $\tau = 4.1 \times 10^{-15}$ sec, are plotted as a function of energy in Fig. 14.11. The calculated values of $[1 - \epsilon_1^{(f)}(E)]$ and $[1 + \epsilon_2^{(f)}(E)]$ are also compared with the experimental quantities in Fig. 14.10. It is seen that there is a well-defined interband transition identified by a zero in $\delta\epsilon_1^{(b)}(E)$ and a maximum in $\delta\epsilon_2^{(b)}(E)$ at (1.2 ± 0.1) ev. This interband transition corresponds to the O_I x-ray absorption edge.

At higher energies the structure in $\delta\epsilon_1^{(b)}(E)$ and $\delta\epsilon_2^{(b)}(E)$ is more complicated, since more than one interband transition contributes to the calculated values of the real and imaginary parts of the dielectric constant due to bound electrons. The most recent measurements of the transmittance of tin films[18] locate the N_{IV} and N_V x-ray absorption edges at (24.9 ± 0.1) ev and (23.8 ± 0.1) ev respectively. These $4d$ to $5p$ electron transitions are unresolved in Fig. 14.11 at 24.5 ev.

The energy loss functions $-\mathrm{Im}\,(1/\epsilon)$ and $-\mathrm{Im}\,[1/(\epsilon + 1)]$ for volume and surface plasmons,[25] respectively, were calculated from the experimentally determined values of ϵ_1 and ϵ_2 (Fig. 14.10) and are plotted vs photon energy in Fig. 14.12. These functions describe the probability that fast electrons traversing the material will lose energy due to induced volume and surface collective electron oscillations respectively. Ritchie[25] predicts that the surface, or lowered, plasma loss should occur at $E_p/\sqrt{2}$ for a plane film, where E_p is the observed volume plasma loss.

[24] N. F. Mott and H. Jones, *The Theory of the Properties of Metals and Alloys*, Dover Publications, Inc., New York, 1958.

[25] R. H. Ritchie, *Phys. Rev.* **106**, 874 (1957).

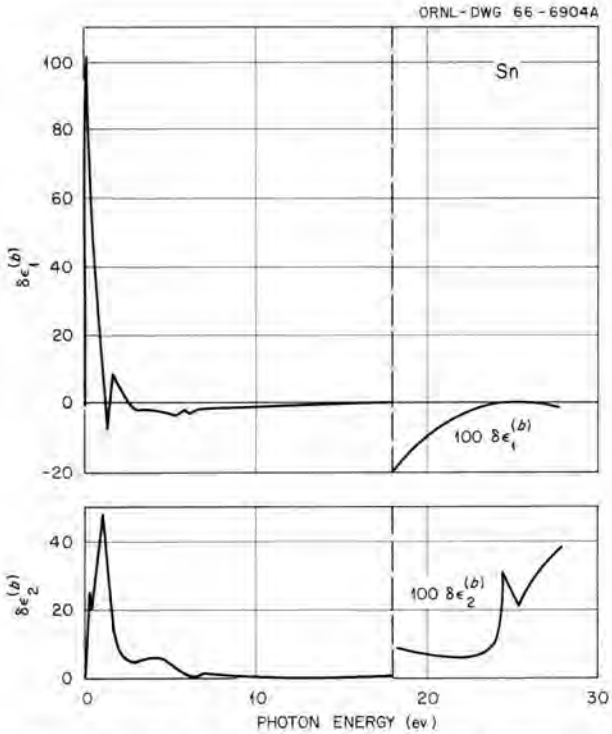

Fig. 14.11. Contributions to ϵ_1 and ϵ_2 Due to Bound Electrons, $\delta\epsilon_1^{(b)}$ and $\delta\epsilon_2^{(b)}$, Respectively, as a Function of Photon Energy.

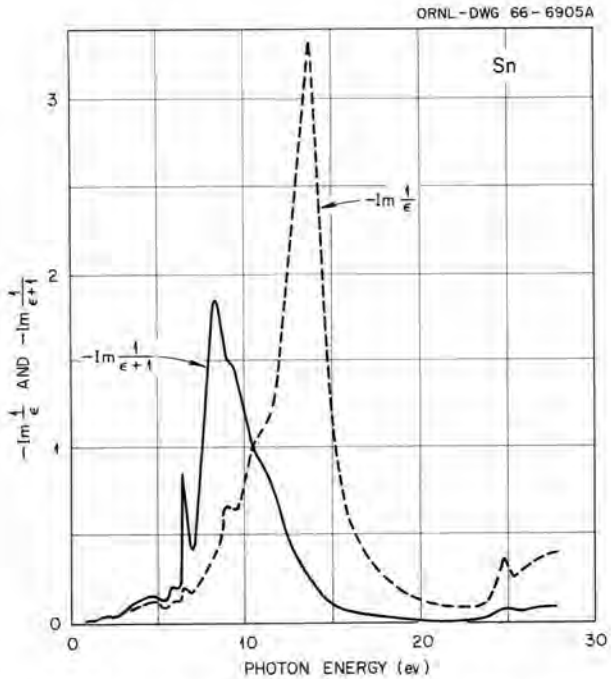

Fig. 14.12. Energy Loss Function, $-\mathrm{Im}\,[1/(\epsilon+1)]$ for Surface Plasmons and $-\mathrm{Im}\,(1/\epsilon)$ for Volume Plasmons, of Tin as a Function of Photon Energy.

In Fig. 14.12 the $-\mathrm{Im}\,(1/\epsilon)$ function shows a sharp maximum at 13.8 ev, and the $-\mathrm{Im}\,[1/(\epsilon+1)]$ function a sharp maximum at 8.5 ev. The sharpness of these maxima indicates that both energy losses should be observed when fast electrons traverse tin films. Characteristic electron energy losses have been observed in tin by Powell[26] at 14.1 and 10.4 ev, with surface oxidation causing the replacement of the 10.4 ev low-lying loss by a modified low-lying loss at (8.3 ± 0.2) ev. The agreement of the maximum of the volume plasma loss function at 13.8 ev with the 14.1 ev electron energy loss observed by Powell is satisfactory. Furthermore, the optical data unambiguously identify this characteristic electron energy loss as due to induced volume electron plasma oscillations, since in this energy region ϵ_1 goes through zero and ϵ_2 is small and shows no structure.[27] If the loss were due to an induced interband transition there would be a relative maximum in ϵ_2. Similarly the maximum of the surface plasma loss function at 8.5 ev is seen to agree with the modified low-lying loss observed by Powell with an oxide layer on the surface of the tin. This is identified as a surface plasma loss for the same reasons as the volume plasma loss since ϵ_1 passes through -1 and ϵ_2 shows no structure in this region. The observed position of this loss is lower than the predicted value $13.8/\sqrt{2} = 9.8$ ev because of surface oxidation.

The observed volume plasma energy, E_p, is displaced from $E_{pa} = 8.3$ ev to $E_p = 13.8$ ev because of the negative value of $\delta\epsilon_1^{(b)}(E)$ in this energy range (Fig. 14.11). Alternatively, we can say that at higher energies there is a greater density of free electrons. At energies well above 1.2 ev, in the region of E_p, all four valence electrons in tin should behave as if they are free or almost free. That this is so is seen from the observed $E_p = 13.8$ ev compared with the theoretical value of 14.3 ev obtained from Eq. (2) with $n_{\mathrm{eff}} = 4$ and m_{eff} put equal to the free-electron mass.

OPTICAL AND ELECTRONIC PROPERTIES OF SODIUM IN THE WAVELENGTH REGION 420 TO 2000 A

The index of refraction, n, of sodium films evaporated onto quartz substrates has been determined

[26] C. J. Powell, *Proc. Phys. Soc. (London)* **A68**, 525 (1955).

[27] H. Frölich and H. Pelzer, *Proc. Phys. Soc. (London)* **A68**, 525 (1955).

in the spectral region between 420 and 2000 A from interference patterns in the reflected beam and from the critical angle marking the onset of near total reflection.[28] Both these effects are shown in Fig. 14.13 for a film 4500 A thick, confirming the high transparency of Na in this wavelength region. The net phase change resulting from reflections at the front and back surface of the film is 0.3π, a result which is independent of wavelength. The growth of an oxide layer on the surface of a film was shown not to alter the position of interference maxima and minima.

We have shown that the extinction coefficient, k, is of the order of 0.015 in the wavelength region 420 to 2000 A. Thus $k^2 \ll n^2$, and the real part of the dielectric constant $\epsilon_1 = n^2 - k^2$ can be calculated from the values of n. In Fig. 14.14 our values of ϵ_1 are plotted vs wavelength squared. The solid line shown in the figure is the result expected for an ideal free-electron metal of the same density as sodium. The fact that the experimental points lie above this line indicates that the optical properties of sodium are slightly influenced by other processes, namely interband transitions. The theoretical expression for ϵ_1 is:

$$\epsilon_1 = 1 - \frac{\lambda^2}{\lambda p^2} + \delta(\lambda) .$$

The free-electron plasma wavelength, λp, is equal to $(\pi m^* c^2/Ne^2)^{1/2}$, where m^* is the reduced electron mass in the conduction band, equal to 0.98 times the mass of free electron in the case of sodium, N is the density of free electrons, and c and e have their usual meanings. The interband contribution is represented by the term $\delta(\lambda)$. Structure can be seen in the values of $\delta(\lambda)$, obtained by subtraction of the calculated free-electron value of ϵ_1 from the experimental value. The point B shown in Fig. 14.14 is the highest energy direct transition possible between the conduction band and the first unoccupied band. Figure 14.14 shows that for long wavelengths $\delta(\lambda)$ is approximately constant. However, as the point B is approached, δ decreases. For the shortest wavelengths shown in Fig. 14.14, δ again increases. This increase is associated with the threshold for excitation of core (L_{III}) electrons, which occurs at 405 A, only 15 A below our lowest measurement.

[28] W. R. Hunter, *J. Opt. Soc. Am.* 54, 15 (1964).

Confusion exists in the comparison of the plasma energy obtained from electron-energy-loss data with that obtained from optical measurements and with the theoretical value of the free-electron plasma energy. The data presented in Fig. 14.14 show clearly the nature of the difficulty. Two distinct plasma energies can be obtained from the data in this figure. The free-electron plasma energy,

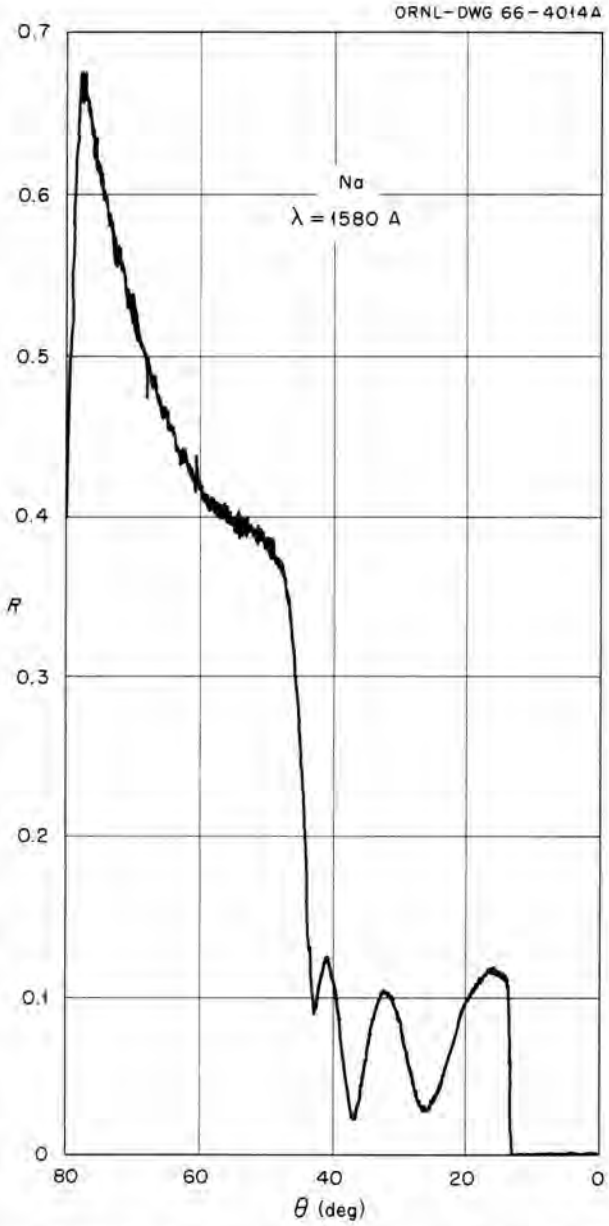

Fig. 14.13. Measured Reflectance vs Angle of Incidence of an Interference Fringe in the Region of Near-Total Reflectance.

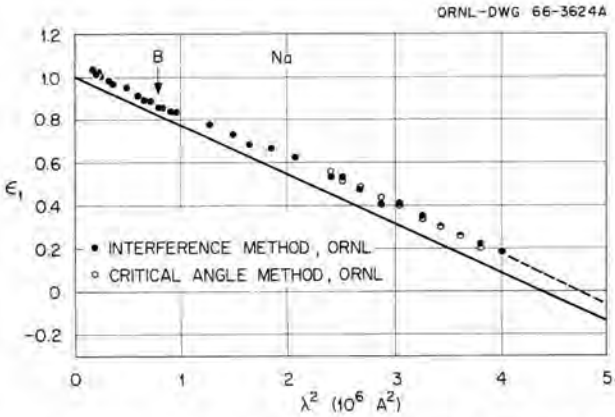

Fig. 14.14. Real Part of the Dielectric Constant vs Wavelength Squared. The solid line is the value of the real part of the dielectric constant expected from a free-electron metal, while the dashed line indicates extrapolation used to determine the wavelength at the real part of the dielectric constant equal to zero.

$\hbar\omega p$(free), is determined from the slope of ϵ_1 vs λ^2 in a wavelength region in which $\delta(\lambda)$ is constant. The effective plasma energy, $\hbar\omega p$(eff), is determined from the wavelength at which $\epsilon_1 = 0$. Clearly $\hbar\omega p$(free) is equal to $\hbar\omega p$(eff) only if $\delta(\lambda) = 0$.

In the data shown in Fig. 14.14, $\delta(\lambda)$ is approximately constant in the region from $\lambda^2 = 2 \times 10^6$ A^2 to 4×10^6 A^2, and $\hbar\omega p$(free) determined from the slope of a line fitted to the experimental points in this region is 5.97 ± 0.05 ev. This value must be compared with the theoretical value of 5.968 ev. The effective plasma energy, $\hbar\omega p$(eff), determined from the extrapolation shown as a dashed line in Fig. 14.14, is 5.69 ± 0.03 ev, in agreement with the value of 5.70 ± 0.05 ev measured in the energy-loss experiment of Kunz.[29]

ELECTRON SLOWING-DOWN SPECTRA IN ALUMINUM

Electron slowing-down spectra in aluminum have been obtained using alloys of the following compositions by weight: 1% Cu, 99% Al; 1% Au, 99% Al; and 5% Pd, 95% Al. All the sources were made of nonradioactive alloys and neutron-activated to produce radioactive ^{64}Cu, ^{198}Au, and ^{109}Pd, which provided uniformly distributed electron sources in the aluminum.

Figure 14.15 shows the electron flux resulting in aluminum from the slowing down of the beta rays from ^{64}Cu. Copper-64 decays by positron emission with an end-point energy of 660 kev and negatron emission with an end-point energy of 570 kev. The experimental flux varies from a maximum of 2.5×10^{-3} electrons cm^{-2} ev^{-1} per primary electron per cubic centimeter at 17 ev above the bottom of the conduction band to a minimum of 5×10^{-8} at 20 kev. The experimental flux is 50% higher than theory at the highest energies and more than an order of magnitude higher at lower energies.

Figure 14.16 shows the electron flux in aluminum from the slowing down of ^{198}Au beta rays. Gold-198 decays by negatron emission with an end-point energy of 1 Mev. The experimental flux varies from a maximum of 8.5×10^{-4} at 15 ev to a minimum of 6×10^{-8} at 13 kev. Again the experimental flux is 50% higher than theory at the highest energies and more than an order of magnitude higher at lower energies.

Figure 14.17 shows the electron flux in aluminum resulting from the slowing down of ^{109}Pd beta

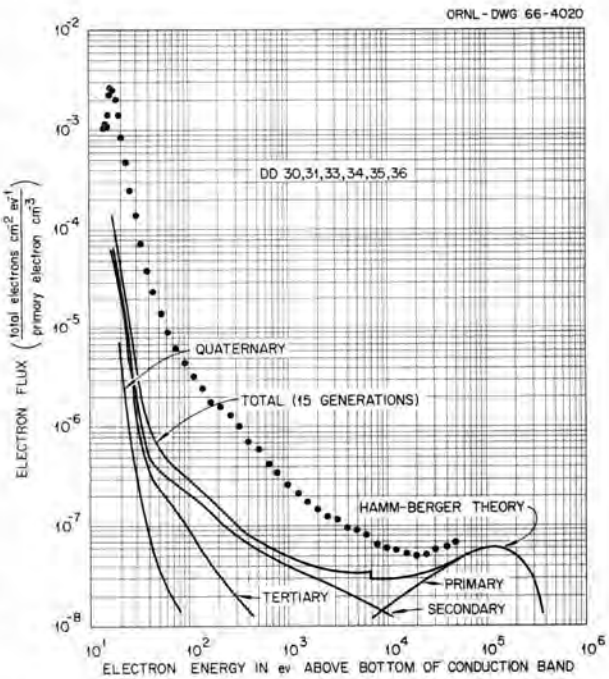

Fig. 14.15. Electron Flux Spectrum Resulting from ^{64}Cu Beta Rays Absorbed in Al-Cu Alloy (99% Al, 1% Cu by Weight).

[29] C. Kunz, *Phys. Letters* 15, 312 (1965).

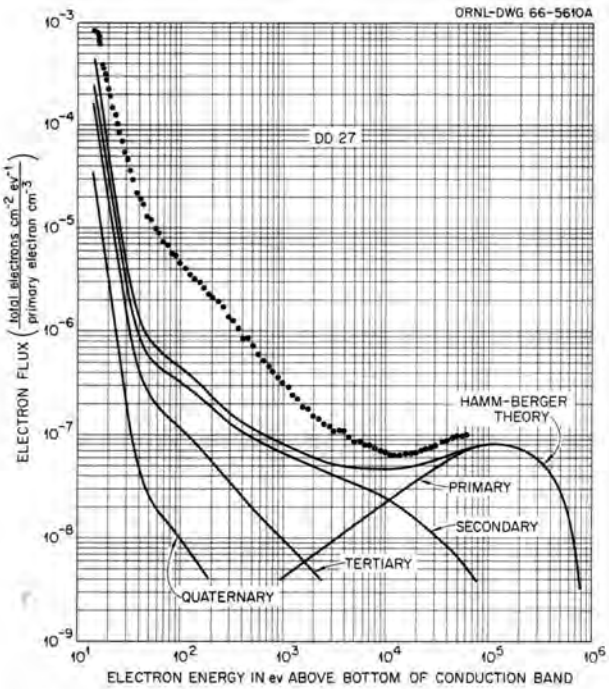

Fig. 14.16. Electron Flux Spectrum of ^{198}Au Beta Rays Absorbed in Aluminum (1% Au, 99% Al).

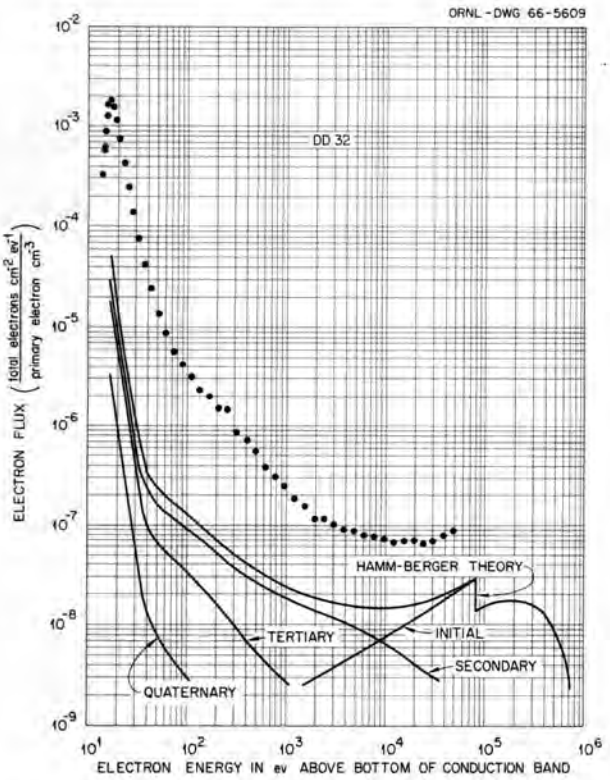

Fig. 14.17. Electron Flux Spectrum of ^{109}Pd Beta Rays Absorbed in Aluminum (5% Pd, 95% Al).

rays. Palladium-109 decays by negatron emission with an end-point energy of 1 Mev to ^{109m}Ag. Silver-109*m* decays by emission of an 88-kev gamma ray, which is converted in the *K* and *L* shells in 92% of the transitions, giving rise to conversion electrons with energies of 63 and 84 kev respectively. The vacancies in the *K* and *L* shells cause an Auger cascade. The experimental flux varies from a maximum of 1.8×10^{-3} at 17 ev to a minimum of 6×10^{-8} at 20 kev. In this case the experimental flux is a factor of four above theory at the highest energies and more than an order of magnitude higher at lower energies.

Distributions of the electron flux as a function of linear energy transfer (LET) were obtained by recognizing that the flux Φ_1 in any energy interval dE can be associated with a flux Φ_2 in some LET interval dL thus:

$$\Phi_1(E)\, dE = \Phi_2(L)\, dL$$

and

$$\Phi_2(L) = \Phi_1(E) \frac{dE}{dL} .$$

Values of dE/dL were obtained from the electron stopping power in aluminum shown in Fig. 14.18. The dashed line is the Bethe-Bloch stopping power, and the solid line is a theory derived by Ritchie which includes electron-plasmon interactions and electron-electron interactions in the conduction band and electron-electron interactions in the *L* shell. Figure 14.19 shows the LET distribution of the electron flux resulting from the slowing down of ^{64}Cu beta rays in aluminum. The flux varies

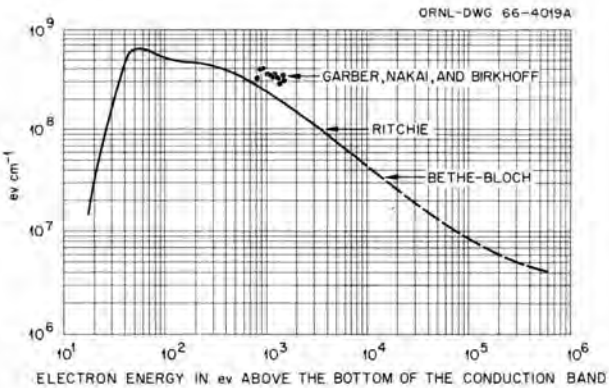

Fig. 14.18. Electron Stopping Power for Aluminum.

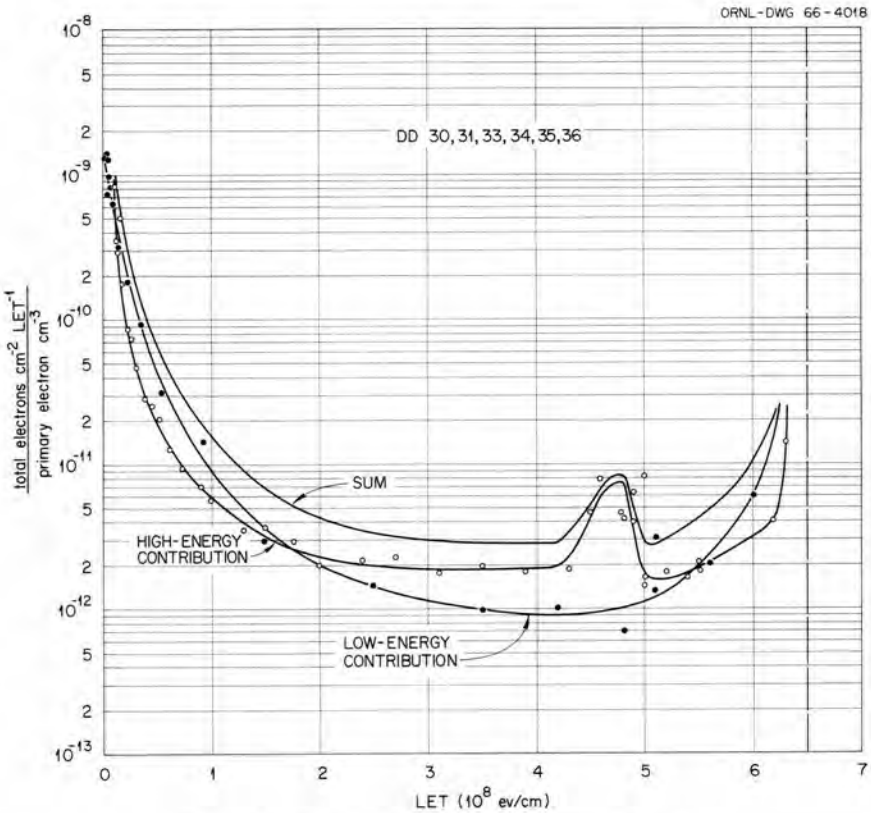

Fig. 14.19. LET Distribution of Electron Flux.

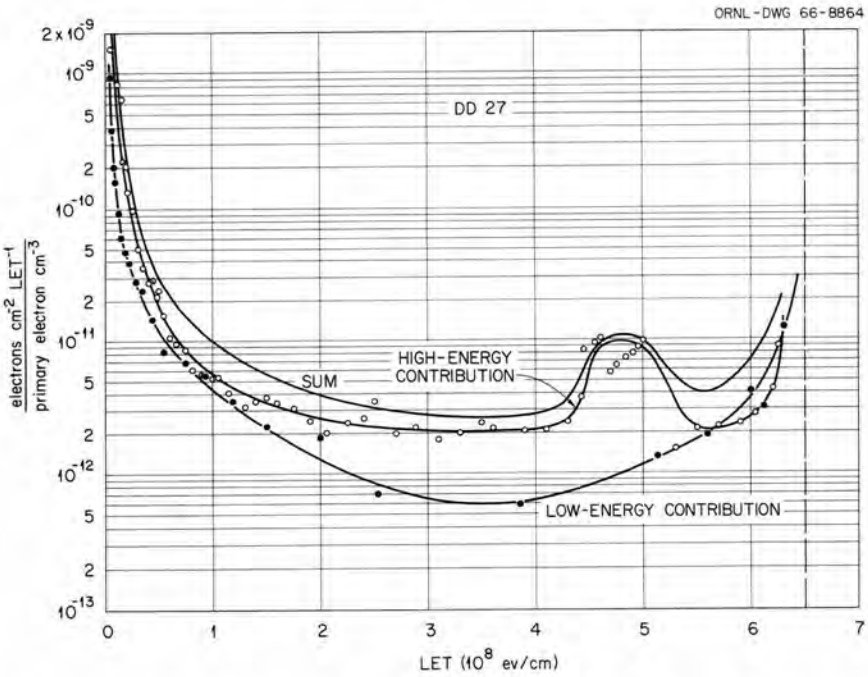

Fig. 14.20. LET Distribution of Electron Flux Resulting from ^{198}Au Beta Rays Absorbed in Aluminum.

from 1×10^{-9} electron cm^{-2} LET^{-1} per primary electron per cubic centimeter at 1×10^{7} ev/cm to 4×10^{-12} at 4×10^{8} ev/cm, peaks to 1×10^{-11} at 4.5×10^{8} ev/cm, and then rises as the maximum stopping power of 6.5×10^{8} ev/cm is approached. The LET distribution of the flux is the sum of two nearly equal contributions, one due to electrons with energy greater than 55 ev and another due to electrons with energy less than 55 ev, shown as the curves labeled "high-energy contribution" and "low-energy contribution" respectively. The peak at 4.5×10^{8} ev/cm is entirely due to the theoretical stopping power, which is nearly flat between 150 and 300 ev, causing a peak in dE/dL. Figures 14.20 and 14.21 show similar LET distribution for the AlAu and AlPd alloys. Figures 14.19 to 14.21 substantiate the assumption usually made in radiobiology that the electron spectrum in an irradiated medium is mono-LET in character.

A special source was constructed to test how well the space between two parallel, coaxial, closely spaced disks approximates a cavity in an infinite isotropic medium. Two aluminum disks, one containing ^{198}Au and one inert, were mounted in the electron spectrometer, first with the source disk and then the inert disk at the focal position. Electron flux spectra identical in magnitude and shape were measured, indicating that planar boundaries, shielding, and escape of electrons do not alter the assumption that measured fluxes are characteristic of those in an infinite isotropic medium. The results also support the energy-independent correction which has been applied for scattering from the disks and shields of the regular source.

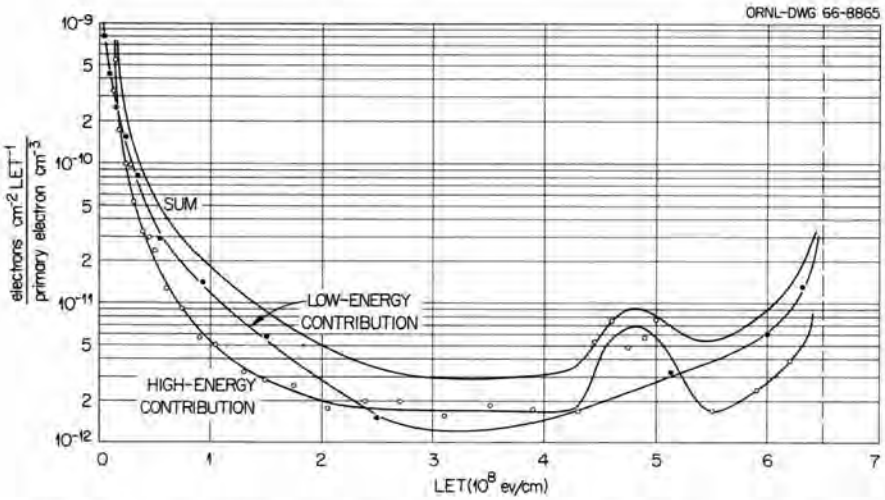

Fig. 14.21. LET Distribution of Electron Flux Resulting from ^{109}Pd Beta Rays Absorbed in Aluminum.

15. Professional Health Physics Training

K. Z. Morgan[1] M. F. Fair[2]

Sixteen fellowship students reported to the Division in June for summer training. Thirteen of the Fellows were supported by the Atomic Energy Commission and two by the U.S. Public Health Service. One student was an alien from Egypt. The first week was spent in the ORAU Special Training Division and the second week at ORNL in a program of orientation. The remainder of the training period included five weeks with the research groups and five weeks in applied health physics.

In the applied health physics training, the student gains practical experience in all phases of radiation protection under the supervision of a senior health physicist. The student learns of all the radiation protection services that are provided for the Physics Division, Reactor Chemistry Division, Metals and Ceramics Division, Solid State Division, Chemical Technology Division, Rolling Mill, Tracer Facilities, High Level Radiochemical Development Laboratory, Fission Products Pilot Plant, Waste Disposal Group, Isolation Laboratory, Pilot Plant Operations, and the Ecology Research Group. In addition, they learn of personnel monitoring, instrument calibration, counting facilities, bioassay techniques, and whole-body counters.

In health physics research, the students are first given a brief summary of all the research projects which are in progress in the Division. They then choose the group in which they will remain for the five-week period doing basic research under senior scientist supervision. The fields of investigation include: interaction of radiation with gases, solids, and matter; theoretical radiation physics; health physics research reactor; dosimetry; radioactive waste disposal; and radiation ecology.

It is felt that during this first summer the student is given sufficient experience in applied health physics to enable him to take a position in this field. Also, he learns of the tremendous breadth in research health physics and is made aware of the diverse problems available for thesis work should he decide to continue his education for the Ph.D. degree under the fellowship.

The course in General Health Physics (Physics 472–473) at the University of Tennessee was completed. This was a two-quarter course which met 3 hr/week. There were five AEC Fellows, two U.S. Public Health Service Fellows, one student from Yugoslavia, and one from the Nuclear Engineering Department.

The course in Applied Radiation Physics (Physics 234) at Vanderbilt University was also completed. This was a one-semester course which met 4 hr/week. There were eight AEC Fellows.

Seventeen students were selected for the 1966–67 Fellowship Program. Eleven will enroll at Vanderbilt University and six at the University of Tennessee in September 1966.

Universities and colleges at which ORNL health physics research and educational activities were discussed are listed below:

Appalachian State College
Augsburg College
Bethany Nazarene College
Carleton College
Catawba College
Central State College
Coe College
Converse College
Cornell College
Murray State College
Purdue University
Roanoke College
Rutgers University
Southern Missionary College
St. Johns University
University of Louisville

[1]Acting Chief, Education and Training Department.
[2]Assistant Chief, Education and Training Department.

The Citadel
Davidson College
Florida State University
Florida Atlantic University
Furman University
Georgia Institute of Technology
Howard College
Lenoir Rhyne College
Macalester College
Mississippi State University
University of Michigan
University of Missouri
University of South Florida
University of Tennessee
University of Virginia
Vanderbilt University
Wofford College

One member of the Radiation Physics Section spent part of his time with the University-ORNL Co-Op Program in setting up a new graduate curriculum at the University of Tennessee. This new course of study includes, in addition to the General Health Physics course, one-quarter courses entitled Radiation Chemical Physics, Radiation Biology, Physics of Polyatomic Molecules, Interaction of Electrons with Solids, and Interaction of Radiation with Matter. These new courses will be taught by University of Tennessee faculty members and by members of the Radiation Physics Section on loan to the University of Tennessee. It is felt that the availability of this new curriculum leading to a Ph.D. in Radiation Physics will prove attractive to Health Physics Fellows who desire education beyond the master's level.

There were 22 Oak Ridge Graduate Fellows, AEC Fellows, and USPHS students in the Division working on theses as partial requirements for advanced degrees. Their theses titles and universities are listed below.

R. P. Blaunstein, "Electron Transport in Carcinogens" (Tennessee).

R. N. Compton, "Electron Capture Cross Sections and Negative Ion Lifetimes" (Tennessee).

W. G. Connor, "Semi-Classical Model of the Photoelectric Effect in Metals" (Vanderbilt).

L. S. Cram, "Investigation of the 'Surface Plasma' Radiation from Electron-Bombarded Ag" (Vanderbilt).

J. Crowell, "Positron Annihilation in an Electron Gas" (Vanderbilt).

H. W. Dickson, "Measurement of Electron Attachment Coefficients in Hydrogen Halides and Water-Bromobenzene Mixtures" (Tennessee).

F. W. Garber, "Electronic Energy Levels in Al and Silver" (Tennessee).

W. F. Hanson, "Investigation of Plasma Radiation from Electron-Bombarded Aluminum Foils as a Function of Angle of Observation and Foil Thickness" (Vanderbilt).

W. G. Hendrick, "Electron Capture in Halogenated Benzene Derivatives – Effects of Temperature Changes" (Tennessee).

R. J. Herickhoff, "Characteristic Energy Loss Studies of Electron-Bombarded Al, Cd, In, Mg, and Zn Foils with Vacuum Ultraviolet Spectroscopy" (Vanderbilt).

H. J. Howe, "Transition Radiation and Low-Energy Bremsstrahlung" (Vanderbilt).

R. H. Huebner, "Optical Constants of Evaporated Metal Films of Silver and Indium" (Vanderbilt).

T. M. Jelinek, "Optical Properties of Evaporated Films of Cadmium, Thallium, and Zinc in the Vacuum Ultraviolet" (Vanderbilt).

D. R. Nelson, "Lifetime of Electrons on Polyatomic Molecules" (Tennessee).

J. E. Parks, "Studies of Electron Transport in Gases, Using Time-of-Flight Swarm Methods" (Tennessee).

H. L. Pray, "Low-Energy Electron Studies in Tl, Mg, and In" (Tennessee).

Linda L. Robinson, "Optical Reflectivity of Water in the Vacuum Ultraviolet" (Tennessee).

J. L. Stanford, "Photoelectric and Optical Properties of Commercial Pt, Au, and Pd Foils and Evaporated Al and Ag Films in the Extreme Ultraviolet" (Tennessee).

J. C. Sutherland, "The Optical Properties of Sodium in the Vacuum Ultraviolet" (Georgia Institute of Technology).

L. H. Toburen, "Charge Exchange Cross Sections for Mev Protons in Various Gases" (Vanderbilt).

R. C. Vehse, "Reflectance of Evaporated Al Films in the Wavelength Region 800 – 2000 A" (Tennessee).

R. E. Wilems, "Collective Interactions in Solids" (Tennessee).

Eight research participants and four ORAU undergraduate students arrived in June to spend the summer in the Division.

Various members of the Division participated in the Traveling Lecture Program, the ORNL Orientation Program, and various other community activities.

The Division, in cooperation with ORAU, presented a ten-week course in health physics for state personnel sponsored by the Atomic Energy Commission. This was part of the overall AEC program to turn over to the individual states the responsibility for regulation and control of radioactive materials. Ten students completed the program.

Three 1-hr lectures in applied health physics were given to personnel of the Biology Division

at the request of the division director. Two 2-hr lectures were presented to the Institute on the Fundamentals of Radiation Protection at the Nashville Center of the University of Tennessee. A two-day lecture and tour program was arranged for the University of Arkansas Radiological Health Course. Two lectures were given for the Medical Radioisotopes Course at ORAU. Several lectures were given at the educational series of the East Tennessee Health Physics Society chapter.

The demands for education in health physics will continue to rise as they have in the past. Emphasis will be on education to the Ph.D. level to provide personnel for positions of leadership in industrial, academic, and medical institutions. Although the advanced program will be emphasized, education will continue to be offered during the summer at the master's level to provide vocational training which includes a knowledge of health physics principles and procedures.

16. Physics of Tissue Damage

R. D. Birkhoff

Ada E. Carter
J. G. Carter
L. G. Christophorou
M. Y. Nakai[1]
D. R. Nelson
H. L. Pray[2]
Linda L. Robinson[3]
E. K. Yeargers[4]

EXCIMER-SCINTILLATOR INVESTIGATIONS

The role of naphthalene in loaded scintillators[5] and the possible role of solvent excimers in enhancing energy transfer and/or enabling the solvent to resist the so-called "solvent quenching" by various materials, suggested that improved scintillators, particularly improved loaded and giant scintillators, might be obtained by using solvents like 2-ethylnaphthalene (2-EN) which form excimers in the liquid state and at room temperature.

Accordingly, various commonly used scintillator solutes in 2-EN oxygen-free solutions were excited by 230-kev x rays, and their emission intensities were observed with a Bausch and Lomb 500-mm grating monochromator. Figure 16.1 gives an example of the data obtained. A comparison was made of the integrated emission intensities, I_{int}, from the present results[6] with those (taken under identical conditions) of two popular liquid scintillators:[7,8] 8 g/liter *p*-terphenyl in toluene (system I), and 5 g/liter *p*-terphenyl + 0.5 g/liter 2,2-*p*-phenylenebis[5-phenyloxazole] (POPOP) in toluene (system II). The I_{int} for a 4.5-g/liter PPO (2,5-diphenyloxazole) in 2-EN + di-*n*-butylmercury (DBM) mixture is a strong function of the DBM

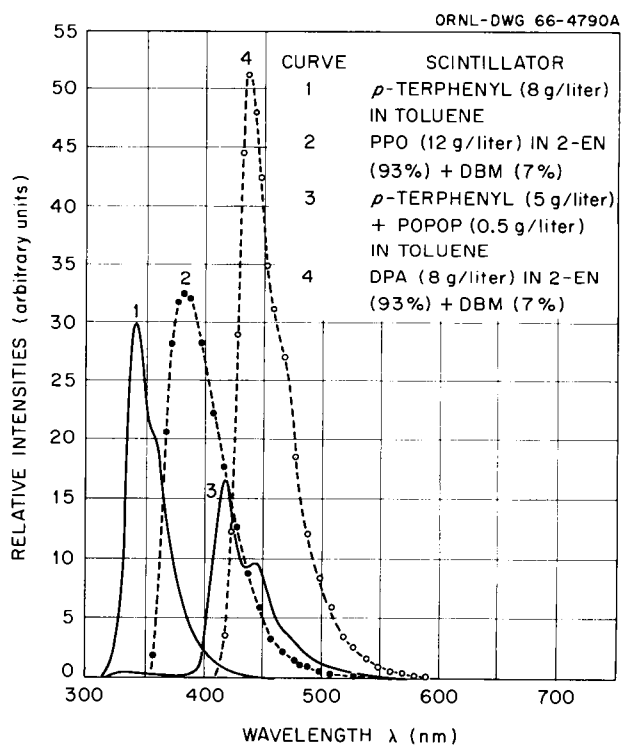

Fig. 16.1. Direct Comparison of the Emission Intensities of Liquid Scintillators.

[1]On loan from Thermonuclear Division.

[2]Radiological Health Physics Fellow.

[3]USAEC Health Physics Fellow.

[4]USAEC Postdoctoral Fellow.

[5]H. Kallmann, M. Furst, and F. H. Brown, *Nucleonics* 13(4), 58 (1955).

[6]I_{int} is a better physical quantity to compare scintillation efficiencies than the usual parameter, *T*, defined as the number of photoelectrons released from the photocathode due to the ionizing radiation.

[7]J. B. Birks, *The Theory and Practice of Scintillation Counting*, chap. 8, p. 269, Pergamon, New York, 1964.

[8]F. N. Hayes, *IRE Trans. Nucl. Sci.* **NS-5**(3), 166 (1958).

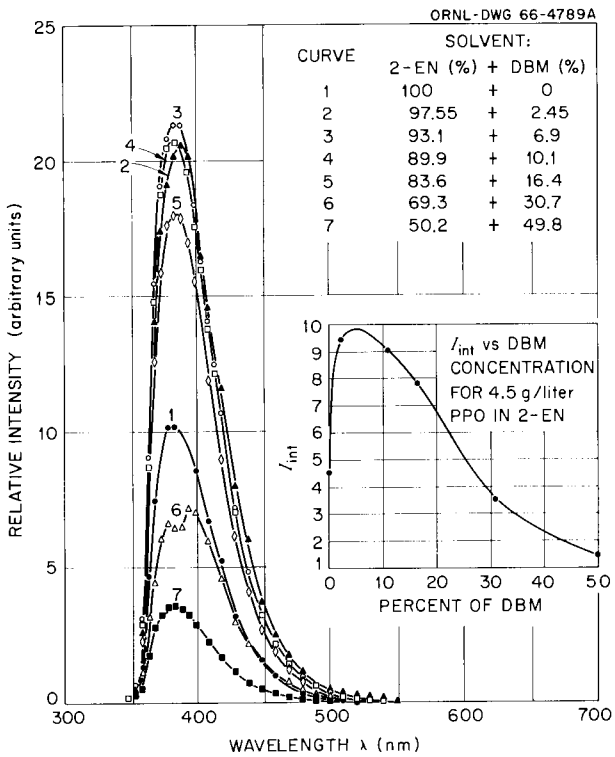

Fig. 16.2. 4.5 g/liter PPO in 2-Ethyl Naphthalene and Di-*n*-butylmercury Solutions.

concentration. Figure 16.2 shows the effect of DBM on the PPO (4.5 g/liter) emission in 2-EN solutions. Fluorescence emission from 2-EN itself is negligible in these mixtures. As can be seen from the inset of Fig. 16.2, I_{int} is maximum when the percentage of DBM (by mass) in 2-EN is ~7%. This maximum value of I_{int} is 1.65 times that of the popular system II [i.e., the overall emission from PPO (4.5 g/liter) in 2-EN (93%) + DBM (7%) is 1.65 times that from system II]. Keeping the percentage of DBM in 2-EN constant at 7% we increased the PPO concentration from 4.5 to 8 to 12 g/liter. The I_{int} increased from 1.65 to 2.23 to 2.5 (relative to the I_{int} of system II, which is taken equal to 1) respectively. System III, a mixture of PPO (18 g/liter) in 2-EN (89.1%) + DBM (10.9%), which has an electron density 1% higher than toluene, gave an I_{int} 2.4 times that of system II. Considering the excellent overlap between the PPO emission in system III [and system IV = PPO (12 g/liter) in 2-EN (93%) + DBM (7%)] with the cathode spectral response of commonly used photomultipliers (e.g., S_{11}), systems III and IV constitute practical, more efficient liquid scintillators.

Another, even more efficient, scintillating system than systems III and IV has been found: 8 g/liter DPA (diphenylanthracene) in 2-EN (93%) + DBM (7%) (system V). For system V, I_{int} is 310% of that of system II. The DPA emission in system V has a maximum at 4400 A (see Fig. 16.1), which allows use of the improved (over Al) reflectivity of TiO_2. Preliminary data indicate that an optimum combination of DPA and DBM in 2-EN can give a scintillating system with I_{int} at least 320% of that of system II. Other scintillator solutes in 2-EN + DBM mixtures are under investigation.

The present results promise better liquid scintillators. In this connection the following two points are important:

(1) the role of the solvent excimer,

(2) the role of the quencher as energy transferrer.

Energy transfer from the singlet excited solvent molecule (M^*) to the solute molecule (S) may be more efficient through the photoassociated excimer, that is,

$$[MM]^{**} + S \longrightarrow S^* + M + M \quad , \qquad (1)$$

where $[MM]^{**}$ is the solvent excimer with excess energy (not thermally stabilized), formed[9] by interaction of singlet excited (M^*) and unexcited (M) solvent molecules. Process (1) seems to be very fast. This is suggested by the fact that the I_{int} from POPOP in 2-EN solutions is not a function of temperature ($298 \leqq T \leqq 413°K$), although the 2-EN excimer dissociates much faster[10] at $T = 413°K$ than at $T = 298°K$. The necessary matching of the energy levels of M and S for efficient transfer becomes less important in view of the broadening of the electronic states caused by the interaction of M and M^* in their mutual association. Enhancement of energy transfer from a donor to an acceptor was observed in aromatic systems by Stevens and was attributed to the sensitization of the acceptor via the excimer of the donor.

---

[9]It should, however, be stressed that MM^* also results from triplet-triplet annihilation [B. Stevens, *Nature* **192**, 725 (1961)]. Also M^+-M^- annihilation results in the formation of an excimer, but this process is not important here. These alternative ways of MM^* formation may contribute to the enhancement of energy transfer from the solvent to the emitting solute.

[10]L. G. Christophorou and J. G. Carter, *Nature* **209**, 678 (1966).

In solvents like 2-EN where the migration of excitation energy is believed to take place through the coupled system $[MM]^{**}$, any quenching of M^* by a quencher Q takes place via the excimer, that is,

$$[MM]^{**} + Q \begin{cases} \longrightarrow M + M + Q^* \ (a) \\ \longrightarrow M + M + Q \ (b) \end{cases} . \qquad (2)$$

Our experimental data and those of others[11] show that I_{int} of PPO in solvents such as xylene and toluene, where little or no excimer is formed at room temperature, decreases much faster with concentration of Q than in solvents where excimers dominate. This suggests that process (2*b*) may be slower and/or process (2*a*) faster than the corresponding ones for M^*.

In the past the effect of Q on the efficiency of a liquid scintillator has been quite generally attributed to the quenching of M^* by Q. This very efficient quenching overshadowed any possible increase in I_{int} through the process

$$Q^* + S \longrightarrow Q + S^* \ , \qquad (3)$$

where Q^* is excited either directly by the incident radiation or through process (2*a*).

From the data shown in Figs. 16.1 and 16.2, however, it becomes apparent that process (3) and/or (2*a*) is more efficient than process (2*b*), thus resulting in increased I_{int}. The falling off of I_{int} at high concentrations of Q, shown in Fig. 16.2, is attributed to strong self-quenching of Q (i.e., $Q^* + Q \longrightarrow Q + Q$), which excludes the possibility of using Q alone as a solvent.

In conclusion, the possible role of excimers to enhance energy transfer from solvent to solute, to enable less quenching of the excited solvent molecules, to act, in a way, as a secondary solute shifting the M^* emission to that of MM^*, suggests that more efficient liquid scintillators, "excimer-scintillators," can be obtained. Detailed investigations are in progress.

[11]M. Furst and H. Kallmann, *Phys. Rev.* **97**, 583 (1955).

RADIATION INTERACTIONS WITH LIQUIDS

The technique to be described measures the dielectric constants of liquid water, which are used to evaluate the electronic energy levels to determine which levels are excited by ionizing radiation. Such data are basic to a better understanding of radiation physics, chemistry, and biology, and the technique may be employed with other body fluids (blood, lymph, etc.). The technique also seems to be directly applicable to photochemical studies of liquids in the vacuum ultraviolet, where no work has previously been reported.

A vacuum ultraviolet monochromator, optical system, and water cell were designed and constructed for measuring the reflectivity of liquid water in the wavelength region from 300 to 2000 A (40 to 6 ev). Ultraviolet light from the Seya-type monochromator enters horizontally into the cell (see Fig. 16.3), where the water in an open dish is in equilibrium with its vapor at about 1°C. The low temperature reduces the vapor pressure, thus decreasing absorption along the optical path. A high vacuum is maintained in the monochromator through the use of cryogenic pumping at the exit slit assembly. The incident light reflects downward from a mirror onto either the water surface or a reference surface and is then specularly reflected onto a phosphor-coated photomultiplier. The angle of incidence may be varied in steps by inserting mirrors inclined at various angles in the optical path. Relative reflectivity values are converted to absolute measurements, and then the real and

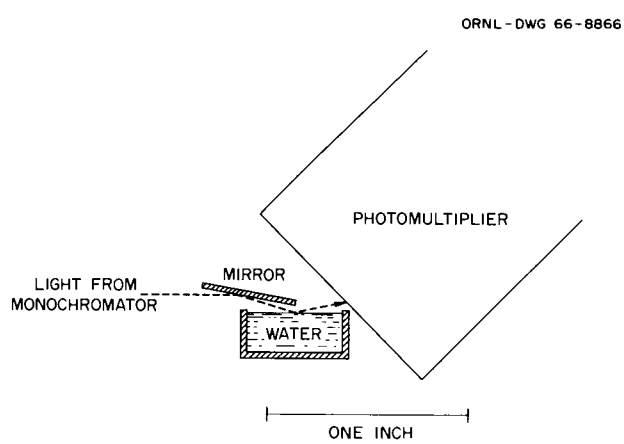

Fig. 16.3. Schematic of Optical Path in Water Reflectivity Experiment.

imaginary parts of the dielectric constant of water are obtained from the Fresnel relations. Reflectivity data obtained this year for the visible region above 3000 A (and with the cell at atmospheric pressure) at incident angles of 20, 45, and 70° are in substantial agreement with literature values. In order to go much below this wavelength the cell was evacuated to the vapor pressure of water at 1°C (5 mm Hg). Difficulty was then experienced with the water sample, which either boiled or froze unless cell temperature, vapor leak through the optical slit into the monochromator, state of aeration of the sample, temperature of the sample, etc., were just right to maintain the liquid state. Relatively crude attempts at temperature and vapor pressure monitoring and control resulted in our being able to maintain a smooth liquid surface for as long as 15 min on several occasions. Problems remain, however, for the liquid, in approaching this equilibrium, boils occasionally and wets the photomultiplier, mirror, and reference surface. Nonetheless, results to date seem encouraging, and we will in all probability be able to obtain the optical and dielectric constants of water within the next year.

OPTICAL PROPERTIES OF POLYSTYRENE

The optical properties of polystyrene have been obtained from 3000 to 400 A. The real (n) and imaginary (k) parts of the complex index of refraction were obtained from reflectance measured at 20 and 70° incidence. That is, a computer program written for the CDC 1604-A computer was used to evaluate n and k from a system of two equations involving the polarization of the incident beam and the reflectivity of the sample at two angles of photon incidence. The computer solves these equations for n and k by means of successive approximations using Newton's method. These calculated values of n and k were then used to obtain the real and imaginary parts of the complex dielectric constant, $\epsilon = \epsilon_1 + i\epsilon_2$. The quantity $-\mathrm{Im}\,(1/\epsilon)$, which is proportional to the energy lost by an electron traversing the medium, was then calculated, and major peaks are observed to occur at 6.5 and 19.2 ev.

The n and k values were obtained from smooth curves drawn through the measured reflectance points as shown in Fig. 16.4. The n and k values are shown in Fig. 16.5, and the real and imaginary parts of the complex dielectric constant calculated using these n and k values are presented in Fig. 16.6. The polystyrene electron energy loss function, $-\mathrm{Im}\,(1/\epsilon)$, is shown in Fig. 16.7 (curve A) and compared with the energy loss spectrum obtained from electron beam experiments by Swanson and Powell[12] (curve B). The loss function shows peaks at 4.6, 5.2, 6.5, and 8.5 ev and a very broad peak at about 19.2 ev. Sum rule calculations of the effective number of electrons participating in these excitations have been carried out, and values of 0.05, 0.03, and 0.94 for the 4.6-, 5.2-, and 8.5-ev losses have been obtained. Sum rule calculations for the 6.5-ev loss give values between 0.7 and 0.9, and the calculations for the 19.2-ev loss give results that indicate that all 40 electrons of the polystyrene monomeric unit are participating.

The electron energy loss peaks at 4.6, 5.2, and 8.5 ev occur in regions where ϵ_1 is large compared

[12] N. Swanson and C. J. Powell, to be published.

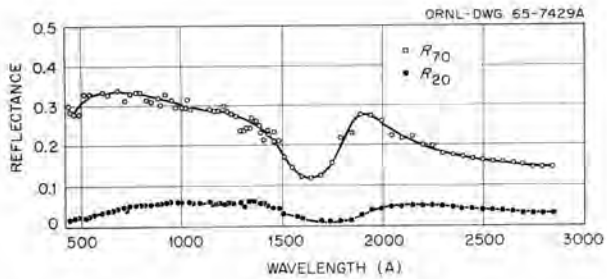

Fig. 16.4. Reflectance of Annealed Polystyrene vs Wavelength for 20 and 70° Photon Incidence.

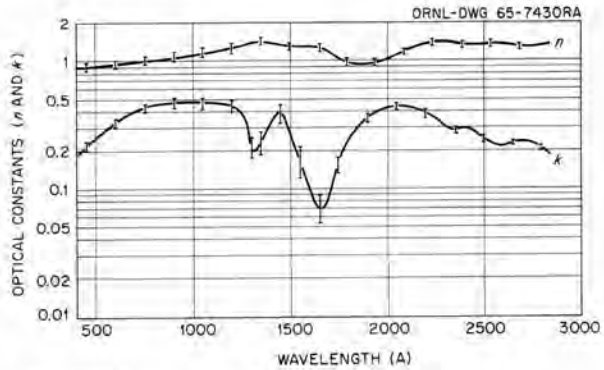

Fig. 16.5. Optical Constants (n and k) of Annealed Polystyrene vs Wavelength.

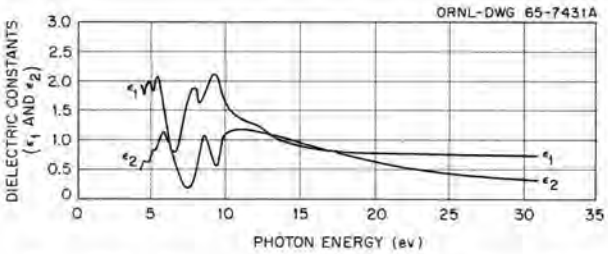

Fig. 16.6. Dielectric Constants (ϵ_1 and ϵ_2) of Annealed Polystyrene vs Photon Energy.

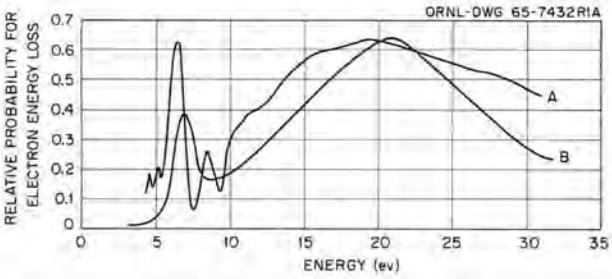

Fig. 16.7. (A) Energy Loss Function Im ($1/\epsilon$) of Annealed Polystyrene vs Photon Energy; (B) Electron Energy Loss Spectrum of Atactic Polystyrene Measured by Swanson and Powell.

to ϵ_2 and result from maxima in the optical loss function, ϵ_2. These losses are, therefore, identified as being due to bound electron excitations. The 6.5-ev loss involves the six π electrons in the benzene ring, and the structure in ϵ_1 at this energy indicates that collective effects may be present. Thus, it is concluded that the 6.5-ev loss in polystyrene is a hybrid resonance between a collective free-electron oscillation and transitions involving the benzene ring π electrons. The 19.2-ev loss seems to correspond to a plasma oscillation in which all 40 electrons of the monomeric unit are involved.

ELECTRONICALLY EXCITED AMINO ACIDS

The purpose of this project is to study the nature of excited states of dry amino acids when irradiated with slow (1- to 100-ev) electrons. The quantum yields and energies of the resultant emitted fluorescence and phosphorescence can give information about initial excitation and subsequent events. Thus, the results should be applicable to protein inactivation by radiation.

In the past three months, studies have been made to determine the electrical conductivity of thin evaporated films of the aromatic amino acids. This was necessitated by the possibility of incident electrons "piling up" in these normally poor conductors and electrostatically preventing further electrons from being absorbed. Preliminary studies with 15- to 50-ev electrons indicate that at least half as many electrons appear at the back of a 200- to 600-A-thick amino acid layer as were incident on the front side. Electron micrographs show no *apparent* holes in the films; thus, these films may be fairly good electrical conductors (unexpected on the basis of bulk and film conductivity measurements), or each incident electron could excite several other electrons into the conduction band ($\sim$2 to 3 ev) giving a "cascade" effect. The latter should lead to trapping at lattice defects (probably numerous in these evaporated layers), impurities, or in surface states. Alternatively, the films may be undergoing dielectric breakdown. The electric field across the amino acid layer is $\sim 10^7$ v/cm – of the right magnitude for this.

LOW-ENERGY ELECTRON TRANSMISSION IN SOLIDS

Studies of electron transmission through vacuum-evaporated thin films ($\sim$200 A) have been continued. An electron beam is normally incident on a thin film supported on a thin Al_2O_3 insulating layer which has been electrolytically formed on an Al substrate. Currents to the film and substrate are amplified by Philbrick P2 amplifiers, and their ratio is measured with a Vidar digital ratiometer. The ratio of film current to incident current is proportional to absorption in the film.

For electrons of energies between 3 ev and 3 kev the general shape of the transmission characteristic for Al as a function of energy at low energies has been found to agree with theoretical calculations which include electron-electron, electron-plasmon, and electron–*L*-electron interactions as shown in Fig. 16.8. The Monte Carlo calculations reveal, for example, that a 40-ev electron is stopped in the first few angstroms of a 200-A foil and gives rise to a burst of perhaps ten low-energy electrons which move relatively unhindered in the foil. At

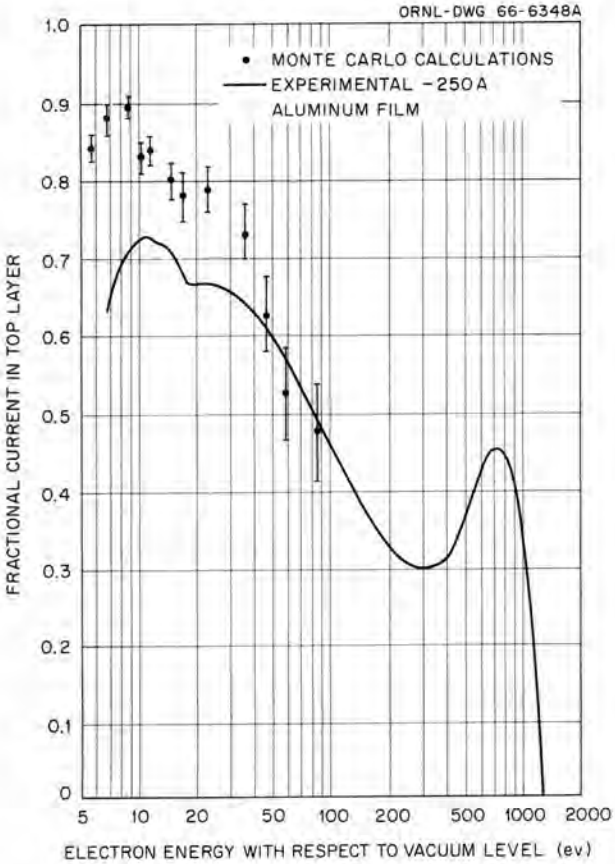

Fig. 16.8. Theoretical Monte Carlo Calculations for Aluminum and Experimental Data.

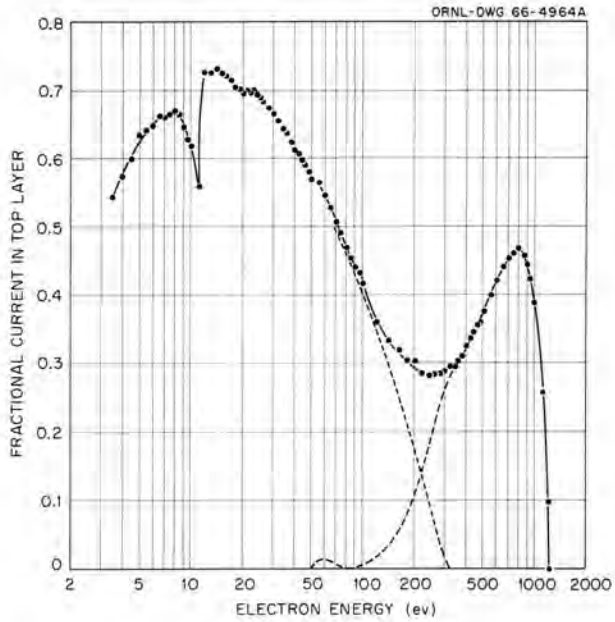

Fig. 16.9. Top Current as a Function of Incident Electron Energy for 470-A Magnesium Foil.

higher electron energies the primary electron itself traverses the foil, and increasing the electron energy increases the probability of traversal. Such data were analyzed to yield the stopping power, which was found to be constant at about 3.5 ev/A between 800 and 1500 ev. Transmission of other foils such as Mg, Tl, In, and Cu was also determined, and although the characteristic reveals electron-plasmon and electron–inner-shell interactions, quantitative comparison has not been made with the Monte Carlo calculations as yet. Particularly interesting are the data on Mg (Fig. 16.9) which show a sharp minimum at 11 ev between the surface plasmon excitation peak (8 ev) and the volume plasmon excitation at higher energies. An ultrahigh-vacuum version of the present apparatus was designed, constructed, and tested, and together with a new electron gun able to operate as low as 0.5 ev and a foil holder which permits nonnormal beam incidence, will be used to study electron–surface-plasmon excitations on atomically clean surfaces.

Part IV. Radiation Dosimetry

J. A. Auxier

17. Ichiban Studies

J. A. Auxier

J. S. Cheka H. H. Hubbell, Jr. T. D. Jones

ICHIBAN LIAISON

On the latest visit to the Atomic Bomb Casualty Commission (ABCC) in Japan from February 10 to April 8, 1966, the redetermined Nagasaki epicenter coordinates, based on burn-shadow measurements collected by S. Nagaoka, were introduced to that organization; a method of estimating exposure to subjects outside of, but shielded by, structures was also presented; procedures were devised for the processing of shielding histories which did not fit criteria of shielding categories exactly; and a procedure was devised for evaluating exposures to individuals shielded by terrain.

A report by H. H. Hubbell, Jr., *et al.*[1] on the redetermination of the Nagasaki epicenter was given to the ABCC. This report, based on data by Nagaoka, will be published as an ABCC Technical Report. The ABCC Statistics Department wishes to use the coordinates in this report as the officially accepted values for Nagasaki and those of E. T. Arakawa *et al.*[2] for Hiroshima. The ORNL group considers that earlier Japanese data, being more internally consistent and having been based on clearer shadows, should not be ignored, and analysis of early Japanese data will continue.

There are many survivors under study by the ABCC who, at the time of the bombing, were outside of, but shielded by, some structure or other obstruction. The fraction of total radiation intercepted can be determined by the use of the spherical coordinate projector[3] and the angular distribution functions for gamma and neutron radiations respectively. Such a projector was supplied to the ABCC in 1960, and the angular distribution functions were supplied in 1963. Most of the cases in this category have been processed to this point, but a method for estimation of exposure was not available. Empirical formulas for the evaluation of neutron and gamma radiation exposures under these conditions were developed on the basis of measurements made during weapons tests and Operation BREN; these were submitted to the ABCC.

The intercepted fraction of each type of radiation is designated Y_1, and the unintercepted fraction $1 - Y_1$ is designated Y_2. If the shielding object is opaque to the radiation being considered, the dose at the location is $Y_2 \times$ air dose (D_{air}) at that point for that radiation. If the shielding object is a Japanese house, the average neutron transmission based on experimental data[4] is 0.15, and the formula becomes $D_n = (0.15Y_1 + Y_2)D_{air_n}$, which can be reduced to $D_n = (0.15 + 0.85Y_2)D_{air_n}$. The evaluation of gamma-ray exposure is complicated by the presence of secondary sources of gamma rays in the walls due to both the degradation of the high-energy component of the gamma radiation and the radiative capture of neutrons. This secondary gamma source is designated Y_3, and its value is approximately

[1] H. H. Hubbell *et al.*, *The Burst Points of the Atomic Bombs in Japan. Part I. A Redetermination for Nagasaki from Shadows on Stones*, to be published as an ABCC Technical Report.

[2] E. T. Arakawa, *Radiation Dosimetry in Hiroshima and Nagasaki Atomic Bomb Survivors*, ABCC TR 14–59 (1959).

[3] J. A. Auxier *et al.*, WT-1725 (1961) (classified).

[4] J. S. Cheka *et al.*, *Distribution of Weapons Radiation in Japanese Residential Structures*, CEX-62.11 (1965).

$(e^{-1.897-0.255x})Y_1$, where x is the distance in meters from the point of interest to a house wall. This equation is based on the data from Operation BREN.[4] The secondary source Y_3 is further divided into $Y_{3(df)}$ for the forward direction (i.e., toward the hypocenter) and $Y_{3(db)}$ for the backward direction. Then

$$D_\gamma = \left[Y_2 + \frac{0.75Y_1}{2} + \frac{0.25Y_1}{2} + 0.7Y_{3(df)} + Y_{3(db)}\right] D_{\mathrm{air}_\gamma},$$

where the first Y_1 term accounts for the hard component and the second Y_1 term accounts for the soft component of the incident gamma radiation;[4] but

$$Y_1 = 1 - Y_2 ;$$

therefore

$$D_\gamma = \left[0.5(1 + Y_2) + 0.7Y_{3(df)} + Y_{3(db)}\right] D_{\mathrm{air}_\gamma}.$$

In the past several years, methods have been submitted by ORNL to the ABCC whereby radiation exposures could be estimated for survivors in locations falling into special environmental categories. In each instance, criteria of applicability were supplied. However, whatever criteria are specified, there exist marginal cases or those where some of the criteria are not met exactly. Because of this difficulty, there has been a tendency on the part of the ABCC to defer calculation of dose estimates based on the 1965 ORNL revised air-dose curves[5] (T65D) until most of these criteria were clarified. In collaboration with Dr. Milton of the Statistics Department a policy was initiated whereby dose calculations can be expedited. According to this policy, all cases which clearly fall into one of the categories for which methods of calculation are given will be processed and placed in class I. These are considered to be good estimates with an uncertainty of ±6% at the 50% confidence level. If most of the criteria of a category are met but there is a perturbing factor which cannot be evaluated exactly, or elements of two categories are present though those of one of them predominate, the evaluation is made on the basis of the dominant category but placed in class II. These should be accurate to within ±15% at the 50% confidence level. For those cases which do not have shielding histories but for which there is nondetailed information on location in the master sample questionnaires, if in the open, D_{air} will be assigned, while if in Japanese houses, values of neutron and gamma-ray doses based on the average values for the shielding factors derived from a large number of class I cases evaluated by the nine-parameter formula[6] will be assigned. These will be "order of magnitude" figures and will be considered class III. Nonevaluated cases will be in class IV and will not be used in statistical studies. Any class IV cases, such as those in heavy structures, which are evaluated later will be reassigned to class I or II depending on the quality of the estimate.

In Nagasaki, where a number of terrain shielding cases exist, a field study was made on terrain shielding, and a method of procedure outlined for evaluation of these cases. Except for very simple geometries, these will all fall into class II.

The question again arose of what to do about high-dose cases (i.e., those showing 1000 rads or more). Evidently some misinformation has entered into the data on which calculations are based. There were 175 of these until the air-dose curves were revised, after which there appear to be about 60. It was recommended that no time be spent on further rechecking of these particular cases because: (1) they amount to only 0.2% of the ~30,000 cases under study and so have little statistical significance; (2) a change in the story on reinterview is not necessarily a correction; and (3) the expenditure of one man-day per case, as is indicated by a sample recheck, would not be justified unless a case is of special interest.

Some time was spent on the study of heavy-shielding cases. The evaluation of many of these will require more study. However, some of the cases of simple geometry, or those in which there is total shielding in a large fraction of the solid angle, may be evaluated as soon as transmission factors for weapons radiation are available for concrete.

Calculation of T65D is getting under way, and there are now available methods which will treat between 80 and 90% of the cases for which there are shielding histories. The balance comprises mainly the heavy-shielding cases and will require more work by ORNL both here and in Japan.

[5] J. A. Auxier *et al.*, *Health Phys.* 12, 425 (1966).

[6] J. A. Auxier *et al.*, *Health Phys. Div. Ann. Progr. Rept. July 31, 1964*, ORNL-3697, p. 155.

18. Spectrometry and Dosimetry Research

J. H. Thorngate

M. D. Brown[1]
D. R. Davy[2]
D. R. Johnson
P. T. Perdue
L. H. Peshori[2]
G. F. Stone[3]
A. H. Sullivan[4]
E. B. Wagner

AN ABSOLUTE NEUTRON DOSIMETER BASED ON A GENERALIZED CONCEPT FOR RADIATION DOSIMETRY

A neutron dosimeter was designed that was based on the generalized concept of radiation dosimetry originally described by Hurst and Ritchie.[5] The interaction products were recoil protons from a hydrogenous radiator, and the energy-loss distribution considered was from the protons passing into or through a surface-barrier radiation detector. Using the generalized dosimetry concept, this dosimeter has (1) the characteristics of an absolute instrument whose response can be fitted to any dosimetry concept, and (2) the possibility of serving as a dose spectrometer. Three dose concepts were considered: tissue kerma in air, tissue first-collision dose, and surface multicollision dose for a 30-cm slab of tissue.

The generalized principle formulated by Hurst and Ritchie can be stated as follows: Let operator $O_i^\alpha(E_p)$ act upon the energy-loss distribution generated in a system of configuration $\beta_1 \beta_2 \ldots \beta_n$. For a medium j and dose distribution k, a given dose function $D_{jk}(E)$ is measurable with errors less than δ in an energy range $E_1 \leqq E \leqq E_2$ provided there exist operators O_i^α and geometrical parameters $\beta_1 \beta_2 \ldots \beta_n$ such that the inequality

$$\left| \sum_{p,\alpha} O_i^\alpha(\epsilon_p) n_{\beta,p}^{(\alpha)}(\epsilon_p, E) - D_{jk}(E) \right| \leqq \delta \qquad (1)$$

is satisfied for all energies in the specified range. Any dose-energy relationship may be used, and the test system can be unrelated, in a direct sense, to the jth material or the kth physical effect.

In carrying out the matching, the operator was found for a specified configuration such that inequality (1) was satisfied. Two configurations for neutron dosimeters using semiconductor detectors were used in which a polyethylene radiator of area A was in contact with the detector.

For the first configuration, the thickness of the radiator and the sensitive depth of the detector were greater than the range of the most energetic proton generated in the radiator by the incident neutrons. Under these conditions, the differential spectrum of protons incident upon the detector, for center-of-mass isotropic scattering, is[6]

$$n(E)\,\mathrm{d}E = \frac{A N_0 \sigma_{n,p}(E)}{(dE/dx)(E)} \left(1 - \left[\frac{E}{E_0}\right]^{3/2}\right), \qquad (2)$$

where dE/dx is the stopping power for protons of energy E in polyethylene of N_0 atoms of hydrogen per gram, E_0 is the incident neutron energy, and

[1]Two days per week graduate student.

[2]Alien guest.

[3]Visiting investigator from TVA.

[4]CERN-ORNL exchange researcher.

[5]G. S. Hurst and R. H. Ritchie, *Health Phys.* 8, 117 (1962).

[6]R. J. Vosser, *The Application of Semiconductor Radiation Detectors to the Observation of Fast Neutrons*, Tech. Doc. Report ASD-TDR-62-838 (1962).

Table 18.1. Fit of Eq. (3) for the Infinite Radiator and Detector Configuration to:

Tissue Kerma in Air. $A = 1.50 \times 10^{-3}$					Absorbed Dose Calculated from Kerma. $A = 7.52 \times 10^{-5}$					Surface Multicollision Dose for an Infinite Slab of Tissue. $A = 1.68 \times 10^{-5}$				
u	E_1	E_2	$r(u)$	$m(u)$	u	E_1	E_2	$r(u)$	$m(u)$	u	E_1	E_2	$r(u)$	$m(u)$
1	0	0.36	1	2	1	0	0.35	1	2	1	0	0.30	0	2
2	0.59	0.92	1	2	2	0.54	0.82	1	2	2	0.34	0.72	0	2
3	1.58	2.05	0	2	3	1.05	1.55	−1	2	3	1.24	1.60	−1	2
4	3.00	4.05	−1	2	4	2.00	2.50	0	2	4	2.30	2.95	−1	2
5	5.35	6.75	−1	2	5	4.00	4.40	0	2	5	3.65	4.70	−2	2
					6	5.8	6.90	−1	2	6	8.20	10.0	−1	2

$\sigma_{n,p}$ is the hydrogen-scattering cross section for neutrons of this energy. Since the entering proton was completely stopped in the detector, the recorded differential pulse spectrum was given by this expression.

For a dosimeter based on this configuration, a convenient form for the operator O_i^{α} was[5]

$$R(E) = A \sum_{u=1}^{u=u_{max}} 2^{r(u)}(-1)^{m(u)} \times \int_{E_1(u)}^{E_2(u)} n(\epsilon, E)\,d\epsilon = AR_u\,, \quad (3)$$

where $R(E)$ was chosen to fit a particular dose concept $D_{jk}(E)$. To keep the analysis suitable for binary multiplication or division, $r(u)$ was limited to zero or a positive or negative integer, and $m(u)$ was either 1 or 2 for subsequent addition or subtraction. The number of energy losses in the ith channel is determined by the range of integration $E_1(u)$ and $E_2(u)$. For a particular neutron energy E, a choice of values may be made for the five parameters $r(u)$, $m(u)$, $E_1(u)$, $E_2(u)$, and u_{max} so that the conditions of Eq. (1) can be satisfied over a wide range of energies for any particular dose concept. Table 18.1 shows the calculation of Eq. (3) for the kerma-like neutron first-collision dose in tissue $Df_1(E)$, the absorbed dose for fast neutrons in tissue $Df_2(E)$, and the surface tissue multicollision dose $D_s(E)$; A is then a calculated constant relating the response per neutron to dose per neutron for the particular configuration and dose concept under consideration.

Table 18.2. Fit of Eq. (3) for Limited Radiator and Detector Configuration to:

Absorbed Dose Calculated from Kerma. $A = 1.57 \times 10^{-5}$					Surface Multicollision Dose for an Infinite Slab. $A = 1.75 \times 10^{-5}$				
u	E_1	E_2	$r(u)$	$m(u)$	u	E_1	E_2	$r(u)$	$m(u)$
1	0	0.31	0	2	1	0	0.30	0	2
2	0.50	0.61	1	2	2	0.33	0.56	0	2
3	1.10	1.24	0	2	3	1.00	1.16	−1	2
4	1.60	1.80	0	2	4	1.50	1.71	0	2
5	2.3	2.80	2	1	5	1.50	1.71	−1	2[a]
					6	2.40	2.60	0	1
					7	2.63	∞	2	1

[a]Requires delay in binary circuit.

As the sensitive depth was increased to cover more energetic incident neutron spectra, the gamma interactions with the detector masked the proton spectrum in the 0-to-1-Mev region. Thus, the resulting proton spectrum could be used only for the energy region above 1 Mev. (See Table 18.2.)

Figure 18.1 indicates the recorded energy-loss distributions obtained at bias voltages which produced sensitive depths approximately equivalent to the ranges of 5-, 2.3-, and 1.5-Mev protons in silicon. Since dE/dx decreases as the proton energy increases, any proton recoiling at angle θ, with respect to the path of the neutron, that passed through the detector gave an energy-loss pulse of

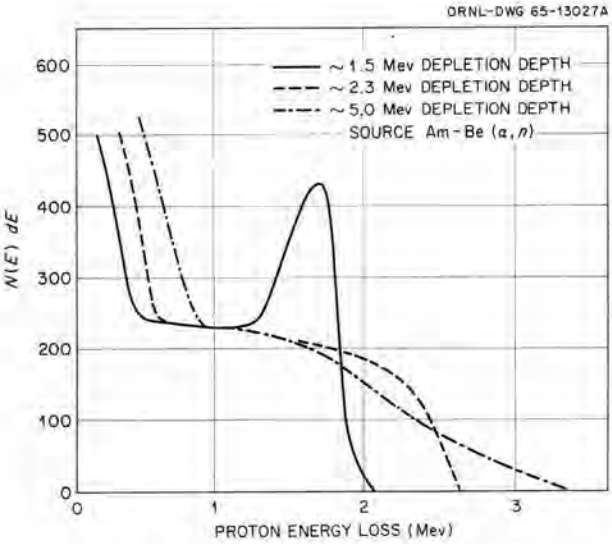

Fig. 18.1. Variation of the Recorded Differential Pulse Distribution from the High-Resistivity Surface-Barrier Radiation Detector with Applied Bias Voltage.

amplitude less than that of a proton with a range $\leq$ than the detector thickness. Thus, as the sensitive depth was decreased, the proton energy-loss distribution curve peaked in the proton energy region immediately below the energy corresponding to the sensitive depth. Consequently, for a particular sensitive depth, a proton energy was found such that, even though the higher energy spectrum distribution had changed, the total number of protons depositing energy above this particular energy value remained constant and therefore the distribution below it was unchanged.

Since the gamma interaction decreased as the bias decreased, the region of the proton spectrum below the critical proton energy was explored in successive steps by using a series of bias voltages. In these measurements, as in all others, a background spectrum was subtracted from the proton spectrum. Since the background was obtained by exposing the detector without radiator to the neutron flux, this procedure eliminates any effect due to interaction between the neutrons and gamma rays with the detector, and thus assisted in the evaluation of gamma-ray interference.

Two experimental complications arose from the first configuration. As noted, when the sensitive depth of the detector was increased, gamma interactions with the detector obscured part of the proton spectrum. Second, for high-energy incident neutrons found in the environs of an accelerator it would be necessary to employ a lithium-drifted detector in order to obtain a sensitive depth greater than the range of the most energetic proton generated. These difficulties were overcome by using a configuration where both the radiator thickness and sensitive depth of the detector were specified as less than the range of the more energetic protons generated by the incident neutrons.

The doses per unit neutron fluence for incident neutron spectra from AmBe, PuBe, and AmB radioactive (α,n) sources and from the Health Physics Research Reactor (HPRR) were measured. The results for dosimeters based on configurations I and II are given in Table 18.3. The emission rates from the (α,n) sources used in these calculations were obtained from an intercomparison employing a calibrated long counter and a National Bureau of Standards calibrated 16-g PuBe source as reference. Because of the directional response of the dosimeters, a value limited to the direct neutron fluence was used in the calculations for exposures to the HPRR. This flux was estimated from a separate measurement involving a ^{239}Pu foil in a ^{10}B sphere shielded from all but the direct radiation. Various reactor runs were normalized via measurements taken with a fixed fast-fission chamber.

In finding the operator [Eq. (3)] fitting a particular dose concept, one may leave the low-energy region of the incident neutron spectrum unbalanced. This can be achieved either directly (say

Table 18.3. Dose per Unit Neutron Fluence Values Using Dosimeters Based on Configurations I and II

Neutron Source	Dose per Neutron Values (ergs/g per unit fluence)					
	First Collision Dose		Tissue Kerma in Air		Multiple Collision Dose	
	I	II	I	II	I	II
	$\times10^{-7}$	$\times10^{-7}$	$\times10^{-7}$		$\times10^{-7}$	$\times10^{-7}$
Pu-Be	4.01	3.92	4.03		4.79	4.60
Am-Be	3.94	4.11	4.04		4.90	5.05
Am-B	3.55	3.51	3.65		4.38	4.23
HPRR	2.70	2.74	2.73		3.28	3.13

for the 0.3-Mev response) or indirectly by choosing the lowest value of $E_1(u)$ in Eq. (3) at some value other than zero. Obviously, in the latter case, the dose delivered by all neutrons of energy less than $E_1(u)$ is disregarded, and the response to neutrons 0.3 Mev > $E_n \geqq E(u)$ is balanced only as well as the dose concept under consideration varies directly with neutron energy. Table 18.4 indicates forms of the operator for tissue kerma in air that contain such imbalances. Table 18.5 shows the relative dose values obtained when the fits of Tables 18.1, 18.4(*a*), and 18.4(*b*) are applied to AmBe, PuBe, and AmB incident spectra. The results indicate that both AmBe and AmB spectra contain a significant (~11 and 8% respectively) low-energy component. For AmBe this would be expected from the recent work of Geiger and Hargrove (16% <1.5 Mev), but no comparative results are available for AmB.

Table 18.6 shows an intercomparison of this and other dosimeters. Because of the difficulty of evaluating the errors in the Monte Carlo code used in reduction of the data for the second configuration, the values appearing in this table are those

Table 18.4. Fit of Eq. (3) for the Infinite Radiator and Detector Configuration to Tissue Kerma in Air, Containing Imbalances for Neutrons of Energy (*a*) <0.13 Mev and (*b*) <0.3 Mev

(*a*) $A = 9.53 \times 10^{-6}$					(*b*) $A = 1.62 \times 10^{-5}$				
u	E_1	E_2	$r(u)$	$m(u)$	u	E_1	E_2	$r(u)$	$m(u)$
1	0.13	0.26	2	2	1	0.3	0.4	2	2
2	0.45	0.84	0	2	2	0.7	0.95	−1	2
3	1.05	1.30	0	2	3	1.5	1.65	0	2
4	2.20	2.65	0	2	4	2.5	3.05	−1	2
5	4.10	5.20	−1	2	5	4.3	4.7	−1	2
6	7.80	8.20	0	2	6	6.75	7.2	−1	2

Table 18.5. Relative Dose Values for Different Incident Spectra with Different Fit Imbalances

Source Fit	Relative Dose Values		
	Am-Be	Am-B	Pu-Be
1(*a*)	1.00	1.00	1.00
5(*a*)	0.96	0.95	0.96
5(*b*)	0.89	0.92	0.94

[a]Neutrons of energy less than 0.13 Mev.
[b]Neutrons of energy less than 0.3 Mev.

Table 18.6. Intercomparison of Dose per Unit Neutron Fluence Values for Different Dosimetry Systems

Neutron Source	Dose per Neutron (ergs/g)								
	Tissue Kerma in Air			First Collision Dose			Multicollision Dose		
	a	*b*	*c*	*a*	*d*	*e*	*a*	*b*	*c*
Am-Be	4.04			3.94		4.05	4.90		
Pu-Be	4.03		3.90	4.01	4.04	3.90	4.79		3.4[f]
Am-B	3.65			3.55		3.51	4.38		
HPRR[g]	2.73	2.69		2.70			3.28	3.65	3.21[h]

[a]Generalized dosimeter.
[b]Fission foils.
[c]Neutron spectrometry or nuclear track emulsions.
[d]Tissue-equivalent ion chamber.
[e]Proportional counter.
[f]On assuming $D_H = 0.1D_P$.
[g]Direct beam.
[h]On assuming 1.30 escape neutrons per fission.

for a dosimeter of the first configuration. However, because of systematic errors, the more accurate dose per neutron values should be those associated with a dosimeter having a "thin" radiator and detector. While the differences between kerma and the first-collision dose, as herein used, are small when compared with the absolute error, they should nevertheless be significant. In obtaining these results, the various operators were applied to the same energy-loss spectrum, and thus the relative results are free of statistical errors and have the same systematic errors.

The good agreement between these results and those obtained by using other dosimetry systems indicates that accurate input data for the design of a dosimeter based on Hurst and Ritchie's generalized principle of radiation dosimetry is now available. The principal advantage of such a dosimeter is that, provided the whole energy-loss spectrum is recorded, the results can be expressed now, or at any later date, in terms of any dose concept.

PREDICTION OF BIOLOGICAL DAMAGE FROM STOPPING-POWER THEORY

With the initial assumption that the necessary and sufficient condition for biological damage to result from irradiation is the ionization of neighboring critical sites, stopping-power theory is used to develop a series of equations that successfully predict the biological effect observed in several experiments. With certain restrictions on the range of the incident charged particles' velocity, the equations simplify to:

Biological effect per unit fluence

$$\psi = \frac{Vb}{2w^2}\left[\frac{dE}{dx}[1 - F(T)]\left\{1 - \frac{b}{w}\frac{dE}{dx}[1 - F(T)]\right\}\right]^2 ,$$

where

$$F(T) = \left[\frac{\ln (2mv^2/T_d)}{2 \ln (2mv^2/I)}\right]\left[1 - \left(\frac{1 - T_d/2mv^2}{\ln 2mv^2/T_d}\right)^2\right]^{1/2} .$$

Here V is the critical volume of the biological system under consideration, b the C–H bond spacing, w the energy expended by the radiation in producing one ionization, m the electron mass, I the ionization potential in tissue, dE/dx and v are the stopping power and velocity of the incident particle respectively, and T_d is the energy of the secondary electron whose range in tissue is equal to the dimensions of the diffusion volume around the critical sites. Using Jaffé's diffusion equation and reported values for solute concentrations within the nucleus, solute collision frequencies, and probabilities for the elimination of an active radical per collision, then

$$T_d = T_0 \ln\left(\frac{N}{N_0}\right)^{0.3} , \qquad \frac{N}{N_0} < 0.95 ,$$

$$= 1.1 \text{ kev} , \qquad \frac{N}{N_0} \geqq 0.95 ,$$

where N is the biological population density at any time during the irradiation and N_0 is its initial value; T_0, a constant whose value is determined by biological parameters, is unimportant because of the finite size of the ion sheath formed by the incident primary particle.

Predictions from this theory are consistent with biological findings. Figures 18.2 and 18.3 compare theoretical and experimental results of RBE values, the biological end point being the colony-forming ability of T_1 cells irradiated to different survival levels. Introducing reasonable mathematical approximations, the maximum RBE occurs when ψ has its maximum value; this occurs for any incident particle when its velocity is given by $V_m = 3cZ/137$, where c is the velocity of light and Z applies to the incident particle; V_m occurs at an energy greater than that corresponding to the Bragg peak. For particles of velocity V_m

$$\psi_{max} = 2.5 \times 10^{-8} a^2 (1 - 6.64 \times 10^{-2} a) , \qquad T_d > 2\, mv^2 ,$$

$$= 0.3 \left(\frac{dE}{dx}\right)_{max}\left(1 - 229 \frac{dE}{dx_{max}}\right)^2 , \qquad T_d \leqq 2\, mv^2 ,$$

where $a = 2 \ln (2mv_m^2/I) - \ln (2mv_m^2/T_d)$ and $(dE/dx)_{max} = 5.77 \times 10^{-4} \ln (2mv_m^2/I)$.

Using these equations, $(\text{RBE})_{max}$ values were calculated for $z = 1$ to 10 and are shown in Fig. 18.3. The smooth curve joining these RBE values

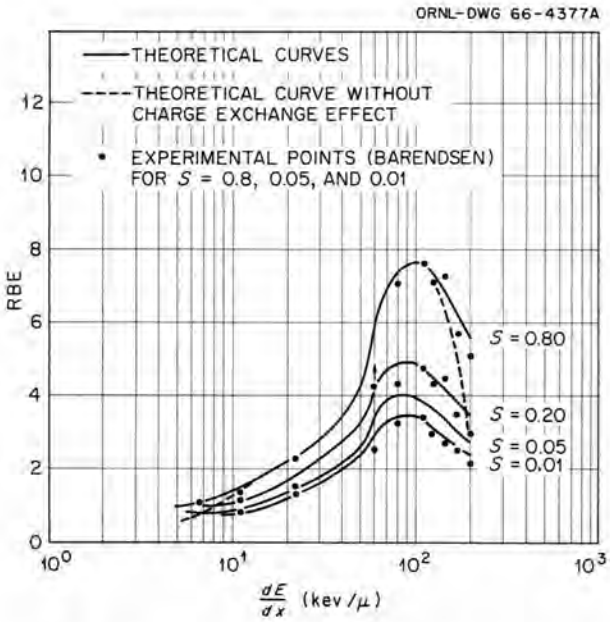

Fig. 18.2. Calculated RBE vs dE/dx Curves for the Inhibition of Colony Formation by T_1 Cells to Various Levels of Survival Following Irradiation with Deuterons and Alpha Particles of Various Energies. The circles indicate experimental results from J. J. Broerse and G. W. Barendsen, *Biological Effects of Neutron and Proton Irradiations*, vol. 1, IAEA, Vienna, 1964.

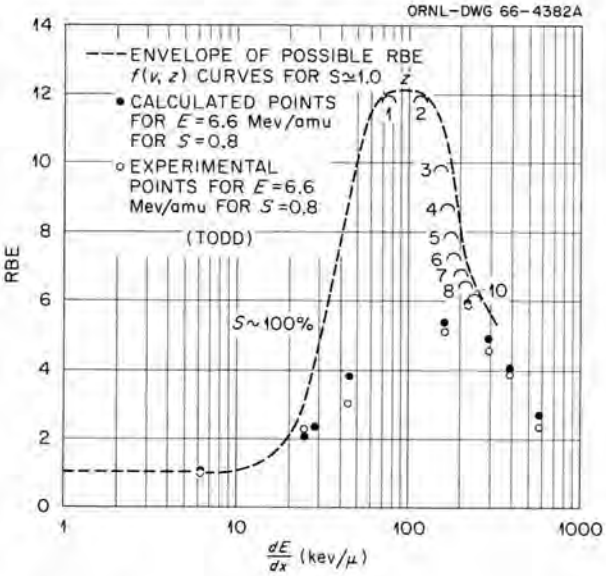

Fig. 18.3. Calculated RBE vs dE/dx Values for the Inhibition of Colony Formation by T_1 Cells to a Survival Level of 80% (●) and Experimental Values (O) Reported by P. W. Todd, *Reversible and Irreversible Effects of Ionizing Radiations on the Reproductive Integrity of Mammalian Cells*, UCRL-11614 (1964), Following Irradiations with Heavy Ions of Equal Velocity. The dotted curve is the theoretical envelope of the possible RBE vs dE/dx curves for varying velocities of incident particles with $z = 1$ to 10.

for a survival level of 95 to 100% is also given in Fig. 18.3. This enveloping curve has a shape similar to that obtained by drawing a smooth curve through the QF vs LET relationship recommended by ICRP, but, in contrast, has a maximum value of RBE $\cong$ 12 for any incident *charged* particle provided dose rate effects are neglected. If the dose rate effects predicted by the theory are introduced, then the ICRP curve would be matched except at the high-LET end. To a good approximation ψ_{max} is constant for $z \geqq 3$, and the high-LET end of the enveloping curve decreases with increasing LET as $1/(dE/dx)$, that is, as $1/\ln v^2$. This, then, is the physical equivalent of the biologist's "overkill" concept.

Some general conclusions based on this theory and the implicit assumptions – see Fig. 18.4 – are listed below. While these are consistent with biological findings, they are nevertheless far more specific than the conclusions reached as a result of such studies.

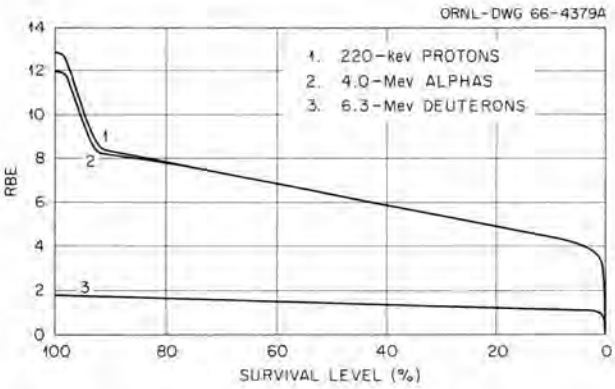

Fig. 18.4. Calculated RBE Values for T_1 Cells Irradiated by 220-kev Protons, 4-Mev Alpha Particles, and 6.3-Mev Deuterons to Different Survival Levels.

1. No unique relationship exists between RBE and LET.
2. The RBE value for a particular radiation is constant for damage levels of 0 to 5%.
3. There is not a critical dE/dx value above which chemical protection is operative, but rather a survival level and incident particle velocity dependence. For example, no chemical protection against neutrons of energy less than a few Mev should exist.

Speculatively interpreting the initial assumption and the values used in the above calculations for the bond spacing (1.1 A) and energy absorbed per ionization (30 ev), one would conclude that the prerequisite for cell inactivation is the production of a carbon atom in a CH_2 grouping with a double bond opening. Assuming this to be the case, the cross section for inactivation applicable to neutron irradiations has four components:

1. direct neutron interaction with one hydrogen atom and the recoiling proton causing the second ionization;
2. direct charge exchange between a recoiling carbon ion and the next carbon atom;
3. that due to the equilibrium recoil proton spectrum; and
4. that due to the equilibrium secondary electron spectrum.

Calculations show that (4) is always small, that (3) is significant but not a major component for incident neutrons of energy <13 Mev, and that (1) and (2) are approximately equal contributors at a neutron energy of 3 Mev, while the direct proton effect dominates at low neutron energies. Because of the importance of the direct interaction effects, neutron doses based on an absorbed energy concept are inadequate and RBE values calculated on the basis of these concepts fall on the irregular curve shown in Fig. 18.5. If instead the biological effectiveness of neutrons is expressed in terms of unit neutron fluence, the curve becomes smooth and the variation of response with depth in tissue is given in Fig. 18.6. Unfortunately, few experimental data exist for the neutron energies covered by the above curves, but what do exist agree well with predicted values (see Fig. 18.5).

Assuming that little difference exists in the physical parameters, for example, nucleus volume,

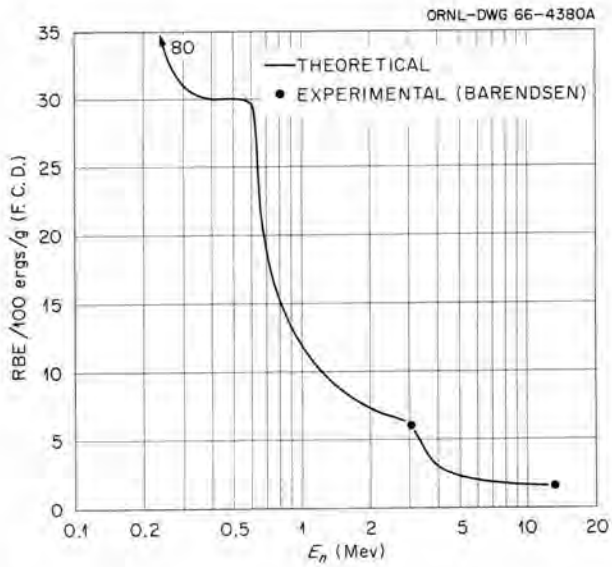

Fig. 18.5. Calculated RBE vs Incident Neutron Energy Curve for the Inhibition of Colony Formation by T_1 Cells to a Survival Level of 80% and Experimental Values for Incident 3 and 13-Mev Neutrons Reported by J. J. Broerse and G. W. Barendsen, *Biological Effects of Neutron and Proton Irradiations*, vol. 1, IAEA, Vienna, 1964. In all cases the RBE is referenced to the first collision rad dose calculated from tissue kerma.

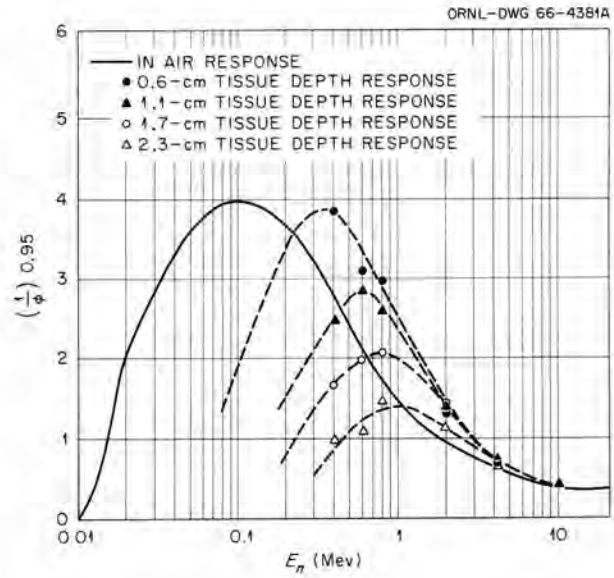

Fig. 18.6. Calculated Effectiveness of Neutrons of Various Energies to Cause Biological Damage at Different Depths in Tissue.

solute concentrates, etc., of cells in various mammalian organs, the theory can be used to yield predictions for a variety of biological end points. For example, Fig. 18.7 shows predicted testes weight loss[7] after exposure to fission neutrons and again the agreement between theory and experiment is quite good. Similarly, using reported reference radiation dose levels for LD_{50}^{30} in mice, then 30-day lethality becomes equivalent to a cell survival level of 1%. Monte Carlo methods were used to generate the ψ function at the center of a mouse for an incident HPRR neutron spectrum, and the predicted RBE value, based on first collision dose at the above damage level, is 3.8, in good agreement with recent measurements. Because of the physical dimensions of the critical assembly, the neutron leakage spectrum from the Hanford recuplex accident should have been very similar to that of the Y-12 accident. Figure 18.8 shows the theoretical RBE–damage-level curve for this spectrum applicable at a tissue depth of 5 cm in a man-sized phantom. Also shown on this curve are measured neutron RBE values for the three most heavily exposed (3 to 25 rads of neutrons) personnel involved in the recuplex accident. The biological end point here is chromosome breakages, and the values are plotted at the total damage level.

[7]A. L. Batchelor *et al.*, *Biological Effects of Neutron and Proton Irradiations*, vol. 2, IAEA, Vienna, 1964.

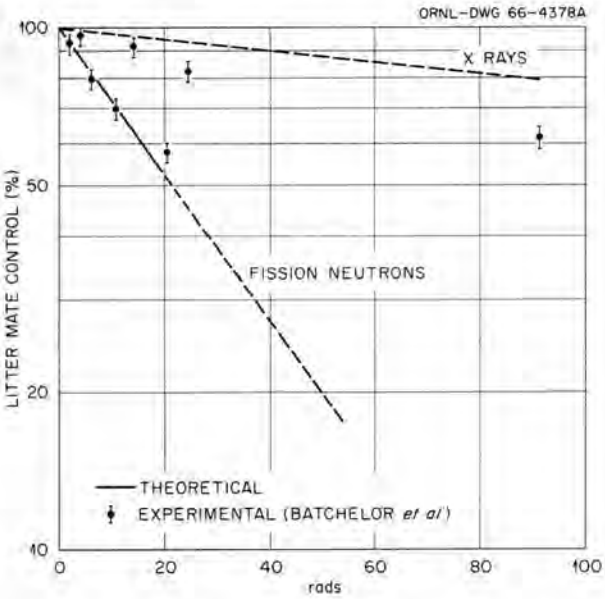

Fig. 18.7. Calculated Testes Weight Loss Following Irradiation with Fission Neutrons and 50-kev$_p$ X Rays. The experimental values are from ref. 7.

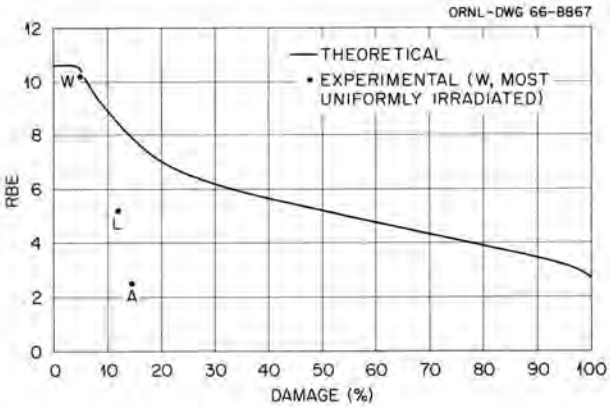

Fig. 18.8. Theoretical RBE Damage Level for Chromosome Breakage at a Tissue Depth of 5 cm in a Man-Sized Phantom (Assume a Y-12 Nuclear Accident Spectrum) and Experimental RBE Values for Three Subjects Exposed to the Recuplex Nuclear Accident at Hanford.

The theory outlined above will not be applicable to all biological systems but rather should be limited to those systems that have evoked the multitarget model. Biological results which require this restriction can be explained in terms of the presence of double helix DNA molecules and the associated nucleoproteins.

TRANSISTORIZED FAST-NEUTRON INTEGRATOR – RADSAN MARK II

A new transistorized fast-neutron integrator (Radsan mark II) has been built based on the ORNL-designed vacuum tube model Q-1995.[8] This instrument was developed to fill the need for an integrator of scaled-down size, weight, and power requirements, and with provisions allowing adaptation to specialized measurements. For example, it is to be used aboard a helicopter during Operation HENRE; this type of operation results in severe environmental problems such as vibration, electrical interference, limitations of space, weight, and available power.

[8]E. B. Wagner and G. S. Hurst, *Rev. Sci. Instr.* 29, 153 (1958).

The mark II weighs about 25 lb, and although designed primarily for ac operation, it is possible to operate it from batteries. The main instrument is mounted on a 19-in. rack-size chassis with a 7-in. panel and is connected by means of a cable to a counter and preamplifier unit. Although the mark II Radsan is similar to Q-1995 in basic design, there are several changes. A simple four-stage binary integrator is retained, but the discriminators are set at 0.4, 0.8, 1.6, and 3.2 v, and less electronic gain is required. A "window" amplifier is used ahead of the two lower discriminators to improve their stability. The timer unit for direct dose readout has been simplified so that it now uses a single transistorized interval timer with a 238-sec nonadjustable interval. This means that for each dose determination it is necessary to multiply the scaler reading by a factor which is determined when each new proportional counter is calibrated to determine the number of digits per second equal to a millirad. More extensive shielding and filtering have been incorporated in the new model.

Commercial transistor plug-in-type modules were used where they were adaptable, and some of the other basic units of the instrument are modified ORNL designs. The high-voltage supply is an ORNL Q-2291A modified to provide switch-selected voltages between 1200 and 1500 v in 50-v steps. The three-decade scaler for readout is adapted from an ORNL transistorized portable scaler design.[9] The transistorized discriminators, window amplifier, and binary integrator utilize circuitry that had been developed for an operational analyzer for generalized dosimetry.[10] The transistor-regulated, low-voltage power supplies are commercial units, and Zener-diode networks have been added for decoupling, filtering, and regulation to supply the individual sections of the instrument. Since the effort put into the design and development of the instrument was intermittent over a period of several years, some of the transistors could be updated to advantage. However, it is planned to direct any further effort toward an entirely new model utilizing recent developments such as microcircuitry which would enable one to design a more sophisticated instrument.

[9] J. H. Thorngate and J. E. Parks, *Health Phys.* **12**, 385 (1966).

[10] R. D. Birkhoff *et al.*, *Health Phys. Div. Ann. Progr. Rept. June 30, 1963*, ORNL-3492, p. 142.

PRODUCTION OF GAMMA RAYS BY NEUTRONS IN AIR

The production of gamma rays by neutron interaction in air in the energy range from 0 to 14 Mev is important to the health physicist. A typical application is the Ichiban program to determine radiation doses received by the Hiroshima and Nagasaki survivors. A study has been made to determine the relative importance of the various gamma-producing cross sections in air. These cross sections fall into three energy regions. From 0 to approximately 1 ev the capture cross section has a $1/V$ dependence. In the energy span from 1 ev to 4.75 Mev there are no significant gamma-producing cross sections. Most neutrons in this region lose their energy through elastic collisions until they reach thermal energies, at which time they interact via thermal reactions. Threshold reactions are responsible for the gamma rays produced directly by neutrons with energies greater than 4.75 Mev.

Relative thermal-neutron capture cross sections are presented in Fig. 18.9. By far the most important is the $^{14}N(n,\gamma)^{15}N^*$ reaction. Table 18.7 gives the transition intensities of the observed

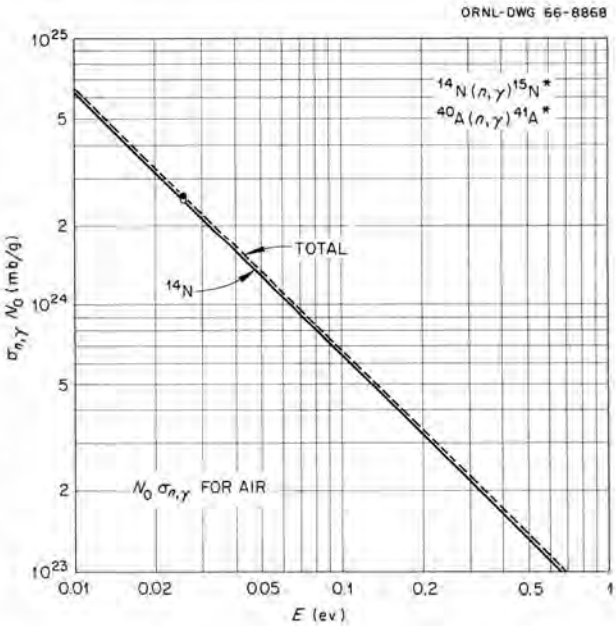

Fig. 18.9. Relative Thermal-Neutron Capture Cross Sections for Air.

gamma rays; these data are taken from Ajzenberg-Selove and Lauritsen.[11] The only other significant cross section is for the $^{40}Ar(n,\gamma)^{41}Ar^*$ reaction, which produces 4.74- and 5.59-Mev gamma rays. However, the ^{40}Ar cross section is only 3% of the total relative thermal cross section.

Threshold reactions are not kinematically possible until the energy of the incoming neutron is sufficient to supply the necessary energy and momentum. When charged particles are emitted, they must have sufficient energy to penetrate the Coulomb barrier of about 3 Mev for protons and twice that for alpha particles. For inelastic scattering, the incident neutron must have sufficient energy to excite the target to one of its excited states. Thus there is an effective threshold for inelastic scattering from each of the excited levels. When the neutrons produce the higher excited states, there is a possibility of cascade gamma rays.

The neutron reactions in ^{16}O and ^{14}N are the only important ones in the threshold region because the abundances of the other isotopes and elements in air are small. There is $4\frac{1}{4}$ times as much ^{14}N as ^{16}O in air. Since ^{16}O is a doubly magic nucleus, it should be much more stable than ^{14}N, which is an odd-odd nucleus.[12] Indeed this is true even though ^{16}O is a more complex many-body system. This effect is observed here since ^{14}N starts producing gamma rays from threshold reactions at about 4.75 Mev, while in ^{16}O the gamma rays are observed at about 6.5 Mev.

Reactions which produce gamma rays in ^{14}N are $^{14}N(n,n')^{14}N^*$ and $^{14}N(n,\alpha)^{11}B^*$,[13–15] of which the most important is the inelastic scattering reaction. These gamma rays have energies from about 1.5 to 12 Mev. The cross sections are shown in Fig. 18.10.

In ^{16}O the reactions which produce gamma rays are $^{16}O(n,n')^{16}O^*$, $^{16}O(n,\alpha)^{13}C^*$, and $^{16}O(n,p)^{16}N^*$;[15–17] the $^{16}N^*$ decays by beta emission with a half-life of 7.35 sec to $^{16}O^*$. Inelastic scattering is the most important gamma-producing cross section. These gamma rays have energies from 3 to 7 Mev. The cross sections are shown in Fig. 18.11.

The cross sections for the production of gamma rays from the interaction of neutrons with air are well known at thermal energies, partially known from threshold to about 9.5 Mev with one additional point at 14 Mev, and unexplored from 9.5 to 14 Mev. The total relative gamma-ray-producing cross sections for ^{14}N and ^{16}O are presented in Fig. 18.12. From this graph, it is evident that ^{14}N is the dominant gamma-producing source in air. Most of the gamma rays come from the inelastic scattering of neutrons by ^{14}N and ^{16}O. There is a region between thermal and threshold in which the neutron interacts predominantly through elastic collisions until it is moderated to thermal energies.

[11] F. Ajzenberg-Selove and T. Lauritsen, *Nucl. Phys.* 11, 1 (1959).

Table 18.7. Gamma Radiation from $^{14}N(n,\gamma)^{15}N$

E_γ (Mev)	Gamma Rays per 100 Captures	Assignment
10.833 ± 0.008	11	C → 0
>9.152	≦0.3	
9.152 ± 0.010	1	9.16 → 0
9.03 ± 0.03	0.2	9.06 → 0
8.54 ± 0.04	0.2	8.57 → 0
8.313 ± 0.013	4	8.32 → 0
7.305 ± 0.012	9	7.31 → 0
(7.164)	≦0.8	
6.323 ± 0.008	17	6.33 → 0
5.559 ± 0.005	14	C → 5.28
5.530 ± 0.008	18	C → 5.31
5.293 ± 0.007	35	5.31 → 0
5.263 ± 0.010	22	5.28 → 0
4.497 ± 0.011	16	C → 6.33
3.669 ± 0.016	17	C → 7.16
3.520 ± 0.016	15	C → 7.31
(3.267)	≦6	

[12] D. Halliday, *Introductory Nuclear Physics*, chap. 8, sect. 10, Wiley, New York, 1950.

[13] J. R. Smith, *Phys. Rev.* **95**, 730 (1954).

[14] A. B. Lillie, *Phys. Rev.* **87**, 716 (1952).

[15] J. R. Stehn *et al.*, *Neutron Cross Sections*, BNL-325, 2d ed., suppl. 2, vol. 1 (1965).

[16] W. J. McDonald *et al.*, *Nucl. Phys.* **75**, 353 (1966).

[17] V. V. Nefedov *et al.*, *Soviet Progress in Neutron Physics* (ed. by Krupchitskii), pp. 241–47 (1961).

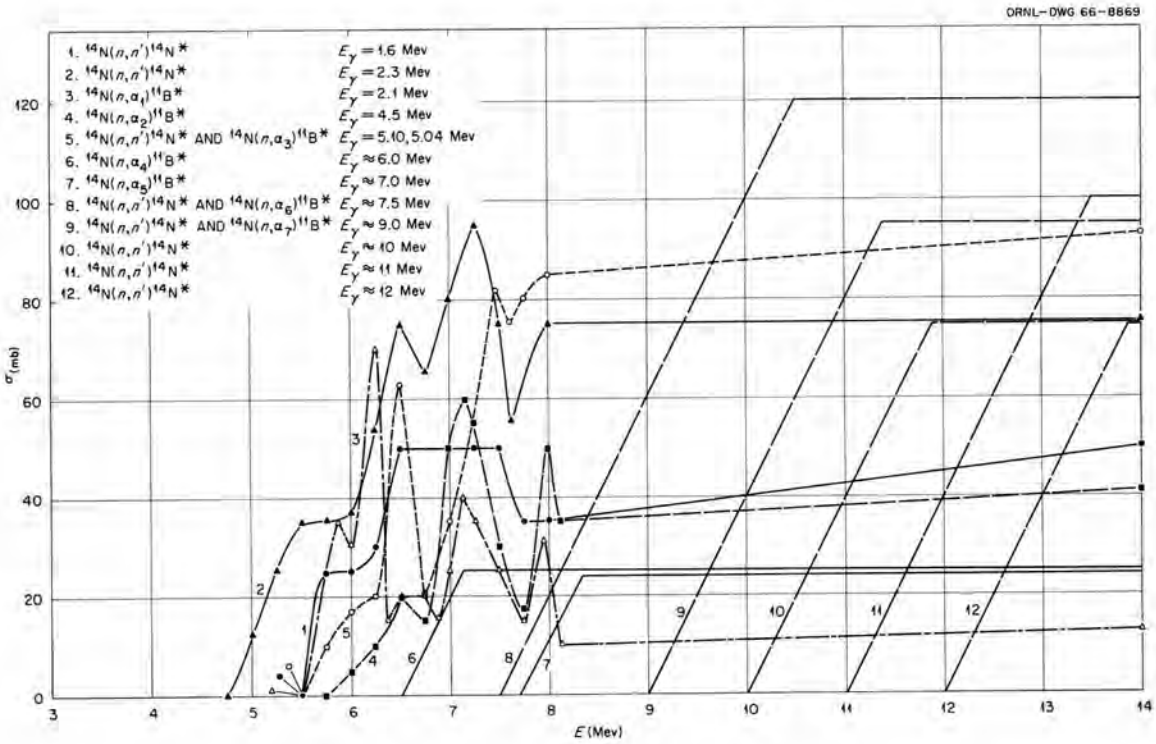

Fig. 18.10. Neutron Cross Sections for Production of Gamma Rays in ^{14}N.

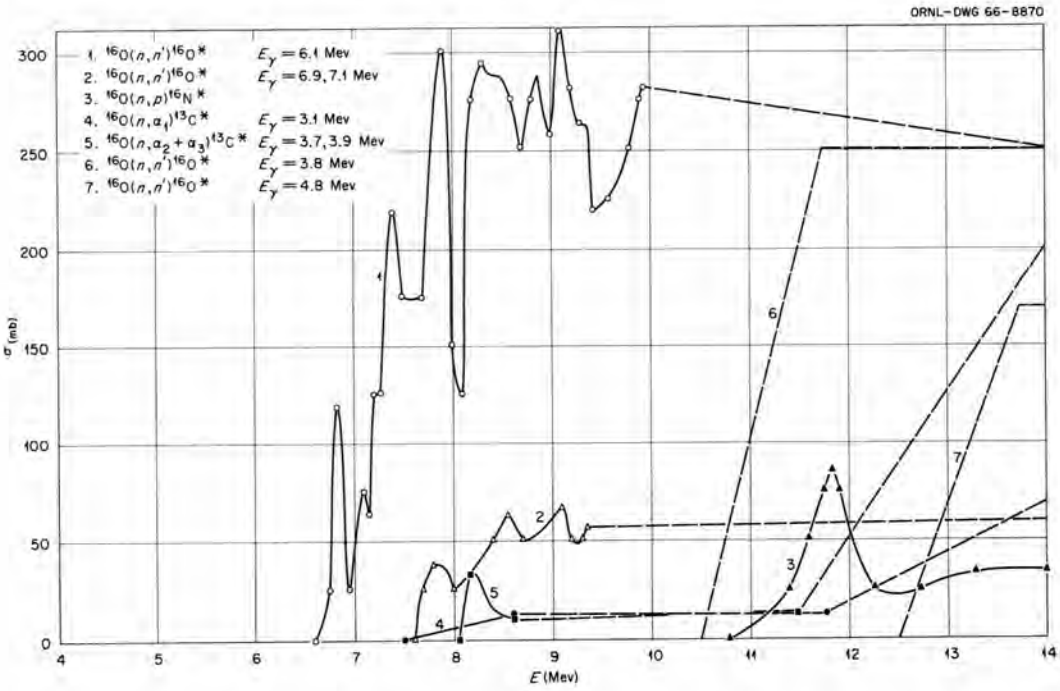

Fig. 18.11. Neutron Cross Sections for Production of Gamma Rays in ^{16}O.

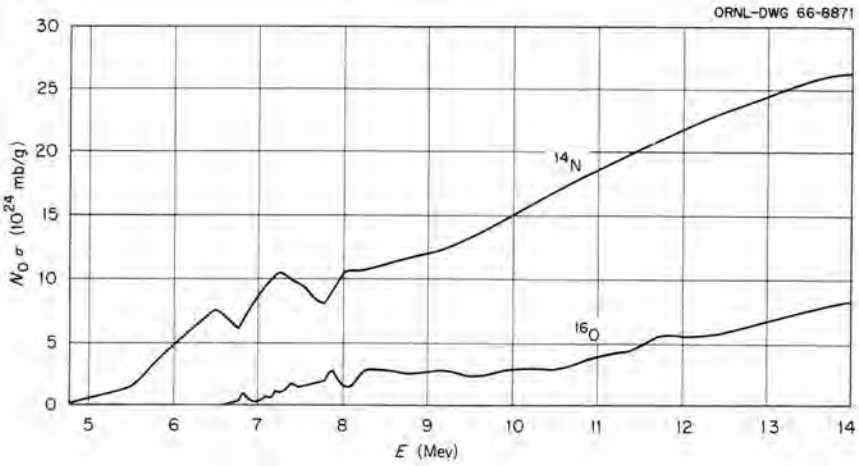

Fig. 18.12. Total Relative Gamma-Ray-Producing Cross Sections for Neutrons in Air.

NEUTRON CROSS SECTIONS FOR THE ELEMENTS IN TISSUE

Work is presently under way to determine the best available data for the cross sections of neutrons in the energy range of 0 to 14 Mev for the elements in tissue. In the energy range of 10 to 14 Mev the cross sections will be approximated when no experimental data are available. It is the purpose of this work to reduce the total neutron cross section into its component parts to be used as input data for a calculation of depth dose in tissue-equivalent phantoms. In this calculation the inelastic reaction products are assumed to come off isotropically with average energy $\overline{E}_3$;

$$\overline{E}_3 = \frac{2M_1M_3E_1}{(M_3+M_4)^2} + \frac{M_4Q + E_1(M_4 - M_1)}{M_3 + M_4},$$

where

E_1, M_1 = energy and mass of incoming neutron,

Q = Q value for reaction,

M_3 = mass of reaction product with energy E_3,

M_4 = mass of other reaction product.

For this choice of $\overline{E}_3$

1. energy is conserved, $E_1 + Q = \overline{E}_3 + \overline{E}_4$;
2. $\overline{E}_3 = M_4Q/M_3 + M_4$ when $E_1 \cong 0$ as it should;
3. $\overline{E}_3 = M_1M_3E_1/(M_3 + M_4)^2$ at threshold and $\theta = 0$ as it should;

$\overline{E}_4$ is the average energy of the other reaction product. One arrives at the above $\overline{E}_3$ by assuming equally probable energies when E_3 is single valued.

IONIZATION RECOMBINATION STUDIES

The biological effectiveness of radiation is known to depend on the local rate of energy loss along the track of the charged radiation and its secondaries. Many physical effects of radiation also depend on this local rate of energy loss, such as the light output from plastic scintillators, the efficiency of chemical dosimeters, and the initial recombination in ionization chambers. The recombination in ionization chambers has been selected for study to determine what information can be obtained about the distribution of the ionization. Recombination was selected because the phenomenon has received much attention, because the parameters affecting recombination in gases can be controlled, and because the empirical relations between recombination and "biological effectiveness" of radiation have been demonstrated.[18,19] Several theories of initial recombi-

[18] M. Zelcinsky, *Nukleonika* 7(3), 175 (1962).

[19] A. H. Sullivan and J. Baarli, CERN Report 63-17 (1963).

nation existed before 1940. These have the fundamental difficulty of either applying only to certain types of radiation or of requiring some knowledge of the type of radiation causing the ionization.

The theory of recombination occurring in long, randomly oriented ion columns has been given by Jaffé,[20] who deduces an equation for ion collection efficiency of:

$$f_1 = \int_0^{\pi/2} \frac{\sin^2\theta}{\sin\theta + \frac{N g_1 p}{y}\int_0^\infty \frac{e^{-s}\,ds}{\sqrt{s\left(1+\frac{s}{y^2\sin^2\theta}\right)}}}\,d\theta\,, \qquad (1)$$

where $y = Bv/p$, which is directly proportional to the ratio of applied voltage to gas pressure, g_1 is a gas constant, and N the number of ion pairs per centimeter at unit gas pressure. The equation has been found to describe well the recombination occurring along the tracks of alpha particles. Both θ and s are arbitrary variables. Ionization occurring in clusters, such as is found in electron ionization, is described by a theory of Lea.[21] This theory can be reduced to an equation for the collection efficiency of an isolated cluster of ν ions of:

$$f_2 = \frac{1}{1 + g_2 \nu p\left[1 - e^{y^2}(1 - 2\,\mathrm{erf}\,\sqrt{2}y)\right]}\,. \qquad (2)$$

The problem, to make the theory universal, is to decide what length of track in a long column is reasonably equivalent to an isolated cluster, and over what range of gas parameters is such an equivalence valid. This is decided by putting N in Eq. (1) equal to $\nu/\Delta x$ and $f_1 = f_2$.

In Fig. 18.13 f_1 and f_2 are plotted as a function of $y = (Bv/p)$, where it is shown that the equality holds reasonably over four decades of ν provided $y > 1$. The value of Δx necessary to obtain this best fit is equivalent to about 0.1 μ of unit density tissue.

Hence Eq. (2) is universal at high v/p when ν refers to the number of ions in a length of track Δx.

Much of the experimental work has been devoted to demonstrating the universality of Eq. (2) and determining the constants to be used. The measurements have been made in a parallel plate tissue-equivalent ionization chamber filled with tissue-equivalent gas, and using as sources of ionization gamma rays, neutrons, and an internal alpha-particle source. The constants have to be

[20] G. Jaffé, *Ann. Physik* **42**, 317 (1913).

[21] D. E. Lea, *Proc. Cambridge Phil. Soc.* **30**, 80 (1933).

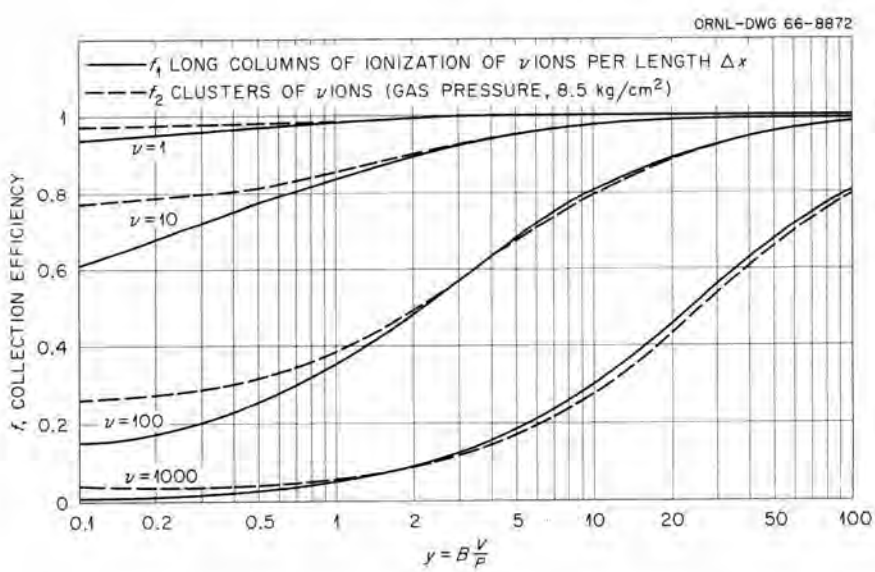

Fig. 18.13. Ionization Collection Efficiencies as a Function of the Number of Ions per Track Length Δx and the Number of Ions in Clusters.

found without assuming a distribution of the ionization as it is this distribution that it is necessary, eventually, to determine. The measurements have shown that the "constants" are reasonably independent of the type of radiation causing the ionization. Using Eq. (2), an absolute determination of ν and its distribution is, in theory, possible. A quantity that is determined readily is the average number of ions per length Δx. Typical values that have been found in conventional units of linear energy transfer of kev per micron in unit density tissue are as follows.

Type of Radiation	Source	LET (kev/μ)
Gamma rays	^{60}Co	3.2
Neutrons and gamma rays	PuBe	18.5
Neutrons	D(d,n)^{3}He	49.0

19. Dosimetry Applications

J. A. Auxier

R. T. Boughner[1]
J. S. Cheka
Mary P. Haydon[2]
D. R. Johnson
T. D. Jones
G. D. Kerr
J. W. Poston
T. D. Strickler

METAPHOSPHATE GLASS DOSIMETRY

In the last few years, silver-activated metaphosphate glass has been greatly improved. The developments have been along the lines of (1) greater sensitivity, achieved both by altering the composition and also by using larger volumes of glass; (2) lower energy dependence, brought about by lowering the average atomic number of the mixture; (3) lower inherent fluorescence or predose reading; and (4) better readers. The glass has reached a stage where it appears feasible to consider its use for personnel monitoring, as a possible replacement of film badges.

Previous studies investigated the additivity of small doses,[3] the dose range, and the long-term stability of the radiation-induced fluorescence with microdosimeter rods (1 mm in diameter by 6 mm).[4]

The glass is commercially available in blocks. Samples of two sizes, 8 × 8 × 4.7 mm and 6 × 6 × 3.3 mm, were tested. These have volumes 64 and 25 times that of the microdosimeter rod respectively. The predose fluorescence of the larger blocks is ~500 mr equivalent and that of the smaller ones ~700 mr equivalent, compared with ~4 r for the rods. In some experimental batches of the larger-size blocks, the predose fluorescence had been reduced to ~380 and 200 mr. With the low predose reading and the high radiation sensitivity, it is possible to measure a few tens of milliroentgens with the same reliability as ~1 r can be measured with a rod.

When using glass to evaluate the low exposures, surface cleanliness is critical; a fingerprint may produce fluorescence equivalent to 300 mr of gamma-ray exposure when placed in the uv light of the reader. Although the rods can be cleaned adequately by a series of baths consisting of acetone, distilled water, and methyl alcohol, this treatment proved insufficient for the blocks. Several commercial detergents were tested, but each left some fluorescent residue on the glass. Excellent reproducibility was obtained by using sodium dichromate–sulfuric acid cleaning solution, diluted about 20 to 1, and a distilled water rinse preceding the acetone, distilled water, and methyl alcohol, all sequentially immersed in the tank of an ultrasonic cleaner.

Heat treatment can be used to "erase" the radiation-induced fluorescence in microdosimeter rods.[3] When this technique was tested on the blocks, it was found that heating at 400°C for 1 hr would accomplish this purpose. However, it took about three weeks for the residual fluorescence to stabilize, the reading 24 hr after heat treatment being 15 to 25% higher than 19 days later, depending on differences in batches of glass.

It was found that the heat treatment reduced the predose fluorescence of the regular glass blocks, but increased that of the experimental low-predose blocks. A group of blocks having a predose fluorescence of about 550 mr equivalent had about 380

[1]Mathematics Division.

[2]Consultant.

[3]J. S. Cheka, *Health Phys.* **8**, 551 (1962).

[4]J. S. Cheka, *Health Phys.* **10**, 303 (1964).

mr equivalent after heat treatment, but the measurements on a group of low-predose blocks were 240 and 290 mr equivalent respectively; the latter number was independent of whether specimens had or had not been exposed to radiation before the heat treatment.

The glass with the lowest average atomic number now available still has too high a response to low-energy radiation (by a factor of 5.5 for 69 kev effective). Work is being done to design a shield which both flattens the energy response and is of convenient size to be contained in a badge.

The lowest-Z glass contains almost 50% $LiPO_3$. Because of this ingredient, this glass is extremely sensitive to thermal neutrons, a characteristic which is troublesome in mixed radiation fields. At our request, one of the suppliers produced a glass using isotopic ^7Li in the $LiPO_3$. Preliminary tests indicate that the neutron response is lower and differs by a factor of ~ 14. The glass is not altogether insensitive to thermal neutrons because the activating silver also responds to these. Further study is required to determine whether the best technique will be to use a lithium filter or to use differential readings between two kinds of glass to obtain correction factors for neutron response in mixed fields of neutrons and gamma rays.

The tests were made using a recent-model fluoroglass reader (Toshiba FD-5). This reader is quite stable, and readings on it are reproducible. The sample holder has interchangeable inserts to accommodate the various sizes of glass dosimeters.

A NEUTRON-ENERGY THRESHOLD DETECTOR SYSTEM EMPLOYING SOLID-STATE NUCLEAR TRACK DETECTORS

The neutron-energy threshold detector units (TDU's) developed by Hurst *et al.*[5,6] have been improved by replacing the conventional fissile foils with fissile radiators and nuclear track detectors. Figure 19.1 shows the fissile radiators and glass detectors in a model suitable for field

[5] G. S. Hurst *et al.*, *Rev. Sci. Instr.* **27**, 153 (1956).

[6] G. S. Hurst and R. H. Ritchie, *Radiation Accidents: Dosimetric Aspects of Neutron and Gamma-Ray Exposures*, ORNL-2748, pt. A (November 1959).

Fig. 19.1. View of Unassembled TDU Using Fissile Radiators and Glass Plates as Nuclear Track Detectors.

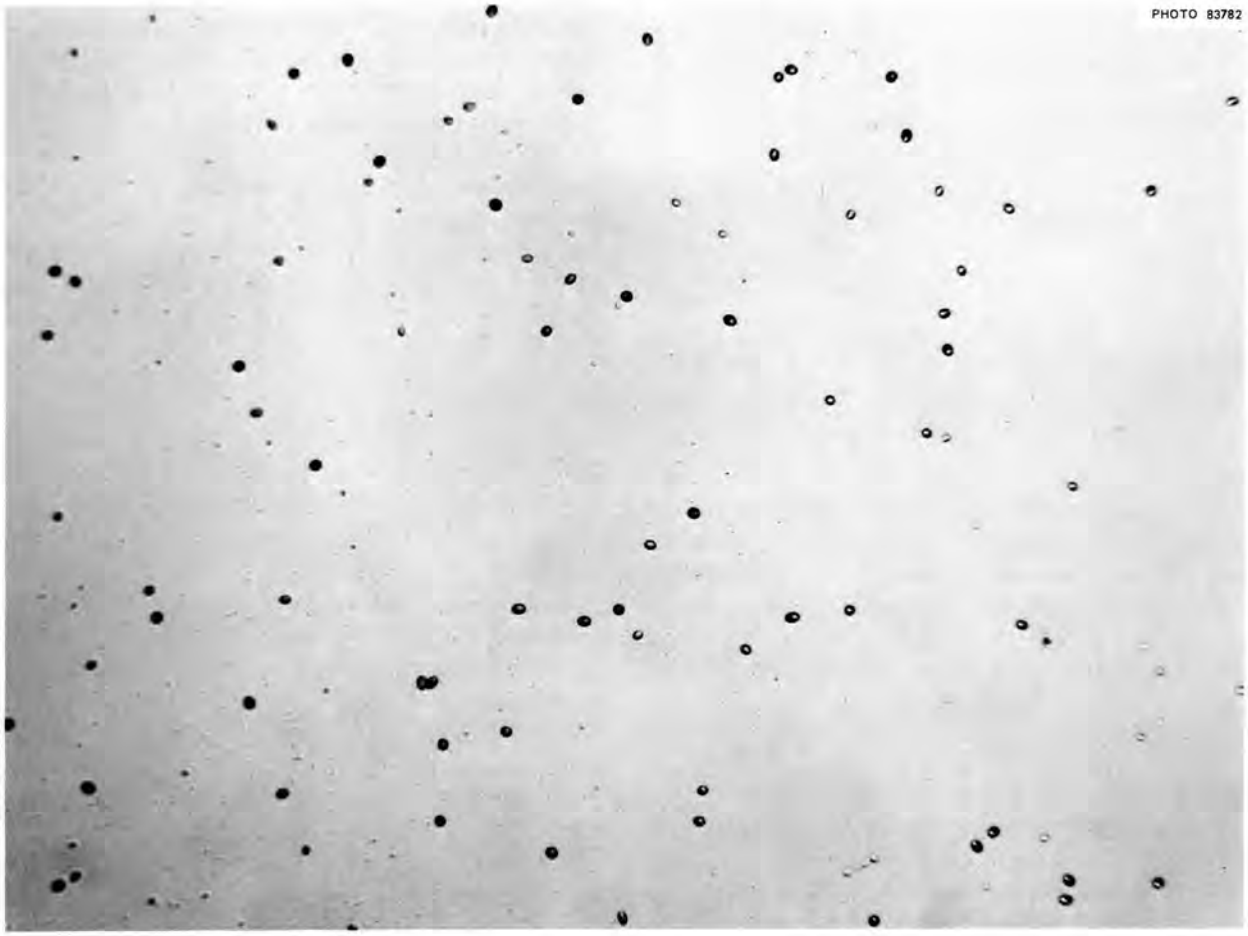

Fig. 19.2. Fission Fragment Tracks (100X) in Micro Cover Glasses Etched in 10% HF Solution for 5 min.

use. These three detector units can be placed inside the boron and cadmium shields presently used in the Hurst-type TDU.

The term "solid-state track detectors" has been applied to insulating solids in which tracks of charged particles can be viewed with an optical microscope after they have been developed by chemical etching.[7] Fission-fragment tracks in micro cover glasses made of Corning brand glass, No. 0211, which have been etched in a 10% HF solution for 5 min are shown in Fig. 19.2.

The track registration efficiency in the glass is 100% since the rate of energy loss of the fission fragments from the thin foils used is above the critical rate of energy loss for track formation in the glass, but the detection efficiency is less than 100% since it depends upon the track registration geometry,[8] as shown in Fig. 19.3. If the rate of chemical etch along the tracks is T and the rate of chemical etch of the surface of the detector is S, the critical angle θ_c for observing a track is arc cos (S/T).

The critical angle for the micro cover glasses was determined to be $58 \pm 2°$ by mounting a point source of fission fragments above a plane surface of the material in a vacuum and observing directly the largest angle at which tracks were formed, since this measure was simpler than measuring the rates of chemical etch. These detectors were chosen because they had surfaces free of irregularities and their small critical angle gave a central region free of edge effects when used with the 1.5-cm^2 fissile radiators at a separation distance of

[7] R. L. Fleischer *et al.*, *Phys. Rev.* **133**, A1443 (1964).

[8] R. L. Fleischer and P. B. Price, *J. Geophys. Res.* **69**, 331 (1964).

ORNL-DWG 66-8873

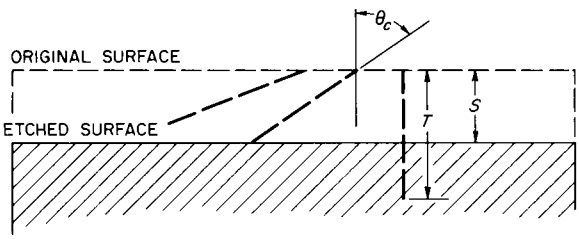

Fig. 19.3. Track Registration Geometry. Developed tracks are observed at angles less than θ_c and those produced by fission fragments incident at angles larger than θ_c are etched away when the detector is developed.

0.04 cm. If the fields of tracks observed with the microscope are limited to this central region of the detector, the detection efficiency ϵ is just the solid angle $d\Omega$ over which tracks will be observed or

$$\epsilon = \frac{d\Omega}{2\pi} = \frac{\int_0^{2\pi}\int_0^{\theta_c} \sin\theta \, d\theta \, d\phi}{2\pi} = 1 - \cos\theta_c \, .$$

The 2π source geometry appears because of the two charged fragments produced in the fission reaction. The detection efficiency for the glass calculated by the above equation is 47 ± 3%.

Once the detector unit has been exposed and the track density N determined with an optical microscope, the neutron fluence Φ above the threshold energy of the fissile radiator may be calculated by the relationship

$$N = \Phi n \sigma \epsilon P \, ,$$

where n is the number of fissile atoms per unit area, σ is the effective fission cross section of the material enclosed by the boron shield, P is a correction factor for the perturbation of the neutron fluence by the boron shield,[9] and ϵ is the efficiency of the detector. The first-collision tissue dose can be calculated from the neutron fluence measurements in the normal manner.[9]

A set of fissile radiators of 15, 85, and 400 $\mu g/cm^2$ of ^{239}Pu, ^{237}Np, and ^{238}U, respectively, has been used with the sulfur foil from the conventional TDU to measure doses of 10 to 10^4 rads of fast neutrons.

One advantage of this TDU system is that immediate retrieval is not necessary because observation of the radioactivity of the fast-decaying fission products has been eliminated, and the ^{32}P produced in the sulfur foil has a 14.2-day half-life. Other advantages are the elimination of the specialized counting system needed for accurate evaluation of the fissile foils used in the conventional TDU's, and the increased sensitivity of the new method requires only microgram quantities of fissionable material compared to the gram quantities of material required with the present TDU.

NUCLEAR ACCIDENT DOSIMETER INTERCOMPARISON STUDY

A second intercomparison of nuclear accident dosimeter (NAD) systems was held at the DOSAR facility during the fall of 1965. Seven groups representing Savannah River Plant (SRP), Pacific Northwest Laboratory (PNL), Phylatron Corporation, and four dosimetry groups from Oak Ridge (Y-12, K-25, X-10, and DOSAR) participated in the study.

The HPRR was pulsed to 9.1×10^{16} fissions with the dosimeters arranged in an arc 3 m from the reactor core and approximately 1.5 m above the floor. A Bomab[10] phantom filled with saline solution (~1.5 mg of Na per cubic centimeter) was instrumented by each organization and placed in a position and orientation unknown to the participants.

The experiment was repeated using a moderated neutron energy spectrum which was produced by placing a 10-in.-thick polyethylene shield 1 m from the reactor core. The dosimeters were placed behind the shield in an arc 3 m from the core and 1.5 m from the floor. Bomab was positioned behind the shield at a distance of 4 m. The second pulse yielded 6.6×10^{16} fissions. Tables 19.1 and 19.2 show the results of both experiments before and after data revisions.

During a discussion session following the experiments, the question of future intercomparisons was raised. The consensus was that such studies are valuable and that they will be more valuable with continuing improvement in NAD systems. In general, the participants knew the causes of the

[9] D. R. Johnson *et al.*, *Health Phys.* 11, 759 (1965).

[10] A commercially available phantom.

Table 19.1. Intercomparison Data for Burst 158, October 19, 1965

Study Group	Date	D_f (rads)	D_{th} (rads)	D_γ (r)	n/γ	Neutron Fluence (neutrons/cm^2) ϕ_{th}	ϕ_{Pu}	ϕ_{Np}	ϕ_U	ϕ_S	ϕ_{In+Cd}	$\phi_{115m_{In}}$	ϕ_{Cu}	ϕ_{tot}	Na (μc/cc)	Bomab Dose Based on ^{24}Na (rads)	Gamma Dose (Bomab)
						$\times 10^{10}$	$\times 10^{10}$	$\times 10^{10}$	$\times 10^{10}$	$\times 10^{10}$	$\times 10^{10}$	$\times 10^{10}$	$\times 10^{10}$	$\times 10^{10}$	$\times 10^{-4}$		
SRP	10-22-65	403		60	6.7	0.37				1.6	0.023	10.7	5.2	16.0	7.26	262 247[f]	
			No revisions submitted														
PNL	10-22-65	417[a] 384[b]		65	5.9	0.6				4.6		5.6	3.5	14.3		127	
	Revisions 11-23-65	362[a] 389[b]	0.13	69[c] 89[d]	5.6[c] 4.4[d]	0.6				3.4	0.15	7.6	2.9	15.3		177[e]	32[c] 34
DOSAR	10-22-65	363	0.22	66	5.5	0.79	14.7	10.4	4.90	2.93				14.7	4.7	211[g] 248	38
	Revisions 12-1-65			51	7.1												
Y-12	10-22-65	316[g] 364[h]	0.26	61	5.2	0.94	15.1	8.34	4.8 5.5	2.76				15.1	6.7	190	
	Revisions 10-27-65															207	
K-25	10-22-65	404[g] 352[h]		55	7.3 6.4	0.66 0.64	17.2	10.5	5.2	2.65		5.8	0.52		6.7	200 235[g]	
	Revisions 12-7-65	364[g] 352[i]	0.18		6.6[g] 6.4[i]		15.3	9.88	4.94							200 237[g]	36 31
Phylatron	10-22-65	353															
	Revisions 11-4-65						14.1									177[e]	
AHP, X-10	10-22-65	360	0.21	52	6.9	0.7	14.8	10.5	4.5	2.6				14.8			
			No revisions submitted														
DOSAR (exptl.)	10-22-65	370					15.3[h]	9.9	4.7	2.6				15.3			
			No revisions submitted														

[a]Single gold foil.
[b]Single gold foil spectrum weighted.
[c]Glass.
[d]Film.
[e]Not based on ^{24}Na activation.
[f]CND.
[g]TDU.
[h]Uranium foil.
[i]ORGDP dosimeter.

Table 19.2. Intercomparison Data for Burst 159, October 20, 1965[a]

Study Group	Date	D_f (rads)	D_{th} (rads)	D_γ (r)	n/γ	Neutron Fluence (neutroms/cm^2) ϕ_{th}	ϕ_{Pu}	ϕ_{Np}	ϕ_U	ϕ_S	ϕ_{In+Cd}	$\phi_{115m_{In}}$	ϕ_{Cu}	ϕ_{tot}	Na (μc/cc)	Bomab Dose Based on ^{24}Na (rads)	Gamma Dose (Bomab)
						$\times 10^{10}$	$\times 10^{10}$	$\times 10^{10}$	$\times 10^{10}$	$\times 10^{10}$	$\times 10^{10}$	$\times 10^{10}$	$\times 10^{10}$	$\times 10^{10}$	$\times 10^{-4}$		
SRP	10-22-65	37		23.5 22.3	1.57	0.21				0.067	0.008	0.60	1.5	2.3	1.12	24	
			No revisions submitted														
PNL	10-22-65	41[a] 22[b]		7	3.1	0.4				0.2			0.9	1.5		12	<5
	Revisions 11-23-65	36[a] 18[f]	0.09	30[c] 37[d]	0.6[c] 0.5[d]	0.4				0.14	0.06	0	0.9	1.5		20[e]	32[c] 34[d]
DOSAR	10-22-65	25	0.14	35	0.7	0.51	1.19	0.61	0.23	0.11				1.19	0.92	19[f] 39	17
	Revisions 12-1-65			22	1.1											31	
Y-12	10-22-65	23[f] 19[g]	<0.1	25	0.92	0.097	1.3	0.54	0.22	0.096				1.3	1.0	24	16
	Revisions 10-27-65		0.17			0.60										26	
K-25	10-22-65	24.3[f] 23.9[h]		23	1.06 1.04	0.448 0.404	1.31	0.325	0.252	0.123 0.116		0.315	0.124		1.10	18 30[f]	
	Revisions 12-7-65	25.5[f] 23.9[h]	0.13[f] 0.11[h]		1.11[e] 1.04		1.22	0.61	0.24								27 17
Phylatron	10-22-65	13.3															
	Revisions 11-4-65	20.7					0.86										
AHP, X-10	10-22-65	26		30	0.87	0.4	1.2	0.7	0.2	0.1				1.2			
			No revisions submitted														
DOSAR (exptl.)	10-22-65	28.8					1.36[g]	0.67	0.33	0.11							
			No revisions submitted														

[a]Symbols are as defined in Table 19.1.

observed differences in response in a given radiation field. During the next year, some of the participants plan changes in instruments and/or techniques which should result in more consistent results in future intercomparisons.

Another intercomparison experiment is planned for which more precise spectral and dose information for the HPRR will be available. Also, a neutron generator is now available at the DOSAR facility which should yield adequate fluences of 14-Mev neutrons for studies of this type as well as 3-Mev neutrons at lower intensity.

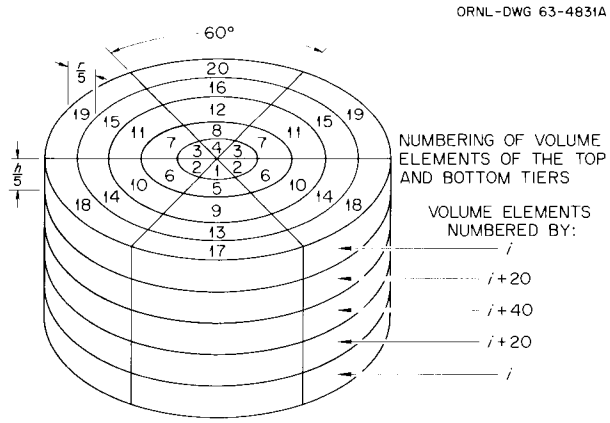

Fig. 19.4. Numbering of Volume Elements in the Cylindrical Phantom.

DEPTH-DOSE STUDIES

Depth dose as a function of energy has been the object of extensive study both experimentally and theoretically via use of a Monte Carlo digital computer code simulating various physical experimental situations. The phantom (Fig. 19.4) was assumed to be a man-equivalent cylinder, 30 cm in diameter and 60 cm in height, composed only of H, C, N, and O in the proportions found in soft tissue.[11] The phantom was divided into 150 volume elements; however, these 150 elements were reduced to 60 for unilateral broad-beam irradiation due to geometrical symmetry, and small volume elements 1, 2, 3, and 4 were combined to improve the statistical accuracy of the results (likewise elements 21, 22, 23, and 24 were combined, as well as 41, 42, 43, and 44), so that the final exposure results could be described adequately by LET spectra for 51 different volume elements. The LET spectra were recorded according to the divisions found in ref. 11. Stopping power as a function of energy was the same as discussed by Snyder;[12] however, due to recent experimental results, there is reason to believe that the low-energy portions of the curves for C, N, and O may be in error, and this possibility is being investigated.

Depth dose and LET spectra have been computed for ten different monoenergetic neutron beams (0.025 ev to 2.5 Mev). The code is being revised so that calculations may be completed for all energies between 0.025 ev and 15 Mev. Prior calculations were precisely valid only for elastic isotropic reactions, which limited the use of the code to incident neutron energies of 2.5 Mev and lower. All reactions, both elastic and inelastic, possessing a significant macroscopic cross section ($\gtrsim$15 mb) are being included, as well as the best stopping-power data obtainable (experimental data were available, but calculated data relative to measured substances were not available) for H, C, N, and O. Also included are the secondary products, consisting of deuterons, tritons, alpha particles, and beryllium and boron ions.

A preliminary study, to determine the dose variation between a strict isotropic treatment and a more general treatment which permitted anisotropic considerations, was undertaken for a 30 × 30 × 60 cm slab subdivided by planes, multiples of 7.5 cm from the face receiving "head-on" irradiation by the incident neutrons. The results are shown in Table 19.3.

The standard error of these numbers is 5 to 10%; hence one can surmise that the more rigorous treatment adds little to the accuracy of the calculations. In a new version of the code it is planned tentatively to allow only isotropic reactions in order to make more efficient use of computing machinery.

Data are shown in Figs. 19.5 and 19.6 for the cylindrical phantom exposed to a beam of 1-Mev neutrons. The dose due to neutrons as a function of penetration depth is shown in Fig. 19.5 and indicates no significant difference in the dose contributed to the different tiers of the phantom.

[11] "Protection Against Neutron Radiation Up to 30 Million Electron Volts," *Natl. Bur. Std. (U.S.), Handbook* **63**, U.S. Govt. Printing Office, Washington, D.C., 1957.

[12] W. S. Snyder, *Biological Effects of Neutrons and Proton Irradiations*, vol. 1, p. 3, IAEA, Vienna, 1964.

Table 19.3. Comparison of Isotropic and Anisotropic Calculations of Dose

Energy (Mev)	Slab No.	Isotropic Scattering of Neutrons (rads neutron^{-1} cm^{-2})	Anisotropic Scattering of Neutrons (rads neutron^{-1} cm^{-2})	Error (%)
		$\times 10^{-8}$	$\times 10^{-8}$	
14	1	0.528	0.467	−11.6
(2.5 Mev cutoff)	2	0.336	0.324	−3.6
	3	0.194	0.197	+1.5
	4	0.0978	0.113	+15.5
14	1	0.556	0.484	−12.9
(only wt cutoff)	2	0.348	0.332	−4.6
	3	0.204	0.214	+4.9
	4	0.126	0.137	+8.7
7	1	0.456	0.448	−1.8
(2.5 Mev cutoff)	2	0.253	0.249	−1.7
	3	0.120	0.126	+4.8
	4	0.0541	0.0593	+9.5

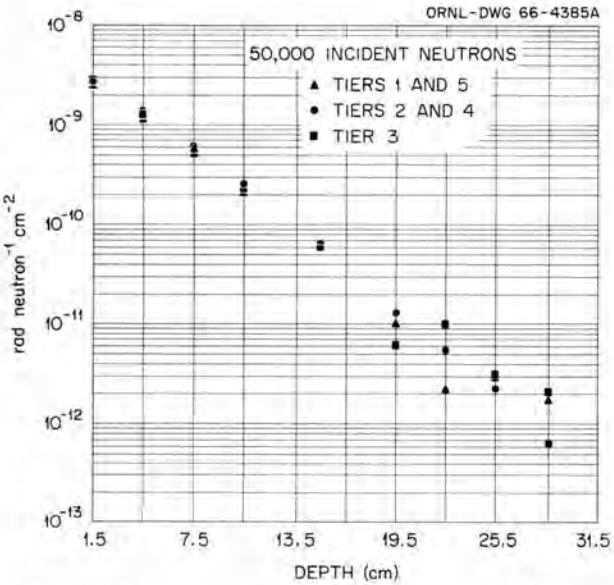

Fig. 19.5. Neutron Dose (rads neutron^{-1} cm^{-2}) in Tiers from 1-Mev Neutrons as a Function of Depth in the Cylindrical Phantom.

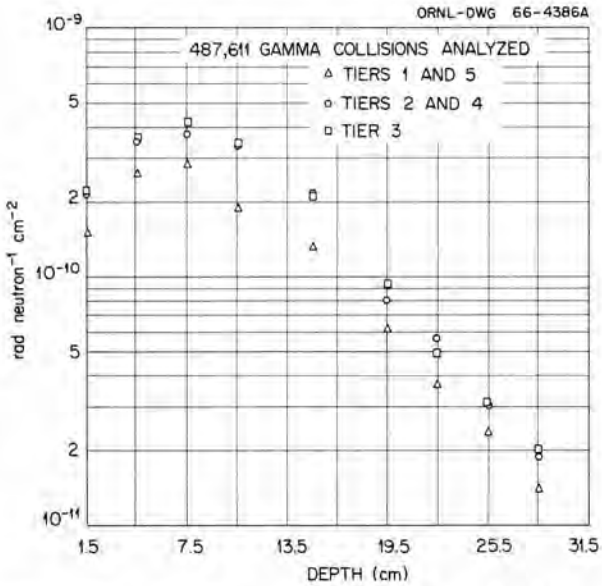

Fig. 19.6. Dose Due to (n,γ) Reactions for 1-Mev Neutrons in Tiers as a Function of Depth in the Cylindrical Phantom.

This fact has been verified experimentally (see the next section). The dose due to (n,γ) reactions as a function of penetration depth is as shown in Fig. 19.6 and does indicate a significant difference in the dose component deposited in the various tiers.

EXPERIMENTAL DEPTH-DOSE STUDIES IN WATER PHANTOMS

The calculational studies of neutron depth-dose distributions in a 30-cm-diam × 60-cm cylindrical phantom were continued. For a special case,

that of a broad beam of neutrons having a fission spectrum, the only volume elements investigated were six 5 × 5 × 12 cm right parallelepipeds extending from front to back and centered vertically in the cylindrical phantom (see Fig. 19.7). These simplifications reduced substantially the amount of computer time required to obtain the desired statistical accuracy using the Monte Carlo technique, but the study was designed primarily to facilitate comparison of calculational and experimental studies. Therefore, the chief consideration that determined the volume element size was the physical size of the dosimeters used. The results of the computations are shown in Fig. 19.7 along with the experimental results.

The experimental work utilized the neutrons from the HPRR; the spectrum closely approximates a fission spectrum. In order to simulate as well as practicable a parallel beam of neutrons impinging on the phantom, it was positioned 6 m from the reactor. To minimize scattered radiation, both the phantom and the reactor were centered 2 m above the floor of the reactor building. In addition, the reactor was positioned above pit 1 so that the experimental distance of 6 m placed the phantom near the center of the reactor building and well away from all other experimental apparatus.

Two Hurst proportional counters ("phantom" size) were used in conjunction with two charge-sensitive preamplifiers and a Radsan dose integrator for neutron dosimetry. One of the counters was used as the "depth dosimeter," while the other one was positioned at the $H = 2$, $D = 6$ m location in air so that depth-dose rates could be determined relative to the "incident" radiation field. The counters were both operated from the same high-voltage supply, the twin preamplifiers were powered by a single remote power supply, and the outputs of each of the preamplifiers were alternately connected to the input of a single Radsan for dose-rate measurements. The reasoning behind this procedure was that if electronic or high-voltage gain drift occurred, it should have occurred equally in both systems so that the depth-dose measurements relative to "in air" measurements were unaffected.

The reactor was operated at 100 w while measurements were made on the front and back sides of the water-filled phantom and inside each of the six

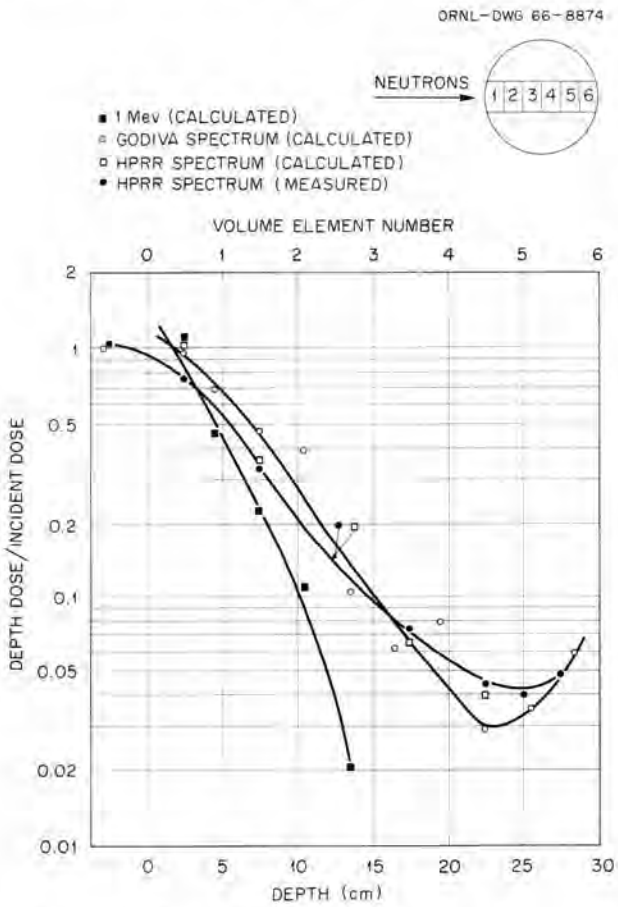

Fig. 19.7. Ratio of Depth Dose to Incident Dose as a Function of Depth in a 30-cm-diam by 60-cm Cylindrical Phantom.

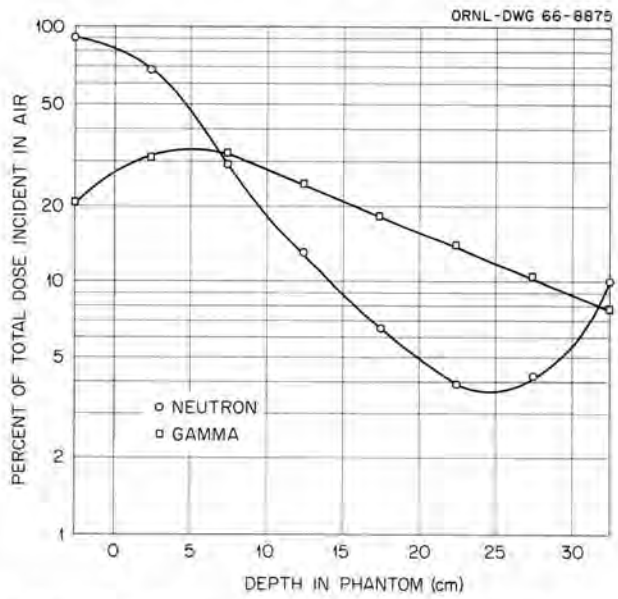

Fig. 19.8. For an Exposure to the HPRR, the Percent of Total Air Dose Is Presented as a Function of Depth in a 30-cm-diam Cylindrical Phantom.

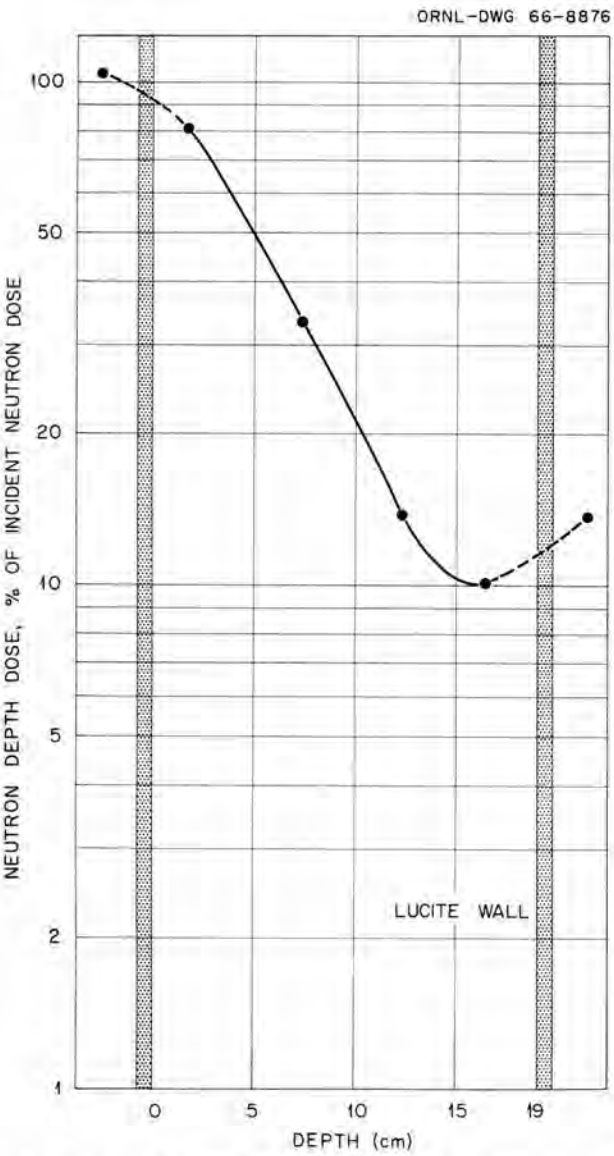

Fig. 19.9. For an Exposure to the HPRR, the Neutron Depth Dose Percent of Incident Neutron Dose Is Presented as a Function of Depth in an Elliptical Phantom 60 cm High and with Major Axis = 30 cm and Minor Axis = 20 cm.

internal volume elements. The results are shown in Fig. 19.8 along with gamma depth-dose distribution, which was determined in the same way using Phil gamma-ray dosimeters.

Finally, owing to the interest in the upturn in the experimental neutron depth-dose curve near the back of the phantom, two additional phantoms were investigated: (1) an elliptical phantom 60 cm deep with major and minor axes of 30 and 20 cm, respectively (the measurements being made along the minor axis), and (2) a 45-cm-diam × 90-cm-deep cylindrical phantom. The results are shown in Figs. 19.9 and 19.10.

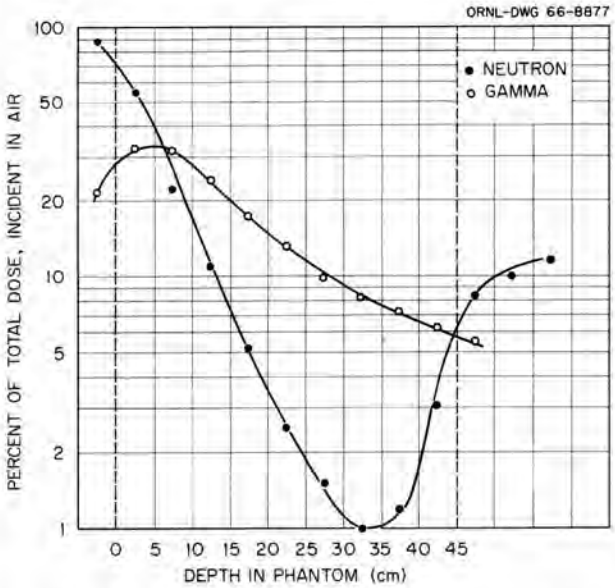

Fig. 19.10. For an Exposure to the HPRR, the Percent of Total Dose in Air Is Presented as a Function of Depth in a 45-cm Cylindrical Phantom.

SENSITIVITY OF CELLULOSE ACETATE BUTYRATE FOR ALPHA-PARTICLE TRACK REGISTRATION

The development of solid-state track-detection techniques has been summarized by Fleischer, Price, and Walker.[13–16] Here the radiation damage produced by the passage of heavy charged particles through insulating solids is used as a basis of detecting these particles. The simplest technique is to place the solid detector in an etching solution which preferentially etches the damaged region along the track until the track itself becomes visible using an optical microscope. Such tracks

[13] R. L. Fleischer *et al.*, *Ann. Rev. Nucl. Sci.* **15**, 1 (1965).

[14] P. B. Price and R. M. Walker, *J. Appl. Phys.* **33**, 3407 (1962).

[15] R. L. Fleischer and P. B. Price, *J. Appl. Phys.* **34**, 2903 (1963).

[16] R. L. Fleischer and P. B. Price, *Science* **140**, 1221 (1963).

have been observed in many materials, including inorganic crystals, glasses, and plastics. Each such material is characterized by a critical rate of energy loss along the track, below which no such preferential etching takes place. Consequently, there is a high-energy limit as well as a low-energy limit to the detection of most particles.

The mechanism of track production has been attributed by some to the creation of "thermal spikes" or "displacement spikes," both of which are commonly referred to in describing radiation damage in crystals.[17] More recently, Fleischer *et al.*[13] introduced the picture of an "ion explosion spike" to account for the fact that tracks are not found in metals or good semiconductors. In this model the strong electrostatic repulsion of the ions remaining in the heavily ionized region of the track is great enough to force them into the lattice, where they remain as interstitials, and leave a high concentration of vacancies along the track.

The etching techniques and critical rates of energy loss for various detectors have been summarized by Fleischer *et al.*,[18] and the application of the detectors in the field of nuclear physics, neutron dosimetry, and geochronology has been described by the same group.[13,16]

In cellulose nitrate, cellulose acetate, and cellulose acetate butyrate, the critical rate of energy loss for preferential etching is below the maximum rate of energy loss for alpha particles in these materials so that low-energy alphas and helium ions can be detected. One such detector can be obtained from the cellulose acetate butyrate film backing found in many commercial photographic films. For example, if the emulsion is removed from the NTA neutron dosimeter film, the film backing provides a detector which is sensitive to alpha particles of energies between approximately 0.1 and 3 Mev.

Sodium hydroxide is a suitable etchant; in a 25% solution (by weight) at 65°C, pits begin to appear along the tracks in this film after about ½ hr of etching. When observed in an optical microscope, these etch pits continue to grow with increased etching time until they become large shallow craters and eventually fade away as the edges become indistinct.

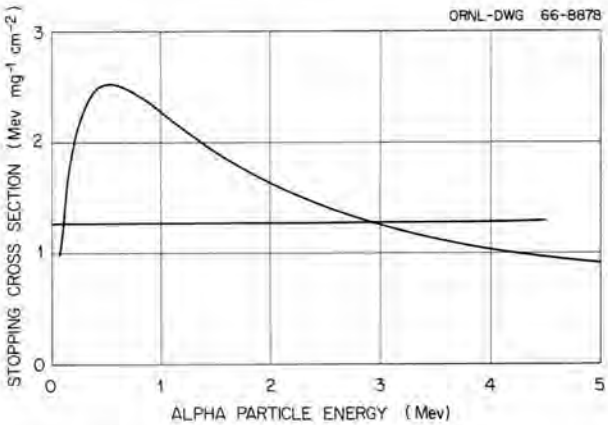

Fig. 19.11. Calculated Rate of Energy Loss (Mev mg^{-1} cm^{-2}) for Alpha Particles as a Function of Alpha-Particle Energy.

The critical rate of energy loss is illustrated in Fig. 19.11, where a plot is made of the calculated rate of energy loss for a particle in cellulose acetate butyrate as a function of energy.[19] By use of alpha particles from ^{239}Pu, degraded in energy by passage through air, it is found that after about 1 hr of etching, tracks can be observed from alphas of energies up to about 3 Mev, but not higher. Also, at low energies, He^+ ions are found to register with energies down to about 100 kev, but not lower. This implies a critical rate of energy loss of approximately 1.3 Mev mg^{-1} cm^2 required for preferential etching of this material and is indicated in Fig. 19.11 by the horizontal line.

Etch pits from alpha particles impinging on the surface may not be registered for any one of several reasons:

1. At high energies the rate of energy loss may be less than the critical rate, so that no selective etching takes place. In this case, by prolonged etching away of the surface of the material, it is sometimes possible to reach the point where the particle has lost enough energy so that its rate of energy loss is no longer below the critical rate, at which time its track will begin to etch preferentially.
2. At low energies it may again have a rate of energy loss less than the critical value, such that it cannot be etched. Even if it is slightly above this energy, it may easily be overetched and indistinct.

[17] L. T. Chadderton, *Radiation Damage in Crystals*, pp. 36–54, Methuen, London, 1965.

[18] R. L. Fleischer *et al.*, *Phys. Rev.* **133**, A1443 (1964).

[19] W. Whaling, *Handbuch der Physik*, vol. 34, pp. 192–217, Springer, Berlin, 1958.

3. It may strike the surface at too large an angle with respect to the normal. In this case the etching along the track may be overshadowed by the etching of the unirradiated surface. This would occur at a critical angle θ_c with respect to the normal given by $\cos \theta_c = V_g/V_t$, where V_g is the rate at which the unirradiated surface is etched away and V_t is the etching rate along the track. Since V_t depends on the rate of energy loss along the track, the critical angle would depend on the type of particle producing the track as well as its energy. As an example, this critical angle has been found to be about 60° for 1.75-Mev alphas in cellulose acetate butyrate.

IRRADIATION OF PLASTICS IN DOSAR LOW-ENERGY ACCELERATOR

A deflection chamber, 1 m long and 15 cm in diameter, was constructed to use with a pair of beam deflection plates on the target end of the DOSAR low-energy accelerator for irradiation of plastics with helium ions and deuterons. Two tantalum-foil apertures defined the beam to a pencil approximately 0.005 in. in diameter before it entered the deflection plates, as shown in Fig. 19.12.

For calibration purposes a ½-in.-thick glass plate was prepared for the target end of the deflection chamber. After spreading a thin layer of vacuum grease on the inside face of this plate, ZnS powder was dusted onto the surface to provide a scintillating surface which could be viewed from outside. This was clamped to the end of the chamber, and the vacuum was sufficient to hold it in place and provide a good seal.

With the beam on, a good spot could be observed where the beam hit the ZnS, and the chamber could be lined up mechanically so that the beam was centered on the axis of the tube.

Voltages from 500 to 4000 v were applied to the deflection plates, and the deflection of the beam spot was measured at different accelerating potentials. Figure 19.13 shows the measured deflection at various accelerating potentials between 60 and 170 kv. At each of these accelerating potentials, a straight line has been drawn according to the equation

$$D = 0.4 \times \frac{V_t}{V_0},$$

ORNL-DWG 66-8879

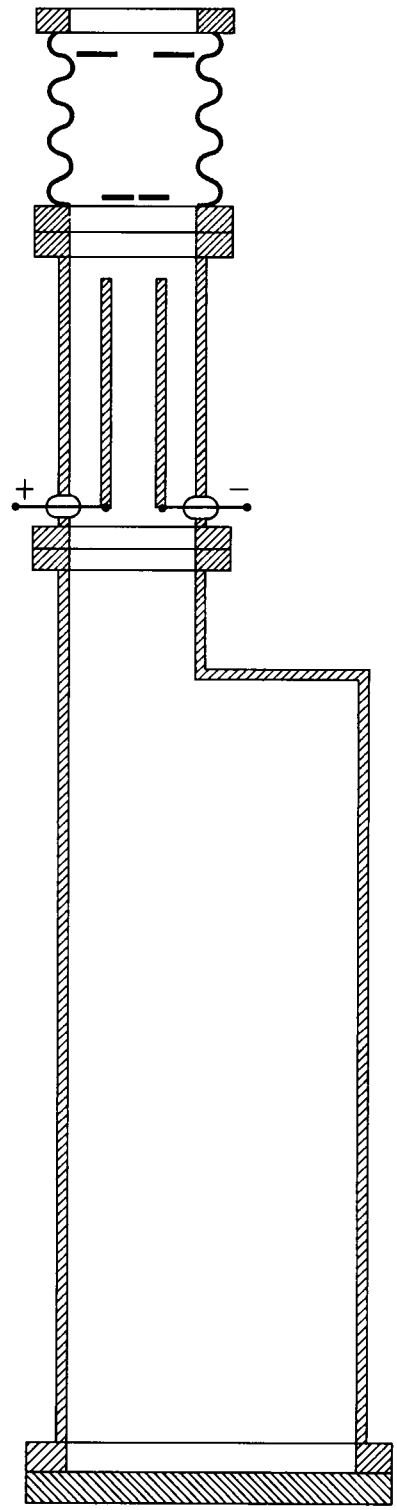

Fig. 19.12. Schematic Arrangement of Target End of the DOSAR Low-Energy Accelerator as Used in Irradiating Plastic Samples with He^+ and D^+ Ions.

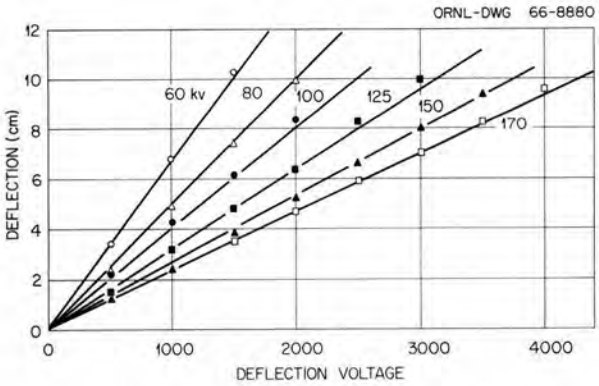

Fig. 19.13. Beam Deflection (cm) as a Function of Deflection Voltage for 60-, 80-, 100-, 125-, 150-, and 170-kv He^+ Ions.

where D is the deflection in centimeters, V_t the transverse voltage of the deflection plates, and V_0 the accelerating potential in kilovolts. Within the experimental error involved in the deflection measurements, this seems to provide an adequate estimate of the deflection for the purposes of this experiment.

The deflection angle θ would be given by

$$\tan \theta = \frac{l}{2d} \frac{V_t}{V_0} \times 10^{-3} ,$$

where l is the length and d the separation of the deflection plates, provided fringing is neglected at the ends of the plates. Since the deflection angle is small, $d = 1.98$ cm, $l = 13.2$ cm, and the distance from the center of the deflection plates to the target is 108.5 cm, the deflection should be about $0.36 V_t/V_0$ cm, which is reasonably close to the measured value given above.

Samples of cellulose acetate butyrate (NTA film base) were taped to the target plate at distances corresponding to deflections of -2, 2, 6, and 10 cm and were irradiated with helium ions using accelerating potentials of 180, 150, 100, and 80 kv respectively. After removing these plastic films, they were etched in a 25% solution of sodium hydroxide at 65°C. With $\frac{1}{2}$ hr of etching, the spot made by the beam could be observed at the three higher energies but not at 80 kv. The spot produced was of the order of $\frac{1}{8}$ in. in diameter, and after 1 hr of etching, shallow individual etch pits could be observed at the edge of the spot. At 100 kv, however, the etch pits were difficult to distinguish and were "washed out" with slightly more etching.

PHOTO 84606

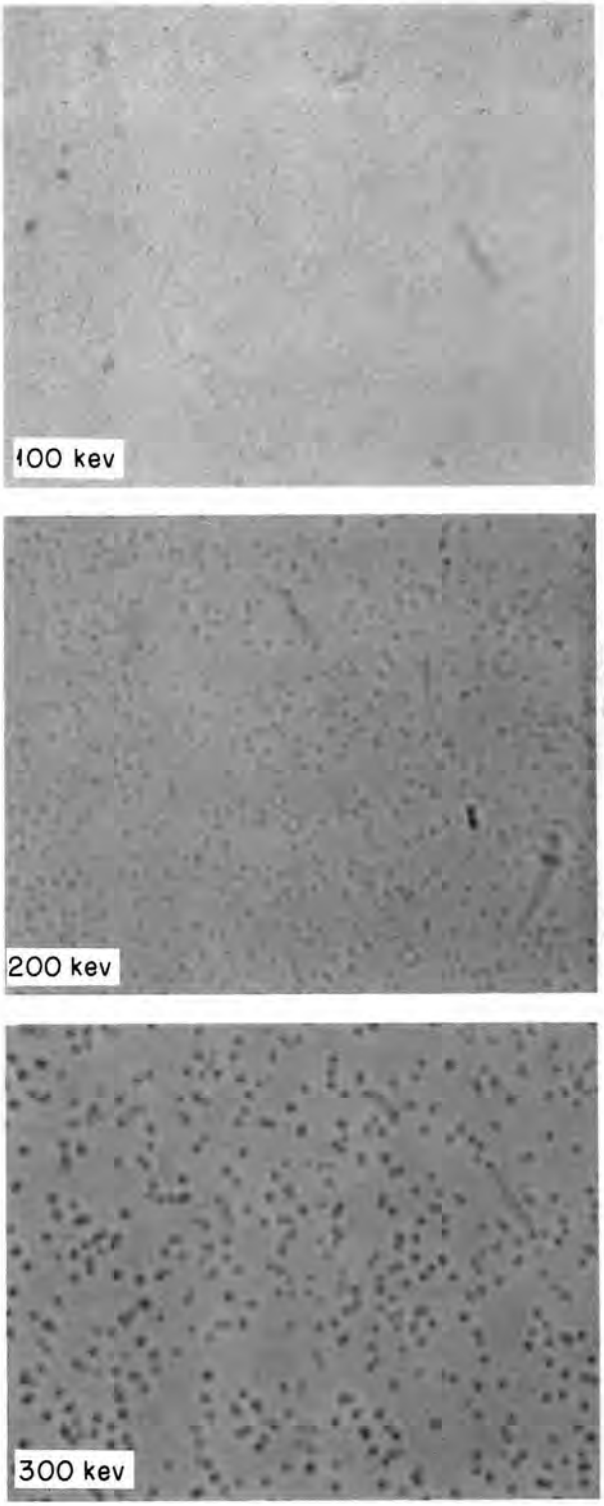

Fig. 19.14. Etched Pits in Cellulose Acetate Butyrate from Bombardment of Singly Ionized He^+ Ions of 100, 200, and 300 kev. Etched 1 hr in 25% NaOH at 65°C. Observed at 400 power.

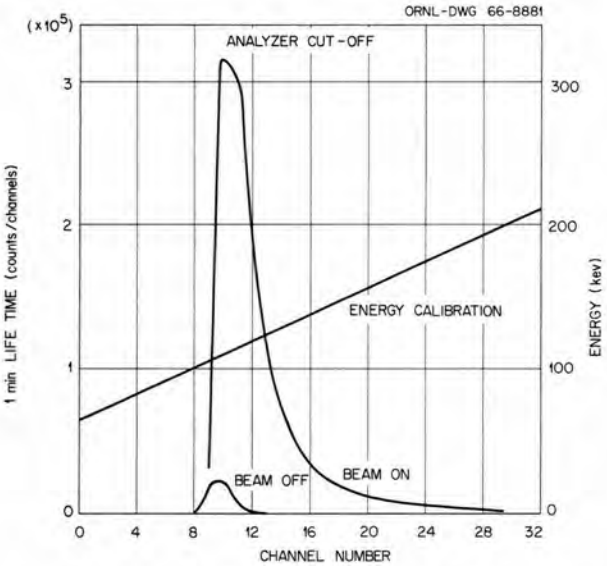

Fig. 19.15. He^+ Spectrum Measurements for 180-kv He^+ Ions and 3600 v on Deflection Plates.

It was not possible to tell if these pits were from He^+ ions or from He^{2+} ions of twice the energy, although at 180 kv there appeared to be two sizes of pits.

A similar irradiation made by C. F. Barnett, however, at a 600-kv accelerator at Y-12 showed distinguishable pits from *singly* ionized helium ions at 300 and 200 kev and tiny dots even at 100 kev. These are shown in Fig. 19.14.

An attempt was made to measure the energy spectrum of the beam from the accelerator in order to determine the relative intensities of the singly and doubly ionized helium nuclei. A surface-barrier detector (ORTEC 3-108G) was mounted in the deflection chamber about 8 cm off the beam axis. With a 512-channel analyzer, a spectrum was run at 180 kv accelerating potential with the beam on and 3600 v on the deflector plates. This spectrum is shown in Fig. 19.15. A rough energy

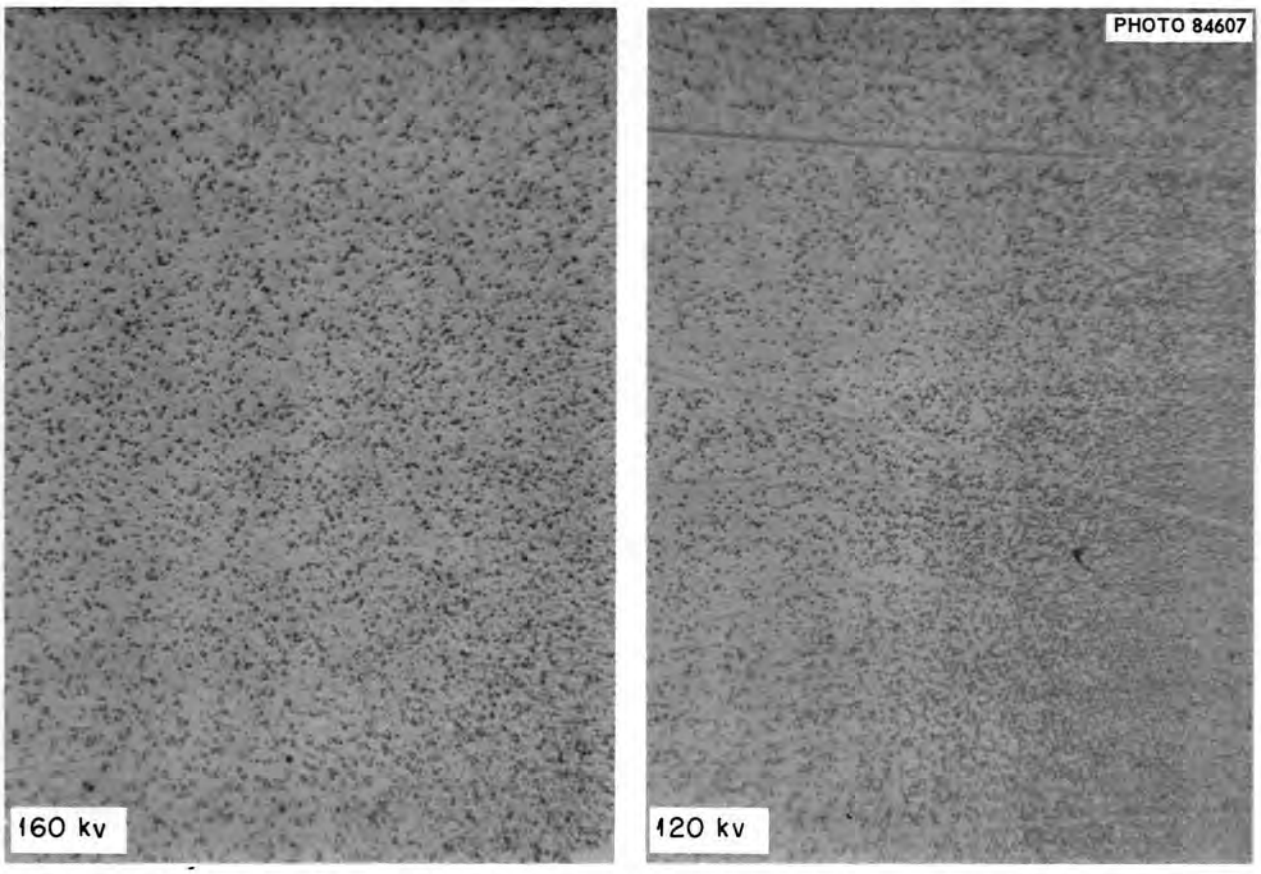

Fig. 19.16. Etched Pits in Cellulose Nitrate from Bombardment by Deuterium Ions in an Accelerating Potential of 160 and 120 kv. Etched 1 hr in 25% NaOH at 23°C. Observed at 400 power.

calibration made with an ORNL Q-1212D mercury-relay pulser and an ^{237}Np source is also shown on this figure and implies that the analyzer low-energy cutoff is at about 100 kev. The lowest attainable beam current through the 0.005-in. aperture yielded far too many ions, and the counting system was unable to indicate the spectrum. Therefore, these efforts were discontinued for the present.

A deuteron beam was also used to irradiate cellulose acetate butyrate (film base) and cellulose nitrate sheet in the accelerator under similar conditions. Although practically no evidence was found of etch pits in the cellulose acetate butyrate, good pits were observed in the cellulose nitrate at accelerating potentials of 160 and 120 kv, as shown in Fig. 19.16.

RADSAN CORRECTION-FACTOR STUDIES

A study was undertaken to provide convenient correction factors to be applied to Radsan neutron dose-rate readings taken in radiation fields of unknown spectra. Previous determinations of the accuracy of the Radsan neutron-dose integrator have been made as a function of neutron energy (i.e., from 0.5 through 14 Mev).[20] However, the use of these published correction factors requires a knowledge of the input neutron energy, which is seldom known accurately. Depending upon the radiation source, whether it be isotopic such as PuBe, AmB, etc., or accelerator or reactor produced, the neutron energies frequently are in the form of a distribution of energies such as that associated with the fissioning of ^{235}U. To add to this problem, the health physicist, as well as the radiobiologist, is frequently faced with not only a complex neutron energy distribution but one that has been modified by experimental apparatus and/or various other scattering media such as the floor and walls, which are apt to be concrete for radiation protection purposes. A good example of this problem is the task of radiobiological dosimetry measurements at the DOSAR facility. This work encompasses experiments utilizing both fission-spectrum neutrons from the HPRR and monoenergetic neutrons from a neutron generator employing the $D(d,n)^3He$ and $T(d,n)^4He$ reactions, yielding energies of 3 and 15 Mev (at 0°) respectively. There is a substantial difference in the overall response of the Radsan neutron-dosimetry system for these different neutron energies. Whereas the Radsan overestimates by several percent the neutron dose rates from isotopic sources such as PuBe, AmB, and from the $D(d,n)^3He$ reaction, it underestimates by approximately 17% the neutron dose rate due to "in air" exposures to the radiation leakage from the HPRR. In addition, an experimenter recently undertook the study of neutron-radiation lethality in mice as a function of variations in the fission-neutron energy spectrum. This was done by exposing the animals to the HPRR both "in air" and behind moderators of various types, including thick polyethylene, graphite, and steel shields. During these experiments, it was estimated that the Radsan integrator was insensitive to as much as 50% of the neutron dose due to the extremely softened neutron energy spectrum associated with the moderated experiments. This suspicion was partially corroborated by measurements made with the Hurst threshold detector system (TDU), which is reasonably accurate down to the threshold energy of ^{239}Pu (a few kev).

When 15-Mev neutrons from the $T(d,n)^4He$ reaction are being measured in the laboratory, the Radsan correction factor is not much different than unity; however, for the HENRE experiment, to be conducted this autumn at the Nevada Test Site, neutron dose rates are to be measured several mean free paths distant from a point source of 14.1-Mev neutrons (90°). The neutron energy spectrum in this case will be modified substantially after passing through 750 to 1000 yd of air, so a routine correction of Radsan readings based on laboratory experiments with 15-Mev neutrons would be undesirable.

In order to provide a set of quick but accurate correction factors for Radsan readings, an experiment was undertaken in which the accuracy of a Radsan-like neutron dose integration was compared with the theoretically "correct" neutron dose obtained by extrapolating the proton recoil distribution to the zero energy intercept as outlined by Wagner and Hurst.[21] However, in order to simplify the "correction factor" technique for unknown neutron energy spectra, it became necessary to measure a "spectrum-sensitive" parameter simultaneously with Radsan dose-rate measurements.

[20] E. B. Wagner and G. S. Hurst, *Rev. Sci. Instr.* **29**, (1958).

[21] E. B. Wagner and G. S. Hurst, *Health Phys.* **2**, 57 (1959).

One possibility for such a parameter is the so-called "5-v counts per dose digit," which is obtained by counting the number of 5-v discriminator pulses associated with each dose-rate measurement. Since the 5-v discriminator triggers for each acceptable pulse above 5 v, it provides a useful means for determining the overall counting statistics of any given radiation measurement and is used routinely in this capacity at ORNL. In addition, however, the 5-v counts per dose digit is rather sensitive to changes in neutron energy spectra and may provide the "spectrum-sensitive" parameter needed for Radsan correction-factor studies. When the Radsan is used in the conventional manner, the 5-v counts per dose digit varies from about 4 for "hard" monoenergetic source energies to greater than 10 for extremely moderated fission spectra. This is logical since it requires fewer large than small pulses to deliver a given absorbed dose.

This study was performed by exposing a Hurst proportional counter to a wide variety of neutron energy spectra. The detector was used in the conventional way with the Radsan dose integrator (i.e., the 5-, 10-, 20-, and 40-v discriminators were carefully calibrated using an oscilloscope and a Q pulser). The counter was operated in the proportional region and was standardized routinely using the internal ^{239}Pu alpha source. In addition, while the discriminators were being calibrated, the Radsan amplifier output pulses were fed into a multicahnnel analyzer to establish the corresponding channel numbers of the four discriminator energies. Then, when the various neutron exposures were made, the amplifier output pulses were sampled with the analyzer and mathematically manipulated two ways:

1. "Theoretical" Radsan dose: The number of pulses in each energy interval defined by the four discriminator channel numbers were weighted by the mean channel number for each energy interval. The actual channel numbers used which corresponded to the 5-, 10-, 20-, and 40-v discriminator energies were numbers 15, 30, 59, and 118, and the weighting factors were 22, 44, 88, and 196.

2. Extrapolated, or "correct," dose: The same analyzer data were plotted on semilog paper and extrapolated to "zero" energy channel after the method of Wagner and Hurst. Then, the dose was calculated channel by channel by integrating the number of counts per channel $N(E)$ times the corresponding channel numbers for the entire proton recoil spectrum. This dose integration included the extrapolated region, which usually was represented by approximately the first 15 of a total of 256 channels. Since there was some question as to the correct slope of the extrapolated data, the data were all extrapolated arbitrarily through the channel number corresponding to the 5-v discriminator on the assumption that all counts above this point were due to recoil protons only. It has been shown previously that this is generally true even for coexistent gamma-ray fields which are orders of magnitude higher than those encountered during these experiments.[21]

Finally, the "correction factors" were calculated as the ratio of "extrapolated dose"/"theoretical Radsan dose" and plotted as a function of 5-v counts per dose digit. The results are shown in Fig. 19.17 and represent data taken using the various neutron spectra mentioned previously.

Since the Radsan dosimetry system is usually calibrated with an NBS-certified PuBe or AmBe source with which a 5-v counts per dose digit of 5.2 is typical, the correction factors must contain data from both the calibration and the unknown neutron energy spectrum (i.e., if used to correct Radsan readings of an unshielded HPRR exposure in which the 5-v counts per dose digit was 6.6, then the factor 1.17/0.97 would be appropriate). When typical Radsan measurements were adjusted in this way and normalized to the HPRR radiation output, good agreement was obtained with similar dose measurements made with Hurst TDU systems regardless of spectrum changes caused by various moderating materials. Thus, the use of this correction technique should greatly reduce uncertainties associated with Radsan-type neutron dose-rate measurements, particularly in radiation fields of unknown quality.

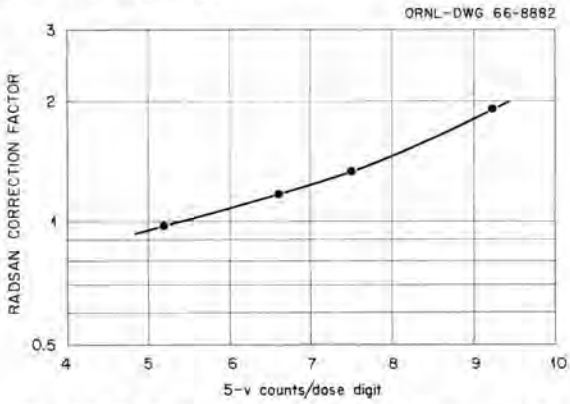

Fig. 19.17. Radsan Dose Correction Factor as a Function of the Number of Counts Above 5 v per Dose Digit.

20. Special Projects and HPRR Operations

F. F. Haywood L. W. Gilley[1]

E. G. Hill[2] J. E. Jackson E. M. Robinson
Robert Sharp[3] W. H. Shinpaugh E. D. Carroll[4]
J. W. Poston D. R. Ward[1]

OPERATION HENRE ACCELERATOR

Most of the studies of the Special Projects Group were of an engineering nature. Of major significance was the final endurance testing of the 150-kev positive-ion accelerator (the development of this machine was reported earlier).[5,6] This testing was finished in January 1966, and the accelerator was shipped to the Nevada Test Site (NTS) for use in Operation HENRE,[7] a field experiment designed to study (1) neutron and gamma-ray distributions in air, (2) shielding factors of field fortifications and idealized large geometry shields, and (3) dose distributions in tissue-equivalent phantoms in air and in various structures.

Throughout the accelerator test period, the stability of the machine was judged to be excellent. Protons were accelerated during this period, and beams of 450 to 500 ma were extracted at 150 kv.

Activities not directly related to Operation HENRE have resulted in a relocation of the BREN tower; this has caused a delay of several months in starting the field experiment. However, the accelerator has been assembled and will be ready for use in the program in the fall of 1966.

HENRE ^{3}H Target Shipping Containers

During this report period, containers for shipping the accelerator targets to NTS by military aircraft have been designed and fabricated. The containers, which were designed in accordance with AEC Appendix 0529, were built to transfer three targets each (see Fig. 20.1). Of major importance in the design of containers for ^{3}H-loaded targets is protection against heavy impact and high temperatures due to fire. As shown in Fig. 20.1, the container is actually a container within another. The three targets are loaded, as shown in Fig. 20.2, in the inner container, which is constructed of aluminum. This section is then closed, flushed with an inert gas to retard oxidation on the surface of the target, and placed inside the large stainless steel outer shell. The minimum spacing between the outer shell and the aluminum container is 5 in.; this space is filled with thermal insulation (Calsilite-Hi 1800°F). Protection is then afforded the inner container should the shipment be engulfed in fire. Each target will be loaded with 1500 to 2000 curies of ^{3}H which is adsorbed in a thin film of erbium metal deposited on the copper target backing. Tritium is not expected to dissociate greatly from the erbium at temperatures less than about 500°F, which is the maximum temperature expected inside the inner container should the entire shipment be engulfed in a 1-hr "standard fire" of 1700°F.

---

[1]On loan from Neutron Physics Division.

[2]Visiting investigator from Edgerton, Germeshausen and Grier, Inc., Las Vegas, Nev.

[3]Visiting investigator from Armed Forces Radiobiology Research Institute, Bethesda, Md.

[4]On loan from Instrumentation and Controls Division.

[5]J. A. Auxier *et al.*, *Health Phys. Div. Ann. Progr. Rept. July 31, 1965*, ORNL-3849, pp. 176–80.

[6]T. G. Provenzano *et al.*, *Feasibility Study: Intense 14 Mev Neutron Source for Operation HENRE*, CEX-65.01 (1966).

[7]Technical Director's Staff, *Operations Plan – Operation HENRE*, CEX-65.03 (1965).

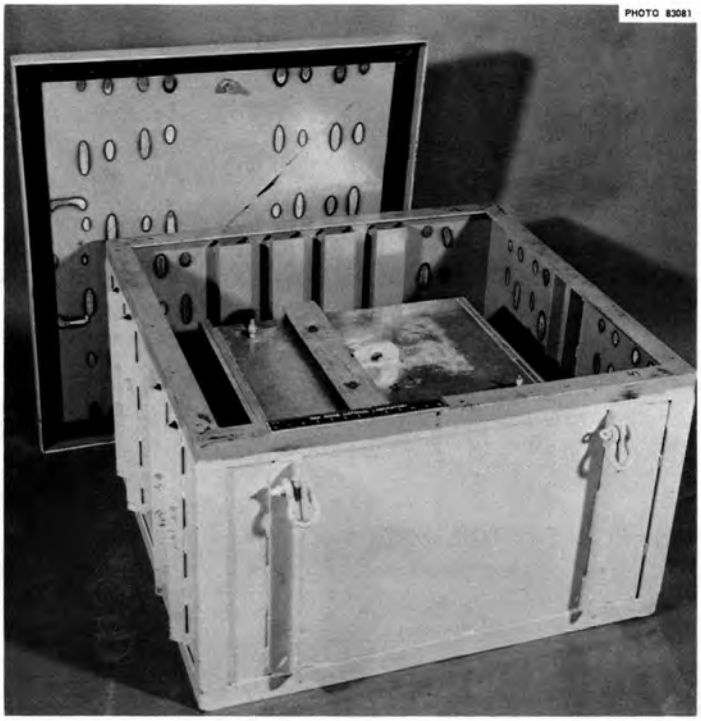

Fig. 20.1. View of Shipping Container for HENRE Targets.

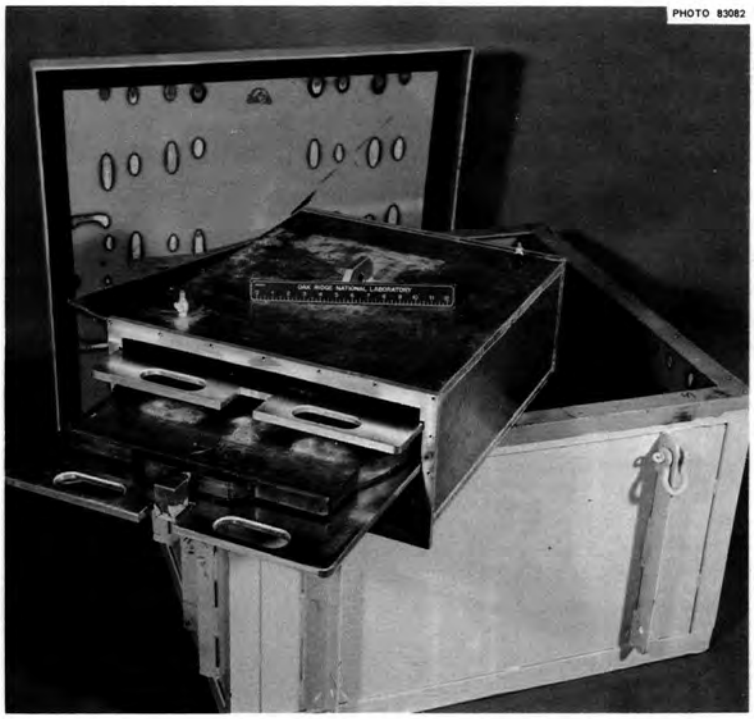

Fig. 20.2. View of Target Arrangement in the Shipping Containers.

This container has been approved by the Bureau of Explosives and has been assigned permit B of E 2202.

DOSAR LOW-ENERGY ACCELERATOR

A 200-kev positive-ion accelerator was purchased and installed at the DOSAR facility in January 1966. This machine serves as a source of monoenergetic radiations for use in the evaluation and calibration of dosimetry and spectrometry systems. Positive ions and electrons can be accelerated in this machine. Beam currents range to 1600 μa for protons, 1000 μa for electrons and deuterons, and progressively lower currents for heavier ions up to and including xenon. Particles may be accelerated from 5 kv to 200 kv.

The accelerator is located in a small 20 × 30 ft "low-scatter" building. Area shielding is afforded by large concrete blocks stacked in and around the building (see Fig. 20.3). Remote controls for the accelerator are located in the trailer shown in Fig. 20.4, which is also shielded by large concrete blocks.

To date, this accelerator has been used to study the response of certain detector systems to monoenergetic neutrons of 14 and 3 Mev. The neutron dose profile for these reactions has been determined for experiment planning purposes, and a normalizing system has been established to correlate results from one run to another. In addition, an experiment has been performed to observe tracks in plastic samples which were bombarded with helium ions inside the accelerator tube (see Fig. 20.5).

Fig. 20.3. View of Concrete Blocks Surrounding Building Containing Accelerator.

Fig. 20.4. View of Accelerator Building and Concrete-Block-Shielded Control Trailer.

Personnel Protection Around the Accelerator

Numerous steps have been taken to provide protection for personnel from both radiation and high-voltage hazards. In the case of radiation protection, signs, barriers, and rotating lights on the outside of the building serve as conspicuous warning devices. To alert personnel of possible radiation fields around the accelerator, an announcement is made over the public address system. Prior to operating the accelerator, a personnel check is made inside the building, and the access door is locked with a key which is kept in the console during all operating periods. An interlock is installed on this door; if the door is opened, the high voltage is turned off and an indicator light on the console is turned on.

Inside the room housing the accelerator, a neutron monitor with audible and visible alarm is used. Two additional red lights in this room indicate, respectively, that the high voltage and ion beam are turned on.

Personnel protection against high voltage is provided as follows: (1) a good earth ground exists on both the high-voltage transformer tank and the accelerator base, (2) a grounding strap attached to a nonconducting rod is available to remove static charges when working on components in the high-voltage section of the accelerator, and (3) a shorting bar is located inside the transformer tank.

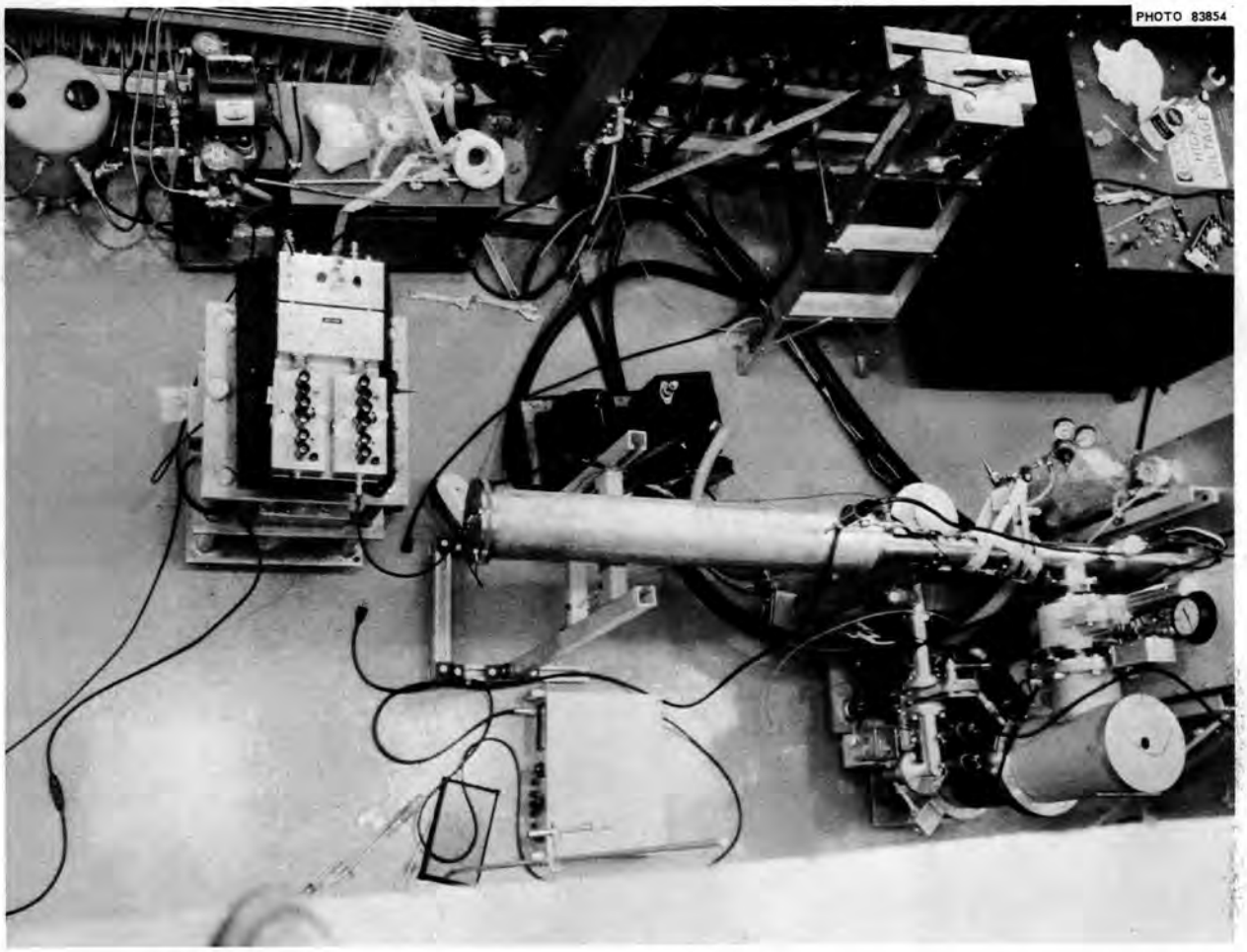

Fig. 20.5. View of Accelerator During Recent Experiment in Which Plastic Samples Were Irradiated with He^+ and D^+ Ions.

HEALTH PHYSICS RESEARCH REACTOR

During the period July 1965 to April 1966, the Health Physics Research Reactor was operated 109 times in the burst mode and 196 times at steady-state power. The total running time was 271 hr, which resulted in an integrated power of 84 kwhr. As in the past years, the reactor has again been used primarily by the DOSAR staff. Other users have included other ORNL divisions, AEC plants and laboratories, universities, and private industry.

Experiments performed included irradiation of animals and plant systems, instrumentation response studies, comparison of nuclear accident dosimetry systems, and depth-dose studies in tissue-equivalent phantoms. Also, the radioactive core has been used to expose tissue-equivalent ion chambers to the gamma-ray field from mixed fission products (reactor not operating).

Reactor Investigations

During this report period, work has been continued in order to improve the reproducibility of burst yield from the HPRR. This work has included installation of a longer burst rod to minimize effects due to burst rod bounce, determination

of the degree of accuracy for measuring the various parameters which affect burst yield, and the installation of an improved burst rod pneumatic system.

The improved pneumatic system serves two purposes. By critically damping the burst rod insertion, rod bounce is eliminated. This, in turn, eliminates the small movements of the safety block due to physical shock caused by the impact of the burst rod upon insertion.

During these investigations, the following information was obtained for each burst: (1) the insertion time of the burst rod, (2) its position at the time of burst, (3) the time between initial insertion of the burst rod and the initiation of the burst, (4) the initial "period" or initial rate of power rise during the burst, (5) the burst shape, and (6) the position of the safety block as a function of time for the first $\frac{1}{2}$ in. of movement from the fully inserted position. These data are still undergoing analysis.

The changes in the burst rod and pneumatic system have made possible the accumulation of data in the range of 1 to 9×10^{16} fissions/burst with only a ±4% variation in reproducibility. It should be pointed out that this success was achieved with a relatively long burst rod insertion time. However, this has resulted in several "pre-ignitions" (a burst initiation before full insertion of the burst rod). A program has been initiated to reduce the burst rod insertion time while maintaining critical damping of the burst rod.

Part V. Internal Dosimetry

W. S. Snyder

21. Internal Dose Estimation

W. S. Snyder
S. R. Bernard
Monica Boyd[1]
Mary Jane Cook
Wallace Davis III[1]
C. F. Holoway
H. L. Fisher, Jr.[2]
Mary R. Ford
Isabel H. Tipton[3]

REVISION OF STANDARD MAN

W. S. Snyder Mary Jane Cook
Isabel H. Tipton

Although standard man, as a typical radiation worker, was established approximately 17 years ago, there has been no systematic revision of the concept since that time, nor has it been extended to include other members of the population. Standard man should include the information needed for estimation of dose, whether from external or from internal sources; it should provide an estimate of the variability of dose due to individual differences and should offer methods of adjusting the estimate to correct for an individual's characteristics.

The original standard man was formalized by the International Commission on Radiological Protection (ICRP) at a conference at Chalk River in 1949.[4] This first standard man consisted of little more than (1) the specifications of the weights of some of the important organs and tissues, (2) specifications of intakes of air, water, and a few elements, and (3) some data on excretion. With increasing use of internally and externally applied radiation, it has become a necessity to expand the concept of standard man and to reevaluate the existing parameters.

The ICRP has organized a Task Group for the Revision of Standard Man, and the authors of this report are members of this group. Although the final values of the organ and tissue weights given here are the responsibility of the authors and not listed as representing the views of the task group, nevertheless, the authors are glad to acknowledge the very considerable influence of the other members of the task group on the work reported here. These members are Dr. L. Karhausen (Euratom) and Dr. G. Parry-Howells (United Kingdom Medical Research Council). The contribution of Dr. E. S. Nasset (formerly of the University of Rochester) should be acknowledged also. In particular, Dr. Karhausen has gathered and evaluated much of the data which are reported here in only slightly modified form in some cases. The authors have attempted to deal with the tissues and organs which present special problems either because little or no data were available or because of wide discrepancies of reported values. Each of these cases is discussed briefly below.

When data are selected or interpreted to define a typical or standard adult, it is necessary to have in mind the type of individual to be defined. Many of the data reported on organ weights or masses of tissues were not obtained from bodies of persons of the desired type. For example, age and weight of the subject may be expected to vary widely for much of the data, and in many cases it is necessary to scale the results to correct for this. A compilation of data without regard to the different characteristics of many of the subjects might give

[1]Summer employee.

[2]U.S. Public Health Service.

[3]Physics Department, University of Tennessee.

[4]Chalk River Conference on Permissible Internal Dose, a conference of representatives from the United Kingdom, Canada, and the United States, held in Chalk River, Canada, September 29–30, 1949, RM-10, 1950.

erroneous ideas of the interrelations of the organs and tissues of the body.

The organ weights of the hypothetical individual defined here are given in Table 21.1. This individual is considered to be a radiation worker who weighs 70 kg (~154.3 lb), is 174 cm (69.1 in.) tall, and is between 20 and 30 years of age. The values selected for the organ weights are taken from many sources and have been adjusted in some cases to correspond to an adult of the above weight, height, and age. Included with the weight of each organ or tissue given in Table 21.1 are the nerves, fascia, blood vessels, and lymphatic tissue such as lymph nodes within the tissue, blood and other fluids which would not be lost when the organ or tissue sample was removed during a postmortem examination, and other connective tissue except tendons and ligaments; tendons and ligaments are considered separately.

Gastrointestinal Tract (GI)

The values for the GI tract are based on the report prepared for ICRP Committee II by Eve.[5]

Lungs

The data are from the ICRP Committee II Task Group on Lung Dynamics.[6]

Skeleton[7-13]

Due to the presence of bone marrow, fat, and water, the weight of the skeleton was one of the most difficult to select. Many investigators have studied only dry, defatted bone or bones rather than the whole skeleton. Because it is so difficult to obtain an entire skeleton by dissection, data on the skeleton as a whole are not plentiful. The estimated total wet skeletal weight of 9400 g given here is intended to include bone marrow but includes neither cartilage nor dense connective tissue which may be cut away.

Adipose Tissue[14-16]

The term "adipose tissue" is used to represent (1) the subcutaneous tissue, which is a patent, fatty tissue underneath the skin, and (2) "other," which includes such fatty tissues as omentum and that which surrounds the individual organs. The term "fat" is restricted to the chemical constituent of all tissues which may be extracted with ether or other organic solvents.

Adipose tissue is one of the most widely variable tissues in weight and proportion since it is the chief factor in obesity. Standard man is assumed to be a well-developed, but nonobese, male by the criteria set by Morse and Soeldner,[15] who reported a value of 18.9% of total body weight for the adipose tissue of a group of healthy male subjects whose average weights and heights are close to those of standard man.

Aorta

Because the aorta is really external to both the heart and the lungs, it is the only blood vessel whose weight has not been considered to be included in that of the organ or tissue with which it is closely associated in the body.

Blood[7,17,18]

Although the total blood in the body of standard man has a weight of 5512 g (volume = 5200 ml),

---

[5] I. S. Eve, *Health Phys.* 12, 131 (1966).

[6] Task Group on Lung Dynamics, *Health Phys.* 12, 173 (1966).

[7] R. P. Custer, *An Atlas of the Blood and Bone Marrow*, Saunders, Philadelphia, 1949.

[8] R. E. Ellis, *Phys. Med. Biol.* 5, 255 (1961).

[9] G. Hudson, *Nature* 205, 96 (1965).

[10] M. W. Ingalls, *Am. J. Anat.* 48, 45 (1931).

[11] A. L. Merz *et al.*, *Am. J. Phys. Anthropol.* 14, 589 (1956).

[12] M. Trotter and R. P. Peterson, *J. Bone Joint Surg.* 44-A, 669 (1962).

[13] H. Q. Woodard and E. Holodny, *Phys. Med. Biol.* 5, 57 (1960).

[14] J. Brozek (ed.), *Ann. N. Y. Acad. Sci.* 110, 1–1018 (1963).

[15] W. I. Morse and J. S. Soeldner, *Metabolism* 12, 9 (1963).

[16] J. P. Schaeffer (ed.), *Morris' Human Anatomy*, McGraw-Hill, New York, 1953.

[17] R. H. Altman, *Blood and Other Body Fluids*, Fed. Am. Soc. Exptl. Biol., Washington, 1961.

[18] M. J. Yiengst and N. W. Shock, *J. Appl. Physiol.* 17, 195 (1962).

Table 21.1. Organs and Tissues of Standard Man

	Mass (g)	Percent of Total Body
Adipose tissue	13,000	18.6
Subcutaneous	[9,500][a]	[13.6][a]
Other	[3,500]	[5.0]
Adrenals (2)	14	0.020
Aorta	100	0.14
Blood - total	[5,512] (5200 ml)	[7.9]
Blood vessels (including pulmonary)		
Contents (blood)	2,862 (2700 ml)	4.1
Brain	1,400	2.0
Cartilage and dense connective tissue	4,000	5.7
Eyes (2)	15	0.021
Fluids, miscellaneous	385	0.55
Gall bladder	10	0.014
GI tract	2,000	2.9
Esophagus	[50]	[0.071]
Stomach	[150]	[0.21]
Intestine	[1,800]	[2.57]
Contents of GI tract	1,005	1.4
Hair	15	0.021
Heart	350	0.50
Contents (blood)	318 (300 ml)	0.45
Kidneys (2)	310	0.44
Larynx	15	0.021
Liver	1,800	2.6
Lungs (2)	1,000	1.4
Muscle	27,000	38.6
Nails	10	0.014
Pancreas	90	0.13
Parathyroid (4)	0.2	0.0003
Pineal	0.2	0.0003
Pituitary	0.6	0.0006
Prostate	16	0.023
Salivary Glands (6)	85	0.12
Skeleton	9,400	13.4
Bone	[6,400]	[9.1]
Red marrow	[1,300]	[1.9]
Yellow marrow	[1,700]	[2.4]
Skin	4,000	5.7
Spinal cord	28	0.040
Contents (cerebrospinal fluid)	221 (220 ml)	0.32
Spleen	175	0.25
Teeth	46	0.066
Testes (2)	60	0.086
Thymus	20	0.029
Thyroid	16	0.023
Tongue	50	0.071
Tonsils (2)	3	0.0043
Trachea	15	0.021
Ureters (2)	16	0.023
Urinary bladder	45	0.064
Contents (urine)	102 (100 ml)	0.15
Urethra	2	0.0029
Total body	70,000	

[a]Numbers in brackets not included in totals.

part of this blood is included in the weights of organs and tissues. Only that blood which can be considered to be flowing in the large blood vessels and thus lost when the organs are removed for weighing during a postmortem examination is included as a separate item, "Contents of Blood Vessels." The remaining blood which would not drain from the organ is termed "trapped blood." The amount of trapped blood has been estimated in all organs except liver, muscle, spleen, and skeleton on the basis of the quantity of iron found in each organ by spectrographic analysis.[19] If we assume 5×10^{-4} g of Fe per milliliter of blood[20] and all of the Fe in the organs except those named specifically above occurred in the trapped blood, the quantity of trapped blood may be calculated by dividing the number of grams of iron in a tissue by 5×10^{-4}. The amount of blood in liver, spleen, and bone was calculated assuming 80% of the iron found in the hemopoietic system to be stored and 20% to be associated with trapped blood.[21] The amount in muscle was estimated, taking into consideration the relative quantities of myoglobin and hemoglobin in muscle.[22,23] Thus, the circulating blood represents the difference between total and trapped blood.

Cartilage and Dense Connective Tissue

We tentatively suggest a value of 4000 g as the weight of cartilage and dense connective tissue. This value was estimated in two ways. (1) Collagen accounts for about one-third of the proteins in the body.[24,25] For soft tissues the words "connective tissue" have been assumed to be synonymous with "collagen," and the amount has been calculated as one-third of the crude protein content of a tissue. By studying drawings of muscle and skeleton in *Gray's Anatomy*[26] and *Morris' Anatomy*[16] which were made carefully to scale, the amount of cartilage and dense connective tissue was estimated to be 4600 g. (2) The suggested organ weights for standard man were totaled (omitting cartilage and dense connective tissue) and the sum subtracted from 70 kg. The difference indicated that approximately 4000 g should be allocated for cartilage and dense connective tissue.

Fluids, Miscellaneous

This heading includes synovial fluid and any other fluids, excluding blood, which might be lost when an organ is dissected for weighing.

Many of the weights in Table 21.1 are tentative and in no way should they be considered final. This study does represent the first attempt so far as we can determine to define a 70-kg man in such detail.

THE ESTIMATION OF EXPOSURE TO AN AEROSOL BASED ON A REVISED STANDARD LUNG MODEL

Mary R. Ford W. S. Snyder

The lung model used by ICRP to estimate values of $(MPC)_a$[27,28] was revised recently by a task group created to advise ICRP Committee II concerning lung dynamics. The report of the task group[29] specifies a more realistic and quantitative scheme for the deposition and clearance of particulate matter from the respiratory tract than did the previous model. It does not, however, discuss the actual computation of dose to the various compartments of the lung or to the lung as a whole. Additional information needed for the estimation of dose to various portions of the lung is discussed here, and methods of obtaining the dose estimates are presented.

---

[19] I. H. Tipton and M. J. Cook, *Health Phys.* 9, 103 (1963).

[20] P. B. Hawk *et al.*, *Practical Physiological Chemistry*, 12th ed., Blakiston, Philadelphia, 1947.

[21] C. V. Moore and R. Dubach, "Iron," in *Mineral Metabolism*, vol. 2, part B, ed. by C. L. Comar and F. Bronner, Academic, New York, 1962.

[22] B. A. Houssay *et al.*, *Human Physiology*, 2d ed., McGraw-Hill, New York, 1955.

[23] E. L. Smith, "Cobalt," in *Mineral Metabolism*, vol. 2, part B, ed. by C. L. Comar and F. Bronner, Academic, New York, 1962.

[24] I. S. Kleiner and J. M. Orten, *Biochemistry*, 6th ed., Mosby, St. Louis, 1962.

[25] J. Gross, *Sci. Am.* 204, 120 (1961).

[26] C. M. Goss (ed.), *Gray's Anatomy of the Human Body*, 27th ed., Lea and Febiger, Philadelphia, 1959.

[27] *Report of Committee II on Permissible Dose for Internal Radiation*, ICRP Publication 2, Pergamon, London, 1959.

[28] J. N. Stannard, "An Evaluation of Inhalation Hazards in the Nuclear Energy Industry," p. 306 in *Peaceful Uses of Atomic Energy*, vol. 23, 1958.

[29] P. E. Morrow, Chairman, Task Group on Lung Dynamics, *Health Phys.* 12, 173 (1966).

The model respiratory tract, as described by the task group, consists of three compartments: the nasopharynx (N-P), beginning with the anterior nares and extending back and down to the level of the larynx; the trachea and bronchial tree (T-B), including the terminal bronchioles; and the pulmonary (P) compartment. The schematic portrayal of these compartments, together with the associated deposition and clearance processes as shown in the report[29] of the task group, are reproduced in Fig. 21.1. The letters D_1 through D_5 indicate the fractions of the inhaled aerosol which are either exhaled or deposited in each of the compartments. The task group finds that these fractions vary with the activity median aerodynamic diameter (AMAD) of the aerosol, and graphs are provided in the report to show this variation. The letters *a* through *j* in the diagram indicate clearance pathways from the compartments into blood, GI tract, and/or lymph. It should be noted that the pulmonary region is not a simple compartment in the usual sense of uniform mixing and elimination, since each pathway clears a prescribed fraction of the material which is deposited, and this fraction varies depending upon the solubility of the material deposited.

ORNL-DWG 66-5772

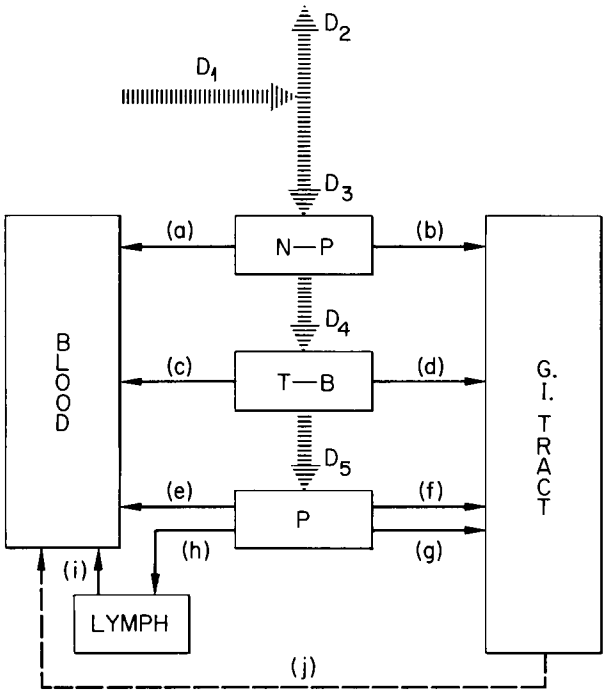

Fig. 21.1. Respiratory Tract Clearance Model.

Table 21.2. Clearance Classification

Class D, Rapid	Class W, Intermediate	Class Y, Slow
< 1 day to 10 days	10 days to 100 days	> 100 days

Both the amount of material following a particular route and the rate at which it is cleared are assigned on the basis of three classes of aerosols, as shown in Table 21.2. Class D material is cleared in <1 day to 10 days, class W in a matter of days or months, and class Y material over a period of months to years.

Using this model, it is a straightforward matter to calculate the microcurie-days of residence in each of the three regions for a given intake of a specified aerosol. The dose delivered to a given region in a specified time period is the product of a constant, the microcurie-days of residence during the period, and the energy absorbed per disintegration divided by the appropriate mass. These formulas for dose to the three regions during the first T days following a single intake of an aerosol follow. For the nasopharynx region:

$$D_{\text{rems}} = \frac{I \times 51 \times \epsilon}{M} \times D_3 \left(f_a \frac{1 - e^{-\lambda_a T}}{\lambda_a} + f_b \frac{1 - e^{-\lambda_b T}}{\lambda_b} \right).$$

For the tracheobronchial region:

(1) Dose from inhaled material deposited in region

$$D_{\text{rems}} = \frac{I \times 51 \times \epsilon}{M} \times D_4 \left(f_c \frac{1 - e^{-\lambda_c T}}{\lambda_c} + f_d \frac{1 - e^{-\lambda_d T}}{\lambda_d} \right);$$

(2) Dose from material cleared from P region through the T-B region to the GI tract

$$D_{\text{rems}} = \frac{I \times 51 \times \epsilon \times t}{M}$$

$$\times D_5 \left(f_f \lambda_f^b \frac{1 - e^{-\lambda_f T}}{\lambda_f} + f_g \lambda_g^b \frac{1 - e^{-\lambda_g T}}{\lambda_g} \right).$$

For the pulmonary region:

$$D_{\text{rems}} = \frac{I \times 51 \times \epsilon}{M} \times D_5 \left(f_e \frac{1 - e^{-\lambda_e T}}{\lambda_e} \right.$$

$$\left. + f_f \frac{1 - e^{-\lambda_f T}}{\lambda_f} + f_g \frac{1 - e^{-\lambda_g T}}{\lambda_g} + f_h \frac{1 - e^{-\lambda_h T}}{\lambda_h} \right),$$

where

I = intake at time zero (μc),

51 = dis/day × g-rad/Mev,

ϵ = effective energy per disintegration (Mev),

M = mass of region considered (g),

D_3, D_4, D_5 = fraction of the inhaled aerosol deposited in the N-P, T-B, and P regions respectively,

t = time of passage through the T-B region of material cleared from the P region to the GI tract (days),

f_a, f_b, etc. = fractions cleared by pathways a, b, etc.,

λ_a, λ_b, etc. = effective elimination constants for pathways a, b, etc.,

λ_f^b and λ_g^b = biological elimination constants for pathways f and g.

As mentioned earlier, these formulas follow directly from the definition of the new lung model except for the two factors ϵ and M, the effective energy absorbed per disintegration and the mass of the particular tissue under consideration respectively. As will be seen, it is not an entirely simple matter to decide on appropriate values for either of these parameters.

Figure 21.2 shows the accumulated dose to the pulmonary region from an instantaneous intake of 1 μc of a standard aerosol, that is, one having an AMAD of 1 μ; but in order to be perfectly general,

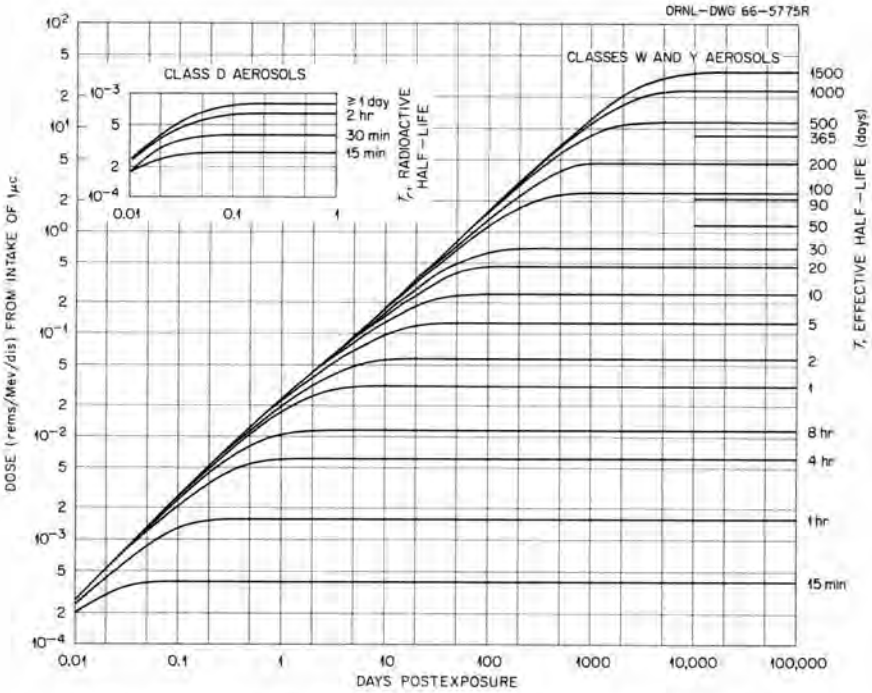

Fig. 21.2. Dose to Pulmonary Region. ϵ = 1 Mev, AMAD = 1 μ.

the effective energy has been taken as 1 Mev. Thus, this graph is universally applicable for any aerosol considered in the report of the task group; one need only select the longest effective half-time for elimination from the P region, read off the ordinate for the desired time, and multiply by the appropriate effective energy. The curves for aerosols of class W or of class Y are labelled with the effective half-time, T, of the long-term component of the retention function. For example, the curve corresponding to $T = 1$ day really represents quite a number of different radionuclides, namely, all of those whose radioactive half-lives, together with the half-lives of the long-term pulmonary retention given in the report, are such that the effective half-time is 1 day. The terms of the formula corresponding to pathways of short elimination time might differ somewhat for some of these radionuclides, but the use of a single curve for all of them does not involve an inaccuracy of more than 5%, which is considered negligible in this context. The mass of the pulmonary region is taken as 500 g, which must be considered to include the capillary, or trapped, blood that is present there.

With a very few exceptions, the elimination half-times for an aerosol of class D do not exceed 30 min, that is, the values given in Table 4 of the report of the task group. Thus, with these very few exceptions, the dose is substantially independent of T_r except when $T_r < 1$ day. The dose to the pulmonary region from an aerosol of class D is given as an insert in Fig. 21.2, and it includes all cases except those where the report of the task group indicates a value of T_b, the biological half-time, which is substantially greater than 30 min.

The estimation of dose to the tracheobronchial region involves more novelty. The tracheobronchial tree consists of the trachea and branching bronchi down to the terminal bronchioles. It is essentially a branching tubular network. The aerosol material is carried by the mucus over the surface of these tubes as the material is cleared by ciliary action. The mass of this region is taken as 400 g, which is arrived at on the basis of estimates of volume given by Weibel[30] and others and on values for the density. Because of the intricate geometrical configuration, a significant portion of the energy released will be absorbed in neighboring tissues. This is true even in the case of an alpha emitter. For example, estimates of the surface area of the T-B region vary from 10 to 20 m^2. If one takes a layer of tissue based on this surface which is 45 μ thick, that is, the range of an alpha particle having an energy of about 5 Mev, he obtains 450 to 900 g. This is far more mass than the T-B region should have according to most estimates and indicates that a significant portion of the energy is absorbed in the surrounding tissue. The mass of 400 g is used here as an estimate of the mass of tissue lying within range of the alpha particles originating in the T-B region. The estimated dose to the T-B region from an aerosol deposited there is shown in Fig. 21.3 by the dashed curves.

In addition to this dose, material cleared from the P region to the GI tract must traverse the T-B region, and hence this material contributes dose during its passage through the region. The estimated dose to the T-B region from this source is shown in Fig. 21.3 by the smooth curves. The assumptions are as before, that is, a standard aerosol with the effective absorbed energy taken as 1 Mev. Estimates for the time of passage of the material cleared from the P region through the T-B region differ rather widely. Estimates based on observation of the movement of the material at certain sites led to estimates of a half-time for clearance of about 15 min, but this estimate may favor the more rapid elimination routes which are more readily observed. Other estimates based on gamma spectrometry indicate clearance times of

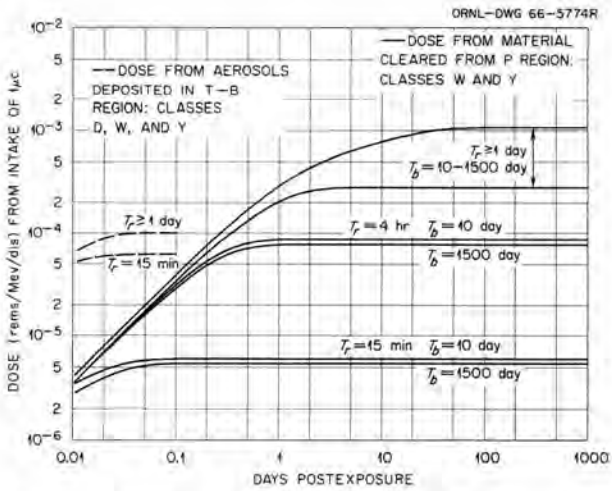

Fig. 21.3. Dose to Tracheobronchial Region. $\epsilon = 1$ Mev, AMAD = 1 μ.

[30]E. R. Weibel, *Morphometry of the Human Lung*, Academic, New York, 1963.

2 hr or more, but these estimates may be influenced somewhat by the presence of the pulmonary deposits. Although the present dose estimate involves this uncertainty, it is clear that material passing from the P region to the GI tract makes a very significant contribution to the total dose received by the T-B region.

The N-P region consists essentially of the nasal passages and pharynx down to the level of the larynx. The aerosol merely deposits on these surfaces and is removed by the movement of the mucus. Thus a surface distribution of the material seems appropriate as a model for estimation of dose. The N-P region has about 300 cm^2 of surface, and the proposed lung model assigns a half-time of 4 min for removal of the deposited material. There is evidence that the material accumulates to a greater degree and resides longer at certain sites than at others, but in this calculation the dose is averaged over the tissue. The dose has been computed primarily for an alpha emitter, and so the dose has been averaged over a layer which is 45 μ thick. This is the range of an alpha particle having an energy of about 5 Mev. Figure 21.4 shows this dose for a standard aerosol with an effective energy of 1 Mev. Because of the short clearance time for this region, the radioactive half-life makes little difference in the dose, and essentially all of the dose is delivered within the first half hour following intake.

A certain fraction of the inhaled material is transported to the lymph nodes. For very insoluble dusts, such as those of class Y, the proposed lung model allows 10% of this material to be eliminated from the lymph nodes with a rather long half-time of 100 to 1500 days, depending on the solubility of the dust. The other 90% remains in the lymph nodes indefinitely, being subject only to radioactive decay. The dose to the lymph nodes has been computed using 15 g as the weight of these respiratory lymph nodes, a value given by Pochin[31] for the tracheobronchial lymph glands. The total mass of lymphatic material in the lung is probably larger than this, and the dose averaged over this mass somewhat smaller than that computed here. As discussed by Pochin,[31] the problem of migrating lymphocytes complicates the problem, and the facts are not in hand which might serve as the basis for a more accurate dose estimate to individual lymph nodes or lymphocytes.

[31]E. E. Pochin, *Health Phys.* 12, 563 (1966).

Figure 21.5 shows a composite of all these calculations for a very insoluble material. The curves apply to any radioactive aerosol of class Y which has the indicated AMAD and effective half-times in the P region. The effective energy per disintegration has been taken as 1 Mev. It is clear that the total dose to lymph nodes is greater than to any of the other three regions of the lungs. Even if one

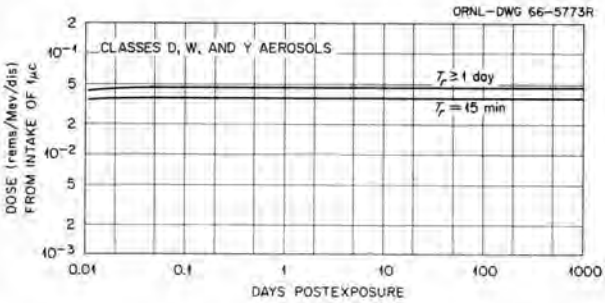

Fig. 21.4. Dose to Nasopharyngeal Region. $\epsilon = 1$ Mev, AMAD = 1 μ.

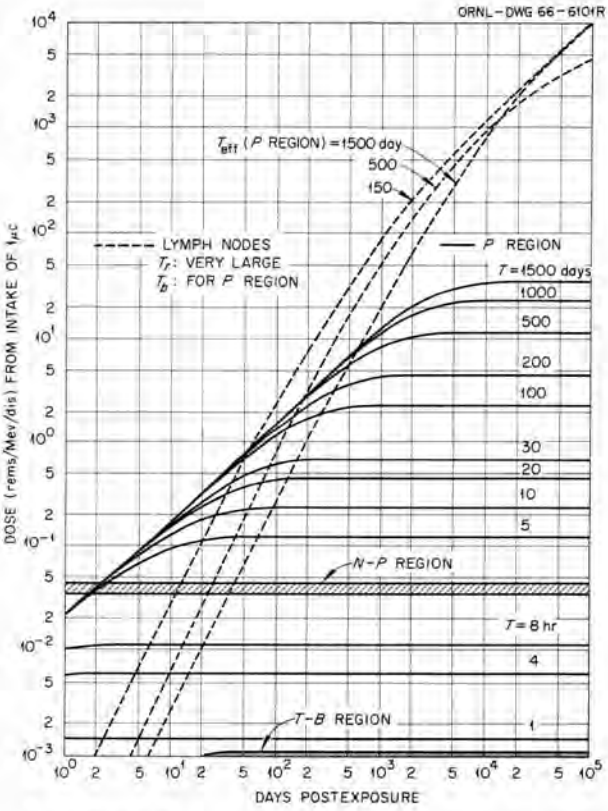

Fig. 21.5. Dose to Respiratory Tract. $\epsilon = 1$ Mev, AMAD = 1 μ.

averages the dose over the entire lymphatic system of the body (which is not done here), the dose to the lymph predominates, but not by such a large factor.

In computing the dose curves given in Figs. 21.2–5, the AMAD has been taken as 1 μ. Since D_3 and D_5 occur as factors in the dose formula, it is possible to give a factor which corrects these curves for aerosols of other AMAD. Since $D_3 = 30$ and $D_5 = 25$ for AMAD = 1 μ, the required correction factors for the N-P and P regions are $D_3/30$ and $D_5/25$ respectively. The proposed lung model gives a constant deposition factor for the T-B region, and so factors for the pulmonary region and the N-P region are the only ones shown. It is clear that the doses vary greatly with the AMAD – the dose to the P region decreasing and that to the N-P region increasing as AMAD increases.

In the foregoing formulas and graphs the effective energy has been taken as 1 Mev. Thus each value must be multiplied by the effective energy absorbed per disintegration of the isotope in order to obtain the actual dose in rems. In the case of alpha particles it seems sufficiently accurate to take the effective energy as the total energy of the alpha particles, for the thickness of the various tissues considered will be at least of the order of the range of the particle. While individual bronchioles may have a diameter this small, these smaller ones are quite closely spaced. This is indicated clearly by considerations of surface area as noted above.

It is clear that not much of the energy of photons will be absorbed near the point of origin of the photon, and hence it seems reasonable to average the dose from photons over the entire lung. A Monte-Carlo-type code has been written to obtain the absorbed fraction of energy for photons of various energies which originate uniformly within the volume occupied by the lungs. These absorbed fractions are given in Table 21.3. A similar study has been made for a surface distribution of photons, and, as would be expected, the fraction of energy absorbed in a layer of 45-μ thickness is generally quite small.

Beta emitters clearly are somewhere between these two extremes. For a beta such as the tritium beta one may use the model for local absorption; and for a beta of long range – say, 1 cm – the model averaging over the entire lung seems more appropriate. Although it is clear that further studies of the problem are indicated, a more detailed consideration of the morphology of these regions of the lung than we have been able to find in the literature seems to be required.

Table 21.3. Absorbed Fraction for a Uniform Distribution of a Gamma Source in the Lungs of a Tissue Phantom

Energy of Gamma (Mev)	Absorbed Fraction, A. F.
0.01	0.97
0.05	0.27
0.1	0.17
0.5	0.16
1	0.15
2	0.13

VARIATION OF DOSE DELIVERED BY ^{137}Cs AS A FUNCTION OF BODY SIZE FROM INFANCY TO ADULTHOOD

H. L. Fisher, Jr. W. S. Snyder

The problem we wish to consider is the following: Given a unit source of ^{137}Cs in the body of man, determine the dose rate at various positions in his body. Since it is relatively easy to determine the beta dose rate, let us dispose of this part before we examine the gamma-dose-rate problem. In Fig. 21.6 is shown the radiological decay scheme of ^{137}Cs. The ranges of both the emitted beta particles and of the electron are less than 0.6 cm in tissue. Since this range is small compared to the dimensions of the body, we will assume, as is usually done, that the entire kinetic energy of these particles is absorbed locally. The surface skin is an exception however. Using an effective

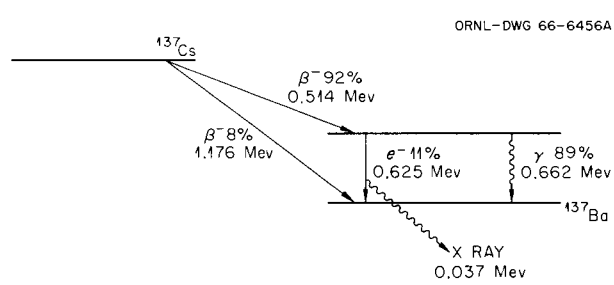

Fig. 21.6. Radiological Decay Scheme of ^{137}Cs.

energy of 0.26 Mev/dis for the betas and the electron, a dose rate of 550 microrads/hr results from a ^{137}Cs concentration in the body of 1 $\mu c/kg$. If a uniform distribution of ^{137}Cs in the body is assumed, every part of the body except the surface will be receiving a beta dose rate of 550 microrads/hr for each $\mu c/kg$ concentration of ^{137}Cs. The surface will receive about one-half of the dose rate. By way of comparison, the total-body gamma dose rate for the adult is about 480 microrads/hr per $\mu c/kg$ as we shall see later.

The problem of determining the gamma dose rate delivered to the body is not as easily resolved, because the mean range in tissue of the 0.662-Mev gamma photon is 12 cm. This value is not small compared to the dimensions of the body, so we have the problem of determining the amount of energy that escapes from the body or, conversely, the amount that is absorbed. The theory of gamma photon interaction with matter has been known for some time. However, to apply this theory to other than thin slabs and simple geometrical shapes involves elaborate mathematical calculations. Understandably, previous attempts at estimating the gamma dose rate usually have not relied on this well-developed theory but have instead employed simplifying assumptions for the purpose of performing the calculations. One such method uses the effective radius concept of the ICRP.[27] The body or organ is assumed to be a sphere of tissue of a given radius with the entire organ burden located at its center. A first-collision calculation of dose to this sphere of tissue is then effected. This method conservatively estimates the gamma dose to the body from ^{137}Cs to be about twice as high as has been found in this report.

Through the use of the high-speed digital computer it has become practical to apply the well-developed theory of gamma photon interaction with matter and dispense with many simplifying assumptions. However, we still need to specify the shape of the human body. In Fig. 21.7 is shown the type of phantom and coordinate system we have chosen. The head and neck are represented by the upper elliptical cylinder; the trunk and arms compose the elliptical cylinder of the center section; and the legs below the buttocks form the elliptical cone of the phantom. This form of the phantom is the same for all ages. Only the heights and axes of the elliptical cylinders and elliptical cone are varied to provide a phantom approximating the body size of grossly normal individuals ranging in age from infancy to adulthood. For this problem, six phantoms representing body sizes of human males of ages 0, 1, 5, 10, 15, and 20 years were constructed. The weights and dimensions completely specifying the phantoms are given in Fig. 21.7. These dimensions were chosen after considering data on body weight, length, breadth, and circumference of body parts obtained from the *Biological Handbook* by Altman.[32] Reference material also was obtained from the phantom constructed by Hayes and Brucer.[33] Data on the relative volume of body parts were obtained from "Growth of Man" in *Tabulae Biologicae* by Krogman.[34]

As shown in Fig. 21.7 the phantom was divided into over a hundred subregions in which the dose rate was determined. There are four layers in the legs in which the dose rate was calculated. There were usually five layers in the trunk section. However, in phantoms for ages 0, 1, and 5 years the trunk was divided into three, three, and four layers, respectively, in order to obtain a reasonably accurate estimate of dose rate in each. Inside the trunk the layers are further subdivided into five concentric bands. These bands are further cut by vertical cross planes to give the final and smallest volume elements in which dose rate was determined. The head section was sectioned into either two or four layers, depending on head size. With this subdivision of the phantom, the vertical variation of dose rate could be determined as well as the the side-to-side and front-to-back variations.

A Monte-Carlo-type method of calculating the dose rate was used. This code is similar to the one used by Ellett, Callahan, and Brownell,[35] but the phantom used here is different. The gamma-ray-attenuation coefficients for the medium were taken from Grodstein.[36] This method requires that the flight of a photon is mathematically followed between interaction sites. Through probabilistic

---

[32] P. L. Altman and D. S. Dittmer, *Growth Including Reproduction and Morphological Development*, Biological Handbook, Fed. Am. Soc. Exptl. Biol., Washington, 1962.

[33] R. L. Hayes and M. Brucer, *Intern. J. Appl. Rad. Isotopes* 9, 111 (1960).

[34] W. M. Krogman, "Growth of Man," pp. 712–15 in *Tabulae Biologicae*, vol. XX, ed. by H. Denzer *et al.*, Den Haag, 1941.

[35] W. H. Ellett, A. B. Callahan, and G. L. Brownell, *Brit. J. Radiol.* 37(433), 45 (1964).

[36] G. W. Grodstein, *X-Ray Attenuation Coefficients for 10 kev to 100 Mev*, NBS Circular 583, 1957; and R. T. McGinnis, *Supplement to NBS Circular 583*, 1959.

ORNL-DWG 66-6436

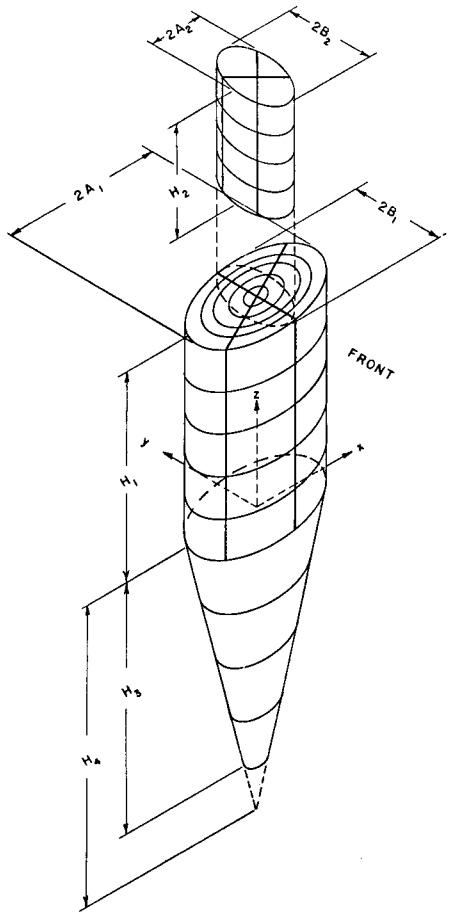

PHANTOM DIMENSIONS AND DOSE REGIONS

Age (yr)	Weight (kg)	H_1 (cm)	H_2 (cm)	H_3 (cm)	H_4 (cm)	A_1 (cm)	B_1 (cm)	A_2 (cm)	B_2 (cm)
0	3.473	23	13	15	20	5.5	5	4.5	5
1	10.171	33	16	27	36	8	7	6.5	7
5	19.654	45	20	46	57.5	11	7.5	6.5	7.5
10	31.902	54	22	64	80	14	8	6.5	8
15	54.041	65	23	78	97.5	18	9	7	9
20	70.037	70	24	80	100	20	10	.7	10

Fig. 21.7. Phantom Dimensions and Dose Regions.

rules, the energy deposition of the photon at an interaction site is recorded. After a large number of such simulated photon histories have been calculated, the average energy deposition per photon in a region is then estimated, and the dose per photon may be calculated. Photons of initial energy 0.662 Mev were randomly generated uniformly in the phantoms as follows: 80,000 in the phantoms for ages of 15 and 20 years; 100,000 in the phantoms for ages 1, 5, and 10 years; and 160,000 in the phantom for the newborn. For each photon the direction of flight was selected randomly. The flight distance to the first interaction site was determined randomly using the cross section of the medium at the energy of the photon. After selecting a new flight direction emanating from this interaction site probabilistically from the Klein-Nishina distribution, the energy deposition at this site can be determined. The process of photon flight is now repeated but with a decreased energy. Let $n - 1$, n, and $n + 1$ be consecutive interaction sites for a photon. The mathematical photon is characterized by eight independent quantities – x, y, and z, the coordinates of the present interaction site; a and b, the direction cosines specifying the direction of flight to the next interaction site; L, the length of the photon's flight path to the next interaction site; E, the energy of the photon during its flight; and W, the weight of the photon during its flight. The weight of a mathematical photon is the probability the photon exists and takes on all values from zero to 1. It is set equal to 1 for a photon just started from the source. However, a real photon has a weight of either zero or 1 at all

times. Suppose a photon, $P_{n-1} = P(x_{n-1}, y_{n-1}, z_{n-1}, a_{n-1}, b_{n-1}, L_{n-1}, E_{n-1}, W_{n-1})$, is in flight between points $n-1$ and n. We wish to know the energy deposition at point n and the location of the point $n+1$, which may be found if we find P_n and use it in conjunction with P_{n-1}. The coordinates x_n, y_n, and z_n may be found by applying algebraic geometry using x_{n-1}, y_{n-1}, z_{n-1}, a_{n-1}, b_{n-1}, and L_{n-1}. The new direction of flight, a_n and b_n, is determined by using E_{n-1} and the Klein-Nishina gamma photon scattering distribution. The new energy E_n is calculated from the angle of scatter, which involves a_{n-1}, b_{n-1}, a_n, and b_n. Length L_n is calculated as follows:

$$L_n = \frac{-1}{\sigma(E_n)} \ln N ,$$

where $\sigma(E_n)$ is the attenuation cross section of the medium and N is a random number chosen uniformly on $0 \leqq N \leqq 1$. The weight W_n is given by

$$W_n = W_{n-1} \frac{\sigma_c(E_n)}{\sigma(E_n)} ,$$

where $\sigma_c(E_n)$ is the cross section for the Compton process. The energy deposition at point n is

$$E\Delta = W_{n-1} \left[\frac{\sigma_p(E_{n-1})}{\sigma(E_{n-1})} E_{n-1} + \frac{\sigma_c(E_{n-1})}{\sigma(E_{n-1})} (E_{n-1} - E_n) + \frac{\sigma_{pp}(E_{n-1})}{\sigma(E_{n-1})} (E_{n-1} - 2e) \right] ,$$

where $\sigma_p(E_n)$, $\sigma_c(E_n)$, and $\sigma_{pp}(E_n)$ are the cross sections for the photoelectric, Compton, and pair production processes, respectively, and e is the rest mass of an electron in energy units. The total flight history of a photon may end in one of three ways. It may end by escaping from the phantom, or when its energy falls below 2 kev, or when its weight falls below 10^{-5}.

Let us look briefly at the restrictions of this method as we are using it. Other than the obvious inaccuracies that the shape of the phantoms only roughly approximates the shape of the human body and that the phantom remains in a fixed standing position and is in free space from which no backscatter occurs, there is one restriction that should be emphasized. This phantom is homogeneous throughout. There is no low density and low cross-sectional area for the lungs, nor is there a high density and modified cross-sectional area for bone. To take these into account would involve a rewriting of the entire code. Although the results obtained with the constant-density phantom will need to be refined in the future, the results presented here are an improvement over past ones.

In Fig. 21.8 is a graph of the total-body gamma dose rate vs age from a ^{137}Cs source uniformly distributed in the phantoms. The units of the ordinate are in dose rate (microrads/hr) per unit activity concentration in the body (μc/kg). Dose rates for the different phantoms are given per unit concentration of activity in the phantoms, but one may convert the values given to other bases of comparison. Throughout this paper we will use the units just described. It is the primary purpose of this report to describe the physical differences in gamma-ray absorption in different size phantoms although biological parameters such as biological half-life, gut absorption, and intake quantity will influence a hazards evaluation.

From this graph we see that the total-body dose rate for the infant is slightly less than one-half that for the adult. This is due to the fact that the 0.662-Mev gamma rays have a higher probability of

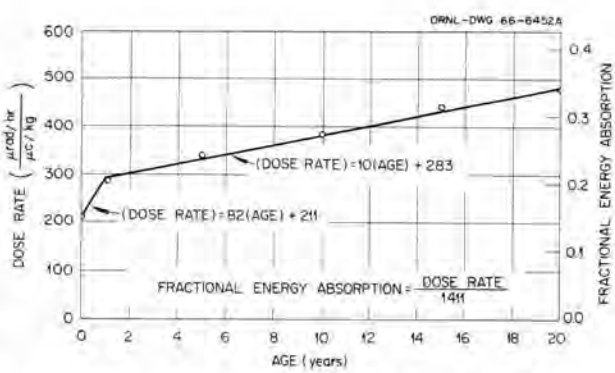

Fig. 21.8. Average Total-Body Gamma Dose Rate from a Uniformly Distributed ^{137}Cs Source.

escaping from the infant phantom than from the adult phantom, which is 20 times larger in the total mass. The total-body dose rate for the adult as determined by this Monte Carlo calculation is about one-half that obtained by an ICRP effective radius calculation. At this point let us refer to the gamma plus beta dose rate. The total dose rate from ^{137}Cs may be obtained by adding 550 to the values given on this graph or on any succeeding dose rate graph for a uniformly distributed source presented in this report. This is true for all of the phantoms.

Since a Monte Carlo computation is an involved and time-consuming procedure, it is more efficient to store the results of the calculation for application to other problems. The results have been stored in three modes – graphically, in tables, and in approximating formulas. As seen in the graph, the gamma dose rate vs age has been approximated by two linear functions. There is no theoretical significance to these approximating functions. They are used as a convenient means of storing the data simply and for retrieving them within a certain range of error.

To show the variation of dose within the phantoms, we have chosen the results for the infant and adult phantoms only. Results for the other phantoms are similar to these two. We shall examine results from the adult phantom first. In Fig. 21.9 is a graph of the average dose rate in horizontal layers from head to foot of the phantom. The error bars on the Monte Carlo points are one standard deviation due to the statistical variability involved in Monte Carlo calculations. We note particularly that the average dose rate along the trunk is nearly constant and is about 15% greater than the average dose rate for the total body. The top of the head and bottom of the feet receive the lowest dose rate, being about a factor of 3 below the trunk average. The Monte Carlo points above those for the layer average are the dose rates along the vertical axis of the trunk. At this location, in the interior, are found the highest dose rates in the body. These are higher than the layer average by about 30%. Let us examine the approximate gonadal gamma dose rates. The ovaries, which would be located near the vertical axis of the trunk, receive this central dose rate. The testes receive a dose rate that is approximately that of the trunk average. As a point of perspective, the vertical distribution of gamma dose rate in the infant has been plotted on this same graph.

The variation of dose rate from the center of the trunk to its surface for the adult phantom is given in Fig. 21.10. Because little variation in dose rate exists among the layers of the trunk, we may average the values from all layers to obtain better statistics. This was done, and the two curves seen here are the dose rates from the center to the front surface and from the center to the side surface. Of course, the dose rate from center to back is identical with the center-to-front dose rate and has been included. Similar remarks apply to the

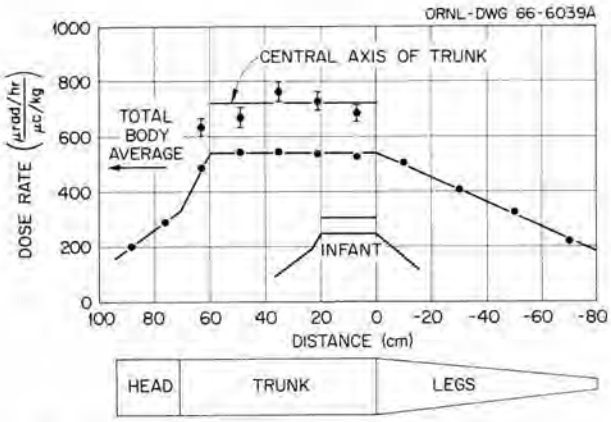

Fig. 21.9. Average Gamma Dose Rate in Horizontal Layers in the Adult Phantom from a Uniformly Distributed ^{137}Cs Source.

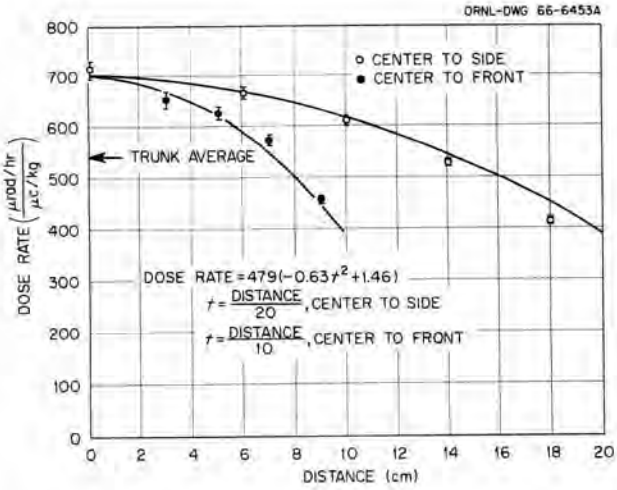

Fig. 21.10. Gamma Dose Rate from Center to Surface of Adult Phantom from a Uniform ^{137}Cs Source.

variation of dose from left to right. From the Monte Carlo estimates, it was noted that the dose rate at the front surface was not very different from that at the side surface. Considering that the trunk is elliptical and twice as wide as it is thick, this result was a little surprising. The other phantoms are not as highly elliptical, and this result is valid for them also. The dose rate at the surface is about one-half the central dose rate.

In Fig. 21.11 is shown the vertical variation of dose rate in the infant phantom. It appears that the relative changes observed from head to foot are about the same as for the adult phantom. However, the entire graph is located at a lower dose rate than the one for the adult. The variation of dose rate from center to surface of the infant phantom is given in Fig. 21.12. Since the infant trunk is nearly cylindrical, being only 1 cm wider than it is thick, there is practically no difference in the center-to-front and center-to-side data. Again, the surface dose rate is about one-half the central dose rate.

Results from the other four phantoms are similar to the ones already shown. Results from all phantoms are shown in Fig. 21.13; also shown here is the normalized dose rate for each phantom. Zero on the abscissa is the center axis of the trunk, while the value 1 is the surface. To normalize the dose rate for a phantom, we divide by the total-body dose rate for that phantom. It may be observed that the variation of dose rates among the phantoms is about 10% after normalization in the manner described.

The equations approximating the data you have seen in the preceding graphs are tools that allow one to retrieve with sufficient accuracy the results found by the Monte Carlo method. All of these equations are given compactly in Fig. 21.14. The first function relates age to total-body gamma dose rate; the second function permits calculation of the average gamma dose rate from foot to head of the phantom; and the third function gives the gamma dose rate at any position inside the trunk. Functions 4 and 5 are derivable from 3, while function 6 is the beta dose rate.

Let us now consider a nonuniform distribution of ^{137}Cs in the phantom. It has been found by Yamagata[37] that the cesium concentration of muscle is

[37] N. Yamagata, *Radiation Res.* 3–1, 9 (March 1962).

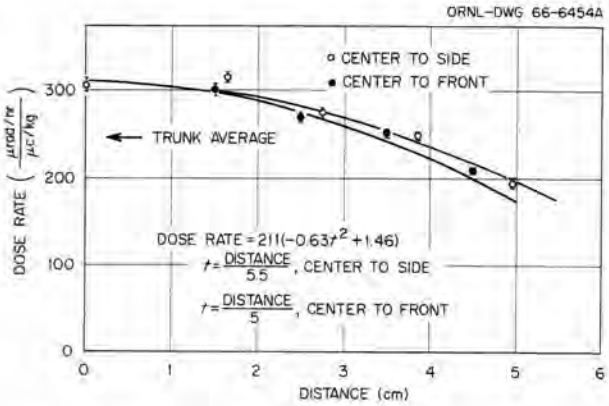

Fig. 21.12. Gamma Dose Rate from Center to Surface of Infant Phantom from a Uniform ^{137}Cs Source.

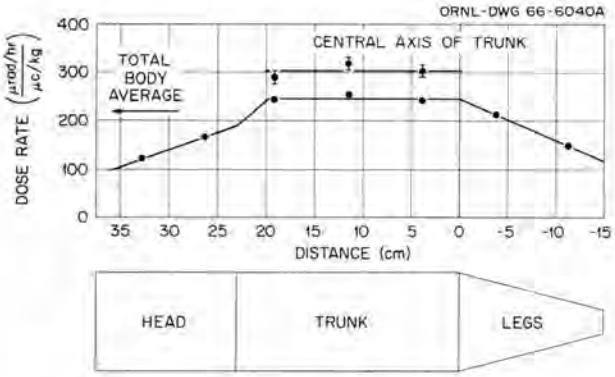

Fig. 21.11. Average Gamma Dose Rate in Horizontal Layers in the Infant Phantom from a Uniformly Distributed ^{137}Cs Source.

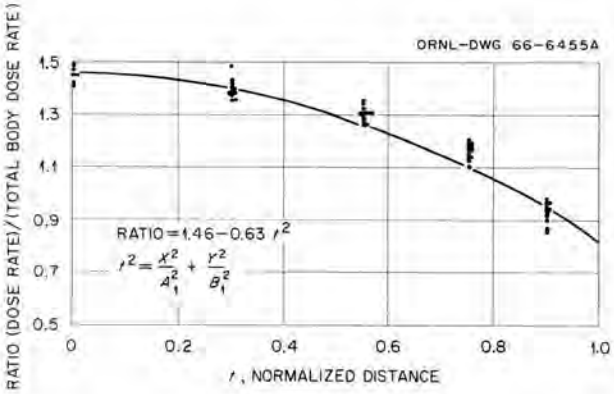

Fig. 21.13. Normalized Gamma Dose Rate from Center to Surface of Normalized Phantoms from a Uniform ^{137}Cs Source.

ORNL DWG 66-6382

(1) $$D_{avtb} = \begin{cases} 82\ (\text{Age, yr}) + 211 \pm 5\%, & 0 \leq \text{Age} \leq 1 \\ 10\ (\text{Age, yr}) + 283 \pm 5\%, & 1 \leq \text{Age} \leq 20 \\ 483, & 20 \leq \text{Age} \end{cases}$$

(2) $$D_{av}(Z) = \begin{cases} D_{avtb}\left[\frac{0.72}{H_3} Z + 1.15\right] \pm 25\%, & -H_3 \leq Z \leq 0 \\ D_{avtb}\left[1.15\right] \pm 5\%, & 0 \leq Z \leq \frac{6}{7} H_1 \\ D_{avtb}\left[-\frac{2.47}{H_1} Z + 3.25\right] \pm 20\%, & \frac{6}{7} H_1 \leq Z \leq H_1 \\ D_{avtb}\left[-Z + H_1 + 2H_2\right] \frac{0.40}{H_2} \pm 20\%, & H_1 \leq Z \leq H_2 \end{cases}$$

(3) $$D(x,y) = D_{avtb}\left[-0.63\left(\frac{x^2}{A_1^2} + \frac{y^2}{B_1^2}\right) + 1.46\right] \pm 10\%, \quad 0 \leq Z \leq \frac{6}{7} H_1, \quad \frac{x^2}{A_1^2} + \frac{y^2}{B_1^2} \leq 1$$

(4) $$D_{center} = 1.46\, D_{avtb} \pm 10\%$$

(5) $$D_{surface} = 0.83\, D_{avtb} \pm 10\%$$

(6) $$D_{\beta} = 550$$

where

D_{avtb} is the total body gamma dose rate

$D_{av}(Z)$ is the gamma dose rate in horizontal layers along the vertical axis Z

$D(x,y)$ is the gamma dose rate at the position (x,y) in the trunk

D_{center} is the gamma dose rate along the Z axis in the trunk

$D_{surface}$ is the gamma dose rate at the surface of the trunk

D_{β} is the beta dose rate everywhere in the phantom

Fig. 21.14. Dose Rate (μrad/hr per μc/kg) in Phantoms from a ^{137}Cs Source Uniformly Distributed in the Phantoms.

about twice that of other soft tissues, the latter being fairly uniform. To simulate this distribution in the adult phantom, the volume of the leg section and about one-half of the trunk volume nearest the surface were taken to represent muscle. The equation separating these volumes is

$$\left(\frac{X}{14}\right)^2 + \left(\frac{Y + 1.5}{7}\right)^2 = 1.$$

In this muscle section the source concentration of ^{137}Cs was twice the remaining sections. Surprisingly, this distribution of the source did not produce any large change in the gamma dose rate anywhere in the body when compared with the uniform distribution of the same body burden. For example, the total-body dose rate for the nonuniform distribution was 2% less than that for the uniform case, while the dose rate along the central axis of the trunk for the nonuniform case was 90% of that in the uniform case. However, the beta dose rate would be twice as large in the muscle as in other soft tissue since all beta energy was assumed to be absorbed locally.

Let us close by considering the total-body beta plus gamma dose received by the infant and the adult when each takes in 1 μc of ^{137}Cs. Let us assume the gut absorption to be 100% and the biological half-times of cesium to be 100 days for the adult and 20 days for the infant. In this case the infant would receive 0.15 rad and the adult 0.05 rad; that is, the infant would receive three times the dose received by the adult.

We see that although the infant receives the same beta dose rate and only one-half the gamma dose rate as the adult per unit ^{137}Cs body concentration, metabolic parameters as well as intake patterns need to be included in the analysis to arrive at meaningful conclusions as to dose commitment or assessment of risk.

Acknowledgement

Appreciation for the coding and computer operations is expressed to Gordon G. Warner of the ORNL Mathematics Division.

IODINE RETENTION

W. S. Snyder H. L. Fisher, Jr.
Monica Boyd

Therapeutic and diagnostic use of radioactive iodine, as well as that available to the population through fallout and the food chain, provides impetus for the study of iodine retention by the thyroid and the body. Several models have been proposed[38,39] which consist of essentially three compartments. It is the purpose of this report to give solutions for the iodine retention model in general and in detail, using typical or normal metabolic parameters.

The model is shown schematically in Fig. 21.15. The Q's are the quantities of iodine in the various compartments, and the K's are rate constants by which transfer occurs between compartments. The system of differential equations governing the kinetics is:

$$\frac{d}{dt} Q_I(t) = -(K_{IE} + K_{IG} + \lambda)\, Q_I(t) + K_{BI}\, Q_B(t)\,,$$

$$\frac{d}{dt} Q_G(t) = K_{IG}\, Q_I(t) - (K_{GB} + \lambda)\, Q_G(t)\,, \qquad (1)$$

$$\frac{d}{dt} Q_B(t) = K_{GB}\, Q_G(t) - (K_{BI} + K_{BF} + \lambda)\, Q_B(t)\,.$$

This system is valid for radioactive iodine with decay constant λ or for stable iodine with $\lambda = 0$.

[38] G. L. Brownell, *J. Clin. Endocrinol. Metab.* 11, 1095 (1951).

[39] D. S. Riggs, *Pharmacol. Rev.* 4, 284 (1952).

ORNL-DWG 66-8883

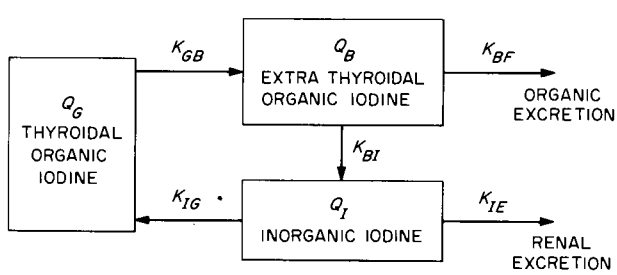

Fig. 21.15. Compartmental Model for Iodine Metabolism.

Activity in a compartment may be obtained by multiplying the quantities Q by λ. This system will be solved for the case of an intake of inorganic iodine of amount $Q_I(0)$ into the inorganic iodine compartment at time zero. The initial conditions are therefore:

$$Q_I(0) = Q_I(0)\,,$$

$$Q_G(0) = 0\,,$$

$$Q_B(0) = 0\,.$$

It is appropriate to emphasize again that this model is for the normal thyroid under normal conditions and may not apply to pathological cases or people on high- or low-iodine diets. The solution to the system is:

$$Q_I(t) = Q_I(0)\frac{1}{D}\left\{(K_{GB} - \lambda_1)Ae^{-(\lambda_1 + \lambda)t} + (K_{GB} - \lambda_2)Be^{-(\lambda_2 + \lambda)t} + (K_{GB} - \lambda_3)Ce^{-(\lambda_3 + \lambda)t}\right\},$$

$$Q_G(t) = Q_I(0)\frac{1}{D}\left\{K_{IG}Ae^{-(\lambda_1 + \lambda)t} + K_{IG}Be^{-(\lambda_2 + \lambda)t} + K_{IG}Ce^{-(\lambda_3 + \lambda)t}\right\},$$

$$Q_B(t) = Q_I(0)\frac{1}{D} \times \left\{(K_{GB} - \lambda_1)(K_{IG} + K_{IE} - \lambda_1)Ae^{-(\lambda_1 + \lambda)t} + (K_{GB} - \lambda_2)(K_{IG} + K_{IE} - \lambda_2)Be^{-(\lambda_2 + \lambda)t} + (K_{GB} - \lambda_3)(K_{IG} + K_{IE} - \lambda_3)Ce^{-(\lambda_3 + \lambda)t}\right\},$$

where

$$D = (\lambda_1 - \lambda_2)[\lambda_3(\lambda_1 + \lambda_2 - \lambda_3) - \lambda_1\lambda_2]\,,$$

$$A = (\lambda_2 - \lambda_3)[K_{GB} + K_{IG} + K_{IE} - (\lambda_2 + \lambda_3)]\,,$$

$$B = (\lambda_3 - \lambda_1)[K_{GB} + K_{IG} + K_{IE} - (\lambda_3 + \lambda_1)]\,,$$

$$C = (\lambda_1 - \lambda_2)[K_{GB} + K_{IG} + K_{IE} - (\lambda_1 + \lambda_2)]\,,$$

and λ_1, λ_2, and λ_3 are the three solutions of

$$-\Lambda^3 + (K_{GB} + K_{IE} + K_{IG} + K_{BI} + K_{BF})\Lambda^2 - (K_{GB}K_{BI} + K_{GB}K_{BF} + K_{GB}K_{IE} + K_{GB}K_{IG} + K_{IE}K_{BI} + K_{IE}K_{BF} + K_{IG}K_{BI} + K_{IG}K_{BF})\Lambda + (K_{IE}K_{GB}K_{BI} + K_{IE}K_{GB}K_{BF} + K_{IG}K_{GB}K_{BF}) = 0\,.$$

Riggs[39] has given typical values determined from experiment for the transfer rates for the normal thyroid and for several pathological conditions. These rates for the normal individual given in units of proportion per hour are:

$$K_{IG} = 0.0389\,,$$
$$K_{IE} = 0.0800\,,$$
$$K_{GB} = 0.000364\,,$$
$$K_{BI} = 0.00222\,,$$
$$K_{BF} = 0.000208\,.$$

Using these constants the retention in the three compartments of any isotope of iodine with radiological decay constant λ (hr^{-1}) is:

$$Q_I(t) = Q_I(0)\,\{1.00e^{-(0.119 + \lambda)t} - 0.00093e^{-(0.00255 + \lambda)t} + 0.00093e^{-(0.000246 + \lambda)t}\}\,,$$

$$Q_G(t) = Q_I(0)\,\{-0.328e^{-(0.119 + \lambda)t} + 0.016e^{-(0.00255 + \lambda)t} + 0.312e^{-(0.000246 + \lambda)t}\}\,,$$

$$Q_B(t) = Q_I(0)\,\{-0.0027e^{-(0.119+\lambda)t} - 0.0478e^{-(0.00255+\lambda)t} + 0.0505e^{-(0.000246+\lambda)t}\},$$

where t is in hours.

For ^{131}I, $\lambda = 0.00359\ hr^{-1}$ and $A(t) = \lambda\ Q(t)$ where $A(t)$ is the activity, the retention equations are:

$$A_I(t) = A_I(0)\,\{1.00e^{-0.122t} - 0.00093e^{-0.00614t} + 0.00093e^{-0.00384t}\},$$

$$A_G(t) = A_I(0)\,\{-0.328e^{-0.122t} + 0.016e^{-0.00614t} + 0.312e^{-0.00384t}\},$$

$$A_B(t) = A_I(0)\,\{-0.0027e^{-0.122t} - 0.0478e^{-0.00614t} + 0.0505e^{-0.0384t}\},$$

where t is in hours.

These retention functions are shown graphically in Figs. 21.16 to 21.18. The equilibrium level in a compartment model may be computed if the intake rate, I, is known. Let

$$\frac{d}{dt}Q(t) = -\Lambda\ Q(t) \qquad (2)$$

be the matrix formulation of the system of differential equations representing the model. Then for a constant intake rate, M,

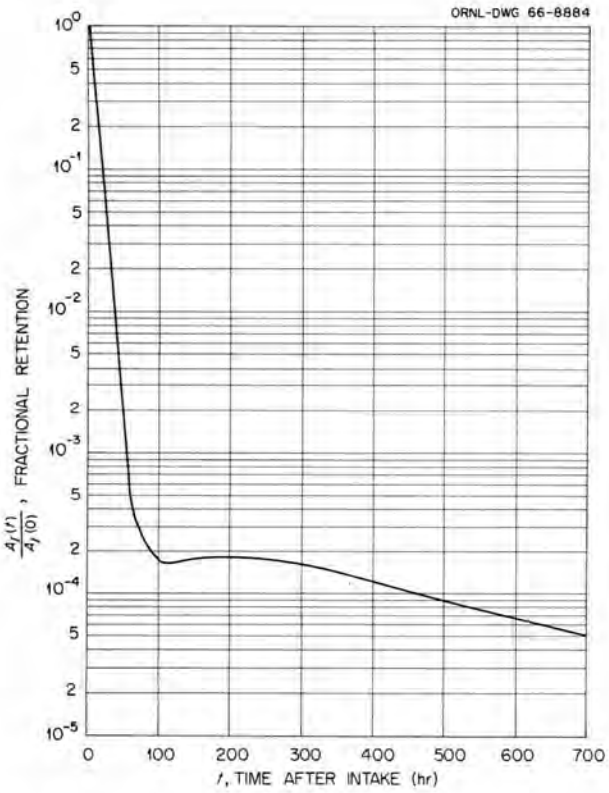

Fig. 21.16. Fractional Retention of Inorganic ^{131}I After Single Intake.

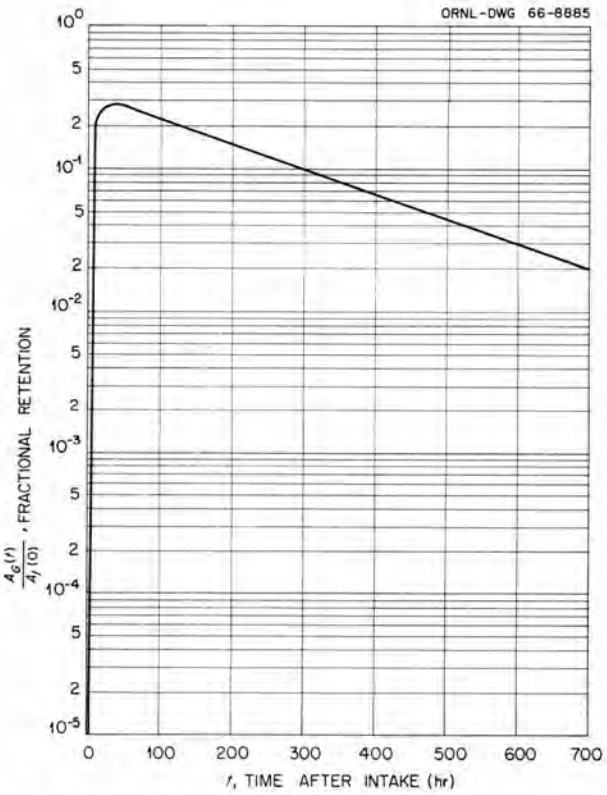

Fig. 21.17. Fractional Retention of Thyroidal Organic ^{131}I After Single Intake.

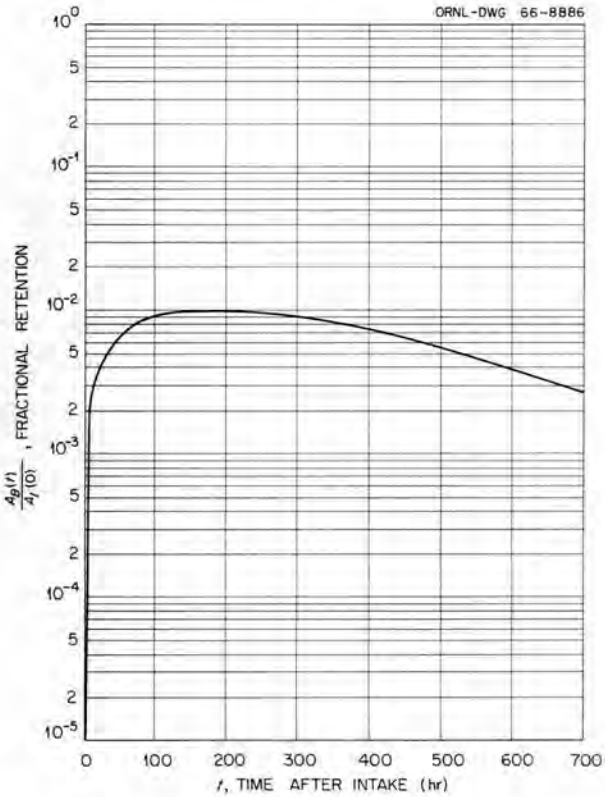

Fig. 21.18. Fractional Retention of Extrathyroidal Organic ^{131}I After Single Intake.

$$\frac{d}{dt}\,Q(t) = -\Lambda\,Q(t) + M\,,$$

$$\left.\frac{d}{dt}\,Q(t)\right]_{t=\infty} = -\Lambda\,Q(\infty) + M\,. \tag{3}$$

It has been shown by Berman and Schoenfeld[40] that for a Λ whose elements satisfy

$$\lambda_{ij} \leqq 0,\ i \neq j\,,$$

$$\lambda_{ii} \leqq \sum_{\substack{j=1\\ j\neq i}}^{n} \lambda_{ji}\,,$$

the roots, x, of $|\Lambda - xI| = 0$ have negative real parts and that pure imaginary roots are impossible. Consequently the solutions of (2) consist of sums of exponentials with negative powers, while (3) is of the same form plus a constant. Therefore,

$$\left.\frac{d}{dt}\,Q(t)\right]_{t=\infty} = 0\,,$$

and the equilibrium activity is

$$Q(\infty) = \Lambda^{-1}M\,.$$

In the case of the three-compartment system for iodine, the equilibrium activity, $A(\infty) = \lambda\,Q(\infty)$, for a constant continuous intake is:

$$\begin{bmatrix} A_I(\infty) \\ A_B(\infty) \\ A_G(\infty) \end{bmatrix} = \frac{I_I}{S}\begin{bmatrix} (K_{BI} + K_{BF} + \lambda)(K_{GB} + \lambda) \\ K_{GB}K_{IG} \\ (K_{BI} + K_{BF} + \lambda)K_{IG} \end{bmatrix},$$

where

$$S = (K_{BI} + K_{BF} + \lambda)(K_{IG} + K_{IE} + \lambda)(K_{GB} + \lambda) - K_{BI}K_{GB}K_{IG}\,,$$

I_I = activity/hr intake into inorganic iodine compartment.

For ^{131}I

$$\begin{bmatrix} A_I(\infty) \\ A_B(\infty) \\ A_G(\infty) \end{bmatrix} = I_I\begin{bmatrix} 11.6 \\ 6.9 \\ 114 \end{bmatrix}.$$

The percentage of the ^{131}I body burden in each compartment at equilibrium is, therefore, 8.7% inorganic, 5.2% extrathyroidal organic, and 86.1% thyroidal organic. For stable iodine, $\lambda = 0$, the equilibrium amounts (g) for a constant continuous intake, M_I (g/hr), are:

$$\begin{bmatrix} Q_I(\infty) \\ Q_B(\infty) \\ Q_G(\infty) \end{bmatrix} = M_I\begin{bmatrix} 12 \\ 192 \\ 1280 \end{bmatrix}.$$

The percentage of the stable iodine body burden in each compartment at equilibrium, therefore, is 0.8%

[40] M. Berman and R. Schoenfeld, *J. Appl. Phys.* 27(11), 1361 (1956).

inorganic, 13% extrathyroidal organic, and 86.2% thyroidal organic.

The total dose to any compartment of a compartmental model from a single intake may be calculated. Let the system

$$\frac{d}{dt} A(t) = -\Lambda\, A(t)$$

with initial conditions $A(0)$ describe this model, where $A(t)$, column vector, is the activity (μc) and Λ the decay matrix (hr^{-1}). Then

$$\int_0^\infty \frac{d}{dt} A(t)\, dt = -\Lambda \int_0^\infty A(t)\, dt\,,$$

$$[A(\infty) - A(0)] = -\Lambda \int_0^\infty A(t)\, dt\,.$$

For the reasons mentioned previously, the solution $A(t)$ consists of exponentials with exponents consisting of negative real parts. Therefore, the μc-hr of residence is

$$\int_0^\infty A(t)\, dt = \Lambda^{-1}\, A(0)\,,$$

and the total dose in rads D_i to compartment i from a single intake may be obtained from

$$\begin{bmatrix} D_1 m_1 \\ D_2 m_2 \\ \vdots \\ D_n m_n \end{bmatrix} = 2.13 \epsilon\, \Lambda^{-1}\, A(0)\,,$$

where ϵ is the effective energy in Mev and m_i the compartment mass. For the three-compartment model for iodine, the total dose (rads) to each compartment from a single intake is:

$$\begin{bmatrix} D_I \\ D_B \\ D_G \end{bmatrix} = \frac{2.13\, A_I(0)}{S} \begin{bmatrix} (K_{BI} + K_{BF} + \lambda)(K_{GB} + \lambda)/M_I \\ K_{GB} K_{IG}/M_B \\ (K_{BI} + K_{BF} + \lambda) K_{IG}/M_G \end{bmatrix},$$

where M_I, M_B, and M_G are the masses of the three compartments I, B, and G; $A_I(0)$ is the initial amount of activity (μc) introduced into compartment I; and

$$S = (K_{BI} + K_{BF} + \lambda)(K_{IG} + K_{IE} + \lambda)(K_{GB} + \lambda) - K_{BI} K_{GB} K_{IG}\,.$$

Assuming the thyroid to weigh 20 g, the total dose from organic thyroidal iodine from a single intake of ^{131}I is:

$$\frac{D_G}{A_I(0)} = 2 \text{ rads}/\mu\text{c}\,.$$

Conclusion

The mathematical equations for a three-compartmental model for iodine metabolism were solved to find the retention functions for the compartments using typical parameters for thyroid function. The equilibrium level for each compartment under constant continuous intake conditions was found as a rational function of the compartmental transfer constants. The activity residence time or total dose for each compartment from a single intake was also found as a rational function of the compartmental transfer coefficients. These equations were given as a function of the radiological decay constant, permitting their use with any radio- or stable isotope of iodine. The use of these equations was demonstrated by employing ^{131}I as an example.

COMPUTER STUDIES OF LINEAR COMBINATION OF EXPONENTIALS REPRESENTING POWER FUNCTIONS

S. R. Bernard W. Davis III

This study was undertaken to compare a sum of exponentials

$$S = \sum_i a_i e^{-\alpha_i t}$$

with a power function. In the sum of exponentials

a_i and α_i are constants and t (the time) is a variable. In our previous reports[41] we showed that the particular case where

$$a_i \propto \alpha_i^{-h}$$

will give rise to a power function where the smallest and largest α's approach zero and infinity, respectively, and all the differences

$$\Delta\alpha_i = \alpha_{i+1} - \alpha_i$$

approach zero as $N \to \infty$. Thus by definition of the Riemann integral

$$\lim_{N \to \infty} \sum_{i=1}^{N} \alpha_i^{-n} e^{-t\alpha_i} \Delta\alpha_i$$

$$\to \int_0^\infty \alpha^{-n} e^{-t\alpha} \, d\alpha = \Gamma(1-n)\, t^{n-1}, \qquad n < 1 ,$$

where

$$\Gamma(1-n) = \int_0^\infty x^{-n} e^{-x} \, dx .$$

This suggests that the sum,

$$\sum_{i=1}^{N} \alpha_i^{-n} e^{-t\alpha_i} , \qquad (1)$$

might be approximately equal to

$$\frac{1}{\Delta\alpha} \Gamma(1-n)\, t^{n-1} , \qquad n < 1 , \qquad (2)$$

over some interval of time not including $t = 0$. Clearly, in Eq. (1) for $t = 0$ and the smallest $\alpha \neq 0$ this function is finite, a property not enjoyed by the function in Eq. (2).

The major reason for undertaking this study is to discover a clue as to why the power function frequently appears to represent data on excretion from and retention in the body when a bone-seeking radionuclide is administered. The power function has been reported by Speckman and Norris,[42] Marshall,[43] Langham *et al.*,[44] Glad *et al.*,[45] and Bernard[46] and others to represent fairly adequately metabolic data.

We present only a brief summary of the results of the studies made using a computer. In the computational work we incremented the α's linearly, that is, we let

$$\alpha_i = \alpha_1 + (i-1)\,\Delta\alpha , \qquad i = 1, 2, \ldots, N , \qquad (3)$$

and we let N range from 10 to 10^4, and $n = -0.5$, 0, 0.333, 0.666, and 0.999. The other two parameters, α_1 and $\Delta\alpha$, took on various values ranging from 10^{-6} to 10^{-2}. Clearly, for the case $n = 0$ one does not need a computer to sum N exponential terms because in that case the sum in (1) under the condition in (3) is a geometric series, and it reduces to the simple expression

$$S = e^{-\alpha_1 t} \frac{1 - e^{-N\,\Delta\alpha\, t}}{1 - e^{-\Delta\alpha t}} . \qquad (4)$$

For the case $n \neq 0$, no simple expression could be found. In the computations made with the CDC 1604 computer, however, we made computations for $n = 0$ to have a point of reference or of accuracy to check the program. In general we found that as N was increased and $\Delta\alpha$ and α_1 approached zero, the finite sum would more closely approximate the power function in (2) over longer periods of time, but only for the case where $n \leqq 0.333$. For $n = 0.666$ or 0.999 the finite sum never did touch the power function as given in (2). Figure 21.19 shows a graph of a typical set of calculations plotted with the Calcomp plotter. Also shown are the power functions which these sums approximate. In this calculation $N = 10^3$, $\alpha_1 = 10^{-6}$, $\Delta\alpha = 2 \times 10^{-6}$, and $n = 0$, 0.333, 0.666, and 0.999. As can be seen, for $n = 0$ and 0.333, the finite sum of terms and the power functions are tangent to one another

[41] *Health Phys. Div. Ann. Progr. Rept. July 31, 1965*, ORNL-3849, p. 201.

[42] T. W. Speckman and W. P. Norris, *Radiation Res.* **23**, 461 (1964).

[43] J. H. Marshall, *J. Theoret. Biol.* **6**, 386 (1964).

[44] W. H. Langham *et al.*, *Distribution and Excretion of Plutonium Administered Intravenously to Man*, LA-1151 (1950).

[45] B. N. Glad, C. W. Mays, and W. Fisher, *Radiation Res.* 12(6), 672 (1960).

[46] S. R. Bernard, *Health Phys.* **1**, 288 (1958).

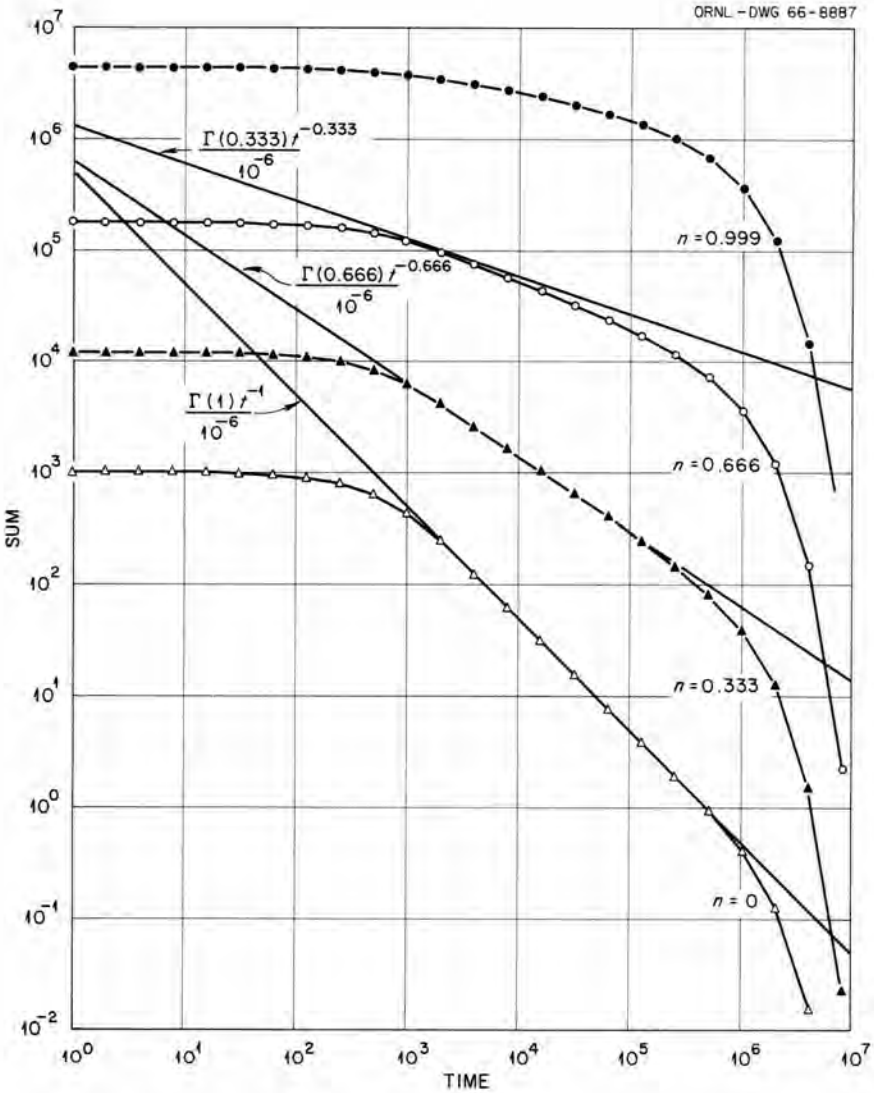

Fig. 21.19. Plot of $\sum_{i=1}^{N} \alpha_i^{-n} e^{-\alpha_i t}$ and $\frac{\Gamma(1-n)}{2 \times 10^{-6}}\, t^{1-n}$ vs t for $\alpha_i = 10^{-6} + (i-1)\, 2 \times 10^{-6}$, $i = 1, 2, \ldots, 1000$, and Various Values of n.

over at least two decades of time, but for $n = 0.666$ the agreement is not as good over as long a period of time. For the case $n = 0.999$ the power function would be

$$\frac{\Gamma(0.001)\ t^{-0.001}}{10^{-6}} \sim 10^9 t^{-0.001},$$

and the value for $t = 1$ is $\sim 10^9$. Note the finite sum at $t = 1$ is $\sim 5 \times 10^6$ and differs from the power function by a factor of ~ 200. We observed in all of our computer studies that the agreement between a finite sum and the power function was always poorest where $n = 0.999$. The reasons for this are not known to us.

We also observed that when $(\alpha_1/\Delta\alpha) < \frac{1}{2}$ then an inflection would occur in the log $\times$ log graph of the sum vs time and would be more pronounced as $|1 - n|$ increased. Figure 21.20 shows a log $\times$ log plot of the sum vs time to illustrate this for $n = -0.5$, 0, 0.333, and 0.999, $\Delta\alpha = 0.01$ and $\alpha_1 = 0.001$. Here $N = 150$ except for the case where $n = -0.5$, in which case $N = 1000$. Note that in all cases except $n = 0.999$ the sum of finite terms intersects the power function twice and undergoes an inflection. It is not difficult to show for the case $n = 0$ that when the condition $(\alpha_1/\Delta\alpha) \geqq \frac{1}{2}$ holds, no inflection will occur. No proof for the case $N \neq 0$ has been found yet. However, in our studies we have observed that when $(\alpha_1/\Delta\alpha) \geqq \frac{1}{2}$ no inflection occurs in the curves.

We also mention that our work reported here is somewhat similar to that carried out and reported by Turner.[47] He approaches the problem by noting that one might represent the spectrum of the a's and α's in the exponential sum by a continuous function (he chooses a gamma distribution); he then takes the integral over the spectrum of the α's. In his gamma distribution approach, a special form of the power function – one which is finite at the origin – is derived.

---

[47] M. E. Turner, *Biometrics* **20**(4), 827 (1964).

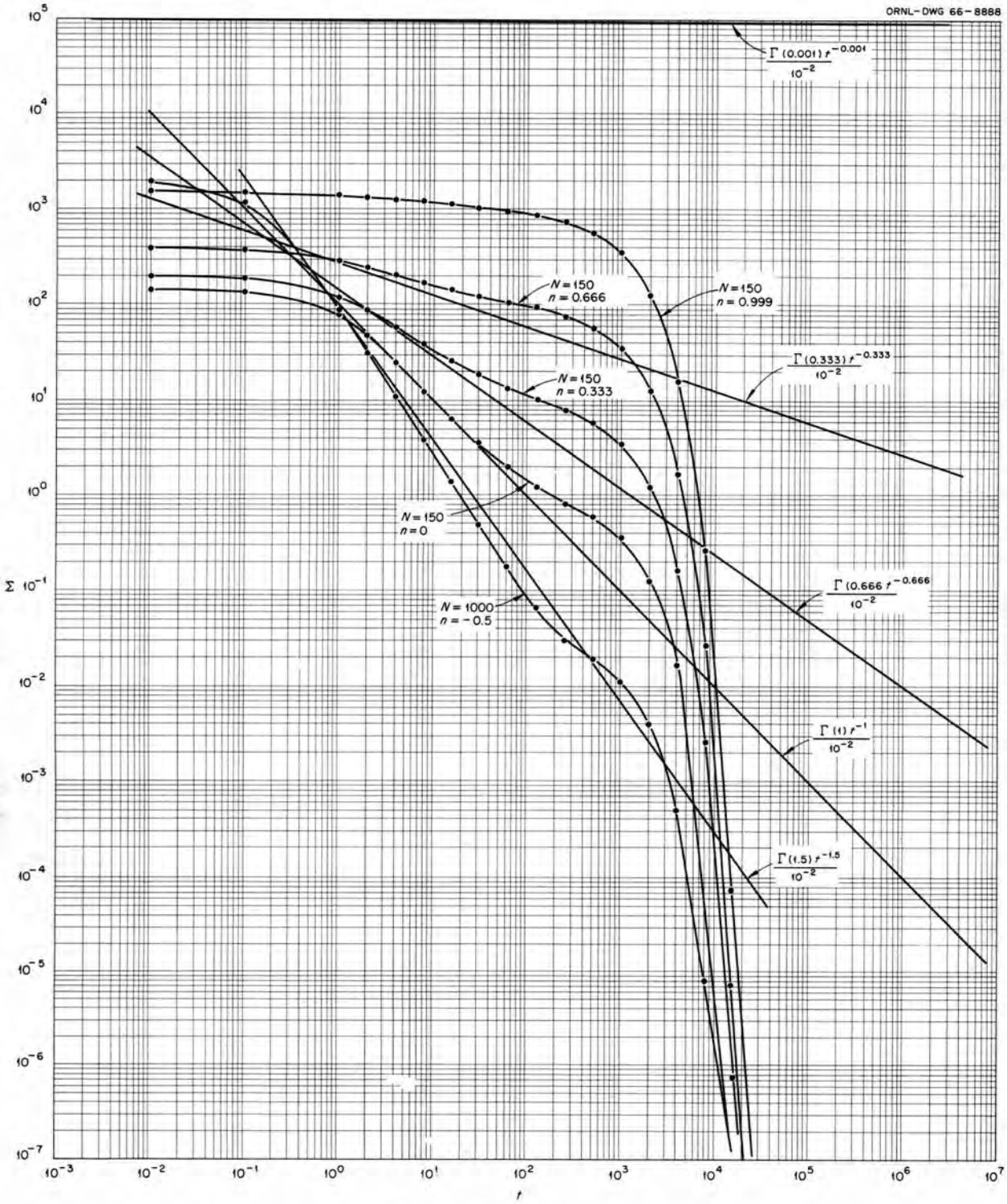

Fig. 21.20. Plot of $\sum_{i=1}^{N} \alpha_i^{-n} e^{-\alpha_i t}$ and $\frac{\Gamma(1-n)}{0.01} t^{1-n}$ vs t for $\alpha_i = 10^{-3} + (i-1) \times 10^{-2}$, $i = 1, 2, \ldots, 150$, and Various Values of n.

22. Stable Element Metabolism

W. S. Snyder
Mary Jane Cook
Cyrus Feldman[1]
F. S. Jones[1]
Peggy L. Stewart[2]
Isabel H. Tipton[2]

Because the primary objective of the Internal Dosimetry Section is to calculate maximum permissible concentration (MPC) values and dose estimates for human exposure, great emphasis is given to relevant human data where such data are available. At present, analysis of human tissue specimens is one of the main sources of these data. Autopsy samples of tissues and total bodies of individuals who were long-term residents of their communities prior to death and who were considered to be grossly normal provide a means of estimating the distribution of various chemical elements in the body that might result from chronic low-level exposure. The data from such samples provide some of the best evidence relating to chronic exposure to certain long-lived radionuclides and yield an estimate of the degree of variability of dose to be expected in a population chronically exposed.

The results of this program are presented under (1) "Tissue Analysis Laboratory," (2) "Inorganic Composition of Ashed Biological Materials," and (3) "Elemental Composition of Standard Man." These data may be used with other information for estimating internal exposure to radionuclides which are isotopes of the stable chemical elements measured in this study.

TISSUE ANALYSIS LABORATORY

Cyrus Feldman F. S. Jones

A chemical preconcentration plus flame photometry method[3] was adapted for the determination of cesium in samples of diets of teen-age children in several cities of the United States. The diets consisted of 21 complete meals plus snacks which were prepared by home economists in widely scattered locations at intervals during the first six months of 1962. All edible materials were composited and homogenized in a Waring Blendor.[4] These diet samples were obtained through the courtesy of Irving Michelson, Consumers Union.

A detailed statistical treatment has not been applied to the 44 samples which were analyzed for stable cesium, but the average is 0.45 μg per gram of food ash; 84% of the measurements lie between 0.20 and 0.60 μg of Cs per gram of food ash, with the extreme values being 0.14 and 2.2. As a check on the method, W. T. Mullins,[5] using neutron activation analysis on four samples, obtained an average of 0.49 μg of Cs per gram of food ash.

These and other similar samples were analyzed for rubidium without chemical separation, using flame photometry alone. Of the 71 samples, the mean value was 170 μg of Rb per gram of food ash, and the concentration ranged from 90 to 280.

These two sets of data will be expressed in terms of daily intake and compared with other published values.

INORGANIC COMPOSITION OF ASHED BIOLOGICAL MATERIALS

Peggy L. Stewart Isabel H. Tipton

Since the anionic as well as the cationic composition of a sample of ash influences the results

[1]Analytical Chemistry Division, ORNL.

[2]Physics Department, University of Tennessee.

[3]C. Feldman and T. C. Rains, *Anal. Chem.* **36**, 405 (1964).

[4]I. Michelson, *Health Phys.* **9**, 944 (1963).

[5]Analytical Chemistry Division, ORNL.

of spectrochemical analysis, standards must have as nearly as possible the same composition as the unknowns. Thus, it is important to know the total composition of ash. Residues resulting from the ashing technique used in analyzing diets and excreta from two individuals[6] were studied in detail for their anionic composition.

The purest obtainable inorganic compounds, oxides, carbonates, phosphates, and chlorides of the major inorganic constituents of diets and excreta and some representative trace elements, as well as a homogenized composite sample of food, were each ashed separately under identical conditions.

All trace and minor element determinations were made by emission spectroscopy. Quantitative curves derived from standards of similar composition afforded the basis of the metal analysis. Sodium and potassium were run on a flame photometer, calcium and magnesium were titrated with EDTA, while phosphorus was estimated by an emission semiquantitative method. Sulfates were precipitated with barium, carbonates were measured as the gas CO_2, and chlorides were analyzed by the titration of an acidified solution at the HgCl equivalence point.

[6]I. H. Tipton, P. L. Stewart, and P. G. Martin, "Trace Elements in Diets and Excreta," *Health Phys.* (in press).

Secondary method checks were made in these ways: Ca^{2+} by $KMnO_4$ titration and by precipitation as the oxalate; Mg^{2+} by emission; CO_3^{2-} by standardization of HCl to a pH of 3 and end point calibration with Na_2CO_3.

On the basis of data obtained from the ashing of inorganic compounds, it appeared that 91.6% of the ash at 450°C without sulfur could be accounted for as CaO (7%), NaCl (41%), KPO_3 (30.4%), and KCl (13.2%). The other 8.4% could be attributed to Mg (1.9%), CO_3^{2-} (2.3%), SO_4^{2-} (3.5%), trace elements (0.5%), and nitrates, silicates, etc. (0.2%).

The primary differences detected among the ashing procedures investigated are the conversion of chlorides to sulfates, the retention of Mg, Ca, and Na, and the loss of CO_3^{2-} and K in the sulfur methods, especially the 550°C ashing condition (Table 22.1).

Since most atoms of minor trace elements and some atoms of K and Na are bound to organic matter, which will decompose during the ashing process, it is important to identify the inorganic ion with which the metal will combine. The conversion of the metals to oxides in dry ashing and conversion to sulfates in the H_2SO_4 digestion are generally accepted as straightforward reactions. In the case of the sulfur addition ashing method at 550°C, however, the resulting anion cannot

Table 22.1. Results of Four Ashing Techniques Employed in the Analysis of a Food Sample

Values are given as percent of total ash as analyzed

Constituent Analyzed	450°C, No Addition	450°C, Sulfur Added	450°C, H_2SO_4 Added	550°C, Sulfur Added
Ca	4.90	4.50	4.20	7.20
Na	15.63	15.63	15.88	17.50
K	16.63	14.00	14.13	13.13
Mg	1.90	1.60	1.40	2.20
P	~8.00	~8.00	~8.00	~8.00
Cl^-	28.00	1.40	0.60	10.90
CO_3^{2-}	2.30	0.70	1.00	0.60
SO_4^{2-}	3.45	39.16	40.73	19.77
Total	80.81	84.99	85.94	79.30
Trace metals	~0.50	~0.50	~0.50	~0.50

Table 22.2. Ash Residue Analyses and Theoretical Compositions of Several Organometallic Compounds

Sample ashed at 550°C – sulfur added

Initial Material	Metal	Theoretical Composition			Experimental Composition			Probable Anion
		Metal Concentration (%)	Percent Ash if Entirely Metal Sulfate	Percent Sulfate in Metal Sulfate	Metal Concentration (%)	Percent Ash of Original Sample	Percent Sulfate in Ash	
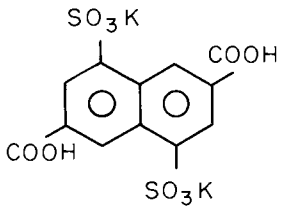	K	17.30%	38.54%		17.38%	39.72%	*a*	Sulfate
Sodium *p*-sulfophenyl-methallyl ether	Na	9.19%	28.29%	67.62%	8.96%	28.01%	67.41%	Sulfate
Aluminum stearate	Al	3.41%	21.6%	84.21%	*a*	21.50%	83.8%	Sulfate
Barium stearate	Ba	19.45%	33.2%	*a*	*a*	33.45%	*a*	Sulfate
Calcium stearate	Ca	6.6%	22.4%	70.59%	6.68%	22.67%	69.6%	Sulfate
Cadmium stearate	Cd	16.5%	30.7%	46.14%	*a*	26.58%	22.26%	Sulfate-sulfide mixture
Iron distearate	Fe	9.0%	32.85%[b]	72.0%	9.2%	14.70%	10.32%	Oxide-sulfate mixture
Lithium stearate	Li	2.4%	19.1%	87.3%	2.38%	19.35%	85.5%	Sulfate
Magnesium stearate	Mg	4.06%	20.7%	79.8%	4.10%	13.42%	51.3%	Sulfate-oxide mixture
Lead stearate	Pb	26.8%	39.1%	*a*	*a*	38.75%	*a*	Sulfate
Dibutyltin oxide[c]	Sn	47.73%	*d*	44.70%	*a*	59.68%	0.48%	Oxide
Dibutyltin oxide[e]	Sn	47.73%	*d*	44.70%	*a*	61.85%	0.75%	Oxide
Zinc dibutyldithio-carbamate	Zn	13.79%	34.05%	59.5%	*a*	18.25%	0.90%	Oxide-sulfide mixture

[a]Not determined.
[b]As Fe_2O_3 = 12.8%.
[c]Sulfur addition ashing method.
[d]As SnO_2 = 60.62%.
[e]H_2SO_4 digestion.

be predicted unequivocally and must be investigated experimentally.

Organometallic compounds of selected elements were ashed at 550°C in the presence of sulfur. Initial materials, experimental data, theoretical compositions, and conclusions are given in Table 22.2. Whenever it was possible, the ash residue was analyzed for metal and sulfate content.

For K, Na, Li, Ba, Pb, Ca, and Al, the anion was found to be the sulfate.

Tin, as dibutyltin oxide, was ashed by both the sulfur addition and H_2SO_4 digestion techniques. The results obtained in both instances confirm the following reaction: $SnSO_4 \xrightarrow{360°C} SnO_2 + SO_2\uparrow$. It may thus be concluded that tin is present as SnO_2 in the ash residues.

The case of cadmium is not straightforward. The theoretical ash content as $CdSO_4$ should be 30.7%; the actual ash content is 26.58%. In addition, the sulfate content of the ash is 22.26%, not 46.14% as it would be if the ash were $CdSO_4$. Two additional observations were made concerning the ash residue; (1) it was yellow and (2) the distinct odor of H_2S was observed when acid was added to the residue. Since $CdSO_4$ is white and CdS is yellow, the evidence indicates the presence of CdS as well as $CdSO_4$ in the ash residue. If one assumes only $CdSO_4$ and CdS to be present in the ash residue, the 26.58% ash residue would require 17.67% Cd in the starting material (theoretical Cd = 16.5%). Based on the data available, it may thus be concluded that the cadmium is present in the ash as a sulfate-sulfide mixture.

An ash content of 13.42% was obtained from magnesium stearate. This is again considerably lower than the 20.7% which would result if the ash were 100% $MgSO_4$. Actually, the ash was found to be 64.1% $MgSO_4$. If the remainder of the ash were assumed to be MgO, this would account for 91% of the ash. Some difficulty was experienced in the sulfate determination with this ash residue. Since sulfate represents 80% of $MgSO_4$, an error of 2% in the sulfate value would bring this material balance near the actual ash content. Based on the excellent agreement between the theoretical (4.06%) and the experimental (4.10%) magnesium content, it may be concluded that the anion assignment of a mixture of sulfate and oxide is correct. It should be noted that when magnesium stearate was ashed by the H_2SO_4 digestion, an ash content of 20.38% was obtained (theoretical $MgSO_4$ = 20.7%).

Iron presents a special case. Theoretically, the ashing reaction should be governed by the following consideration: ferric sulfate decomposes at temperature >480°C. Since the ashing is carried out at a temperature of 550°C, ferric sulfate is not expected to be present in the ash residue. The iron content of the test sample (iron distearate) is 9.0%. This would yield an ash content of 32.85% expressed as $Fe_2(SO_4)_3$ or an ash content of 12.8% expressed as Fe_2O_3. The experimental ash content was found to be 14.7%. In addition, the ash was found to contain 10.2% sulfate. Based on these results, the iron balance was calculated to be 15% $Fe_2(SO_4)_3$ and 85% Fe_2O_3. This gave a theoretical value for iron content of 9.0%, which agreed with the observed value of 9.2%.

It can be concluded that the anion in the iron ash residue is a mixture of sulfate and oxide. This also indicates that the decomposition of $Fe_2(SO_4)_3$ is about 85% complete at 550°C.

The most surprising case encountered was that of zinc. When zinc dibutyldithiocarbamate was ashed, the ash content was found to be 18.25%. If it were $ZnSO_4$, an ash content of 34.05% would have resulted. As in the case of cadmium, the ash residue was yellow and the distinct odor of H_2S resulted when acid was added to the ash residue. Both zinc oxide and zinc sulfate are white. There does exist, however, a compound of zinc (the oxysulfide, ZnO·ZnS) which is yellow. If one assumes 0.51% $ZnSO_4$ in the ash and the remainder as ZnO·ZnS, this will account for 13.2% Zn in the original sample, the theoretical zinc content of which is 13.8%.

The results of this study show the sulfate to be the predominant anion, but some oxides and sulfides will also be present.

ELEMENTAL COMPOSITION OF STANDARD MAN

Isabel H. Tipton W. S. Snyder
Mary Jane Cook

In most cases the radioactive form of an element will be metabolized in the same way as the stable form of an element; therefore, much time has been devoted to the study of the elemental composition of many human organs and tissues. From these

The table below should be inserted in the section "Elemental Composition of Standard Man," page 240 of the subject report.

Elemental Composition of Total Body of Standard Man

Element	Symbol	Percent by Weight	Amount in 70-kg Man (g)
Oxygen	O	60	42,000
Carbon	C	24	16,700
Hydrogen	H	10	7,000
Nitrogen	N	2.9	2,000
Calcium	Ca	1.2	880
Phosphorus	P	1.1	800
Sulfur	S	0.24	170
Potassium	K	0.20	140
Sodium	Na	0.20	140
Chlorine	Cl	0.20	140
Magnesium	Mg	0.03	20
Iron	Fe	0.007	4.7
Zinc	Zn	0.003	2.2
Rubidium	Rb	5×10^{-4}	0.33
Strontium	Sr	4×10^{-4}	0.28
Lead	Pb	1.7×10^{-4}	0.12
Copper	Cu	1.3×10^{-4}	0.09
Aluminum	Al	1×10^{-4}	0.07
Barium	Ba	7×10^{-5}	0.05
Cadmium	Cd	7×10^{-5}	0.05
Iodine	I	5×10^{-5}	0.036
Bromine	Br	4×10^{-5}	0.027
Titanium	Ti	4×10^{-5}	0.027
Manganese	Mn	4×10^{-5}	0.026
Tin	Sn	3×10^{-5}	0.02
Boron	B	$<3 \times 10^{-5}$	<0.02
Nickel	Ni	2×10^{-5}	0.014
Chromium	Cr	2×10^{-5}	0.014
Molybdenum	Mo	1.7×10^{-5}	0.012
Gold	Au	$<1.4 \times 10^{-5}$	<0.010
Cobalt	Co	2×10^{-6}	0.0017
Silver	Ag	2×10^{-6}	0.0013
Cesium	Cs	1.4×10^{-6}	0.001
Vanadium	V	$<1.4 \times 10^{-6}$	<0.001
Bismuth	Bi	$<1.4 \times 10^{-6}$	<0.001
Uranium	U	3×10^{-8}	2×10^{-5}
Beryllium	Be	1.3×10^{-9}	9×10^{-6}
Radium	Ra	4×10^{-14}	3×10^{-11}

data one may determine the principal organ of deposition for many radionuclides occurring in chemical forms similar to those encountered in the diet and in the environment.

In calculating maximum permissible concentration (MPC) and q (maximum permissible burden in total body) values, one often needs to know the values of f_2, which is the fraction of an element in the organ of the amount in the total body. Because no total bodies have been analyzed for trace elements, the amount in the total body must be determined as the sum of the quantities in each organ and tissue. Although information on all tissues and organs was not available for every element, values were found for the amounts of most of the commonly occurring elements in at least 90% of the total body, and a good estimation of the amount in the balance could be made, depending on the nature of the tissues or organs in which the amounts were unknown. If the concentration was approximately the same in all tissues for which information was available, that is, "known" tissues, the concentration in those tissues for which no information was available, that is, "unknown" tissues, was assumed to be the same as for the known. If the concentration of an element in one or more tissues was much higher than the average of the other known tissues, the concentration in the unknowns was assumed to have this average value. For example, calcium and radium have exceptionally high concentrations in bone, so in calculating the quantity of calcium and radium in the total body, the unknown tissues, being for the most part soft tissues, were assumed to have the average concentration of the known soft tissues.

The amounts of the major elements, O, C, H, N, were calculated on the basis of the composition of the constituents of tissue, water, protein, fat, and carbohydrate. The values for the elements Ca, P, K, Mg, Fe, Zn, Sr, Pb, Cu, Al, Ba, Cd, Ti, Mn, Sn, B, Ni, Cr, Mo, Au, Co, Ag, V, and Bi came, for the most part, from spectrographic analyses of tissues from 150 adults from the United States. The "less than" sign in the table indicates that the element was observed in fewer than half of the samples analyzed. The values for S, Na, Cl, Rb, I, Br, Cs, V, Be, and Ra were taken from many different sources. For a complete bibliography the reader is referred to unpublished data, "Elemental Composition of Standard Man," I. H. Tipton (March 1966).

Part VI. Health Physics Technology

B. R. Fish

23. Aerosol Physics

B. R. Fish

R. H. Boyett
T. G. Clark
G. W. Royster, Jr.
F. G. Karioris[1]
J. L. Thompson
R. L. Walker
W. H. Wilkie, Jr.
C. F. Parrish[2]

ADHESION OF SOLID PARTICLES TO SOLID SURFACES

B. R. Fish
R. L. Walker
T. D. Calton[3]
F. G. Karioris[1]
C. F. Parrish[2]

The accidental resuspension of radioactive particles from surfaces in the working environment depends upon the forces of adhesion existing between the particles and the surface as well as the forces available for resuspension. Deliberate resuspension, as in decontamination, also depends upon the adhesion and resuspension force balance. Similarly, retention of deposited particles in sampling and air-cleaning devices is controlled by the same mechanisms that determine the probability of resuspension. Efforts to predict and to control particle retention require knowledge of the basic forces affecting deposition, adhesion, and removal.

There are four principal mechanisms for adhesion of particles to surfaces – capillary, electrostatic, and molecular forces, and a time-dependent viscous-flow resistance to particle removal. Preliminary studies reported earlier[4,5] have indicated that capillary and electrostatic forces predominate in many cases; consequently, we have examined these mechanisms in more detail.

Capillary Force

Surfaces exposed to moist air are continually being bombarded by water molecules, which impinge on the surface at a rate depending upon the partial pressure of water vapor in the local environment and the ambient temperature. The return of water molecules to the gas phase depends upon local physical-chemical interactions, which determine the vapor pressure over the surface of the given deposit of water. If we consider the region of contact between a sphere of radius r and a plane surface, assuming both are wetted by water, it is seen that this region constitutes a capillary and that any water accumulating in the capillary will have a curved surface. From the Gibbs-Thomson relation (Kelvin equation) it is possible to predict that a water surface having a constant total curvature a will be in equilibrium with an ambient partial pressure p according to:

$$a = \frac{\gamma M}{\rho R T \ln (p/p_\infty)} ,$$

where

γ = free surface energy of the liquid (surface tension),

[1]Temporary summer employee, Marquette University, Milwaukee, Wis.

[2]Research participant, Indiana State College, Terre Haute.

[3]Mathematics Division.

[4]B. R. Fish *et al.*, *Health Phys. Div. Ann. Progr. Rept. July 31, 1965*, ORNL-3849, p. 220.

[5]R. L. Walker and B. R. Fish, *Adhesion of Particles to Surfaces in Liquid and Gaseous Environments*, Proc. 4th Ann. Tech. Mtg. and Exhibit, AACC, Miami, Fla., May 25–28, 1965; and ORNL-TM-1209 (Aug. 2, 1965).

M = molecular weight of the liquid,

ρ = liquid density,

R = the gas constant,

T = absolute temperature,

p_∞ = saturation vapor pressure for local conditions.

For conditions under which $p < p_\infty$, that is, less than 100% relative humidity (% R.H. $= 100 \times p/p_\infty$), the curvature is negative. The surface of revolution having a constant negative total curvature is a nodoid,[6] Fig. 23.1. The requirement that all forces be in balance makes it possible to calculate the parameters of the capillary layer in equilibrium with a given relative humidity. Thus, it is possible to calculate the normal component of force holding the particle to the surface for various conditions of temperature and relative humidity.

Furthermore, molecular kinetic considerations suggest that the growth of the capillary layer, hence the normal force, should require a finite time to reach equilibrium. Thus, an aging effect is predicted in which the adhesive force is expected to increase with time and approach a maximum value.

Experimental observations of the number of 45-μ-diam glass beads remaining on a glass surface after application of a fixed removal force are shown in Fig. 23.2. It is seen that the number of particles requiring more than 5000 times the force of gravity for removal increases approximately as an exponential function of time. The half-time, T,

[6]A. G. Greenhill, *Applications of Elliptic Functions*, Dover, New York, 1959.

ORNL-DWG 66-8889

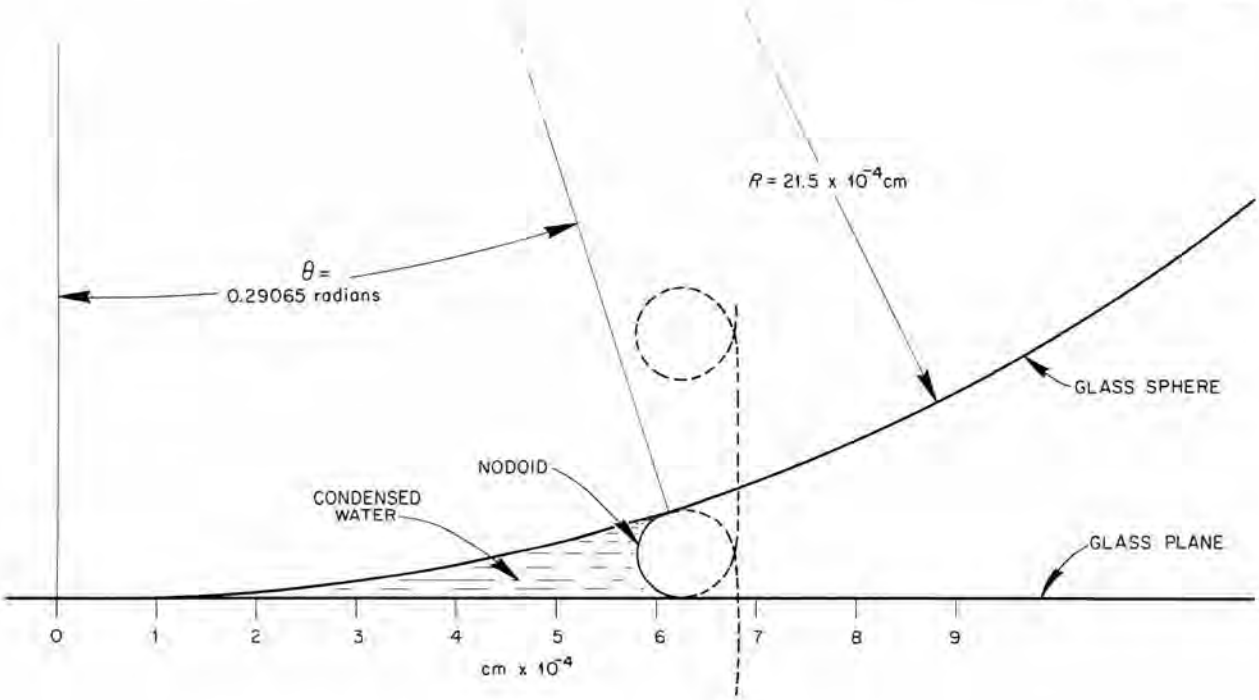

EQUILIBRIUM CAPILLARY
SPHERE-TO-PLANE GEOMETRY

Fig. 23.1. Equilibrium Capillary Layer Calculated for a Relative Humidity of 99.9% (Table 23.1).

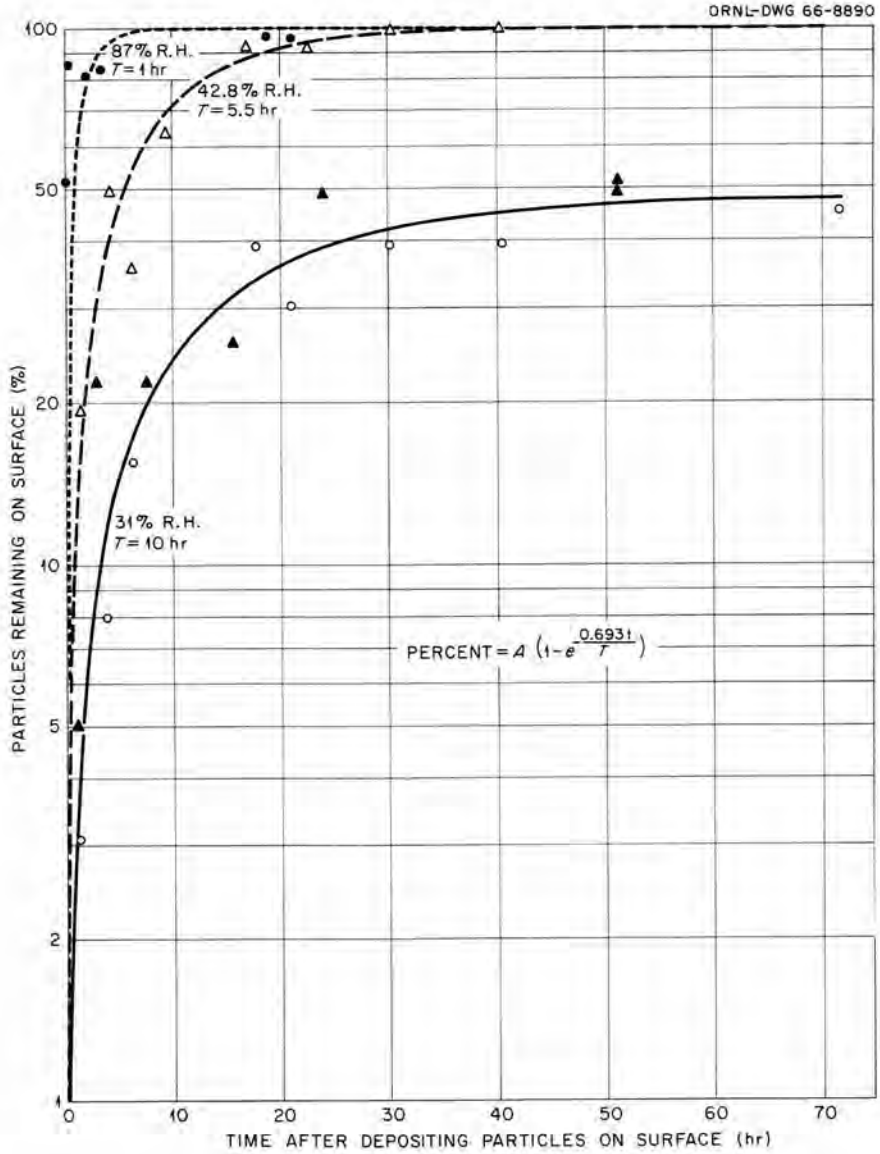

Fig. 23.2. Retention of Glass Spheres (45 μ diam) on a Glass Surface After Application of 5000 g – Effect of Relative Humidity and Aging.

increases as the relative humidity decreases. The observed effects of relative humidity and of aging are in qualitative agreement with predictions based on the capillary model. However, the observed maximum force required to remove all particles as a function of relative humidity does not agree with quantitative estimates of force based on the simple model, Table 23.1.

To date, no clearly successful test of the Gibbs-Thomson relation has been performed for microscopic capillaries. On the contrary, work of Shereshevsky[7,8] over the past 30 years seems to indicate that the condensation of a polar liquid in a microscopic conical capillary yields somewhat erratic results, but frequently the amount is much more than would be predicted based on the Gibbs-Thomson equation. A possible explanation is that,

[7]J. L. Shereshefsky, *J. Am. Chem. Soc.* **50**, 2966 (1928).

[8]M. Folman and J. L. Shereshefsky, *J. Phys. Chem.* **59**, 607 (1955).

Table 23.1. Comparison of Observed Maximum Sphere-to-Plane Adhesive Forces with Calculations Based on a Simple Capillary Condensation Model

Measurements were made using 45-μ-diam soda-lime glass spheres on a soda-lime glass plane. For calculations the free surface energies were assumed to be $\gamma_{lg} = 72$ (ergs/cm^2), $\gamma_{ls} = 230$ (ergs/cm^2), and $\gamma_{sg} = 300$ (ergs/cm^2)

Relative Humidity (%)	Theory		Experiment
	Calculated θ (deg)	Calculated Maximum Force (dynes)	Observed Maximum Force (dynes)
31	0.37	0.00017	1.08
43	0.44	0.00023	1.93
58	0.55	0.00037	2.05
87	1.10	0.0015	3.03
99.9	16.62	0.33	
100	90	4.05	3.23 (±0.71)

due to the proximity of much of the capillary volume to solid walls, a long-range orientation may be imposed on the molecules of the liquid, thereby lowering the effective vapor pressure over the liquid surface. A further test of this hypothesis may be possible by solving the equations required to determine the nodoids consistent with the observed forces and then calculate the saturation vapor pressures required to produce the associated total curvatures.

Electrical Force

Although the importance of electrical forces in adhesion of particles has been recognized,[9,10] the various references to electrical effects are rather vague and do not discuss the physical mechanisms involved. Despite clear indications of the significance of these forces, no systematic effort to study electrical effects in adhesion has been reported.

Of the several physical processes of adhesion, the only case in which the force is operative over an appreciable distance is that of electrical force. Thus, depending on the surface charge and the charge on the particle, deposition may be induced on preferred locations where adhesion is enhanced (bound, or persistent charges) or reduced (conductive particle on a charged, conductive surface). Various other electrostatic processes, for example, image charge induction and contact potential charging, always lead to attractive forces which add to the adhesive force.

The only one of these cases that consistently leads to a net electrostatic repulsion is that of a conductive particle on a charged conductive surface. Because of the possibility that this repulsive mechanism might contribute significantly to resuspension or that it might be utilized in decontamination, it is being studied in some detail.

From elementary electrostatics it can be shown that the force of repulsion on a unit area of a charged conductor is given by

$$F_e = 5.65 \times 10^{15} \frac{\sigma^2}{k} \text{ dynes/cm}^2 ,$$

where σ is the surface charge density (coulombs/cm^2) and k is the dielectric constant of the surrounding medium. This may be applied to the case of a flat conductive flake (or a flat conductive agglomerate approximating a flake) on a charged conductive surface. It is instructive to compare the electrical force with the gravitation

[9] B. V. Deryagin and A. D. Zimon, *Kolloidn. Zh.* **23**, 454 (1961) (translated by Consultants Bureau, Chicago, Ill.).

[10] M. Corn and F. Stein, *Am. Ind. Hyg. Assoc. J.* **26**, 325 (1965).

force, for a flake of thickness t (cm) and density ρ (g/cm^3); thus

$$G = \frac{F_e}{mg} = 5.77 \times 10^{12} \frac{\sigma^2}{kt\rho} .$$

In dry air the maximum charge density that can be maintained on a flat surface is usually assumed to be approximately 2.7×10^{-9} coulomb/cm^2; hence the thickest unit-density flake for which the electrical force is as great as the gravitational force is 0.4 μ thick (of arbitrary shape in the other two dimensions). Under ordinary environmental conditions (moist air, etc.) the maximum attainable surface charge density is commonly taken to be about half of the above figure or less; however, for flakes consisting of agglomerated small particles the density may be considerably less than 1. Consequently, this effect may be significant for thin agglomerates but not for unit-density solid flakes in excess of about 0.2 μ thick.

The case of a conductive spherical particle resting on a charged conductive surface is not readily soluble in closed form and was treated experimentally to provide an estimate of the electrical force. The simple apparatus used in this study included a parallel-plate capacitor with gold-plated electrodes immersed horizontally in a viscous silicone oil (η = 9.35 poises; dielectric constant k = 2.74). A constant dc voltage was applied across the capacitor, and the movement of small gold spheres up and down between the plates was photographed using a microscope and a pulsed light source.

Several anomalies were seen to occur in connection with the negative electrode, including inconstant contact times, erratic deceleration of the sphere on approaching the negative electrode, and nonreproducible velocities after contact. These results, along with the observed behavior of extraneous debris in the apparatus, suggest a variable interference of contact because of a layer of debris adhering to the negative plate. Contact with the positive plate was quite reproducible; the observed velocities of a 50- and a 110-μ-diam gold sphere after contacting the positive (lower) electrode are shown in Fig. 23.3 as a function of the square of the field strength. The observed upward velocities are fitted adequately by the expression

$$v = 4.29 \times 10^{-6} r^{1.46} E^2 - v_g ,$$

where

r = radius of the sphere (cm),

E = electrical field intensity (v/cm),

v_g = Stokes settling velocity (cm/sec).

By defining the velocity due to the electrical force as $v_e = v + v_g$ and applying the Stokes

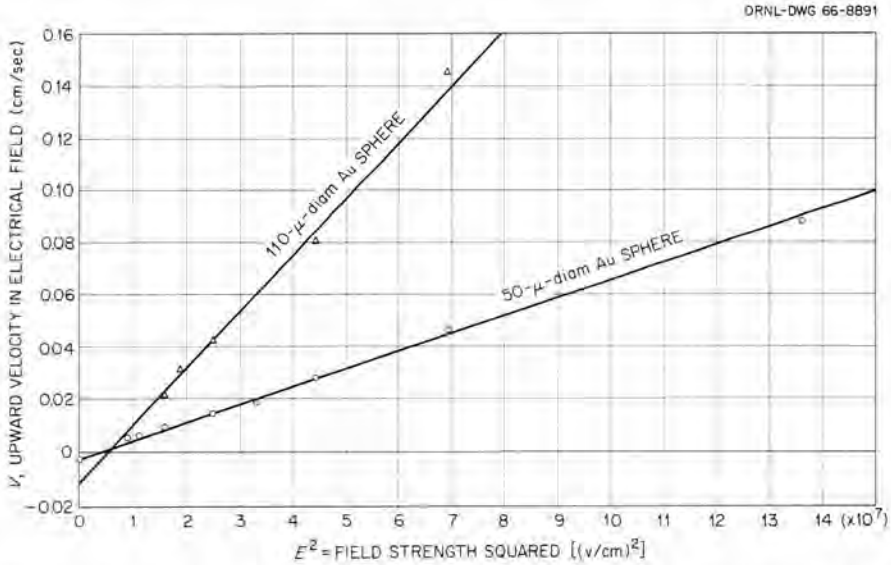

Fig. 23.3. Upward Velocity of a Conductive Sphere After Contacting a Charged Surface (in Silicone Oil – η = 9.35 poises).

equation for viscous resistance to movement of the sphere (note: Reynolds number <0.001 in every case), it is seen that the electrical force is

$$F_e = 8.85 \times 10^{-5} \pi k r^{2.46} E^2 \text{ dynes,}$$

or in terms of the surface charge density,

$$F_e = 3.55 \times 10^{18} \frac{\sigma^2}{k} r^{2.46} \text{ dynes} .$$

Again, as in the case for the flat flake, the G factor is defined as

$$G = \frac{F_e}{mg} = 8.65 \times 10^{14} \frac{\sigma^2}{k r^{0.54} \rho} .$$

Assuming that this empirical relation holds also for smaller spheres, the largest unit-density sphere for which this electrical force just equals the gravitational force in dry air is 1.7 μ in diameter. However, the radius varies approximately as the fourth power of the surface charge density; thus under ordinary environmental conditions the largest such unit-density sphere probably does not exceed about 0.13 μ diameter, comparable with the thickness of a unit-density flake for which the maximum electrical force just balances the gravitational force.

Additional work is being done to confirm these estimates for spheres, flakes, and agglomerates. Pending more complete data, it may be concluded tentatively that particles, flakes, and flat agglomerates of thickness not exceeding about 0.2 μ on a charged conductive surface will not be resuspended as a result of local electrical forces alone except under optimum conditions. However, these forces should not be ignored, since they can amount to as much as 10% of the gravitational force for 9-μ-diam unit-density spheres and for 2-μ-thick flakes. For optimum conditions this would be 120-μ-diam spheres and 4-μ-thick flakes.

SURVEY OF ADVENTITIOUS ELECTRICAL FIELDS IN THE WORKING ENVIRONMENT

R. L. Walker J. L. Thompson
B. R. Fish

The only long-range mechanism by which airborne particles are attracted to surfaces is the interaction of the particles with an electrostatic field. This force, given by Coulomb's law, is

$$F = \frac{qq'}{4\pi\epsilon_0^2} .$$

A preliminary survey of two hot-cell facilities has been conducted to determine the existence and the magnitude of electrical fields related to charged

Table 23.2. Observations of Charged Surfaces in Two Hot-Cell Facilities

	Surface Charge Density[a] (coulombs/cm^2)		Remarks
	Average	Maximum	
Hot-cell window, Facility A	1.78×10^{-11}	2.84×10^{-11}	All cell windows charged
Hot-cell window, Facility B	5.27×10^{-12}	6.56×10^{-12}	All cell windows charged
Glass windows in partitions and doors	2.73×10^{-11}	4.37×10^{-11}	50% charged
Strip-chart recorder windows, glass	9.95×10^{-12}	2.84×10^{-11}	All windows charged
Strip-chart recorder windows, Plexiglas	3.06×10^{-11}	4.81×10^{-11}	All windows charged
Floor tile (vinyl asbestos)	5.13×10^{-12}	6.56×10^{-12}	100% charged
Sponge rubber floor mats	2.48×10^{-11}	3.28×10^{-11}	100% charged

[a]Measurements made with a Keithly model 250 static meter employing a capacitor-divider network.

surfaces. Charged areas have been found ranging up to 4.8×10^{-11} coulomb/cm^2. The highest charges were found on cell windows, door and partition glass, chart recorder windows, and sponge rubber floor mats, Table 23.2. All the observed charges are negative.

Assuming that a hot-cell window represents a uniformly charged disk 1 m in diameter and has a surface charge density of 4.8×10^{-11} coulomb/cm^2 and assuming that most airborne particles bear a charge proportional to their radii in centimeters [$q \approx 3.2 \times 10^{-14}$r coulombs, based on work of J. M. Dalla Valle, C. Orr, and B. L. Hinkle, *Brit. J. Appl. Phys.* **5**, suppl. 3, S198 (1954)], it is seen that the electrical force on unit-density particles is equal to or greater than the gravitational force for $\leqq 0.5$-μ-diam particles within 2 m of the surface, $\leqq 0.9$-μ particles within 1 m of the surface, and approximately $\leqq 3$-μ particles within 10 cm of the surface. Thus, it is seen that electrical fields do exist in some areas of the working environment and that their intensity is sufficient to affect the site of deposition of airborne particles.

STUDIES OF SURFACE CONTAMINATION

G. W. Royster, Jr. B. R. Fish

In carrying out an area monitoring program the health physicist familiarizes himself with existing and potential radiation fields and the conditions under which they occur in order to advise the user of the local facility on methods to minimize unnecessary radiation exposure in his work. As an aid to the exercise of professional judgment in such matters, there are tabular summaries suggesting maximum permissible radiation exposures for various categories of workers and for various periods of time. Similarly, information is available to help judge the relative seriousness of a given airborne concentration of a radionuclide. However, no comparable body of recommendations exists with regard to the significance of radioactive surface contamination. Despite the economic and operational importance of controlling radioactive contamination, there remain wide areas of disagreement on contamination control criteria and practices. There are several reasons for this disparity, but the fundamental problem is the lack of an adequate technical basis for understanding the behavior of radioactive contamination in the working environment. The ORNL aerosol physics group has directed its major emphasis to providing a body of data which the health physicist may use in interpreting professionally the measurements and meanings of radioactive surface contamination.

In previous reports[11–15] we have discussed various techniques for monitoring "removable" surface contamination, their areas of application, and some of their deficiencies. Because of its long history of use, much attention has been given to the wipe test (smear test). While the wipe test can provide useful information in regard to changing levels of contamination and to the probability of contaminating skin, wounds, and clothing, it is *not* in general related to the likelihood of internal exposure via resuspension and subsequent inhalation. A resuspension test (smair test) has been developed which is positively correlated with the probability of inhaling particles resuspended from environmental surfaces. Although correlations between these two types of measurements may be obtained for a given set of conditions, one should not expect consistent agreement between the wipe and the resuspension tests, inasmuch as they are intended to measure two different modes of transferring contaminants from surfaces. Both measurement techniques can provide useful information to the health physicist for evaluating the resuspension and the cross-contamination potentialities of a given situation involving radioactive surface contamination.

Resuspension studies, performed in a large, room-size, test chamber, provide a means of comparing the inhalation probability per unit time for various types of contaminants under selected environmental conditions. Data obtained in this study can be used along with tabulated maximum permissible concentrations $(MPC)_a$ for radionuclides in air[16] to provide an estimate for the

---

[11] B. R. Fish *et al.*, *Health Phys. Div. Ann. Progr. Rept. July 31, 1962*, ORNL-3347, p. 142.

[12] G. W. Royster, Jr., *Health Phys. Div. Ann. Progr. Rept. June 30, 1963*, ORNL-3492, pp. 185–87.

[13] G. W. Royster, Jr., *Health Phys. Div. Ann. Progr. Rept. July 31, 1964*, ORNL-3697, pp. 215–16.

[14] G. W. Royster, Jr., and B. R. Fish, *Health Phys. Div. Ann. Progr. Rept. July 31, 1965*, ORNL-3849, pp. 217–18.

[15] G. W. Royster, Jr., and B. R. Fish, *Techniques for Assessing "Removable" Surface Contamination*, ORNL-TM-1045 (Feb. 4, 1965).

[16] *Report of Committee II on Permissible Dose for Internal Radiation*, ICRP publication 2, Pergamon, New York, 1959.

level of freshly deposited dust which may result in resuspension equal to the MPC. The values listed in Table 23.1 are the factors which must be multiplied by the $(MPC)_a$, $\mu c/cm^3$, to obtain the related surface contamination level, dis/min per 100 cm^2. It is seen that for a rather wide range of ordinary surface conditions the factor $1.72 \times 10^{13} \times (MPC)_a$ yields a reasonably low variation. However, it is clear that vigorous activity may lower this (i.e., increase resuspension) by as much as a factor of 60 or more, and deliberate attempts to reduce resuspension may increase this index by a factor of more than 1000. These studies show that the wide range of resuspension factors reported by various authors[17] may occur and can, in fact, occur in consequence of differences in surface conditions alone.

In addition to the variation in resuspension related to the condition of the surface, other factors also can be of importance. Both laboratory-scale and resuspension-room studies have shown the importance of particle size in regard to resuspension. Figure 23.4 shows the particle-size distribution in the resuspension room (asphalt tile floor) during dispersion and after sweeping the floor. As has been shown previously[18] a larger fraction of the particles above 2 μ in diameter were redispersed than of the smaller particles. In Fig. 23.5 is shown the total particle distribution in the room during the dispersion and redispersion periods. It is seen that after the particles settled for 26 hr and the air concentration in the room returned to the background level, sweeping in the room for 5 min raised the air concentration to about one-half the peak concentration reached during the initial dispersion period.

It should be clear that the multiplicative factors listed in Table 23.3 apply only to particles having properties, including size distribution, similar to the ones used in this study. Thus, attempts to derive a universal "permissible" contamination level are likely to be unfruitful. A more promising approach is the definition of a standard sampling technique that can be correlated with resuspension

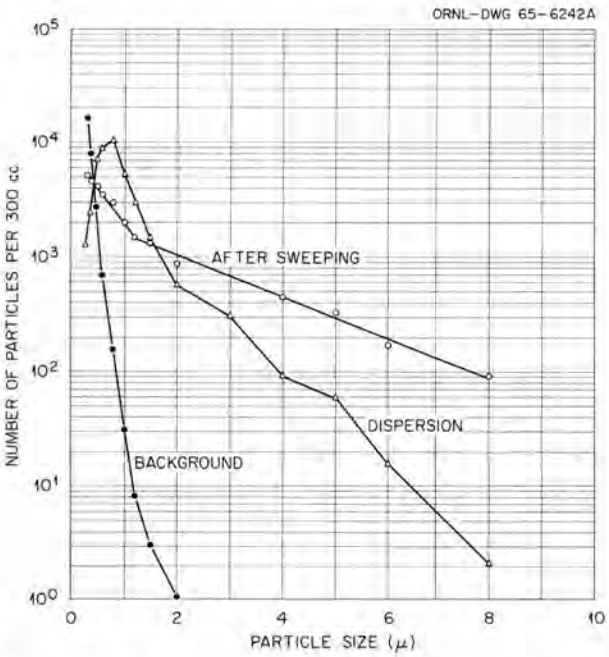

Fig. 23.4. Particle Size Distribution of CuO Dust.

probability independent of surface and particle properties. The smair, resuspension, sampler is being tested to determine to what extent it may be adapted for this purpose. As an example of the results obtained using the smair sampler, the average factor relating the smair sample test results to the $(MPC)_a$ was $K = 0.334 \times 10^{13}$ (±60%) for all the surface conditions studied [i.e., $0.334 \times 10^{13} \times (MPC)_a$ = smair sample dis/min], including the oiled surface.

While the major emphasis has been placed on resuspension of settled dusts, some work has been done on surface contamination resulting from solution spills. In the case of liquid spills there is the possibility of chemical reaction with the surface, penetration into the surface, or evaporation of the liquid leaving a film on the surface. This latter case has been investigated by spraying a solution of cupric nitrate in ethyl alcohol onto a stainless steel surface and allowing the alcohol to evaporate. The resulting deposit of cupric nitrate is extremely adherent and could not be removed by air impingement. The wiping action of the smear test, however, removed 80% of the deposit. Examination of the deposit under a microscope showed the copper crystals to be very

[17] G. W. Royster, Jr., and B. R. Fish, *Redispersion of Surface Dust in a Room*, 4th National Tech. Meeting, American Association for Contamination Control, May 25–28, 1965, Miami, Fla., and A. C. Chamberlain and G. R. Stansbury, AERE HP/R737.

[18] G. W. Royster, Jr., and B. R. Fish, *Health Phys.* 11, 835 (1965) (abstract).

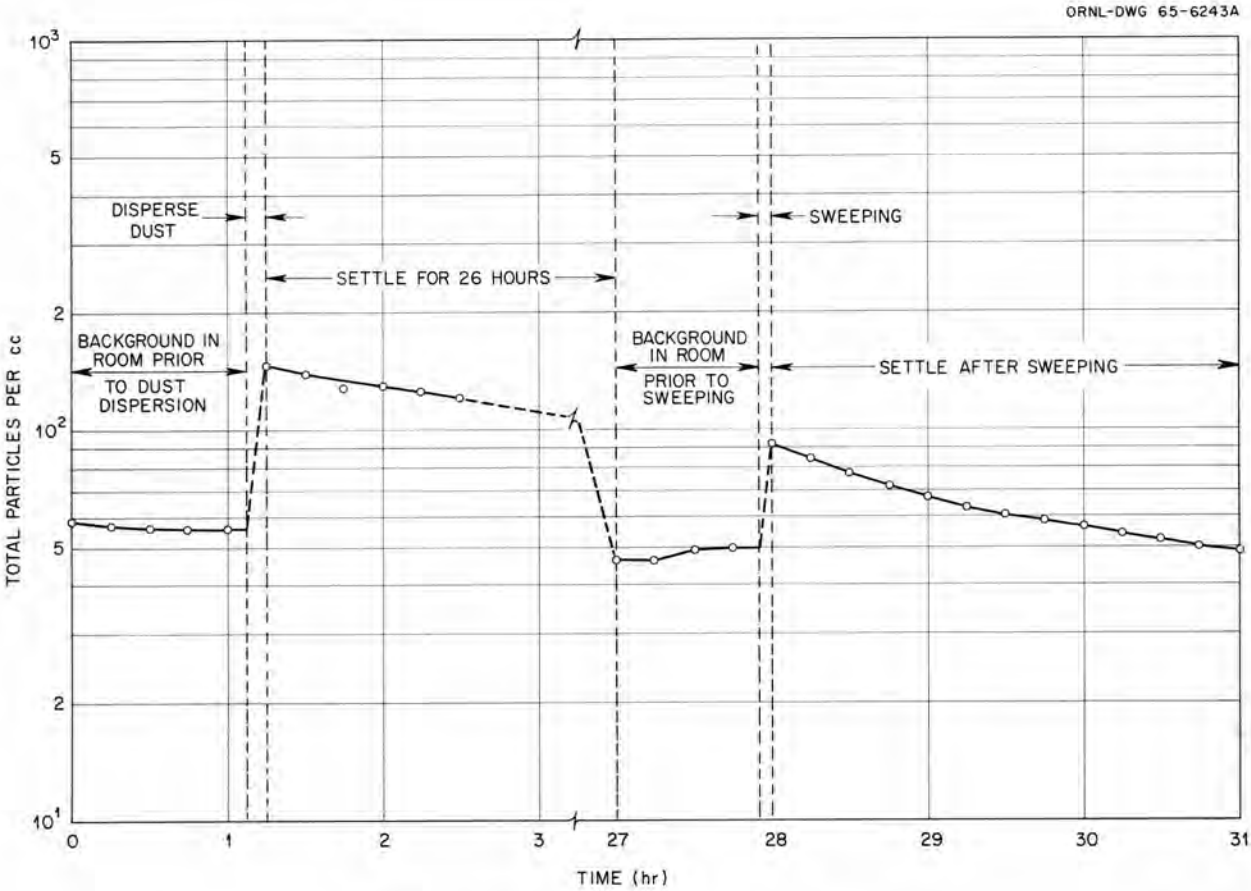

Fig. 23.5. Dispersion of CuO Dust in a Room.

Table 23.3. Resuspension Multiplication Factor, K, to Provide an Estimate of Surface Contamination Level (dis/min per 100 cm^2) Likely to Produce $(MPC)_a$

$$\mu c/cm^3 = K \times (MPC)_a$$

Floor Conditions	K, Moderate Activity	K, Sweeping
Waxed floor tile		
Very clean	0.99×10^{13}	1.52×10^{12}
Very clean	0.57×10^{13}	1.07×10^{12}
Average clean	1.85×10^{13}	2.13×10^{12}
Dirty (gummy)	3.47×10^{13}	
Dirty (dry dust)	1.32×10^{13}	2.67×10^{11}
Concrete (clean, unsealed)	2.13×10^{13}	4.48×10^{11}
Average of above	1.72×10^{13} (±55%)	1.09×10^{12}
Oiled floor tile	$>1.85 \times 10^{16}$	$>1.85 \times 10^{15}$

moist, which condition is dominated by capillary and viscous forces of adhesion which significantly reduce the potential for resuspension by aerodynamic forces. It is planned to test other solutions which do not yield hygroscopic evaporates and to observe the resuspension of the deposits from surfaces by the action of air currents.

ENVIRONMENTAL STUDIES

T. G. Clark B. R. Fish
J. L. Thompson

A complete analysis of the hazards arising from the accidental fragmentation of nuclear reactors or isotopic power sources requires a knowledge of the deposition and adhesion of radioactive debris on the skin. In addition to information on radiobiological effects and on the dosimetry of small particles, some estimate of source-skin contact probability is needed. A study has been initiated to determine the degree of initial retention on the arm of particles falling vertically in a uniform fallout field.

Figure 23.6 shows the device designed and constructed to give such a distribution pattern. The closed copper chamber is cylindrical, measuring 6.5 cm in diameter and 4.5 cm high with two 1-cm ports. Perforations in the base plate are made with a No. 52 twist drill (0.0635 in. diameter) and are in a hexagonal array with 1-cm spacing. A double-faced sticky tape is applied to this plate, small holes are punched in the tape at the 36 orifices, and Eaton-Dikeman No. 953 sharkskin filter paper is placed over the tape. Suction is applied to the top port, providing an air flow of 66 lin ft/min. This assures a face velocity sufficient to retain a wax particle up to 500 μ in diameter at each orifice.

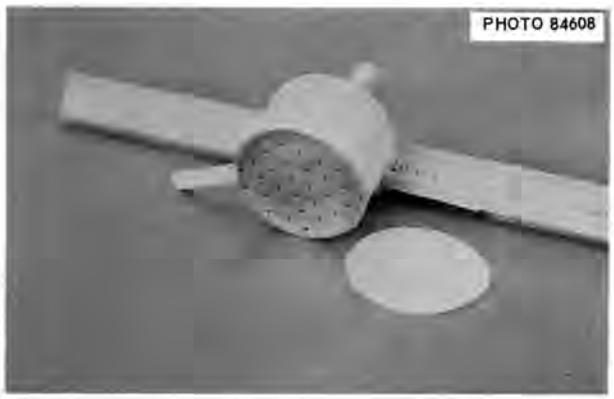

Fig. 23.6. Particle Dispersion Device.

After loading, the chamber is positioned above the forearm with the aid of small plumb bobs in a draft-free area. The particles are released by simultaneously interrupting the vacuum, instituting a momentary backflow in the side port, and mechanically vibrating the chamber. Particle deposition is observed to be uniform for a drop of several centimeters under normal room conditions.

In the experiments the device is held at a height that will assure that the particles have attained their terminal velocity before impaction on the arm. For unit-density particles of 150 μ diameter, this is on the order of a few centimeters.

Preliminary results show that initial deposition is proportional to particle size and skin surface moisture. In the size range of 297 to 500 μ from 6.2 to 44% of the particles impacting on arms of average dryness were retained long enough to observe them ($\gtrsim$1 min). In one trial, sweating was induced before exposure by enclosing the arm in a polyethylene envelope. Under these conditions, simulating natural occurrence of perspiration, retention values approached 100% for 104 to 125 μ spheres. Only 55% were retained by this individual under normal conditions using this size particle.

Hazards arising from the deposition of micron-size radioactive particles on the skin are proportional to the residence time of these sources. Efforts are continuing to determine the variation of this time as a function of particle size and density. Earlier studies showed an inverse relationship between particle diameter and retention time. These data are shown in Fig. 23.7, where the vertical lines are standard deviations of the retention time and the horizontal lines indicate the size range of the particles used.

Although some particles are entrapped by hairs, adhesion is due primarily to capillary forces acting between particles and the surface layer of skin oils and moisture. The nature of this layer, in turn, varies widely because of environmental and physiological differences between individuals.

Trial runs were made with simulated reactor debris on the forearms of three subjects. Depleted uranium dicarbide spheres, carbon coated, were dropped onto the arm from a height of a few centimeters, the subjects engaged in routine

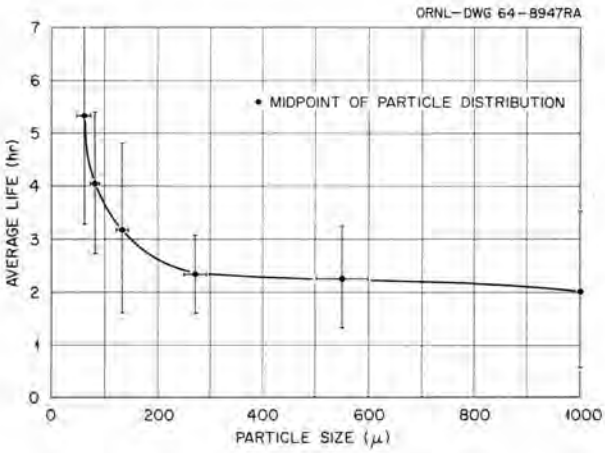

Fig. 23.7. Particle Retention on Skin.

laboratory or clerical activity, and periodic counts were made of the rate of loss of particles. Low magnification was required in visualizing these 230-μ-diam spheres among the hairs of the arm. Kraft paper was taped onto the floor and lower edge of walls of the room in which these experiments took place to assure recovery of all the test material, even though the radiotoxicity of the depleted uranium is negligible. Figure 23.8 shows the wide range of retention times observed, which was not unexpected. Subjects TGC and BRF are moderately hirsute, with hair of the arm measuring 2.5 to 3.0 cm long and quite dense ($\sim$20 hairs/cm^2). Under low magnification the surface of the skin appears moist. Subject JLT's arm is almost devoid of hair [12 hairs/cm^2, which are fine and short (0.68 cm], and the surface appears somewhat drier. Numerical integration of the areas under the curves gives a range of average particle retention times from 0.73 to 6.9 hr.

Decontamination of Skin

A series of tests were carried out on one individual to determine the effectiveness of simple countermeasures in removing small spherical particles. Experiments were conducted in an air-conditioned laboratory where the temperature varied from 68 to 70°F and the relative humidity was 60%. Test material consisted of fluorescent wax spheres from 100 to 1000 μ in diameter; 50 to 170 of these were dropped onto the surface of the left arm, and counts were made under ultraviolet light before and after the decontamination process. These trials were carried out "blind," that is, under standard laboratory illumination. During brushing, etc., the particles were not visible to the experimenter, and no conscious effort was made to restrict the removal forces to the test contaminants.

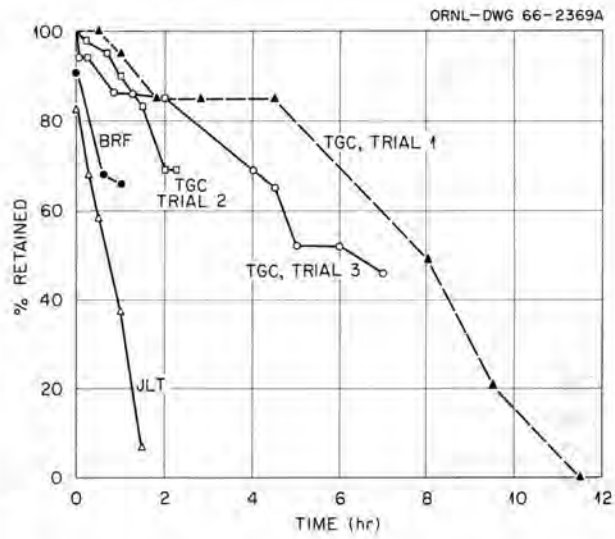

Fig. 23.8. Retention of 230-μ-diam UC_2 Beads on the Arm.

Table 23.4. Decontamination of Particulate Contamination[a] on Skin

Particle Diameter (μ)	Percent Removed		
	Brushing	Rinsing	Washing
500–1000	100	100	100
297–500	100	100	100
250–297	97	100	100
210–250	95	100	100
179–210	98	100	100
125–149	92	100	100
104–125	89	98	100
88–104	86	97	97
1–2	<0.1	<0.1	>99

[a]Fluorescent carnauba wax spheres.

Three techniques were used: (1) brushing with the right hand and finger for a short time (less than 5 sec), (2) rinsing under running tap water for a few seconds, and (3) washing with soap and water with the right hand and rinsing off under running water. Results are shown in Table 23.4. Brushing would not be quite so efficacious were the skin moist or oily. It can be seen that decontamination of the arm is a natural consequence of simple sanitary habits.

EMPIRICAL DOSE MODEL FOR REACTOR DEBRIS PARTICLES

R. H. Boyett B. R. Fish

Determination of radiation dose to tissue from a discrete beta-emitting source is a notoriously difficult problem. The most successful and widely applicable approach to date is an empirical treatment due to Loevinger.[19] Loevinger dealt with the homogeneous case in which the radioactive material is uniformly distributed in a volume of tissue and where the activity, absorption, and backscatter media are assumed to be of unit density. This case is applicable to a wide variety of problems, but differs significantly from the situation in which a high-Z radioactive source is in contact with tissue (e.g., a neutron-irradiated UC_2 particle on the skin). These two cases are contrasted in Fig. 23.9. Preliminary results of spectrum and radiation dose measurements, which we have initiated to provide a basis for an empirical treatment suggested by us for application to the inhomogeneous case,[20] are discussed in this report.

These data are specific for the case of 1-cm-diam sources composed of graphite containing 17 wt % of uranium; however, additional measurements are planned using UC_2 sources of various sizes. The principle is that of approximating the spectrum for which a dose estimate is desired by superposition of dose and spectral data from a library of known measurements made using the desired geometry and source composition. Obviously, application of the technique is not limited to UC_2 and, in principle, could be used for other compositions including particles of activated structural materials.

The spectra shown in Fig. 23.10 were obtained from two 1-cm-diam sources of UC_2 plus graphite, one of which contained ^{45}Ca and the other contained ^{89}Sr (plus 3% ^{90}Sr + ^{90}Y contaminants). These emission spectra were measured with a $\frac{1}{4}$-in.-thick by $\frac{1}{2}$-in.-diam anthracene crystal, under 100 μ Hg vacuum. Surface and depth dose measurements were made on the 1-cm-diam

[19] R. Loevinger *et al.*, "Discrete Radioisotope Sources," in *Radiation Dosimetry* (ed. by G. Hine and G. L. Brownell), Academic, 1956.

[20] R. H. Boyett and B. R. Fish, *Health Phys.* 11, 803 (1965) (abstract).

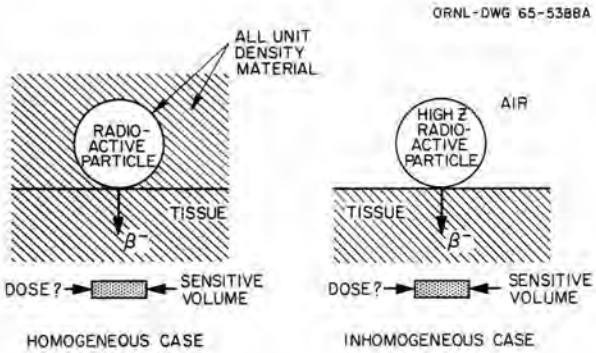

Fig. 23.9. Beta Dosimetry of Discrete Sources.

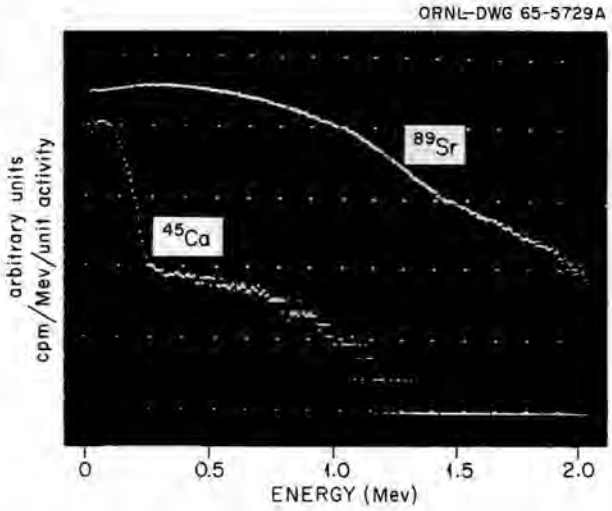

Fig. 23.10. ^{89}Sr and ^{45}Ca Spectra from 1-cm-diam Particle (High Z Material).

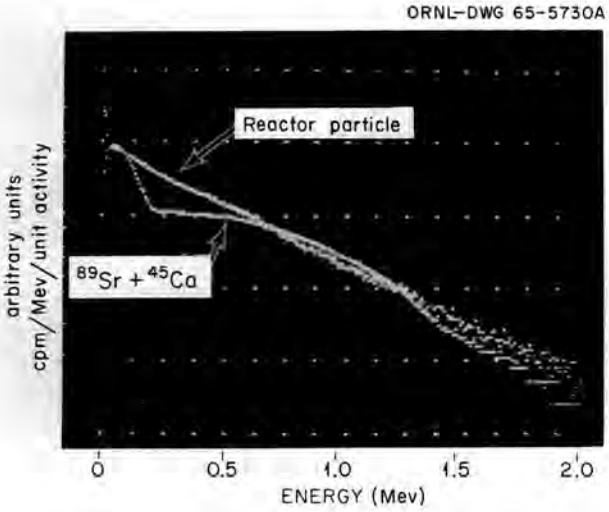

Fig. 23.11. Simulation of Arbitrary Beta Spectrum.

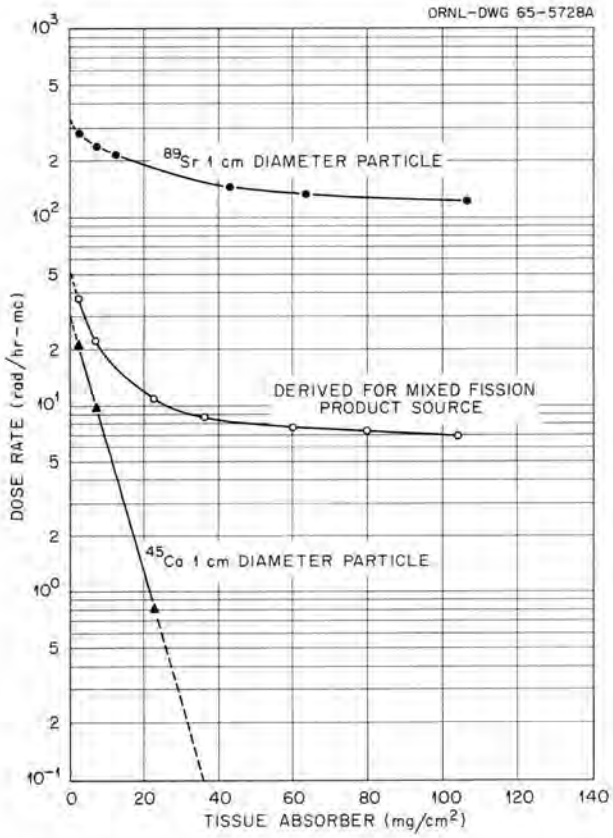

Fig. 23.12. Depth Dose Measurements Average over a 3-mm-diam Collecting Electrode.

particles with an extrapolation chamber using a 3-mm-diam collecting electrode.

An example of this approach is shown in Fig. 23.11. A linear combination of the spectra from two known sources is compared with that of an approximately 200-μ-diam irradiated reactor fuel particle (NRX-A2 test). Obviously, a closer simulation could be made by the use of spectra from additional radionuclides having intermediate energies or energies higher than that of ^{89}Sr. For this example, it was necessary to add 27% of the standard ^{45}Ca spectrum and 3% of the standard ^{89}Sr spectrum to approximate the spectrum from the reactor fuel particle. Thus an estimate of the dose rate from the reactor particle can be obtained by adding the same fractions of the measured dose rates obtained from the two standard sources. Dose rate estimates as a function of depth in tissue are shown in Fig. 23.12. This approach is adaptable to automatic curve fitting on a computer or to simplified techniques of hand calculation, for example, using energy bands and solving a set of simultaneous linear equations.

DOSIMETRY OF SMALL PARTICLES

R. H. Boyett W. H. Wilkie

The significance of intense beta irradiation of limited areas of the skin and GI tract of man exposed to small radioactive particles should be considered in establishing radiological health protection practices and in radiation safety evaluations. Such particles may arise from many sources – contaminated surfaces, fallout, nuclear debris, etc. – and may present considerable civil defense problems in the event of nuclear war. In contrast to established criteria for whole-body and whole-organ exposure, there are few guidelines for assessing the hazards of high exposure to limited volumes of tissue. The importance of assessing the biological effects of ionizing radiation to humans and of relating tissue damage to the radiation dose delivered has prompted considerable research effort in the field of dosimetry. Primarily, the experimental approach has been focused on attempts to measure directly or indirectly the rate of energy absorption in tissue.

The techniques of extrapolation dosimetry as applied to small particles have been described in

previous reports.[21,22] Two specific techniques are briefly discussed, and data obtained by each technique from small irradiated UC_2 particles are compared.

The scintillation method (anthracene extrapolation)[23] is used to obtain values of absorbed dose to tissue-equivalent volumes approaching the volumes of cells. The method incorporates a series of scintillators (anthracene or NE 102-A plastic) mounted on Lucite light pipes with dimensions ranging from 11 mm diameter × 0.5 mm thick to 1 mm diameter × 0.005 mm thick. Pulse-height spectra are recorded using each scintillation assembly with absorbing thicknesses from zero to several hundred milligrams per square centimeter. A schematic is shown in Fig. 23.13. These pulse-height spectra are converted to energy spectra using a computer program to apply appropriate corrections and to calculate the absorbed dose.

[21]W. H. Wilkie, Jr., and B. R. Fish, *Health Phys. Div. Ann. Progr. Rept. July 31, 1965*, ORNL-3849, p. 227.

[22]B. R. Fish *et al.*, ORNL-1053 (classified).

[23]W. H. Wilkie and B. R. Fish, paper to be presented at the Symposium on Solid-State and Chemical Radiation Dosimetry in Medicine and Biology, Vienna, Austria, Oct. 3–7, 1966.

These dose measurements are then assembled into extrapolation curves in order to extract dose information to given volumes at specified absorbing thicknesses. This technique is suitable for measurements using sources with activities in the range of 0.05 to 500 μc. These source strengths are below the level required for use with an ionization extrapolation chamber having the same diameter sensitive volume.

Although the anthracene method of dosimetry is about three orders of magnitude more sensitive, the ionization extrapolation chamber is a very useful dosimetry method for measuring dose levels beyond the limit of the scintillation method. A very useful comparison can be made also from ionization chamber data and the derived dose data obtained from spectroscopy methods.[20] The ionization extrapolation chamber, Fig. 23.14, employs a variety of collecting electrodes ranging in size from 1 mm to 3 cm in diameter.[24]

Figure 23.15 shows a comparison of data from the two methods. Reactor-irradiated UC_2 particles, 145 ± 5 μ and 120 ± 2 μ diameters, were used to estimate the dose rate that would be delivered to

[24]R. Loevinger and N. G. Trott, *Intern. J. Appl. Radiation Isotopes* **17**, 103–11 (1966).

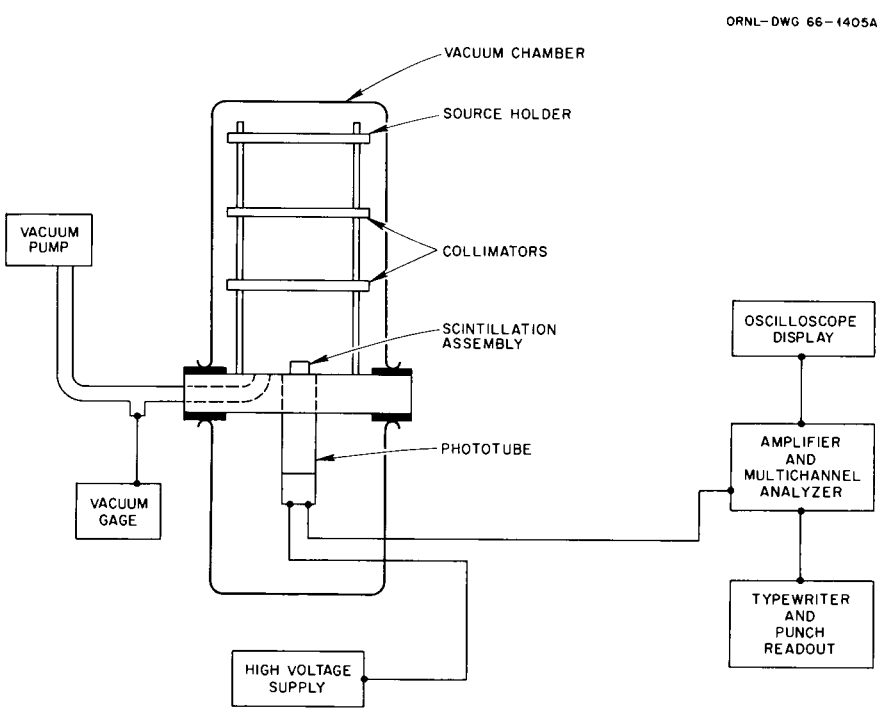

Fig. 23.13. Schematic of Anthracene Extrapolation Method.

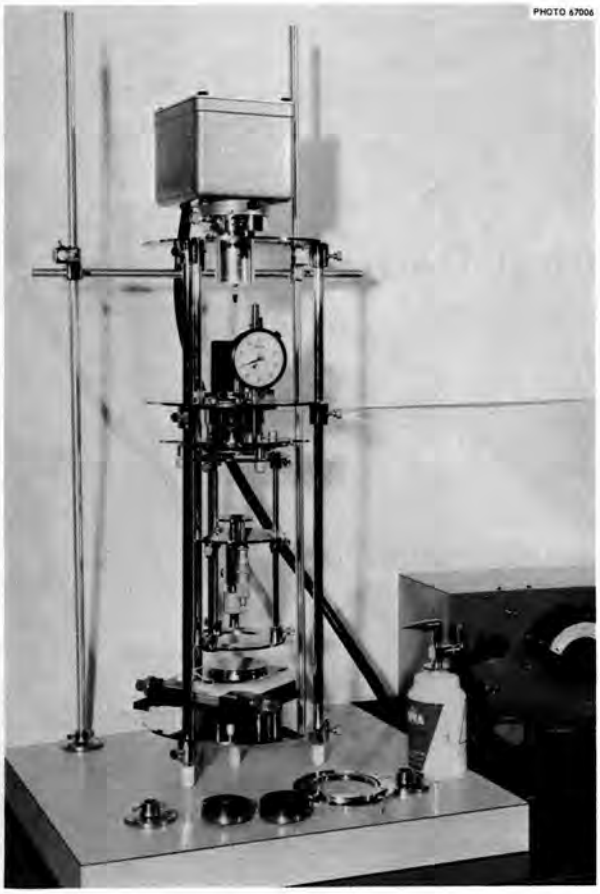

Fig. 23.14. Ionization Extrapolation Chamber.

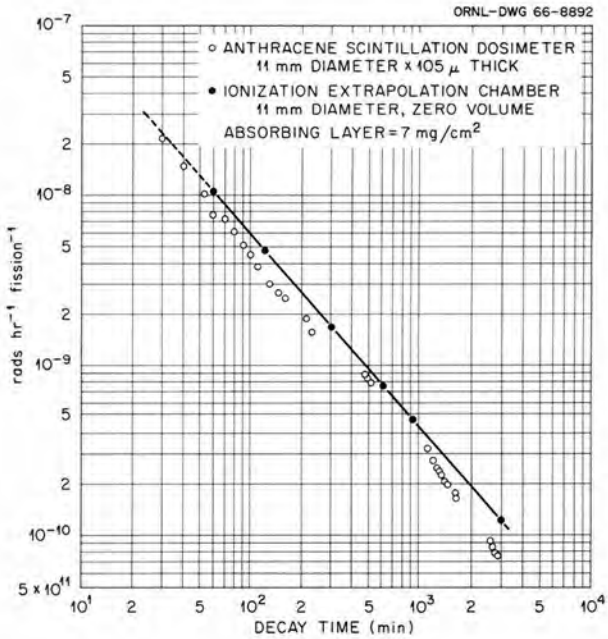

Fig. 23.15. Comparison of Anthracene and Ionization Extrapolation Methods.

tissue-equivalent material of 1 cm^2 area as a function of decay time. An absorbing layer of 7 mg/cm^2 Mylar was placed between the particle and the sensitive volumes. The activation times were 10 min, with the 120-μ-diam particle exposed to a flux level three orders of magnitude higher to obtain an activity level suitable for use with the ionization extrapolation chamber. The data reported for the anthracene measurements were determined using a crystal of 105 μ thickness. Preliminary measurements using a series of crystals with the same diameter with thicknesses ranging from 500 to 70 μ indicated that a dose rate increase of approximately 28% would be necessary in order to correct to zero thickness. The data were normalized to a per fission basis for comparison.

24. Applied Internal Dosimetry

B. R. Fish

P. E. Brown L. B. Farabee
G. R. Patterson, Jr. R. J. Rawls[1]
J. A. Bains[2]

ORNL IN VIVO GAMMA-RAY SPECTROMETRY FACILITY

P. E. Brown L. B. Farabee
G. R. Patterson, Jr. R. J. Rawls[1]
J. A. Bains[2]

With the beginning of Fiscal Year 1966 the ORNL in vivo counting program entered its fourth phase of operation. The initial phase of developmental operation covered the period June 1960 to July 1961[3] and utilized a 200-channel, tube-type analyzer and a 4 × 4 in. NaI(Tl) crystal. The last six months of this phase included limited routine human counting. The second phase, covering the period July 1961 to November 1962,[4] required additional research and development activities in order to change over to an 8 × 4 in. NaI(Tl) crystal and a transistorized 512-channel analyzer. The third phase, covering the period December 1962 to May 1965,[5,6] was devoted to obtaining base-line counts on essentially everyone with any significant potential for future exposure. The first three phases included slightly more than 4000 human counts. The fourth phase, toward which all the others were directed, is the routine monitoring and evaluation of the extent of exposure to gamma-emitting radioisotopes of all Laboratory employees.

The job of determining which employees should be counted, the frequency with which they should be recounted, and preparing the necessary schedule cards and lists is requiring more time than had been anticipated. The new routine counting program is expected to get under way with the beginning of the new fiscal year. During this interim period, the routine counting of employees has proceeded at a reduced rate; however, several employees thought to have sustained internal exposures have been counted, and other free counter time has been used to advantage in counting standards or performing calibrations needed to evaluate human counts.

During the period from July 1, 1965, through May 31, 1966, a total of 593 counts were made on 463 persons; approximately 89% of the persons counted showed a normal human spectrum on at least one of their counts. In addition to the 593 whole-body counts, 35 counts were made on two persons to determine the location of a contaminant or the amount of activity in a particular organ or part of the body. Table 24.1 summarizes the data for those cases in which measurable amounts of internal radioactivity other than normal ^{40}K and ^{137}Cs were observed. In addition to the human counts a total of 278 calibration and development counts were made; 93

[1]Present address: Hughes Aerospace, Los Angeles, Calif.

[2]Temporary summer employee, Centenary College, Shreveport, La,

[3]B. R. Fish *et al.*, *Health Phys. Div. Ann. Progr. Rept. July 31, 1961*, ORNL-3189, pp. 222–24.

[4]B. R. Fish *et al.*, *Health Phys. Div. Ann. Progr. Rept. July 31, 1962*, ORNL-3347, pp. 147–48.

[5]B. R. Fish *et al.*, *Health Phys. Div. Ann. Progr. Rept. June 30, 1963*, ORNL-3492, pp. 195–205.

[6]B. R. Fish *et al.*, *Health Phys. Div. Ann. Progr. Rept. July 31, 1964*, ORNL-3697, pp. 222–25.

Table 24.1. Measurable Radioactivity Found in Routine Whole-Body Monitoring Program, July 1, 1965, to May 31, 1966

Isotope	Persons Counted	Maximum Detected (μc)	Percent of MPBB
^{46}Sc	1	0.004	0.008
^{57}Co	2	0.065	0.033
^{60}Co	13	0.012	0.12
^{90}Sr-^{90}Y	4	0.626[a]	43.4
^{95}Zr-^{95}Nb	8	0.039	0.2
^{106}Ru-^{106}Rh	5	0.03	1.0
^{131}I	6	0.006	0.86
^{137}Cs	6[b]	0.092	0.31
^{144}Ce-^{144}Pr	3	0.05	1.0
^{203}Hg	5[c]	0.022	0.55
^{226}Ra	1[d]	<0.0005 μg	0.5
^{235}U	1	Trace possible	
Activity unidentified	7		
Indications of bremsstrahlung	3		

[a]This is the maximum amount detected early in the year for one of two exposure cases which have been followed since January 1964. The average amount for the year was 0.594 μc, which is the equivalent of 39.1% of the permissible lung burden for the equilibrium mixture ^{90}Sr-^{90}Y. The maximum amount of ^{90}Sr detected in persons other than these two known exposures was 0.154 μc, which compared with the MPBB for ^{90}Sr (in equilibrium) is approximately 8% (assuming all in bone).

[b]Radioactive fallout ^{137}Cs is detected in everyone because of assimilation from the diet. The number reported here represents only those who showed 0.045 μc, or roughly three times the average for persons not occupationally exposed.

[c]One person not included in this tabulation was counted following a medical procedure injection of ^{197}Hg. At the time of his first counting, 28 days post injection, the 0.279-Mev peak of ^{203}Hg completely overshadowed the peaks of ^{197}Hg. His whole-body burden of ^{203}Hg at this time was estimated to be 41 μc, or 10.25 times the MPBB.

[d]Three employees of another federal agency installation were counted because of suspected exposure to ^{226}Ra. Only one showed a possibly positive trace of ^{226}Ra.

of these were standards or calibrations for use in the routine human counting program, and 185 of them were counts made to investigate and/or improve counting techniques and capabilities.

IN VIVO DETECTION AND MEASUREMENT OF ^{90}Sr-^{90}Y INTERNAL CONTAMINATION

In January 1964, three laboratory employees were exposed to airborne particulate $^{90}SrTiO_3$.[7,8] The employee who had the smallest indicated deposit originally was, at the time of his last counting, showing <5% of the permissible lung burden; he is no longer being counted frequently. The other two employees are still being counted at approximately one-month intervals using the 8 × 4 in. lead-collimated NaI(Tl) crystal. Figure 24.1 shows the estimated chest burdens for these two employees since their first counts. During this fiscal year their chest counts have averaged approximately 39% of the permissible lung burden for the equilibrium mixture ^{90}Sr-^{90}Y. Judging from the portion of the curves from 180 days post exposure up to 849 days post exposure, it appears that the half-time for lung clearance may be in excess of 1000 days.

COMPUTER ANALYSIS OF WHOLE-BODY COUNT DATA

G. R. Patterson, Jr. E. Schonfeld[9]
M. T. Harkrider[10]

Program WBC,[11,12] written especially for analysis of the ORNL whole-body counting data and in limited use since March 1963, proved to be unsatisfactory from the standpoint of its limited capabilities and its cost of operation. It was capable of evaluating only normal human spectra, or about 75 to 85% of the counts, and required excessive programmer time to correct errors in the program

[7]B. R. Fish *et al.*, *Health Phys. Div. Ann. Progr. Rept. July 31, 1964*, ORNL-3697, pp. 223–24.

[8]B. R. Fish *et al.*, *Health Phys. Div. Ann. Progr. Rept. July 31, 1965*, ORNL-3849, pp. 227–28.

[9]Chemical Technology Division.

[10]Mathematics Division.

[11]B. R. Fish *et al.*, *Health Phys. Div. Ann. Progr. Rept. June 30, 1963*, ORNL-3492, pp. 202–04.

[12]B. R. Fish *et al.*, *Health Phys. Div. Ann. Progr. Rept. July 31, 1964*, ORNL-3697, p. 225.

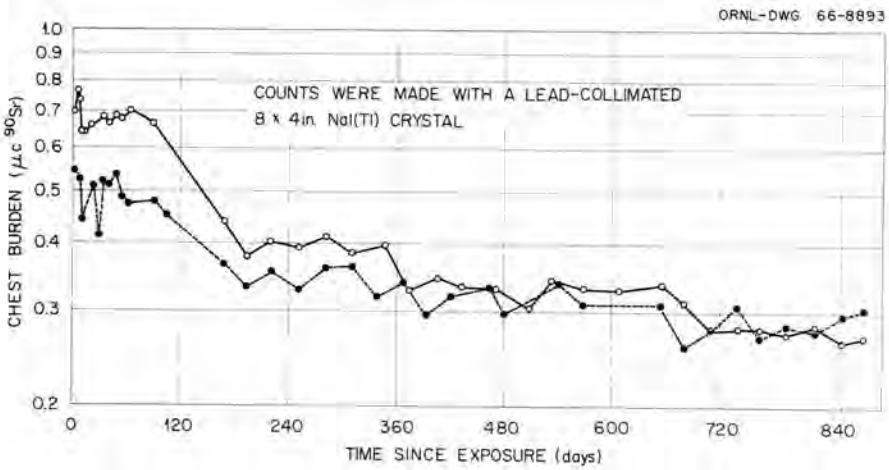

Fig. 24.1. Estimated Lung Burdens of Subjects Inhaling $^{90}SrTiO_3$.

as they became evident. In addition to program deficiencies, we experienced frequent mechanical difficulties in generating punched paper data tapes acceptable by the photoelectric tape reader at the ORNL computing center.

We now have in use a new computer program which can analyze almost any human count we are likely to make and for which we have the necessary calibration standards. An additional advantage is that the new program utilizes punched card data input. The electromechanical equipment used to translate paper data tape to punched cards accepts many tapes which the photoelectric tape reader would not; furthermore, tape errors are easier to spot and correct in the card format.

In July 1965 we evaluated the application to whole-body count data of a new computer program written for the quantitative analysis of the gamma-ray spectra from very low-level radioactive samples. The FORTRAN 63 program ALPHA[13,14] was written by E. Schonfeld of the Chemical Technology Division for analyzing low-level liquid waste samples by least-squares resolution of their gamma-ray spectra. Two test series of routine human counts proved program ALPHA to be directly applicable to whole-body count data analysis without any changes in its original format. The program provides for all the analysis capabilities we desired and is quite flexible. Some of the features of ALPHA which are of particular interest in connection with analysis of in vivo data follow.

1. Evaluation of both normal and abnormal spectra. ALPHA will estimate the amount and standard error of any isotope for which there is a standard in the "library." It will indicate the presence of "suspicious" channels where peaks may exist in the data for which a standard was not available. ALPHA can be instructed to reject a standard and reevaluate the spectrum without reference to that standard if the amount of that activity in the spectrum is less than a prescribed rejection level.

2. The standards "library" has a capacity of up to 80 calibration standards; as many as 20 of these standards can be called for in the analysis of any one "unknown" sample. The "library" can be loaded each time as a punched card deck, or a large "library" can be loaded onto magnetic tape to be used repeatedly.

3. ALPHA can compensate for gain and/or threshold shifts; it can be instructed to match standard and sample peaks automatically or to shift gain and threshold by specified amounts.

4. Both standards and sample data can be input from punched cards or from magnetic tape, or one can be on tape and the other on cards. Spectral data can be in any format as long as the standards and samples are in the same format.

---

[13] E. Schonfeld, *Alpha – a Computer Program for the Determination of Radioisotopes by the Least-Squares Resolution of the Gamma-Ray Spectra*, ORNL-3810 (July 1965).

[14] E. Schonfeld, A. H. Kibbey, and W. Davis, Jr., *Determination of Nuclide Concentrations in Solutions Containing Low Levels of Radioactivity by Least-Squares Resolution of the Gamma-Ray Spectra*, ORNL-3744 (January 1965).

```
CARD M=1     20925  1   =0     =0          1  2.000E+01  2.000E+01          =0          =0          =0
                                6356   4430  4501     1 24 66  601  M 12  1812 27 40 36 665 44
     0     88   187   194   231   327   397   357   460   482   561   520   549   583   581
   591    620   558   525   507   472   511   491   420   446   438   447   418   324   343
   336    277   313   306   331   315   220   301   241   245   281   266   179   133   181
   153    151   224   167   168   200   207   219   190   181   219   238   167   180   169
   225    205   215   242   202   149   174   116   138   177   137   150   147   103    75
   104     94    53   149   112   188   224   252   268   282   257   223   221   176   168
   184    211   304   300   452   493   539   539   470   458   342   277   226   163    77
    57     35    42    42    10    22    14    20    22     9    10    23    20    25    39
    11     20    23     6    18    21    45     8    30    34    38    32    15     8    21
    =3      0    44     0     4   =12    38    24    19    20    15    16    47    34     8
   =11     23     5    31    =6    11    14     9    =1     2     7     9    19     7    17
    11      7    15    18    =2     7    33    38    17    17    41    42    60    81    88
    85     74   137   123   123   119   115    76    82    58    66    44    50    37    16
     6     40     8     1    17    10     0    10   =13    10     6    11     3    11    =2
     3    =13     3     2     2    =3    =9     1    =4     1   =11    =8   =11    =1   =21
   =16      3     6   =16     3     0    =3     3   =12     9    =4     7     4    =3     2
   =13    =10    =5    =2    =7     0     2    =1     8    =5     0    =3    =4    =2    =4
    10
BACKGD SUM=    4.100E+04     SAMPLE SUM=    3.196E+04
CARD M=6       3 1=0=0 1     =0=0 1 210
FIT=  1.816E+00 THR SHIFT=  .47 GAIN SHIFT= .9944
FIT=  1.452E+00 THR SHIFT=  .80 GAIN SHIFT= .9907
ALPHA FACTORS
 6.9089E=01  7.0578E=01  8.6832E=01
RESULTS=CONCENTRATIONS AND EST STANDARD ERRORS

                TOTAL=K    1.2729E+02   5.86E+00    137=CS     7.2963E+00   6.10E=01    95=ZR=NB   3.6602E+01   7.37E=01
RATIO OF RESIDUALS OVER STD DEV PER CHANNEL
    =0     =0     =0    1.2    1.8    2.2    1.0     .5    1.1    1.7    2.0    1.5    2.2    2.2
   2.1    2.9    2.6    1.4    1.4     .6     .8    1.2     .1    =.5    =.2    =.2     .2   =1.3   =1.6
   =.9   =1.5    =.8    =.5     .4     .9    =.9     .3    =.3    =.4    1.2    1.0    =.7   =2.1   =1.4
  =1.3   =1.9     .3    =.6   =1.1     .3     .8    1.3     .6     .0    1.5    2.7     .8     .1     .3
   2.3    2.0    2.4    3.4    2.4     .2     .8    =.9    =.3    1.7     .2    1.0    1.3    =.5   =1.9
    =.6    =.9   =2.8    =.1   =1.9    =.4    =.2    =.1     .1     .6    =.3   =1.3   =1.4   =3.3   =4.0
   =4.2   =4.3   =2.4   =3.2    1.1    1.0    2.3    2.3     .9    2.0    =.7    =.5     .0    =.7   =2.2
   =1.8   =1.7    =.3     .2   =1.2    =.4    =.7    =.1    =.4   =1.0    =.5     .2    =.1     .5     .9
    =.9     .0    =.2    =.8     .1     .6    1.3    =.5    1.1    1.3    1.4     .4    =.6    =.7    =.4
   =1.4    =.6     .7   =1.2   =1.6   =1.1    1.0    =.0    =.3    =.3    =.6     .4    1.7     .3   =1.6
   =1.3    =.2    =.2    =.0   =1.3    =.1    =.2    =.9   =1.0    =.6    =.3     .0     .2     .1     .5
    =.2     .3     .5    =.5    =.6    1.0    1.6     .1    =.7     .0     .2     .1     .6     .5    =.5
   =1.4     .1     .6    =.0    =.0    =.1   =1.3   =1.0    =.8    =.3    =.1     .4     .2    =.7    =.9
    1.4     .1    =.8     .7     .5    =.2     .3   =1.2     .1    1.0     .9     .4     .8    =.3     .2
   =1.2    =.2     .2     .2    =.3    =.8    =.2    =.4    =.2   =1.1    =.9   =1.1    =.4   =1.8   =1.8
    =.1     .4   =1.5    =.1     .0    =.3     .2   =1.2     .7    =.5     .6     .7    =.6     .1   =1.9
   =1.3    =.7    =.4   =1.2    =.1     .1     .0    1.1   =1.0    =.2
SUSPICIOUS CHANNELS
 15  16  17  62  63  64
```

Fig. 24.2. Human Body Count Record Sheet – Program ALPHA Printed Output.

5. Sample data can be input either as gross counts or net counts. ALPHA corrects both the sample and the background for counting time, adjusts for counter dead time if instructed to, and either subtracts the background or not as instructed.

6. ALPHA can evaluate several counts individually, then combine the results (concentrations and estimated errors) and compute the averages.

Output from program ALPHA is both printed and punched into cards. The printed output, Fig. 24.2, includes all information identifying the sample, estimates of isotope concentrations with standard error, estimates of goodness of fit of standards and samples, the ratio of the residual count over the standard deviation per channel, and indications of which channels may have some activity for which no standard was called from the library. These sheets are filed in chronological order for ready reference to results. The punched card output includes all the identifying information and the estimates of isotope concentration with standard errors. These punched cards can be used in auxiliary programs for plotting of spectra or sorting, tabulating, or compiling data reports, etc. M. T. Harkrider has already written a new program with which we can tabulate weekly or other periodical reports of counting activities using the punched card output deck.

At the present time a library of 86 standards is available on IBM cards; this comprises multiple counts on 20 different isotopes with differing distributions in the calibration phantom or counted in different count configurations. A library of 36 different standards applicable to the latest in vivo counts has been loaded on magnetic tape; this represents multiple counts with differing distributions or different counting configurations of 12 different isotopes. This library, of course, does not include all of the isotopes we may expect to encounter with in vivo counting, and new spectra are being added continually to the library.

CORRECTION OF ^{239}Pu-^{241}Am WOUND COUNT FOR ATTENUATION IN TISSUE AND FOR DIFFERENT RATIOS OF ^{241}Am TO ^{239}Pu

P. E. Brown

There are three main factors that make ^{239}Pu measurement in wounds difficult: (1) the low energy of the photons and the poor yield per disintegration, (2) the varying amounts of ^{241}Am accompanying the ^{239}Pu (this depends on the amount of ^{241}Pu present and age of the source since separation from americium), and (3) the confusion caused by the fact that many of the ^{241}Am photons have almost the same energy as photons from ^{239}Pu.

For counting the low-energy photons a special NaI(Tl) thin-crystal counter, manufactured by Harshaw Chemical Company, Cleveland, Ohio, is used. The background is about 0.5 count/min in the energy bands used, and contribution from gamma rays having energies above 100 kev is very small. The crystal is 1 in. in diameter by $\frac{1}{32}$ in. thick and is covered with a 0.005-in. beryllium window.

Correction for attenuation of these weak photons in the wound tissue can be accomplished approximately by observing the ratio of counts in peaks of different energy. These peaks should be separated as widely as possible. For pure ^{239}Pu the 17- and 53-kev peaks are the only ones that have sufficient difference in energy for this purpose. For ^{241}Am alone the 26- and the 60-kev peaks could be used but are too close in energy to give a good index of attenuation. The 17-to-20-kev band of both ^{239}Pu and ^{241}Am and the 55-to-65-kev band of ^{241}Am have the required difference in energy, but this means that both components must be handled together.

An empirical approach was undertaken by simulating several ^{241}Am/^{239}Pu ratios to represent sources of different ages and different ^{241}Pu content. This was done by the use of a pure ^{239}Pu source (^{241}Am freshly separated) and a pure ^{241}Am source. The two were combined by adding fractional parts of the ^{241}Am and of the pure ^{239}Pu source spectra. A 512-channel Nuclear Data analyzer was used to prepare spectra of counts made with each source separately, using vinyl absorbers ranging from 0.75 to 16 mm thick. Corresponding absorption counts on each source were combined to give five different ^{241}Am/^{239}Pu ratios for each absorber. With these data a graph was prepared to show the thickness of absorber vs the ratio of counts per minute in the 17-kev band to counts per minute in the 60-kev band. Curves for five ^{241}Am/^{239}Pu ratios are shown,

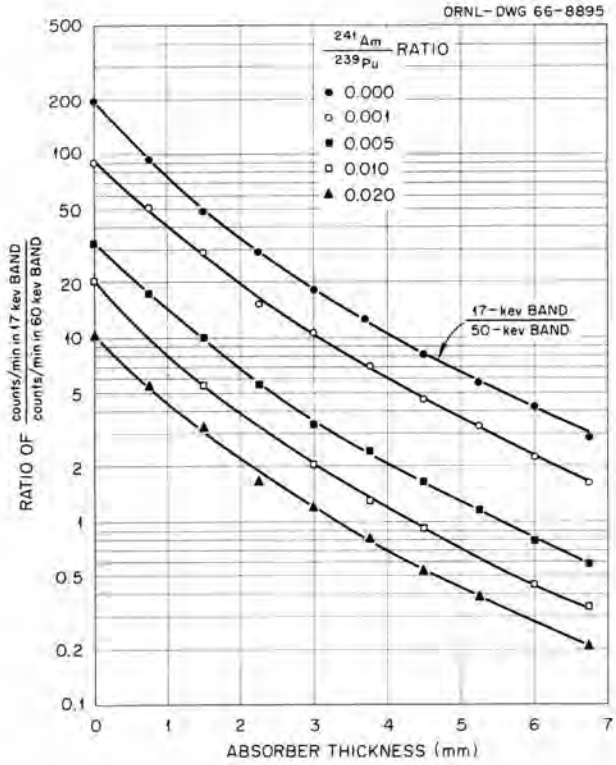

Fig. 24.3. Relative Count Rate in 17- and 60-kev Bands as a Function of Absorber Thickness for Different $^{241}Am/^{239}Pu$ Ratios.

Fig. 24.3. Another graph was prepared showing counting efficiencies for the 17- and 60-kev bands vs thickness of absorber, Fig. 24.4.

It is necessary to know the ratio of ^{241}Am to ^{239}Pu. If such information is not available, it is possible to obtain an estimate using the data given here. A sample of the contaminating material is counted using a few plastic absorbers in the range of those in the graphs. The 17 kev/60 kev counting ratios are plotted in Fig. 24.3, and by comparison of $^{241}Am/^{239}Pu$ ratios already plotted there the proper ratio to use in counting the wound can be estimated. A single count is made in contact with the wound to determine the 17 kev/60 kev counting ratio. Figure 24.4 may then be used to find the counting efficiency. The 17-kev band has the best efficiency for shallow wounds and low $^{241}Am/^{239}Pu$ ratios. The 60-kev band is better for deep wounds and high $^{241}Am/^{239}Pu$ ratios. The least detectable activity (three times the standard deviation of the smallest detectable counting rate) varies with attenuation in tissue and the $^{241}Am/^{239}Pu$ ratio, Fig. 24.5.

The purpose of this investigation was to find a method of correcting ^{239}Pu wound counts for attenuation in tissue and for ratio of ^{241}Am to ^{239}Pu. Additional investigation is under way of the effect of large particle sizes on attenuation. It has not been determined how well the above corrections apply to this problem. Without any such correction an approximately 50% underestimate would occur for 50-μg ^{239}Pu particles in the wound. It is desirable also to know the distribution of activity within the wound, but this procedure gives only the overall or averaged attenuation.

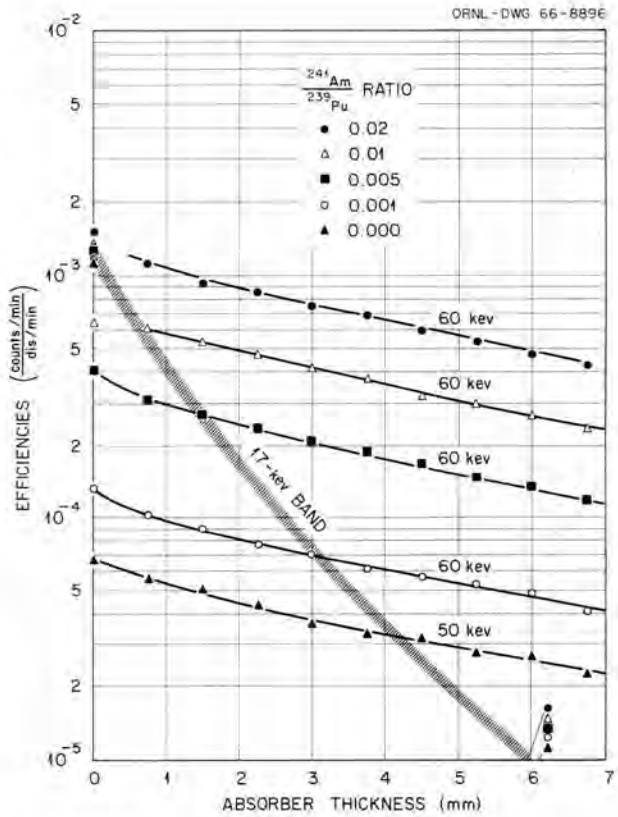

Fig. 24.4. Counting Efficiencies (Counts in Band per Disintegration of ^{239}Pu) vs Absorber Thickness for Different $^{241}Am/^{239}Pu$ Ratios.

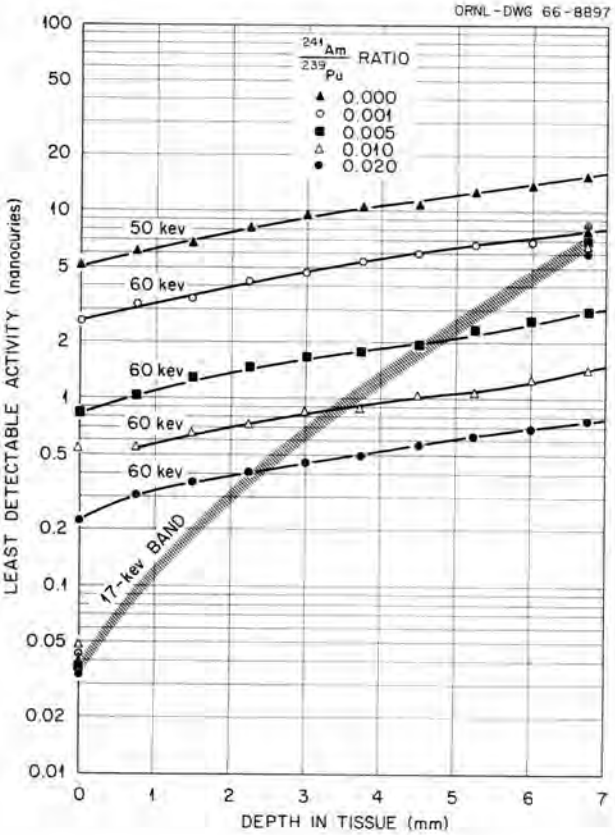

Fig. 24.5. Least Detectable Amount of ^{239}Pu (30-min Count) as a Function of Depth in Tissue for Different $^{241}Am/^{239}Pu$ Ratios.

ABSORPTION OF ^{90}Sr FROM A PUNCTURE WOUND

L. B. Farabee

An employee accidentally received a puncture wound on the volar surface of the tip of the left index finger from a stainless steel wire 1 mm in diameter which was contaminated with ^{90}Sr + ^{90}Y. The absorption of the ^{90}Sr into the body was studied by analysis of blood and urine, while the residual ^{90}Y remaining in the finger was determined by counting the beta activity with an end-window GM beta counter (1.4-mg/cm^2 window).

Although the employee was wearing full protective clothing including four pairs of rubber gloves, the wire pierced the gloves and entered the finger to an estimated depth of about 2 to 3 mm. This depth was estimated by counting the 2.18-Mev beta of ^{90}Y in the finger using layers of polyethylene sheets, and comparing the shape of the absorption curve obtained with that of a known curve derived from a ^{90}Sr-^{90}Y source in a simulated finger counted under similar conditions using the same polyethylene absorbers. The average depth of the ^{90}Y was estimated to be about 1.5 mm. Essentially all of the 0.61-Mev ^{90}Sr was absorbed in the muscle and skin.

In Fig. 24.6 is shown the ^{90}Y content of the finger as determined by the average of four different methods of counting. The ^{90}Y in the first several determinations is abnormally large due to a nonequilibrium condition that existed on the wire. Decontamination of the cell prior to the accident had removed much of the ^{90}Sr, but the ^{90}Y daughter remained on the wire at a level 4.8 times what would have been present in an equilibrium mixture at the time of exposure.

The amount of ^{90}Sr absorbed from the wound was estimated to be 0.051 μc on the basis of a single urine sample collected 4 hr after the incident. And a comparable estimate, 0.073 μc of ^{90}Sr, was obtained from the analysis of a blood sample taken 6 hr after exposure. A urine sample taken five days after the accident indicated an uptake of 0.066 μc. These estimates were obtained by comparison with known human exposures to ^{85}Sr injections.[15]

[15] M. Bishop *et al.*, *Intern. J. Radiation Biol.* **2**, 125 (1960).

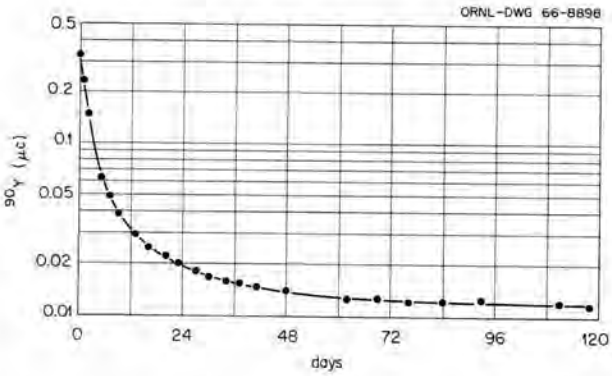

Fig. 24.6. ^{90}Y Content of the Finger as Determined by the Average of Four Different Methods of Counting.

Due to the initial excess of ^{90}Y, it was difficult to estimate the absorption of ^{90}Sr by direct counting in the first six to eight days after the accident. However, from day 12 to about day 60, about 0.012 μc was absorbed. After day 60 the rate of absorption has been very low, the indicated half-life for elimination being on the order of 500 days.

At present our best estimate is that the initial intake was 0.33 μc of ^{90}Y plus 0.07 μc of ^{90}Sr. Of this, approximately 0.06 μc of ^{90}Sr was absorbed rapidly into the bloodstream and 0.008 μc of ^{90}Sr remained in the wound and is being eliminated very slowly.

PREVENTING RADIOSTRONTIUM LOSS IN THE PRECIPITATION OF ALKALINE-EARTH PHOSPHATES FROM URINE WITH NH_4OH

L. B. Farabee

In a urinalysis program it is sometimes necessary to analyze an individual sample for more than one radionuclide. Since urine contains large quantities of calcium, magnesium, and phosphates, the precipitation of alkaline-earth phosphates in a basic medium is usually the first step in the concentration of both transuranic radionuclides and radiostrontium from a urine sample. It has been shown[16] that quantitative recovery of radiostrontium is obtained when NaOH is used. However, since the first step in the ORNL urinalysis procedure for the transuranic radionuclides employs NH_4OH to precipitate the alkaline-earth phosphates, it is necessary to determine the efficiency of radiostrontium recovery in order that both analyses may be made on one sample.

Although ^{90}Sr is the isotope of greatest interest in the urinalysis program, ^{85}Sr (0.51-Mev gamma) is used in the developmental work to facilitate the study of solubility losses since direct counting can be done on liquid samples using an NaI(Tl) crystal and a multichannel analyzer. Since it was found that large losses of ^{85}Sr occurred when alkaline-earth phosphates were precipitated from dilute urine samples, 500-ml aliquots of dilute urine (sp gr 1.007) were used in an attempt to study variables which might improve recovery. In the ORNL procedure, 25 ml of concentrated HNO_3 is added to a 500-ml aliquot of urine, and the sample is heated for 1 hr at 80°C; then NH_4OH is added to give a visible precipitate at a pH of about 8 to 9.

By varying the conditions of the alkaline-earth phosphate precipitation using NH_4OH, it is seen that best results are obtained when (1) excess calcium (60 mg per 500 ml of urine) is added, (2) excess H_3PO_4 is added to give a 0.1 M solution, (3) excess NH_4OH to give a pH of 9, and (4) the exclusion of atmospheric CO_2 from the sample after precipitation by covering the beaker with a plastic wrap (this single step increases the recovery of ^{85}Sr by 4%). A constant recovery of 95.0% (±0.3) is obtained when the precipitation is carried out using the above conditions for processing urine samples ranging in volume from 500 to 1500 ml.

---

[16] L. B. Farabee, *A.M.A. Arch. Ind. Health* 17, 200 (1958).

Theses, Papers, Publications, and Lectures

Theses

L. G. Christophorou, A. Hajiantoniou, and G. S. Hurst
Interaction of Thermal Electrons with Polarizable and Polar Molecules, ORNL-TM-1262 (November 1965).

R. N. Compton, G. S. Hurst, L. G. Christophorou, and P. W. Reinhardt
Electron Capture Cross Sections and Negative Ion Lifetimes, ORNL-TM-1409 (March 1966).

W. G. Connor and R. H. Ritchie
Semi-Classical Model of the Photoelectric Effect in Metals, ORNL-TM-1458 (May 1966).

Julian Crowell and R. H. Ritchie
Positron Annihilation in an Electron Gas, ORNL-TM-1443 (May 1966).

F. W. Garber
Electronic Energy Levels in Aluminum and Silver, ORNL-TM-1153 (August 1965).

H. J. Howe and R. H. Ritchie
Transition Radiation and Low-Energy Bremsstrahlung, ORNL-TM-1105 (August 1965).

T. M. Jelinek, E. T. Arakawa, and R. N. Hamm
Optical Properties of Evaporated Films of Cadmium, Thallium, and Zinc in the Vacuum Ultraviolet, ORNL-TM-1164 (July 1965).

T. P. O'Farrell, S. I. Auerbach, and P. B. Dunaway
Incorporation of a Thymidine Analog by Indigenous Rodents, ORNL-3907 (March 1966).

J. E. Parks and G. S. Hurst
Studies of Electron Transport in Gases, Using Time-of-Flight Methods, ORNL-TM-1287 (December 1965).

J. L. Stanford, E. T. Arakawa, and R. D. Birkhoff
Photoelectric and Optical Properties of Commercial Pt, Au, and Pd Foils and Evaporated Al and Ag Films in the Extreme Ultraviolet, ORNL-TM-1392 (in preparation).

Papers

E. T. Arakawa and R. N. Hamm
Studies of Collective Electron Oscillations in Metals by Optical Methods, International Colloquium on the Optical Properties and Electronic Structure of Metals and Alloys, September 13–16, 1965, Paris, France.

J. C. Ashley, J. Crowell, and R. H. Ritchie
Effective Mass of a Slow Charged Particle in an Electron Gas, American Physical Society, Southeastern Section, November 1–3, 1965, Charlottesville, Virginia.

Leroy Augenstein, Edward Yeargers, James Carter, and DeVaughn Nelson
Excitation, Dissipative and Emissive Mechanisms in Tryptophan, Symposium on Space Biology, 1965, Berkeley, California.

J. A. Auxier
Physical Problems of Dosimetry of Neutrons and Protons, Symposium on Accidental Irradiation at Place of Work, April 25–29, 1966, Nice, France.

J. A. Auxier and D. R. Johnson
Nuclear Accident Dosimetry Tests, AEC and Contractor Health Protection Meeting, January 13, 1966, Chicago, Illinois (presented by D. R. Johnson).

R. D. Birkhoff, R. N. Hamm, and W. J. McConnell
Measurements of Electron Slowing Down Spectra in Infinite Isotropic Media, Third International Congress of Radiation Research, June 26–July 2, 1966, Cortina, Italy.

B. G. Blaylock
A Cytogenetic Study of a Natural Population of Chironomus Inhabiting an Area Contaminated by Radioactive Waste, IAEA Symposium on the Disposal of Radioactive Wastes into Seas, Oceans, and Surface Waters, May 16–20, 1966, Vienna, Austria.

W. J. Boegly, Jr., F. L. Parker, and E. G. Struxness
Radioactive Waste Disposal in Underground Formations: Possible Applications for Industrial Waste Disposal, Annual Conference of Water Pollution Control Federation, October 10–14, 1965, Atlantic City, New Jersey.

R. L. Bradshaw, W. L. Beck, H. W. Dickson, and W. F. Hanson
High Dose Response of Glass Rod Dosimeters Irradiated at Temperatures Up to 250°C, Health Physics Society Meeting, June 26–30, 1966, Houston, Texas.

R. L. Bradshaw, T. F. Lomenick, W. C. McClain, W. J. Boegly, Jr., F. M. Empson, and F. L. Parker
Project Salt Vault: Effects of Temperature and Radiation on Plastic Flow and Mine Stability, Symposium on Solidification and Long-Term Storage of Highly Radioactive Wastes, February 13–17, 1966, Richland, Washington.

G. N. Brown
Irradiation–Photo Period Interactions in Xanthium, AIBS Meetings, August 17, 1965, Urbana, Illinois.

Nuclei Acid Changes in Mimosa Following Fast Neutron Irradiation, AIBS Meetings, August 18, 1965, Urbana, Illinois.

Soluble RNA Changes in Mimosa Following Fast Neutron Irradiation, Association of Southern Agricultural Workers, February 7, 1966, Jackson, Mississippi.

J. G. Carter, T. M. Jelinek, R. N. Hamm, and R. D. Birkhoff
Optical Properties of Polystyrene in the Vacuum Ultraviolet, American Physical Society, Southeastern Section, November 1–3, 1965, Charlottesville, Virginia.

L. G. Christophorou, G. S. Hurst, R. N. Compton, and P. W. Reinhardt
Low-Energy Electron Capture Cross Sections for Dissociative Processes in Complex Molecules, American Physical Society, Southeastern Section, November 1–3, 1965, Charlottesville, Virginia.

L. G. Christophorou, G. S. Hurst, R. N. Compton, and P. W. Reinhardt
Study of Electron Capture in Benzene Derivatives, Third International Congress of Radiation Research, June 26–July 2, 1966, Cortina, Italy.

L. G. Christophorou, G. S. Hurst, and A. Hadjiantoniou
Interaction of Thermal Electrons with Polarizable and Polar Molecules, 18th Annual Gaseous Electronics Conference, October 20–22, 1965, Minneapolis, Minnesota.

T. G. Clark, B. R. Fish, and R. H. Boyett
Health Physics Aspects of Particle Retention on Skin, Tennessee Valley Industrial Health Conference, Gatlinburg, Tennessee, September 30–October 1, 1965.

R. N. Compton, L. G. Christophorou, G. S. Hurst, and P. W. Reinhardt
Nondissociative Electron Capture and Autodetachment Lifetimes in Complex Molecules, American Physical Society, Southeastern Section, November 1–3, 1965, Charlottesville, Virginia.

K. E. Cowser
Radioactive Waste Management, 26th Meeting of Illinois Public Health Association, April 13–15, 1965, Springfield, Illinois.

K. E. Cowser, L. C. Lasher, L. Gemmell, and S. G. Pearsall
Operational Experience in the Treatment of Radioactive Waste at Oak Ridge National Laboratory and Brookhaven National Laboratory, IAEA-ENEA Symposium on Practices in the Treatment of Low and Intermediate Level Radioactive Wastes, December 6–10, 1965, Vienna, Austria.

K. E. Cowser, W. S. Snyder, C. P. McCammon, C. P. Straub, O. W. Kochtitzky, R. L. Hervin, E. G. Struxness, and R. J. Morton
Evaluation of Radiation Dose to Man from Radionuclides Released to the Clinch River, IAEA Symposium on the Disposal of Radioactive Wastes into Seas, Oceans, and Surface Waters, May 16–20, 1966, Vienna, Austria.

L. S. Cram, E. T. Arakawa, and R. D. Birkhoff
Investigation of the Surface Plasma Radiation from Electron-Bombarded Ag, American Physical Society, April 25–28, 1966, Washington, D.C.

D. A. Crossley, Jr.
Relation of Arthropod Activities to Leaf Litter Breakdown, Annual Meeting, Ecological Society of America, August 19, 1965, Urbana, Illinois.

Radiation Effects Studies with Insects, Health Physics Division Annual Information Meeting, October 28, 1965.

Arthropod Predator-Prey Transfer of Radioactive Cesium, Annual Meeting, Association Southeastern Biologists, April 15, 1966, Raleigh, North Carolina.

Julian Crowell and R. H. Ritchie
Positron Annihilation in a Free Electron Gas, American Physical Society, Southeastern Section, November 1–3, 1965, Charlottesville, Virginia.

Patricia Dalton and J. E. Turner
Calculation of Atomic Mean Excitation Energies (I Values) from Stopping Power Measurements, American Physical Society, Southeastern Section, November 1–3, 1965, Charlottesville, Virginia.

F. J. Davis and E. B. Wagner
Time-of-Flight Measurements of Diffusion Coefficients and Drift Velocities in Electron Swarms (Differential Pumping Method), 18th Annual Gaseous Electronics Conference, October 20–22, 1965, Minneapolis, Minnesota.

D. R. Davy
Prediction of Biological Damage from Stopping Power Theory, Health Physics Society, June 27–30, 1966, Houston, Texas.

D. R. Davy and L. H. Peshori
An Absolute Neutron Dosimeter Based on a Generalized Concept for Radiation Dosimetry, Health Physics Society, June 27–30, 1966, Houston, Texas.

P. B. Dunaway
Radiosensitivity of Indigenous Rodents in Eastern Tennessee, Annual Meeting of the Ecological Society of America, August 15–20, 1965, University of Illinois, Urbana, Illinois.

L. C. Emerson and E. T. Arakawa
Absolute Photon Intensity Measurements in the Energy Region Below 30 eV, Health Physics Society, June 27–30, 1966, Houston, Texas.

F. M. Empson, R. L. Bradshaw, W. J. Boegly, Jr., W. C. McClain, F. L. Parker, and W. F. Schaffer, Jr.
Project Salt Vault: Design and Operation, International Symposium on the Solidification and Long-Term Storage of Highly Radioactive Wastes, February 14–18, 1966, Richland, Washington.

Henry L. Fisher, Jr.
A Computer Code for Estimation of Body Burden of ^{90}Sr Based on O.R. and Bone Remodeling Which Are Age Dependent, Eleventh Annual Bio-Assay and Analytical Chemistry Meeting, October 7–8, 1965, Albuquerque, New Mexico.

Variation of Radiological Dose Delivered by Cesium-137 as a Function of Body Size from Infancy to Adulthood, Eleventh Annual Health Physics Society Meeting, June 27–30, 1966, Houston, Texas.

Mary R. Ford and W. S. Snyder
The Estimation of Exposure to an Aerosol Based on a Revised Standard Lung Model, Eleventh Annual Health Physics Society Meeting, June 27–30, 1966, Houston, Texas.

Kenneth Fox and J. E. Turner
Variational Calculation for Bound States in an Electric Dipole Field, American Physical Society, April 25–28, 1966, Washington, D.C.

F. W. Garber, Y. Nakai, and R. D. Birkhoff
Stopping Power of Aluminum for Electrons Between 800 and 1500 eV, American Physical Society, Southeastern Section, November 1–3, 1965, Charlottesville, Virginia.

W. F. Hanson and E. T. Arakawa
Reflectivities of Concave Diffraction Gratings for Polarized Light in the Vacuum Ultraviolet, American Physical Society, Southeastern Section, November 1–3, 1965, Charlottesville, Virginia.

F. F. Haywood
Recent Experimental Observations in Radiation Free-Field Studies, DASA Nuclear Initial Radiation Measurements Working Group, December 8 and 9, 1965, San Francisco, California.

F. F. Haywood and E. M. Robinson
A Shipping Container for Accelerator Targets Loaded with Kilocurie Quantities of Tritium, Health Physics Society, June 27–30, 1966, Houston, Texas.

H. Hollister and J. E. Turner
Quantum Theory of RBE. II. Interpretation of Cell Survival Data, Third International Congress of Radiation Research, June 26–July 2, 1966, Cortina, Italy.

G. S. Hurst, L. G. Christophorou, R. N. Compton, and P. W. Reinhardt
A Swarm-Beam Method for Measurement of Electron Capture Cross Sections, American Physical Society, Southeastern Section, November 1–3, 1965, Charlottesville, Virginia.

G. S. Hurst and J. E. Parks
Time-of-Flight Measurement of Diffusion Coefficients and Drift Velocities in Electron Swarms, 18th Annual Gaseous Electronics Conference, October 20–22, 1965, Minneapolis, Minnesota.

D. G. Jacobs
Desorption of Radioiodine from Clays, Clay Mineral Society Meeting, August 22–26, 1965, Berkeley, California.

D. G. Jacobs
Negative Sorption by Alumino-Silicates Having a Limited Degree of Lattice Expansion, International Clay Conference, June 20–24, 1966, Jerusalem, Israel.

G. E. Jones, S. Cram, and E. T. Arakawa
Radiation from Thick Silver Foils Bombarded by Grazing Incidence Electrons, American Physical Society, Southeastern Section, November 1–3, 1965, Charlottesville, Virginia.

N. R. Kevern
The Feeding Rate and Energy Requirements of Carp (Cyprinus carpio Linnaeus), AIBS Meetings (Ecology Section), August 15–20, 1965, Urbana, Illinois.

N. R. Kevern, D. J. Nelson, J. L. Wilhm, and N. A. Griffith
An Estimate of Periphyton Mass and Stream Bottom Area Using Phosphorus-32, 14th Annual Meeting of the Midwest Benthological Society, April 13–15, 1966, Mt. Pleasant, Michigan.

R. A. MacRae, E. T. Arakawa, and R. N. Hamm
Optical Properties of Mo and Sn in the Vacuum UV, Optical Society of America, March 14–18, 1966, Washington, D.C.

W. J. McConnell, R. N. Hamm, and R. D. Birkhoff
Electron Slowing Down Spectrum of Cu-64 Beta Rays Absorbed in Aluminum, American Physical Society, April 25–28, 1966, Washington, D.C.

W. C. Moldenhauer, A. S. Rogowski, and D. Kirkham
Relationship Between the Energy Necessary to Initiate Runoff and the Energy of Rupture for Aggregates of Eight Iowa Soils, American Society of Agronomy, 1965 Annual Meeting, October 31 to November 5, 1965, Columbus, Ohio.

K. Z. Morgan
Dose Commitments, International Symposium on Radiological Protection in Industrial Use of Radioisotopes, Paris, France, December 13, 1965.

Maximum Permissible Exposure to Ionizing Radiation, Public Health Conference on the Use of X-Rays in Medicine and Industry, University of Miami, Miami, Florida, April 14, 1966.

D. J. Nelson
Ecological Aspects of Radionuclides in Streams, American Association for the Advancement of Science, Pacific Division, June 21–26, 1965, Riverside, California.

Prediction of ^{90}Sr Uptake in Fish, Ecological Society of America, August 15–20, 1965, Urbana, Illinois.

Microchemical Constituents in Contemporary and Pre-Columbian Clam Shell, International Association for Quaternary Research, VIIth Congress, August 30–September 5, 1965, Boulder, Colorado.

The Prediction of ^{90}Sr Uptake in Fish Using Data on Specific Activities and Biological Half-Lives, International Symposium on Radioecological Concentration Processes, April 25–29, 1966.

Jacob Neufeld and Harvel Wright
Excitation of Hydromagnetic Waves by a Helical Proton Stream, Symposium on Electromagnetic Wave Theory, September 6–11, 1965, The Netherlands.

J. S. Olson

Lake Michigan Dune Development 4, Vegetation, Dune, and Climatic History, Field Conference C., International Association for Quaternary Research, August 23, 1965.

Postattack Ecology and Environmental Defense, National Academy of Science Committee for Office of Emergency Planning, June 20, 1966.

F. L. Parker, W. J. Boegly, Jr., R. L. Bradshaw, F. M. Empson, W. C. McClain, and W. F. Schaffer, Jr.
Disposal of Solid Radioactive Wastes in Rock Salt, American Chemical Society Meeting, September 12–17, 1965, Atlantic City, New Jersey.

F. L. Parker, M. A. Churchill, R. W. Andrew, B. J. Frederick, P. H. Carrigan, Jr., S. L. Jones, E. G. Struxness, and R. J. Morton
Dilution, Dispersion, and Mass Transport of Radionuclides in the Clinch-Tennessee Rivers, IAEA Symposium on the Disposal of Radioactive Wastes into Seas, Oceans, and Surface Waters, May 16–20, 1966, Vienna, Austria (paper presented by K. E. Cowser).

B. C. Patten
A Method for Determining Productivity of Individual Phytoplankton Species in Mixed Species Samples, Atlantic Estuarine Research Society, April 22–23, 1966, Morehead City, North Carolina.

R. J. Pickering, P. H. Carrigan, Jr., Tsuneo Tamura, H. H. Abee, J. W. Beverage, and R. W. Andrew
Radioactivity in Bottom Sediment of the Clinch and Tennessee Rivers, IAEA Symposium on the Disposal of Radioactive Wastes into Seas, Oceans, and Surface Waters, Vienna, Austria, May 16–20, 1966.

J. W. Poston
Physical Aspects of Seed Irradiations, Study Group on Coordination of Research on the Use of Neutrons in Seed Irradiation, July 25–29, 1966, Vienna, Austria.

D. E. Reichle
Cesium-134 Behavior and Energetics in Terrestrial Isopods, AIBS Meetings (Symposium on Bioenergetics of Animals), August 15–22, 1965, Urbana, Illinois.

The Behavior of Radiocesium During Insect Metamorphosis, ASB Meetings (Invertebrate Ecology and Radiobiology Section), April 14–16, 1966, Raleigh, North Carolina.

R. H. Ritchie
The Interaction of Low-Energy Electrons with Solids, Third International Congress of Radiation Research, June 26–July 2, 1966, Cortina, Italy.

R. H. Ritchie and J. Crowell
Ladder Corrections to the Static RPA Dielectric Constant, American Physical Society, Southeastern Section, November 1–3, 1965, Charlottesville, Virginia.

G. W. Royster, Jr., and B. R. Fish
Redispersion of Surface Dust in a Room, Tennessee Valley Industrial Health Conference, Gatlinburg, Tennessee, September 30–October 1, 1965.

W. F. Schaffer, Jr., W. J. Boegly, Jr., F. L. Parker, R. L. Bradshaw, F. M. Empson, and W. C. McClain
Project Salt Vault: Design and Demonstration of Equipment, International Symposium on the Solidification and Long-Term Storage of Highly Radioactive Wastes, Feburary 14–18, 1966, Richland, Washington.

H. C. Schweinler
A Course in Dimensional Analysis, American Physical Society, Southeastern Section, November 1–3, 1965, Charlottesville, Virginia.

W. S. Snyder
The Variation of Dose in Man from Unilateral Exposure to Gamma Rays, Tennessee Valley Industrial Health Conference, September 30 and October 1, 1965, Gatlinburg, Tennessee.

A Dose Estimate Based on Stable Isotope Data, Eleventh Bio-Assay and Analytical Chemistry Meeting, October 7–8, 1965, Albuquerque, New Mexico.

The Variation of Dose in Man from Exposure to a Point Source of Gamma Rays, International Conference on Radiological Protection in Industrial Uses of Radioisotopes, December 13–15, 1965, Paris, France.

The Standard Man in Relation to Internal Radiation Dose, American Industrial Hygiene Conference, May 16–20, 1966, Pittsburgh, Pennsylvania.

J. L. Stanford, E. T. Arakawa, and R. D. Birkhoff
Photoelectric and Optical Properties of Evaporated Ag Films in the Extreme Ultraviolet, American Physical Society, April 25–28, 1966, Washington, D.C.

E. G. Struxness, W. deLaguna, T. Tamura, H. W. Weeren, and R. C. Sexton
Ultimate Disposal of Intermediate-Level Liquid Waste in Bedded Shale by Hydraulic Fracturing, Health Physics Society, Tenth Annual Meeting, Los Angeles, California, June 14–17, 1965.[1]

---

[1]Omitted from *Health Phys. Div. Ann. Progr. Rept. July 31, 1965,* ORNL-3849.

T. Tamura and H. D. Waller
Sorption and Desorption of Radiocesium by Three Contrasting Soils, Annual Meeting of the American Society of Agronomy, November 1–4, 1965, Columbus, Ohio.

F. G. Taylor
Morphological Effects of Ionizing Radiation on Woody Species, Tennessee Academy of Science, December 10, 1965, Oak Ridge, Tennessee.

J. E. Turner
Theoretical Methods in the Dosimetry of High-Energy Particles, First AEC Symposium on Accelerator Radiation Dosimetry and Experience, Brookhaven National Laboratory, November 3–5, 1965, Upton, Long Island, New York.

J. E. Turner and K. Fox
On the Question of Bound States in a Dipole Field, American Physical Society, Southeastern Section, November 1–3, 1965, Charlottesville, Virginia.

J. E. Turner and H. Hollister
Quantum Theory of RBE. I. Velocity and Charge Dependence, Third International Congress of Radiation Research, June 26–July 2, 1966, Cortina, Italy.

G. M. Van Dyne
Recent Advances in Range Nutrition Research Techniques, Southern Section Annual Meeting, Amererican Society of Range Management, October 1965, Kissimmee, Florida.

The Optimum Site Problem – An Application and Integration of Multiple Linear Regression and Linear Programming Analyses, National Annual Meeting, American Society of Range Management, February 1966, New Orleans, Louisiana.

R. C. Vehse, E. T. Arakawa, and J. L. Stanford
Reflectance of Evaporated Al Films in the Wavelength Region 800 to 2000 A, American Physical Society, April 25–28, 1966, Washington, D.C.

J. L. Wilhm
Species Diversity of Benthic Macroinvertebrates in a Stream Receiving Domestic and Oil Refinery Effluents, AIBS Meetings (Ecology Section), August 15–20, 1965, Urbana, Illinois.

J. P. Witherspoon
Responses of Pinus strobus *to Acute Gamma Irradiation of Roots and Shoots,* AIBS Meetings, August 17, 1965, Urbana, Illinois.

Harvel Wright and J. Neufeld
Excitation of Hydromagnetic Waves by a Gyrating Proton Stream, American Physical Society, Division of Plasma Physics, November 8–11, 1965, San Francisco, California.

Publications

G. A. Andrews, J. A. Auxier, and C. C. Lushbaugh
"The Importance of Dosimetry to the Medical Management of Persons Accidentally Exposed to High Levels of Radiation," pp. 3–16 in *Personnel Dosimetry for Radiation Accidents,* IAEA, Vienna, 1965.

E. T. Arakawa and R. N. Hamm
Report of Trip Abroad by E. T. Arakawa and R. N. Hamm During the Period September 3–22, 1965, ORNL-CF-65-10-32 (Oct. 18, 1965).

E. T. Arakawa, R. N. Hamm, W. F. Hanson, and T. M. Jelinek
"Studies of Collective Electron Oscillations in Metals by Optical Methods," pp. 374–85 in *Proc. Intern. Colloquium on Optical Properties and Electronic Structure of Metals and Alloys, Paris, September 13–16, 1965,* North-Holland, Amsterdam, 1966.

E. T. Arakawa and J. C. Sutherland
"Optical Properties of Sodium in the Vacuum Ultraviolet," submitted for publication in the *Physical Review.*

J. C. Ashley, L. S. Cram, and E. T. Arakawa
"Photon Emission from Al Foils Bombarded by Non-Normally Incident Electrons," submitted for publication in the *Physical Review.*

S. I. Auerbach
"Radionuclide Cycling: Current Status and Current Needs," *Health Phys.* **11**, 1355 (1965).

Report on the International Symposium on Radioecological Concentration Processes and on a Visit to the Swedish Phytotron, ORNL-CF-66-5-72 (May 1966).

Leroy Augenstein, Edward Yeargers, James Carter, and DeVaughn Nelson
"Excitation, Dissipative and Emissive Mechanisms in Tryptophan," *Proceedings of Symposium on Space Biology, 1965, Berkeley, California* (in press).

J. A. Auxier
"Ichiban: The Dosimetry Program for Nuclear Bomb Survivors of Hiroshima and Nagasaki," pp. 121–26 in *Proceedings of the Symposium on Protective Structures for Civilian Populations,* Natl. Acad. Sci.–Natl. Res. Council, Washington, D.C., 1966.

"Physical Problems of Dosimetry of Neutrons and Protons," to be published in *Proceedings of Symposium on Accidental Irradiation at Place of Work, Euratom, Nice, France.*

Report of Trip Abroad by J. A. Auxier During Period April 24, 1966–May 1, 1966, ORNL-CF-66-5-54 (June 2, 1966).

J. A. Auxier, J. S. Cheka, F. F. Haywood, T. D. Jones, and J. H. Thorngate
"Free-Field Radiation-Dose Distributions from the Hiroshima and Nagasaki Bombings," *Health Phys.* **12**(3), 425–29 (1966).

R. E. Blanco and F. L. Parker
Waste Treatment and Disposal Semiannual Progress Report, July–December 1965, ORNL-TM-1465 (June 1966).

B. G. Blaylock
"Chromosomal Aberrations in a Natural Population of *Chironomus tentans* Exposed to Chronic Low-Level Radiation," *Evolution* **19**(3), 421–29 (1965).

"A Cytogenetic Study of a Natural Population of *Chironomus* Inhabiting an Area Contaminated by Radioactive Waste," to be published in *Proceedings of the IAEA Symposium on the Disposal of Radioactive Wastes into Seas, Oceans, and Surface Waters, Vienna, Austria, May 16–20, 1966* (in press).

"Chromosomal Polymorphism in Irradiated Natural Populations of *Chironomus,*" *Genetics* **53**(1), 131–36 (1966).

Report on Symposium on the Disposal of Radioactive Wastes into Seas, Oceans, and Surface Waters, Vienna, Austria, May 16–20, 1966, ORNL-CF-66-6-50 (June 1966).

W. J. Boegly, Jr., R. L. Bradshaw, F. M. Empson, W. F. Schaffer, Jr., F. L. Parker, and J. O. Blomeke
"Project Salt Vault: A Demonstration Disposal of High Level Radioactive Solids in Lyons, Kansas, Salt Mine," *Health Phys.* **12**, 417–24 (1966).

R. L. Bradshaw
"Management of Radioactive Waste" (book review), *Nucl. Appl.* **1**(5), 495–96 (October 1965).

R. L. Bradshaw, J. O. Blomeke, W. J. Boegly, Jr., F. M. Empson, F. L. Parker, J. J. Perona, and W. F. Schaffer, Jr.
"Disposal of High Activity Power Reactor Wastes in Salt Mines: A Concept and Field Scale Demonstration," *Nucl. Struct. Eng. (Amsterdam)* **2,** 438–46 (1965).

R. L. Bradshaw and W. C. McClain
Roof Bolt Test Analysis and Recommendations, ORNL-CF-66-4-66.

G. N. Brown and F. G. Taylor
"Interaction of Radiation and Photoperiodism in *Xanthium chinense,*" *Radiation Botany* **6,** 145 (1966).

J. G. Carter, T. M. Jelinek, R. N. Hamm, and R. D. Birkhoff
"Optical Properties of Polystyrene in the Vacuum Ultraviolet," *J. Chem. Phys.* **44,** 2266–69 (1966).

J. G. Carter, D. R. Nelson, and L. G. Augenstein
"The Effect of Temperature on X-Ray Induced Light Emission from Powders of Amino Acids and Trypsin," *Arch. Biochem. Biophys.* **3,** 270–82 (1965).

J. S. Cheka
Report of Trip Abroad by J. S. Cheka During Period February 10, 1966–April 8, 1966, ORNL-CF-66-5-31 (May 13, 1966).

J. S. Cheka, F. W. Sanders, T. D. Jones, and W. H. Shinpaugh
Distribution of Weapons Radiation in Japanese Residential Structures, CEX-62.11 (August 1965).

L. G. Christophorou and J. G. Carter
"Excimer X-Ray Investigation," *Nature* **209,** 678–80 (1966).

"Improved Organic Scintillators in 2-Ethyl Naphthalene; the Role of Excimers," submitted for publication in the *Physical Review.*

L. G. Christophorou, R. N. Compton, G. S. Hurst, and P. W. Reinhardt
"The Determination of Electron Capture Cross Sections with Swarm-Beam Techniques," *J. Chem. Phys.* **43,** 4273–81 (1965).

"Interactions of Low-Energy Electrons with Benzene Derivatives," *J. Chem. Phys.* (in press).

L. G. Christophorou, G. S. Hurst, and A. Hadjiantoniou
"Interaction of Thermal Electrons with Polarizable and Polar Molecules," *J. Chem. Phys.* **44,** 3506–13 (1966).

L. G. Christophorou, G. S. Hurst, and W. G. Hendrick
"Swarm Determination of the Cross Section for Momentum Transfer in Ethylene and in Ethylene Mixtures," *J. Chem. Phys.* (in press).

R. N. Compton, L. G. Christophorou, G. S. Hurst, and P. W. Reinhardt
"Nondissociative Electron Capture and Negative Ion Lifetimes for Complex Molecules," submitted for publication in the *Journal of Chemical Physics.*

R. N. Compton and P. W. Reinhardt
"Excitation of He, N_2, H_2O, and D_2O by Electron Impact," submitted for publication in the *Journal of Chemical Physics.*

G. E. Cosgrove and T. P. O'Farrell
"Papillomas and Other Lesions in the Stomachs of Pine Mice," *J. Mammal.* **46,** 510 (1965).

K. E. Cowser and W. S. Snyder
Safety Analysis of Radionuclide Release to the Clinch River, ORNL-3721, suppl. 3 (May 1966).

L. S. Cram and E. T. Arakawa
"Investigation of the 'Surface Plasma' Radiation from Electron-Bombarded Ag," submitted for publication in the *Physical Review.*

D. A. Crossley, Jr.
"Radioisotope Measurement of Food Consumption by a Leaf Beetle Species, *Chrysomela knabi* Brown," *Ecology* **47**(1), 1–8 (Winter 1966).

D. A. Crossley, Jr., and M. Witkamp
"Effects of Pesticide on Biota and Breakdown of Forest Litter," Transactions of 8th International Congress of Soil Science in Bucharest, vol. III (in press).

Julian Crowell, V. E. Anderson, and R. H. Ritchie
"Ladder Corrections to the Static RPA Dielectric Constant and to Positron Annihilation in Metals," to be published in the *Physical Review*.

J. W. Curlin
Forest Management Plan, AEC Oak Ridge Reservation, ORNL-TM-1317 (September 1965).

D. R. Davy
"Personnel Dosimetry for Radiation Accidents" (book review), to be published in *Health Physics*.

"Prediction of Biological Damage from Stopping-Power Theory," to be published in *Health Physics*.

D. R. Davy and L. H. Peshori
"An Absolute Neutron Dosimeter Based on a Generalized Concept for Radiation Dosimetry," to be published in *Health Physics*.

D. R. Davy, L. H. Peshori, and J. W. Poston
"Sodium-24 Production in Saline-Filled Phantoms Under Neutron Irradiations," to be published in *Health Physics*.

Wallace de Laguna
Chemical Quality of Water, Brookhaven National Laboratory and Vicinity, Suffolk County, New York, U.S. Geological Survey Bulletin 1156-D, U.S. Government Printing Office, Washington, D.C., 1964.

"Disposal of Radioactive Wastes by Hydraulic Fracturing: Part I, General Concept and First Field Experiments," *Nucl. Struct. Eng. (Amsterdam)* **3**(2), 338–52 (1966).

"Disposal of Radioactive Wastes by Hydraulic Fracturing: Part II, Mechanics of Fracture Formation and Design of Observation and Monitoring Wells," *Nucl. Struct. Eng. (Amsterdam)* **3**(3), 432–38 (1966).

A Hydrologic Analysis of Postulated Liquid-Waste Releases, Brookhaven National Laboratory, Suffolk County, New York, U.S. Geological Survey Bulletin 1156-E, U.S. Government Printing Office, Washington, D.C., 1966.

"Management of Radioactive Wastes" (book review), *Health Phys.* **12**(1), 109 (January 1966).

P. B. Dunaway and G. E. Cosgrove
"Skin Carcinoma in a Cotton Rat," *Am. Midland Naturalist* **75**, 535 (1966).

P. B. Dunaway, J. A. Payne, L. L. Lewis, and J. D. Story
"Effects of *Cuterebra angustrifrons* Infesting *Peromyscus leucopus* in Tennessee," in press.

F. M. Empson, W. J. Boegly, Jr., R. L. Bradshaw, W. C. McClain, F. L. Parker, W. F. Schaffer, Jr.
"Demonstration of Disposal of High-Level Radioactive Solids in Salt," *Proceedings of Second Symposium on Salt, Cleveland, Ohio, May 3–5, 1965* (in press).

H. G. Fisser and G. M. Van Dyne
"Effect of Variation in Number and Spacing of Points on Accuracy and Precision of Estimates of Basal Cover of Foothill Grassland," *J. Range Management* **19**, 205–11 (1966).

B. R. Fish
Trip Report – Second International Symposium on Inhaled Particles and Vapours, Cambridge, England, September 28–October 1, 1965, ORNL-CF-65-12-85 (Dec. 27, 1965).

B. R. Fish and R. L. Walker
"Aerosol Physics of Radioactive Particles," *Proceedings of International Symposium on Fission Product Release and Transport Under Accident Conditions, Oak Ridge, Tennessee, April 5–7, 1965,* vol. I, CONF-650407.

B. R. Fish, T. G. Clark, R. H. Boyett, W. H. Wilkie, Jr., W. C. McWhorter, and J. L. Thompson
Environmental Studies: Radiological Significance of Nuclear Rocket Debris, Semi-Annual Progress Report for Period January 1–June 30, 1965, ORNL-TM-1159 (January 1966).

Kenneth Fox
"Reduced Matrix Element of an Irreducible Spherical Tensor Operator – New Derivation and Applications," *J. Mol. Spectry.* **17,** 247–51 (1965).

"Theory of Vibration-Rotation Interactions in Spherical Top Molecules. I. A New Overtone Band," *J. Mol. Spectry.* **16,** 35–55 (1965).

"Theory of Vibration-Rotation Interactions in Spherical Top Molecules. I. A New Overtone Band," (Proceedings of International Symposium on Atomic and Molecular Quantum Theory, January 18–23, 1965, Sanibel Island, Florida), *J. Chem. Phys.* **43,** S25–S26 (1965).

Kenneth Fox and J. E. Turner
"Variational Calculation for Bound States in an Electric Dipole Field," *J. Chem. Phys.* (in press).

"WKB Treatment of Bound States in an Electric Dipole Potential," *Am. J. Phys.* (in press).

R. N. Hamm, R. A. MacRae, and E. T. Arakawa
"Polarization Studies in the Vacuum Ultraviolet," *J. Opt. Soc. Am.* **55,** 1460–63 (1965).

W. F. Hanson and E. T. Arakawa
"Reflectivities of Concave Diffraction Gratings for Polarized Light in the Vacuum Ultraviolet," *J. Opt. Soc. Am.* **56,** 124–25 (1966).

F. F. Haywood, T. G. Provenzano, and J. A. Auxier (eds.)
Operations Plan – Operation HENRE (prepared by Operation HENRE Technical Director's Staff), CEX-65.03 (September 1965).

W. R. Hendee and J. L. Ellis
"Scattering of Gamma Radiation from Semi-Infinite Slabs," *Health Phys.* **12,** 673–81 (1966).

R. J. Herickhoff, W. F. Hanson, E. T. Arakawa, and R. D. Birkhoff
"The Angular Distribution and Thickness Dependence of Transition Radiation from Thin Al Foils," *Phys. Rev.* **139,** A1455–58 (1965).

H. Hollister and J. E. Turner
"The Possible Role of Momentum in Radiation Dosimetry. III. Remarks on the 1962 ICRP/ICRU Report," to be published in *Health Physics.*

H. H. Hubbell, Jr., E. T. Arakawa, Shogo Nagaoka, Shoichi Ueda, and Sunao Tanaka
"The Burst Points of the Atomic Bombs in Japan. Part I. A Redetermination for Nagasaki from Shadows on Stones," to be published as an ABCC Technical Report.

G. S. Hurst and J. E. Parks
"Time-of-Flight Determinations of Electron Diffusion Coefficients and Electron Drift Velocities in Ethylene and in Water Vapor," *J. Chem. Phys.* (in press).

D. G. Jacobs
"Use of Negative Sorption in Studies of Ion Fixation by Hydrobiotite," *Clays and Clay Minerals, Proceedings of the 13th National Conference, Madison, Wisconsin, October 5–8, 1964,* Pergamon, New York (1965).

"Negative Sorption by Alumino-Silicates Having a Limited Degree of Lattice Expansion," *Proc. Intern. Clay Conf.* **1,** 319–29 (1966).

T. M. Jelinek, R. N. Hamm, E. T. Arakawa, and R. H. Huebner
"The Optical Constants of Vacuum Evaporated Films of Cd and Tl in the Vacuum Ultraviolet," *J. Opt. Soc. Am.* **56**, 185–88 (1966).

D. R. Johnson
"Neutron Dose Conversion Factors for AmBe and AmB Sources," *Health Phys.* **12**, 856–57 (1966).

D. R. Johnson, J. H. Thorngate, P. W. Reinhardt, and F. J. Davis
"An Experimental Calibration of Fission Foil Threshold Detectors," *Health Phys.* **11**, 759–62 (1965).

G. E. Jones, L. S. Cram, and E. T. Arakawa
"Radiation from Thick Silver Foils Bombarded by Grazing-Incident Electrons," submitted for publication in the *Physical Review*.

K. Katoh and J. E. Turner
"A Study of Elementary Particle Interactions for High-Energy Dosimetry," submitted for publication in *Health Physics*.

G. D. Kerr and T. D. Strickler
"The Application of Solid-State Nuclear Track Detectors to the Hurst Threshold Detector System," to be published in *Health Physics*.

C. E. Klots
"Energy Partition Parameters in Radiation Studies of Molecular Gases," *J. Chem. Phys.* **44**, 2715–18 (1966).

C. E. Klots and V. E. Anderson
"Finite Medium Effects in Gas Phase Radiation Chemistry," submitted for publication in the *Journal of Physical Chemistry*.

L. L. Lewis and P. B. Dunaway
Techniques for Hematological Studies of Wild Mammals, ORNL-3806 (June 1965).

T. F. Lomenick and T. Tamura
"Naturally Occurring Fixation of Cesium-137 on Sediments of Lacustrine Origin," *Soil Sci. Soc. Am. Proc.* **29**(4), 383–87 (1965).

T. F. Lomenick and H. J. Wyrick
Geohydrological Evaluation of Solid Waste Storage Area 6, ORNL-TM-1327 (December 1965).

C. A. Mawson and K. E. Cowser
"Review of Health Physics Society Papers on Environmental Monitoring, Hazards, Analysis, and Waste Disposal," *Nucl. Safety* **7**(3) (Spring 1966).

W. J. McConnell, H. H. Hubbell, Jr., and R. D. Birkhoff
"Slowing Down Spectrum of Au-198 Beta Rays in Gold," *Health Phys.* **12**, 693–98 (1966).

W. C. McClain
Surface Uplifts Associated with the Hydraulic Fracturing Disposal Techniques, ORNL-CF-66-5-48.

"Time-Dependent Behavior of Pillars in the Alsace Potash Mines," pp. 489–500 in *Proceedings of the 6th Symposium on Rock Mechanics, October 1964, University of Missouri at Rolla* (1964).

K. Z. Morgan
"Graduate Programs for the Health Physicist in the United States," *Health Phys.* **11**, 895–915 (1965).

P. E. Morrow (Chairman), D. V. Bates, B. R. Fish, T. F. Hatch, and T. T. Mercer
"Deposition and Retention Models for Internal Dosimetry of the Human Respiratory Tract" (report prepared for Committee II of the International Commission on Radiological Protection, and reviewed by the Committee on 20 April 1965), *Health Phys.* **12**(2), 173–207 (February 1966).

R. J. Morton (ed.)
Status Report No. 5 on Clinch River Study, ORNL-3721 (October 1965).

Y. Nakai, F. W. Garber, R. H. Ritchie, and R. D. Birkhoff
"Electronic Energy Levels in Aluminum – A Solid State Franck and Hertz Experiment," *J. Phys. Chem. Solids* **26,** 1621–22 (1965).

D. J. Nelson
Book review, *"Ecology and the Industrial Society," Health Phys.* (in press).

"Microchemical Constituents in Contemporary and Pre-Columbian Clam Shell," *Quaternary Paleoecology,* Yale University Press, New Haven (in press).

"Prediction of ^{90}Sr Uptake in Fish," *Bull. Ecol. Soc. Am.* **46,** 101 (1965) (abstract).

"The Prediction of ^{90}Sr Uptake in Fish Using Data on Specific Activities and Biological Half-Lives," *Proc. Intern. Symp. Radioecological Concentration Processes,* Pergamon, New York (in press).

"Report on International Symposium on Radioecological Concentration Processes," Stockholm, Sweden, 25–29 April 1966, ORNL-CF-66-5-69 (May 1966).

"Strontium in Calcite: New Analyses," *Inst. Marine Sci.* (University of Texas) **10,** 76–79 (1965).

D. J. Nelson, N. R. Kevern, J. L. Wilhm, and N. A. Griffith
"Estimates of Periphyton Mass and Stream Bottom Area Using Phosphorus-32," *Limnology and Oceanography* (submitted).

D. J. Nelson, T. C. Rains, and J. A. Norris
"High Purity Calcium Carbonate in Freshwater Clam Shell," *Science* **152**(3727), 1368–70 (1966).

D. J. Nelson (with G. M. Rosenthal and D. A. Gardiner)
"Deposition of Strontium and Calcium in Snail Shell," *Nature* **207**(4992), 51–54 (1965).

J. Neufeld
Report of Trip Abroad by J. Neufeld During the Period September 5–21, 1965, ORNL-CF-65-11-6 (Nov. 3, 1965).

J. Neufeld, W. S. Snyder, J. E. Turner, and Harvel Wright
"Calculation of Radiation Dose from Protons and Neutrons to 400 MeV," *Health Phys.* **12,** 227–37 (1966).

Jacob Neufeld and C. L. Wiginton
"Cyclotron Excitation of Electromagnetic Waves by a Gyrating Electron Beam," *Phys. Rev.* (in press).

Jacob Neufeld and Harvel Wright
"Comments on Paper by John M. Cornwall on 'Cyclotron Instabilities and Electromagnetic Emission in the Ultra Low Frequency and Very Low Frequency Ranges,'" *J. Geophys. Res.* (in press).

"Excitation of Hydromagnetic Waves by a Gyrating Proton Stream," *Phys. Fluids* **8,** 2281–87 (1965).

"Instabilities Produced in a Plasma by a Helical Proton Beam," *Phys. Rev.* **141,** 211–16 (1966).

T. P. O'Farrell
"Home Range and Ecology of Snowshoe Hares in Interior Alaska," *J. Mammal.* **46,** 406 (1965).

"The Rabbits of Middleton Island, Alaska," *J. Mammal.* **46,** 525 (1965).

J. S. Olson
"Equation for Cesium Transfer in a Liriodendron Forest," *Health Phys.* **11**(12), 1385–92 (1965).

"Progress in Radiation Ecology: Radionuclide Movement in Major Environments," *Nucl. Safety* **8**(1) (1966) (in press).

"Use of Tracer Techniques for the Study of Biogeochemical Cycles," *Proc. First Intern. Symp. Ecosystems, Copenhagen,* UNESCO, Paris (in press).

J. S. Olson, G. Cristofolini, and S. Cristofolini

Oak Ridge, Tennessee, Flora: 1. Preliminary Alphabetic Inventory of Vascular Plants, ORNL-TM-1232 (March 1966).

F. L. Parker

(Book review) "*Management of Radioactive Wastes* by C. A. Mawson," *Nucl. Sci. Eng.* 310–11 (July 1966).

Proposed Revision of ORNL Policy for Treatment and Disposal of Intermediate- and Low-Level Wastes, ORNL-CF-65-11-56.

Treatment of Reactor Pool Water, report to the Government of Pakistan, TA Report No. 255, International Atomic Energy Agency (June 1, 1966).

"United States and Soviet Union Waste-Disposal Standards," *Nucl. Safety* **6**(4), 433–36 (1965).

B. C. Patten

"The Biocoenetic Process in an Estuarine Phytoplankton Community," ORNL-3946 (in press).

"Equilibrium Specific Activity Relationships in Two-Compartment Exchange Systems," *Health Phys.* **12**, 521–24 (1966).

"Systems Ecology: A Course Sequence in Mathematical Ecology," *BioSci* (in press).

"Vertical Distribution and Sinking Characteristics of Seston in the Lower York River," *Chesapeake Sci.* **7**, 20–29 (1966).

B. C. Patten (with R. L. Iverson)

"Photosynthesis and 85-Sr Uptake in Freshwater Plankton," *Nature* (in press).

J. A. Payne

"A Summer Carrion Study of the Baby Pig, *Sus scrofa* Linnaeus," *Ecology* **46**, 592–602 (1965).

J. A. Payne and G. E. Cosgrove

"Tissue Changes Following *Cuterebra* Infestation in Rodents," *Am. Midland Naturalist* **75**, 205–13 (1966).

J. A. Payne and D. A. Crossley, Jr.

Animal Species Associated with Pig Carrion, ORNL-TM-1432 (April 1966).

J. A. Payne, P. B. Dunaway, G. D. Martin, and J. D. Story

"Effects of *Cuterebra angustifrons* on Plasma Proteins of *Peromyscus leucopus,*" J. Parasitol. **51**, 1004–8 (1965).

P. T. Perdue

"Inexpensive Liquid Nitrogen Level Control for Cold Traps," to be published in *Nuclear Instruments and Methods.*

R. J. Pickering, P. H. Carrigan, Jr., and F. L. Parker

The Clinch River Study – An Investigation of the Fate of Radionuclides Released to a Surface Stream (prepared in cooperation with Oak Ridge National Laboratory and the U.S. Atomic Energy Commission), Geological Survey Circular 497, Washington, D.C., 1965.

T. G. Provenzano, E. J. Story, F. F. Haywood, and H. T. Miller

Feasibility Study: Intense 14-MeV Neutron Source for Operation HENRE, CEX-65.01 (May 1966).

D. E. Reichle

"Bryophyte Succession in a Northern Illinois Bog," *The Bryologist* **68**(4), 463–70 (1965).

"The Temperature and Humidity Relations of Some Bog Pselaphid Beetles," *Ecology* (in press).

D. E. Reichle and D. A. Crossley, Jr.

"Investigations on Heterotrophic Productivity in Forest Insect Communities," Working Meeting on Principles and Methods of Secondary Productivity of Terrestrial Ecosystems (in press).

"Radiocesium Dispersion in a Cryptozoan Food Web," *Health Phys.* **11**(12), 1375–84 (1965).

D. E. Reichle, J. D. Palmer, and O. Park
"Persistent Rhythmic Locomotor Behavior in the Cave Cricket, *Hadenoecus subterraneus,* and Its Ecological Significance," *Am. Midland Naturalist* **74**(1), 57–66 (1965).

R. H. Ritchie
"Coupled Electron Hole Cascade in a Free Electron Gas," *J. Appl. Phys.* **37,** 2276 (1966).

"Photon Excitation of Surface Plasmons," *Surface Sci.* **3,** 497–99 (1965).

R. H. Ritchie and V. E. Anderson
"The Use of Fourier Transforms in the Unfolding of Experimental Data," submitted for publication in *Nuclear Instruments and Methods.*

R. H. Ritchie and J. C. Ashley
"The Interaction of Hot Electrons with a Free Electron Gas," *J. Phys. Chem. Solids* **26,** 1689–94 (1965).

R. H. Ritchie and A. L. Marusak
"The Surface Plasmon Dispersion Relation for an Electron Gas," *Surface Sci.* **4,** 234–40 (1966).

R. H. Ritchie, M. Y. Nakai, and R. D. Birkhoff
"Low-Energy Electron Mean Free Paths in Solids," to be published in *Advances in Radiobiology,* vol. 3.

A. S. Rogowski and T. Tamura
"Movement of ^{137}Cs by Runoff, Erosion, and Infiltration on the Alluvial Captina Silt Loam, *Health Phys.* **11,** 1333–40 (December 1965).

G. W. Royster, Jr., and B. R. Fish
"Redispersion of Surface Dust in a Room," *Proceedings of Fourth Annual Technical Meeting and Exhibit, American Association for Contamination Control, Miami Beach, Florida, May 25–28, 1965;* and ORNL-TM-1209 (Aug. 2, 1965).

W. S. Snyder
"A Review of Recent FRC and NCRP Publications," *Nucl. Safety* **6**(4), 368 (1965).

"A Review of FRC Report No. 7 on Protective Action Guides for Strontium-89, Strontium-90, and Cesium-137," *Nucl. Safety* (in press).

J. L. Stanford, R. N. Hamm, and E. T. Arakawa
"Effect of Photon Refraction on Angular Dependence of Photoelectric Yields in the Wavelength Region 300 A to 1200 A," *J. Opt. Soc. Am.* **56,** 124 (1966).

E. G. Struxness
Clinch River Study Steering Committee (E. G. Struxness, chairman), Subcommittee on Water Sampling and Analysis (M. A. Churchill, chairman, J. S. Cragwall, Jr., R. W. Andrew, and S. Leary Jones), *Concentrations, Total Stream Loads, and Mass Transport of Radionuclides in the Clinch and Tennessee Rivers,* supplement No. 1 to *Status Report No. 5 on Clinch River Study* (R. J. Morton, ed.), ORNL-3721 (August 1965).

(Book review) "*Handling and Disposal of Radioactive Materials in Hospitals and Medical Research Establishments,* ICRP Publication No. 5; Report of Committee V; 1964." For publication in *Nuclear Safety,* 1966.

(Book review) "*Low-Level Radioactive Wastes: Their Handling, Treatment, and Disposal,* by Conrad P. Straub, 1964." To be published in *Health Phys,* 1966.

(Abstract) "Ultimate Disposal of Intermediate-Level Liquid Waste in Bedded Shale by Hydraulic Fracturing," E. G. Struxness, W. de Laguna, T. Tamura, and H. O. Weeren, *Health Phys.* **11**(8), 819 (August 1965).

(Abstract) book review, "*Handling and Disposal of Radioactive Materials in Hospitals and Medical Research Establishments,* ICRP Publication No. 5; Committee V." To be published in *Nuclear Safety,* 1966.

(Book review) "*Principles of Environmental Monitoring Related to Handling of Radioactive Materials,* ICRP Publication 7; Report of Committee 4 of ICRP, 1966." To be published in *Nuclear Safety,* 1966.

Tsuneo Tamura

"Development and Applications of Minerals in Radioactive Waste Disposal," *Proc. Intern. Clay Conf.* **1**, 425–39 (1966).

"Selective Sorption Reactions of Strontium with Soil Minerals," *Nucl. Safety* **7**, 99–103 (1965).

F. G. Taylor, Jr.

"Predicted Seasonal Radiosensitivity of Southeastern Tree Species," *Radiation Botany* (in press).

"Supernumerary Incisors in *Lynx rufus* Schreber," *J. Mammal.* **46**, 507 (1965).

J. H. Thorngate

An Interval Timer Designed for Use During Irradiations at the Health Physics Research Reactor, ORNL-TM-1559 (in press).

J. H. Thorngate and E. T. Loy

Post Pulse Gamma-Radiation Spectrum – Operation BREN, CEX-62.13 (June 1966).

J. H. Thorngate and J. E. Parks

"A Portable Scaler," *Health Phys.* **12**(3), 385–94 (1966).

J. H. Thorngate, D. R. Johnson, and P. T. Perdue

Neutron and Gamma-Ray Leakage from the Ichiban Critical Assembly, CEX-64.7 (June 1966).

I. H. Tipton, Peggy L. Stewart, and Polly G. Martin

"Trace Elements in Diets and Excreta," *Health Phys.* (in press).

J. E. Turner

"Book review of *Kernkrafte: Einfuhrung in die theoretische Kernphysik,* von G. Elder. G. Braun, Germany, 1965, 342 pp.," *Health Phys.* **12**, 723 (May 1966).

(Book review) "*Personnel Dosimetry for Radiation Accidents,*" *J. Nucl. Sci. Eng.* **25**, 310 (1966).

"Electron Capture by Rotational Excitation of Polar Molecules," *Phys. Rev.* **141**, 21–26 (1966).

"The Possible Role of Momentum in Radiation Dosimetry. II. Extension to Charged Particles and Further General Considerations," *Health Phys.* **11**, 1163–75 (1965).

J. E. Turner and Kenneth Fox

On the Bound States of an Electron in the Field of a Permanent Electric Dipole, ORNL-3895 (December 1965).

J. E. Turner and Hal Hollister

"Relationship of Collision Theory to the Interpretation of Relative Biological Effectiveness," submitted for publication in *Nature.*

"On the Relationship of the Velocity of a Charged Particle to Its Relative Biological Effectiveness (RBE)," *Nature* **208**, 36–37 (1965).

V. R. Rao Uppuluri, L. R. Shenton, and S. R. Bernard

Stochastic Models for the Distribution of Radioactive Material in a Connected System of Compartments, ORNL-3809 (1965).

G. M. Van Dyne

"Application of Some Operations Research Techniques to Food Chain Analysis Problems," *Health Phys.* **11**(12), 1511–19 (1965).

"Chemical Composition and Digestibility of Range Plants from Annual Range and from Pure-Stand Plots," *J. Range Management* **18**(6), 332–37 (1965).

Chemical Composition of Individual Range Plants from the U.S. Range Station, Miles City, Montana, from 1955–1960, ORNL-TM-1279 (September 1965).

Regress – a Multiple Regression and Correlation Program with Graphic Output for Model Evaluation, ORNL-TM-1288 (December 1965).

Data on Chemical and Botanical Composition of Dietary Samples Grazed by Cattle and Sheep, ORNL-TM-1376 (March 1966).

Ecosystems, Systems Ecology, and Systems Ecologists, ORNL-3957 (June 1966).

"Use of a Vacuum-Clipper for Harvesting Herbage," *Ecology* (in press).

G. M. Van Dyne and H. F. Heady
"Botanical Composition of Sheep and Cattle Diets on a Mature Annual Range," *Hilgardia* **36**(13), 465–92 (1965).

G. M. Van Dyne and I. Thorsteinsson
"Intraseasonal Changes in Height Growth Rate of Range Plants in Response to Nitrogen and Phosphorus," *Proc. Xth. Intern. Grassland Congr.* (in press).

W. G. Vogel and G. M. Van Dyne
"Vegetation Responses to Grazing on a Central Montana Foothill Sheep Range," *J. Range Management* **19**(2), 80–85 (1966).

R. L. Walker and B. R. Fish
"Adhesion of Particles to Surfaces in Liquid and Gaseous Environments," *Proceedings of Fourth Annual Technical Meeting and Exhibit, American Association for Contamination Control, Miami Beach, Florida, May 25–28, 1965;* and ORNL-TM-1228 (Aug. 30, 1965).

J. L. Wilhm
"Species Diversity of Benthic Macroinvertebrates in a Stream Receiving Domestic Refinery Effluents," *Am. Midland Naturalist* (in press).

J. P. Witherspoon
"Radiation Damage to Forest Surrounding an Unshielded Fast Reactor," *Health Phys.* **11**, 1637 (1965).

J. P. Witherspoon and G. N. Brown
"Translocation of Cesium-137 from Parent Trees to Seedlings of *Liriodendron tulipifera,*" *Botan. Gaz.* **126**(3), 181 (1965).

Martin Witkamp
"Decomposition of Leaf Litter in Relation to Environmental Conditions, Microflora, and Microbial Respiration," *Ecology* **47**, 194–201 (1966).

"Environmental Influences on Microbial Populations and Activity of the Forest Floor," Transactions of 8th International Congress of Soil Science in Bucharest, vol. III (in press).

"Macroflora, Mycoflora, and Soil Relationships in a Pine Plantation," *Ecology* **47**, 238–44 (1966).

"Rates of Carbon Dioxide Evolution from the Forest Floor; Measurement, Environmental Effects, and Relation to CO_2 from Litter," *Ecology* **47**(3) (1966) (in press).

Harvel Wright, C. L. Wiginton, and J. Neufeld
"Almost Longitudinal Instabilities in a Plasma-Beam System," *Phys. Fluids* **8**, 1375–84 (1965).

Lectures

J. C. Ashley
Effective Mass of Positrons in a Free Electron Gas, Department of Physics, University of Tennessee, April 4, 1966, Knoxville.

S. I. Auerbach

Radiation Ecology, Radiation Biology Conference, Oak Ridge Associated Universities, August 3, 1966, Oak Ridge, Tennessee.

Ecology and Ecological Research at ORNL, ORAU Nuclear Science Seminar (Navy), August 1965, Oak Ridge, Tennessee.

J. A. Auxier

The Health Physics Research Reactor and Its Role at the DOSAR Facility, University of Illinois, May 24, 1966, Urbana.

Radiation Dosimetry, 102d Session of Basic Research Course, ORINS, October 18, 1965, Oak Ridge, Tennessee.

S. R. Bernard

Work in the Information Center for Internal Exposure, Monthly Luncheon Meeting of Information Centers, April 1966, Alexander Hotel, Oak Ridge, Tennessee.

R. D. Birkhoff

Generation and Slowing Down of Electrons in Irradiated Media, Pfeiffer College, November 17, 1965, Misenheimer, North Carolina; Davidson College, November 18, 1965, Davidson, North Carolina.

Evidence for the Existence of Plasmons in Solids, Catawba College, November 18, 1965, Salisbury, North Carolina.

B. G. Blaylock

Chromosomal Aberrations in Natural Populations Exposed to Chronic Low-Level Radiation, Radioecology Institute, ORINS, July 6, 1965, Oak Ridge, Tennessee.

Cytogenetic Effects of Chronic Environmental Radiation on a Natural Population of Chironomidae, Department of Biology, University of Notre Dame, Notre Dame, Indiana, December 7, 1965; Department of Biology, West Virginia University, Morgantown, West Virginia.

R. L. Bradshaw

Salt Studies, University of Arkansas Radiological Health Faculty and Students, Oak Ridge National Laboratory, April 21, 1966, Oak Ridge, Tennessee.

J. G. Carter

Graduate Fellowships in Health Physics; Research Conducted in the Health Physics Division at the Oak Ridge National Laboratory, Department of Physics, Murray State College, November 23, 1965, Murray, Kentucky.

J. S. Cheka

Luminescence Dosimetry, ORINS-ORNL Ten-Week Health Physics Course, ORINS, September 24, 1965, Oak Ridge, Tennessee.

R. N. Compton

Electron Capture Cross Sections and Negative Ion Lifetimes, Department of Physics, University of Tennessee, March 3, 1966, Knoxville.

K. E. Cowser

Clinch River Safety Analysis, University of Arkansas Radiological Health Faculty and Students, Oak Ridge National Laboratory, April 21, 1966, Oak Ridge, Tennessee.

D. A. Crossley, Jr.

Radioisotope Accumulation by Predaceous Arthropods, Zoology Seminar, May 24, 1966, University of Tennessee, Knoxville.

L. C. Emerson

Radiation Physics Research at ORNL; the AEC Special Fellowship Program in Health Physics, Furman University, November 11, 1965, Greenville, South Carolina; Wofford and Converse Colleges, November 12, 1965, Spartanburg, South Carolina; The Citadel, November 19, 1965, Charleston, South Carolina.

The Determination of the Optical Properties of Solids, Department of Physics, University of Tennessee, February 28, 1966, Knoxville.

Radioactivity and Radioactive Decay, Health Physics Society, East Tennessee Chapter Educational Lecture, ORINS Medical Division, March 24, 1966, Oak Ridge, Tennessee.

B. R. Fish

Radioactivity in Man, ORINS-ORNL Ten-Week Health Physics Course, October 19, 1965.

W. R. Garrett

Elastic Electron Scattering from Atoms, Department of Physics, University of Tennessee, May 16, 1966, Knoxville.

R. N. Hamm

Dielectric Constants and Energy Losses in Solids, Department of Physics, University of Tennessee, February 23, 1966, Knoxville.

G. S. Hurst

Scope of ORNL-HP Division's Radiation Physics Program, Southern Missionary College, January 11, 1966, Collegedale, Tennessee.

D. G. Jacobs

Tank Safety Studies, University of Arkansas Radiological Health Faculty and Students; Oak Ridge National Laboratory, April 12, 1966, Oak Ridge, Tennessee.

Waste Disposal Practices and Research, Oak Ridge Naval Reserve, October 13, 1965, Oak Ridge, Tennessee.

D. R. Johnson

Radiobiological Dosimetry of External Radiation Sources, Summer Institute in Radiation Botany, UT-AEC Agricultural Research Laboratory, July 18, 1966, Oak Ridge, Tennessee.

N. R. Kevern

Feeding Rate of Carp Estimated by a Radioisotopic Method, Department of Fisheries and Wildlife, Michigan State University, March 11, 1966, East Lansing.

T. F. Lomenick

Disposal of High-Level Wastes in Subterranean Salt Deposits, AEC Fellowship Program, Oak Ridge National Laboratory, June 15, 1966, Oak Ridge, Tennessee.

The Nature and Origin of Radioactive Wastes, AEC Fellowship Program, Oak Ridge National Laboratory, June 15, 1966, Oak Ridge, Tennessee.

Solid Waste Disposal, Southern Interstate Nuclear Board Briefing on Waste Disposal, Oak Ridge National Laboratory, August 18–19, 1965, Oak Ridge, Tennessee.

W. J. McConnell

Opportunities for Graduate Study Under the Health Physics Fellowship Program, Cornell College, October 19, 1965, Mt. Vernon, Iowa; Coe College, October 21, 1965, Cedar Rapids, Iowa.

K. Z. Morgan

Maximum Permissible Exposure, Lenoir Rhyne College, Hickory, North Carolina, November 4, 1965; Rutgers University, New Brunswick, New Jersey, November 10, 1965.

Current Concept of MPD, University of Tennessee–AEC Agricultural Experiment Station, Oak Ridge, Tennessee, November 17, 1965.

History of Health Physics, ORINS Banquet, Oak Ridge, Tennessee, November 17, 1965.

Health Physics – a New Science and a Challenging Profession, Howard College, Birmingham, Alabama, November 23, 1965; Bethany Nazarene College, Bethany, Oklahoma, March 8, 1966; Central State College, Edmond, Oklahoma, March 9, 1966; Maryville College, Maryville, Tennessee, April 1, 1966.

Report to the ORNL Research Committee, ORNL Research Committee, X-10, dining room, December 1, 1965.

Permissible Exposure to Ionizing Radiation, Purdue University, Lafayette, Indiana, January 12, 1966.

The Calculations of Maximum Permissible Concentrations of Radionuclides in Food, Air, and Water, University of Missouri, Columbia, January 14, 1966.

Health Physics Lecture Course, University of Tennessee AEC Fellowship Students, January 18, 19, 21, 26, and February 2, 4, 1966; Vanderbilt University AEC Fellowship Students, March 21, 22, 28, 29, and April 4, 5, 1966.

Health Physics, Atlanta Chapter of Health Physics Society, Atlanta, Georgia, April 19, 1966.

An Introduction to Internal Dose Problems, Visiting Radiological Health Students from the University of Arkansas, ORNL Conference Room 3504, April 21, 1966.

New Recommendations of the ICRP, NCRP, and FRC, Health Physics Society Annual Meeting, Refresher Course, Houston, Texas, June 27, 1966.

Health Physics Program, U.S. Army Nuclear Science Seminar, Oak Ridge Playhouse, Oak Ridge, Tennessee, July 19, 1966.

D. J. Nelson

The Importance of Specific Activity in Problems of Environmental Radioactivity, Radioecology Institute, July 8, 1965, Oak Ridge, Tennessee.

D. R. Nelson

Health Physics: The Profession – Graduate Educational Opportunities; Current Research at ORNL, Macalester College, November 18, 1965; St. Paul, Minnesota; Augsburg College, November 19, 1965, Minneapolis, Minnesota; Carleton College, November 19, 1965, Northfield, Minnesota; St. John's University, November 21–22, 1965, Collegeville, Minnesota.

J. S. Olson

Ecology and Environmental Monitoring, ORAU course for public officials on radiation safety, October 20, 1965.

Mineral Cycling in Forest Ecosystems, July 28, 1966.

F. L. Parker

Disposal in Salt Formations, Southern Interstate Nuclear Board Briefing on Waste Disposal, Oak Ridge National Laboratory, August 18–19, 1965, Oak Ridge, Tennessee.

D. E. Reichle

Radiocesium Turnover Rates and Energy Flow in Terrestrial Isopod Populations, Department of Zoology and Entomology, The University of Tennessee, March 1, 1966, Knoxville.

Radioactive Tracers in Ecological Research: Energetics of Arthropod Populations, Department of Biology, West Virginia University, February 2, 1966, Morgantown.

Radiotracer Studies of Food Chain Kinetics in a Forest Ecosystem, Department of Zoology, University of Kentucky, February 22, 1966, Lexington.

R. H. Ritchie

Opportunities for Graduate Study Under the Health Physics Fellowship Program, Department of Physics, University of Louisville, December 8, 1965, Louisville, Kentucky.

Monte-Carlo Solutions of Some Many-Body Problems, Department of Physics, University of Tennessee, May 9, 1966, Knoxville.

A. S. Rogowski

Environmental Research, AEC Fellowship Students, Oak Ridge National Laboratory, June 16, 1966, Oak Ridge, Tennessee.

Erosion Research at Oak Ridge National Laboratory, Erosion Conference, United States Department of Agriculture, Agricultural Research Service, Soil and Water Conservation Research Division, January 17–19, 1966, Chicago, Illinois.

H. C. Schweinler
Dimensional Analysis, Department of Physics, Roanoke College, November 3, 1965, Salem, Virginia.

W. S. Snyder
ICRP, NCRP, and FRC Committees, ORINS-ORNL Ten-Week Health Physics Course, October 21, 1965, ORNL, 4500S.

J. L. Stanford
Extending Optical Studies into the Vacuum Ultraviolet – Experimental Considerations, Department of Physics, University of Tennessee, March 2, 1966, Knoxville.

E. G. Struxness
Waste Disposal, Nuclear Geology Group, ORINS, January 15, 1965;[1] ORINS Special Training to a Group of Exhibit Managers, ORINS, Oak Ridge, July 29, 1965;[1] University of Tennessee students, ORNL, June 16, 1966.

Plow Share Program, Oak Ridge High School, March 16, 1965.[1]

Waste Disposal and Environmental Monitoring, Vanderbilt University, AEC Fellowship Students, March 29 and 30, 1965;[1] Vanderbilt University, AEC Fellowship Students, April 5 and 6, 1965;[1] University of Tennessee, May 12, 14, 19, 21, and 26, 1965.[1]

Problems Pertaining to Environmental Research of Radioactivity, Summer Institute in Radioecology, ORINS, Oak Ridge, June 25, 1965.[1]

Presite Monitoring Program, Ten-Week Health Physics Course, ORINS Special Training lectures to people responsible for licensing and inspecting of radioisotope users, etc., ORINS, Oak Ridge, October 20, 1965.

Fracturing Experiments in Waste Disposal Section at ORNL, Oak Ridge High School, March 8, 1966.

Tsuneo Tamura
How Do We Dispose of Radioactive Wastes, Patterson State College, April 14, 1966, Wayne, New Jersey (American Society of Agronomy–National Science Foundation's Visiting Scientist Lecturer Program); Slippery Rock State College, May 3, 1966, Slippery Rock, Pennsylvania (American Society of Agronomy–National Science Foundation's Visiting Scientist Lecturer Program.

Hydrofracture Studies, University of Arkansas Radiological Health Faculty and Students, Oak Ridge National Laboratory, April 21, 1966, Oak Ridge, Tennessee.

Radioactive Waste Disposal, Advanced Reactor Group, July 29, 1965, Oak Ridge, Tennessee; Nuclear Science and Engineering Department, Pennsylvania State University, May 5, 1966, College Station.

Radioactive Waste Disposal by Hydrofracturing, AEC Fellowship Program, Summer 1966, Oak Ridge National Laboratory, June 16, 1966, Oak Ridge, Tennessee; Southern Interstate Nuclear Board, Oak Ridge National Laboratory, August 19, 1965, Oak Ridge, Tennessee.

Reactions of Fission Products with Minerals, Patterson State College, April 15, 1966, Wayne, New Jersey (American Society of Agronomy–National Science Foundation's Visiting Scientist Lecturer Program); Slippery Rock State College, May 4, 1966, Slippery Rock, Pennsylvania (American Society of Agronomy–National Science Foundation's Visiting Scientist Lecturer Program).

Retention of Fission Products by Soils, Rural Civil Defense Specialist at USAEC-UT Farm, October 26, 1965, Oak Ridge, Tennessee.

Soil Mineral Reactions, AEC Fellowship Program, Summer 1966, Oak Ridge National Laboratory, June 16, 1966, Oak Ridge, Tennessee.

---

[1]These lectures were omitted from *Health Phys. Div. Ann. Progr. Rept. July 31, 1965,* ORNL-3849.

I. H. Tipton

Radioactivity in Man, Institute in the Fundamentals of Radiation and Radiological Protection, March 10, 1966, Vanderbilt University, Nashville, Tennessee.

J. E. Turner

Research in the Theory of Radiation Dosimetry, Department of Physics, University of Michigan, January 19, 1966, Ann Arbor.

Interaction of Radiation with Matter, University of Virginia, February 14, 1966, Charlottesville; University of Roanoke, February 15, 1966, Roanoke, Virginia.

G. M. Van Dyne

Ecosystems, Systems Ecology, and Systems Ecologists, Zoology Department, University of Georgia, December 1965, Athens.

The Pasture Ecosystem, Animal Science Department, November 1965, University of Tennessee, Knoxville.

Linear Programming Applications in Applied Ecology, January 1966, Botany Department, University of Tennessee, Knoxville.

Ecosystems, and Systems Ecology, February 1966, College of Forestry and Natural Resources, Colorado State University, Fort Collins.

Computers and Natural Resource Management, February 1966, Fishery and Wildlife Biology Department, Colorado State University, Fort Collins.

The Optimum Site Problem, February 1966, Range Service Department, Colorado State University, Fort Collins.

Recent Advances in Range Nutrition Research, February 1966, Range Service Department, Colorado State University, Fort Collins.

J. L. Wilhm

Evaluation of Community Structure with Diversity Indices Derived from Information Theory, Kansas State Teachers College, November 5, 1965, Emporia.

Estimation of Productivity and Standing Crop of Periphyton in a Stream, University of Florida, January 14, 1966, Gainesville.

J. P. Witherspoon

Cycling of Radiocesium in Forest Ecosystems, Department of Botany, November 3, 1965, University of North Carolina; School of Forestry, November 5, 1965, Duke University; Department of Botany, December 13, 1965, University of Missouri.

Interactions of Environmental Factors and Ionizing Radiation on Native Tree Species, Department of Botany, November 3, 1965, University of North Carolina; Department of Biology, February 17, 1966, University of South Carolina; Department of Biology, December 7, 1965, Alabama College; Department of Biology, December 8, 1965, Vanderbilt University; Department of Biology; March 28, 1966, West Virginia University; Department of Botany, February 25, 1966, University of Tennessee.

Ecological Dosimetry, June 28, 1966, ORINS Radioecology Institute.

Cesium Cycling in Forest, June 29, 1966, ORINS Radioecology Institute.

Radiation Effects on Plants, July 7, 1966, ORINS Radioecology Institute.

HEALTH PHYSICS DIVISION

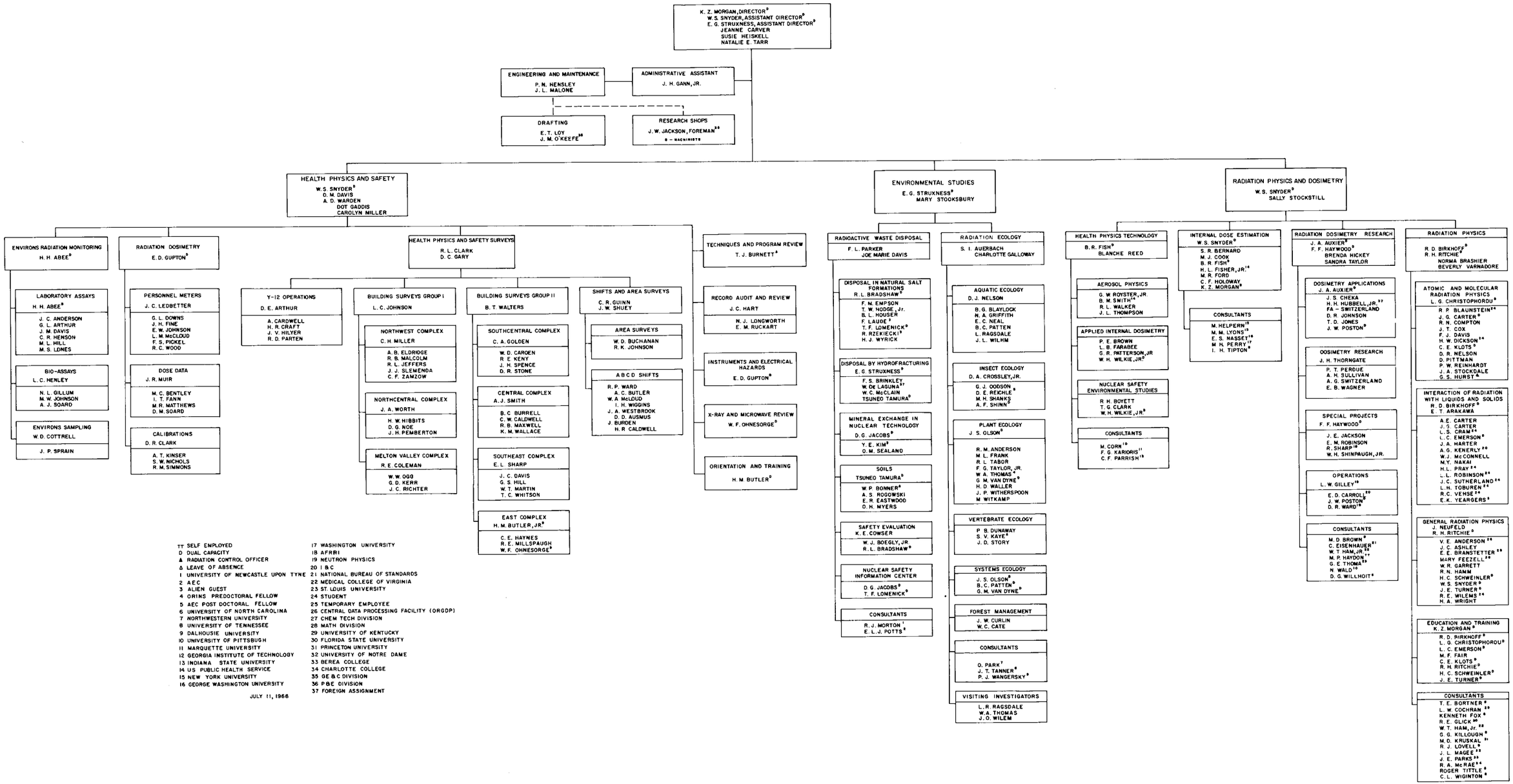

TT SELF EMPLOYED
D DUAL CAPACITY
▲ RADIATION CONTROL OFFICER
Δ LEAVE OF ABSENCE
1 UNIVERSITY OF NEWCASTLE UPON TYNE
2 AEC
3 ALIEN GUEST
4 ORINS PREDOCTORAL FELLOW
5 AEC POST DOCTORAL FELLOW
6 UNIVERSITY OF NORTH CAROLINA
7 NORTHWESTERN UNIVERSITY
8 UNIVERSITY OF TENNESSEE
9 DALHOUSIE UNIVERSITY
10 UNIVERSITY OF PITTSBUGH
11 MARQUETTE UNIVERSITY
12 GEORGIA INSTITUTE OF TECHNOLOGY
13 INDIANA STATE UNIVERSITY
14 US PUBLIC HEALTH SERVICE
15 NEW YORK UNIVERSITY
16 GEORGE WASHINGTON UNIVERSITY
17 WASHINGTON UNIVERSITY
18 AFRRI
19 NEUTRON PHYSICS
20 I B&C
21 NATIONAL BUREAU OF STANDARDS
22 MEDICAL COLLEGE OF VIRGINIA
23 ST. LOUIS UNIVERSITY
24 STUDENT
25 TEMPORARY EMPLOYEE
26 CENTRAL DATA PROCESSING FACILITY (ORGDP)
27 CHEM TECH DIVISION
28 MATH DIVISION
29 UNIVERSITY OF KENTUCKY
30 FLORIDA STATE UNIVERSITY
31 PRINCETON UNIVERSITY
32 UNIVERSITY OF NOTRE DAME
33 BEREA COLLEGE
34 CHARLOTTE COLLEGE
35 GE B&C DIVISION
36 P&E DIVISION
37 FOREIGN ASSIGNMENT

JULY 11, 1966

ORNL-4007
UC-41 – Health and Safety

INTERNAL DISTRIBUTION

1. Biology Library
2. Reactor Division Library
3–5. Central Research Library
6. Laboratory Shift Supervisor
7–8. ORNL, Y-12 Technical Library
Document Reference Section
9–68. Laboratory Records Department
69. Laboratory Records Department, ORNL RC
70. H. H. Abee
71. V. E. Anderson
72. E. T. Arakawa
73. J. C. Ashley
74. S. I. Auerbach
75. J. A. Auxier
76. S. E. Beall
77. S. R. Bernard
78. R. D. Birkhoff
79. W. J. Boegly
80. P. E. Brown
81. F. R. Bruce
82. T. H. J. Burnett
83. J. G. Carter
84. L. G. Christophorou
85. R. L. Clark
86. T. G. Clark
87. W. E. Cohn
88. R. N. Compton
89. M. J. Cook
90. D. A. Crossley, Jr.
91. F. L. Culler
92. D. M. Davis
93. F. J. Davis
94. P. B. Dunaway
95. L. C. Emerson
96. M. F. Fair
97. L. B. Farabee
98. B. R. Fish
99. M. R. Ford
100. J. A. Gabbard
101. W. R. Garrett
102. J. H. Gillette
103. E. D. Gupton
104. R. N. Hamm
105. C. S. Harrill
106. J. A. Harter
107. A. Hollaender
108. L. B. Holland
109. C. F. Holoway
110. A. S. Householder
111. L. C. Johnson
112. W. H. Jordan
113. M. T. Kelley
114. C. E. Klots
115. C. E. Larson
116. T. A. Lincoln
117. J. L. Liverman
118. R. S. Livingston
119. H. G. MacPherson
120. F. C. Maienschein
121. W. J. McConnell
122. A. J. Miller
123. K. Z. Morgan
124. M. Y. Nakai
125. D. J. Nelson
126. D. R. Nelson
127. J. Neufeld
128. J. S. Olson
129. F. L. Parker
130–131. R. B. Parker
132. G. R. Patterson
133. R. W. Peelle
134. H. P. Raaen
135. M. L. Randolph
136. P. W. Reinhardt
137. R. M. Richardson
138. R. H. Ritchie
139. G. W. Royster
140. H. C. Schweinler
141. H. E. Seagren
142. M. J. Skinner
143. W. S. Snyder

144. J. A. Stockdale
145. E. G. Struxness
146. C. D. Susano
147. N. E. Tarr
148. E. H. Taylor
149. J. L. Thompson
150. J. E. Turner
151. A. C. Upton
152. A. D. Warden
153. A. M. Weinberg
154. G. C. Williams
155. H. A. Wright
156. E. K. Yeargers
157. G. Young
158. J. E. Cantlon (consultant)
159. J. C. Frye (consultant)
160. J. B. Hursh (consultant)
161. J. L. Magee (consultant)
162. H. O. Wyckoff (consultant)
163. J. B. Birks (consultant)
164. M. D. Brown (consultant)
165. L. W. Cochran (consultant)
166. Charles Eisenhauer (consultant)
167. Ugo Fano (consultant)
168. Kenneth Fox (consultant)
169. R. E. Glick (consultant)
170. M. P. Haydon (consultant)
171. W. T. Ham, Jr. (consultant)
172. R. J. Lovell (consultant)
173. R. A. MacRae (consultant)
174. R. J. Morton (consultant)
175. J. E. Parks (consultant)
176. T. D. Strickler (consultant)
177. G. E. Thoma (consultant)
178. I. H. Tipton (consultant)
179. Neil Wald (consultant)
180. D. G. Willhoit (consultant)
181. M. R. Williams (consultant)

EXTERNAL DISTRIBUTION

182. R. J. Anderson, Assistant Surgeon General, Chief, Bureau of State Services, USPHS, Department of Health, Education and Welfare, Washington, D.C.
183. G. A. Andrews, Medical Division, Oak Ridge Associated Universities, Oak Ridge, Tennessee
184. Leroy Augenstein, Michigan State University, East Lansing, Michigan
185–189. Walter Belter, Division of Reactor Development, AEC, Washington, D.C.
190. W. P. Bennett, University of California, Radiation Laboratory, P.O. Box 808, Livermore, California
191. M. J. Berger, Division 231.01, National Bureau of Standards, Washington, D.C. 20234
192. C. H. Bernard, Department of Physics, Midwestern University, Witchita Falls, Texas
193. M. A. Biondi, Physics Department, University of Pittsburgh, Pittsburgh, Pa. 15213
194. T. E. Bortner, 615 Pennsylvania Avenue, Oak Ridge, Tennessee
195. J. F. Burns, 131 Georgia Avenue, Oak Ridge, Tennessee
196. H. J. Carey, Jr., The Carey Salt Company, Hutchinson, Kansas
197. D. R. Chadwick, Div. Radiological Health, USPHS, Room 5094, South Building HEW, Washington, D.C.
198. D. C. Conway, Department of Chemistry, Texas A and M University, College Station, Texas 77843
199. Earl Cook, Division of Earth Sciences, National Academy of Sciences, National Research Council, Washington, D.C.
200. M. Corn, School of Public Health, University of Pittsburgh
201. J. S. Cragwell, Jr., U.S. Geological Survey, 144 Federal Office Building, Nashville, Tennessee
202. L. W. Crevoiserat, Allied Maintenance Corp., Empire State Building, New York, New York 10001
203. Julian Crowell, Department of Physics, Roanoke College, Salem, Virginia
204. C. E. Dady, Watertown Arsenal, Ordnance Material Research Office, Watertown, Massachusetts

205. Maxwell Dauer, Department of Radiology, University of Miami, School of Medicine, Miami, Florida 33136
206. J. J. Davis, Environmental Sciences Branch, Division of Biology and Medicine, USAEC, Washington, D.C.
207. R. S. Decker, Space Nuclear Propulsion Office, USAEC, Washington, D.C.
208. Cdr. John Ebersole, USN, 9711 De Paul Drive, Bethesda, Maryland 20034
209. Gordon M. Fair, Pierce Hall, Harvard University, Cambridge, Massachusetts
210. Wade L. Fite, Department of Physics, University of Pittsburgh, Pittsburgh, Pa. 15213
211. Frank Foley, Kansas State Geological Survey, Lawrence, Kansas
212. F. Gabbard, Department of Physics, University of Kentucky, Lexington, Ky. 40506
213. Luis Garcia, Nuclear Utilities Services, Washington, D.C.
214. H. N. Gardner, Division of Medical Sciences, National Academy of Sciences, National Research Council, 2101 Constitution Avenue, N.W. Washington, D.C.
215. E. F. Gloyna, Department of Civil Engineering, University of Texas, Austin 12, Texas
216. W. W. Grigorieff, Assistant to the Executive Director, Oak Ridge Associated Universities
217. Richard Hamburger, Division of Peaceful Nuclear Explosives, U.S. Atomic Energy Commission, Washington, D.C.
218. William Happer, Columbia University, Radiation Laboratory, New York, New York
219. Ray Hefferlin, Physics Department, Southern Missionary College, Collegedale, Tennessee 37315
220. R. J. Herickhoff, Div. of Sperry-Rand Corp., UNIVAC, St. Paul, Minn. 55116
221. G. R. Holeman, Dept. of University Health, Health Physics Division, Yale University, New Haven, Conn.
222. J. I. Hopkins, Box 327, Davidson College, Davidson, N.C. 28036
223. John R. Horan, P.O. Box 2108, Idaho Falls, Idaho 83401
224. W. R. Hunter, U.S. Naval Research Laboratory, Washington 25, D.C.
225. G. S. Hurst, Dept. of Physics, University of Kentucky, Lexington, Ky. 40506
226. A. H. Jaffey, Argonne National Laboratory, 9700 S. Cass Ave., Argonne, Illinois 60440
227. W. P. Jesse, Physical Sciences Laboratory, St. Procopius College, Lisle, Illinois
228. Paul Jones, U.S. Geological Survey, Washington, D.C.
229. S. Leary Jones, Tennessee Department of Public Health, Cordell Hull Building, Nashville, Tennessee
230. F. G. Karioris, Marquette University, Milwaukee, Wisconsin
231. H. P. Kallmann, New York University, Radiation and Solid State Laboratory, New York, New York
232. Michael Kasha, Dept. of Chemistry, Florida State University, Tallahassee, Florida
233. Jacob Kastner, Argonne National Laboratory, 9700 S. Cass Avenue, Argonne, Illinois 60440
234. W. J. Kaufman, University of California, Berkeley, California
235. O. W. Kochtitzky, Tennessee Valley Authority, 717 Edney Building, Chattanooga, Tennessee
236. H. A. Kornberg, Biology Dept., Battelle Northwest, P.O. Box 999, Richland, Washington
237. P. A. Krenkel, Vanderbilt University, School of Engineering, Nashville, Tennessee
238. J. B. Lackey, University of Florida, Gainesville, Florida
239. W. J. Lacy, Office of Civil Defense, Pentagon, Washington, D.C.
240. J. A. Lieberman, Div. of Reactor Development, AEC, Washington D.C.
241. S. A. Lough, Division of Biology and Medicine, USAEC, Washington, D.C.
242. Lola Lyons, Librarian, Olin Industries, Inc., East Alton, Illinois
243. R. P. Madden, National Bureau of Standards, Far UV Physics Division, 222 National Bureau of Standards, Washington, D.C. 20234
244. L. D. Marinelli, Argonne National Laboratory, 9700 Cass Avenue, Argonne, Ill. 60440
245. L. Marton, Electron Physics Division, National Bureau of Standards, Washington, D.C. 20234
246. Lee Mayes, Kansas State Board of Health, Topeka, Kansas
247. Charles W. Mays, Jr., Radiobiology Laboratory, University of Utah, Salt Lake City, Utah
248. E. W. McDaniel, Dept. of Physics, Georgia Institute of Technology, Atlanta, Georgia 30332
249. A. H. Nielson, Dept. of Physics, University of Tennessee, Knoxville, Tennessee 37916

250. C. Orr, Georgia Institute of Technology, Atlanta, Georgia
251. C. F. Parrish, Indiana State College, Terre Haute, Indiana
252. Frank L. Pascal, Jr., General Dynamics/Ft. Worth, Plant Zone Y-42, P.O. Box 748, Fort Worth, Texas 76101
253. C. M. Patterson, E. I. duPont de Nemours, Savannah River Laboratory, Aiken, South Carolina 29801
254. A. V. Phelps, Westinghouse Research Laboratories, Churchill Borough, Pittsburgh 35, Pa.
255. R. B. Platt, Dept. Biology, Emory University, Atlanta, Georgia
256. R. L. Platzman, University of Chicago, Chicago, Illinois
257. C. J. Powell, National Bureau of Standards, Electron Physics Section, Washington, D.C. 20234
258. R. D. Present, Physics Dept., University of Tennessee, Knoxville, Tennessee 37916
259. E. P. Resner, States Marine Lines, c/o New York Shipbuilding Corp., Camden, New Jersey
260. W. C. Roesch, Battelle Northwest, P.O. Box 999, Richland, Washington
261. C. E. Roos, Dept. of Physics, Vanderbilt University, Nashville, Tennessee
262. Miriam Sachs, Department of Health, Metropolitan State Health District, 1100 Raymond Blvd., Newark 2, New Jersey
263. J. A. R. Samson, Experimental Physics Dept., Geophysics Corp. of America, Physics Research Division, Bedford, Massachusetts 01730
264. G. J. Schulz, Westinghouse Research Laboratories, Pittsburgh, Pa. 15235
265. Vincent Schultz, Dept. Zoology, Washington State University, Pullman, Washington
266. R. L. Shearin, Environmental Radiological Health Training, R. A. Taft Sanitary Engineering Center, 4676 Columbia Parkway, Cincinnati, Ohio 45226
267. C. S. Shoup, Biology Division, USAEC, Oak Ridge, Tennessee
268. S. C. Sigoloff, Office of the Executive Vice President, Electro-Optical Systems, Inc., 300 North Halstead Street, Pasadena, California 91107
269. J. A. Simpson, Electron Physics Section, National Bureau of Standards, Washington, D.C. 20234
270. D. S. Smith, 12576 Clifton Blvd., Lakewood, Ohio
271. J. N. Stannard, University of Rochester School of Medicine and Dentistry, Dept. of Radiation Biology and Atomic Energy Project, P.O. Box 287, Station 3, Rochester 20, New York
272. H. E. Stokinger, Bureau of State Service, Dept. of Health, Education and Welfare, Penn 14 Broadway, Cincinnati 2, Ohio
273. C. P. Straub, University of Minnesota, College of Medical Sciences, School of Public Health, Minneapolis, Minnesota 55455
274. J. A. Swartout, 270 Park Avenue, New York 17, New York
275. H. A. Thomas, Jr., Division of Engineering and Applied Physics, Harvard University, Cambridge, Massachusetts
276. H. C. Thomas, Chemistry Department, University of North Carolina, Chapel Hill, N.C.
277. James Thomas, Instructor of Public Health, Yale University
278. H. H. Waesche, AEC Liaison Officer, Geochemical and Petrology Branch, U.S. Geological Survey, Naval Gun Factory, Building 213, Washington 25, D.C.
279. R. W. Wallace, University of California, Radiation Laboratory, Berkeley 4, California
280. J. W. Watkins, U.S. Bureau of Mines, Washington, D.C.
281. G. L. Weissler, Dept. of Physics, University of Southern California, Los Angeles, California
282. K. T. Whitby, Dept. of Mechanical Engineering, University of Minnesota, Minneapolis
283. E. G. Williams 6560 Colgate Road, Jacksonville, Florida 32217
284. John Wolfe, Div. of Biology and Medicine, U.S. Atomic Energy Commission, Washington, D.C.
285. Robert W. Wood, Div. of Biology and Medicine, U.S. Atomic Energy Commission, Washington, D.C.
286. Paul Zigman, USNRDL, San Francisco, California
287. Toshio Aoki, J.A.E.R.I., Takai-Mura, Naka-Gun, Ibaraki-Ken, Japan
288. H. Boersch, Physical Institute, Technical University of Berlin, Berlin, West Germany
289. P. R. J. Burch, Dept. of Med. Phys, University of Leeds, General Infirmary, Leeds 1, England
290. G. Cavalleri, Centro Information Studi Esperienze, casella postale 3986, Milano, Italy

291. R. M. Chaudhri, High Tension and Nuclear Research Laboratory, Church Road, Government College, P.O. Box 701, Lahore, West Pakistan
292. R. W. Crompton, Research School of Physical Sciences, The Australian National University, Ion Diffusion Unit, Box 4, G.P.O. Canberra A.C.T., Australia
293. Florence Fayard, Laboratoire de Chimie Physique, Faculte des Sciences, Orsay (Seine-et-Oise), France
294. Yehuda Feige, Health Physics Department, IAEC, Yavne, Israel
295. I. M. Frank, Joint Institute for Nuclear Research, Laboratory of Neutron Physics, Dubna, U.S.S.R.
296. R. M. Fry, Health Physics Research Section, A.A.E.C., Private Mail Bag, Sutherland, NSW, Australia
297. A. K. Ganguly, Health Physics Division, Atomic Energy Establishment, Trombay, Bombay 73, India
298. Anthony Hadjiantoniou, 22 Evias Street, Piraeus 87, Greece
299. Jens Lindhard, Institute of Physics, Aarhus University, Aarhus, Denmark
300. K. A. Mahmoud, Radiation Protection and Civil Defense Dept., Atomic Energy Establishment, Abou-Zaabal Post Office, Cairo, U.A.R. (Egypt)
301. John Myhill, The Royal North Shore Hospital of Sydney, Crows Nest, Sydney, N.S.W., Australia
302. Yasushi Nishiwaki, Tokyo Kogyo Daigaku, Inst. of Tech., Ohkayamo, Meguro-Ku, Tokyo, Japan
303. H. Raether, Institute for Applied Physics, University of Hamburg, Hamburg, West Germany
304. S. Robin, Spectroscopy Laboratory, University of Rennes, Rennes, France
305. Claudio Sennis, Chief, Hazards Evaluation Branch, Safety and Control Division, Comitato Nazionale Per L'Energia Nucleare, Divisione Sicurezza E. Controlli, Roma, Via Belisario 15, Italy
306. Sakai Shimizu, Institute for Chemical Research, Kyoto University, Kyoto, Japan
307. Kazuo Simokawa, Library of Faculty of Science, Osaka City University, Sugimoto-Cho, Sumiyoshi-Ku, Osaka, Japan
308. W. Steinmann, University of Munich, Munich, West Germany
309. J. B. Swan, University of Western Australia, Nedlands, Western Australia
310. W. L. Templeton, Health and Safety Division, U.K. Atomic Energy Authority, Seascale, Cumberland, England
311. M. Vidmar, Boris Kidrich Institute, Vinca, Yugoslavia
312. Radiation Physics Division, Health and Safety Laboratory, New York Operations
313. Research and Development Division, USAEC, Oak Ridge Operations, Oak Ridge, Tennessee
314. Physics Library, Vanderbilt University, Nashville, Tennessee

315–628. Given distribution as shown in TID-4500 under Health and Safety category (25 copies – CFSTI)